UNIVERSITÄT LEIPZIG

REPORT
Institute für Physik
The Physics Institutes

2015

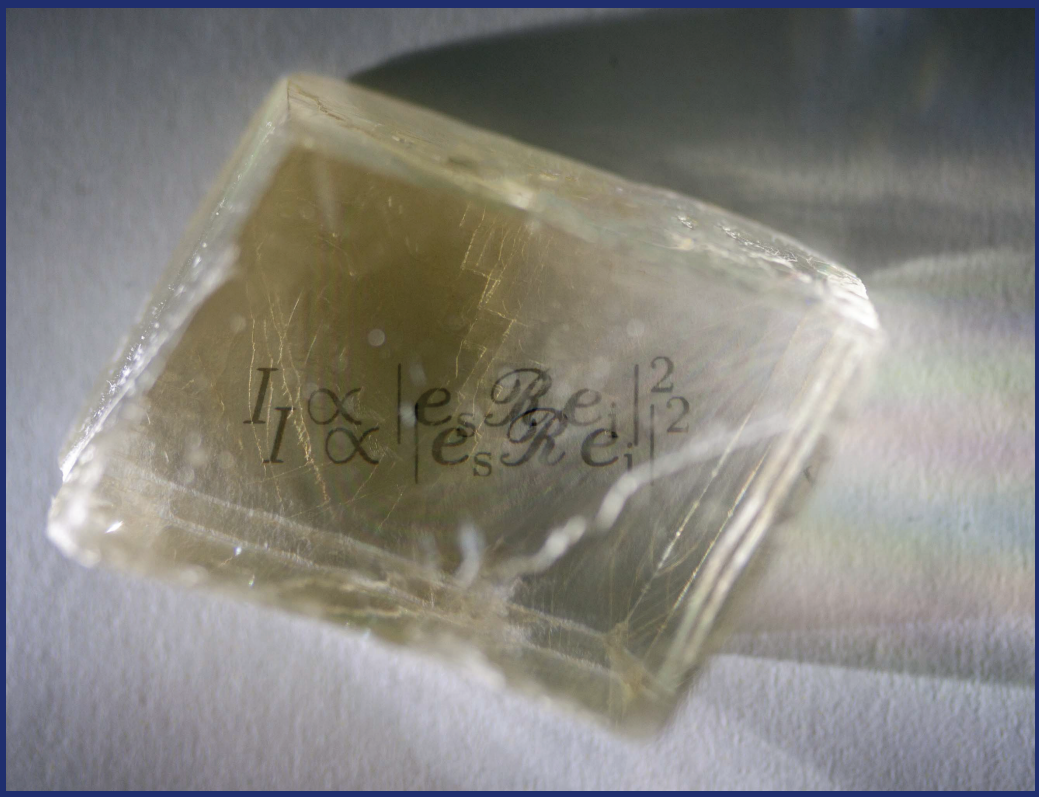

The Physics Institutes of Universität Leipzig, Report 2015
M. Grundmann (Ed.)

Technical Editor: Anja Heck

Printed in Germany by
MERKUR Druck und Kopierzentrum GmbH, Leipzig

online available at
http://nbn-resolving.de/urn:nbn:de:bsz:15-qucosa-151238

Front cover

■ Raman scattering formula seen through a birefringent crystal (calcite). A theory of Raman scattering from all crystal systems including optically anisotropic crystals has been established (see section 9.18).

Back covers

■ Recent publications.

Institut für Experimentelle Physik I
Institut für Experimentelle Physik II
Institut für Theoretische Physik

Fakultät für
Physik und Geowissenschaften

Universität Leipzig

Institute for Experimental Physics I
Institute for Experimental Physics II
Institute for Theoretical Physics

Faculty of Physics and Earth Sciences

Universität Leipzig

Report 2015

Addresses

Institute for Experimental Physics I

Linnéstraße 5
D-04103 Leipzig, Germany
Phone: +49 341 97-32470
Fax: +49 341 97-32479
WWW: https://www.physgeo.uni-leipzig.de/fakultaet/institutebereiche/experimentelle-physik-i/

Institute for Experimental Physics II

Linnéstraße 5
D-04103 Leipzig, Germany
Phone: +49 341 97-32650
Fax: +49 341 97-32668
WWW: https://www.physgeo.uni-leipzig.de/fakultaet/institutebereiche/experimentelle-physik-ii/

Institute for Theoretical Physics

Brüderstr. 14 - 16
D-04103 Leipzig, Germany
Phone: +49 341 97-32420
Fax: +49 341 97-32548
WWW: https://www.physgeo.uni-leipzig.de/fakultaet/institutebereiche/theoretische-physik/

Preface

The 2015 Report of the Physics Institutes of the Universität Leipzig presents an interesting overview of our research activities in the past year. It is also testimony of our scientific interaction with colleagues and partners worldwide. We are grateful to our guests for enriching our academic year with their contributions in the colloquium and within the work groups.

Our colleague Wolfhard Janke, heading the computational physics group, was awarded an Adjunct Professorship of the University of Georgia, USA.

Klaus Kroy, together with Prof. Erwin Frey, has edited a Focus Issue on "Soft mesoscopics: Physics for biology at a mesoscopic scale" in the New Journal of Physics (an established pioneer of open-source scientific publishing), which gathered over 40 original paper contributions from international research groups [New Journal of Physics **17**(11), 110203 (2015).

Marius Grundmann has edited together with Prof. Saskia F. Fischer (Humboldt-Universität zu Berlin) a special issue of Semiconductor Science and Technology on "Semiconductor Functional Oxides" [Semic. Sci. Technol. **30**(2), 020301 (2015)].

Marius Grundmann, Dr. Andreas Rahm and Dr. Holger von Wenckstern have guest edited selected papers from the TCO2014 conference in physica status solidi (a) "Transparent Conductive Oxides" [phys. stat. sol. (a) **212**(7), 1408 (2015)].

From 12–15 January an International Workshop on *Nonequilibrium Dynamics of Low-dimensional Electronic Sysems* combinded with a Winter School for graduate students was organized by Bernd Rosenow together with Yuval Gefen (Weizmann) and Natan Andrei (Rutgers). Topics covered by the 29 invited speakers included: Non-equilibrium physics and equilibration of edge modes and 1d conductors, non-equilibrium superconductivity, relaxation and thermalization in Mott insulators, quantum quenches and equilibration in cold atomic gases.

The BuildMoNa Minisymposium on "Quantum Coherent Structures – Unconventional Superconductivity" end of September was organized by Bernd Rosenow and Marius Grundmann with eight invited speakers.

At the end of November the by now traditional 16th International Workshop on Recent Developments on Computational Physics "CompPhys15" organized by Wolfhard Janke took place in Leipzig. Around 60 scientists from over 10 different countries exchanged ideas and discussed recent progress in several fields of computational physics.

Work has successfully continued in the Centers of Excellence (Sonderforschungsbereiche) SFB 762 "Functionality of Oxide Interfaces" and SFB TRR102 "Polymers under Multiple Constraints: Restricted and Controlled Molecular Order and Mobility". In January 2015, the SFB TRR102 has successfully defended the extension application for the 2nd funding period from July 2015 – June 2019. SFB762 was renewed for its

third funding period (2016–2019). Work also continues in DFG Forschergruppe 1616 on photonic nanowires. New challenges are pursued in H2020 project "LOMID", the DFG/ANR project "Ulysses" and in the newly established DFG Schwerpunktprogramm 1796 "FFlexCom". A joint project with Leibniz-Institute for Surface Modification (IOM) started on "Sensors based on single atoms".

A major upgrade of the LIPSION accelerator is under way with an ECR ion source.

Our activities and success is only possible with the generous support from various funding agencies for which we are very grateful and which is individually acknowledged in the brief of reports.

Leipzig,
August 2016

F. Cichos
M. Grundmann
W. Janke
Directors

Contents

1

Structure and Staff of the Institutes

1.1 Institute for Experimental Physics I

1.1.1 Office of the Director

Prof. Dr. Josef A. Käs (director)

1.1.2 Molecular Nano-Photonics, Molekulare Nanophotonik [MON]

Prof. Dr. Frank Cichos

Technical staff

Dipl.-Phys. Andrea Kramer
Dipl.-Phys. Uwe Weber

PhD candidates

Subhasis Adhikari, M.Sc.
Dipl.-Phys. Nicole Amecke
Dipl.-Phys. Marco Braun
Dipl.-Phys. Andreas Bregulla
André Heber, M.Sc.
Santiago Muiños Landin, M.Sc.
Dipl.-Phys. Romy Schachoff
Tobias Thalheim, M.Sc.
Dipl.-Phys. Rebecca Wagner

Students

Alice Abend
Alexander Fischer
Nikolai Kortenbruck
Sascha Loebel

David Plotzki
Falko Schmidt

1.1.3 Molecular Physics, Molekülphysik [MOP]

Prof. Dr. F. Kremer

Secretary

Kerstin Lohse

Technical staff

Dipl.-Phys. Cordula Bärbel Krause
Dipl.-Ing. (FH) Jörg Reinmuth
Dipl.-Phys. Wiktor Skokow

Academic staff

Dr. Martin Treß
Dr. Emmanuel Urandu Mapesa

PhD candidates

Dipl.-Phys. Markus Anton
M. Edu. Falk Frenzel
M. Sc. Wycliffe Kiprop Kipnusu
Dipl.-Phys. Wilhelm Kossack
M. Sc. Emmanuel Urandu Mapesa
Dipl.-Phys. Nils Neubauer
Dipl.-Phys. Tim Stangner

Students

cand. M. Edu. Patricia Prinz

1.1.4 Soft Matter Physics, Physik der weichen Materie [PWM]

Prof. Dr. Josef A. Käs

Secretary

Claudia Brück

Technical staff

Dr. Undine Dietrich
Dipl.-Phys. Bernd Kohlstrunk
Ing. Elke Westphal

Academic staff

Dr. Mareike Zink

PhD candidates

Uta Allenstein, M. Sc. (zusammen mit Prof. Mayr)
Martin Glaser, M. Sc.
Tom Golde, M. Sc.
Dipl.-Phys. Chris Händel
Dipl.-Phys. Tina Händler
Paul Heine, M. Sc.
Hans Kubitschke, M. Sc.
Jürgen Lippoldt, M. Sc.
Erik Morawetz, M. Sc.
Dipl.-Phys. Steve Pawlizak
Saddam Moyazur Rahman, M. Sc. (BBZ, Forschergruppe M. Zink)
Dipl.-Phys. Sebastian Schmidt
Dipl.-Phys. Jörg Schnauß
Dipl.-Phys. Carsten Schuldt
Dipl.-Phys. Enrico Warmt
Emilia Wisotzki, M. Sc.

Students

Sabrina Friebe
Gregor Haider
Konrad Jahn
Till Möhn
Linda Oswald
Erik Schmidt
Markus Sommerfeld
Astrid Weidt

1.1.5 Biological Physics, Biologische Physik [BIP]

Prof. Dr. Claudia Mierke

Secretary

Kerstin Lohse

Technical staff

Dipl.-Ing. Kathrin Koch

PhD candidates

M. Sc. Stefanie Puder
Dipl.-Phys. Tony Fischer
M. Sc. Tom Kunschmann
M. Sc. Jeremy Perez
M. Sc. Nils Wilharm
M. Sc. Frank Sauer

Students

Alexander Hayn
Anthony Ogbuehi
Sebastian Ronneberger

1.1.6 Molecular Biophysics, Molekulare Biophysik [MBP]

Prof. Dr. Ralf Seidel

Secretary

Kerstin Lohse

1.2 Institute for Experimental Physics II

1.2.1 Office of the Director

Prof. Dr. Marius Grundmann (director)
Prof. Dr. Pablo Esquinazi (vice director)

1.2.2 Magnetic Resonance of Complex Quantum Solids, Magnetische Resonanz Komplexer Quantenfestkörper [MQF]

Prof. Dr. Jürgen Haase

Secretary

Sophie Kirchner

Technical staff

Gert Klotzsche
Tilo Pilling
Stefan Schlayer
Horst Voigt
Björn Kamke

Academic staff

PD Dr. Marko Bertmer
Prof. Dr. Dieter Freude
Prof. Dr. Andreas Pöppl

PhD candidates

Nina Dvoyashkina, M.Sc.
Stefan Friedländer, M.Sc.
Nataliya Georgieva, M.Sc.
Robin Gühne, M.Sc.
Dipl.-Phys. Alexander Jäger
Michael Jurkutat, M.Sc.
Arafat Hossain Khan, M.Sc.
Dipl.-Phys. Jonas Kohlrautz
Anastasiia Kultaeva, M.Sc.
Alexander Lauerer, M.Sc.
Kathrin Lorenz, M.Sc.
Thomas Meier, M.Sc.
Dipl.-Phys. Matthias Mendt
Steven Reichardt, M.Sc.
Dipl.-Phys. Sebastian Sambale
Daniel Schneider, M.Sc.
Emmanouil Veroutis, M.Sc.
Marufa Zahan, M.Sc.

Students

Felix Gutt
Felix Höfer, B.Sc.
Felix Bolling, B.Sc.

1.2.3 Nuclear Solid State Physics, Nukleare Festkörperphysik [NFP]

Prof. Dr. Jan Meijer

Secretary

Birgit Wendisch

Technical staff

Dipl.-Phys. Steffen Jankuhn
Carsten Pahnke
Dipl.-Ing. Joachim Starke

Academic staff

Dr. Sébastien Pezzagna
Dr. Daniel Spemann (till October 2015)
Dr. Jürgen Vogt (till May 2015)

PhD candidates

Dipl.-Math. Roger John, B.Sc.
Jan Lehnert, M.Sc.
Nicole Raatz, M.Sc.
Paul Räcke, M.Sc. (since November 2015)
Robert Staacke, M.Sc.
Ralf Wunderlich, M.Sc.

Students

Youssef Albanay, B.Sc.
Sascha Becker, B.Sc.
Janson Dwan (since May 2015)
Christopher Eames (till March 2015)
Jakob Helbig, B.Sc. (till February 2015, since November 2015)
Johannes Küpper, B.Sc. (till February 2015, since November 2015)
Tobias Lühmann, B.Sc. (till June 2015)
Michael Mensing, B.Sc.
Maximilian Quaas (till July 2015)
Julian Vogel, B.Sc. (till July 2015)
Erik Wiedemann, B.Sc.

1.2.4 Semiconductor Physics, Halbleiterphysik [HLP]

Prof. Dr. Marius Grundmann

Secretary

Anja Heck
Birgit Wendisch

Technical staff

Dipl.-Phys. Gabriele Benndorf
Monika Hahn
Dipl.-Ing. Holger Hochmuth
Maik Hoffmann
Dipl.-Phys. Jörg Lenzner
Dipl.-Phys. Axel Märcker
Gabriele Ramm
Roswitha Riedel

Academic staff

Dr. Kerstin Brachwitz
Dr. Helena Franke
Dr. Heiko Frenzel
Dr. Fabian Klüpfel
Dr. Christian Kranert
Prof. Dr. Michael Lorenz
Dr. Florian Schmidt
PD Dr. Rainer Pickenhain
Prof. Dr. Bernd Rheinländer (retired)
Dr. Rüdiger Schmidt-Grund
Dr. Chris Sturm
Dr. Holger von Wenckstern
Dr. Chang Yang

PhD candidates

Sofie Bitter, M.Sc.
Michael Bonholzer, M.Sc.
Marcus Jenderka, M.Sc.
Robert Karsthof, M.Sc.
Sherzod Khujanov, M.Sc.
Abdurashid Mavlonov, M.Sc.
Tom Michalsky, M.Sc.
Dipl.-Phys. Stefan Müller
Anna Reinhardt, M.Sc.
Steffen Richter, M.Sc.
Dipl.-Phys. Friedrich-Leonhard Schein
Peter Schlupp, M.Sc.
Peter Schwinkendorf, M.Sc.
Alexander Shkurmanov, M.Sc.
Daniel Splith, M.Sc.
Martin Thunert, M.Sc.
Haoming Wei, M.Sc.
Marcel Wille, M.Sc.

Zhang Zhipeng, M.Sc.
Vitaly Zviagin, M.Sc.

Students

Tobias Abel
Philipp Bischoff
Francesco Boschi Raffael Deichsel
Felix Gutt
Oliver Herrfurth
Alexander Holm
Max Kneiß
Evgeny Krüger
Oliver Lahr
Stefan Lange
Steffen Lanzinger
Manuel Raphael Lindel
J. Msasi Makumbi
Karim Nafis Imtiaz
Ahsan Rasheed
Michael Scheibe
Laurenz Thyen
Benjamin Wehr
Anna Werner
Tim Wolter

1.2.5 Solid State Optics and Acoustics, Festkörperoptik und -akustik [FKO]

vacant

1.2.6 Superconductivity and Magnetism, Supraleitung und Magnetismus [SUM]

Prof. Dr. Pablo Esquinazi

Secretary

Sandy Ehlers

Technical staff

Dr. Winfried Böhlmann
Dipl.-Krist. Annette Setzer

Academic staff

Prof. Dr. Michael Ziese
Dr. José Barzola-Quiquia
Dr. Israel Lorite Villalba
Dr. Yogesh Kumar

PhD candidates

M. Sc. Francis Bern
M. Sc. Santiago Muiños Landín
M. Sc. Bogdan Semenenko
M. Sc. Christian Eike Precker

Students

cand. B. Sc. Lukas Botsch
cand. B. Sc. Artiom Zaitev
cand. B. Sc. Tiago Rafael Silva Cordeiro
B. Sc. Markus Stiller
B. Sc. Mahsa Zoraghi

1.3 Institute for Theoretical Physics

1.3.1 Office of the Director

Prof. Dr. Wolfhard Janke (director)
Prof. Dr. Rainer Verch (vice director)

Secretary

Susan Hussack
Gabriele Menge
Lea Voigt

1.3.2 Computational Quantum Field Theory, Computerorientierte Quantenfeldtheorie [CQT]

Prof. Dr. Wolfhard Janke

Technical staff

–

Academic staff

Dr. Stefan Schnabel
Dr. Niklas Fricke
Dr. Jonathan Gross
Dr. Suman Majumder
Dr. Johannes Zierenberg

PhD candidates

M.Sc. Johannes Bock
M.Sc. Momchil Ivanov
M.Sc. Ravinder Kumar ("co-tutelle" with Coventry University, UK)
Dipl.-Phys. Martin Marenz
Dipl.-Phys. Marco Müller
Dipl.-Phys. Hannes Nagel
Dipl.-Phys. Andreas Nußbaumer
M.Sc. Philipp Schierz

Students

Kieran Austin
Marius Bause
Henrik Christiansen
Jan Meischner
Fabio Müller
David Oberthür
Simon Schneider
Benjamin Schott
Paul Spitzner
Ronja Stübel
Tobias Weiss
Shane Carlson
Lisa Fiedler
Adrian Häußler
Philipp Hess
Michel Michalkow
Felix Neduck
Katharina Tholen
Robert Wiesen
Chris Allen

1.3.3 Quantum Field Theory and Gravity, Quantenfeldtheorie und Gravitation [QFG]

Prof. Dr. Gerd Rudolph (Speaker)
Prof. Dr. Rainer Verch

Academic staff

PD Dr. Michael Bordag
Dr. Gandalf Lechner
Dr. Matthias Schmidt

PhD candidates

Zhirayr Avetisyan
Benjamin Eltzner
Erik Fuchs
Michael Gransee
Thomas Ludwig
Jan Zschoche

Students

Tobias Diez
Kevin Knauer
Adam Reichold
Johannes Zähle

1.3.4 Statistical Physics, Statistische Physik [STP]

Prof. Dr. Bernd Rosenow

Academic staff

Dr. Casper Drukier

PhD candidates

Giovanni Frigeri, M.Sc.
Lukas Kimme, M.Sc.
Martin Treffkorn, M.Sc.

1.3.5 Theory of Condensed Matter, Theorie der kondensierten Materie [TKM]

Prof. Dr. Ulrich Behn (Speaker)
Prof. Dr. Klaus Kroy

Prof. Dr. Dieter Ihle (retired)
Prof. Dr. Adolf Kühnel (retired)

PhD candidates

Sven Auschra, M.Sc.
Dipl.-Phys. Jakob T. Bullerjahn
Gianmaria Falasco, M.Sc.
Dipl.-Phys. Andrea Kramer
Rüdiger Kürsten, M.Sc.
Dipl.-Phys. Marc Lämmel
Anne Meiwald, M.Sc.
Richard Pfaller, M.Sc.
Stefano Steffenoni, M.Sc.
Dipl.-Phys. Sebastian Sturm
Guillermo Zecua, M.Sc.

Students

Mona Guthardt, B.Sc.
Tim Herpich, M.Sc.
Constantin Huster, B.Sc.
Stefan Landmann, B.Sc.
Johann Müller, B.Sc.
Claudio Schöller, B.Sc.
Felix Schramm, B.Sc.
Benjamin Streitz, B.Sc.
Meike Will, B.Sc.

1.3.6 Theory of Elementary Particles, Theorie der Elementarteilchen [TET]

Prof. Dr. Stefan Hollands

Prof. Dr. Klaus Sibold (retired)

Academic staff

PD Dr. Roland Kirchner
PD Dr. Holger Perlt
Dr. Ko Sanders
PD Dr. Arwed Schiller
Dr. Jochen Zahn

PhD candidates

Giovanni Collini, M.Sc.
Steffen Pottel, M.Sc.

Mojtaba Taslimitehrani, M.Sc.

Students

Onirban Islam
Tobias Jerabek
Maximilian Schambach

I

Institute for Experimental Physics I

2

Molecular Nano-Photonics

2.1 Introduction

Studying dynamic processes at the level of single molecules and particles in soft materials, the group has recently started to explore the release of heat from single molecules and nanoparticles. These absorbing chromophores are able to convert optical energy into heat, if their fluorescence quantum yield is low. This released heat is generating a steady state spatial temperature profile as they are embedded in a large heat bath, which is their solvent environment. This local temperature profile allows a number of new studies, which range from fundamental physical aspects of Hot Brownian Motion (HBM) to the active motion of self-propelled particles. In particular this field of research of the group addresses

- Thermally propelled particles and micromachines
- Manipulation and trapping of single nano-objects in solution
- Transmission microscopy of Rayleigh- and Mie-particles
- Manipulation of living cells by local temperature fields
- Heat conduction at the nanoscale

During the year 2015 the Molecular Nanophotonics Group has celebrated a number of achievements. Among them are:

- Prof. Dr. Cichos has been a guest professor at the University of Bordeaux working with Prof. Dr. Alois Würger.
- The group is part of the Collaborative Research Center (CRC) TRR 102 "Polymers under Multiple Contraints", which has been successfully extended in the year 2015.
- André Heber has been awarded with the 2nd BuildMoNa price for the development of a photothermal light modulator.

Collaborations with the groups of Prof. Dr. Klaus Kroy (Universität Leipzig), Prof. Dr. Michael Mertig (TU Dresden), Prof. Dr. Alois Würger (University of Bordeaux)

and Prof. Dr. Haw Yang (Princeton University) have been very fruitful. Collaborative measurements with the groups of Prof. Dr. Friedrich Kremer and Prof. Dr. Marius Grundmann have been carried out.

Frank Cichos

2.2 Interaction of Single Macro-Molecules with Inhomogeneous Temperature Fields in a Thermophoretic Trap

M. Braun, A.P. Bregulla, T. Thalheim, F. Cichos

The manipulation and trapping of single molecules that undergo Brownian motion are of considerable interest to soft matter sciences as it for example would allow for controlled studies of protein aggregation dynamics or molecular reactions and interactions. Conventional trapping techniques such as optical tweezing become unsuitable for nanometer-sized objects. Molecular trapping can be achieved e.g. by a technique called Anti-Brownian Electrokinetic trap (ABEL trap), which exploits the feedback controlled electric field of four electrodes. However, the latter technique requires electrical contacts, which introduce difficulties when fabricating multiple traps.

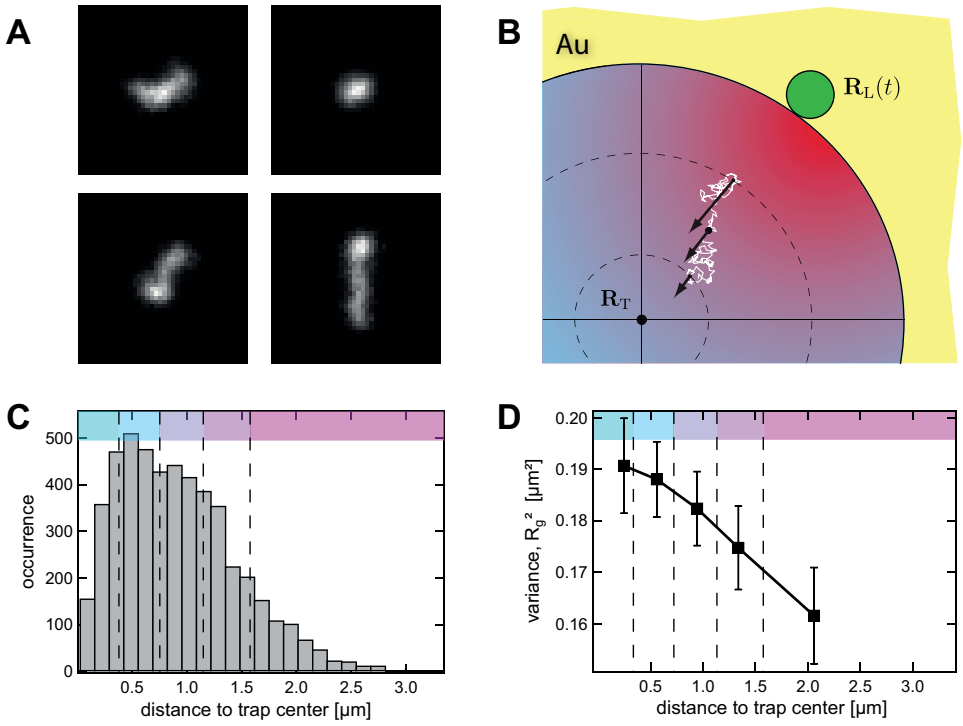

Figure 2.1: A) Four snapshots ($4.6 \times 4.6\,\mu m^2$) of a trapped single λ-DNA molecule. **B)** Illustration of the thermophoretic trap. The heating laser beam (green) is driven such that the molecule (white) is driven to the center. Thereby, the different monomers can experience a different thermophoretic drift (arrows). **C)** Radial position distribution histogram divided into five concentric regions. **D)** Radius of gyration of the DNA molecule for the different concentric regions. Trap diameter: $d_{trap} = 15\,\mu m$.

In this project we have developed an all-optical technique which replaces the electric fields by highly localized thermal fields and is therefore scalable to large arrays [1]. The so-called thermophoretic trap exploits thermophoretic interactions of a molecule placed in a temperature gradient in solution. In our approach the temperature field is generated by a circular gold nanostructure optically heated by a focused laser beam. Due to the small dimensions of the heat source, even a small temperature elevation introduces large temperature gradients causing a strong thermophoretic drift by which the motion of a diffusing particle can be manipulated controlled via real-time position feedback [2]. This new all-optical technique for the manipulation of nano-objects enables long-time observations of not only single but also multiple nano-objects without applying strong optical or electric fields. Being based on temperature gradients, the method also becomes particularly interesting for the investigation of thermal non-equilibrium problems and the interaction of molecules with temperature fields.
The temperature fields employed for trapping decay approximately with the inverse distance from the heat source. The resulting temperature gradients thus appear strongly inhomogeneous over the trapping region. They can be used to thermophoretically confine the center-of-mass (COM) motion of a single macro-molecule, demonstrated for λ-DNA (Figure 2.1A). If the inhomogeneity is strong enough, the temperature gradient varies non-negligibly over the extent of the molecule inducing a different thermophoretic drift for the different monomers. For the particular geometry used in our trap, stronger temperature gradients are exerted to the monomers in the outer region of the trap than to those in the central region (see illustration in Figure 2.1A). Thus, a net compression of the DNA density is expected in addition to the overall induced COM motion. This is readily verified by experiments of trapped λ-DNA. Figure 2.1C shows the radial COM position distribution histogram of a single DNA molecule in the trap. The trapping area is divided into five concentric regions (see color scaling) and the molecule's radius of gyration R_g is measured for each region independently by image analysis. Figure 2.1D plots R_g for the different radial intervals. As can be seen, the DNA conformation is considerably compressed in the outer regions, where the temperature gradient variation over the molecule is the highest.
While thermophoretic stretching of long DNA molecules confined in nano-channels has been demonstrated before, here, we demonstrated for the first time a compression of free DNA molecules purely caused by temperature gradients.
The project is funded within the CRC TRR 102 "Polymers under Multiple Constraints".

[1] M. Braun, F. Cichos: ACS Nano **7**, 11200 (2013), doi:10.1021/nn404980k
[2] M. Braun et al.: Nano Lett. **15**, 5499 (2015), doi:10.1021/acs.nanolett.5b01999

2.3 Thermo-osmotic Flow in Thin Films

A.P. Bregulla, F. Cichos

Within this project we have investigated the flow arising from a non-uniform heat content along a solid/liquid interface. At the very vicinity of the solid/liquid interface an interaction layer occurs, as depicted in Figure 2.2A, which is defined by the interactions (electrostatic, Van-der-Waals, hydrogen bonds, . . .) of the surface with the liquid and its

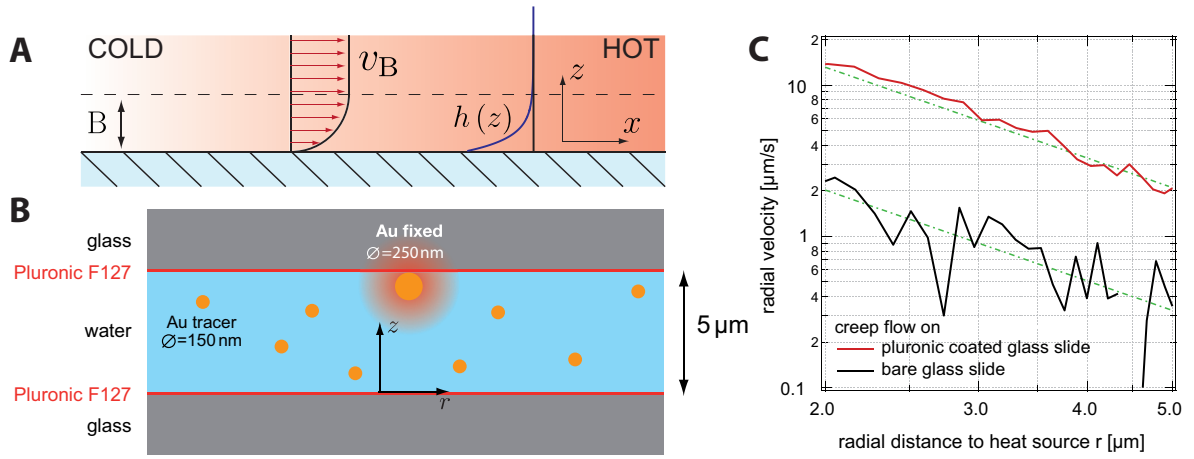

Figure 2.2: A) Occurrence of an interaction layer with the length scale B at a solid interface immersed by a liquid. In the case of a non-uniform temperature distribution across the surface a thermo-osmotic flow arises within the interaction layer with an effective slip velocity v_B beyond this layer. **B)** Principal design of the experiment. The fluid is contained between two glass cover slides in a sandwich structure with a gap of about 5 μm. A R = 125 nm gold nanoparticle is immobilized at the top surface and used as the heat source. **C)** The slip velocity on both glass and Pluronic-coated glass beyond two microns from the heated spot.

solutes. Electrostatic interactions, for example, between a charged surface and mobile ions available in the liquid medium, lead to an accumulation of charges at the surface. They create a diffusive charged double layer called the Debye layer. Additionally, the properties of water at solid interfaces differ from the bulk and depend on the chemical as well as mechanical surface properties, such as surface roughness or patterning. In a physical context these effects can be characterized by a local excess specific enthalpy h in the interfacial layer compared to the bulk. If the liquid phase is attracted at the molecular level, then $h < 0$. The excess specific enthalpy is maximum at the interface and vanishes beyond the boundary layer, as depicted in Figure 2.2A. Since the most physical parameters describing the system and the corresponding interactions are sensitive to temperature, also the excess specific enthalpy is a function of temperature. In case of a non-isothermal surface, the excess enthalpy varies across the interface resulting in a stress in the interfacial layer, leading to a thermo-osmotic surface flow and due to mass conservation to an extended flow pattern in the bulk. To verify and quantify such a flow, an experiment has been designed as sketched in Figure 2.2B. The fluid cell consists of two glass cover slips containing the water film in a sandwich structure. A gold colloid (R_{au} = 125 nm) was used as a local heat source to generate the temperature gradient along the glass/water interface. A focused laser beam was used to first immobilize the colloid at the upper slide by the radiation pressure of the beam and afterwards to heat the gold colloid with an incident power of P_0 = 5 mW. The wavelength was chosen to match the plasmonic properties of the gold colloid. When the particle is heated, the absorbed energy dissipates into the environment and a static temperature profile arises in its surrounding, decaying with the reciprocal distance to the heat source. Small gold particles (R_{tr} = 75 nm) were used to trace the resulting bulk velocity field. By comparing the experimental result and the numerical calculation the thermo-osmotic boundary velocity and the phoretic mobility of the substrate can be obtained. This experiment

has been reported in [1] for two fundamentally different substrate properties. The first one is a bare glass slide and the second one a Pluronic F-127 covered glass surface. While bare glass slides exhibit surface charges, Pluronic F-127 is non-ionic. As depicted in Figure 2.2C, it turns out that the thermo-osmotic flow on the uncharged polymer surface is by one magnitude larger than on the charged surface.
The project is funded within the DFG-ANR project "Thermoelectric Effects at the Nanoscale".

[1] A.P. Bregulla et al.: PRL **16**, 188303 (2016), doi:10.1103/PhysRevLett.116.188303

2.4 Interactions of Self-Thermophoretic Microswimmers

A.P. Bregulla, S. Muiños Landin, F. Cichos

Based on previous own work [1], we used the photon nudging technique to continue our study of the interactions of self-thermophoretic microswimmers. This method consists of the real-time measurement of the position and orientation of a microswimmer to drive it towards a well-defined point of a sample, harnessing thereby rotational fluctuations of the particle.
The microswimmer employed in these studies is a Janus type particle which is heated by a focused laser beam. Given the asymmetry of its thermal conductivity, a temperature gradient can be created on the surface of the particle which in turn causes a propulsion velocity of the particle. Once heated, the particle creates a temperature and a hydrodynamic flow field that, when other particles are present in the environment,

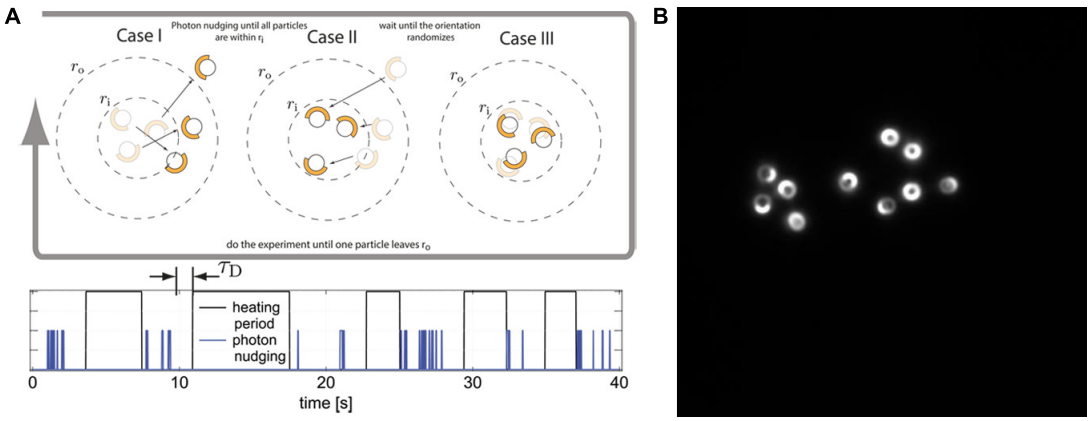

Figure 2.3: A) Experimental concept for the measurement of the interactions. Using the photon nudging a well-defined number of Janus particles is collected (see time line where the photon nudging events are indicated in blue). Once the particles are collected, the system waits a time to erase any preferred alignment induced by the photon nudging. After that all particles are heated via a wide-field laser beam (marked with a black trace in the time line) until they leave a defined area (r_i and r_o). This procedure is repeated until enough data for statistics is obtained. **B)** A large number of particles during their expansion until they leave the big area (r_o) and after collected in a well-defined region of the sample (r_i) via the photon nudging mechanism. During this time the multiple trajectories and orientations are recorded and analyzed.

leads to interactions of the different particles. Here we explore the details of their interaction. We do this by separating the individual contributions of temperature and hydrodynamic flow field. The current experiment employs a gold nanoparticle to create an inhomogeneous temperature field for a Janus particle. The Janus particle is kept close to the heat source by photon nudging to study the interaction with the temperature field. We find a repulsion and preferred alignment of the swimmer in the external temperature field. Thereby, different contributions of the individual hemispheres of the Janus particle to the mother can be quantitatively separated. This experiment is now extended to investigate the interactions of two particles and also multiple particles with the objective of characterizing this interactions and studying the possibility of a collective motion.
The project is funded within the Priority Program 1726 "Microswimmers".

[1] A.P. Bregulla et al.: ACS Nano **8**, 6542 (2014), doi:10.1021/nn501568e

2.5 Thermal Diffusivities Studied by Single Particle Photothermal Microscopy

A. Heber, M. Selmke, F. Cichos

The study of thermal transport is of considerable interest for the understanding of fundamental processes and engineering. Today thermal transport is typically studied at interfaces and not inside the medium. We have advanced photothermal single particle microscopy to provide a method that is able to measure thermal diffusivities on the nano- and microscale with far-field optical readout in liquids and solids. This application of photothermal microscopy is based on recent advances in the modeling of the photothermal signal using a generalized Lorenz-Mie theory.
Photothermal microscopy has proven to be a sensitive imaging technique for investigations of single absorbing nanoparticles, nanostructures and molecules. A single absorbing nano-object is optically excited at its absorption resonance. The excitation energy is dissipated as thermal energy. A localized temperature profile is established. In combination with thermal expansion, a localized refractive index profile is created that alters the transmission of a detection laser beam that is off-resonant. As this transmission change is typically in the order of 10^{-4} and temperature profiles are build-up within microseconds for nanometer-sized objects the heating laser is harmonically modulated at the frequency f. A lock-in amplifier measures the amplitude of transmission of the detection signal at f, which is called photothermal signal.
As temperature changes of the nano-object's surface do not propagate instantaneously due to finite thermal diffusivities the amplitude of the photothermal signal will decrease with growing modulation frequency of the optical heating. Therefore, the frequency dependence of the photothermal signal can be used to measure thermal diffusivities. Earlier attempts have yielded unrealistic values due to simplified models. We use exact electromagnetic calculations to model the transmission of a focussed detection laser beam in the presence of a gold nanoparticle that is surrounded by a time dependent refractive index profile. We measure the photothermal amplitude and phase with respect

to the optical heating for the transmission of the detection laser as in Figure 2.4A and B, respectively in a polymer (Polydimethylsiloxan – PDMS). The photothermal amplitude deviates as much as 40 % from the average, which is explained by the proportionality of the photothermal amplitude to the nanoparticle's volume and variations of the nanoparticle's radius of ~ 10 %. The photothermal phase shows much lower variations and is therefore better suited for the analysis.

After the measurement we perform the analysis. We find that the modeling with Gaussian beams yields thermal diffusivities that are a factor three lower as compared to macroscopic measurements. The frequency dependences of experimental data and model agree very well. Therefore, the modeling is repeated with aberrated beams. This approach gives very good agreement with macroscopic laser flash measurements. We measure an average thermal diffusivity of $(1.3 \pm 0.1) \cdot 10^{-7} \mathrm{m}^2\,\mathrm{s}^{-1}$. Concluding from the measurement systematic errors are likely to occur due to imperfect modeling of the

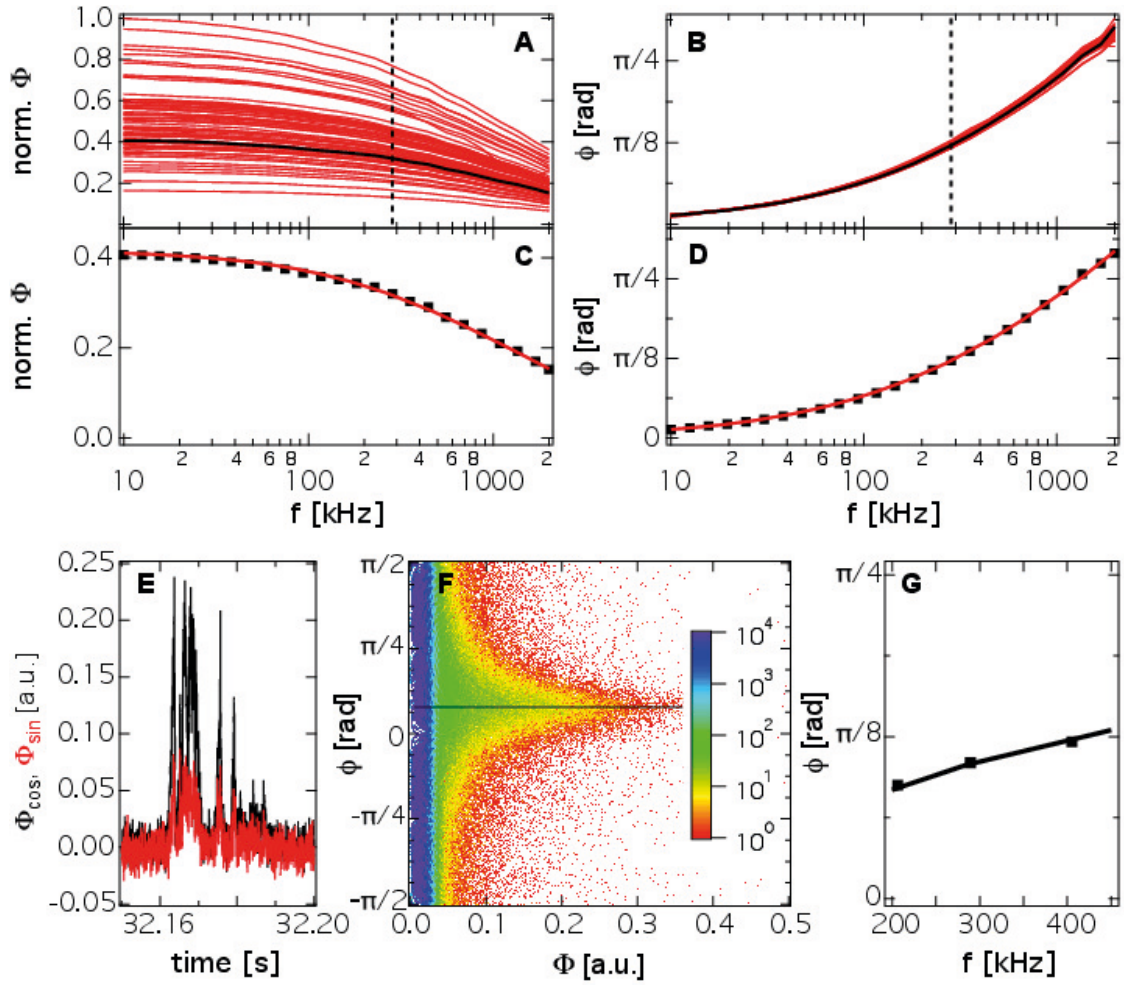

Figure 2.4: A) Photothermal amplitude and **B)** phase delay with respect to the optical heating for 62 different particles. Fit of the experimental to one data set (black in **A)** and **B)**) to the photothermal **C)** amplitude and **D)** phase delay. **E)** Phase sensitive photothermal signal of diffusing nanoparticles. In-phase (black, $\Phi_{\cos}$) and out-of-phase signal (red, $\Phi_{\sin}$). **F)** Histogram counts of the events having a certain amplitude and phase delay. **G)** Plot of the average measured and the modeled photothermal phase delay.

laser beam. The statistical errors result from the manual focussing. The deviations of the thermal diffusivity for two different measurements of the same particle are comparable to the measurements for different particles in the sample. Therefore, we were not able to measure heterogeneities of the thermal diffusivity in PDMS which is an expected result.
The same measurement principle can also be applied for liquids. In contrast to solid samples the position of the nanoparticle is not fixed. The nanoparticles diffuse freely in water. Whenever a particle passes the co-aligned laser beams short signal bursts are detected as shown in Figure 2.4E which also have a well-defined phase delay with respect to the heating laser. From time traces containing a large number of these events a histogram is created that counts the events having a certain amplitude and phase delay (see Figure 2.4F). The average phase delay is determined for the large amplitudes and plotted in Figure 2.4F. The comparison of the phase delays with scattering calculations yields the thermal diffusivity $(1.4 \pm 0.2) \cdot 10^{-7} \mathrm{m}^2\,\mathrm{s}^{-1}$. This new all-optical technique for the study of thermal transport will enable measurements in heterogeneous samples such as cells. Currently the method is advanced to simplify the modeling and enable studies of thermal transport in anisotropic media.

[1] A. Heber et al.: Phys. Chem. Chem. Phys. **17**, 20868 (2015), doi:10.1039/C5CP02920A

2.6 Photothermal Detection and Correlation Spectroscopy of Single Gold Nanoparticles in Living Cells

R. Schachoff, A. Abend, F. Cichos

For better insights into complex cellular processes fluorescence microscopy on the single molecule level has gained large importance. As this technique relies on emission processes, it is restricted to fluorescent probes and hampered by their photophysical processes such as bleaching and blinking. Recently, photothermal microscopy, which is based on the absorption of light, has been pushed to a new level of sensitivity allowing even the detection of single molecules. The technique employs the conversion of optical energy into heat by an absorbing non-fluorescent species. The released heat has been shown to create a nano-lens deflecting a focused probe laser in a microscopy setup. This lensing feature causes a split-focus geometry, the so-called twin-focus, where two lobes with different signal sign exist. Since both signal lobes are sharply separated with no overlap a number of new experimental possibilities arise. The twin-focus is extending the recently developed photothermal correlation spectroscopy (PhoCS), which is the photothermal counterpart of fluorescence correlation spectroscopy.
Gold nanoparticles down to 5 nm in size exhibit large absorption cross sections and high photo-stability and thus deliver intense and stable optical signals in photothermal microscopy with large signal to noise ratios even in heterogeneous environments. Since this method is highly sensitive to the absorbing species and non-invasive, we implement photothermal detection and correlation spectroscopy in living cells to study local dynamics in biological samples. For that purpose, gold nanoparticles are introduced into the cellular matrix of living cells via mechanodelivery, a technique that is based

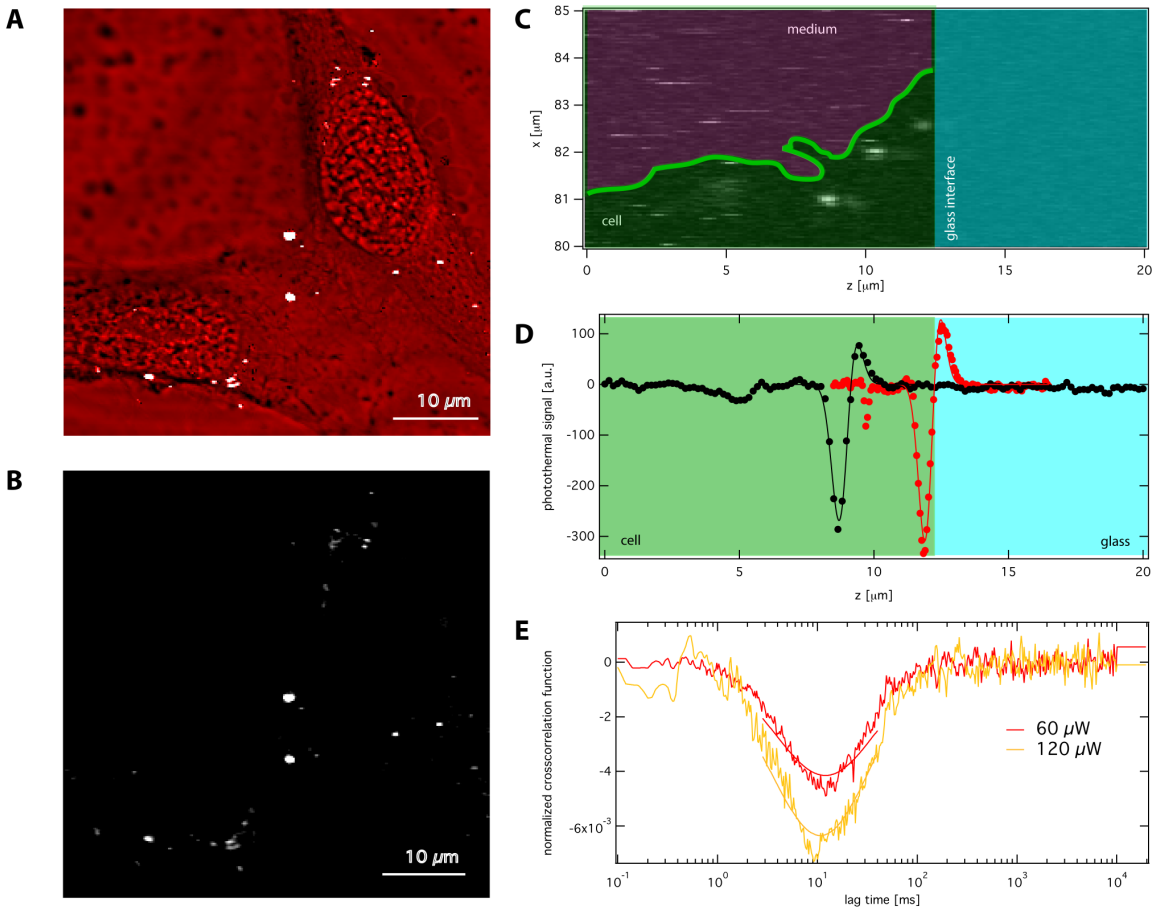

Figure 2.5: A) Scattering image of a fibroblast cell superimposed with the photothermal (pt) signal of gold nanoparticles (white markers). **B)** Background free pt image of the same sample site showing only the signal from gold nanoparticles. **C)** zx-scans of the pt signal. **D)** Line scan through a fixed gold nanoparticle on the glass surface (red markers) and through a gold nanoparticle in the cell (black markers) and their corresponding fits of the photothermal twin-focus characteristic. **E)** Cross-correlation functions at two different heating laser powers, 60 μW and 120 μW.

on mechanically desrupting the cell membrane leading to the delivery of nonspecific-functionalized gold nanoparticles to the cytoplasm. We have shown that the unique two-lobed structure of the detection volume in photothermal single particle microscopy is preserved even in an optical heterogeneous medium such as a cell, so that we are able to differ the photothermal signal of absorbing tracers from two well separated regions. Thus, an additional length scale in the detection volume allows to extract spatial information within the tracer dynamics and axial flow velocities well below 100 nm/ms from the cross-correlation function between the lobes of the twin-focus.

2.7 Hot Brownian Motion

A. Fischer, F. Cichos

We have recently in collaboration with the group of Prof. Kroy at the theory department

shown, that the Brownian motion of heated spherical nanoparticles can be described be new effective parameters for the temperature and the viscosity of the surrounding medium. One of the interesting effects is that the effective temperature is now coupled to the hydrodynamic flow field created by the motion of the nanoparticle thereby dissipating its kinetic energy. Thus, different degrees of freedom such as the rotational and translational motion possess in this thermal non-equilibrium different effective temperatures. In this project we study the instantaneous velocity distribution of a heated microparticle. At very short times, when the above described flow fields have not yet been established, the particle is supposed to show a new effective temperature, which is defined by its kinetic energy or its velocity. In thermal equilibrium this corresponds to the Maxwell–Boltzmann distribution. In thermal non-equilibrium there are so far no experimental results on this effective temperature. To measure this effective temperature we use an optical tweezer setup as depicted in Figure 2.6. Particles which can be heated by a solid state laser at 532 nm are trapped by an infrared laser (1064 nm). The laser heating is supplied in counter-propagating beams to prevent a displacement of the particle due to radiation pressure. The fluctuations of the particle are imaged onto a knife-edge prism and recorded by a balanced photodiode and a fast analog to digital converter. With the help of this setup we will be able to measure the velocity autocorrelation function of a single heated microparticle at nanosecond time resolution.

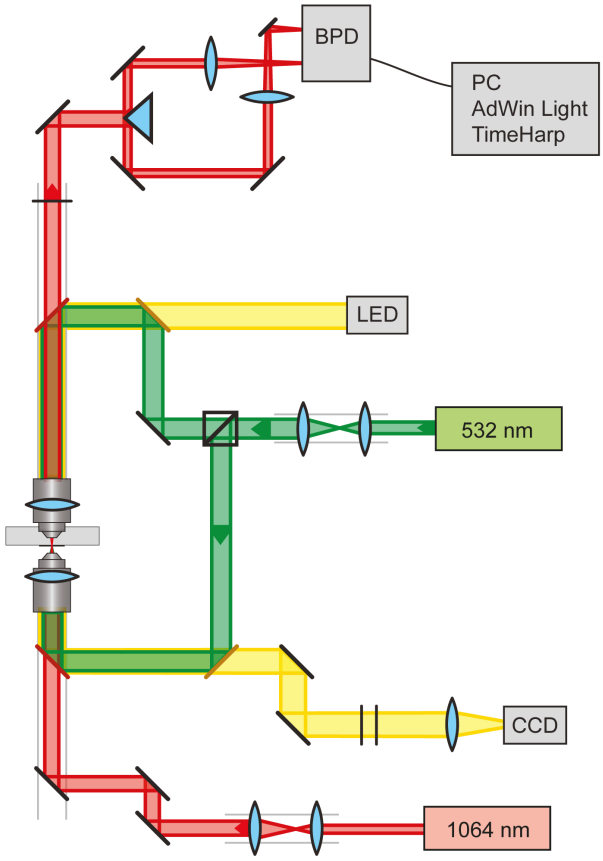

Figure 2.6: Scheme of the experimental optical tweezer setup to measure the instantaneous velocity of a heated microparticle in solution.

2.8 Funding

FOR 877, TP 2: Static and Dynamic Properties of DNA-based Polymer Structures under Constraints and Confinement
F. Cichos in collaboration with M. Mertig (TU Dresden), R. Seidel
DFG, CI 33/11-2

FOR 877: From Local Constraints to Macroscopic Transport
F. Cichos et al.
DFG, CI 33/12-1

DFG-ANR: Thermoelectric Effects at the Nanoscale
F. Cichos in collaboration with A. Würger (Université de Bordeaux, France)
DFG, CI 33/14-1

DFG SPP 1726, TP Propulsion and Interaction of Hot Brownian Swimmers
F. Cichos in collaboration with K. Kroy
DFG, CI 33/16-1

SFB/TRR 102, TP B10: Interaction of Single Polymer Chains in a Thermophoretic Trap
F. Cichos
DFG SFB/TRR 102

Leipzig School of Natural Sciences – Building with Molecules and Nano-objects (BuildMoNa)
F. Cichos (Principal Investigator)
founded as DFG GSC 185

2.9 Organizational Duties

Frank Cichos

- Speaker of the DFG Research Unit 877 "From Local Constraints to Macroscopic Transport"
- Vice Speaker of the Collaborative Research Center Transregio 102 "Polymers under Multiple Constraints"
- Member of the Steering Committee of the Graduate School BuildMoNa
- Head of the Aptitude Commission (M.Sc. Physics)
- Vice head of the PhD Board of the Faculty
- Vice head of the Board of the Faculty for Quality Management
- Member of the Examination Board (Physics/Meteorology)
- Referee: Phys. Rev. B, Phys. Rev. Lett., Nature, Nature Photonics, Chem. Phys. Lett., Appl. Phys. Lett., ACS Petroleum Research Fund, Medical Research Council

2.10 External Cooperations

Academic

- TU Dresden
  Prof. Dr. Michael Mertig
- Université de Bordeaux
  Prof. Dr. Alois Würger
- TU Chemnitz
  Prof. Dr. Christian von Borczyskowski
- Universität Mainz
  Prof. Dr. Thomas Basché
- Princeton University
  Prof. Dr. Haw Yang
- MPI Kohlenforschung Mühlheim
  Dr. Frank Marlow
- Universität Stuttgart
  Prof. Dr. Clemens Bechinger
- MPI Intelligente Systeme
  Prof. Dr. Peer Fischer

2.11 Publications

Journals

M. Braun, A.P. Bregulla, K. Günther, M. Mertig, F. Cichos: *Single molecules trapped by dynamic inhomogeneous temperature fields*, Nano Lett. **15**, 5499–5505 (2015)

A. Heber, M. Selmke, F. Cichos: *Thermal diffusivity measured with a single plasmonic nanoparticle*, Phys. Chem. Chem. Phys. **17**, 20868–20872 (2015)

M. Selmke, F. Cichos: *Comment on "Optimal detection angle in sub-diffraction resolution photothermal microscopy: Application for high sensitivity imaging of biological tissues"*, Opt. Express **23**, 6747–6750 (2015)

A. Bregulla, F. Cichos: *Size dependent efficiency of photophoretic swimmers*, Faraday Discuss. **184**, 381–391 (2015)

T. Cordes, W. Moerner, M. Orrit, S. Sekatskii, S. Faez, P. Borri, H.P. Goswami, A. Clark, P. El-Khoury, S. Mayr, J. Mika, G. Lyu, D. Cross, F. Balzarotti, W. Langbein, V. Sandoghdar, J. Michaelis, A. Chowdhury, A.J. Meixner, N. van Hulst, B. Lounis, F. Stefani, F. Cichos, M. Dahan, L. Novotny, M. Leake: *Plasmonics, tracking and manipulating, and living cells: General discussion*, Faraday Discuss. **184**, 451–473 (2015)

R. Schachoff, M. Selmke, A. Bregulla, F. Cichos, D. Rings, D. Chakraborty, K. Kroy, K. Günther, A. Henning-Knechtel, E. Sperling, M. Mertig: *Hot Brownian motion and photophoretic self-propulsion*, diffusion-fundamentals.org **23(1)**, 1–19 (2015)

H. Brutzer, E. Sperling, K. Günther, J. Dikic, F. Schwarz, D. Klaue, F. Cichos, M. Mertig, R. Seidel: *DNA under confinement and the use of DNA as confinement*, diffusion-fundamentals.org **23(2)**, 1–16 (2015)

Talks

F. Cichos: *Manipulating single nano-objects with dynamic temperature fields*, CeNS Colloquium, Munich, 23 January 2015, invited

M. Braun, F. Cichos: *Thermophoretic trapping of single and multiple nano-objects by actively controlled temperature fields*, DPG Spring Meeting, Berlin, 15–20 March 2015

A. Bregulla, F. Cichos: *Reorientation of passive Janus type swimmers in an external temperature profile*, DPG Spring Meeting, Berlin, 15–20 March 2015

F. Cichos, M. Braun, A. Bregulla: *Towards single molecule trapping and manipulation with dynamic temperature gradients*, DPG Spring Meeting, Berlin, 15–20 March 2015

A. Heber, M. Selmke, M. Braun, F. Cichos: *Single laser beam photothermal microscopy*, DPG Spring Meeting, Berlin, 15–20 March 2015

F. Cichos: *Mapping the interactions of photophoretic microswimmers by photon nudging*, Microswimmers – From Bulk to Interfaces, Pessac, France, 13–15 April 2015, invited

F. Cichos: *Propulsion and interaction of photophoretic microswimmers*, COST Workshop: Experimental Flowing Matter, Ankara, Turkey, 23–24 April 2015, invited

F. Cichos, K. Kroy: *Hot Brownian motion: theory and experiment*, Diffusion Fundamentals VI, Dresden, 23–26 August 2015, invited

A.P. Bregulla, F. Cichos: *Size dependent efficiency of photophoretic swimmers*, Single-Molecule Microscopy and Spectroscopy: Faraday Discussion, London, 14–16 September 2015

T. Thalheim, M. Braun, A. Bregulla, F. Cichos: *Single DNA molecules and colloids in a thermophoretic trap*, Minisymposium CRC TRR 102, Leipzig, 19 November 2015

T. Thalheim, M. Braun, A. Bregulla, F. Cichos: *Thermophoretic trapping of single and multiple colloids and DNA molecules*, 2nd iRTG Workshop CRC TRR 102, Wittenberg, 30 November – 01 December 2015

Posters

F. Cichos, M. Braun, A. Bregulla: *Trapping and manipulating single nano-objects with dynamic temperature fields*, APS March Meeting, San Antonio, USA, 2–6 March 2015

A. Heber, M. Selmke, M. Braun, F. Cichos: *Single laser beam photothermal microscopy*, APS March Meeting, San Antonio, USA, 2–6 March 2015

R. Schachoff, A. Abend, F. Cichos: *Photothermal detection and correlation spectroscopy of single gold nanoparticles in living cells*, DPG Spring Meeting, Berlin, 15–20 March 2015

M. Braun, A. Bregulla, F. Cichos: *Trapping and manipulating single nano-objects with dynamic temperature fields*, Annual BuildMoNa Conference, Leipzig, 23–24 March 2015

A. Heber, M. Selmke, M. Braun, F. Cichos: *Single laser beam photothermal microscopy*, Annual BuildMoNa Conference, Leipzig, 23–24 March 2015

A. Heber, M. Selmke, F. Cichos: *Single metallic nanoparticle measure thermal diffusivities using photothermal microscopy*, Single-Molecule Microscopy and Spectroscopy: Faraday Discussion, London, 14–16 September 2015

R. Schachoff, M. Braun, A. Heber, M. Selmke, F. Cichos: *Twin focus photothermal correlation spectroscopy*, 2nd Workshop: FCS in Polymer Science, Aachen, 24–25 September 2015

2.12 Graduations

Doctorate

- Subhasis Adhikari
  Heterogeneous single molecule dynamics in polymers
  May 2015
- Nicole Amecke
  Characterization of single quantum dot blinking
  May 2015
- Rebecca Wagner
  Local structural and optical characterization of photonic crystals by back focal plane imaging and spectroscopy
  March 2015

Master

- Sascha Loebel
  Flow fields and interactions around optically heated Janus particles in the vicinity of walls
  September 2015
- David Plotzki
  Optically detected electrochemistry on semiconductor nanocrystals
  February 2015

2.13 Guests

- Moritz Kreysing
  Max Planck Institute of Molecular Cell Biology and Genetics, Dresden
  9 December 2015

3

Molecular Physics

3.1 Introduction

This is my last report as an active professor; in March 2015 I have retired. But this does not mean that I intend to move away from research. Instead, I plan to focus on the fields of Broadband Dielectric and Fourier Transform Infrared Spectroscopy; in both we have profound expertise and the two have proven to be complementary and highly versatile in the physics of soft and hard condensed matter. In detail it is planned to study the dielectric properties of polymeric Ionic Liquids (PIL), a project already being funded by the German Science Foundation within a "Knowledge-transfer-project (Erkenntnistransferprojekt)" together with Prof. Veronika Strehmel, FH Krefeld and Merck KGaA in Darmstadt. Currently under review for the second funding period (2015 - 2019) is an application - titled "Broadband Dielectric and IR Spectroscopy to study molecular dynamics and order in nanometer domains of end-fixed polymers" - within the Collaborative Research Center (CRC) of the universities in Halle and Leipzig, "Polymers under multiple constraints: restricted and controlled molecular order and mobility". Furthermore the new common endeavor for the "Establishment of spectroscopic techniques for operational in ovo-gender determination in domestic chicken (Gallus gallus f. dom.)" (Coordinator: Prof. Dr. Maria-Elisabeth Krautwald-Junghanns, GZ: 2813IP003 (2015 - 2017) requires the utmost commitment. Additionally, several book projects are in course or envisaged within the series "Advances in Dielectrics". So I look forward to pursue research in soft matter physics with highest engagement and ambition.

Friedrich Kremer

3.2 Structure and Dynamics of Asymmetric Poly(styrene-*b*-1,4-isoprene) Diblock Copolymer under 1D and 2D Nanoconfinement

W.K. Kipnusu, M.M. Elmahdy*, E.U. Mapesa, J. Zhang†, W. Böhlmann‡, D-M. Smilgies§, C.M. Papadakis†, F. Kremer

*Department of Physics, Mansoura University, Mansoura 35516, Egypt
†Physik weicher Materie, Technische Universität München, 85748 Garching, Germany
‡Institute for Experimental Physics II, University of Leipzig, 04103 Leipzig, Germany
§Cornell High Energy Synchrotron Source, Cornell University, Ithaca, New York 14853, US

The impact of 1- and 2-dimensional (2D) confinement on the structure and dynamics of poly(styrene-*b*-1,4-isoprene) P(S-b-I) diblock copolymer is investigated by a combination of Scanning Electron Microscopy (SEM), Atomic Force Microscopy (AFM), Grazing-Incidence Small-Angle Xray Scattering (GISAXS), and Broadband Dielectric Spectroscopy (BDS). 1D confinement is achieved by spin coating the P(S-b-I) to form nanometric thin films on silicon substrates, while in the 2D confinement, the copolymer is infiltrated into cylindrical anodized aluminium oxide (AAO) nanopores. After dissolving the AAO matrix having mean pore diameter of 150 nm, the SEM images of the exposed P(S-b-I) show straight nanorods. For the thin films, GISAXS and AFM reveal hexagonally packed cylinders of PS in a PI matrix. Three dielectrically active relaxation modes assigned to the two segmental modes of the styrene and isoprene blocks and the normal mode of the latter are studied selectively by BDS. The dynamic glass transition, related to the segmental modes of the styrene and isoprene blocks, is independent of the dimensionality and the finite sizes (down to 18 nm) of confinement, but the normal mode is influenced by both factors with 2D geometrical constraints exerting greater impact. This reflects the considerable difference in the length scales on which the two kinds of fluctuations take place.[1]

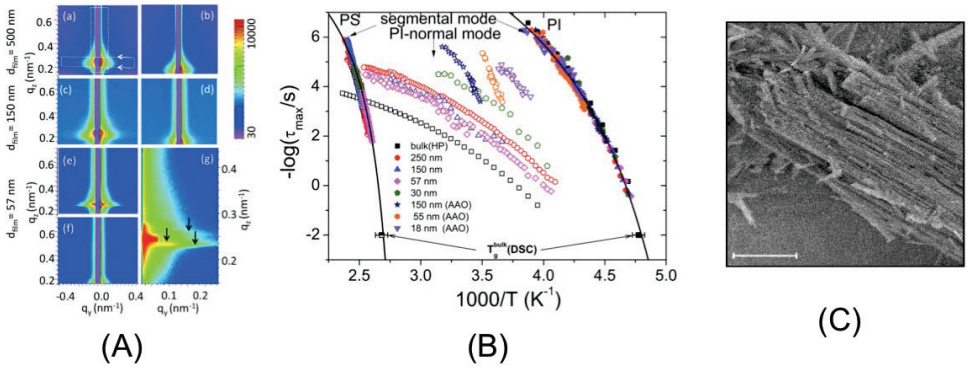

Figure 3.1: (A) 2D GISAXS images of P(S-b-I) films with $f_{PI} = 0.73$, (b-d,h): $\alpha_i = 0.14°$, and (e-g) $\alpha_i = 0.09°$. (B) Activation plot for the relaxation processes in P(S-b-I). The film thicknesses and pore sizes are indicated. (C) SEM micrograph of the nanorods of P(S-b-I) that was contained in 150 nm AAO pores.

[1] W.K. Kipnusu, M.M. Elmahdy, J. Zhang, W. Böhlmann D-M. Smilgies, C.M. Papadakis and F. Kremer, ACS Appl Mater Interfaces, 7, 23, 12328-12338 (2015)

3.3 Confinement for More Space: A Larger Free Volume and Enhanced Glassy Dynamics of 2-Ethyl-1-hexanol in Nanopores

W.K. Kipnusu, M. Elsayed[*†], W. Kossack, S. Pawlus[‡], K. Adrjanowicz[§], M. Tress, E.U. Mapesa, R. Krause-Rehberg[*], K. Kaminski[‡], F. Kremer

[*]Department of Physics, Martin Luther University Halle, 06099 Halle, Germany
[†]Department of Physics, Faculty of Science, Minia University, 61519 Minia, Egypt
[‡]Institute of Physics, University of Silesia, ul. Uniwersytecka 4, 40-007 Katowice, Poland
[§]DNRF Centre "Glass and Time", Dep. of Sciences, Roskilde University, Roskilde, Denmark

Broadband dielectric spectroscopy and positron annihilation lifetime spectroscopy are employed to study the molecular dynamics and effective free volume of 2-ethyl-1-hexanol (2E1H) in the bulk state and when confined in unidirectional nanopores with average diameters of 4, 6, and 8 nm. Enhanced α-relaxations with decreasing pore diameters closer to the calorimetric glass-transition temperature (T_g) correlate with the increase in the effective free volume. This indicates that the glassy dynamics of 2D constrained 2E1H is mainly controlled by density variation.[1]

[1] W.K. Kipnusu, M. Elsayed, W. Kossack, S. Pawlus, K. Adrjanowicz, M. Tress, E. U. Mapesa, R. Krause-Rehberg, K. Kaminski, F. Kremer, J Phys Chem Lett, 6, 3708–3712 (2015)

3.4 Inverse piezoelectric effect in high permittivity siloxanes

M. Tress, S.J. Dünki[*†], F. Kremer, S. YKo[*†], F.A. Nüesch[*]2, C.-D. Varganici[‡], C. Racles[‡], D.M. Opris[*]

[*]Empa, Swiss Federal Laboratories for Materials Science and Technology, Switzerland
[†]Ecole Polytechnique Fédérale de Lausanne
[‡]Petru Poni Institute of Macromolecular Chemistry, Romania

Recently, a homologous series of novel siloxane polymers with fine-tuned glass transition temperatures and dielectric properties by utilizing thiol-ene post-polymerization reactions has been established.[1] Due to the presence of polarizable thioether and nitrile groups, these polymers exhibit large permittivities up to 18.4 for the most polar composition. This high permittivity makes these polymers attractive candidates for dielectric elastomer actuators and flexible electronics. To improve the mechanical stability, the polymer has been cross-linked.

A custom-made setup (Fig. 3.3 left)[2] has been employed to measure the inverse piezoelectric effect. It consists of a piezo-element driven by a frequency generator, a force transducer and two Lock-In amplifiers which use the excitation frequency and the detected force oscillation as reference signals for recording the induced voltage in

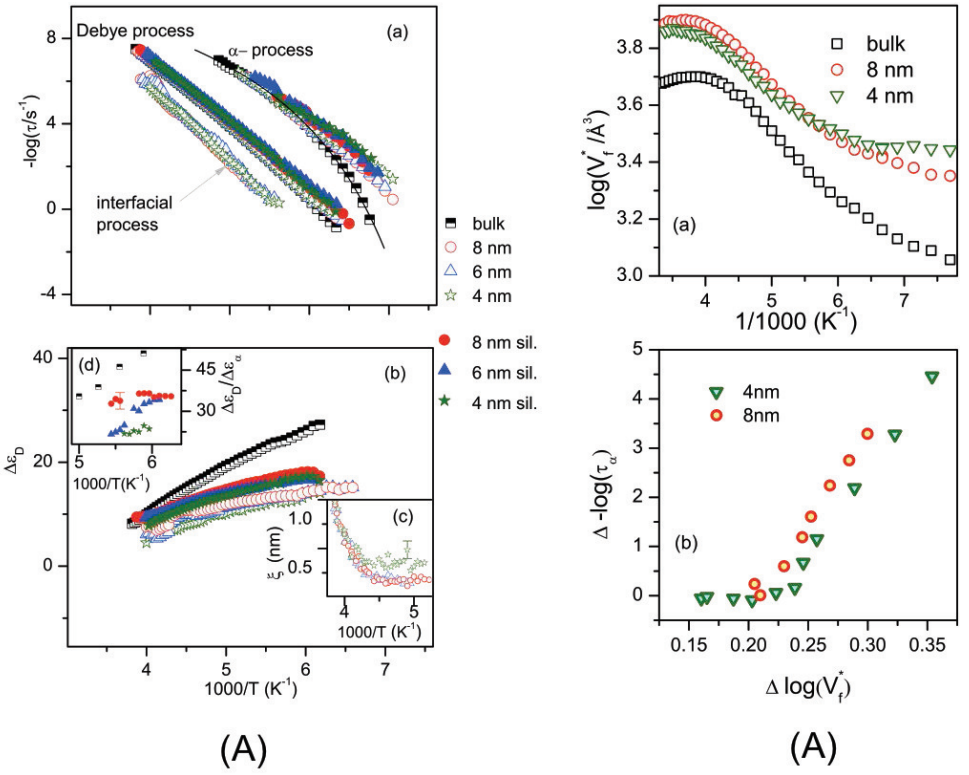

Figure 3.2: (A) Figure 2. (a) Activation plots for 2E1H in the bulk state (half-filled symbols), in native silica pores (open symbols), and in silanized pores (filled symbols). (b) Dielectric relaxation strength ($\Delta\epsilon$) of the Debye-like contribution for bulk (half-filled symbols) and 2E1H confined in 4, 6, and 8 nm native silica pores (open symbols) and silanized pores (closed symbols). Insets: (c) The approximate thickness of the interfacial layer of 2E1H in hydrophilic pores and (d) the ratio $\Delta\epsilon_D/\Delta\epsilon_\alpha$. (B) Temperature dependence of the effective free volume (V_f^*)for the bulk and confined 2E1H molecules. (b) Change or ratio of the α-relaxation with respect to the bulk values plotted as a function of similar change in the V_f^*. The changes were calculated at lower temperatures where confinement effects of τ_α) dominate . Only the last point indicating the largest deviation of $\Delta - \log(\tau_\alpha)$ was obtained from the extrapolated bulk value.

the sample. The latter exhibits a clear increase with increasing force amplitude (Fig. 3.3 right). The origin of a saturation and even drop in the voltage at the highest investigated force amplitudes is not yet clear but might be due to irreversible mechanical deformation since the material is rather soft. Additionally, a pronounced frequency dependence is found with a much stronger voltage at mechanical excitations of higher frequencies. This is indicates a decrease of polarization with time which is subject of further investigations.

[1] S.J. Dünki, M. Tress, F. Kremer, S. Y. Ko, F.A. Nüesch, C.-D. Varganici, C. Racles and D. M. Opris, RSC Adv 5, 50054 (2015)
[2] P. Papadopoulos, P. Heinze, H. Finkelmann and F. Kremer, Macromol 43 6666 (2010)

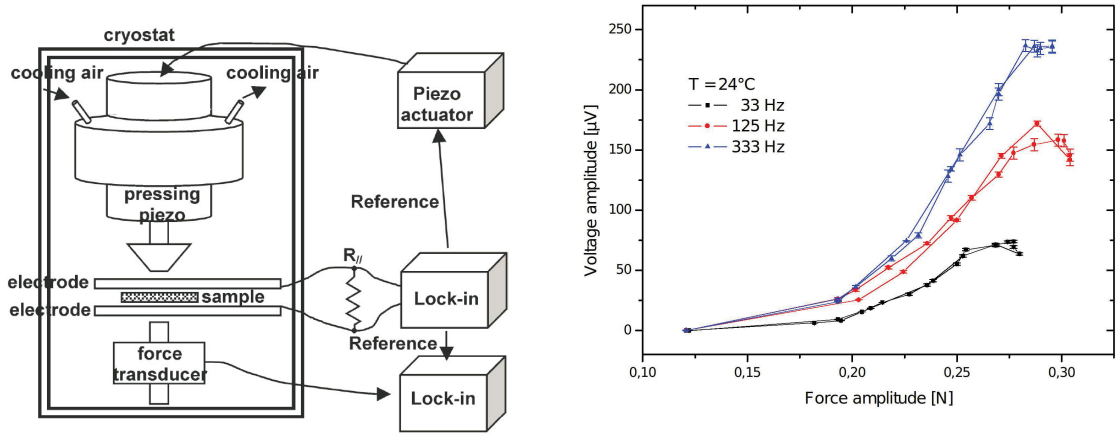

Figure 3.3: Left: Scheme of the custom-made setup to measure the inverse piezoelectric effect. A piezo element above the sample applies a sinusoidal force which is recorded by a force transducer. Electrodes tap the induced voltage and direct it to a Lock-In amplifier with the excitation frequency as reference (taken from [2]). Right: Induced voltage amplitude of the functionalized polysiloxane foil *vs.* amplitude of the applied sinusoidal force at different oscillation frequencies as indicated.

3.5 Enhanced segmental motion in a polymer/inorganic hybrid material

M. Tress, M. Vielhauer*, M. Reiche†, P. Lutz†, F. Kremer

*University of Freiburg
†Max-Planck-Institute for Microstructures, Halle

Covalent bonding of octafunctional polyhedral oligomeric silsesquioxanes (POSS) to polymers introduces an inorganic, rigid component of molecular size to typically flexible amorphous materials (Fig. 3.4 left). Due to the chemical bonding, phase separation is suppressed and hybrid materials are formed which can exhibit significantly changed physical properties. In the present study, we use POSS kernels linked to isotactic polystyrene (iPS) chains resembling star-like molecules with 6 to 8 arms (POSS-iPS$_{6\text{-}8}$).[1]

Being a semi-crystalline polymer, iPS forms crystalline regions in the nanometer range in a cold-crystallization process above its glass transition temperature (T_g = 344 K) and below its melting point (T_m = 479 K). A recently developed nano-structured electrode arrangement[2] enables us to study the segmental dynamics in this system while its morphology might change due to the crystallization process. Since crystallization implies local order, each chain typically consists of both crystalline and amorphous parts. This means that it covers regions of strongly different dynamics. While chain segments in the amorphous regions exhibit a pronounced mobility (glassy dynamics), their pendants in the crystalline phase are highly immobilized and do not conduct such motions. Consequently, these segments in the amorphous region which connect the crystalline with the amorphous part of a chain conduct a significantly slower relaxation.[3]

In contrast, the incorporation of POSS kernels adds another constraint which hinders

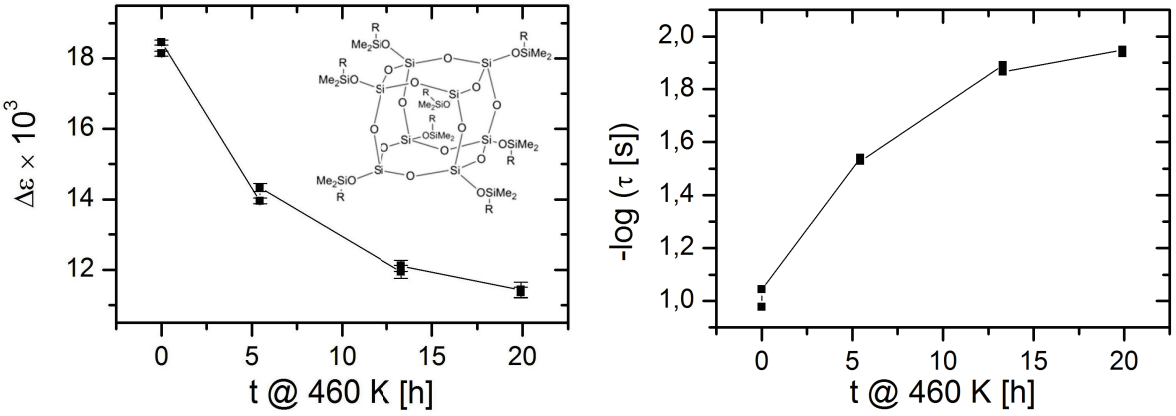

Figure 3.4: Left: Dielectric strength $\Delta\epsilon$ of POSS-iPS6-8 *vs* annealing time t at T_{ann} = 460 K following the sample from amorphous to semi-crystalline state. Inset: Chemical structure of POSS-iPS6-8. Right: Mean relaxation rate τ (at T = 360 K) of POSS-iPS6-8 *vs* annealing time t at T_{ann} = 460 K following the sample from amorphous to semi-crystalline state. Inset: Dielectric relaxation spectra ϵ'' *vs* f recorded at T = 360 K after annealing for different times as indicated.

optimal packing of the chains. Although the degree of crystallinity seems to be unaffected as suggested by the drop in the dielectric strength by roughly one third (Fig. 3.4) which matches the literature value of ∼ 30–35% crystallinity for pure iPS, the segmental dynamics is increased by about one decade in the amorphous parts of the semi-crystalline sample (Fig. 3.4 right). The latter implies a pronounced packing frustration which yields more space for each segment.

[1] M. Vielhauer, P. J. Lutz, G. Reiter and R. Mülhaupt, J Polym Sci Part A: Polym Chem 51, 947 (2013)
[2] A. Serghei and F. Kremer, Rev Sci Inst 79, 026101 (2008)
[3] B. Natesan, H. Xu, B. Seyhan Ince and P. Cebe, J Polym Sci Part B: Polym Phys 42, 777 (2004)

3.6 Epitope mapping of monoclonal antibody HPT-101: a study combining dynamic force spectroscopy, ELISA and molecular dynamics simulations

T. Stangner, S. Angioletti-Uberti* D. Knappe,† D. Singer†, C. Wagner R. Hoffmann† F. Kremer

*Beijing University of Chemical Technology, Beijing, People's Republic of China
†Center for Biotechnology and Biomedicine (BBZ),University of Leipzig, Leipzig, Germany

By combining enzyme-linked immunosorbent assay (ELISA) and optical tweezers-assisted dynamic force spectroscopy (DFS) [1–3], we identify for the first time the binding epitope of the phosphorylation specific monoclonal antibody (mAb) HPT-101 to the Alzheimer's disease relevant peptide tau[pThr231/pSer235] on the level

of single amino acids. In particular, seven tau isoforms are synthesized by replacing binding relevant amino acids by a neutral alanine (alanine scanning). From the binding between mAb HPT-101 and the alanine-scan derivatives, we extract specific binding parameters such as bond lifetime τ_0, binding length x_{ts}, free energy of activation ΔG (DFS) and affinity constant K_a (ELISA, DFS, Fig. 3.5). Based on these quantities, we propose criteria to identify essential, secondary and nonessential amino acids, being representative of the antibody binding epitope. The obtained results are found to be in full accord for both experimental techniques. In order to elucidate the microscopic origin of the change in binding parameters, we perform molecular dynamics (MD) simulations of the free epitope in solution for both its parent and modified form. By taking the end-to-end distance $d_{\text{E-E}}$ and the distance between the α-carbons $d_{\text{C-C}}$ of the phosphorylated residues as gauging parameters, we measure how the structure of the epitope depends on the type of substitution. In particular, whereas $d_{\text{C-C}}$ is sometimes conserved between the parent and modified form, $d_{\text{E-E}}$ strongly changes depending on the type of substitution, correlating well with the experimental data. These results are highly significant, offering a detailed microscopic picture of molecular recognition.

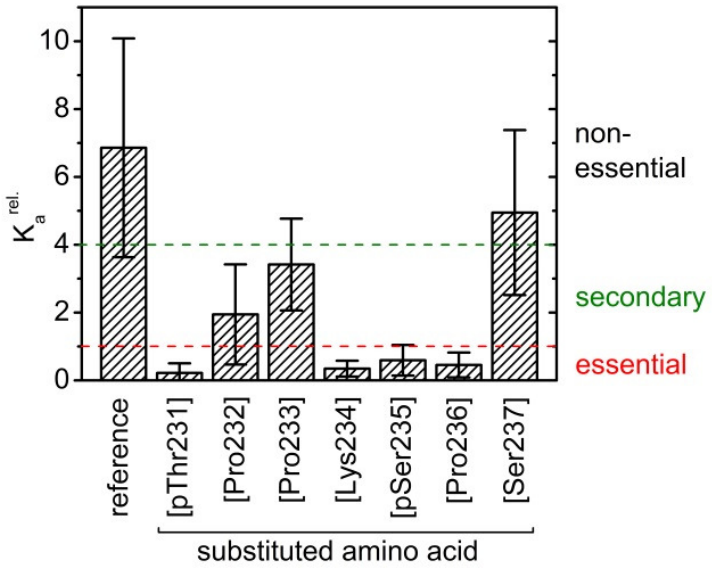

Figure 3.5: Relative affinity constant K_a^{rel}. for the binding of mAb HPT-101 to the different peptides as derived from DFS measurements. The peptide amino acids listed on the x-axis are replaced in the parent peptide tau[pThr231/pSer235] by an alanine and are representative of the different tau isoforms. Four essential (tauIso[pThr231]/[Lys234]/ [pSer235]/[Pro236]), two secondary (tauIso[Pro232]/[Pro233]) and one non-essential (tauIso[Ser237]) are identified, showing a similar trend to our ELISA measurements.

[1] T. Stangner et al., ACS Nano, 7, 12, 11388, DOI:10.1021/nn405303u (2013)
[2] T. Stangner et al., Phys Biol, 10, 046004, DOI:10.1088/1478-3975/10/4/046004 (2013)
[3] T. Stangner et al., Phys Biol, 12, 066018, DOI:10.1088/1478-3975/12/6/066018 (2015)

3.7 Charge transport, molecular dynamics and mesoscopic structure in Polymeric Ionic Liquids (PILs)

F. Frenzel, M.Y. Folikumah*, M. Schulz*, A.M. Anton, W.H. Binder*, F. Kremer

*Martin-Luther-University Halle-Wittenberg, Institute of Chemistry, Halle, Germany

A homologous series of 16 polymeric ionic liquids (PILs) are investigated based on polyisobutylene (PIB) carrying the IL-like cationic headgroup in composition with Br, NTf_2, OTf and pTOS as counteranions. Molecular dynamics, charge transport, polarization effects and the mesoscopic structure are analyzed over a wide frequency (10^{-2} - 10^{7}Hz) and temperature range (200–400 K) by means of broadband dielectric spectroscopy.[1] The net conductivity of the PILs as a whole is quantitatively described by an effective medium approach (EMA) and confirmed by transmission electron microscopy (TEM) investigations reflecting the microphase-separated character between high conductive IL-like micelles embedded in an insulating polymeric matrix of the PILs under study (Fig. 3.6). [2, 3]

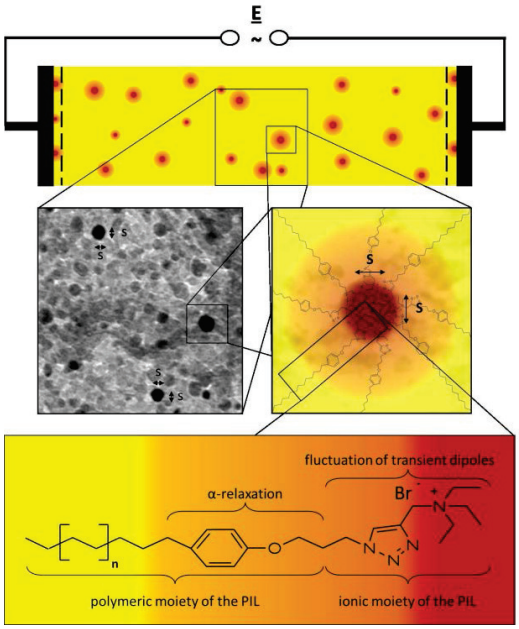

Figure 3.6: Top: Schematic display of the sample cell, upon which an electric field is applied. The area between the electrodes and the dashed lines shows the EP-zone. Center left: Representative TEM micrograph displaying a pronounced phase separation between high-conductive IL-like (volume fraction: 7%) micelles imbedded in a insulating polymeric matrix. Center right: The diffusion length $S \approx 3$–10 nm of the micelles (diameter: ≈ 5–20 nm) through the polymer matrix is indicated. Hence, the charge transport takes primarily place within the IL-like micelles. Bottom: Representation of the dynamics within the PILs under study. The process determining the glassy behavior of the PILs is characterized by the α-relaxation of the benzene-oxygen-unit within the polymeric mainchain, whereas the dynamics of the IL-like functionalization giving rise to the resulting charge transport, is given by the fluctuation of transient dipoles in micelle interior. This demonstrates the decoupling of charge transport from glassy dynamics, which is the - so far known - key-signature of this novel class of materials.

[1] Frenzel, F., Folikumah, M. Y., Schulz, M., Anton, A. M., Binder, W. H., Kremer, F. Molecular Dynamics and Charge Transport in Polymeric Polyisobutylene-Based Ionic Liquids. Macromolecules, 2016
[2] Frenzel, F., Binder, W. H., Sangoro, J. R., Kremer, F. Glassy dynamics and Charge Transport in Polymeric Ionic Liquids. Springer Dielectric Properties of Ionic Liquids, 2016
[3] Sangoro, J. R., Iacob, C., Agapov, A. L., Wang, Y., Berdzinski, S., Rexhausen, H., Strehmel, V., Friedrich, C., Sokolov, A. P., Kremer, F. Decoupling of ionic conductivity from structural dynamics in polymerized ionic liquids. Soft Matter, 2014

3.8 Methods to determine the pressure dependence of the molecular order parameter in (bio)macromolecular fibers

A.M. Anton, C. Gutsche W. Kossack F. Kremer

The experimental realization and an algorithm for analyzing the pressure dependence of the molecular order parameter of specific structural moieties in (bio)macromolecular fibers has been developed. By employing a diamond anvil cell (DAC) the polarization-dependent IR-transmission at hydrostatic pressure is recorded. In parallel, using an integrated microscope, the macroscopic orientation of the fibers is determined (Fig. 3.7). Because the apparent spectral dichroism (Fig. 3.8) originates from the *convolution* of the *macroscopic* distribution of the fibers and the *microscopic* distribution of transition moments within one fiber, one is able to separate between order and disorder at macroscopic and microscopic scales. Using the example of major ampullate spider silk the pressure dependence of the molecular order parameter of alanine groups being located within nanocrystalline building blocks is deduced and found to decrease reversibly by 0.01 GPa^{-1} when varying the external hydrostatic pressure between 0 and 3 GPa.[1]

[1] A. M. Anton, C. Gutsche, W. Kossack, F. Kremer, Soft Matter (2015) 11, 1158-1164

3.9 IR transition moment orientaional analysis (IR-TMOA) on the surface-induced orientation in thin layers of a high electron mobility n-type copolymer (P[NDI2OD-T2])

A.M. Anton, R. Steyrleuthner*†, W. Kossack D. Neher*†, F. Kremer

*Institut für Experimentalphysik, Freie Universität Berlin, Berlin, Germany
†Institut für Physik und Astronomie, Universität Potsdam, Potsdam, Germany

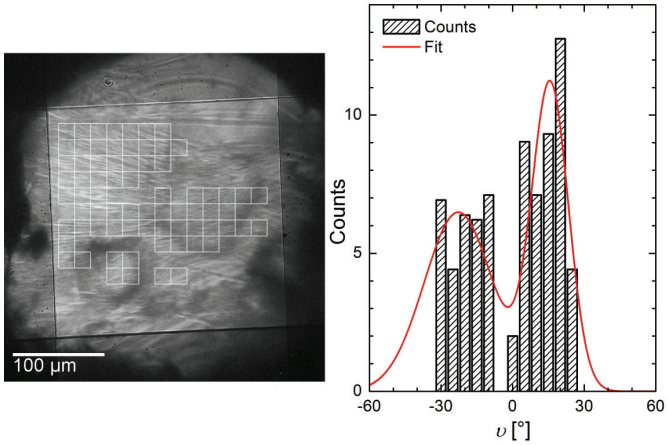

Figure 3.7: The macroscopic orientation distribution of the fibers is evaluated by determining the mean orientation within a reference volume (square region) and compiling a histogram or distribution function (red line) of these reference volumina.

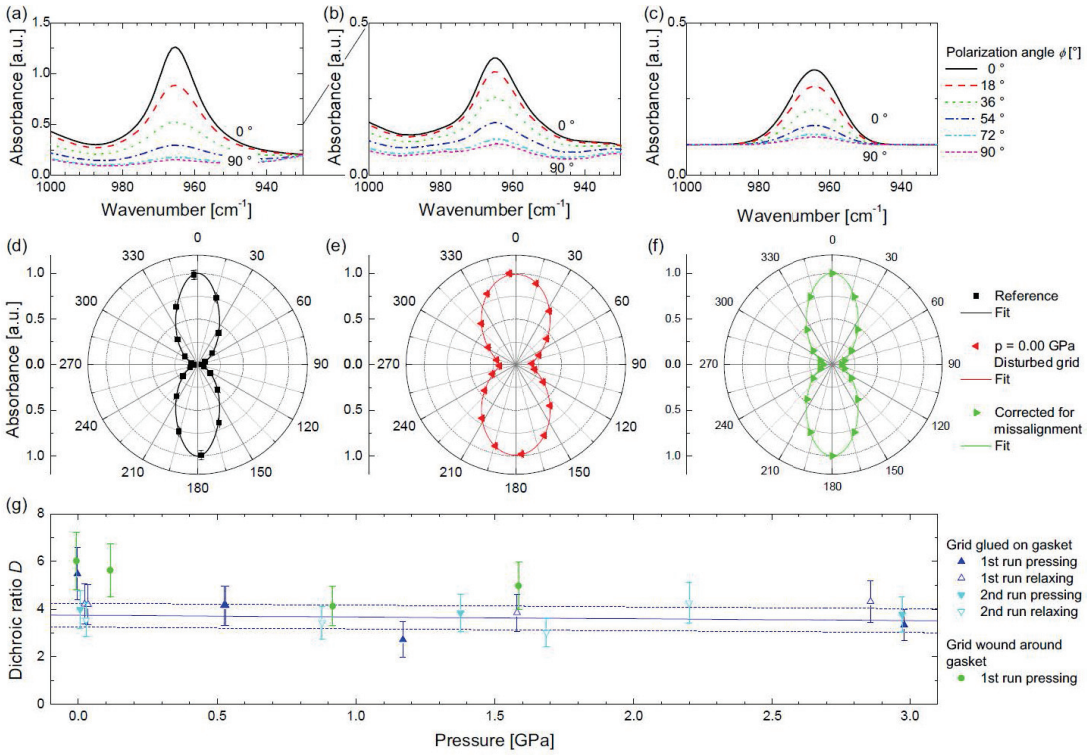

Figure 3.8: (a) The spectral dichroism of parallel fibers is used as a standard for the microscopic distribution of transition moments at ambient conditions (d). (b) Applying hydrostatic pressure causes the grating of parallel fibers to distort on expense of the apparent dichroism (e). (c) Utilizing the macroscopic distribution of the fibers (Fig. 3.7) and anticipate the apparent dichroism as the convolution of the macroscopic distribution and the microscopic distribution of the transition moments within one fiber one is able to separate pressure effects on the macroscopic and microscopic scale and to extract the microscopic transition moment distribution for a deformed grating. (g) This procedure is used to determine the pressure dependence of the molecular order parameter of a alanine-specific vibration located within the nanocrystalites.[1]

By means of the novel IR technique of infrared transition moment orientational analysis (IR-TMOA, Fig. 3.9) the molecular orientation and order in thin layers of the semiconducting polymer *poly[N,N′-bis(2-octyldodecyl) - 1,4,5,8-naphthalenediimide - 2,6-diyl] -alt- 5,5′-(2,2′-bithiophene)* (P(NDI2OD-T2)) is revealed. Structure-specific vibrational bands are analyzed in dependence on polarization and inclination of the incoming light with respect to the sample film. Due to that the molecular order parameter tensor for the respective molecular moieties relative to the sample coordinate system is deduced. Making use of the IR specificity we determine independently the orientation of atomistic planes defined through the *naphthalenediimide* (NDI) and *bithiophene* (T2) units relative to the substrate, and hence, relative to each other (Fig. 3.10). A pronounced solvent effect has been observed: While chlorobenzene causes the T2 planes to align preferentially parallel to the substrate (angle of 29°), 1:1 chloronaphthalene:xylene mixture as solvent results in a reorientation of the T2 units from a *face on* into an *edge on* arrangement. The NDI part, instead, remains unaffected.[1] The derived orientation is well correlated with the direction of π-π-stacking.[2]

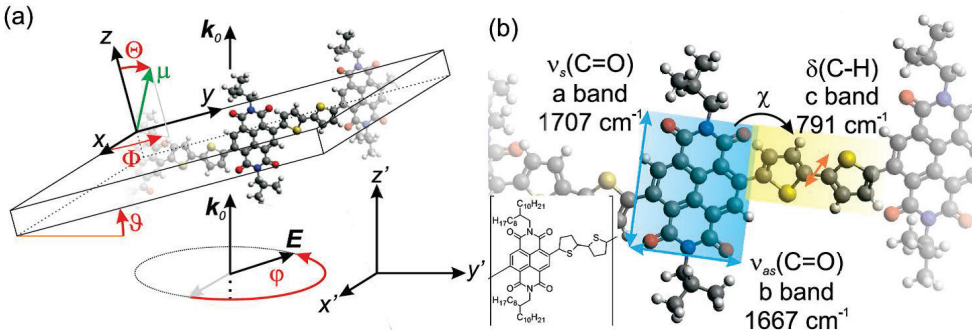

Figure 3.9: (a) For IR-TMOA the sample coordinate system (x,y,z) is inclined relative to the laboratory frame (x',y',z') while the polarization (φ)- and inclination (ϑ)-dependent absorbance is measured. (b) Schematic of a sample fragment and the transition moments (arrows). The C8H17 and C10H21 alkyl side chains are replaced by methyl groups.

[1] A.M. Anton, R. Steyrleuthner, W. Kossack, D. Neher, F. Kremer, J am Chem S 137, 6034–6043 (2015)
[2] R. Steyrleuthner, R. Di Pietro, et al., J Am Chem Soc 136, 4245-4256 (2014)

3.10 Spatial Orientation and Order of Structure-Defining Subunits in Thin Films of a High Mobility n-Type Copolymer

A.M. Anton, R. Steyrleuthner*†, W. Kossack D. Neher*†, F. Kremer

*Institut für Experimentalphysik, Freie Universität Berlin, Berlin, Germany
†Institut für Physik und Astronomie, Universität Potsdam, Potsdam, Germany

Orientation and order of distinct molecular subunits in solid layers of the high mobility n-type copolymer *poly[N,N′-bis(2-octyldodecyl) - 1,4,5,8-naphthalenediimide -*

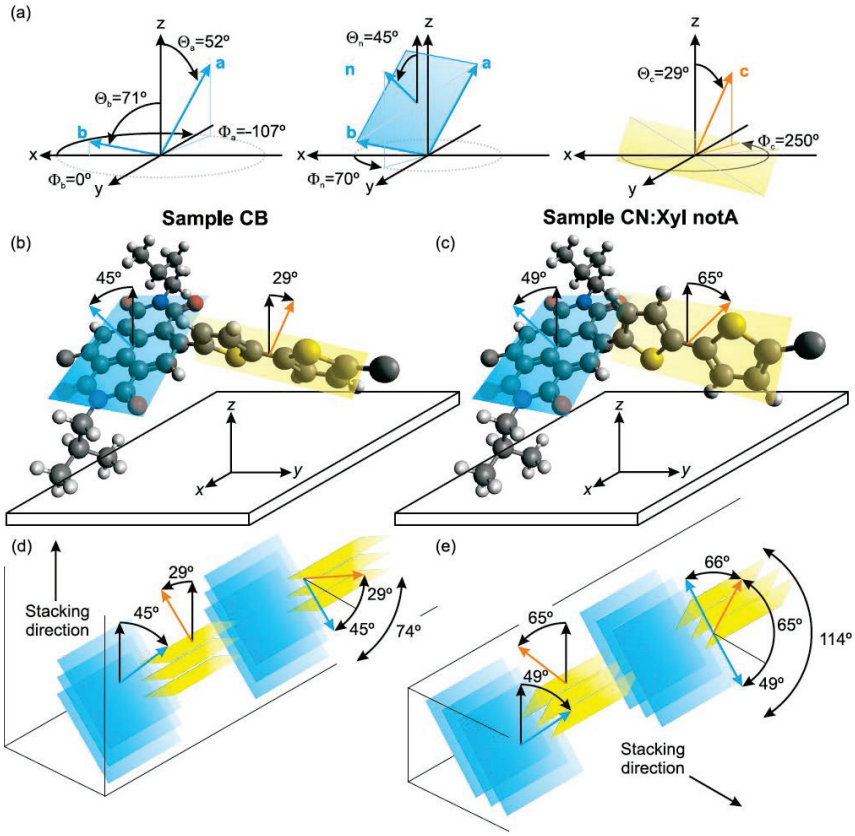

Figure 3.10: (a) Microscopic orientation of the molecular planes. (b) For chlorobenzene as solvent, the NDI unit (blue) is inclined by 45° relative to the substrate, whereas the T2 part (yellow) features an angle of 29° and a face on orientation. (c) For a chloronaphthalene:xylene mixture a distinct edge on orientation of the T2 unit is founde, whereas the NDI block retains its alignment. (d,e) Interpretation of the π-π-stacking direction correlated to the orientation of the T2 unit.

2,6-diyl] -alt- 5,5′-(2,2′-bithiophene) (P(NDI2OD-T2)) are investigated by means of infrared transition moment orientational analysis (IR-TMOA). This novel spectroscopic technique based on concurrent absorbance measurements of structure-specific bands in dependence on inclination and polarization of the incoming light (Fig. 3.9a) enables to determine the complete tensor of absorption independently for each transition moment. As a result, for nm-thin films pronounced in-plane anisotropy arising from self-aggregated order is detected, which, however, is no longer discernable for μm-thick samples. In contrast, the out of plane orientation (inclination of molecular subunits) is retained irrespective of the widely varying layer thicknesses (150 nm *vs* 1.4 μm). Thus, the conception of the sample morphology occurs as stratification of slightly misaligned layers of oriented polymers; with increasing film thickness the macroscopic in plane order diminishes, whereas the out of plane orientation is preserved (Fig. 3.11).

[1] A. M. Anton, R. Steyrleuthner, W. Kossack, D. Neher, F. Kremer, Macromol 49, 1798-1806 (2016)

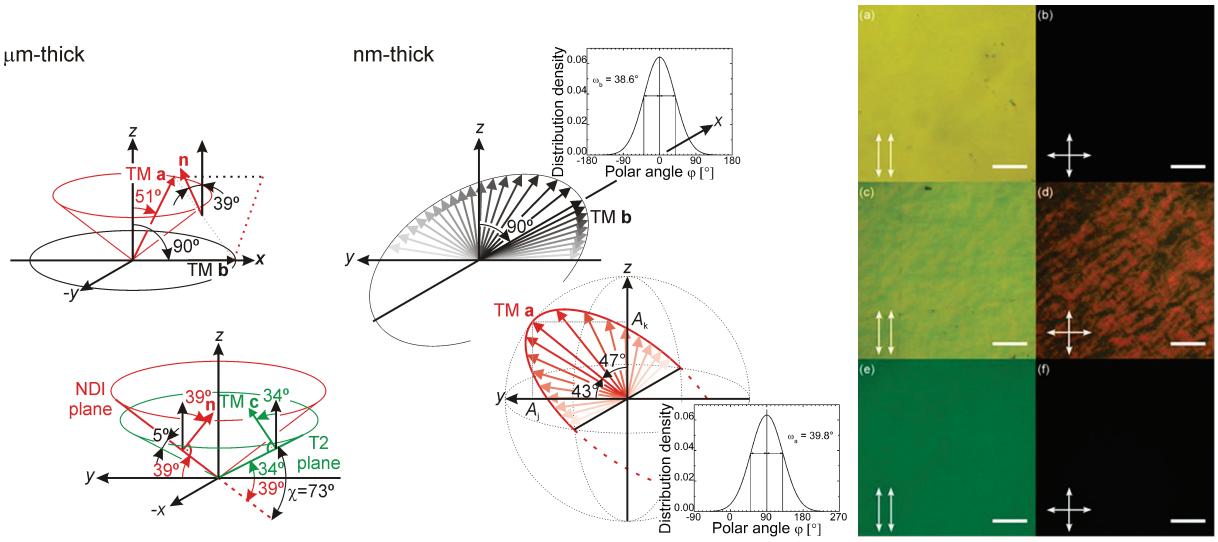

Figure 3.11: For the μm-thick sample TM a (red) is equally distributed at the lateral surface of a cone (opening angle Θ = 51°); TM b (black) is found within the xy-plane (Θ = 90°). Their vector cross product gives the NDI plane's normal vector **n** (red; Θ = 39°), which is consequently rotationally symmetric distributed. The same holds true for TM c (T2 unit, green). The cutting angle results either as sum of or difference between the particular inclinations (Θ = 73° or 5°) The micrographs of the blank ZnSe window (top row), as well as, the μm-thick film (bottom row) at linear-polarized light or with crossed polarizers (arrows) exhibit no birefringent properties. For the nm-thick sample macroscopic anisotropy in absorption arises (middle row, domains indicating long range order): TM b is distributed only within the xy-plane; TM a is symmetrically tilted (Θ = 47°, only one direction is shown). Each scale bar represents a length of 100 μm.[1]

3.11 Biomimetic spider silk's high toughness based on the similar morphology as the natural template

A.M. Anton, A. Heidebrecht*, N. Mahmood†, M. Beiner†, T.R. Scheibel*, F. Kremer

*Faculty of Engineering Science, Universität Bayreuth, Bayreuth, Germany
†Department of Physics, Martin-Luther-University Halle-Wittenberg, Halle, Germany

Spiders' dragline silk exhibits remarkable characteristics as exceptional biocompatibility or high tensile strength combined with great elasticity. Its mechanical properties are based on a refined architecture on the molecular scale: Proteins with highly repetitive core motifs aggregate into nanometer-sized crystals rich on alanine in β-sheet secondary structure and surrounded by an amorphous glycine-rich matrix. During spinning the amorphous parts are elongated which orients both substructures and, in addition, give rise to an inherent non-equilibrium state. Thus, external stress is directly transferred to the nanocrystals, while the tendency to contract is counterbalanced by surrounding fiber structure. However, it was not possible to recreate artificially this exceptional architecture so far.

The combination of wet spinning and post-treatment on the basis of a biomimetic protein results in fibers with similar nanostructure and comparable toughness than the natural template.[1] We found that unoriented alanine-rich β-sheet nanocrystals

with the same size as in natural silk (Fig. 3.12a) are already formed during wet spinning, while the glycine-rich motifs establish the amorphous section. Furthermore, post-spinning strain orients this composite (Fig. 3.12b) leading to a non-equilibrium on nanoscale that is, in addition, accompanied by enhanced mechanical properties. Our results demonstrate in detail how macroscopic mechanical properties originate from the molecular organization: Pre-stressed chains apportion applied stress directly to the crystallites (Fig. 3.12c–e) enabling to dissipate huge mechanical load as identical to the mechanism in natural dragline silk.[2]

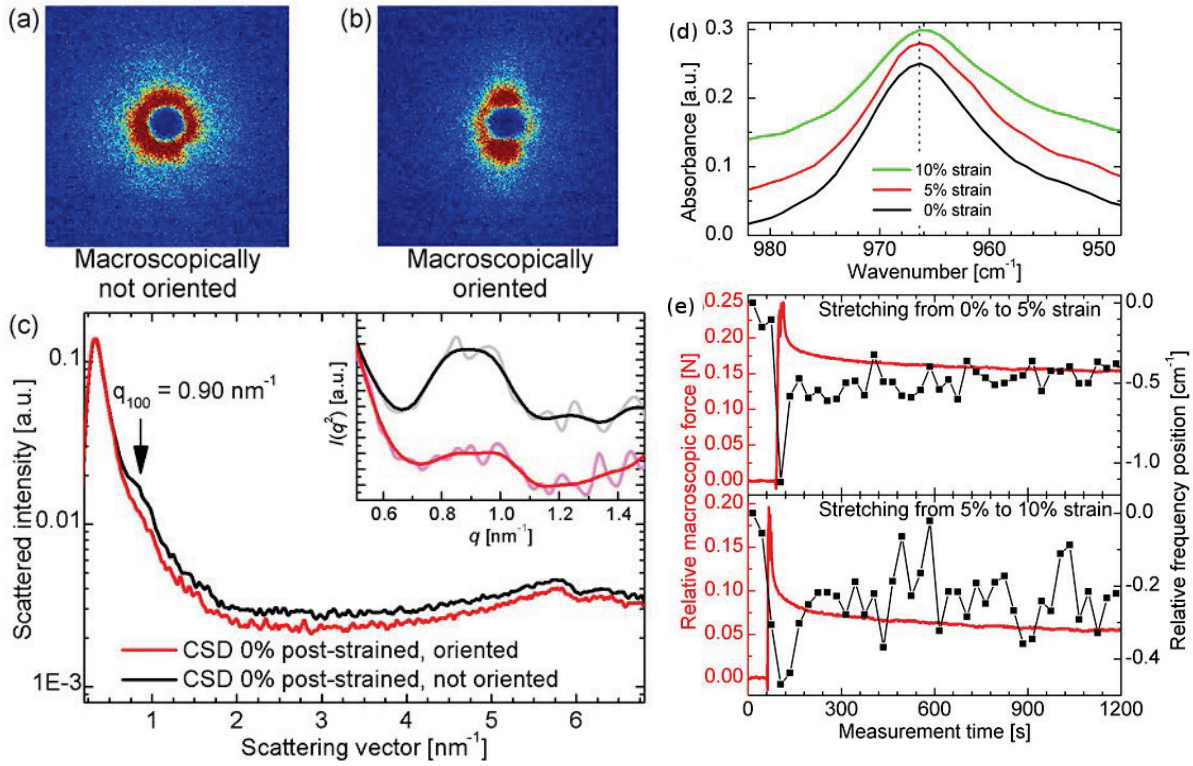

Figure 3.12: SAXS pattern of biomimetic fibers macroscopically (a) not and (b) well oriented. (c) Integrated intensity reveals the crystal size of 7.0 nm. (d) The frequency position of the polyalanine peak is shift as a conse-quence of the applied force (d) Relative force (red) and relative frequency position (black) during the elongation of the biomimetic, post-treated sample from (top) 0 to 5% ana (bottom) 5 to 10% strain. The difference between the black and the red curve in panel d corresponds to the first and the last position in the top diagram of panel e; the difference between the red and the green curve reflects the first and the last position in the bottom diagram.

[1] A. Heidebrecht, L. Eisoldt, J. Diehl, A. Schmidt, M. Geffers, G. Lang, and T. R. Scheibel, Adv Mater 27, 2189-2194 (2015)
[2] R. Ene, P. Papadopoulos, F. Kremer, Soft Matter 22, 4568-4574 (2009)

3.12 Influence of the remanent polarisation on the liquid crystal alignment in composite films

W. Kossack, L. Holländer*, M. Kollosche*, W. Wirges*, R. Gerhard*, F. Kremer

*Institut für Physik und Astronomie, Universität Potsdam, Potsdam, Germany

Polymer dispersed liquid crystals are prepared from a solution of Poly(Vinylidene-Fluoride-*co*-Trifluoro-Ethylene) (PVDF-TrFE) and 4-cyano-4'-n-pentylbiphenyl (5CB) or 4-cyano-4'-n-hexylbiphenyl (6CB). In the resulting films approximately equal fractions of the Liquid Crystals (LC, ≈ 5 wt%) are dissolved within the matrix or reside in slightly oblate inclusions of about 1 μm in diameter (Fig. 3.13).

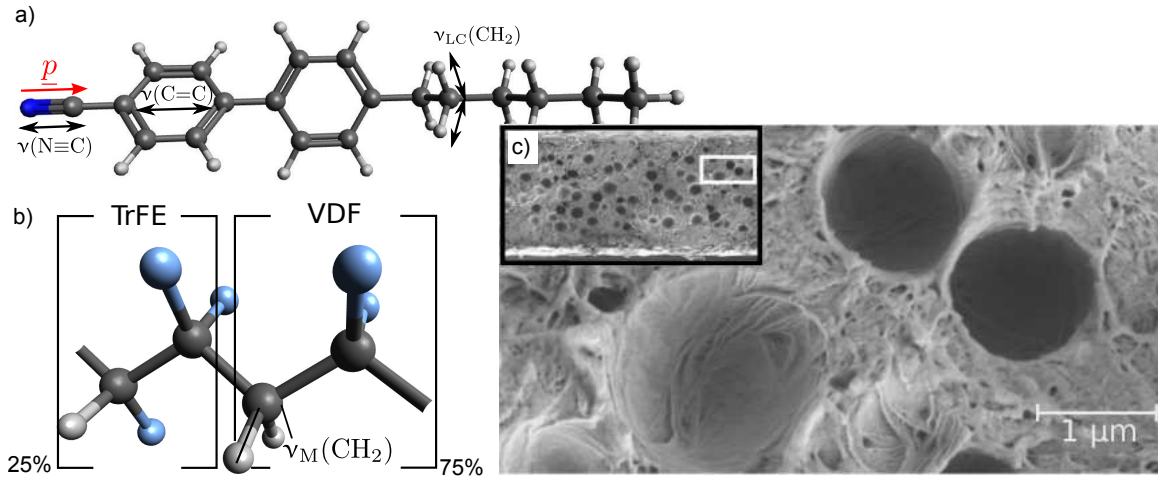

Figure 3.13: Chemical structure of 6CB (a) and PVDF-TrFE (b) including the vibrational tranisition moments under study. In c) an electron micrograph is shown.

Samples are subjected to external electric fields, which polarize the ferroelectric matrix and orient the LCs. Using Infrared Transition Moment Orientational Analysis, the three-dimensional order of the matrix and the LCs is characterized in the native, poled, and annealed state (Fig. 3.14). For all temperatures, the order is lower than expected from model calculations. In agreement with dielectric measurements and light transmission experiments, we attribute this result to the shielding effect of mobile charge carriers within the liquid crystal inclusions.[1]

[1] L. Holländer,W. Kossack, M. Kollosche, W. Wirges, F. Kremer, R. Gerhard, Liquid Crystals, DOI:10.1080/02678292.2016.1185174, (2016)

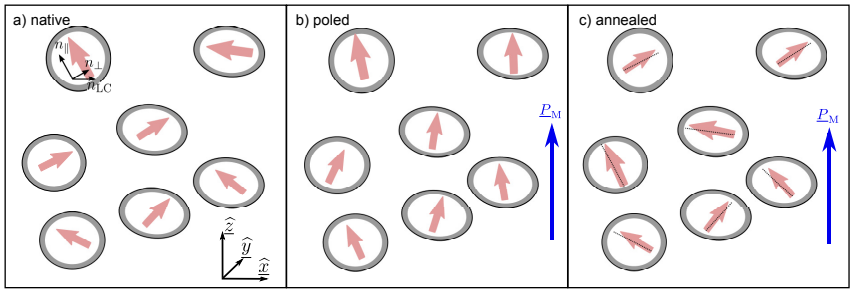

Figure 3.14: Local nematic directors within droplets (Fig. 3.13) after different pre-treatment. The coordinate direction of the remanent polarization ($\underline{P}_M$) of the matrix is showns as blue arrow. The region of interfacial interactions is grey-shaded.

3.13 Interface and Confinement Induced Order in Thin Films of Poly-Caprolactone

W. Kossack, A. Seidlitz*, T. Thurn-Albrecht*, F. Kremer

*Department of Physics, Martin-Luther-University Halle-Wittenberg, Halle, Germany

Infrared transition moment orientational analysis (IR-TMOA), X-ray Diffraction (XRD) and model calculations are combined to study interface and confinement induced order and orientation in thin ($h \approx 11$ μm) films of Poly-Caprolactone (PCL), as prepared by drop-casting on silicon wafers. Depending on the crystallization temperature, 303 K $\leq T_x \leq$ 333 K, non-banded spherulites with a diameter of 1 μm $\leq d_S \leq$ 500 μm form (Fig. 3.15).

Macroscopic order of the crystalline lamellae is imposed by interfacial layers and geometrical confinements of the spherulitc structures ($d_S > h$): radial crystal growth is restricted to a disc of aspect ratio d_S/h. Order is quantified by IR-TMOA and XRD pole figure measurements, which measure, in the case of PCL, the orientation distribution of *complementary* crystal directions. This enables one to correlate the directions of the transition moments with the crystal axes; and estimate the volume fractions of flat on- or edge on lamellae as induced by the substrate or the free interface, as well as the fractions of surface-induced- or bulk-nucleated spherulites in dependence on crystallization temperature. It turns out that the contribution of substrate induced spherulitic structures rises with $T_x = 323$ K up to a value of $\sim$ 12 vol%, whereas no indications of edge on lamellae at the free surface are found. For $T_x \leq 30$ K non-confined spherulites ($d_S < h$) dominate the morphology, and no substrate induced layer is found.[1]

[1] Kossack, W., A. Seidlitz, T. Thurn-Albrecht, F. Kremer, Macromol, 49, 3442-3451 (2016)

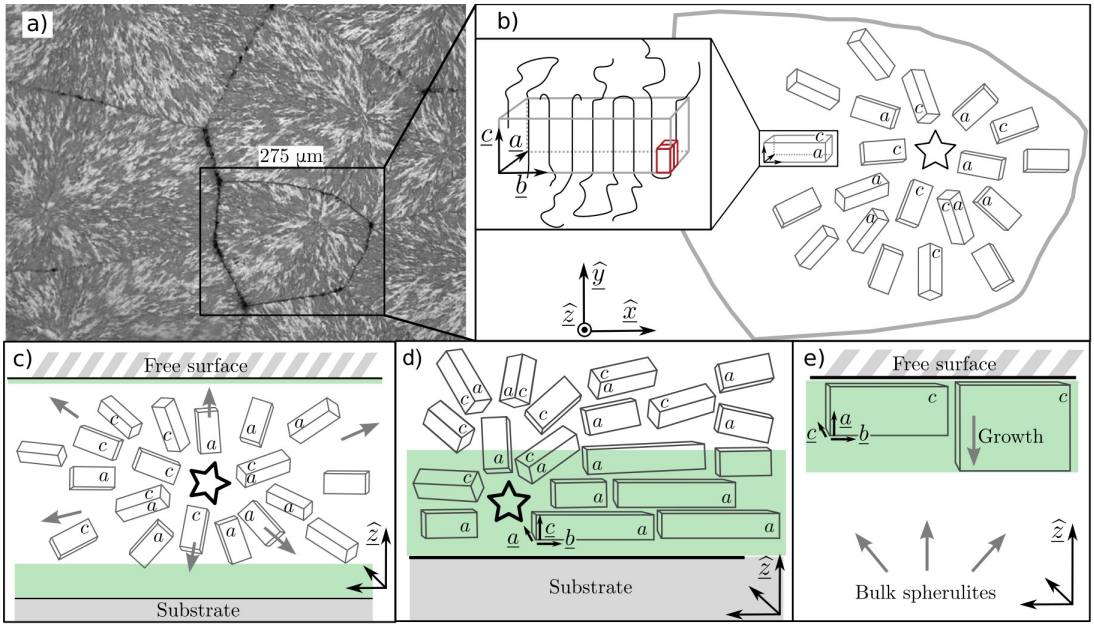

Figure 3.15: Micrograph and scheme of a substrate supported, spherulite (not to scale); a) Micrograph of PCL crystallized at T_x = 323 K; The framed region is 275 μm wide. Non-spherical, flat spherulitic objects form, that impinge each other. b) Lamellar crystallite grow radially out of a nucleation seed (star) and form a non-banded spherulite, that is confined by the film boundaries and neighbouring spherulites. The inset depicts a lamella with polymer backbones indicated by black lines and unit cells in red. Panel c) depicts geometrically confined crystallization within the thin film, whereas d) shows a flat on layer (shaded in green) as induced by the substrate and (e) and edge on layer (shaded in green) as induced by the free surface. The lamellar crystallites grow (grey shaded arrows) preferentially along the $\underline{b}$-direction. Crystal directions are indicated by $\underline{a}$ ([100]), $\underline{b}$ ([010]), and $\underline{c}$ ([001]).

3.14 Molecular dynamics of swollen poly(2-vinyl-pyridine) brushes

N. Neubauer, R. Winkler*, M. Tress, P. Uhlmann*, M. Reiche†, W.K. Kipnusu, F. Kremer

*Leibniz-Institut für Polymerforschung Dresden, Dresden, Germany
†Max Planck Institute of Microstructure Physics, Halle (Saale), Germany

The influence of swelling on the molecular dynamics of poly(2-vinyl-pyridine) (P2VP) brushes is measured by Broadband Dielectric Spectroscopy (BDS) in a broad temperature (350 K – 420 K) and spectral (0.1 Hz – 1 MHz) range with nanostructured, highly conductive silicon electrodes, separated by 35 nm-high insulating silica spacers.

A "grafting-to" method is applied to prepare P2VP-brushes with a grafting density $\sigma = 0.12\,\mathrm{nm}^{-2}$ and a film thickness d = 7.3 nm as measured by ellipsometry. Swelling of the P2VP-brushes is realized with tetrahydrofuran (THF) vapor using a flow-cell. In the dry state, the segmental dynamics of the P2VP brushes coincides with the dynamic glass transition of the bulk system while in the swollen state it becomes faster by up to 1 – 2 decades due to the plasticizing effect of THF.[1, 2]

[1] N. Neubauer, R. Winkler, M. Tress, P. Uhlmann, M. Reiche, W.K. Kipnusu, F. Kremer,

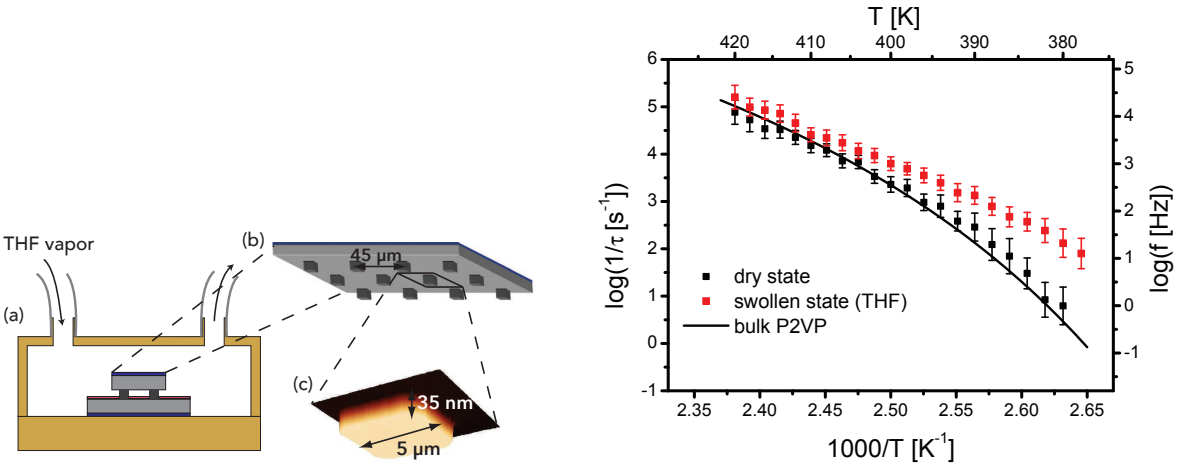

Figure 3.16: Left: Sample arrangement: (a) measurement flow-cell with a sample capacitor and a controllable THF vapor flow, which enables dielectric measurements of THF swollen P2VP brushes. The capacitor is composed of two highly doped silicon electrodes (bottom electrode: 10 x 20 mm^2, top electrode: 1 x 1 mm^2), where the top electrode is covered by an array of insulating silica nanostructures, serving as spacers (b). The spacers have a height of 35 nm, as confirmed by AFM scans (c) to allow dielectric measurements of thin films with a free upper surface. Right: Activation plot of the P2VP α-relaxation of a P2VP brush (σ_{P2VP} = 0.12 nm^{-2}) in the dry state and swollen by THF vapor. The dry P2VP brush (black squares) follows a Vogel-Fulcher-Tammann temperature dependence similar to the mean relaxation rate of bulk P2VP (solid line). In the swollen state, the temperature dependence of the mean relaxation rate is shifted (red squares) due to a solvent induced enhancement of the P2VP α-relaxation. The error bars show the accuracy for determining the mean relaxation rate as a parameter from the Havriliak-Negami fits.

Soft Matter 11, 3062–62015 (2015)
[2] N. Neubauer, M. Tress, R. Winkler, E.U. Mapesa, P. Uhlmann, W.K. Kipnusu, F. Kremer, Macromol, under review (2016)

3.15 Sex-determination of 80-88 hours-old chicken embryos from Raman measurements

E.U. Mapesa, W. Kossack, F. Kremer

Every year billions of layer chicks are produced across the world and the male ones culled since they are of no use in as far as egg production goes. The culling of male chicks, which is in the order of tens of millions per year for Europe alone, is unacceptable both from the point of view of animal rights proponents and in terms of waste disposal.[1, 2] In an on-going consortium, focus is set on developing a practically usable Raman-spectroscopy-based prototype for sexing 3–4 day-old chicken embryos, which is well before the onset of pain perception at day 10.[3] Based on the fact that there is a difference of about 2% in cellular DNA content between male and female chicken, [4] Raman spectroscopy is a versatile tool for this application.

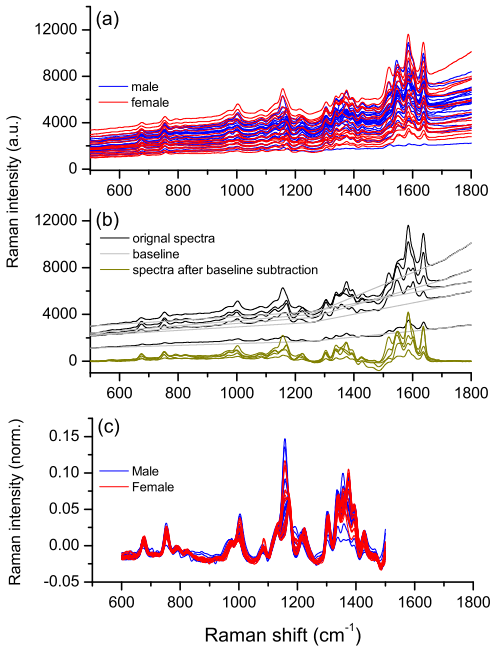

Figure 3.17: (a) Raw Raman spectra as measured from 80–88 hours old embryos using 532 nm excitation with a spectral resolution of 9 cm^{-1}, each spectrum comprising 20 accumulations with an integration time of 1 s. (b) demonstrates the baseline subtraction from the raw data, and (c) vector-normalized data used in the classification algorithm.

In a present focus, Raman spectra are acquired from blood vessels using green excitation (532 nm), the spectra are pre-treated (*ie*, baseline corrected and adjusted, and standardized by vector normalization, Fig. 3.17) before applying linear discriminant analysis (LDA) for classification. By varying the measurement parameters and checking the respective level of correct gender assignment, it is aimed to reduce the measurement time from typically one minute to less than 30 s per egg.

[1] T. Steiner, T. Bartels, A. Stelling, M.-E. Krautwald-Junghanns, H. Fuhrmann, V. Sablinskas, E. Koch, Anal Bioanal Chem 400, 2775–2782 (2011)
[2] M. Harz, M. Krause, T. Bartels, K. Cramer, P. Rösch, J. Popp, Anal Chem 80, 1080–1086 (2008)
[3] A. Weissmann, S. Reitemeier, A. Hahn, J. Gottschalk, A. Einspanier, Theriogenology 80, 199–205 (2013)
[4] T. Tiersch, Worlds Poult Sci J 59, 24–31 (2003)

3.16 Funding

SFB/TRR 102 "Polymers under multiple constraints: restricted and controlled molecular order and mobility", TP B05 "Structural levels of organisation in spider-silk - a combined mechanical and IR-spectroscopic study" (2011–2015), TP B08 "Broadband Dielectric Spectroscopy to study the molecular dynamics in nanometer thin layers of block copolymers" (2011–2019)
Prof. Dr. F. Kremer

New Polymer Materials on the Basis of Functionalized Ionic Liquids for Application in Membranes "Knowledge Transfer Project"
Prof. Dr. F. Kremer, Prof. Dr. Veronika Strehmel (Hochschule Niederrhein)
KR 1138/24-1; STR 437/5-3; (2014–2017)

Establishment of spectroscopic techniques for operational in ovo-gender determination in domestic chicken (Gallus gallus f. dom.)
Prof. Dr. Frierich Kremer, Prof. Dr. Maria-Elisabeth Krautwald-Junghanns (Veterinärmedizinische Fakultät)
GZ: 2813IP003 (2015–2017)

3.17 Organizational Duties

Friedrich Kremer

- Principal Investigator in the "Leipzig School of Natural Sciences - Building with Molecules and Nano-Objects" in the framework of a Graduate School funded by the "Ferderal Excellence Initiative". This supports several Ph.D. projects.
- Deputy chairman of the SFB-TRR 102 on "Polymers under multiple constraints: restricted and cotrolled molecular order and mobility" of the Universities of Halle and Leipzig

3.18 External Cooperations

Academic

- Max-Planck-Institute for Microstructure Physics, Halle
  Dr. Manfred Reiche
- Cornell University, Ithaca, New York
  D.M. Smilgies
- Technische Universität München
  Prof. Dr. C.M. Papadakis, J. Zhang
- Leibniz-Institut für Polymerforschung Dresden
  Dr. P. Uhlmann, R. Winkler
- Martin-Luther-Universität Halle-Wittenberg
  PD Dr. M. Beiner, N. Mahmood

- Fraunhofer Institut für Werkstomechanik IWM, Halle
  PD Dr. M. Beiner
- Helmholtz-Zentrum Berlin für Materialien und Energie, Berlin
  Prof. Dr. J. Dzubiella, Dr. S. Angioletti-Uberti
- Department of Chemical and Biomolecular Engineering, University of Tennessee, Knoxville
  Dr. J. R. Sangoro
- Department of Materials Science and Engineering, Penn State University
  C. Iacob, Ph. D.
- Hochschule Niederrhein, Institute of Organic Chemistry
  Prof. Dr. Strehmel
- Medizinische Fakultät Carl Gustav Carus der Technischen Universität Dresden
  Priv.-Doz. Gerald Steiner

Industry

- Novocontrol, Hundsangen, Germany
- MERCK KGaA, Darmstadt, Germany
- Lohmann Tierzucht GmbH
- EVONTA-Technology GmbH

3.19 Publications

Journals

Kremer, F., M. Treß, E.U. Mapesa "Glassy dynamics and glass transition in nanometric layers and films: A silver lining on the horizon", Journal of Non-Crystalline Solids 407 277-283 (2015) DOI: 10.1016/j.jnoncrysol.2014.08.016

Anton, A.M., C. Gutsche, W. Kossack, F. Kremer "Methods to determine the pressure dependence of the molecular order parameter in (bio) macromolecular fibres" Soft Matter 11, 1158-1164 (2015) DOI: 10.1039/C4SM01142B

Kipnusu, W.K., M.M. Elmahdy, E.U. Mapesa, J. Zhang, W. Böhlmann, D.-M. Smilgies, C.M. Papadakis, F. Kremer "Structure and Dynamics of Asymmetric Poly(styrene-b-1,4-isoprene) Diblock Copolymer under 1D and 2D Nanoconfinement" ACS Appl Mater Interfaces, 7, 12328–12338 (2015) DOI: 10.1021/am506848s

Griffin, P.J., A.P. Holt, K. Tsunashima, J.R. Sangoro, F. Kremer and A. P. Sokolov "Ion transport and structural dynamics in homologous ammonium and phosphonium-based room temperature ionic liquids" The Journal of Chemical Physics 142, 084501 (2015) DOI: 10.1063/1.4913239

Neubauer, N., R. Winkler, M. Tress, P. Uhlmann, M. Reiche, W.K. Kipnusu, F. Kremer "Glassy dynamics of Poly(2-Vinyl-Pyridine) brushes with varying grafting density" Soft Matter 11, 3062–62015 (2015) DOI: 10.1039/C5SM00213C

Anton, A.M.,R. Steyrleuthner, W. Kossack, D. Neher, F. Kremer "Infrared transition moment orientational analysis (IR-TMOA) on the structural organization of the distinct molecular subunits in thin layers of a high mobility n-type copolymer" J Am Chem Soc., 137 (18), 6034–6043 (2015) DOI: 10.1021/jacs.5b01755

Kathrein C.C., W.K. Kipnusu, F. Kremer, A. Böker "Birefringence Analysis of the Effect of Electric Fields on the Order-Disorder Transition Temperature of Lamellae Forming Block Copolymers" Macromolecules 48, 3354-3359 (2015) DOI: 10.1021/acs.macromol.5b00512

Dünki, S.J., M. Tress, F. Kremer, S.Y. Ko, F.A. Nüesch, C.-D. Varganici, C. Raclesd, D.M. Opris "Fine-tuning of the dielectric properties of polysiloxanes by chemical modification" RSC Advances 5, 50054–50062 (2015) DOI: 10.1039/c5ra07412f

Kipnusu, W.K., M. Elsayed, W. Kossack, S. Pawlus, K. Adrjanowicz, M. Tress, E.U. Mapesa, R. Krause-Rehberg, K. Kaminski, F. Kremer "Confinement for More Space: A Larger Free Volume and Enhanced Glassy Dynamics of 2-Ethyl-1-hexanol in Nanopores" J Phys Chem Lett 6, 3708–3712 (2015) DOI: 10.1021/acs.jpclett.5b01533

Stangner T., S. Angioletti-Uberti, D. Knappe, D. Singer, C. Wagner, R. Hoffmann, F. Kremer "Epitope mapping of monoclonal antibody HPT-101: a study combining dynamic force spectroscopy, ELISA and molecular dynamics simulations" Phys Biol 12, 066018 (2015) DOI: 10.1088/1478-3975/12/6/066018

3.20 Graduations

Doctorate

- M. Sc. Wycliffe Kiprop Kipnusu
  Effects of Nanoscale Confinement on the Structure and Dynamics of Glass-forming Systems
- Dipl.-Phys. Tim Stangner
  Einzelmolekül-Kraftspektroskopie zur Untersuchung der Wechselwirkungen zwischen Tau-Peptiden und monoklonalen Antikörpern
- Dipl.-Phys. Wilhelm Kossack
  Infrared Transition Moment Orientational Analysis on polymeric systems

3.21 Guests

- Prof. Dr. Michael Vogel
  TU Darmstadt
  30. April 2015
- Prof. Dr. Bernd Stühn
  TU Darmstadt
  11. June 2015

4

Molecular Biophysics

4.1 Introduction

The Molecular Biophysics group moved in Mai 2015 to Leipzig and has meanwhile established its experimental work. The research of the Molecular Biophysics group aims at dissecting the mechanisms of biomolecular machines that are involved in genome processing and at understanding the interplay with the forces that compact their nucleic acids substrates. To this end the group develops and applies methods that allow studying such machines on the level of a single molecule. This involves force-based methods such as magnetic tweezers as well as fluorescence approaches in particular localization microscopy and Förster resonance energy transfer. Additionally the group uses gained knowledge about biological systems in order to build artificial mimics based on DNA nanostructures. This involves mimics of membrane proteins as well as the biomolecule templated synthesis of inorganic nanostructures. The following specific topics have been pursued in 2015:

- High-resolution magnetic tweezers based on GPU assisted particle tracking
- Combined force spectroscopy and single-molecule fluorescence approaches
- Target recognition by CRISPR-Cas enzymes
- Mechanisms of helicases motors that are involved in double-strand DNA break repair
- 1D diffusion of enzymes along DNA
- DNA nanostructures that mimic membrane protein functions
- DNA templated synthesis of complex metallic nanostructures

The group became part of the Collaborative Research Center (CRC) TRR 102 "Polymers under Multiple Contraints" that started its second funding phase in July 2015. Ralf Seidel was named as an investigator in the cluster of excellence "Center for Advancing Electronics Dresden" (cfaed, TU Dresden), where he is active in the Biomolecular Assembled Circuits path.

Ralf Seidel

4.2 Camera-based three-dimensional real-time particle tracking at kHz rates and Ångström accuracy

A. Huhle, D. Klaue, H. Brutzerl, P. Daldrop, S. Joo, O. Otto, O. Otto, U.F. Keyser, R. Seidel

In magnetic tweezers experiments single biomolecules are subjected to an external force by tethering them to a magnetic particle (bead) and applying a strong magnetic field gradient. The typical read-out parameter that is monitored is the length of the molecule. It is obtained by tracking the position of the magnetic particle in real-time in all three dimensions. To monitor smallest length changes on DNA (e.g. structural DNA rearrangements, movement of motor proteins along DNA) on the order of a single base pair - the fundamental building block of duplex DNA - we constructed high accuracy magnetic tweezers [1]. We introduced two improvements compared to previously used instruments: (i) an enhanced mechanical stability of the whole setup and (ii) the establishment of a high-speed GPU (graphics processing unit) accelerated bead tracking routine. The position of the beads in magnetic tweezers experiments is determined in all three dimensions from microscope images taken in overfocus. Using an illumination in transmission with a low numerical aperture the bead images exhibit diffraction rings. While from cross-correlations with a mirror image the bead positions in the imaging plane can be determined, the axial position is determined from the diffraction rings around the bead that become more expanded when the bead moves towards higher overfocus. Central part of the determination of the axial position is the calculation of a radial intensity profile with respect to the center of the bead. This process requires significant computational resources. So far we typically imaged beads with a CCD camera at 120 Hz, with which 1 nm bead position changes can be resolved in the axial direction. The limiting factor that prevents a better tracking accuracy is shot noise, i.e. the number of photons that are collected with each image. Thus, the only way to improve the tracking accuracy in a given time window is to increase the number of evaluated photons. Since the number of photons a single pixel can acquire is limited by the pixel well depth of the corresponding camera chip, more photons can only be evaluated by faster imaging and/or using an increased magnification of the microscope configuration with correspondingly brighter illumination. To do so we employed a CMOS camera that allows imaging at rates of several kHz and a fiber-coupled mercury arc lamp that provides sufficient light for high speed imaging. In order to allow real-time analysis of the massive acquired image data, the time-consuming radial intensity calculation was outsourced to a state-of-the art graphics card (GPU). The graphics card was programmed in Cuda C built into a DLL and integrated in the Labview-based tweezers operation software. The improved bead tracking methodology allowed us to perform real-time tracking of two beads (each imaged at 160x160 pixel resolution) in parallel at a frame rate of about 3 kHz (Fig. 4.1A). Though the tracking accuracy for a single image is still in the sub-nm range (about 0.2 nm RMS in lateral and 0.3 nm RMS in vertical direction), an accuracy in the 1 Å range was obtained for fixed particles at the time scale of 10 ms (comparable to the CCD tracking rate) . This way 3 Å position changes of a bead corresponding to the height of a single base pair could be conveniently resolved (Fig. 4.1A). This is currently the most precise real-time particle tracking based on imaging and (despite being much more simpler and robust in design) performs equally well as position-sensitive-device based particle tracking as applied

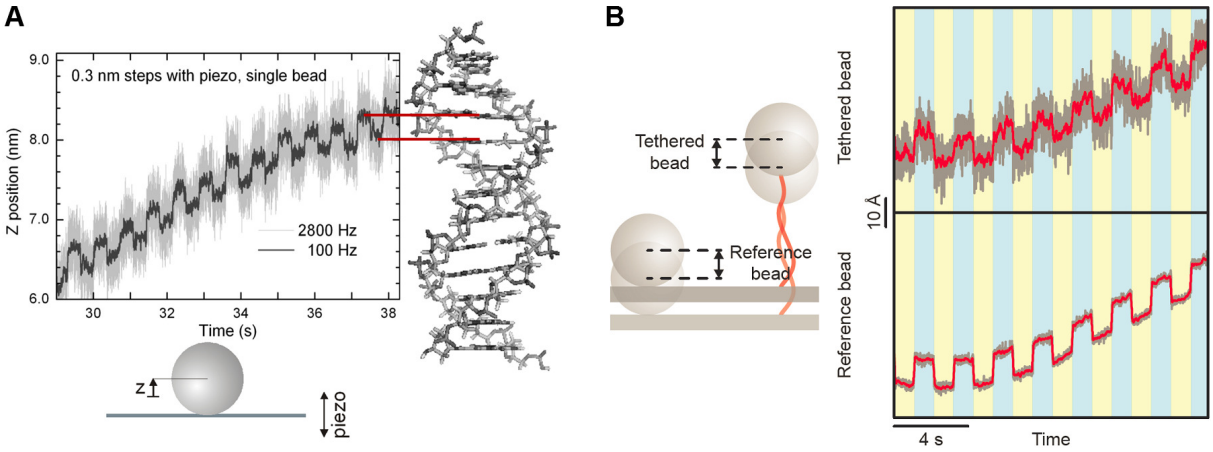

Figure 4.1: High resolution magnetic tweezers experiments. A) Tracking the position of a 3 μm polystyrene bead along the direction of the optical axis of the microscope composing the magnetic tweezers. The bead is fixed to the bottom cover slip of the used fluidic cell, which itself is mounted onto a high resolution piezo-electric nanopositiong stage. The stage is moved periodically up and down by 3 Å every 0.5 s. Data was taken at 2.8 kHz (light gray) and smoothed to 100 Hz (dark gray) using a sliding average. B) Parallel tracking the axial positions of a 1 μm magnetic bead that stretches a 700 nm long DNA molecule with a force of 12 pN (top) and a 3.2 μm polystyrene bead fixed at the bottom of the fluidic cell (lower). The piezoelectric stage moves the fluidic cell and thus the beads periodically up and down by 1 nm every 1 s.

in optical tweezers.

We also tested the tracking accuracy for DNA tethered magnetic beads being pulled in the magnetic tweezers. These beads are subjected to residual Brownian motion that is not suppressed by the stretching of the DNA. Thus for these beads a lower tempo-spatial resolution would be expected. For DNA tethered beads one can still resolve 1 nm steps with sub-second time resolution (Fig. 4.1B). Routinely we track the position of the magnetic bead always with respect to the position of a polystyrene bead that is fixed at the bottom of the fluidic cell. The latter bead serves as a reference that removes slow thermal instrument drift from the difference coordinate. Thus relative changes of the DNA length of only 1 nm can be determined over a long (> 100 s) time scale.

[1] A. Huhle, D. Klaue, H. Brutzer, P. Daldrop, S. Joo, O. Otto, U.F. Keyser, R. Seidel: Nat. Commun. **6**, 5885 (2015)

4.3 Extending the range for force calibration in magnetic tweezers

P. Daldrop, H. Brutzer, A. Huhle, D.J. Kauert, R. Seidel

Quantitative single-molecule mechanical measurements require precise knowledge of the applied forces. In magnetic tweezers experiments the fluctuations of a biomolecule-tethered magnetic bead perpendicular to the force direction are used to calibrate the applied magnetic force. In typical magnetic tweezers experiments the force acts in the

vertical direction along the optical axis of the microscope, while the actual magnetic field is oriented in the horizontal (further referred to as lateral) direction. Due to the attached biomolecule tether (e.g. DNA) the magnetic particle moves due to Brownian fluctuations in a pendulum geometry. However, the applied magnetic microbeads exhibit a magnetization anisotropy, such that they align themselves with their preferred axis to the magnetic field. This results in two different pendulum geometries (see sketches in Fig. 4.2a, b): For fluctuations along the magnetic field (further referred to as y-direction) the pendulum length equals the DNA length L due to the pinned bead orientation. In the horizontal direction perpendicular to the magnetic field lines (further referred to as x-direction) it equals the sum of L and the bead radius R, since the bead is free to rotate around its center axis in direction of the field.

When displacing the pendulum laterally along the short pendulum axis by a distance y, the back-driving force is given by $F_y = -F_{mag}/L \cdot y$. This expression is equivalent to the behavior of a Hookean spring with the spring constant $k_y = F_{mag}/L$. Using the equipartition theorem, one can write for the thermally induced mean square displacement of the pendulum: $1/2k_y\langle y^2\rangle = 1/2k_BT$, from which an expression for the acting magnetic force as function of the lateral bead fluctuations is obtained.

In practice, the magnetic force is not directly derived from the mean-square lateral displacement, but rather from the frequency spectrum of the displacement. The dynamics of a Hookean spring coupled to an element with viscous drag coefficient γ_y is described by a Lorentzian function for the power-spectral-density (PSD) with the characteristic cut-off frequency $f_c = k_y/(2\pi\gamma_y$. For force calibration, time trajectories are recorded and their PSD spectra are fitted with a modified single Lorentian that comprises corrections for acquisition artifacts of the bead position [1]. This provides k_y and γ_y and thus, respectively, also the applied force and the radius of the bead. For the short pendulum geometry, forces can be precisely calibrated using this methodology. Recent high-resolution magnetic tweezers experiments demand however the use of short DNA molecules (tether length shorter than bead radius), for which large cut-off frequencies can be obtained that may exceed the frequency of the bead position detection. At such conditions a reliable force calibration is impeded.

To overcome this limitation the long pendulum geometry may be used for calibration, at which lower cut-off frequencies would be obtained. We therefore tested whether correct forces would be obtained for this geometry. However, applying PSD fitting with a single Lorentzion in this direction provided a significant underestimation of the force and the bead radius (see Ref. [1] for data and full details). This behavior was supported by Brownian dynamics simulations, which modeled the motion of the translational motion in all three dimensions and the rotation of a bead attached to a tether. The difference between the short and the long pendulum geometry are the additional rotational fluctuations of the magnetic bead for the latter case. Using a set of two coupled Langevin equations we derived a theoretical expression for the PSD of the coupled translational and rotational motion of the bead in the long pendulum geometry. This provided a more complex PSD that consisted of a sum of two Lorentzians. The new function of the PSD for the long pendulum geometry provided now correct forces and bead radii for the experimental and the simulated data (Fig. 4.2b). Depending on the DNA length considerably larger forces could be calibrated with this method as compared to the short pendulum geometry. Furthermore, we demonstrated that also the absolute force accuracy was improved [1].

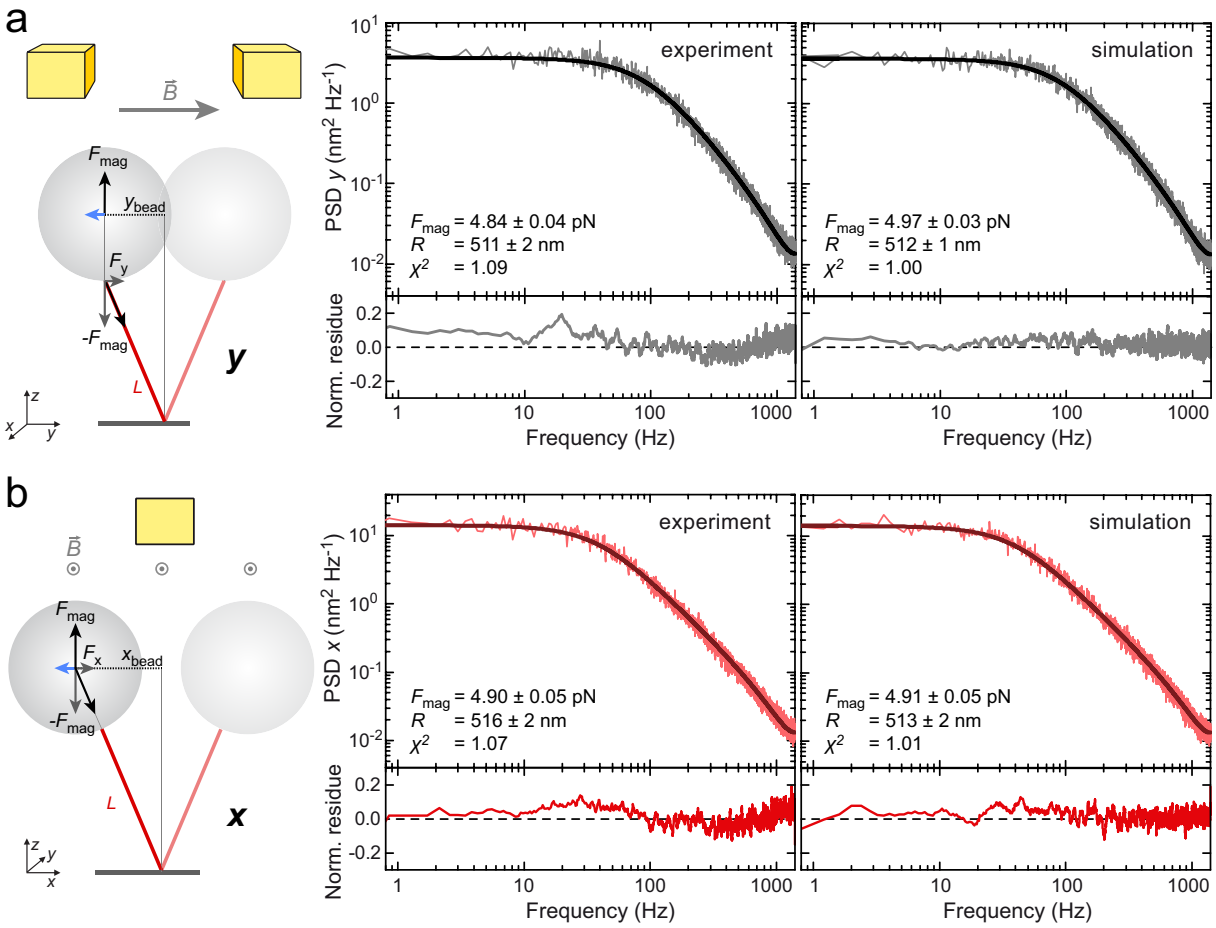

Figure 4.2: PSD analysis of the motion of a DNA attached magnetic particle. a) Short pendulum geometry. (left) Sketch of the lateral bead motion along the magnetic field lines, where the particle orientation is pinned. Results of the PSD analysis using the single-Lorentzian model are shown for experimental (middle) and simulated (right) data. The dark gray line represents the best fit to the data shown in light gray. Obtained fit parameters are given in the plot. b) Long pendulum geometry in which the particle is free to rotate. Sketch and plots are according to a. The data was fitted with the double-Lorentzian model. Figures were taken from Ref. [1].

[1] P. Daldrop, H. Brutzer, A. Huhle, D.J. Kauert, R. Seidel: Biophys J. **108**, 2550 (2015)

4.4 Combining magnetic tweezers and single-molecule fluorescence measurements

F.E. Kemmerich, D.J. Kauert, R. Seidel

We have devised and constructed a setup for a novel hybrid single-molecule technique-combining magnetic tweezers and Förster resonance energy transfer (FRET) measurements (Fig. 4.3. The magnetic tweezers consist of a pair of permanent magnets mounted on a translatable and rotatable stage that facilitates the application external forces and torques to biomolecules attached to a superparamagnetic sphere. Using the infrared

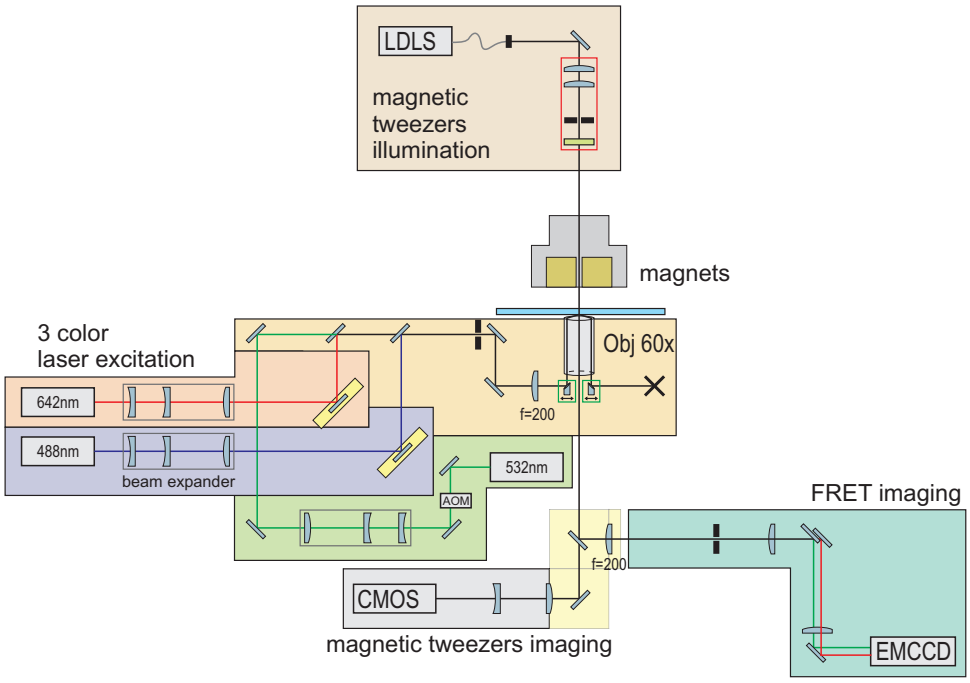

Figure 4.3: Schematics of the setup combining magnetic tweezers and single-molecule FRET detection.

portion of a laser driven light source (LDLS), the magnetic sphere is imaged in overfocus onto a CMOS camera. Applying our in-house developed tracking routines [1] to the live stream of bead images, it is possible to determine the position of the bead with nanometer precision in real time. In this way, for example the extension of stretched DNA incurred by the action of a DNA unwinding helicase can be followed.

FRET measurements allow determining the distance between a donor-acceptor fluorophore pair- either in absolute terms to determine an unknown length on a biomolecule of interest, or alternatively the dynamic variations of the relative separation between the fluorophores can be observed, in order to follow interconversion between conformational states. To achieve this 3 laser lines are coupled in through the objective with a tuneable exit angle that allows total internal reflection fluorescence (TIRF) conditions. The evanescent wave that emanates into sample excites donor fluorophores and depending on their separation distance, the donor and acceptor fluorophores fluoresce with varying relative intensities. Fluorescence emission is collected by the objective and separated from the magnetic tweezers illumination by a dichroic mirror, and then split into a donor and acceptor spectral region which are imaged as two channels onto the halves of an electron multiplying (EM-CCD) camera.

Spectrally splitting the magnetic tweezers (infrared) and fluorescence (visible region) in this way, allowed us to combine the two techniques into a single hybrid instrument. The two cameras can be operated in a triggered mode, which facilitates synchronization of the two data streams at any suitable choice of acquisition frame rates.

Therefore, it becomes possible to stretch or twist biomolecules while measuring their overall length response, and simultaneously to obtain additional orthogonal information about a length scale on the biomolecule defined by the position of the FRET

fluorophore pair. Thus the information content available from an experiment can be expanded. For example, tracking movements of individual motor proteins under force (e.g., DNA interacting motors) and correlating their trajectories with particular conformational states, could deepen our insight into the molecular mechanisms at play.

[1] A. Huhle, D. Klaue, H. Brutzer, P. Daldrop, S. Joo, O. Otto, U.F. Keyser, R. Seidel: Nat. Commun. **6**, 5885 (2015)

4.5 Directional zipping as target recognition mechanism by CRISPR-Cas enzymes

M. Rutkauskas, A. Krivoy, R. Seidel

Type I and Type II CRISPR-Cas systems are core elements of prokaryotic adaptive immunity and tools for the emerging genome editing and gene silencing technologies. Molecular recognition by these systems is achieved by directional base-pairing between the crRNA-component of a ribonucleoprotein surveillance/effector complexes and the corresponding target DNA. Base pairing causes local DNA untwisting and exclusion of the non-complementary strand, providing that a so-called R-loop structure is formed. Upon full base-pairing of the crRNA with the target DNA conformational changes within the surveillance effector complexes are triggered that cause downstream DNA degradation. We use single-molecule DNA twisting (supercoiling) experiments to investigate the recognition and verification of the target sequence for the Type IE surveillance complex Cascade from Streptococcus thermophilus. In these experiments, the local DNA untwisting during R-loop formation translates into a DNA length change (Fig. 4.4A). Full R-loop formation causes a single sudden DNA length increase on negatively supercoiled DNA. This changes in the presence of a single mutation (mismatch between the crRNA and the DNA sequence) in the middle of the target [1]. We observed the occurrence of intermediate R-loops which lengths correspond exactly to the distance of the mutation from the start of the target sequence. These intermediate R-loops are unstable (Fig. 4.4B) and also their stability directly correlates with their length (Fig. 4.4C). When a mismatch is eventually overcome, a full R-loop forms that becomes "locked" through conformational changes of the enzyme. These observations provide direct evidence for a directional R-loop zipping and suggest a dynamic target scanning of Cascade that is mediated through R-loop intermediates. Early encountered mutations challenge R-loop propagation and cause its collapse while distal mutations enable more stable and longer lived R-loops to overcome them. The target verification takes place exclusively at the end of the sequence when the full R-loop formation induces conformational changes that initiate DNA degradation. Such a dynamic and directional R-loop propagation scheme offers several advantages for the recognition of targets with sufficient complementarity: The complex spends little time on targets with low complementarity that from the beginning on carry mismatches. It nonetheless supports that point mutations can be tolerated thus precluding invading viruses to escape degradation by mutations in their genome.

[1] M. Rutkauskas, T. Sinkunas, I. Songailiene, M.S. Tikhomirova, V. Siksnys, R. Seidel: Cell Rep.**10**, 1534 (2015)

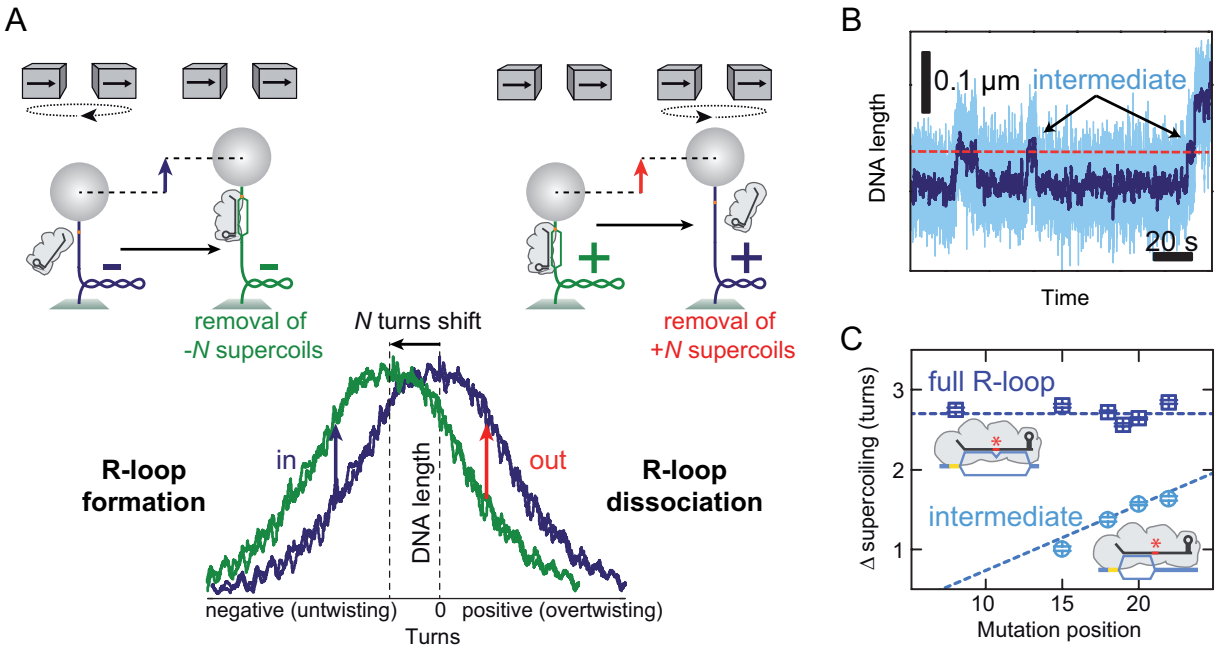

Figure 4.4: A) Using DNA supercoiling to detect target binding by CRISPR-Cas enzymes. R-loop formation causes local DNA unwinding and thus induces removal of negative supercoils on DNA. This can be observed as an abrupt increase of the DNA length (blue arrow) or as a shift of the characteristic rotation curve (black arrow). B) Time-trajectory of R-loop formation on the sequence containing single mismatch in the middle of the target sequence. Multiple intermediates form and collapse in between the R-loop initiation point and the mismatch. Finally the mismatch is overcome and a full R-loop forms. C) Change of supercoiling induced by R-loop formation on target sequences containing mismatches on different positions. Placing the mismatch further away from the R-loop initiation point causes a larger supercoiling change for intermediate R-loops. This provides evidence for a directional zipping of the R-loop.

4.6 Shape-Controlled Synthesis of Gold Nanostructures Using DNA Origami Molds

S. Helmi, R. Seidel

On the nanoscale fundamental properties and potential applications are greatly influenced by the size and shape of the material. We recently introduced a new concept that allows the synthesis of inorganic nanoparticles with programmable shape [1]. For this, we used a three dimensional DNA origami nanostructure with a programmable cavity as a "nanomold". A small gold nanoparticle (AuNP) was site-specifically anchored within the internal cavity of the mold and acts as a nucleation center for subsequent metal deposition leading to mold filling. This allowed the growth of the AuNP into a nanostructure in which its shape and size is controlled by the nanomold cavity. We demonstrated the concept by fabricating a 40 nm rod-like gold nanostructure with a quadratic cross-section. We also showed the metallization of higher order mold assemblies. Currently the mold-based synthesis scheme is further developed into a modular assembly scheme for inorganic nanostructures of complex shapes.

[1] S. Helmi, C. Ziegler, D.J. Kauert, R. Seidel: Nano Lett.**14**, 6693 (2014)

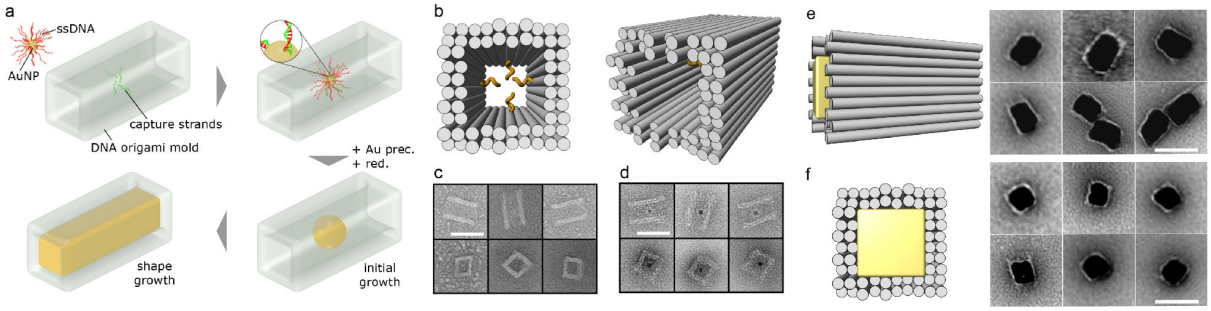

Figure 4.5: a) Scheme of the nanostructure synthesis. b) Cartoon of the DNA mold with capturing strands as orange spirals. c) TEM images of the mold. d) TEM images of the mold with bound gold nanoparticle seed. In c and d, the top and bottom rows show views onto a mold side wall and along the cavity axis, respectively. Gold nanoparticles grown within origami molds, e) TEM images of grown particles viewed from a side view, and (f) viewed along the cavity axis, as illustrated by the cartoon on the left. Scale bars correspond to 40 nm. Image was taken from Ref. [1]

4.7 Amphipathic DNA origami nanostructrures to scaffold and deform lipid membrane vesicles.

D.J. Kauert, R. Seidel

In this work a synthetic biology inspired approach was followed in which amphipathic DNA origami structures were engineered to become scaffolding tools for lipid membranes. DNA origami is a method that emerged in the past decade and allows to design and fabricate nanostructures from DNA in a programmable fashion. A long single stranded DNA ("scaffold") is joined with small oligos ("staples") each one hybridizing to different regions of the single strand, thus folding it into the desired shape. If those structures are modified with functional groups they can be applied in new, interesting ways.
Here block-like DNA origami structures were functionalized with cholesterol anchors at their bottom-side resulting in a flat lipid membrane-binding interface (Fig. 4.6a). Sticky oligonucleotide overhangs on their side facets enabled lateral interactions. By placing them at appropriate positions, the origami structures would arrange themselves into a planar brick wall-like superstructure (Figs. 4.6b, c). Incorporation of fluorescent labels on the top facet of the origami platform allowed to image the structures in confocal laser scanning microscopes as well as to carry out fluorescence (cross) correlation spectroscopy to characterize their tarnslation and rotational mobilities [2].
These multi-functional DNA origami platforms were able to attach to freestanding lipid membranes (giant unilaminar vesicles) through their cholesterol anchors. The lateral interactions between individual structures resulted in the formation of higher order planar assemblies. These superstructures proved to be rigid enough to deform (sculpture) the membranes they bound to (Fig. 4.6d, e). In contrast, control origami structures without sticky end-mediated interactions showed neither multimerizing nor membrane sculpting capabilities.
The tight and regular arrangement of the formed DNA origami structures capable of deforming freestanding lipid membranes represents a mimic of the biological activity

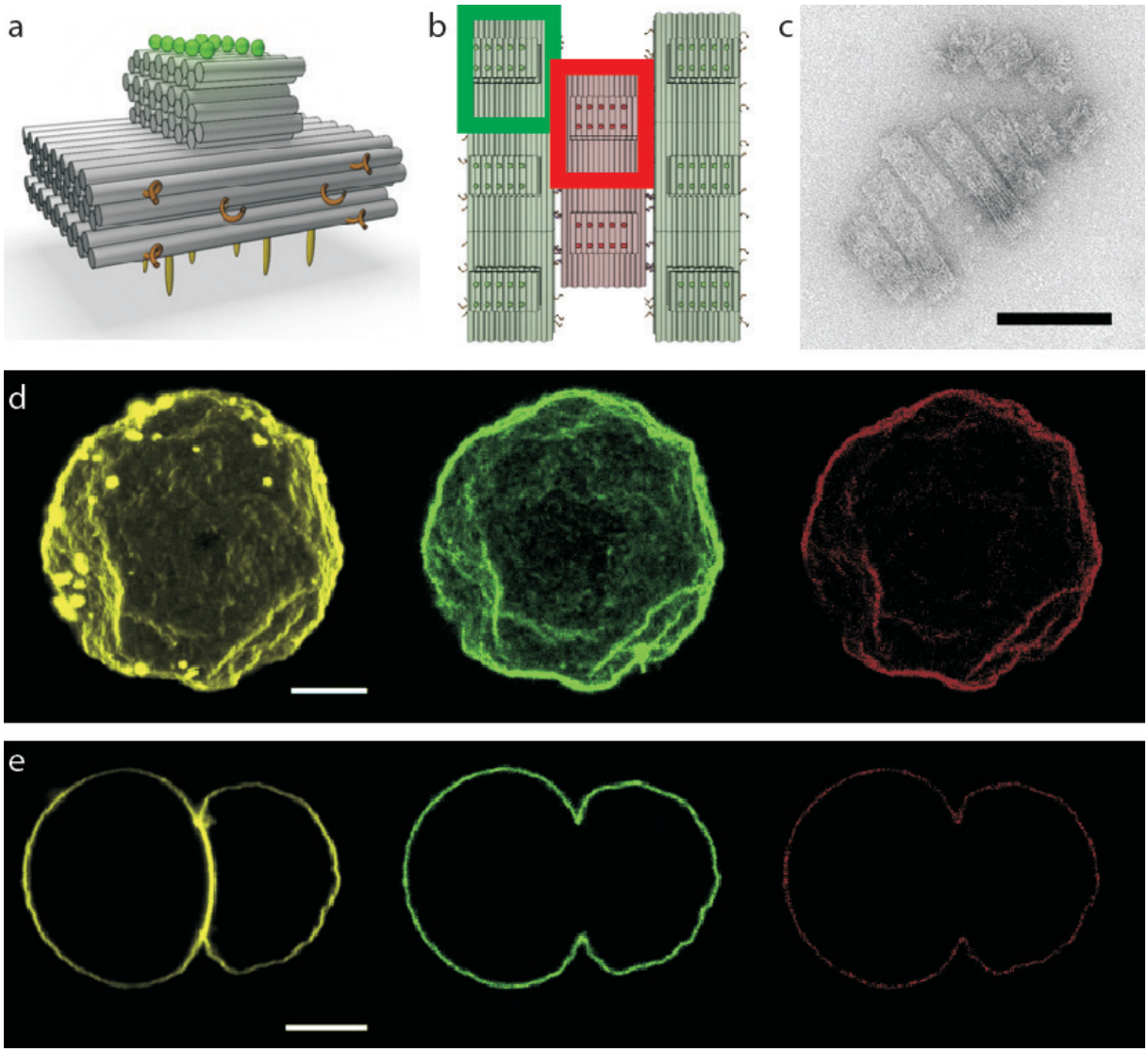

Figure 4.6: a) 3D representation of an origami monolith. Fluorophores are shown as green spheres, Sticky overhangs for multimerization are shown as orange helices. Cholesterol modifications are shown in yellow. b) multimerization scheme of the origami monoliths. The sticky ends were designed in a fashion so that a brick wall like superstructure, where each origami would bind to 4 neighbours, would form. c) TEM image of a formed superstructure. d, e) Deformed giant unilamellar vesicle due to origami superstructures in 3D (d, stacked planes) and 2D (e, single imaging plane) representations. Image was taken from Ref. [1]

of coat-forming proteins, e.g. from the I-/F-BAR family.[1]

[1] A. Czogalla, D.J. Kauert, H.G. Franquelim, V. Uzunova, Y. Zhang, R. Seidel, P. Schwille: Angew. Chem. Intl. Ed. **54**, 6501 (2015)
[2] A. Czogalla, D.J. Kauert, R. Seidel, P. Schwille, E.P. Petrov: Nano Lett. **15**, 649 (2015)

4.8 Funding

DNA based nanometry: Exploring chromatin structure and molecular motors
R. Seidel
ERC GA 261224

Preparation and self-assembly of noble metal nanoparticles with freely programmable shapes based on DNA origami molds
R. Seidel
DFG TRR 61, TP C8

Structure-function analysis of a molecular switch for long-range diffusion on DNA
R. Seidel together A. Aggarwal, Mt. Sinai School, New York, and M. Szczelkun, University of Bristol
NIH 1R01GM111507 - 01

Probing structural transitions of single-polymer chains with mechanical stress
R. Seidel
DFG TRR 102, TP B13

Static and Dynamic Properties of DNA-based Polymer Structures under Constraints and Confinement
R. Seidel in collaboration with M. Mertig (TU Dresden) and F. Cichos
DFG FOR 877, TP2, SE 1646/6-2

Long-range communication of Type III restriction enzymes between their cleavage sites based on ATP-triggered 1D diffusion
Ralf Seidel
DFG SE 1646/7-1

4.9 Organizational Duties

Ralf Seidel

- Board member of the Division of Physics in Life Sciences of the European Physical Society
- Manuscript reviewing for Nature, Cell, Science, eLife, Nat. Nanotech., Nat. Commun., Sci. Rep., ACS Nano, Biophys. J., Nucleic Acids Res., Nanoscale

4.10 External Cooperations

Academic

- Vilnius University (Lithuania)
  Prof. Dr. Virginijus Siknys
- Bristol University (UK)
  Prof. Dr. Mark Szczelkun

- Zurich University (Switzerland)
  Prof. Dr. Petr Cejka
- Skolkovo Institute of Technology (Russia)
  Prof. Dr. Konstantin Severinov
- Johns Hopkins University, Baltimore, MA
  Prof. Dr. Scott Bailey
- Max Planck Institute of Biochemistry, Martinsried
  Prof. Dr. Petra Schwille
- University of Wroclaw
  Dr. Aleksander Czogalla
- Cambridge University
  Prof. Dr. Ulrich Keyser
- Karlsruhe Institute of Technology
  Prof. Dr. Holger Puchta
- Technische Universität Dresden
  Prof. Dr. Yixin Zhang
- Technische Universität Dresden
  Dr. Michael Schlierf

4.11 Publications

Journals

P. Daldrop, H. Brutzer, A. Huhle, D.J. Kauert, R. Seidel: *Extending the range for force calibration in magnetic tweezers*, Biophys J. **108**, 2550 (2015)

M. Rutkauskas, T. Sinkunas, I. Songailiene, M.S. Tikhomirova, V. Siksnys, R. Seidel: *Directional R-Loop Formation by the CRISPR-Cas Surveillance Complex Cascade Provides Efficient Off-Target Site Rejection*, Cell Rep.**10**, 1534 (2015)

A. Czogalla, D.J. Kauert, H.G. Franquelim, V. Uzunova, Y. Zhang, R. Seidel, P. Schwille: *Amphipathic DNA Origami Nanoparticles to Scaffold and Deform Lipid Membrane Vesicles*, Angew. Chem. Intl. Ed. **54**, 6501 (2015)

A. Huhle, D. Klaue, H. Brutzer, P. Daldrop, S. Joo, O. Otto, U.F. Keyser, R. Seidel: *Camera-based three-dimensional real-time particle tracking at kHz rates and Ångström accuracy*, Nat. Commun. **6**, 5885 (2015)

A. Czogalla, D.J. Kauert, R. Seidel, P. Schwille, E.P. Petrov: *DNA origami nanoneedles on freestanding lipid membranes as a tool to observe isotropic-nematic transition in two dimensions.*, Nano Lett. **15**, 649 (2015)

H. Brutzer, E. Sperling, K. Günther, J. Dikic, F. Schwarz, D. Klaue, F. Cichos,M.Mertig, R. Seidel: *DNA under confinement and the use of DNA as confinement*, diffusionfundamentals.org **32**, 1-16 (2015)

Talks

R. Seidel: *Single-molecule insights into the target recognition by Type I CRISPR-Cas surveillance complexes*, Colloquium of SFB 1101, University Tübingen, 03. February 2015

M. Rutkauskas, T. Sinkunas, M. S. Tikhomirova, V. Siksnys, R. Seidel: *Dynamic DNA Target Proofreading in a CRISPR-Cas System*, Biophysical Society Meeting, Baltimore, USA, 07-11. February 2015

R. Seidel: *Single-molecule insights into the target recognition by Type I CRISPR-Cas surveillance complexes*, Colloquium of the Institute of Biochemistry, University Münster, 21. April 2015

R. Seidel: *Directional R-loop formation by the CRISPR-Cas surveillance complex Cascade provides efficient off-target site rejection*, CRISPR 2015, Rockefeller University, New York, USA, 18-20. June 2015

R. Seidel: *R-loop zipper mechanism for the CRISPR-Cas surveillance complex Cascade and control of downstream DNA degradation by the helicase/nuclease Cas3*, FASEB meeting on Helicases and nucleic acid translocases, Steamboat Springs, CO, 26.-31. July 2015

R. Seidel: *A genetic code for the synthesis of inorganic nanostructures with programmable shape*, Nanoscience seminar, Institute for Materials Science and Nanotechnology TU Dresden, 15. October 2015

R. Seidel: *Single-molecule nanomechanics*, Colloquium, IOM Leipzig, 05. November 2015

S. Helmi: *Controllable Synthesis of Gold Nanowires Using DNA Origami Molds*, DNA Mitteldeutschland workshop, Fraunhofer Institute IZI, 27. November 2015

S. Helmi: *Controllable Synthesis of Gold Nanowires Using DNA Origami Molds*, DNA nanotechnology meets plasmonics, Bad Honnef, 07. December 2015

R. Seidel: *Biomimetics with DNA origami*, Colloquium, Institute for Physical Chemistry, University Braunschweig, 01. December 2015

Posters

M. Rutkauskas, M. S. Tikhomirova, Ch. Rouillon, T. Sinkunas, V. Siksnys, R. Seidel: *Single-molecule analysis of R-loop formation by St-Cascade ribonucleorotein complex*, XIIIth Annual UK Workshop on Archaea, The University of Nottingham, Nottingham, UK, 08-09. January 2015

Felix E. Kemmerich, Peter Daldrop, Maryna Levikova, Petr Cejka, Ralf Seidel: *Force Regulated Association Dynamics of RPA on Forked DNA*, Biophysical Society 59th Annual Meeting, Baltimore, Maryland, USA. 7-11. February 2015.

S. Helmi: *Shape-controlled synthesis of gold nanostructures using DNA origami molds*, Symposium of the TRR61, University Münster, Münster, 17. April 2015

M. Rutkauskas, T. Sinkunas, V. Siksnys, R. Seidel: *Quantifying the fate of R-loop intermediates for the Type IE CRISPR-Cas surveillance complex Cascade*, CRISPR 2015, Rockefeller University, New York, USA, 18-20. June 2015

J. Dikic, J. Toth, M.D. Szczelkun, R. Seidel: *The influence of ATP on the long-range diffusion of EcoP15I along DNA*, 7th NEB Meeting, University of Gdansk, Poland, 24th-29th of August 2015, 1st poster prize

4.12 Graduations

N.A.

5

Soft Matter Physics

5.1 Introduction

The Soft Matter Physics group focuses on a quantitative understanding of biological cell phenotype and function from a complex, emerging materials perspective encompassing all length scales from molecules to tissues, which places us in a pioneering and leading position in the novel area Physics of Cancer.

As illustrated in our article "Emergent complexity of the cytoskeleton: from single filaments to tissues", which is among the most read papers in Advances in Physics (IF 20.833) every year, the emphasis of our group is on the material properties of biological cells as key determinants of their character and functions, including tumor progression. This requires an integral approach that spans the length scales from molecules to tissues. For this research our group is uniquely positioned by the ability to concurrently purify cytoskeletal proteins and have access to clinical tissue samples.

The primary objective is to investigate the physical mechanisms which are responsible for the observed active and passive behavior of biological soft matter. In this context we focuse on the study of mechanical properties and behavior of biological cells and as well as polymer networks.

The function of biological cells is investigated from nanometer to macroscopic length scales in order to understand the forces and underlying mechanisms which are required for cell motion and functions such as proliferation. Moreover, we want to know, how and to what extent cellular mechanisms can change during malignant transformation and how these changes can be described from a physical perspective.

Mechanical and material properties of cells such as differential adhesion and contractility, cell stiffness and crowding, differences in cell motility, and differences in extracellular matrix confinement have joined genetic factors and signal transduction as critical to the process of cancer cell escape. Cancer cells, escaped from the tumor to the surrounding microenvironment, generate a mechanical footprint that can be detected by analyzing the regional changes in elastic and viscous properties between tumor core and peripheral regions. Combining quantitative ideas and tools from theoretical physics with a unique set of cutting-edge experimental techniques, the group's work aims at the combination of Soft Matter Physics, Biophotonics and Medical Physics with a redefining impact on medical diagnosis and therapy.

This could bring new perspectives to cancer research and trigger efforts to begin to understand the potential physical underpinnings of cancer. In addition to the enorm-

ously complex molecular networks required for the functioning of normal cells, tumors have an inherently high molecular diversity due to the stochastic nature of the mutations that cause cancer. Moreover, all cells in a tissue can be motile and are viscous on long time scales, behaving very much like a liquid droplet. Consequentially, tissue boundaries are comparable to fluid boundaries and can be described as a new form of fluid matter, which is a significant topic in the novel research area of active soft matter physics.

Josef A. Käs

5.2 Formation of regularly spaced networks as a general feature of actin bundle condensation by entropic forces

F. Huber [*], D. Strehle[†], J. Schnauß, J.A. Käs

[*]FOM Institute AMOLF, Amsterdam
[†]Université de Bordeaux, Institut d'Optique, LP2N

Networks of biopolymers are responsible for the mechanical integrity and functional organization of cellular systems [1]. An omnipresent biopolymer is the protein actin, which forms a large variety of network architectures, ranging from isotropic networks to anisotropic bundles [1]. The network shape is directly linked to cell mechanics and is essential for according physiological functions. A comprehensive understanding of architecture-determining mechanisms and their physical constraints remains elusive. We employed a novel experimental approach based on evaporation to study the formation of confined actin networks by entropic forces.

Molecular crowding as well as counterion condensation were used to form networks of actin bundles without crosslinking proteins. Our study revealed a generic tendency of homogeneous filament solutions to aggregate into regular actin bundle networks connected by aster-like centers which was formerly attributed to dissipative processes [2, 3]. Although starting from identical biochemical compositions, arising network architectures were highly diverse. We were able to decouple various parameters and found that the evolving architecture crucially depends on the network formation history. Drastic changes in network architecture were observed as a consequence of initially biased filament orientation or mixing-induced perturbations [2]. These findings suggest that the formation of regularly spaced bundle networks is a rather general feature of solutions of isotopically distributed filaments subject to attractive potentials [2, 3]. Although arising patterns do not develop a long-range order (no order parameter), they displayed an increased probability for finding a next-neighbor in a distance of about 5-10 μm (Figure 5.1). Due to the fundamental nature of the considered interactions, we expect that the investigated type of network formation further implies severe physical constraints for cytoskeleton self-organization on the more complex level of living cells.

[1] F. Huber et al.: Adv. in Physics **2013** 62(1), 1 -112
[2] F. Huber et al.: New Journal of Physics **2015** 17, 043029
[3] J. Schnauß et al.: Diffusion Fundamentals **2015** 23, 1 -15

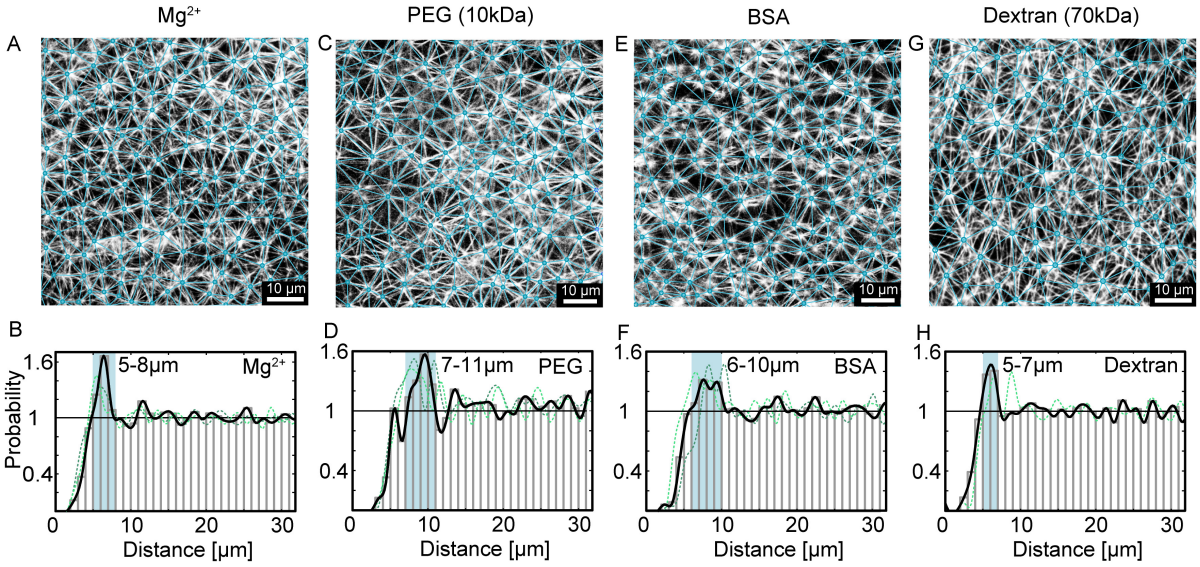

Figure 5.1: Top row: aster-based actin networks induced by Mg2+ ions or various crowding agents (PEG 10 kDa, BSA, dextran 70 kDa) with detected aster centers and bundle contours. **Bottom row:** detected center points were used to derive the radial distribution function for all four networks, which display an increased probability for finding a next-neighbor in a distance of about 5-10 μm. Green curves were derived from networks formed under identical conditions to illustrate the variability of the network structure and spacing. Taken from [2].

5.3 Cell membrane softening in human breast and cervical cancer cells

C. Händel, B.U.S. Schmidt, J. Schiller*, U. Dietrich, T. Möhn, T.R. Kießling, S. Pawlizak, A.W. Fritsch, L.-C. Horn†, S. Briest‡, M. Höckel‡, M. Zink, J.A. Käs

*Medical Faculty, Institute of Medical Physics and Biophysics
†Division of Breast, Urogenital and Perinatal Pathology, Institute of Pathology
‡Department of Obstetrics and Gynecology, University Hospital Leipzig

Biomechanical properties are key to many cellular functions such as cell division and cell motility and thus are crucial in the development and understanding of several diseases, for instance cancer. The mechanics of the cellular cytoskeleton have been extensively characterized in cells and artificial systems. The rigidity of the plasma membrane, with the exception of red blood cells [1], is unknown and membrane rigidity measurements only exist for vesicles composed of a few synthetic lipids [2]. In this study, thermal fluctuations of giant plasma membrane vesicles (GPMVs) directly derived from the plasma membranes of primary breast and cervical cells, as well as breast cell lines, are analyzed. Cell blebs or GPMVs were studied via thermal membrane fluctuations and mass spectrometry. It is shown that cancer cell membranes are significantly softer than their non-malignant counterparts. Figure 5.2 (a) and (b) show representative measurements of the bending rigidity from cell membranes of primary breast and cervical cells. For primary breast cancer cells we found a significantly increased number of GPMVs with lower bending rigidities in contrast to GPMVs obtained from healthy tissue. This result could be confirmed by measurements at cell lines. As

reference, the bending rigidities of GPMVs of non-malignant MCF-10A and malignant MDA-MB-231 breast epithelial cells were also determined and are shown in figure 5.2 (c).

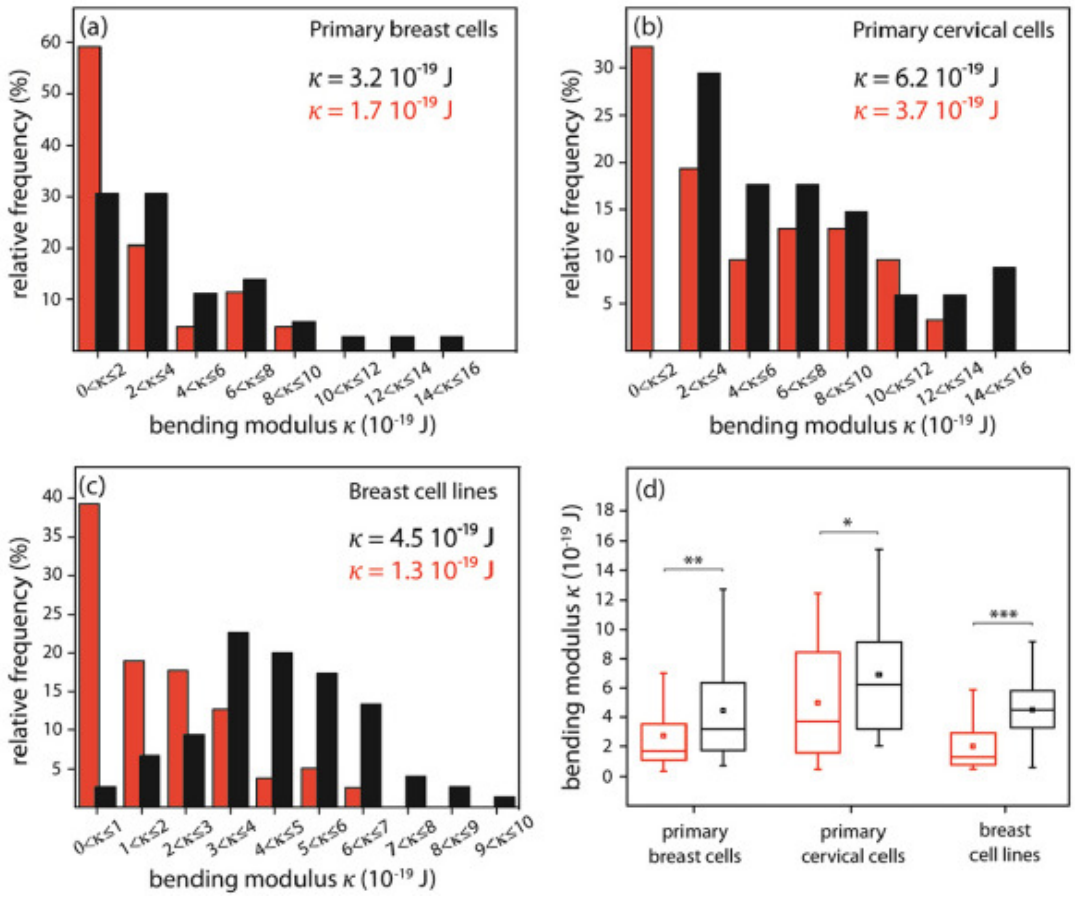

Figure 5.2: Biomechanical behaviour of human carcinoma cell membranes (red) in contrast to membranes obtained from nonmalignant cells (black). Distribution of bending elastic moduli κ of GPMVs obtained from (a) primary breast epithelial cells, (b) primary cervical epithelial cells and (c) breast epithelial cell lines MDA-MB-231 and MCF-10A. (d) Boxplots of bending elastic moduli κ of GPMVs obtained from primary cells and cell lines displaying upper quartile, median, mean value, lower quartile, and a 10% to 90% whisker range (Mann-Whitney *U* test, * $p < 0.05$, ** $p < 0.01$, *** $p < 0.001$).

In order to investigate possible changes of the membrane (phospho)lipid compositions in cancer cells, compared to their non-malignant counterparts, positive ion MALDI-TOF (matrix-assisted laser desorption and ionization time-of-flight) mass spectrometry was employed to investigate the (bio)chemical compositions of all samples in more detail [3]. Two significant differences could be unequivocally monitored. First, a decreased level of sphingomyelin (SM 16:0) in primary cancer cells was observed in contrast to normal ones. Secondly, the proportion of phosphatidylcholines (PC) with shorter, more saturated fatty acyl chains (oleoyl (18:1) in comparison to arachidonoyl (20:4) in malignant cells increases, compared to non-malignant cells (figure 5.3).Thus, the mass spectrometric measurements show two molecular reasons for softening in malignant cell membranes: a decreased level of SM 16:0 and an increased level of PCs with shorter acyl chains. Thus both, chain lengths and SM content, result in a more

bendable membrane. These results indicate that the reduction of membrane rigidity promotes aggressive blebbing motion in invasive cancer cells.

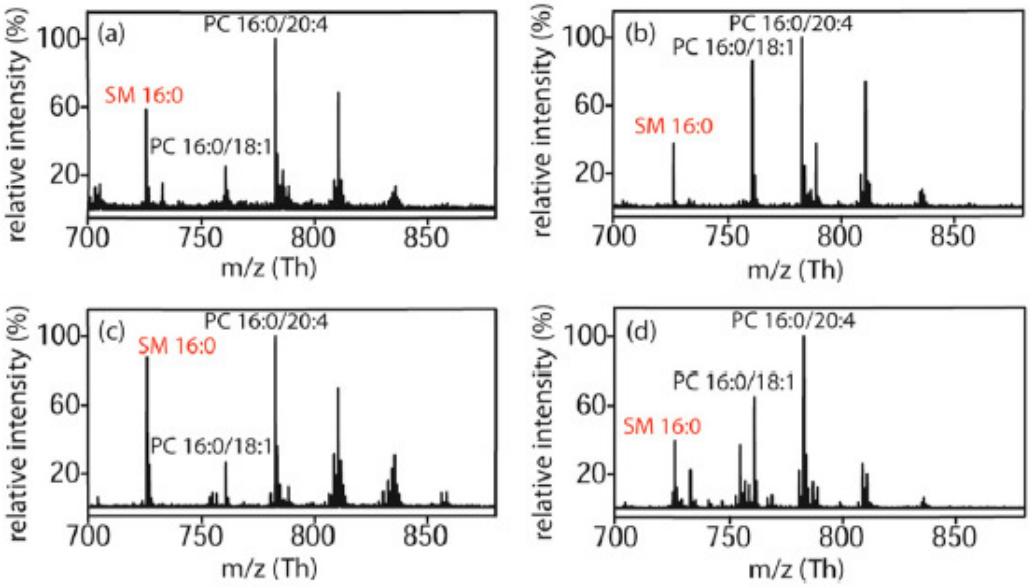

Figure 5.3: Positive ion MALDI-TOF mass spectra of primary cells. Spectra show the mass ranges of most common phospholipids such as phosphatidylcholines (PC 16:0/18:1 and PC 16:0/20:4) as well as sphingomyelin (SM 16:0). The mass spectra of (a) normal primary mammary cells and (b) primary mammary carcinoma cells were obtained from the same patient. Mass spectra of (c) normal primary cervical cells and (d) primary cervical carcinoma cells.

[1] Betz T et al.: PNAS **2009** 106, 15320-15325
[2] Gracià RS et al.: Soft Matter **2010**, 6, 1472-1482
[3] Fuchs B et al.: Prog Lipid Res **2010**, 49(4), 450-475

New Journal of Physics 17(2015)083008

5.4 Pharmacological targeting of membrane rigidity: implications on cancer cell migration and invasion

S. Braig*, B.U.S. Schmidt, K. Stoiber*, C. Händel, T. Möhn, O. Werz†, R. Müller‡, S. Zahler*, A. Koeberle†, J.A. Käs, A. Vollmer*

*Dept. of Pharmacy, Center for Drug Research, Ludwig Maximilians University, Munich
†Institute of Pharmacy, University Jena
‡Helmholtz Institute for Pharmaceutical Research Saarland, Saarland University

The invasive potential of cancer cells strongly depends on cellular stiffness, a physical quantity that is not only regulated by the mechanical impact of the cytoskeleton but also influenced by the membrane rigidity. To analyze the specific role of membrane rigidity in cancer progression, we treated cancer cells with the Acetyl-CoA carboxylase

inhibitor Soraphen A and revealed an alteration of the phospholipidome via mass spectrometry.

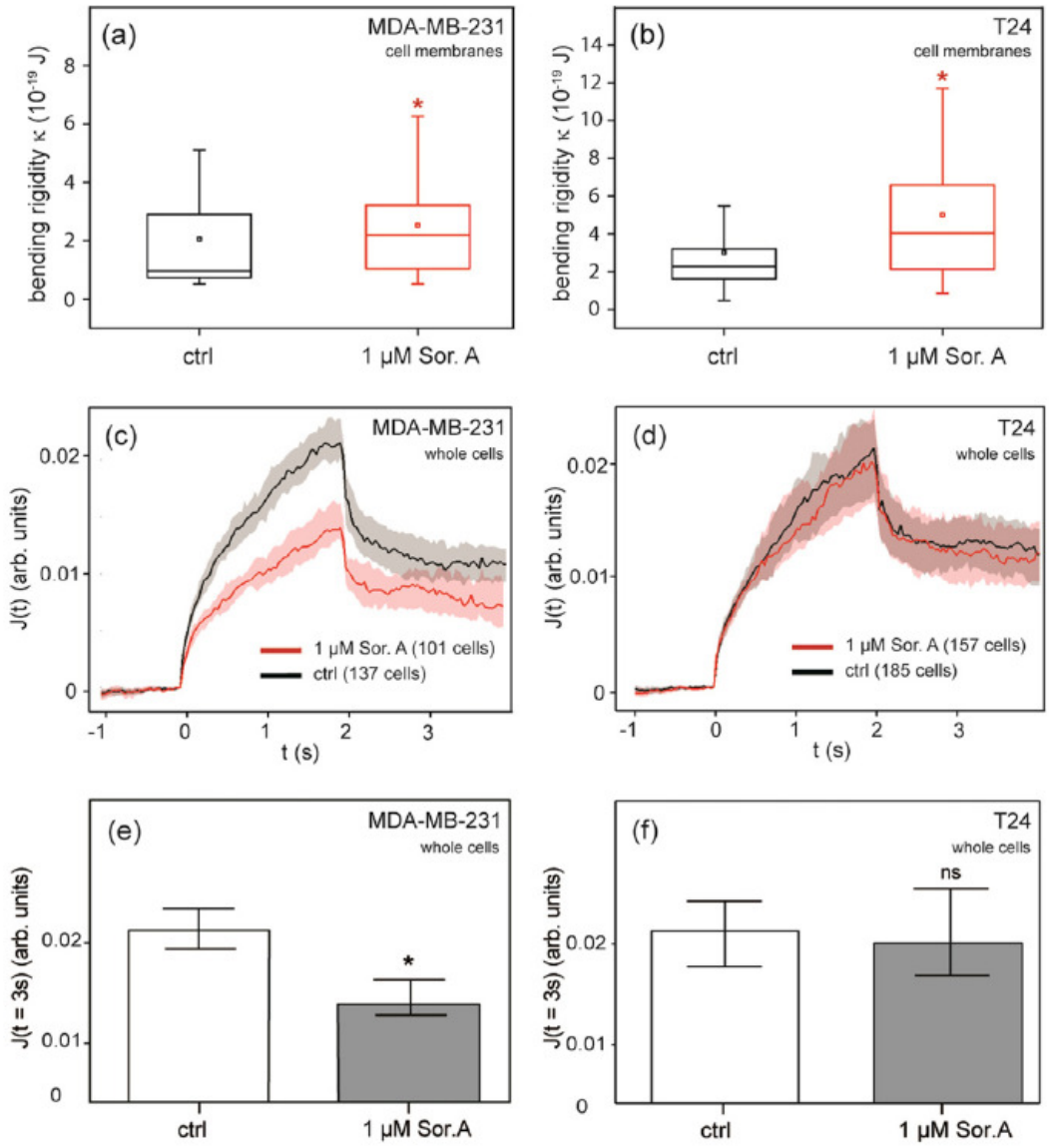

Figure 5.4: Biomechanical behavior of human carcinoma cells and their plasma membranes after Soraphen A treatment. Boxplots of bending elastic moduli κ of cell membranes (GPMVs) obtained from the mammary carcinoma cell line MDA-MB-231 (a) and the bladder carcinoma cell line T24 (b). Both show the impact of 1 μMSoraphen A on cell membrane rigidity, displaying upper quartile, median, mean value, lower quartile and a 10-90% whisker range for κ (Kolmogorov-Smirnov test, * $p < 0.05$). Median relative deformation of whole MDA-MB-231 cells (c) and T24 cells (d) in optical stretcher measurements plotted over time with 800 mW stretch phase from 0 to 2 s. (e), (f) Comparison of optical stretcher measurements at the end of the stretch phase (Kolmogorov-Smirnov test, * $p < 0.05$, ns: not significant).

It could be shown that Soraphen A (as an ACC1 inhibitor) changes the phospholipid composition towards a higher chain length and polyunsaturated lipid species. Further, Soraphen A hinders cancer cell migration as well as invasion and alters the mechanical properties of the plasma membrane. To distinguish influences of cytoskeleton and

plasma membrane on mechanical properties, optical stretcher measurements of whole cells were performed in addition to fluctuation assays of GPMVs (see figure 5.4).

This allowed an interpretation regarding the role of membranes in the context of migration. Migration, invasion, and cell death assays were employed to relate this alteration to functional consequences, and a decrease of migration and invasion without significant impact on cell death has been recorded (see figure 5.5). Fourier fluctuation analysis of giant plasma membrane vesicles showed that Soraphen A increases membrane rigidity of carcinoma cell membranes. The modulation of membrane rigidity and cell stiffness with the chemical compound Soraphen A allowed us to investigate these important mechanical features with respect to migration and invasion. These results point to the important role of membrane rigidity in migratory processes, even with unaffected cell stiffness, and suggest that membrane rigidity is more closely related to cancer progression than previously assumed [1]. Thus, targeting membrane features of cancer cells offers new therapeutic perspectives in membrane research and possibly cancer biology.

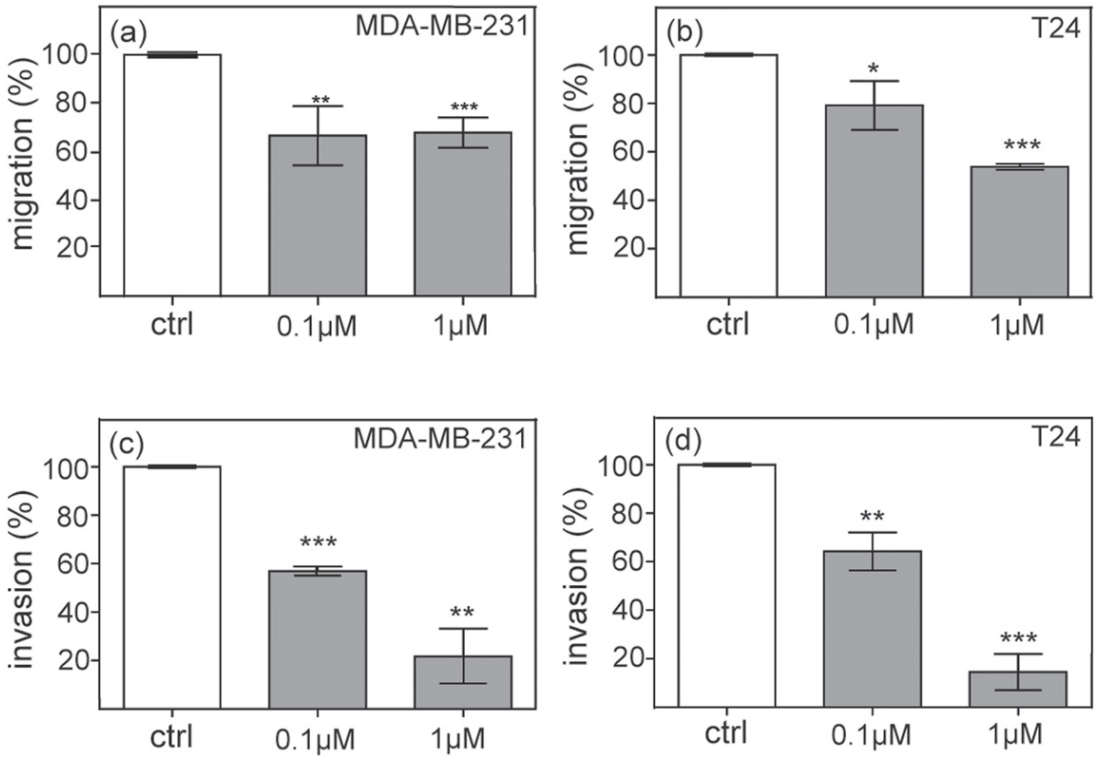

Figure 5.5: Effect of Soraphen A on migration and invasion. Cells were treated with increasing Soraphen A concentrations for 2 h. Migration of (a) MDA-MB-231 and (b) T24 cells was analyzed by a Boyden chamber migration assay. To analyze invasion of cells a modified Boyden chamber assay for (c) MDA-MB-231 and (d) T24 cells was performed. (* $p < 0.05$, ** $p < 0.01$, *** $p < 0.001$.)

[1] Huber F et al.: Adv Phys **2013**, 1, 1-112

5.5 Contractile cell forces deform macroscopic cantilevers and quantify biomaterial performance

U. Allenstein, S.G. Mayr*, M. Zink

*Leibniz-Institut für Oberflächenmodifizierung, Translationszentrum für Regenerative Medizin

Cells require adhesion to survive, proliferate and migrate, as well as for wound healing and many other functions. The strength of contractile cell forces on an underlying surface is a highly relevant quantity to measure the affinity of cells to a rigid surface with and without coating. By employing a self-designed setup, we show that these forces create surface stresses that are sufficient to induce measurable bending of macroscopic cantilevers [1]. In detail, a titanium cantilever with and without coatings was employed as substrate for NIH 3T3 fibroblast cells (Figure 5.6). Prior to measurements, cells were seeded onto the cantilever and adhered, which results in a stress acting onto the cantilever. The resulting cantilever bending was determined with a laser beam reflected on the cantilever's bottom and monitored with a position sensitive detector (PSD). Subsequently, trypsin was added to the cells to detach them. As a result, contractile cell forces were not acting on the cantilever anymore and it relaxed to its initial without cells. For quantitative analysis, we performed finite element simulations on the beam bending to back up the calculation of contractile forces from cantilever bending under non-homogenous surface stress.

In our study *in vitro* fibroblast adhesion on the magnetic shape memory alloy Fe-Pd and on the L-lysine derived plasma-functionalized polymer PPLL was determined. We show that cells on Fe-Pd are able to induce surface stresses three times as high as on pure titanium cantilevers. A further increase was observed for PPLL, where the contractile forces are four times higher than on the titanium reference. Our findings consolidate the role of contractile forces as a meaningful measure of biomaterial performance

[1] U. Allenstein et al.: Soft Matter **2015** 11(25), 5053-5059

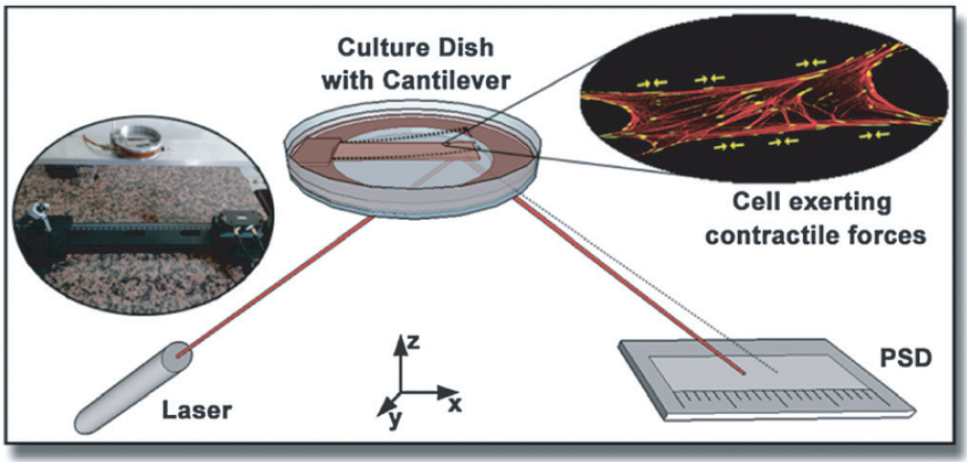

Figure 5.6: Schematic and inset photograph of the bending beam setup to measure the deflection of a cantilever exposed to contractile forces of living cells. The change in position of a laser beam deflected on the bended beam is measured with a position sensitive detector.

5.6 Complex thermorheology of living cells

S. Schmidt, T. Kießling, E. Warmt, A. Fritsch, R. Stange, J.A. Käs

Temperature has a reliable and nearly instantaneous influence on mechanical responses of cells. As recently published [1], MCF-10A normal epithelial breast cells follow the time-temperature superposition (TTS) principle. In 2015, we investigated these feature in more detail and measured thermorheological behavior of eight common cell types within physiologically relevant temperatures and applied TTS to creep compliance curves.

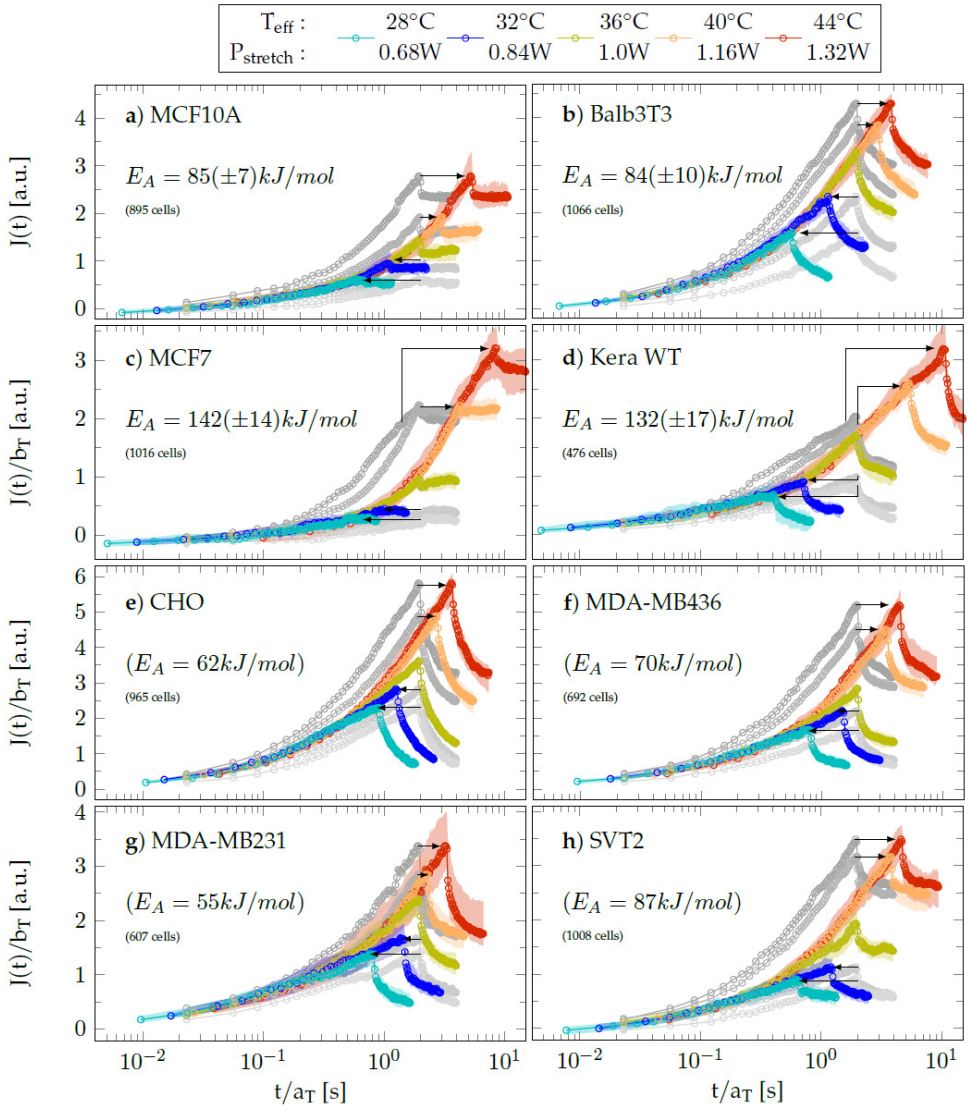

Figure 5.7: Different cell lines show different thermorheological behavior. Only cell lines (a) MCF10 breast epithelial and (b) Balb3T3 mouse fibroblasts behave thermorheologically simple. Cells in (c) MCF7 breast tumor cell line and (d) Mouse keratinocytes superpose only by additional scaling via bT classified as thermorheologically complex. Cells (e)-(h) Chinese hamster ovarian, MDA-MB231 breast tumor cell line, MDA-MB431 breast tumor cell line and SVT2 transformed mouse cell line cannot be scaled to overlap on a single curve.

Our results showed that superposition is not universal and was seen in four of the eight investigated cell types. For the other cell types, transitions of thermorheological responses were observed at 36°C. Activation energies (presenting the sensitivity of cell deformability concerning temperature changes) were calculated for all cell types and ranged between 50 and 150 kJ/mol. The scaling factors of the superposition of superposition of creep curves were used to group the cell lines into three categories. They were dependent on relaxation processes as well as structural composition of the cells in response to mechanical load and temperature increase. This study supports the view that temperature is a vital parameter for comparing cell rheological data and should be precisely controlled when designing experiments.

[1] T. Kießling et al.: New Journal of Physics **2013** 15(4), 383-394

New Journal of Physics 17(2015)073010

5.7 Testing the differential adhesion hypothesis across the epithelial-mesenchymal transition

S. Pawlizak, A. Fritsch, S. Grosser, D. Ahrens, T. Thalheim, S. Riedel, T. Kießling, L. Oswald, M. Zink, M.L. Manning*, J.A. Käs

*Syracuse University, Dept. of Physics, Syracuse, U.S.A.

The spatial segregation of different cell populations in distinct compartments and the formation of well-defined lineage boundaries in-between is a fundamental process during the embryonic development. While normal cells will, in general, never cross these boundaries, metastatic cancer cells undergoing an epithelial-mesenchymal transition (EMT) may eventually acquire the ability to do so. To evaluate the role of cell cohesion in cell sorting and compartmentalization across the EMT, we analyzed the mechanical properties of three cell lines (MCF-10A, MDA-MB-231, MDA-MB-436) exhibiting a shift in E-, N- and P-cadherin levels characteristic of an EMT.

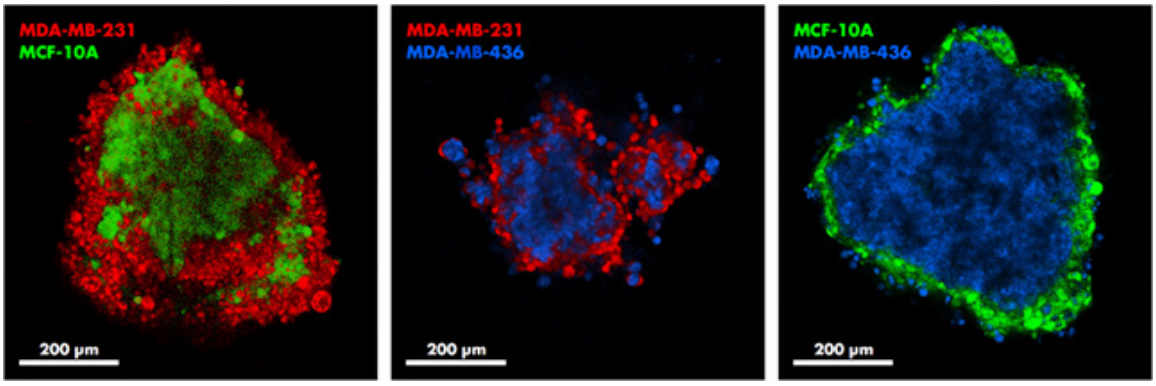

Figure 5.8: The segregation experiments show a clear sorting hierarchy. MDA-MB-231 cells (red) envelop MCF-10A (green) which in turn envelop MDA-MB-436 (blue). Hence, according to the DAH, we would expect MDA-MB-436 to have the highest adhesiveness and MDA-MB-231 to have the lowest.

We applied a diverse set of methods to measure cell-cell adhesiveness, cell stiffness, and cell shapes, and compared the results to predictions from cell sorting in mixtures of cell populations. Although the final sorted state was extremely robust among all three cell lines (see figure 5.8), suggesting that cell sorting may play an important role in organization and boundary formation in tumors, we surprisingly found that the differential adhesion hypothesis (DAH) does not correctly predict the final sorted state. Surface densities of adhesive molecules did not correlate with measured cell-cell adhesion, but did correlate with cell shapes, cell stiffness, and the rate at which cells sort, in accordance with an extended version of the DAH. However, neither of these measures correlated with the final sorted state (see figure 5.9). This mismatch suggests that these tissues do not behave like immiscible fluids, and that dynamical effects such as directional motility, friction, and jamming may play a much more important role in tissue compartmentalization than previously expected.

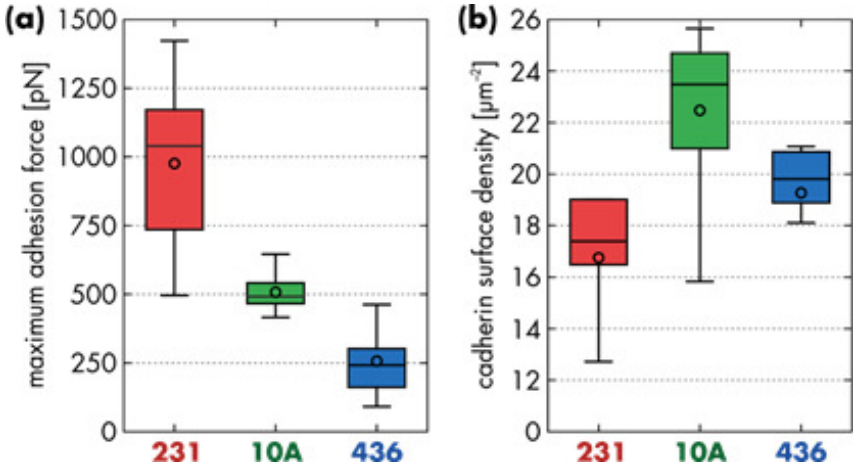

Figure 5.9: (a) Maximum adhesiveness estimated from AFM-based cell-cell separation experiments. (b) surface density of cadherins (which are the molecular origin of cellular adhesion) estimated via image analysis of super-resolution STED images. Both results contradict the adhesiveness expected from the segregation experiments (see figure 5.8).

New Journal of Physics 17(2015)083049

5.8 Liquid-like and Solid-like Behaviour of Breast Cancer Cell Lines in 3D Aggregates

L. Oswald, S. Grosser, S. Pawlizak, A.W. Fritsch, J.A. Käs

Three-dimensional aggregates of biological cells become increasingly relevant in research as they resemble *in vivo* situations much closer than two-dimensional assays. These tissue models are usually described by viscous liquid theories on long time scales [1]. Recent experiments on 3D segregation of breast cancer cell lines questioned this approach. Based on this finding, we create aggregates of MCF-10A, MDA-MB-436, which form compact spheroids, and of MDA-MB-231 cells, forming loose aggregates only. We

perform fusion experiments (see Fig. 5.10) of the spheroids allowing to assess the ratio of tissue surface tension to viscosity.

While MDA-MB-436 spheroids fuse mainly as expected from the viscous liquid theory, MCF-10A spheroids show a rich diversity in fusion behaviour, such as changing rearrangement velocities (see Fig. 5.11) and complete fusion arrest accompanied by superficial morphological changes. The rearrangement velocity is proportional to the ratio of surface tension and viscosity, which is time-independent for Newtonian liquids. The fusion arrest (see Fig. 5.10, upper panel), reminiscent of a jammed state, suggests that the fusion process is no longer governed by surface tension, as the spheroids do not end up with a minimal surface area. Thus, changing rearrangement velocity and fusion arrest both suggest non-Newtonian behaviour.

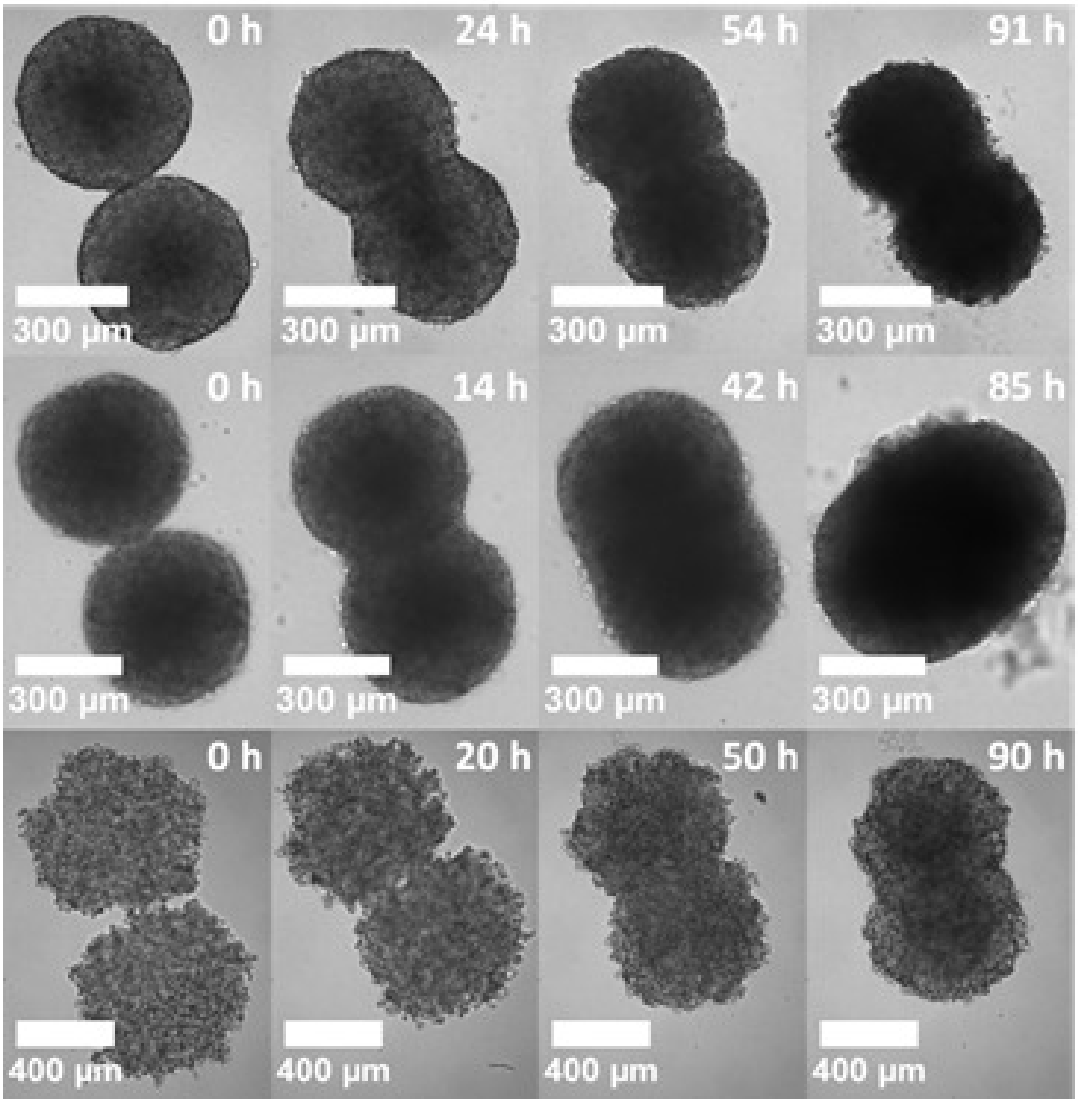

Figure 5.10: Brightfield images of the fusion process of multicellular aggregates of MCF-10A (upper panel, 10000 seeded cells each), MDA-MB-436 (middle panel, 5000 seeded cells each) and MDA-MB-231 (lower panel, 5000 seeded cells each) cells depending on time. The fusion process was started after two days of growth time.

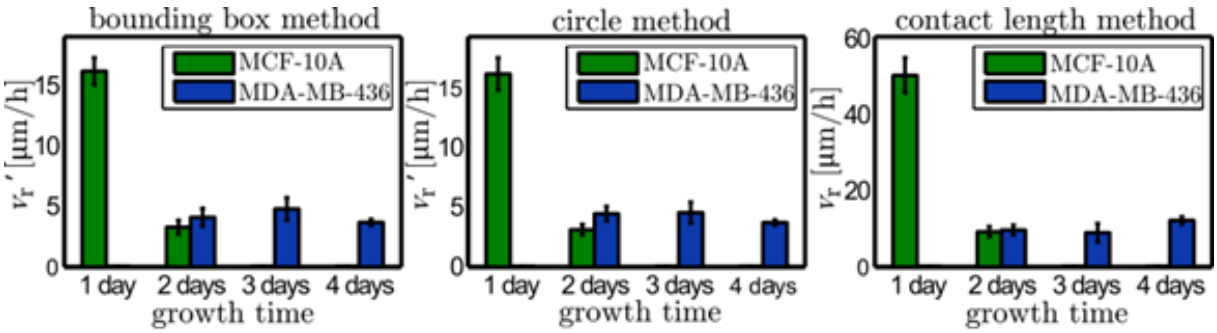

Figure 5.11: Rearrangement velocity v_r' and v_r depending on growth time for MCF-10A and MDA-MB-436 aggregate fusion. Error bars indicate 95% confidence interval. All three analysis methods show a similar behaviour. The rearrangement velocity of MDA-MB-436 aggregates stays nearly constant with increasing growth time, while that of MCF-10A aggregates decreases.

[1] Flenner E et al.: Phys. Rev. E **2012** 85, 031907

5.9 Neuronal and metastatic cancer cells: Unlike brothers

P. Heine, A. Ehrlicher*, J.A. Käs

*Dept. of Bioengineering, McGill University, Montreal, Canada

Even though neuronal and cancer cells have quite different purposes in the body, both must traverse substantial distances in the body. During development neuronal cells traverse substantial distances across the developing tissue. In the mature organism, however, they are bound to the confines of the nervous system. Likewise metastatic cancer cells have the potential to establish auxiliary tumor sites in remote tissues or entirely different organs. It is not wholly identified why neurons can only navigate within the confines of a defined microenvironment, while cancer cells are able to migrate through diverse settings. We review similarities in both form and function of these two unique cell types and inspect which aspects are shared between cancer and neuronal cells and how they employ these features for both dissimilar and shared purposes. Specifically, we examine substrate effects particularly in respect to extracellular matrix (ECM) modifications and constrictions, intracellular mechanics, cellular pushing forces, cytoskeletal filaments, and filopodia of neuron and cancer cells, explaining how these unique cell types achieve their specialized purposes, while sharing a variety of features. This review provides a first look into the similarities and differences between physical aspects of neuronal and cancerous cell lines. It is intended to begin a discussion on the valuable lessons to be learned from comparing these unique cell types in the course of their development.

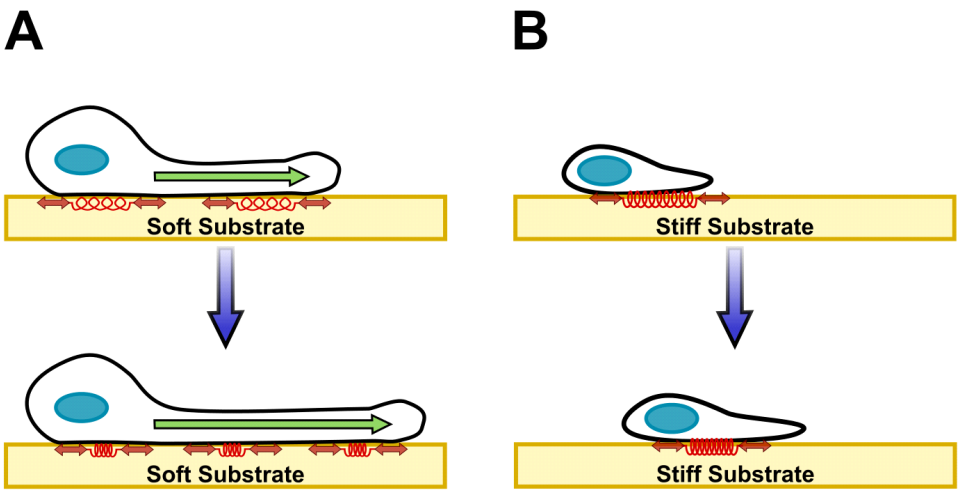

Figure 5.12: Diverse motility modes: A) The soft environment on which neurons grow transforms most of the motile forces exerted by the cell into substrate deformation resulting in a fairly static soma. This does not affect growth cone mobility, since it is from this stationary point that stiff microtubules extend into the neurite to provide the pushing forces for translocation. B) On stiff substrates less energy is transferred into substrate deformation, which results in highly motile cancer cells. Not depicted here is the case of cancer cells on soft substrates in which they enter an immobile but highly proliferative state.

This review paper is part of the Biochimica et Biophysica Acta (BBA) - Molecular Cell Research Special Issue entitled; Mechanobiology

5.10 Funding

Leipziger Schule der Naturwissenschaften - Bauen mit Molekülen und Nano-Objekten (BuildMoNa)
Prof. Dr. E. Hey-Hawkins, Prof. Dr. M. Grundmann und Prof. Dr. J. A. Käs
GSC 185/1

Von lokalen Einschränkungen bis zum makroskopischen Transport - From local constraints to macroscopic transport
Prof. Dr. J. Käs, Dr. Stephan Diez et al.
DFG Forschergruppe FOR 877, Teilprojekt 6, KA 1116/ 7-1

Untersuchung funktioneller Änderungen von Tumorzellen als Ursache unsymmetrischer Verteilungsfunktionen des Zelldeformationsverhaltens
Prof. Dr. J. A. Käs, Dr. M. Zink
DFG, KA 1116/9-1

Blebbing Driven or Actin Protrusive-Force Driven Cancer Cell Migration
Prof. Dr. J. A. Käs, Prof. Dr. C. T. Mierke
DFG, KA 1116/17-1

Mechanismen Aktin-vermittelter Krafterzeugung, Morphodynamik und Motilität einzelner Zellen
Prof. Dr. J. A. Käs, Prof. Dr. K. Rottner, Prof. Dr. M. Falcke
DFG, KA 1116/14-1

Dynamisch-mechanische Manipulation and Charakterisierung von Zellen mit Hilfe magnetischer Dehnung
Dr. M. Zink
DFG, Zi-1330/2-1

5.11 Organizational Duties

Prof. J. A. Käs

- Senator der Universität Leipzig
- Direktor des Instituts für Experimentelle Physik I
- Member of the Organizing Committee: 6th Annual Symposium - Physics of Cancer, Leipzig, September 2015
  involved organizers: Prof. H. Herrmann, Prof. J. Spatz, Jun.-Prof. Franziska Lautenschläger, D. Köster
- PWM Winterschool Kleinwalsertal, A, March 2015
- Journal review: Nature, Science, Cell, Physical Review Letters, Biophysical Journal, Biophysica and Proceedings of the National Academy of Science, Langmuir, Angewandte Chemie, Nature Physics, Journal of Biophotonics, Cytoskeleton, Optics Express, New Journal of Physics
- Grant review: National Science Foundation, Div. of Materials Research; National Science Foundation, Div. of Cellular Organization; National Science Foundation, Div. of Computational Biology; National Science Foundation, Div. of Physics, Special Programs; Deutsche Forschungsgemeinschaft, Alexander von Humboldt Foundation, Deutsche Studienstiftung, Centre National de Recherche
- Fellow, American Physical Society
- Full Member, Saxonian Academy of Sciences

5.12 External Cooperations

Academic

- Syracuse University, USA
  Prof. M. E. Manning
- Syracuse University, USA
  Prof. M. C. Marchetti
- University of Maryland, USA
  Prof. W. Losert
- Albert Einstein College of Medicine, USA
  Prof. J. S. Condeelis

- King's College London, Biomedical Engineering Department, GB
  Prof. R. Sinkus
- Deutsche Gesellschaft für Zellbiologie (DGZ)
  Prof. Dr. H. Herrmann
- Max-Delbrück-Zentrum für molekulare Medizin
  Dr. M. Falcke
- Charité Berlin, MR Elastographie
  Prof. Dr. I. Sack
- Ludwig-Maximilians-Universität München, Fakultät für Chemie und Pharmazie
  Prof. Dr. A. Vollmar
- Technische Universität Braunschweig, Zoologisches Institut
  Prof. Dr. K. Rottner
- Universität Leipzig, Klinik u. Poliklinik für Frauenheilkunde
  Prof. Dr. M. Höckel
- Universität Leipzig, Institut für Pathologie
  Prof. Dr. L.-C. Horn
- Universität Leipzig, Klinik u. Poliklinik f. Mund-, Kiefer- u. Plast. Gesichtschirurgie
  Dr. T. Remmerbach
- Universität Leipzig, Klinik u. Poliklinik f. Dermatologie, Venerologie u. Allergologie
  Prof. Dr. J. Simon
- Universität Leipzig,Translationszentrum für Regenerative Medizin
  Prof. Dr. T. Magin
- Universität Leipzig, Abteilung für Neuroradiologie
  Prof. Dr. K.-T. Hoffmann
- Universität Leipzig, Institut für Experimentelle Physik I
  Prof. Dr. C. Mierke

Industry

- RS Zelltechnik GmbH, Leipzig
  S. Rönicke
- Nanosurf AG, Liestal, Switzerland

5.13 Publications

Journals

S. Grosser, A. W. Fritsch, T. R. Kießling, R. Stange, J. A. Käs: *The lensing effect of trapped particles in a dual-beam optical trap*, Optics Express, **23**, Issue 4, 5221-5235 (2015)

A. C. De Luca, M. Zink, A. Weidt, S. G. Mayr, A. E. Markaki: *Effect of microgrooved surface topography on osteoblast maturation and protein adsorption*, J. of Biomedical Materials Research Part A, **103**, Issue 8, 2689-2700 (2015)

F. Huber, D. Strehle, J. Schnauß, J. A. Käs: *Formation of regularly spaced networks as a general feature of actin bundle condensation by entropic forces*, New Journal of Physics, **17**, 043029 (2015)

U. Allenstein, S. G. Mayr, M. Zink: *Contractile cell forces deform macroscopic cantilevers and quantify biomaterial performance*, Soft Matter, **11**, Issue 25, 5053-5059 (2015)

D. Michalski, W. Härtig, M. Krueger, C. Hobohm, J. A. Käs, T. Fuhs: *A novel approach for mechanical tissue characterization indicates decreased elastic strength in brain areas affected by experimental thromboembolic stroke*, Neuro Report, **26**, Issue 10, 583-587 (2015)

S. B. Schmidt, T. R. Kießling, E. Warmt, A. W. Fritsch, R. Stange, J. A. Käs: *Complex thermorheology of living cells*, New Journal of Physics, **17**, 073010 (2015)

U. Allenstein, S. Selle, M. Tadsen, C. Patzig, T. Höche, M. Zink, S. G. Mayr: *Coupling of Metals and Biominerals: Characterizing the Interface between Ferromagnetic Shape-Memory Alloys and Hydroxyapatite*, ACS Applied Materials & Interfaces, **7**, Issue 28, 15331-15338 (2015)

S. Braig, S. U. Schmidt, K. Ferkaljuk, C. Händel, T. Möhn, O. Werz, R. Müller, S. Zahler, A. Koeberle, J. A. Käs, A. M. Vollmer: *Pharmacological targeting of membrane rigidity: Implications on cancer cell migration and invasion*, New Journal of Physics, **17**, 083007 (2015)

C. Händel, S. Schmidt, J. Schiller, U. Dietrich, T. Möhn, T. Kießling, S. Pawlizak, A. W. Fritsch, L.-C. Horn, S. Briest, M. Höckel, M. Zink, J. A. Käs: *Cell membrane softening in human breast and cervical cancer cells*, New Journal of Physics, **17**, 083008 (2015)

P. Heine, A. Ehrlicher, J. A. Käs: *Neuronal and metastatic cancer cells: Unlike brothers*, Biochim. Biophys. Acta (BBA) - Molecular Cell Research, **1853**, Issue 11, 3126-3131 (2015)

S. Pawlizak, A. W. Fritsch, S. Grosser, D. Ahrens, T. Thalheim, S. Riedel, T. R. Kießling, L. Oswald, M. Zink, M. L. Manning, J. A. Käs: *Testing the differential adhesion hypothesis across the epithelial-mesenchymal transition*, New Journal of Physics, **17**, 083049 (2015)

Talks

J. A. Käs: *Thermorheology of Living Cells - Impact of Temperature Variations on Cell Mechanics*, Trends in Optical Micromanipulation III, Universitätszentrum Obergurgl (Medizinische Universität Innsbruck, Österreich), January 2015 - Invited

J. A. Käs: *Expanded experimental parameter space of semiflexible polymer assemblies through programmable nanomaterials*, APS Meeting, San Antonio, USA, March 2015

M. Glaser, T. Tschirner, M. Moebius-Winkler, C. Schuldt, T. Golde, J. A. Käs, D. M. Smith, J. Schnauß: *Higher ordered assembly of rigid biopolymers induced by depletion forces*, PWM Winterschool, Kleinwalsertal, A, March 2015

J. Lippoldt, T. Golde, C. Schuldt, J. A. Käs: *Cell motility at the leading edge: Measuring membrane fluctuations with an optical tweezer setup*, PWM Winterschool, Kleinwalsertal, A, March 2015

E. Warmt, S. Schmidt, T. Kießling, A. W. Fritsch, R. Stange, J. A. Käs: *Complex thermorheology of cells* , PWM Winterschool, Kleinwalsertal, A, March 2015

L. Oswald, S. Grosser, S. Pawlizak, A. W. Fritsch, J. A. Käs: *Investigating cellular compartmentalisation using in vitro model systems - Spheroid fusion*, PWM Winterschool, Kleinwalsertal, A, March 2015

M. Glaser, T. Tschirner, M. Moebius-Winkler, C. Schuldt, T. Händler, T. Golde, D. M. Smith, J. Schnauß, J. A. Käs: *Higher ordered assembly of rigid biopolymers induced by depletion forces*, Annual conference BuildMona, Leipzig, March 2015

J. Lippoldt, T. Golde, C. Schuldt, J. A. Käs: *Cell motility at the leading edge: Measuring membrane fluctuations with an optical tweezer setup*, Annual conference BuildMona, Leipzig, March 2015

J. Schnauß: *Contractile actin bundles without molecular motors*, DPG Spring Meeting, Berlin, March 2015

M. Glaser, T. Händler, C. Schuldt, T. Golde, J. A. Käs, J. Schnauß, D. M. Smith: *Reptation of single filaments within entangled networks of tunable biopolymers*, DNA Nanotechnology Mitteldeutschland, Jena, May 2015

J. A. Käs: *Self-organisation and Pattern Formation in Carcinomas and their Microenvironment*, 8^{th} International Conference: Engineering of Chemical Complexity, TU München, June 2015 - Invited

L. Oswald, S. Grosser, S. Pawlizak, A. W. Fritsch, J. A. Käs: *Cell aggregation and segregation in in vitro model systems - Jamming*, PWM Summerschool Zingst, June 2015

J. Schnauß: *Dynamics of actin bundle and higher ordered assemblies*, PWM Summerschool Zingst, June 2015

M. Glaser, T. Händler, C. Schuldt, T. Golde, J. A. Käs, J. Schnauß, D. M. Smith: *Reptation of single filaments within entangled networks of tunable biopolymers*, PWM Summerschool Zingst, June 2015

J. Lippoldt, C. Händel, S. Schmidt, J. A. Käs: *The Influence of Cholesterol on Membrane Stiffness and Actin Anchorage*, PWM Summerschool Zingst, June 2015

J. A. Käs: *Biophysics in Cells and Tumors*, 7^{th} DFG Workshop for Early Career Investigators in Medical Technology and Medical Physics, Charité Campus Mitte, Berlin, August 2015 - Invited

M. Glaser, T. Tschirner, C. Schuldt, T. Händler, T. Golde, J. A. Käs, J. Schnauß, D. M. Smith: *Exploring the formation of higher ordered phases by programmable DNA nanotubes*, DNA Nanotechnology Workshop Mitteldeutschland, Dresden, September 2015

J. A. Käs: *The EMT, an Unjamming Transition?*, 6^{th} Annual Symposium - Physics of Cancer, Leipzig, September 2015

S. Schmidt, C. Händel, J. A. Käs: *Membrane Softening in Malignant Cells*, 6^{th} Annual Symposium - Physics of Cancer, Leipzig, September 2015

S. Schmidt, C. Händel, J. A. Käs: *Membrane rigidity and thermorheology of cells*, Biophysics Seminar, Department of Physics, University of Maryland, U.S.A., September 2015

J. Schnauß: *Artificial DNA-based cross-linker drastically alter actin networks*, DNA Nanotechnology Workshop Mitteldeutschland, Leipzig, November 2015

Posters

M. Glaser, T. Tschirner, M. Moebius-Winkler, C. Schuldt, T. Händler, T. Golde, J. Schnauß, D. M. Smith, J. A. Käs *Higher ordered assembly of rigid biopolymers induced by depletion forces*, DPG Spring Meeting, Berlin, March 2015

E. Warmt, S. Schmidt, T. Kießling, A. W. Fritsch, R. Stange, J. A. Käs: *Complex thermorheology of cells* , DPG Spring Meeting, Berlin, March 2015

T. Händler, C. Schuldt, M. Glaser, J. Schnauß, J. A. Käs, D. M. Smith: *Microrheological characterization of DNA nanotube networks*, DPG Spring Meeting, Berlin, March 2015

J. Schnauß, T. Golde, C. Schuldt, S. Schmidt, M. Glaser, D. Strehle, C. Heussinger, J. A. Käs: *Collective dynamics in a multi-filament actin bundle*, Diffusion Fundamentals VI, Dresden, August 2015

M. Glaser, T. Tschirner, M. Moebius-Winkler, C. Schuldt, T. Golde, J. A. Käs, D. M. Smith, J.Schnauß: *Higher ordered assembly of rigid biopolymers induced by depletion forces*, 6^{th} Annual Symposium - Physics of Cancer, Leipzig, September 2015

J. Schnauß, T. Golde, C. Schuldt, S. Schmidt, M. Glaser, D. Strehle, C. Heussinger, J. A. Käs: *Motor-free contraction and collective dynamics in a multi-filament actin bundle*, 6^{th} Annual Symposium - Physics of Cancer, Leipzig, September 2015

S. Grosser, L. Oswald, S. Pawlizak, A. W. Fritsch, J. A. Käs: *Fluidity and Jamming in 3D Aggregates of Breast Cancer Cell Lines*, 6^{th} Annual Symposium - Physics of Cancer, Leipzig, September 2015

P. Heine, E. Warmt, J. A. Käs: *Cellular jamming and invasive behavior in epithelial cell layers*, 6^{th} Annual Symposium - Physics of Cancer, Leipzig, September 2015

M. Glaser, T. Tschirner, C. Schuldt, T. Händler, T. Golde, J. A. Käs, J.Schnauß, D. M. Smith: *Higher ordered assembly of rigid biopolymers induced by depletion forces*, World Conference on Regenerative Medicine, Leipzig, October 2015

5.14 Graduations

Doctorate

- Valentina Dallacasagrande
  Novel approaches to study the biomechanics of intact central nervous tissue
  02.04.2015
- Jörg Schnauß
  Self-assembly effects of filamentous actin bundles
  14.09.2015
- Sebastian Schmidt
  Accessing Novel Material Parameters in Single Cell Biomechanics
  14.12.2015

Master

- Dave Ahrens
  Temporal Adhesion Dynamics in Mammary Cancer Cell Lines
  February 2014
- Sabrina Friebe
  Biomechanical Properties of Multicellular Spheroids
  March 2015

Bachelor

- Gregor Hayder
  Membrane stiffness in the context of cancer
  February 2015
- Paul Birkenmeyer
  Impact of LRP1 on biomechanical properties of tumor cells
  February 2015

6

Biological Physics

6.1 Introduction

Cellular Biophysics in the Field of Cancer Research Most cancer-related deaths during the malginant cancer progression are caused by the ability of cancer cells to metastasize. The process of metastasis follows a linear propagation of several steps. It starts with the spreading of cancer cells from the primary tumor, which then migrate into the local tumor microenvironment. The cancer cells can transmigrate into blood or lymph vessels (intravasation), get transported through the vessel flow, adhere to the endothelial cell lining, grow and form a secondary tumor directly inside the vessel or the cancer cells possibly transmigrate through the endothelial vessel lining (extravasation) into the extracellular matrix of connective tissue. After this step, the cancer cells migrate further into the targeted tissue (possibly another organ), grow and form a secondary tumor (i.e. the tumor metastasizes). Despite of all current findings based on biochemistry and even the novel approaches based on genomics and proteomics cancer research did not fundamentally change cancer death rates, but still improved clinical diagnosis substantially in the field of cancer research regarding the classification and detailed staging of tumors, numerous marker proteins and mapping of specific human cancer-types. Thus, a main criticism to these methods is that the expression levels of numerous genes and molecules, which are differently regulated during cancer progression, depend on the cancer disease stage. In particular, it is still not fully understood how they regulate cancer progression. A reason may be that these genomic and proteomic based methods do not account for the localization of the molecules in special compartments such as lipid rafts, their activation or assembly state, their life-time, turn-over-, modification- and recycling rate. Thus, we and others propose that the biomechanical properties are crucial for the efficiency and speed of cancer cell invasion and subsequently, for metastases formation. In more detail, classical physical approaches will be adopted to complex soft matter such as cancer cells and novel biophysical methods will be developed in order to adopt them to cancer research. These novel physical approaches have so far changed or will still alter the direction of recent cancer research. Moreover, even the role of the endothelium during the transmigration and invasion of cells is not clear, it has been seen as passive barrier, but this could not explain all novel findings as our finding that this endothelial layer of vessels can enhance the invasiveness of cancer cells. Thus, we will investigate how cancer cells alter the structural, biochemical and mechanical properties of the endothelium to regulate their own invasiveness through

extracellular matrices and hence, through the tissue microenvironment. Moreover, we will investigate how the mechanical properties of cancer cells regulate the functional properties such as cancer cell invasion and transendothelial migration. Finally, our research will shed light on the mechanical properties of cancer cells and the interacting endothelium and will point out the importance of the mechanical properties as a critical determinant for the efficiency of cancer cell invasion and the overall progression of cancer. In conclusion, we suggest that the regulation of the endothelial cells biomechanical properties by cancer cells and the mechanical properties of cancer cells are a critical determinants of cancer cell invasiveness and may affect the future development of new cancer treatments.

Claudia Mierke

6.2 Motility of human cancer cells through biomimetic collagen matrices

C.T. Mierke

The migration and invasion of cells in three-dimensional (3D) extracellular matrices is on the one hand a prerequisite for tissue assembly, homeostasis and regeneration, immune cell trafficking upon cell injury such as wounds and on the other hand cellular motility plays a role in numerous diseases such as cancer. During the malignant progression of cancer disease, the process of metastasis depends on the migration of single cancer cells that spread out of the primary tumor and breach through endothelial vessel linings. In more detail, the migration of cancer cells through the extracellular matrix protein network building connective tissue is a cyclic process involving several steps, including: firstly the actin polymerization-dependent protrusion of pseudopods at the leading edge; secondly the integrin-facilitated adhesion to the extracellular microenvironment; thirdly the degradation of the nearby extracellular matrix proteins evoked by its cleavage through membrane exposed proteases such as matrix-metalloproteinases; fourthly the actomyosin-driven contraction of the cell's body, enhancing longitudinal tension; and fifthly the retraction of the cell's rear part in the direction of the cell migration front leading to a translocation of the whole cell (Doyle et al 2013). These five steps describe only one special migration mode that can be chosen by aggressive and metastatic cancer cells of epithelial origin. This mode of migration is named the protrusive migration mode (Maruthamuthu and Gardel 2014). However, there seems to be other modes of cancer cell migration, such as the blebbing migration mode. In this blebbing mode, the cells extend and retract suddenly membrane blebs, in which the membrane has no contact to the actin cytoskeleton (Laser-Azogui et al 2014). When cells use this kind of migration mode, it not yet well understood and still ongoing research. Moreover, it is not clear whether the protrusive and the blebbing migration modes are clearly distinguishable from each other or whether mixtures exist involving both phenomena, the formation of protrusions and the rapid extension and retraction of blebs on these protrusions. Which migration mode is preferred by a specific type of cancer cell and how the switch of migration modes is affected by the specific biomimetic environmental conditions is still elusive. In addition to these two migration modes,

there is another migration mode described, which is named the lobopodial migration mode which seems to represent a partial switch between the migration modes. This lobopodial mode has not been observed in cancer cells, however, so far it has only been detected for fibroblasts. Thus, we suggest that cancer cells also choose this lobopodial migration mode under certain circumstances. Hence, further effort is needed to analyze whether and how cancer cells are able to use this fibroblastoid lobopodial migration mode. The capability of cancers to metastasize depends on the cancer cell's ability to migrate out of the primary tumor and invade connective tissue, adhere, and possibly breach through and transmigrate a barrier such as basal membrane and the endothelium of blood and lymphoid vessels. Alternatively, cancer cells can enter the vascular system directly in the primary tumor as many tumor-endothelial vessels are leaky or consist of cancer cells mimicking endothelial cells. However, what specifies a certain migration mode and how the appearance or the switch between the different migration modes is regulated, is not yet well understood. In more detail, the individual migration mode is proposed to play a central role for the regulation of the basement membrane or endothelial barrier-crossing ability of certain cancer cells and is supposed to have an impact on their migration speed through biomimetic matrices such as collagen type I gels. How efficient a migrating cancer cell overcomes the different obstacles such as steric restrictions found in dense 3D biomimetic matrices is supposed to depend strongly on its mechanical properties. In more detail, how a cancer cell strongly is able to generate and transmit its protrusive forces seems to impact its migration mode and speed. Hence cellular forces and material properties of biomimetic matter such as pore-sizes or elastic modulus determine which migration mode of is favored for a special cancer cell type or cancer cell subpopulation. Indeed, it has been reported that cancer cells with a certain cellular mechanical phenotype such as increased contractile force transmission and generation are capable to migrate through 3D biomimetic networks such as dense collagen fiber matrices more efficiently than less contractile cancer cells (Mierke et al 2008, Mierke et al 2011). Nonetheless, what kind of migration mode is chosen when cancer cells seems to squeeze through narrower pores or interendothelial junctions of vascular endothelial cell walls? In this special case of transendothelial migration and the migration through the dense basal membrane of the vessels a blebbing migration mode seems to be more likely than a protrusive migration mode. However, also an invadopodia-like protrusive mode may be well suited for transmigration of cancer cells. In preliminary results it has been observed that membrane stiffness pronouncedly softens in primary human mamma and human cervix carcinoma cells, supporting the blebbing migration mode. Finally, we hypothesize that the mechanical properties of cells and biomimetic matter as well as the type of force generation of cancer cells determine the migration mode and regulates the switch between individual migration modes. The following questions still need to be answered: What are the mechanisms determining the individual migration mode of cancer cells? What role do microenvironmental properties of biomimetic matter such as the material mechanics and structure of the extracellular matrix play regarding the switch of the migration mode by the cancer cells? In order to investigate this, one needs to dissect the crosstalk between the migration modes of the cancer cells and the environmental confinements such as pore-size, overall cellular stiffness, plasma membrane surface tension and extracellular matrix rigidity, and the proteomics of the cellular adhesion machinery as well as the extracellular protein composition of the biomimetic matrix network. To understand the mechanism how

migrating cancer cells interact with their biomimetic environmental confinement and why individual cancer cells use a certain invasion mode such as blebbing or protrusive migration modes, the following major problems seems to be addressed. What roles do the influence of cytoskeletal stiffness and cell contractility play regarding the switch of the migration modes and cellular migration speed in biomimetic matrices? To what extent do mechanical properties favor either the protrusive or blebbing-based migration modes of cancer cells? How does the surface tension of the cells membrane impact on the cellular migration behavior, such as protrusive-driven or blebbing-driven motility? What effect does the adhesion strength of cancer cells have on the preferred migration mode? Moreover, is the blebbing migration mode indeed preferred by small pore-sizes of the microenvironmental confinement and biomimetic matrices, such as the connective tissue matrix scaffold, whereas the protrusive migration mode is supported by large pore-sizes? Can the blebbing or protrusive migration modes of cancer cells impact the transmigration of cancer cells through barriers such as vascular endothelial cell linings and basal membranes of vessels? Knowing the answers to these questions will contribute to the understanding of how cancer cells utilize a specific migration mode to migrate through the 3D microenvironment and what role the cellular mechanical properties and material properties of biomimetic microenvironments and connective tissue play. Moreover, this knowledge will contribute to reveal the individual impact of the mechanical properties of cancer cells and the mechanical properties of their microenvironments in supporting the migratory behavior and capacity of epithelial-derived carcinomas, during the malignant progression of cancers (metastasis).

6.3 Funding

Blebbing Driven or Actin Protrusive-Force Driven Cancer Cell Migration
Prof. C. T. Mierke
DFG

6.4 Organizational Duties

Prof. C. T. Mierke

- Referee: Cancer Research, Journal of Cell Science, Advanced Biomaterials,Acta Biomaterials, British Journal of Cancer, Journal of Pharmacy and Pharmacology, Molecular Vision, International Journal of Nanomedicine, Plos One, Eur. J. Biophysics
- Special Issue Guest Editor for Physical Biology

6.5 External Cooperations

Academic

- Imperial College London, Department of Materials, London,UK
  Prof. Dr.-Ing. habil. Aldo R. Boccaccini

- Netherlands Cancer Institute Amsterdam, Netherlands
  Dr. Arnoud Sonnenberg
- University of Regensburg, Institute for Molecular and Cellular Anatomy, Regensburg, Germany
  Prof. Dr. Ralph Witzgall
- Philipps-University Marburg, Department of Neurosurgery, Germany
  Prof. Dr. J. W. Bartsch
- Department of Paediatric Kidney, Hannover medical School, Germany
  Prof. Dr. Hermann Haller , Dr. rer. nat. Wolfgang Ziegler
- University of Bonn, Institute of Genetics Actin Dynamics and Motility Unit, Germany
  Prof. Dr. Klemens Rottner
- University of Leipzig, Translational Center for Regenerative Medicine, Germany
  Prof. Dr. Thomas Magin
- University of Leipzig, Center for Biotechnology and Biomedicine (BBZ), Germany
  Prof. Dr. A. Robitzki

6.6 Publications

Journals

J. Sapudom, S. Rubner, S. Martin, T. Kurth, S. Riedel, C. T. Mierke, T. Pompe: *The phenotype of cancer cell invasion controlled by fibril diameter and pore size of 3D collagen networks*, doi:10.1016/j.biomaterials.2015.02.022

Books

C. T. Mierke: *Physics of Cancer*, iop science, doi:10.1088/978-0-7503-1134-2

Helim Aranda-Espinoza, C. T. Mierke: *Mechanobiology of the Endothelium, Cancer Metastasis and Biomechanics of the Endothelium*, CRC Press 2015, 47-79, doi:10.1201/b18060-4

6.7 Graduations

Diploma

- Sebastian Haupt
  Fibroblast cell invasion behaviour into engineered 3D collagen/fibronectin matrices in microfluidi devices
  22.05.2015

Master

- Stefanie Riedel
  Effect of the Microenvironmental Structure on Tumor Cell Motility
  22.01.2015

Bachelor

- Jacek Zlotowski
  Effect of TNF-alpha on the mechanical properties of cells expressing keratins or deficient of keratins
  19.02.2015
- Monica Tamara Heredia Munoz
  Effect of interleukin-1beta on the deformability of keratin wildtype and deficient cells
  10.02.2015
- Mirko Kirchner
  Einfluss von Fibronektin auf die Motilität von Krebszellen in 3D Kollagenmatrizen
  12.05.2015

II

Institute for Experimental Physics II

7

Magnetic Resonance of Complex Quantum Solids

7.1 Introduction

The electronic properties of quantum-solids in which the electrons exhibit strong correlations with each other or with the lattice are particularly rich and will be of special importance in future functional materials. In addition, such solids are challenging for experiment, as well as theory, as the more than twenty five-year history of high-temperature superconductivity shows: we still do not understand the electronic structure of these systems. One particular aspect of strongly correlated electronic materials is their tendency towards nano-scale electronic phase separation. Even in perfect lattices, electronic nano-structures can form. The investigation of such materials requires the use of methods that can give detailed information. Here, magnetic resonance, on nuclei and electrons, is of particular interest as they not only have atomic scale resolution, but also yield bulk information in contrast to surface techniques. We explore the properties of these materials with tailored new techniques at the frontiers of magnetic resonance. For example, we are the leading laboratory when it comes to NMR at highest pressures and magnetic fields.

Jürgen Haase

7.2 High-sensitivity NMR beyond 200,000 atmospheres of pressure

T. Meier, S. Reichardt, J. Haase

Pressure-induced changes in the chemical or electronic structure of solids require pressures well into the Giga-Pascal (GPa) range due to the strong bonding. Anvil cell designs can reach such pressures, but their small and mostly inaccessible sample chamber has severely hampered NMR experiments in the past. With a new cell design that has a radio frequency (RF) micro-coil in the high pressure chamber, NMR experiments beyond 20 Giga-Pascal are reported for the first time. ^{1}H NMR of water shows sensitivity and resolution obtained with the cells, and ^{63}Cu NMR on a cuprate superconductor

($YBa_2Cu_3O_{7-\delta}$) demonstrates that single-crystals can be investigated, as well. Imagine NMR of the ternary chalcogenide $AgInTe_2$ discovers an insulator-metal transition with shift and relaxation measurements. The pressure cells can be mounted easily on standard NMR probes that fit commercial wide-bore magnets with regular cryostats for field- and temperature-dependent measurements ready for many applications in physics and chemistry.

7.3 Anvil cell gasket design for high pressure nuclear magnetic resonance experiments beyond 30 GPa

T. Meier, J. Haase

Nuclear magnetic resonance (NMR) experiments are reported at up to 30.5 GPa of pressure using radiofrequency (RF) micro-coils with anvil cell designs. These are the highest pressures ever reported with NMR, and are made possible through an improved gasket design based on nano-crystalline powders embedded in epoxy resin. Cubic boron-nitride (c-BN), corundum (α-Al_2O_3), or diamond based composites have been tested, also in NMR experiments. These composite gaskets lose about 1/2 of their initial height up to 30.5 GPa, allowing for larger sample quantities and preventing damages to the RF micro-coils compared to precipitation hardened CuBe gaskets. It is shown that NMR shift and resolution are less affected by the composite gaskets as compared to the more magnetic CuBe. The sensitivity can be as high as at normal pressure. The new, inexpensive, and simple to engineer gaskets are thus superior for NMR experiments at high pressures.

7.4 ^{77}Se nuclear magnetic resonance of topological insulator Bi_2Se_3

N.M. Georgieva, D. Rybicki*, R. Gühne, G.V.M. Williams†, S.V. Chong‡, I. Garate§, J. Haase

*Faculty of Physics and Applied Computer Science, AGH University of Science and Technology, Department of Solid State Physics, al. A. Mickiewicza 30, 30-059 Krakow, Poland
†School of Chemical and Physical Sciences, Victoria University of Wellington, PO Box 600, Wellington 6140, New Zealand
‡Robinson Research Institute, Victoria University of Wellington, PO Box 33436, Lower Hutt 5046, New Zealand
§Département de Physique and Regroupement Québécois sur les Matériaux de Pointe, Université de Sherbrooke, Sherbrooke, Québec, Canada J1K 2R1

Topological insulators (TIs) constitute a new class of materials with an energy gap in the bulk and peculiar metallic states on the surface. To date, most experiments have focused on probing the surface electronic structure of these materials. Here, we report on new and potentially interesting features resulting from the *bulk* electronic structure. Our findings are based on a comprehensive nuclear magnetic resonance (NMR) study of ^{77}Se on Bi_2Se_3 and $Cu_{0.15}Bi_2Se_3$ single crystals. First, we find two resonance lines and

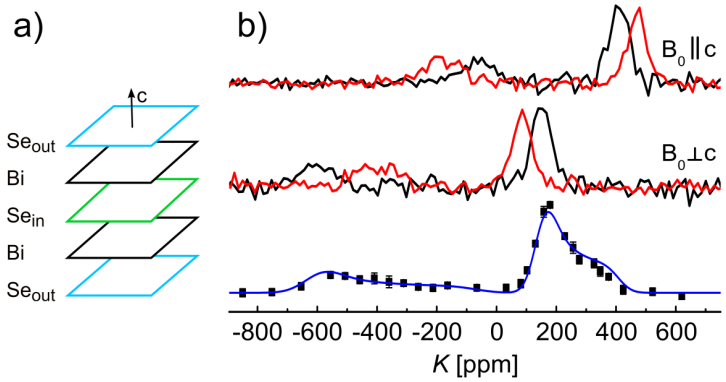

Figure 7.1: a) Sketch of a quintuple layer of five atomic sheets containing two equivalent Bi sites, two equivalent "outer" Se sites (Se_{out}) and another "inner" Se site (Se_{in}) located at the center of inversion. The crystal structure of Bi_2Se_3 consists of stacked, van der Waals bonded quintuple layers, with the *c*-axis normal to the layers. b) ^{77}Se NMR spectra at B_0 = 17.6 T and room temperature of Bi_2Se_3 (black) and $Cu_{0.15}Bi_2Se_3$ (red) single crystals for two crystal orientations (top two), and of Bi_2Se_3 powder (squares) with simulation based on single crystal data (solid blue line). Shifts (*K*) are given with respect to $(CH_3)_2Se$. The stronger (weaker) signal originates from Se_{out} (Se_{in}).

show that they originate from the two inequivalent Se lattice sites. Second, we observe unusual field-independent linewidths, and attribute them to an unexpectedly strong internuclear coupling mediated by bulk electrons. These results call for a revision of earlier NMR studies and add insight into the bulk electronic properties of TIs.

7.5 Electronic spin susceptibilities and superconductivity in $HgBa_2CuO_{4+\delta}$ from nuclear magnetic resonance

D. Rybicki*, J. Kohlrautz, J. Haase M. Greven†, X. Zhao† ‡, M.K. Chan†, C.J. Dorow†, M.J. Veit†

*Faculty of Physics and Applied Computer Science, AGH University of Science and Technology, Department of Solid State Physics, al. A. Mickiewicza 30, 30-059 Krakow, Poland

†School of Physics and Astronomy, University of Minnesota, Minneapolis, Minnesota 55455, USA

‡College of Chemistry, Jilin University, Changchun 130012, China

Nuclear magnetic resonance (NMR) experiments on single crystals of $HgBa_2CuO_{4+\delta}$ are presented that identify two distinct temperature-dependent spin susceptibilities: one is due to a spin component that is temperature-dependent above the critical temperature for superconductivity T_c and reflects pseudogap behavior; the other is Fermi-liquid-like in that it is temperature independent above T_c and vanishes rapidly below T_c. In addition, we demonstrate the existence of a third, hitherto undetected spin susceptibility: it is temperature independent at higher temperatures, vanishes at lower temperatures ($T_0 \neq T_c$), and changes sign near optimal doping. This susceptibility either arises from the coupling between the two spin components, or it could be given by a distinct third spin component.

7.6 The line width of the EPR signal of gaseous nitric oxide as determined by pressure and temperature dependent X-band continuous wave measurements

M. Mendt, A. Pöppl

The electron paramagnetic resonance (EPR) signal of gaseous nitric oxide (NO) has been measured by continuous wave X-band experiments at room temperature at gas pressures between 1 mbar and 60 mbar and at a gas pressure of 48 mbar at different low temperatures. A phenomenological spin Hamiltonian approach allows simulating each EPR signal of NO by changing only a single line width parameter. At room temperature, this line width depends linearly on the NO gas pressure which can be explained by kinetic gas theory. An effective collisional cross section has been determined by this way which is about twice as large as the known cross section for NO derived from viscosity measurements. Experiments with NO gas at low temperatures are consistent to the line width interpretation by kinetic theory. In total, the results demonstrate that in NO adsorption and desorption experiments at different temperatures and NO gas pressures below 60 mbar the amount of desorbed NO can simply be determined in situ by the line width of this signal, which one can obtain easily from a conventional simulation procedure.

7.7 Adsorption of nitric oxide in metal-organic frameworks: Low temperature IR and EPR spectroscopic evaluation of the role of open metal sites

B. Barth*, M. Mendt, A. Pöppl, M. Hartmann*

*Erlangen Catalysis Resource Center (ECRC), Friedrich-Alexander-Universität Erlangen-Nürnberg, Egerlandstr. 3, 91058 Erlangen, Germany

The metal-organic framework materials M-MIL-100 (M = Al, Fe) and M-CPO-27 (M = Co, Ni) have been studied with respect to the adsorption of nitric oxide employing low-temperature ESR and IR spectroscopy. Exposure of the previously desolvated Ni (II) and Co (II) sites in CPO-27 leads to the formation of metal nitrosyl complexes that are stable up to temperatures of 393 K. A weaker bond is formed between the iron metal centers in the Fe-MIL-100 type materials and the nitric oxide molecule. Using in-situ DRIFT and EPR spectroscopy at low temperatures, the formation of Co-, Ni- and Fe-NO adducts is evident from the respective spectra, while specifically strong interactions are absent in Al-MIL-100 and Al/Cr-Mil-53.

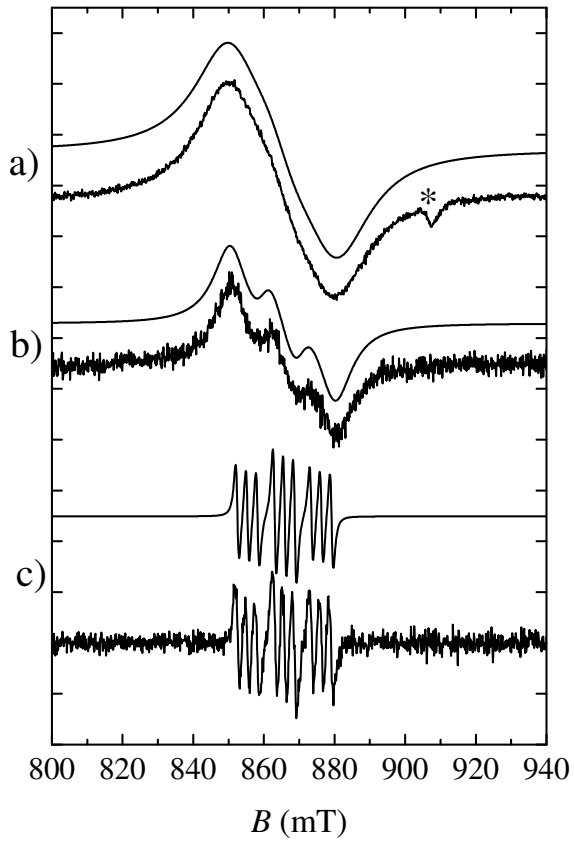

Figure 7.2: Room temperature X-band EPR signals (below) of samples of pure NO with room temperature gas pressures of (a) 60 mbar, (b) 30 mbar and (c) 1 mbar. Simulations are also shown above the corresponding spectra. The asterisk marks an artefact.

7.8 Synthesis, Structure, and Electron Paramagnetic Resonance Study of a Mixed Valent Metal Organic Framework Containing Cu_2 Paddle–Wheel Units

M. Simenas*, M. Kobalz†, M. Mendt, P. Eckold‡, H. Krautscheid†, J. Banys*, A. Pöppl

*Faculty of Physics, Vilnius University, Sauletekio 9, 10222 Vilnius, Lithuania
†Faculty of Chemistry and Mineralogy, Universität Leipzig, Johannisallee 29, 04103 Leipzig, Germany
‡Institute of Inorganic Chemistry, University of Stuttgart, Pfaffenwaldring 55, 70569 Stuttgart, Germany

We report synthesis and composite study of a novel metal organic framework (MOF) compound of chemical formula $^{3}_{\infty}\left[Cu^{I}_{2}Cu^{II}_{2}\{H_2O\}_2\{(\text{Me-trz-}m\text{ba})_2\,\text{thio}\}_2\right]Cl_2$ where $(\text{Me-trz-}m\text{ba})_2\,\text{thio}^{2-}$ stands for

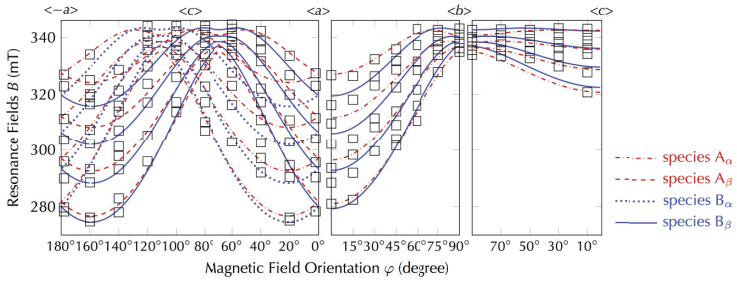

Figure 7.3: X-band EPR signal (b) and simulation (a) of an Al-NO adsorption species in an NO loaded EPR sample of the metal-organic framework Al-MIL-100. The EPR spectrum was measured at 9 K.

3, 3 – (5, 5 – (thiophene – 2, 5 – diyl) -bis (3-methyl-4H-1,2,3-triazole-5,4-diyl)) dibenzoate. This coordination polymer was synthesized by solvothermal synthesis. The crystal structure was determined using single crystal X-ray diffraction. The main building block of this compound is a so-called Cu_2 paddle-wheel (PW) unit, which contains two Cu^{2+} ions connected via four carboxylate groups. Magnetic properties of the investigated MOF were studied by continuous-wave electron paramagnetic resonance (EPR) spectroscopy at X- and Q-band frequencies in a wide temperature range. Mononuclear Cu^{2+} ions were observed in the EPR spectra and characterized by spectral simulations. In addition, the obtained EPR data allowed us to detect and investigate three distinct magnetic interactions related to the Cu^{2+} pairs. At higher temperatures the fine structure pattern was observed in the EPR spectra and the spin spin interaction tensor $\boldsymbol{D}$ was determined. The origin of this pattern was assigned to the thermally populated excited triplet states of the Cu^{2+} pairs. It was found that two Cu^{2+} ions within a single PW unit couple antiferromagnetically with the exchange coupling constant $J = -258\ \mathrm{cm}^{-1}$. Moreover, the EPR spectra of dehydrated MOF samples show a broad, poorly resolved spectral feature, the origin of which is an exchange of the spin triplets between neighboring Cu_2 PW units. By simulating the powder pattern of this interdinuclear exchange line, we estimated the exchange coupling between neighboring PW units ($|J'| = 4.9\ \mathrm{cm}^{-1}$). It was also found that the interdinuclear exchange gradually disappears, if the dehydrated samples are allowed to interact with air, demonstrating that this exchange can be rather easily manipulated in the investigated MOF.

7.9 Single Crystal Electron Paramagnetic Resonance with Dielectric Resonators of Mononuclear Cu^{2+} Ions in a Metal-Organic Framework Containing Cu_2 Paddle-Wheel Units

S. Friedländer, M. Simenas*, M. Kobalz†, P. Eckold‡, O. Ovchar§, A.G. Belous§, J. Banys*, H. Krautscheid†, A. Pöppl

*Faculty of Physics, Vilnius University, Sauletekio 9, 10222 Vilnius, Lithuania
†Faculty of Chemistry and Mineralogy, Universität Leipzig, Johannisallee 29, 04103 Leipzig, Germany

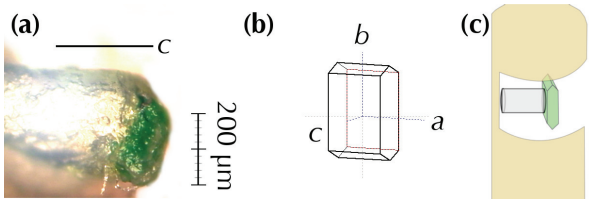

Figure 7.4: (a) The single crystal of **1** taken for all experiments reported. (b) Depicted crystal outline with crystallographic axes indicated. (c) Sketch of the bevelled quartz glass rod with 1 mm diameter housing the crystal glued to the fibre.

‡Institute of Inorganic Chemistry, University of Stuttgart, Pfaffenwaldring 55, 70569 Stuttgart, Germany
§Institute of General and Inorganic Chemistry, National Academy of Sciences of Ukraine, Academian Palladin Avenue 32-34, 03680 Kyiv, Ukraine

Dielectric resonator aided sensitivity-enhancing electron paramagnetic resonance was successfully applied to small single crystals of the previously reported metal-organic framework compound ${}^{3}_{\infty}[Cu^{I}_{2}Cu^{II}_{2}(H_2O)_2L_2Cl_2]$ in a conventional X-band EPR spectrometer at 7 K sample temperature to reveal the nature of mononuclear Cu^{2+} ion defect species. We found that these paramagnetic defects are not related to an impurity phase or extraframework species of the parent metal-organic framework material but are formed within the framework. Novel angular resolved single crystal continuous wave electron paramagnetic resonance supported by powder measurements and single crystal X-ray diffraction on this metal-organic framework compound identified defective copper paddle wheel units with one missing Cu^{2+} ion as the observed mononuclear paramagnetic species in this compound. The sensitivity enhancement by an estimated factor of 8.6 for the single crystal electron paramagnetic resonance spectroscopy is required to efficiently record the Cu^{2+} ion signals in single crystals of typical sizes of $200 \times 50 \times 50\,\mu m^3$ at X-band frequencies. The results demonstrate that conventional electron paramagnetic resonance spectrometers operating at X-band frequencies and equipped with dielectric resonators can successfully be used to perform single crystal studies of these porous, low density materials with very small volume samples at low temperatures.

7.10 Dielectric ceramic EPR resonators for low temperature spectroscopy at X-band frequencies

S. Friedländer, O. Ovchar*, H. Voigt, R. Böttcher, A.G. Belous*, A. Pöppl

*Institute of General and Inorganic Chemistry, National Academy of Sciences of Ukraine, Academian Palladin Avenue 32-34, 03680 Kyiv, Ukraine

The performance of new dielectric ceramic resonators (DRs) for continuous wave (cw) X-band electron paramagnetic resonance (EPR) spectroscopy is investigated at room temperature and low temperatures (77 K, 6 K). The DRs with high dielectric constants of about $\varepsilon_r = 80$, featuring low residual paramagnetic impurities, have been developed and produced on the basis of barium lanthanide titanates solid solutions (BLTss) with

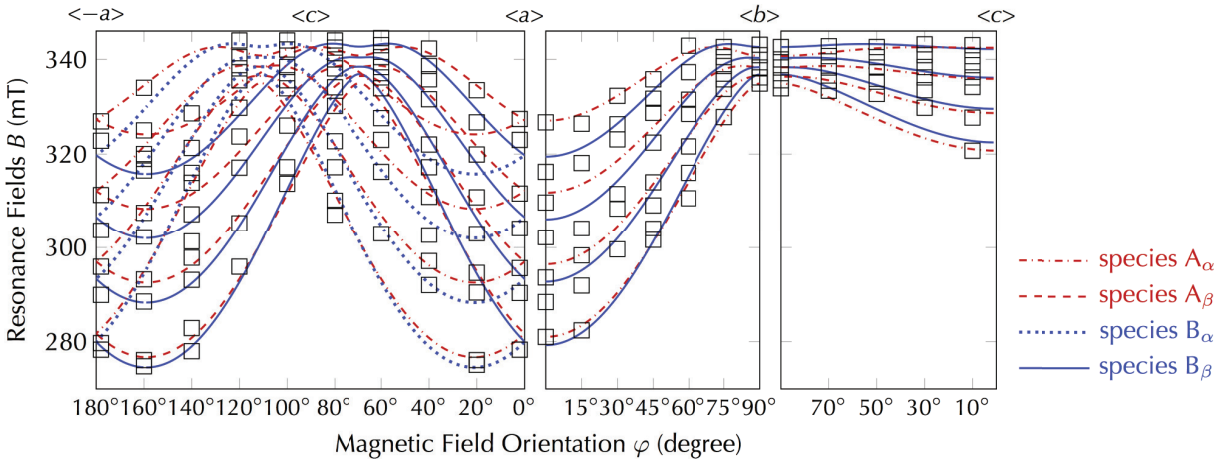

Figure 7.5: Angular dependent resonance field positions of the mononuclear Cu^{2+} species measured in three orthogonal planes (the size of the black open squares resembles error limits) and the simulated angular dependencies of the single crystal (red, blue lines).

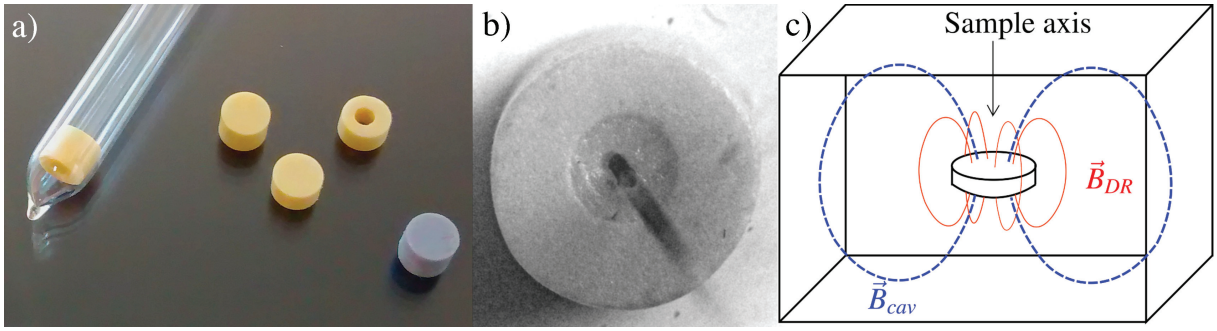

Figure 7.6: a) DRs (from left to right): K80-H in sample tube, K80, K80′, K80-H′ next to the differently colored K85. b) The samples can be inserted in a capillary and positioned inside the DR to achieve the highest SNR gains. Here, a thin capillary (= 200 μm) is positioned with grease inside the hole of K80 (= 1 mm). c) Superposition of $TE_{01\delta}$-mode of a DR (thin, red) and TE_{102} mode of the cavity resonator (dashed blue) in the notation of [**?**].

the general formula $Ba_{6-x}Ln_{8+2x/3}Ti_{18}O_{54}$ (Ln = Sm, Nd) that demonstrate at once low dielectric losses in the microwave range ($\tan\delta = 7\ldots14{\cdot}10^{-4}$ at 10 GHz) and appropriate temperature stability of the dielectric constant ($\tau_\varepsilon = \pm5$ ppm/K). They were optimized for samples with small dimensions and can be used in commercial OXFORD instruments flow cryostats if the coupling is done via cavity resonators. We found a maximal EPR signal enhancement by a factor up to 74 at 6 K. The increases of quality and filling factors as well as that of the microwave (mw) B_1-field in the resonator setup are discussed in dependence on temperature. We show that the absolute sensitivity gain must be related to that increase in the mw field and the remaining relative gain of the SNR is about 18 for small samples. The developed DRs have shown a good potential in EPR application as reliable and easy-to-use components allowing research of thin films and in particular small crystalline structures.

7.11 NO adsorption in amino-modified $Cu_3(btc)_2$-type MOFs studied by solid-state NMR

A.H. Khan, K. Peikert*, M. Fröba*, M. Bertmer

*Department of Chemistry, Institute of Inorganic and Applied Chemistry, University of Hamburg, Martin-Luther-King Platz 6, 20146 Hamburg, Germany

Adsorption of nitric oxide (NO) in the MOFs $Cu_3(btc)_2$ (HKUST-1) and $Cu_3(NH_2btc)_2$ (UHM-30) was studied via ^1H solid-state NMR. Changes to the electronic properties by adding paramagnetic molecules to antiferromagnetically coupled copper ions is evident in ^1H NMR shift, hyperfine coupling, and spin lattice relaxation times (T_1). Furthermore, in the case of $Cu_3(NH_2btc)_2$, the results indicate the formation of NONOates.

7.12 ^{113}Cd Solid-State NMR for Probing the Coordination Sphere in Metal-Organic Frameworks

A.V. Kuttatheyil, M. Handke*, J. Bergmann*, D. Lässig*, J. Lincke*, J. Haase, M. Bertmer, H. Krautscheid*

*Faculty of Chemistry and Mineralogy, Universität Leipzig, Johannisallee 29, 04103 Leipzig, Germany

Spectroscopic techniques are a powerful tool for structure determination, especially if single-crystal material is unavailable. ^{113}Cd solid-state NMR is easy to measure and is a highly sensitive probe because the coordination number, the nature of coordinating groups, and the geometry around the metal ion is reflected by the isotropic chemical shift and the chemical-shift anisotropy. Here, a detailed investigation of a series of 27 cadmium coordination polymers by ^{113}Cd solid-state NMR is reported. The results obtained demonstrate that ^{113}Cd NMR is a very sensitive tool to characterize the cadmium environment, also in non-single-crystal materials. Furthermore, this method allows the observation of guest-induced phase transitions supporting understanding of the structural flexibility of coordination frameworks.

7.13 Tuning the nitric oxide release behavior of amino functionalized HKUST-1

K. Peikert*, L.J. McCormick†, D. Cattaneo†, M.J. Duncan†, F. Hoffmann*, A.H. Khan, M. Bertmer, R.E. Morris†, M. Fröba*

*Department of Chemistry, Institute of Inorganic and Applied Chemistry, University of Hamburg, Martin-Luther-King Platz 6, 20146 Hamburg, Germany

†EaSTChem School of Chemistry, University of St. Andrews, Purdie Building, St. Andrews KY16 9ST, United Kingdom

Four new secondary amino functionalized trimesic acid ligands ($H_3RNHbtc$, R= Me, Et, ^{n}Pr, and ^{i}Pr) were synthesized. When used in combination with H_3btc these ligands

lead to four new mixed-linker metal organic frameworks (MOFs) which we call UHM-36, UHM-37, UHM-38, and UHM-39. All MOFs are isostructural to HKUST-1. We tested these MOFs as nitric oxide storage and release materials and investigate the influence of the amine groups on the NO storage capacity of the MOFs. The results were compared to the unfunctionalized HKUST-1, i. e., $Cu_3(btc)_2$.

7.14 Micro-imaging of liquid-vapor phase transition in nano-channels

A. Lauerer, P. Zeigermann J. Lenzner, C. Chmelik, M. Thommes*, R. Valiullin, J. Kärger

*Quantachrome Instruments, Boynton Beach, FL, USA

Mesoporous silicon accommodating structured nano-channels is employed as a host material for recording the evolution of liquid-vapor phase transitions in nanoporous materials upon molecular adsorption and desorption. Analysis is based on the application of micro-imaging via IR microscopy revealing the spatial-temporal dependence of guest concentrations within the material as a function of the chosen pressure steps. In this way, phase transitions become observable in the context of their local environment and may be correlated with the pore architecture by immediate experimental evidence.

7.15 Uphill diffusion and overshooting in the adsorption of binary mixtures in nanoporous solids

A. Lauerer, T. Binder C. Chmelik, E. Miersemann*, J. Haase, D.M. Ruthven†, J. Kärger,

*Department of Mathematics, University of Leipzig, Augustusplatz 10/11, 04109 Leipzig, Germany
†Department of Chemical and Biological Engineering, University of Maine, 5737 Jenness Hall, Orono, Maine 04469, USA

Under certain conditions, during binary mixture adsorption in nanoporous hosts, the concentration of one component may temporarily exceed its equilibrium value. This implies that, in contrast to Ficks Law, molecules must diffuse in the direction of increasing rather than decreasing concentration. Although this phenomenon of overshooting has been observed previously, it is only recently, using microimaging techniques, that diffusive fluxes in the interior of nanoporous materials have become accessible to direct observation. Here we report the application of interference microscopy to monitor uphill fluxes, covering the entire period of overshooting from initiation until final equilibration. It is shown that the evolution of the profiles can be adequately predicted from the single-component diffusivities together with the binary adsorption equilibrium data. The guest molecules studied (carbon dioxide, ethane and propene) and the host material (ZSM-58 or DDR) are of practical interest in relation to the development of kinetically selective adsorption separation processes.

7.16 Diffusion of propene in DDR crystals studied by interference microscopy

A. Lauerer, T. Binder J. Haase, J. Kärger, D.M. Ruthven*

*Department of Chemical and Biological Engineering, University of Maine, 5737 Jenness Hall, Orono, Maine 04469, USA

This paper presents the results of a detailed experimental study of the diffusion of propene in large crystals of DDR zeolite (the pure silica analog of ZSM-58) carried out by interference microscopy (IFM). Diffusion is very slow as the propene molecules are only just small enough to pass through the distorted 8-ring windows of the DDR structure. This makes it possible to measure many concentration profiles during the available time and thus to study the diffusional behavior at a level of detail that would be impossible in faster systems. In an ideal DDR crystal diffusion should occur only in the radial direction. In the actual system radial diffusion was dominant but there is also a small but significant axial component which complicates the interpretation of the experimental data. The diffusivity increases strongly with loading but the apparent magnitude of this effect may be increased by the small contribution from axial diffusion. The activation energy for radial diffus ion is about 34 kJ/mole.

7.17 Microimaging of transient intracrystalline concentration profiles during two-component uptake of light hydrocarbon - carbon dioxide mixtures by DDR-type zeolites

T. Binder A. Lauerer, C. Chmelik, J. Haase, J. Kärger, D.M. Ruthven*

*Department of Chemical and Biological Engineering, University of Maine, 5737 Jenness Hall, Orono, Maine 04469, USA

We report here the application of interference microscopy to study intracrystalline diffusion in a binary adsorbed phase. Hitherto the application of interference microscopy to the study of intracrystalline diffusion has been limited to single-component systems since only for a single-component system is the measured phase shift directly related to the concentration. However, when the difference in diffusivity between the components is sufficiently large, the faster component reaches equilibrium on a time scale that is short compared with the diffusion time for the slower component. Under these conditions, which are fulfilled for the system studied ($CO_2C_2H_6$ in a large crystal of zeolite DDR), it is possible to determine the transient concentration profiles for both components and hence to determine the influence of the fast component on diffusion of the slower species. It is shown that measurements of this type offer a possible approach for experimental determination of the diffusion matrix. For the system studied, diffusion of ethane was found to be essentially unaffected by the presence of CO_2, in conformity with the results of an earlier study carried out by the zero length column technique.

7.18 Funding

Aufklärung des Ladungstransports in funktionalisierten porösen Organosilikaten und Kompositmembranen mit MAS-NMR-Spektroskopie und Diffusometrie
Prof. Dr. Jürgen Haase, Prof. Dr. Michael Wark
DFG, HA 1893/9-1

Deuterium-Festkörper-NMR und ^1H MAS PFG NMR-Untersuchungen der Beweglichkeit des Wirtsgerüsts und der Gastmoleküle in nanoporösen Materialien
Prof. Dr. Jürgen Haase
DFG, HA 1893/16-1

Micro-Imaging transienter Konzentrationsprofile von Gastgemischen in Zeolithkristallen
Prof. Dr. Jürgen Haase, Prof. Dr. Jörg Kärger
DFG, HA 1893/15-1

Metalle unter extremen Bedingungen
Prof. Dr. Jürgen Haase
DFG, HA 1893/12-1

Energy efficient MOF-based Mixed Matrix Membranes for CO_2 Capture
Prof. Dr. Jürgen Haase
EU, 608490

Anwendungen der NMR-Spektroskopie zur Erforschung von Struktur-Beweglichkeits-Beziehungen an nanoporösen Wirt-Gast-Systemen im konzentrierten Einsatz mit dem Micro-Imaging
Prof. Dr. Jürgen Haase, Prof. Dr. Jörg Kärger
DFG

NMR in Pulsed High-Field Magnets
Prof. Dr. Jürgen Haase, Prof. Dr. Jochen Wosnitza
Drittmittel aus Kooperation HZDR

Leibniz-Graduiertenschule Aerosole, Wolken, Strahlung: Mineralstaub, AG: Heterogene Eisnukleation an Mineralstaubpartikeln
Prof. Dr. Jürgen Haase
Leibniz-Gemeinschaft

MOFs as carrier for nitric oxide delivery in biological systems - microscopic fundamentals of adsorption and controlled release studied by infrared and electron and nuclear spin resonance spectroscopy
PD Dr. Marko Bertmer, Prof. Dr. Andreas Pöppl, Prof. Dr. Martin Hartmann, Prof. Dr. Michael Fröba
DFG, BE 2434/4-2, PO 426/8-2

Charakterisierung der [2+2]-Photodimerisierung von photoaktiven Substanzen auf der Basis von Zimtsäure eingebaut in Polymeren oder in supramolekularen Strukturen mit Festkörper-NMR-Spektroskopie

PD Dr. Marko Bertmer
DFG, BE 2434/2-3

Paramagnetic adsorption sites in microporous crystalline solids studied by electron paramagnetic resonance spectroscopy from single crystals to oriented thin films
Prof. Dr. Andreas Pöppl
DFG, PO 426/11-1

NMR-Untersuchungen der physikalischen Eigenschaften von Materialien, die in nanoporösen Festkörpern eingebettet sind
Prof. Dr. Dieter Michel, Prof. Dr. Elena V. Charnaya
DAAD Leonard-Euler-Programm

Mikrostruktur und molekulare Beweglichkeit organischer Moleküle in wässrigen Lösungen
Prof. Dr. Dieter Michel, Prof. Dr. Vladimir I. Chizhik
DAAD Leonard-Euler-Programm

7.19 Organizational Duties

Professor Dr. Jürgen Haase
- Dean of the Faculty
- Vice Director of the Magnetic Resonance Center Leipzig
- Board Member of the Heisenberg Gesellschaft e. V.
- Full Member of the Saxonian Academy of Sciences in Leipzig
- Member of the German Physical Society
- Member of the American Physical Society
- Member of the ICAM Board of Governors of the institute for Complex Adaptive Matter
- Referee: Physical Review, Science, IOP, German-Israeli Foundation for Scientific Research and Developement

Prof. Dr. Andreas Pöppl
- Referee: Journal of Magnetic Resonance, Journal of the American Chemical Society, Physical Chemistry Chemical Physics, Chemical Physics Letters
- Project Reviewer: German-Israeli Foundation for Scientific Research and Development

PD Dr. Marko Bertmer
- Referee: Angewandte Chemie, Chemistry of Materials, Journal of Physical Chemistry, Solid State Nuclear Magnetic Resonance

Prof. Dr. Dieter Michel
- Full Member of the Saxonian Academy of Sciences in Leipzig
- Member of the German Physical Society
- Member of the Society of German Chemists
- German Coordinator of the German-Russian Centre Applied and Computational Physics (ACOPhys) at the St. Petersburg State University

- Member at the International Advisory Committee of the International Meeting of Ferroelectricity
- Member at the International Advisory Committee of the European Meeting of Ferroelectricity
- Member at the International Advisory Committee of the Conference NMR of Condensed Matter St. Petersburg
- Member of the German-Israeli Foundation for Scientific Research and Developement
- Referee: Physical Review, Journal of Physics: Condensed Matter, Langmuir, Journal of Magnetic Resonance, Phys. Stat. Sol., Materials Chemistry and Physics, German-Israeli Foundation for Scientific Research and Developement

Prof. Dr. Rolf Böttcher

- Referee: Physical Review, Journal of Physics: Condensed Matter, Langmuir, Journal of Magnetic Resonance

7.20 External Cooperations

Academic

- Technical University Munich, Physics Department, Crystal Lab, Garching, Germany
  Prof. Dr. Andreas Erb
- Cavendish Laboratory, Cambridge, UK
  S. K. Goh, P. Alireza
- Washington University, St. Louis, MO, USA
  J. Schilling, M. Conradi
- Victoria University, Physics Department, Wellington, New Zealand
  Dr. Grant V. M.Williams
- Helmholtz-Zentrum Dresden-Rossendorf, Dresden, Germany
  Prof. Dr. J. Wosnitza
- University of Minnesota, School of Physics and Astronomy, USA
  Prof. Dr. M. Greven
- University of Illinois at Urbana-Champaign, Department of Physics, USA
  Prof. Dr. C. P. Slichter
- Laboratoire National des Champs Magnétiques Pulsés, Toulouse, France
  Prof. Dr. G. Rikken
- University of New South Wales, School of Physics, Sydney, Australia
  Prof. Dr. O. Sushkov
- Washington University, Department of Chemistry, St. Louis, MO, USA
  Sophia E. Hayes
- Universität Koblenz-Landau, Abteilung Chemie, Landau, Germany
  Prof. Dr. Gabriele Schaumann
- Martin-Luther-Universität Halle-Wittenberg, Halle, Germany
  Dr. H. T. Langhammer

- Kazan State University, Tartastan, Russian Federation
  Prof. Dr. E. N. Kalabukhova
- Universität Erlangen-Nürnberg, Erlangen Catalysis Resource Center - ECRC, Erlangen, Germany
  Prof. Dr. Martin Hartmann
- Université du Maine, Laboratoire de Physique de l'Etat Condensé, Le Mans, France
  Prof. Dr. A. Kassiba
- University of Vilnius, Faculty of Physics, Vilnius, Lithuania
  Prof. Dr. J. Banys
- Argonne National Laboratory, Illinois, USA
  Prof. Dr. P. Littlewood
- Georgetown University Department of Chemistry, Washington, DC, USA
  Prof. Dr. YuYe Tong
- Max Planck Institute of Solid State Research, Stuttgart, Germany
  Prof. Dr. B. Keimer
- University of Illinois at Chicago, USA
  Prof. Dr. D. K. Morr
- IFW-Dresden, Dresden, Germany
  M. Richter, H. Eschrig
- Ruhr-University Bochum, Bochum, Germany
  R. A. Fischer

Industry

- NMR-Service GmbH, Erfurt, Germany
  M. Braun
- Bruker BioSpin GmbH, Rheinstetten, Germany
  F. Engelke

7.21 Publications

Journals

S. S. Arzumanov, D. I. Kolokolov, D. Freude, A. G. Stepanov
Methane Mobility in Ag/H-ZSM-5 Zeolite in the Presence of Ethene: A View Based on PFG ^{1}H MAS NMR Analysis of Methane Diffusivity
J. Phys. Chem. C 119 (2015) 18481-18486.

A. Lauerer, P. Zeigermann, J. Lenzner, C. Chmelik, M. Thommes, R. Valiullin, J. Kärger
Micro-imaging of liquid-vapor phase transition in nano-channels
Microp. Mesop. Mater. 214 (2015) 143-148.

Barth, M. Mendt, A. Pöppl, M. Hartmann
Adsorption of nitric oxide in metal-organic frameworks: Low temperature IR and EPR spectroscopic evaluation of the role of open metal sites
Microp. Mesop. Mater. 216 (2015) 97-110.

T. Binder, A. Lauerer, C. Chmelik, J. Haase, J. Kärger, D. M. Ruthven
Microimaging of Transient Intracrystalline Concentration Profiles during Two-Component Uptake of Light Hydrocarbon-Carbon Dioxide Mixtures by DDR-Type Zeolites
Ind. Eng. Chem. Res. 54 (2015) 8997-9004.

R. Böttcher, M. Lorenz, A. Pöppl, D. Spemann, M. Grundmann
Local zincblende coordination in heteroepitaxial wurtzite $Zn_{1-x}Mg_xO$:Mn thin films with $0.01 \leq x \leq 0.04$ identified by electron paramagnetic resonance
J. Mater. Chem. C 3 (2015) 11918-11929.

S. Friedländer, M. Simenas, M. Kobalz, P. Eckold, O. Ovchar, A. G. Belous, J. Banys, H. Krautscheid, A. Pöppl
Single Crystal Electron Paramagnetic Resonance with Dielectric Resonators of Mononuclear Cu^{2+} Ions in a Metal-Organic Framework Containing Cu_2 Paddle Wheel Units
J. Phys. Chem. C 119 (2015) 19171-19179.

S. Friedländer, O. Ovchar, H. Voigt, R. Böttcher, A. Belous, A. Pöppl
Dielectic Ceramic EPR Resonators for Low Temperature Spectroscopy at X-band Frequencies
Appl. Magn. Reson. 46 (2015) 33-48.

C. Gabriel, P. Karakosta, A. A. Vangelis, C. P. Raptopoulou, A. Terzis, V. Psycharis, M. Bertmer, C. Mateescu, A. Salifoglou
pH-Specific Crystalline Binary and Ternary Metal-Organic Framework Materials of Pb(II) with (Di)Tricarboxylate Ligands and N,N′-Aromatic Chelators. Structure, Architecture-Lattice Dimensionality, and Electronic Spectroscopic Property Correlations
Cryst. Growth Des. 15 (2015) 1665-1682.

N. Georgieva, D. Rybicki, R. Gühne, G. V. M. Williams, S. V. Chong, I. Garate, J. Haase
^{77}Se nuclear magnetic resonance of topological insulator Bi_2Se_3
arXiv: 1511.01727.

A. Jäger, J. Schwarz, Y. K. Mouvenchery, G. E. Schaumann, M. Bertmer
Physical long-term regeneration dynamics of soil organic matter as followed by ^1H solid-state NMR methods
Environm. Chem. 13 (2015) 50-57.

A. H. Khan, K. Peikert, M. Fröba, M. Bertmer
NO adsorption in amino-modified $Cu_3(btc)_2$-type MOFs studied by solid-state NMR
Microp. Mesop. Mater. 216 (2015) 111-117.

A. V. Kuttatheyil, M. Handke, J. Bergmann, D. Lässig, J. Lincke, J. Haase, M. Bertmer, H. Krautscheid

^{113}Cd Solid-State NMR for Probing the Coordination Sphere in Metal-Organic Frameworks
Chem. Eur. J. 21 (2015) 1118-112.

A. Lauerer, T. Binder, C. Chmelik, E. Miersemann, J. Haase, D. Ruthven, J. Kärger
Uphill diffusion and overshooting in the adsorption of binary mixtures in nanoporous solids
Nature Commun. 6 (2015) 7697.

A. Lauerer, T. Binder, J. Haase, D. Ruthven, J. Kärger
Diffusion of Propene in DDR Crystals Studied by Interference Microscopy
Chem. Eng. Sci. 138 (2015) 110-117.

I. Lorite, C. Zandalazini, P. Esquinazi, D. Spemann, S. Friedländer, A. Pöppl, T. Michalsky, M. Grundmann, J. Vogt, J. Meijer, S. P. Heluani, H. Ohldag, W. A. Adeagbo, S. K. Nayak, W. Hergert, A. Ernst, M. Hoffmann
Study of the negative magneto-resistance of single proton-implanted lithium-doped ZnO microwires
J. Phys.: Cond. Matter 27 (2015) 256002.

M. V. Luzgin, D. Freude, J. Haase, A. G. Stepanov
Methane Interaction with Zn^{2+}-Exchanged Zeolite H-ZSM-5: Study of Adsorption and Mobility by One- and Two-Dimensional Variable-Temperature ^{1}H Solid-State NMR
J. Phys. Chem. C 119 (2015) 14255-14261.

T. Meier, S. Reichardt, J. Haase
High-sensitivity NMR beyond 200.000 atmospheres of pressure
J. Magn. Reson. 257 (2015) 39-44.

T. Meier, J. Haase
Anvil Cell Gasket Design for High Pressure Nuclear Magnetic Resonance Experiments Beyond 30 GPa
Rev. Sci. Instr. 86 (2015) 123906.

M. Mendt, A. Pöppl
The Line Width of the EPR Signal of Gaseous Nitric Oxide as Determined by Pressure and Temperature-Dependent X-band Continuous Wave Measurements
Appl. Magn. Reson. 46 (2015) 1249.

S. Welzmiller, F. Heinke, P. Huth, G. Bothmann, E.-W. Scheidt, G. Wagner, W. Scherer, A. Pöppl, O. Oeckler
The influence of Mn doping on the properties of $Ge_4Sb_2Te_7$
J. Alloys Compd. 652 (2015) 74 82.

L. V. Meyer, J. Voigt, H. Schäfer, M. Steinhart, R. Böttcher, A. Pöppl, M. Mai, C. Feldmann, K. Müller-Buschbaum
Organic melt, electride, and CVD induced in situ deposition of luminescent lanthanide imidazolate MOFs on nanostructured alumina
Inorg. Chem. Front. 2 (2015) 237-245.

K. Peikert, L. J. McCormick, D. Cattaneo, M. J. Duncan, F. Hoffmann, A. H. Khan, M. Bertmer, R. E. Morris, M. Fröba
Tuning the nitric oxide release behavior of amino functionalized HKUST-1
Microp. Mesop. Mater. 216 (2015) 118-126.

A. Pochert, D. Schneider, J. Haase, M. Linden, R. Valiullin
Diffusion and Molecular Exchange in Hollow Core-Shell Silica Nanoparticles
Langmuir 3 (2015) 110285-10295.

D. Y. Podorozhkin, E. V. Charnaya, M. K. Lee, L.-J. Chang, J. Haase, D. Michel, Y. A. Kumzerov, A. V. Fokin
Diffusion slowdown in the nanostructured liquid Ga-Sn alloy
Ann. Phys. (Berlin) 527 (2015) 248-253.

D. Rybicki, J. Kohlrautz, J. Haase, M. Greven, X. Zhao, M. K. Chan, C. J. Dorow, M. Veit
Electronic spin susceptibilities and superconductivity in $HgBa_2CuO_{4+\delta}$ from nuclear magnetic resonance
Phys. Rev. B (R) 92 (2015) 081115-5.

D. Savchenko, E. Kalabukhova, B. Shanina, A. Pöppl, V. Yukhymchuk, J. Lancok, E. Ubyivovk, E. Mokhov
EPR, ESE, and pulsed ENDOR study of the nitrogen donors in 15R SiC grown under carbon-rich conditions
Phys. Status Solidi B 252 (2015) 566-572.

M. Simenas, M. Kobalz, M. Mendt, P. Eckhold, H. Krautscheid, J. Banys, A. Pöppl
Synthesis, Structure, and Electron Paramagnetic Resonance, Study, of a Mixed Valent Metal-Organic Framework Containing Cu_2 Paddle-Wheel Units
J. Phys. Chem. C 119 (2015) 4898 4907.

S. Welzmiller, R. Schlegel, A. Pöppl, G. Bothmann, E.-W. Scheidt, W. Scherer, O. Oeckler
Doping $GeSb_2Te_4$ with $Cr3^{3+}$: Structure and Temperature-Dependent Physical Properties
Z. Anorg. Allg. Chem. 641 (2015) 2350-2356.

T. Titze, A. Lauerer, L. Heinke, C. Chmelik, N. E. R. Zimmermann, F. J. Keil, D. M. Ruthven, J. Kärger
Transport in nanoporous materials including MOFs: the applicability of Ficks laws
Angew. Chem. Int. Ed. 54 (2015) 14580-14583.

M. Simenas, A. Ciupa, M. Maczka, A. Pöppl, J. Banys
EPR Study of Structural Phase Transition in Manganese-Doped $[(CH_3)_2NH_2][Zn(HCOO)_3]$ Metal Organic Framework
J. Phys. Chem. C 119 (2015) 24522-24528.

J. Kohlrautz, S. Reichardt, E. V. Green, H. Kühne, J. Wosnitza, J. Haase
NMR shift and relaxation measurements in pulsed high-field magnets up to 58 Tesla
J. Magn. Reson. 263 (2015) 1-6.

C. M. Kropf, J. Kohlrautz, J. Haase, B. V. Fine
Anomalous longitudinal relaxation of nuclear spins in CaF_2
arXiv:1510.06589.

D. Rybicki, M. Jurkutat, S. Reichardt, C. Kapusta, J. Haase
New Perspective on the Phase Diagram of Cuprate High-Temperature Superconductors
arXiv:1511.02408

M. Simenas, B. Jee, M. Hartmann, J. Banys, A. Pöppl
Adsorption and Desorption of HD on the Metal-Organic Framework $Cu_{2.97}Zn_{0.03}(Btc)_2$ Studied by Three-Pulse ESEEM Spectroscopy
J. Phys. Chem. C 119 (2015) 28530-28535.

M. Simenas, M. Kobalz, M. Mendt, P. Eckold, H. Krautscheid, J. Banys, A. Pöppl
Synthesis, Structure, and Electron Paramagnetic Resonance Study of a Mixed Valent Metal-Organic Framewok Containing Cu_2 Paddle-Wheel Units
J. Phys. Chem. C 119 (2015) 4898-4907.

Talks

A. Pöppl
EPR spectroscopy of paramagnetic centers and adsorption complexes in porous metal organic frameworks: Development and application of dielectric resonators and microresonators for investigations of small single crystals
SPP 1601/2
Göttingen, Germany, January 2015

Jürgen Haase
Charge transfer and distribution, and the uniform spin susceptibility of the cuprate superconductors from Nuclear Magnetic Resonance Studies
AMN-7
Nelson, New Zealand, February 2015

Jürgen Haase
Elektronische und chemische Eigenschaften von Festkörpern - Neue Erkenntnisse von extremer NMR
MDR-35
Leipzig, Germany, May 2015

Jürgen Haase
Extreme high-pressure NMR applications in physics and chemistry
Euromar 2015
Prague, Czech Republic, July 2015

Jürgen Haase
Implications of a Different Phase Diagram for Cuprate Superconductivity
Quantum Design
Dresden, Germany, July 2015

Jürgen Haase
Uniform Spin Susceptibility and a New Phase Diagram from NMR of Cuprate Superconductors
Itinerant Electron Magnetism
Kyoto, Japan, September 2015

Elisabeth Vonhof
Water adsorption on aerosols from nuclear magnetic resonance
Pacifichem 2015
Honolulu, HI, USA, December 2015

Posters

S. Friedländer, A. Kultaeva, F. Bolling, M. Simenas and A. Pöppl
Electron Paramagnetic Resonance with Dielectric Resonators of Small Single Crystals of Metal-Organic Frameworks, Development and application of dielectric resonators for investigations of small, low density, porous MOF single crystals
37th Discussion Meeting of the GDCh-Division of Magnetic Resonance FGMR Joint Meeting with German and British MR Societies and DFG SPP 1601
Darmstadt, September 2015

N. Dvoyashkina
Composite fuel cell materials studied by MAS PFG NMR diffusometry and MAS NMR spectroscopy
Diffusion Fundamentals VI
Dresden, Germany, 23.08.-26.08.2015

A. Lauerer, P. Zeigermann, J. Lenzner, C. Chmelik, R. Valiullin, J. Kärger
IR Micro-Imaging of Mesoporous Silion as a Model System for the Investigation of Hysteresis Phenomena
27. Deutsche Zeolith-Tagung
Oldenburg, Germany, 25.02.-27.02.2015.

A. Lauerer, C. Chmelik, J. Haase, J. Kärger
Interference and IR-Microscopy for Studies of Nanoporous Materials: An Insightful View on Intracrystalline Molecular Transport
Jahrestreffen der Fachgruppn Trocknungstechnik und Wärme- und Stoffübertragung
Leipzig, Germany, 04.03.-06.03.2015.

A. Lauerer, C. Chmelik, J. Haase, J. Kärger
Interference and IR-Microscopy for Studies of Nanoporous Materials: An Insightful View on Intracrystalline Molecular Transport
Diffusion Fundamentals VI
Dresden, Germany, 23.08.-26.08.2015.

M. Zahan
Solid-state NMR study of cation effects on the photodimerization of cinnamate salts
Euromar 2015
Prague, Czech Republic, July 2015

A. H. Khan
Nitric oxide adsorption in amino-modified $Cu_3(btc)_2$-type MOFs studied by solid-state NMR
Euromar 2015
Prague, Czech Republic, July 2015

A. Kultaeva, S. Friedländer, F. Bolling, J. Bergmann, O. Ovchar, H. Voigt, A. Belous, A. Pöppl
High sensitivity EPR spectroscopy of paramagnetic centers in metal-organic framework single crystals
SPP 1601 Young Researchers' Workshop 2016
Konstanz, Germany, 11.04.-14.04.2015

S. Friedländer, H. Voigt, R. Böttcher, A. Pöppl
EPR spectroscopy of paramagnetic centers and adsorption complexes in porous metal organic frameworks - Development an application of dielectric resonators and microresonators for investigations of small single crystals
SPP 1601/2
Göttingen, Germany, January 2015

7.22 Graduations

Doctorate

- Michael Jurkuatat, M. Sc.
  NMR of Electron-Doped High-Temperature Superconductor $Pr_{2-x}Ce_xCuO_4$
  April 2015
- Dipl.-Phys. Sebastian Sambale
  Magnetic and electronic properties of iron-based superconducting systems
  September 2015

7.23 Guests

- Prof. Dr. Thomas Heine
  Jacobs University Bremen gGmbH, Bremen/Germany
  January 2015
- Prof. Dr. Boris Fine
  University of Heidelberg/Germany
  February 2015
- Dr. Alexey Donets
  St. Petersburg State University/Russia
  May 2015
- Professor Elena Charnaya
  St. Petersburg State University/Russia
  May – June 2015

- Roman Dmitriev
  St. Petersburg State University/Russia
  May – June 2015
- Prof. Dr. Alexander Shengelaya
  Ivane Javakhishvili Tbilisi State University, Tbilisi/Georgia
  June 2015
- Dr. Michael Fechner
  Swiss Federal Institute of Technology, Zurich/Switzerland
  July 2015
- Dr. Karl Syassen
  Max Planck Institute for Solid State Physics, Stuttgart/Germany
  July 2015
- Mantas Simenas
  Vilnius University, Vilnius/Lithuania
  August – September 2015
- Prof. Dr. Jeff Tallon
  Robinson Research Institute, Victoria University of Wellington/New Zealand
  September 2015
- Denis Nefedov
  St. Petersburg State University/Russia
  October – December 2015
- Andrei Uskov
  St. Petersburg State University/Russia
  November 2015
- Anastasiia Olegovna Antonenko
  St. Petersburg State University/Russia
  November – December 2015
- Prof. Dr. Clemens Ulrich
  University of New South Wales, Sydney/Australia
  December 2015
- Dmitry Yurievich Podorozhkin
  St. Petersburg State University /Russia
  December 2015 – January 2016
- Min Kai Lee
  National Cheng Kung University, Tainan/Taiwan
  December 2015 – January 2016

8

Nuclear Solid State Physics

8.1 Introduction

Magnetic resonance tomography (MRT) is one of the most important tools of today's modern medicine diagnostics. The technique based mainly on the work of F. Bloch and E. Purcell, who invented the method of Nuclear Magnetic Resonance (NMR) independently. The sensitivity of MRT is limit on the fraction of up to down spins of H in a given magnetic field and is determined by the Boltzmann distribution (only 10^{-5} at RT and standard MRT condition in human medicine). An enhancement of this factor is indirectly related to the lateral resolution and could increase the quality of MRT by orders of magnitude. One possibility to enhance this factor is the so-called hyperpolarization technique. One idea is to use NV centres as polarization agencies and was firstly shown in Berkeley and Ulm. Now R. Wunderlich in cooperation with J. Kohlrautz of the group of J. Haase show that ^{13}C spins in diamond could be hyperpolarized. Thus in 2 min a NMR signal to noise ratio could be acquired corresponding to a conventional NMR measurement of about one day. The question is now would it be possible to polarize H, e.g. by cross polarization and by using nano diamonds to increase the transfer surface. If this became possible it could open the door to perform histological diagnostic within the body.

Beside this exciting result, our group set up a new 100 kV implantation system to find new diamond artificial colour centres. Colour centres in diamond are of great interest since the NV centre was discovered. One new colour centre is now found in Leipzig, named L1 (the first letter of the city where the discovery takes place) with a photoluminescence at 581 nm. This colour centre is extremely bright and shows a very low phonon coupling. The origin is not yet clear and matter of further discussions. We also continue our work on deterministic ion implantation and could set up successfully the 30 kV ionLINE system of the company Raith (in cooperation with the group of B. Rauschenbach).

All this nice results are only possible due to our founding agencies, which we would like to express our deepest gratitude in particular the VolkswagenStiftung, DFG FOR1493, the European Social Founding (ESF) the EU Project DIADEMS and CHIST-ERA, HBFG Project and the SAW Project of the Leibniz Association.

Jan Meijer

8.2 Hyperpolarization via nitrogen vacancy centres

R. Wunderlich, J. Kohlrautz*, J. Haase*, J. Meijer

*Division of Magnetic Resonance of Complex Solids

The spin dynamics of the negatively charged Nitrogen–Vacancy centre (NV) in diamond is used to polarize ^{13}C nuclei in a bulk single crystal. The NV centre can be polarized in its $m = 0$ ground state just by shining green light on it. Here we use the hyperfine coupling between the NV electron spin and the ^{13}C nuclei spin in the exited level anti crossing (ESLAC) at about 50 mT to swop the spin polarization to nearby ^{13}C nuclei. For this reason we designed a home-build low field irradiation unit and a shuttling system to the NMR measurement probe in a 7 T solenoid. With this technique we obtain a signal to noise ratio of SNR = 31 in about 2 min which corresponds to a 23 h standard measurement without hyperpolarization.

Figure 8.1(a) shows the NMR signal at different magnetic fields around the ESLAC in a range of several Gauss. The NMR signal changes in its strength as well as in its

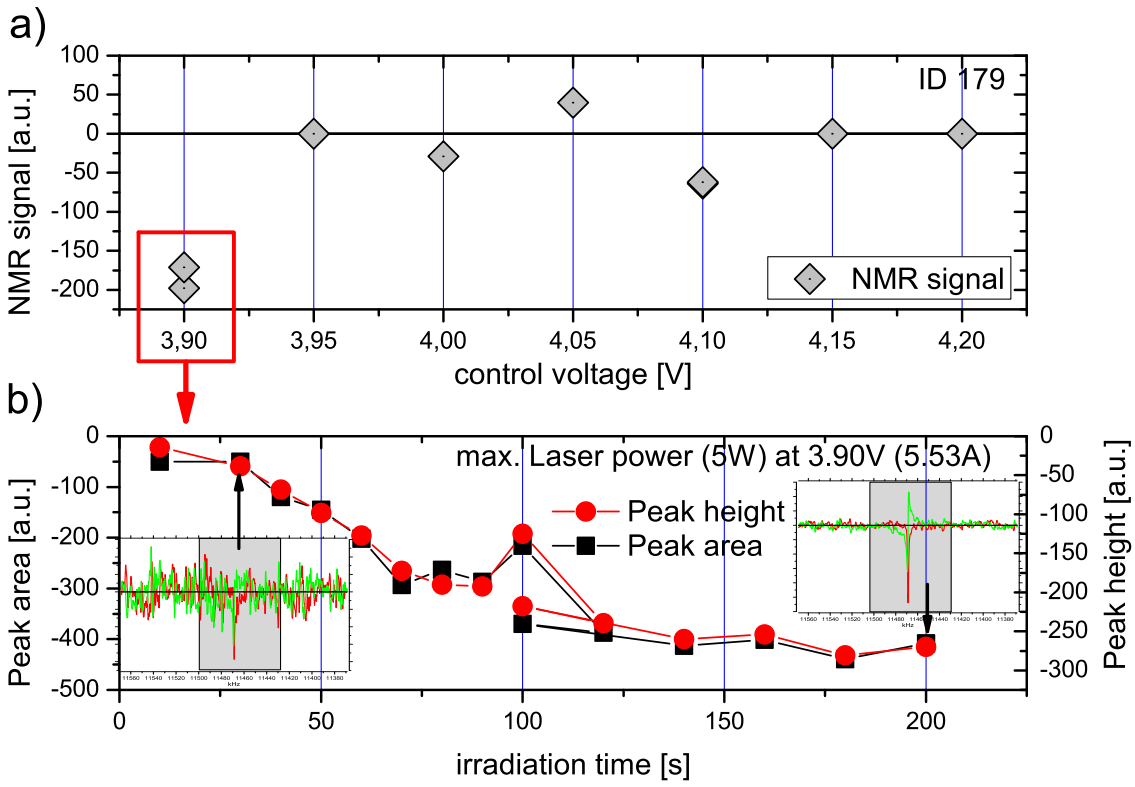

Figure 8.1: (a) NMR signal shown for different magnetic fields near the ESLAC at 50 mT during the laser irradiation. **(b)** The signal depicted with increasing irradiation time at a fixed magnetic field.

sign due to different dominant hyperfine couplings with varying magnetic fields. In Fig. 8.1(b) the saturation of the hyperpolarization effect with increasing irradiation time at a fixed laser output of 5 W at 532 nm is depicted. The competition between

the polarization transfer from the NV centre and the spin–lattice relaxation results in a saturation at about 2 min light exposure.

In ongoing experiments we investigate the different hyperfine coupling strengths and try to extend this technique to diamond micro particles as well as to other material systems like SiC.

8.3 Artificial colour centres with nearly phonon-free fluorescence at room temperature produced by ion beam implatation

J. Lehnert, R. John, M. Mensing, D. Spemann, S. Pezzagna, J. Meijer

Using shallow ion beam implantation of ions and molecules with masses around 26 amu in diamond, a new artificial optical centre with unique properties is formed. The bright L1 centre shows a linear polarized single narrow fluorescence line at 581 nm with nearly no phonon side band at room temperature. Additional the implantation procedure formed the well known ST1 centre. A spin resonance is found at 985 MHz and 1265 MHz with a line width less than 4 MHz. A coherent control of the spin state is shown with a $T_1 = 2.5\,\mu s$ for centres near the surface.

Defect centres in diamond become more and more in focus for a large range of application in physics, material science and bio-technology. Due to its high atomic density and its high Debye temperature, this material is an ideal candidate for quantum information processing and quantum sensing. The wide transparency range of diamond and the large amount of optically active defect centres also offer the possibility to engineer single-photon sources operating at room temperature. The optical properties of such non-classical light emitters can furthermore be controlled or improved by use of adequate photonic structures. For biomedical applications, fluorescent nanodiamonds containing Nitrogen–Vacancy (NV) centres are widely used for imaging and therapy. Furthermore, the unique spin and optical properties of the NV centres in diamond have lead to single molecule NMR. The main important features of the NV centre that provide these kinds of applications are the optical readout and coherent control of single spins with extremely long coherence time at room temperature. Among hundreds of defect centres known in diamond, these exceptional properties have been found up to now only for the NV centre and the ST1 centre. Whereas the NV centre can be produced using ion beam implantation or diamond growth in a controlled way, the ST1 centre was found on an ion beam etched HPHT diamond surface and could not be reproduced up to now. However, despite its prosperousness, the NV centre has some disadvantages. It is formed after annealing and involves a C vacancy, therefore a deterministic fabrication by ion implantation is not possible. Additionally, the centre shows a very large phonon coupling. This leads to a broad emission spectrum, thus coherent coupling schemes using photons are limited to low temperature. In order to find new applicable defect centres, we have set up an ion accelerator which is able to implant all types of elements, at the exception of noble gases. Our aim is to search for all possible diamond colour centres created by ion implantation. Ion implantation is the best way to address single atoms and defects with high spatial resolution. Using this method, the production of

an entangled quantum register and quantum sensors at room temperature has already been demonstrated using NV centres. Due to the extremely small diffusion constant in diamond, atoms placed by ion implantation remain at the same crystal position even after high temperature treatments. This stability reduces bleaching effects or formation change due to laser irradiation. The new centre emitting at 581 nm (hereafter termed the L1 centre following the convention commonly applied by the electron spin resonance (ESR) community). This L1 centre was created by ion implantation technique and, to our knowledge, could not be found in any natural diamond. Additional we refound the ST1 centre in the same samples.

8.4 ST1 colour centre in implanted and plasma treated diamond

R. John, J. Lehnert, S. Pezzagna, J. Meijer

The ST1 colour centre originally found in a diamond with fabricated nano pillars [1] was discovered in two diamonds that were subjected to through a Cu grid with a fluence of 10^{10} cm^{-2}, afterwards annealed at 800 ℃ for 2 h and then cleaned in O plasma at 40 Pa for 1.5 h. Fluorescence images (Fig. 8.2(a)) and spectra (Fig. 8.2(b)) as well as optical detected magnetic resonance (ODMR) spectra (Fig. 8.3(a)) and coherent spin manipulation (Fig. 8.3(b)) were measured for identification. The exact origin of the defect is yet to be determined.

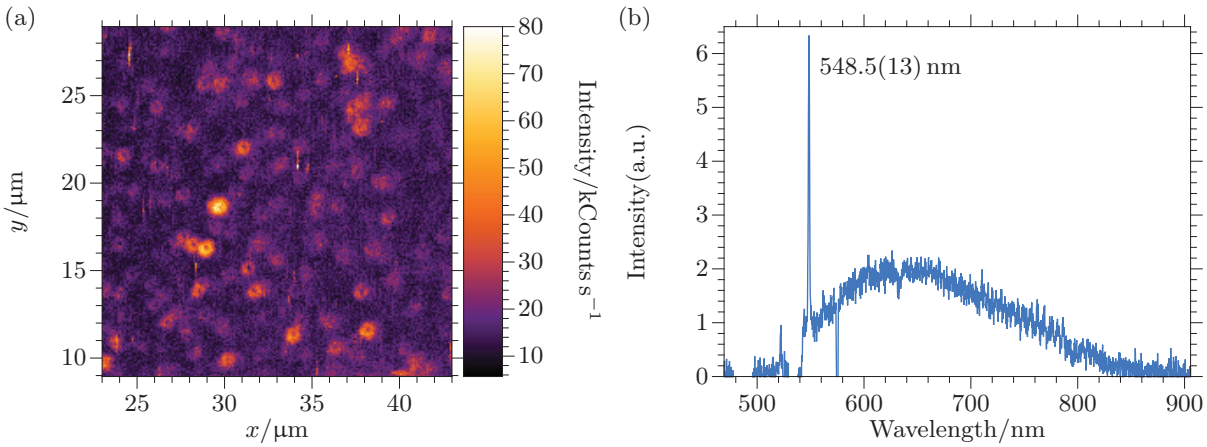

Figure 8.2: (a) Confocal scan of the surface of the diamond showing donut-shaped ST1-centres (caused by the high population of the metastable and non-radiative decaying triplet state [1] under high illumination power) and various other colour centres like the L1. **(b)** Exemplary background corrected PL-spectrum recorded at 300 K and 600 µW for 5 min in air immersion showing a strong ZPL at ≈ 550 nm with a phonon sideband characteristic for ST1.

[1] S.-Y. Lee et al.: Nat. Nanotechnol. **8**, 487 (2013), doi:10.1038/nnano.2013.104
[2] F. Jelezko et al.: phys. stat. sol. (a) **203**, 3207 (2006), doi:10.1002/pssa.200671403

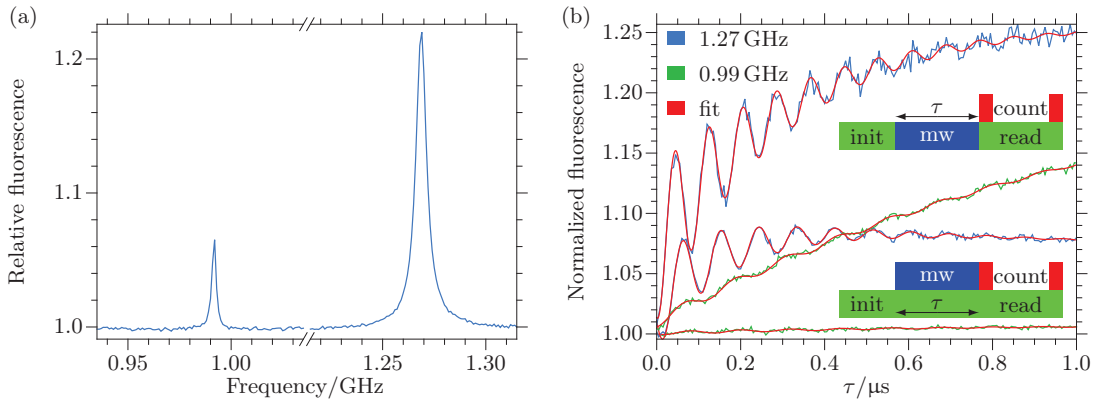

Figure 8.3: (a) ODMR spectrum showing two positive peaks at ≈ 0.99 GHz and ≈ 1.27 GHz indicating a spin triplet with zero field splitting $D \approx 1.13$ GHz and strain $E \approx 140$ MHz. **(b)** Rabi oscillations on the indicated resonance frequency with either pulsed light (upper right curves and pulsing scheme) or constant illumination (lower right curves). The measurement scheme is similar to NV [2], but the initialization laser pulse used was 7 μs, and the two 250 ns counting windows were 5.5 μs apart in time to accommodate for the long shelving state lifetime.

8.5 Increasing the quality of single ion implantation with high spatial resolution

N. Raatz, S. Pezzagna, S. Becker, St. Jankuhn, M. Holz*, I.W. Rangelow†, J. Meijer

*Nano Analytik GmbH, Ilmenau
†Institute of Micro and Nanoelectronics, TU Ilmenau

The Nitrogen-Vacancy (NV) centre in diamond is the most prominent candidate for a solid state quantum device. In order to couple the spins of nearby NV centres one need to place them with a distance about a few nanometer. Our setup to place single ions in solids is the nanoimplanter, a combination of low energy implantation and an atomic force microscope (AFM) with a pierced hollow tip [1].

In the last year we worked mainly on increasing the efficiency of the nanoimplanter to produce better and more deterministic results. This includes two main factors: increasing the spacial resolution and enhancing the creation yield of the NV centre formation. For the first mentioned point we installed a new AFM system which works both in AC (non contact) and DC (contact) mode. Working without contact allows us to determine the size of the aperture of the AFM tip directly in the nanoimplanter chamber by implanting a row of ions on PMMA and subsequent scanning in AC mode. With the help of the image the dimension of the hole can be estimated. Scanning with no contact ensures also a long lifetime of the AFM-tip and avoids the clogging of the hole due to dirt on the sample. With this system we are allowed to implant single ions in nano pillars, nano holes (Fig. 8.4(a),(b)) or photonic crystals [2] by initially scanning the area and subsequent implanting through the aperture of the AFM tip.

To reach the best resolution in all dimensions we also made first measurements of the depth distribution of implanted N ions with a new method which is called atom probe tomography (ATM) [3]. The region of interest is firstly formed to a nanoscaled tip. With a combination of high voltage and laser pulses the single atoms are evaporated

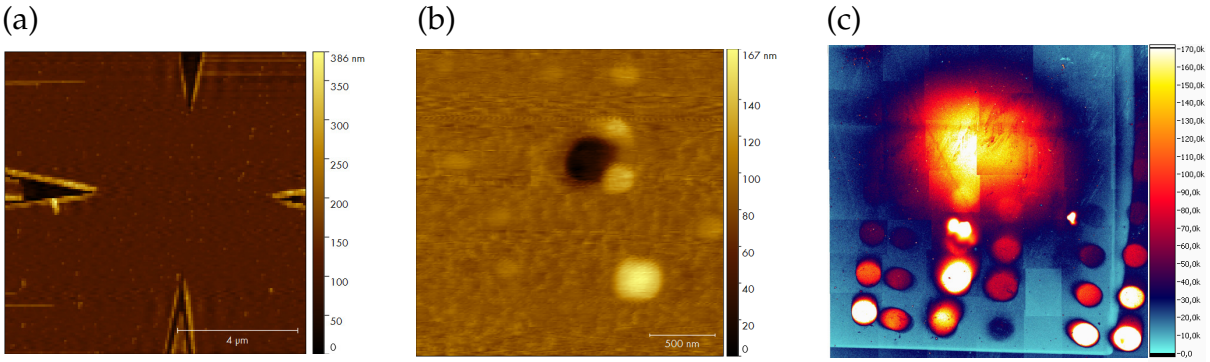

Figure 8.4: (a) AFM scan of a ZnSe layer with a metal mask. A small hole about a few hundred nm is located the middle of the four markers. **(b)** A zoom-in of the same hole as in (a). **(c)** Confocal image of the electron irradiated area. The very bright spot in the middle are NV centres which were formed by the electron irradiation and an followed annealing step (800 ℃ for 2 h). The smaller spots were implanted with N and different low energies ((1 – 5) keV) and different doses ($\left(10^8 - 10^{14}\right)$ cm^{-2}).

and can then be detected by a two dimensional ion detector. In the last step the tip can be reconstructed on the atomic level. With this technique it is possible to measure effects, for instance ion channeling, which influences the depth distribution of the implanted and thus the spacial resolution. Besides these experiments for increasing the resolution we also discovered a simple method for creating NV centres through electron irradiation in a common scanning electron microscope (SEM). For this we made some spots of NV centres with different energies and doses. Afterwards we irradiated the hole area with electrons. After an annealing step we found also NV centres at places which were originally not implanted (Fig. 8.4(c)). This method could make ion implantation possible for nearly every university which is in possession of an usual SEM.

[1] J. Meijer et al.: Appl. Phys. A **91**, 567 (2008), doi:10.1007/s00339-008-4515-1
[2] J. Riedrich-Möller et al.: Appl. Phys. Lett. **106**, 221103 (2015), doi:10.1063/1.4922117
[3] R. Schirhagl et al.: Ann. Rev. Phys. Chem. **65**, 83 (2014), doi:10.1146/annurev-physchem-040513-103659

8.6 Ion beam writing in diamond in mutable depth by using an flexible mask-system and investigation of the annealing process

T. Lühmann, R. Wunderlich, R. Schmidt-Grund*, J. Meijer

*Division of Semiconductor Physics

The variable depth of implantation is important for the doping process in semiconductor physics. In the case of diamond as a special semiconductor differ defects and doping leads to p- and n-type regions by locally irradiation [4] for example the p-i-p

diode in a diamond anvil cell [7]. The nanoprobe of the LIPSION allows diamond irradiation and ion beam writing. The generated 3D structures in our work are basics for modern 3D integrated circuit [5].

Not many studies dealing with the investigation and generation of 3D graphite structures buried in diamond. Pioneers in this field are Olivero and Gippius [1–3].

Huge implantation radiant exposures transform non conductive diamond in a conductive graphite like diamond phase [6]. Inside the diamond target the space-resolved change is determined by the ion species, the energy and the ion beam spot. The problem of variable depth implantation is solved by a practical possibility of variable ion energy. We use He^+ ions with an energy of $E_0 = 1.8\,\text{MeV}$ as an focused beam. The beam diameter is $d = 3\,\mu\text{m}$. In this investigation we present a flexible masking system to vary the energy and the space-resolved depth of the transformation in single-crystal diamond (Fig. 8.5(a)). This makes it possible to create 3D structures buried in diamond

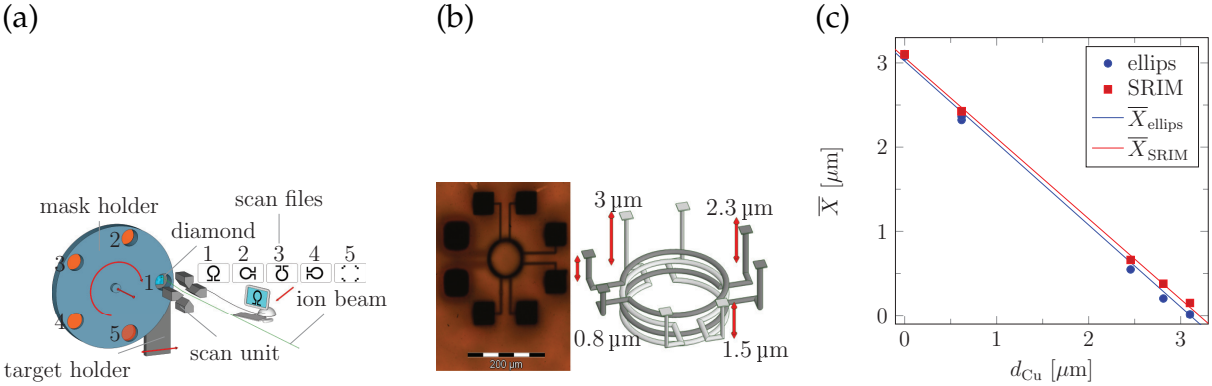

Figure 8.5: (a) Illustration of flexible mask system (not to scale). The rotating mask holder include holes with different masks. A suitable mask can be chosen for each scan file. The mask and scan file no. 5 are for the grid lift off. The scan file includes only the contact areas of the coil structure. The mask holder is mobile in beam direction. The diamond surface needs to be touched by the mask to minimize the ion straggling. **(b)** Microscopical picture and 3D sketch of a graphite like diamond coil inside diamond. **(c)** The depth of the buried structure vs. the Cu foil thickness for the simulated and measured data.

(Fig. 8.5(b)). The physical and chemical properties of the buried structure are completely different to the properties of diamond. The amorphisation depth was simulated by Stopping and Range of Ions in Matter (SRIM [8]) considering different thicknesses of Cu masks and measured by spectroscopic ellipsometry (SE) (Fig. 8.5(c)). The ellipsometry measurements are performed by differed annealing temperatures from 700 °C to 1200 °C in steps of 100 °C and direct after irradiation. We observe in the conductive graphite like diamond phase the change in optical constants dependant on annealing temperatures. The used optical Effective-Medium-Approximation-model (EMA) is in good agreement with structural description of the conduction mechanism in heavy irradiated diamond.

[1] A.A. Gippius et al.: Diamond Relat. Mater. **8**, 1631 (1999), doi:10.1016/s0925-9635(99)00047-3
[2] P. Olivero et al.: Europ. Phys. J. B **75**, 127 (2009), doi:10.1140/epjb/e2009-00427-5
[3] P. Olivero et al.: Diamond Relat. Mater. **18**, 870 (2009), doi:10.1016/j.diamond.2008.10.068

[4] J. O. Orwa et al.: Phys. Rev. B **62**, 5461 (2000), doi:10.1103/physrevb.62.5461
[5] R.S. Patti: Proc. IEEE **94**, 1214 (2006), doi:10.1109/jproc.2006.873612
[6] V.S. Vavilov et al.: Radiat. Eff. **22**, 141 (1974), doi:10.1080/00337577408232161
[7] A.M. Zaitsev et al.: phys. stat. sol. (a) **185**, 59 (2001), doi:10.1002/1521-396x(200105)185:1<59::aid-pssa59>3.0.co;2-c
[8] J.F. Ziegler et al.: *SRIM – The Stopping and Range of Ions in Matter* (2008), http://www.srim.org

8.7 Production of nano-structured bulk NV centres by shallow implantation and diamond CVD overgrowth

S. Pezzagna, M. Lesik*, N. Raatz, A. Tallaire†, R. John, J.-F. Roch*, J. Meijer

*Laboratoire Aimé Cotton, CNRS, Université Paris-Sud and ENS Cachan, Université Paris-Saclay, France
†Laboratoire des Sciences des Procédés et des Matériaux (CNRS UPR 3407), Université Paris 13, Sorbonne Paris Cité, France

The nanometre-scale engineering of single nitrogen-vacancy (NV) centres in diamond can be obtained by low-energy (keV) N implantation with limited straggling [1]. In this energy range, the ion straggling is typically in the order of a few nanometres or less. This is necessary for application in quantum information processing based on coupled NV centres in diamond which require NV−NV distance to be in the range (10 – 30) nm. A high level of precision in the formation of the NV defects by ion implantation is needed. The necessary use of keV energies implies however that the NV centres are produced close to the surface, a few nm deep. For such shallow NV centres, there are issues concerning the charge state stability and the spin coherence properties of the negatively charged NV^-. As a consequence, shallow NV centres generally have inferior overall properties than deeply implanted or deep native NV centres, due to the surface proximity.

In this work, we aim to overgrow a thin layer of diamond on top of the sample in order to bury the NV centres and improve their overall properties (Fig. 8.6). We have continued our search for optimised overgrowth conditions (in collaboration with the LSPM laboratory) in which the shallow NV centres survive after the overgrowth and have improved properties. It has already been shown in reference [2] that the spin coherence time of shallow NVs is improved by overgrowth of a thin diamond layer. This demonstration is an encouraging result, however the influence of the overgrowth on the optical properties and charge state of the centres has not been studied in this reference, and neither the survival rate of the NV centres.

In optimised conditions, we have shown that a pattern of very shallow NV centres (2 nm deep) could be successfully buried and found again after a few μm thick CVD overgrowth (Fig. 8.6). Furthermore, we could demonstrate the stabilisation of the charge state of the NV centres into the negative charge state, which is the one of interest for most of NV^- based application. Figure 8.7 shows how the main charge state of ensembles and single NV centres is shifted from NV^0 to NV^- after overgrowth. The coherence properties are currently under measurement and a new sample is under preparation.

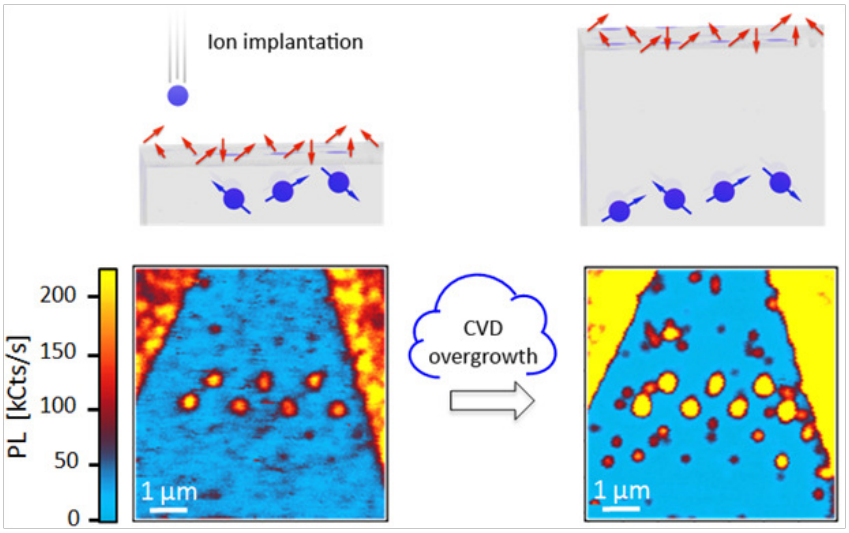

Figure 8.6: Implanted pattern of very shallow NV centres (depth ≈ 2 nm) using a pierced AFM tip (*left*). Same pattern after CVD overgrowth of a 6 µm-thick diamond layer (*right*).

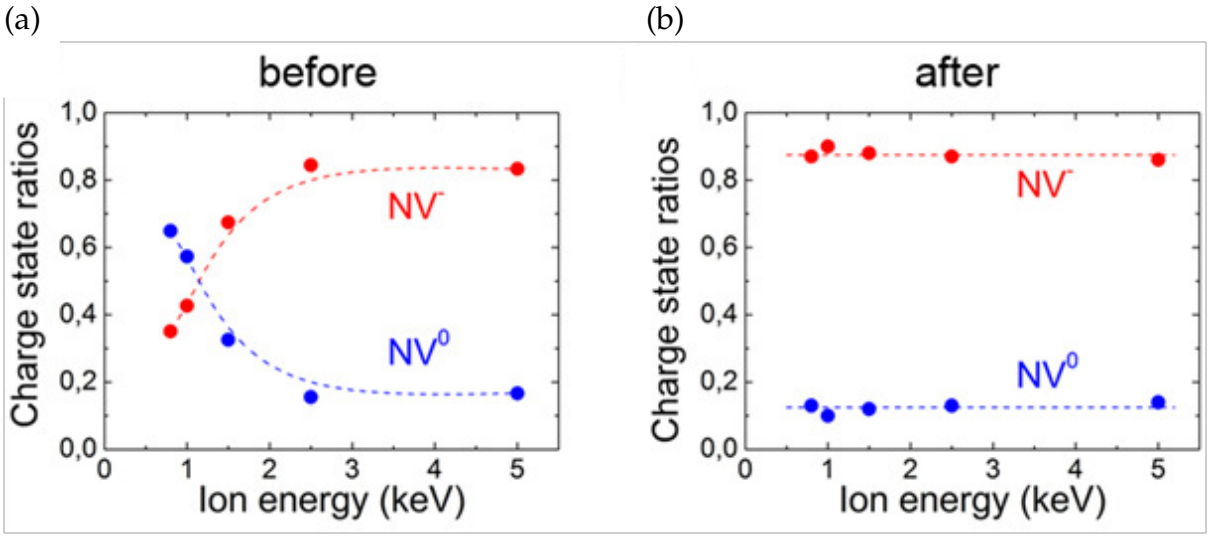

Figure 8.7: Charge state ratio of ensembles of NV centres as a function of their implantation depth or ion energy: **(a)** before and **(b)** after overgrowth.

We have further found that not only surface etching at the regrowth start but also hydrogen diffusion (building NVH complexes and leading to passivation of the NV centres [3]) needed to be considered. Figure 8.8 illustrates how NV centres are passivated by H when a H plasma is applied to the diamond sample. This will be further studied in order to find the overgrowth process avoiding at most the etching of the NV centres at the growth start and the passivation of the NV centres due to H diffusion.

The combination of low-energy high-resolution ion implantation and optimised high-purity chemical vapour deposition (CVD) overgrowth procedures opens the way towards the fabrication of scalable and efficient quantum devices based on single defects in diamond.

[1] S. Pezzagna et al.: Small **6**, 2117 (2010), doi:10.1002/smll.201000902

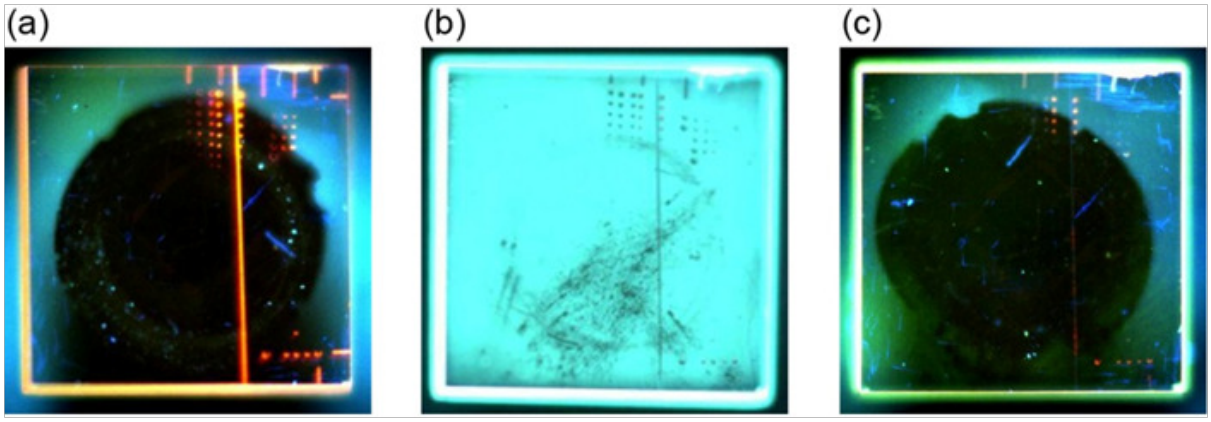

Figure 8.8: Passivation of shallow NV centres due to H diffusion. **(a)** Fluoresence image (UV excitation) of a diamond sample in which shallow NV centres have been implanted (red fluorescence). **(b)** Fluorescence image after a 30 min H plasma (1000 W, 500 °C). The diamond is now H-terminated. The plasma conditions are softer than during CVD overgrowth. **(c)** Fluorescence image after a boiling acid mixture bath (in order to re-O-terminate the diamond surface). The red fluorescence from the NV centres is retrieved but a high amount of them is passivated.

[2] T. Staudacher et al.: Appl. Phys. Lett. **101**, 212401 (2012), doi:10.1063/1.4767144
[3] A. Stacey et al.: Appl. Phys. Lett. **100**, 071902 (2012), doi:10.1063/1.3684612

8.8 Study of the transmission behaviour of ion beams through pores in muscovite foil

C. Scheuner, St. Jankuhn, J. Vogt, S. Pezzagna, C. Trautmann*, J. Meijer

*GSI Helmholtzzentrum für Schwerionenforschung GmbH, Darmstadt

For the creation of NV centres in diamond and other important applications very tiny ion beams are needed. In this paper the collimation of ion beams with pores in Muscovite foil was studied. The foils were prepared at the GSI Darmstadt with high energetic Sm ions which penetrated the foil and subsequent etching with hydrofluoric acid. This created diamond shaped pores where the two diagonals had the average length of $b = 123\,\text{nm}$ and $c = 231\,\text{nm}$. To study the transmission behaviour, beams of N^+- and N^{++}-ions with 4 MeV, 2 MeV, and 0.8 MeV where shot on the foil. The foil thickness of 7 µm is sufficient to stop N ions with energies up to 11 keV. Thus, the ions can just penetrate the foil at the pores. The foil was mounted on a goniometer between the ion beam and a Scanning Transmission Ion Microscopy (STIM) detector in order to measure the number of transmitted ions with respect to the angle between ion beam and the pores. The N beam was unfocused in order to have the divergence as small as possible. As a theoretical approach to explain the transmission behaviour the geometric explanation was not enough because especially at low energies ions still passed the foil where the pore was already so far that it appeared to be closed to the ion beam. Thus, the theory of crystal channelling was applied. Therefore small angle scattering between target material and ions are assumed that deflect the ion beam. Due

to the complicated structure of the Muscovite crystal the theoretical treatment was done for two extremal cases: axial and planar channelling on the inner pore walls which are made up of O planes. A comparison between the measured angle distribution and the calculated values can be seen in Fig. 8.9. There it can be seen that the measurement is

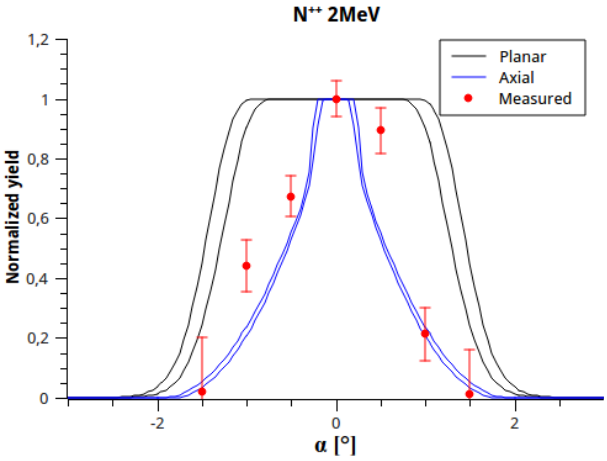

Figure 8.9: Example of the shape of the angle distribution for 2 MeV N^{++}. Here the distribution for axial and planar channelling are given as extremal values with their error region.

in between the two extremal values and also more close to the planar case. Both are physically reasonable taking the crystal structure of muscovite into account. With that also a prediction of the half-width and critical angles in a certain energy region can be made.

Also it was measured that the energy loss of the ions after the transmission is smaller than the measurement error. This can also be confirmed by a rough estimate of the energy loss using the Rutherford back scattering theory.

Furthermore the stability of the foil against ion radiation was checked briefly with a comprehension of STIM measurements done with 2.25 MeV H^+ ions and Scanning Electron Microscopy (SEM) measurements before and after the transmission measurement. In both cases no influence on several days of radiation with N ions of different energies could be observed.

8.9 A new method for deterministic ion implantation at the nano-scale

P. Räcke[*†], D. Spemann[‡†], S. Liedtke[‡†], J.W. Gerlach[‡†], B. Rauschenbach[‡†], J. Meijer[*†]

[*]Division of Nuclear Solid State Physics
[†]Leibniz Joint Lab "Single Ion Implantation", Leipzig
[‡]Leibniz Institute of Surface Modification e.V., Leipzig

A team of physicists from NFP and the IOM Leipzig is working together in the Leibniz Joint Lab "Single Ion Implantation" to develop a new ion implanter. The aim of this project funded by the Leibniz Association and the EU is to enable the implantation of counted single ions with a sub-10 nm resolution.

Ion implantation is a powerful tool for the creation of specific impurities and defects, such as colour centres in solid state matrices. Future developments of conventional and especially quantum mechanical devices require deterministic implantation of single ions with nanometre spatial resolution.

Our approach to deterministic ion implantation is based on a commercial FIB system equipped with a new electron beam ion source (EBIS) and a specifically designed image charge detector (see Fig. 8.10(a)). It consists of alternatingly contacted electrodes

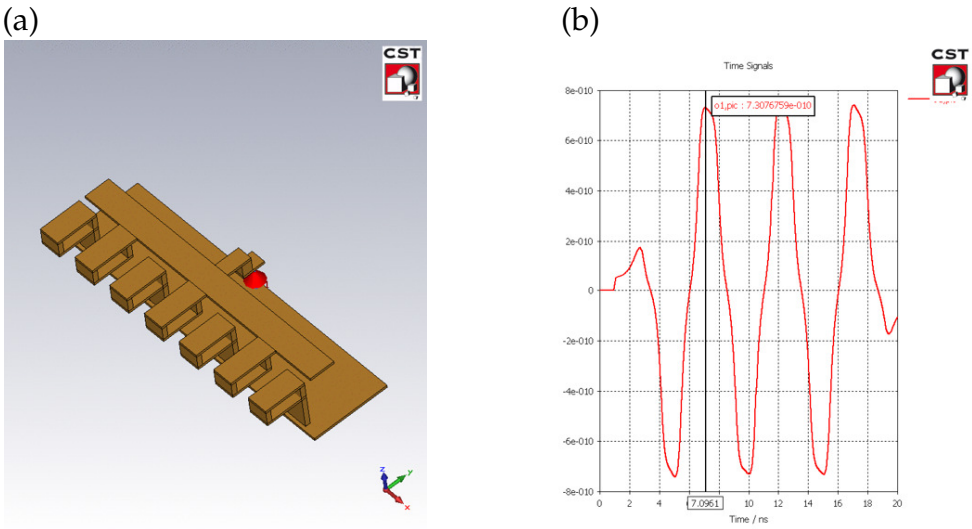

Figure 8.10: (a) One segment of an image charge detector design optimised by simulations of a single ion passing through the electrodes. **(b)** The resulting signal is an approximated sine wave in the time domain. The amplitude depends on a variety of parameters and is in the range of 10 nV.
Simulations of the image charge detector were carried out by F.-J. Schmückle and W. Heinrich (Ferdinand-Braun-Institut, Leibniz-Institut für Höchstfrequenztechnik, Berlin).

around the ion optical axis, in which the ion induces an image charge, which will be measured via the voltage signal (Fig. 8.10(b)) by ultra-low noise electronics. The detection principle, which is employed in a similar form in single particle mass spectrometry, makes the unimpeded fly-by detection of charged objects feasible so that a counted number of ions can be implanted. The new system thus promises to allow for mask-less implantation of low-energy ions offering advantages compared to other approaches. Making the principle independent from the properties of both the charged object to be implanted and the sample structure, a variety of new applications is made possible.

In 2015, the main part of simulations of the electrical detector behaviour was carried out to evaluate the feasibility of the image charge detection principle for our purposes. In parallel, the FIB system was installed in the lab and prepared for fitting the new ion source.

8.10 NV magnetometry of non-classical conduction in zinc-tin-oxide thin films

R. Staacke, R. John, P. Schlupp*, J. Lehnert, M. Grundmann*, J. Meijer

*Division of Semiconductor Physics

Shallow NV centres can be used to measure magnetic fields of electronics deposited on top of a diamond. They can be produced by ion implantation and annealing of the sample. We used CN^- ions with an energy of 11.2 keV to produce shallow NV centres at an average depth of about 9 nm. We deposited a 20 µm broad and 200 nm thick zinc-tin-oxide (ZTO) line by pulsed laser deposition (PLD) [3, 4] and photolithography on an implanted and annealed diamond surface. The measured $T^{-1/4}$-dependence of the conductivity from 50 K up to 310 K indicates a non-classical conduction mechanism which could be either percolation conduction [1] or variable range hopping [2]. We were able to measure the magnetic field (in the range of several 100 nT) of the ZTO-line for different currents up to 20 µA with an accuracy of 54 nT by using pulsed optical detected magnetic resonance (ODMR) (Fig. 8.11). The magnetic field shows the same linear current dependence as in classical conducting materials, but the gradient is about 3 to 4.5 times higher than expected.

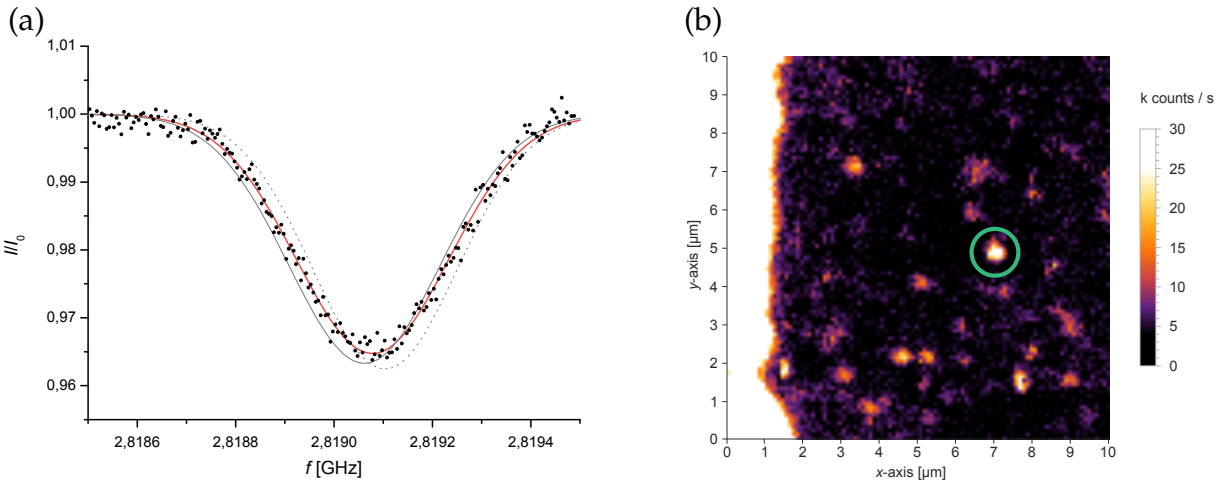

Figure 8.11: (a) Normalised NV fluorescence for 0 µA current through the ZTO-line. The fit of the plotted data (—), the fit for a current of −10 µA (···) and for 10 µA (—) are shown. **(b)** Fluorescence intensity under continuous excitation of (1.0 ± 0.1) mW. The ZTO line is in the left side of the picture. The used NV centre is marked (○).

[1] D. Adler et al.: Solid State Commun. **12**, 9 (1973), doi:10.1016/0038-1098(73)90333-5
[2] N.F. Mott: Phil. Mag. **19**, 835 (1969), doi:10.1080/14786436908216338
[3] P. Schlupp et al.: MRS Proc. **1633**, 101 (2014), doi:10.1557/opl.2014.117
[4] P. Schlupp et al.: Adv. Electron. Mater. **1**, 1400023 (2015), doi:10.1002/aelm.201400023

8.11 Quantification and subcellular localization of iron in brain tissue of patients with Parkinson's disease and age-matched controls

I. Weigelt*, St. Jankuhn, J. Meijer, W. Müller†, T. Arendt*, M. Morawski*

*Paul Flechsig Institute for Brain Research
†Department of Neuropathology

The versatile function of Fe in the cell metabolism makes it essential for cell viability. On the other hand, high concentrations of Fe ions induce oxidative stress via the Fenton reaction. The resulting toxic radicals lead to cell death. Therefore, Fe plays a key role in neurotoxic damage and causes neurological disorders and degeneration. In neurodegenerative diseases such as Parkinson's disease (PD), the Fe concentration in the degenerating brain areas (*substantia nigra pars compacta*) is increased. At the cellular level it is striking that in the Fe-rich areas, certain nerve cell populations are altered early in the disease process, while other neuron populations in the same regions are not or only secondarily affected. By contrast, knowledge about the quantitative Fe concentration and accumulation in other cell types such as astroglia, microglia and oligodendrocytes (myelin) is scarce.

The project aims at examining the cellular and subcellular localization and concentration of Fe in Parkinson's disease in the main cell types (neurons, astrocytes, microglia, and oligodendrocytes) of the human brain. In previous studies of the working groups [1, 2], we were for the first time able to perform a differential quantitative analysis (detection limit 50 µmol/l) of intraneuronal Fe by means of ion beam microscopy (PIXE, Particle induced X-ray emission) in the human *substantia nigra* (Fig. 8.12). Furthermore, the PIXE method could be combined with classic immunohistochem-

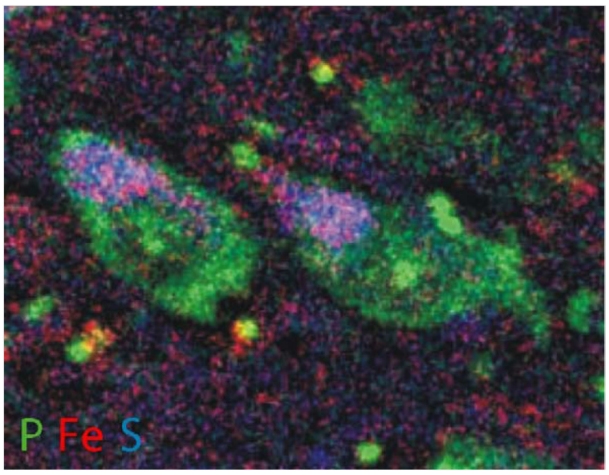

Figure 8.12: Three-element map of P (*green*), Fe (*red*), and S (*blue*) of a human *substantia nigra pars compacta* neuron in PD. The neurons can be localised by its P-rich somata. The *violet* colour is an overlap of *red* and *blue* which shows a clear spatial correlation of Fe and S, i.e. the binding of Fe to neuromelanin.

istry/histopathology with Ni-DAB enhancement, to obtain a wide-ranging variety of

cellular and subcellular markers, to very precisely determine the localization of Fe in various cell types, subcellular fractions (e.g. neuromelanin) and in protein association (e.g. ferritin) in Parkinson's disease and age-matched controls.

[1] M. Morawski et al.: Nucl. Instrum. Meth. Phys. Res. B **231**, 224 (2005), doi:10.1016/j.nimb.2005.01.061
[2] M. Morawski et al.: Nucl. Instrum. Meth. Phys. Res. B **231**, 229 (2005), doi:10.1016/j.nimb.2005.01.062

8.12 Funding

Integration of Molecular Components in Functional Macroscopic Systems: Coupling color centers into macroscopic quantum systems with an atomic nano-assembler
Prof. Dr. J. Meijer
VolkswagenStiftung

DIAmond Devices Enabled Metrology and Sensing (DIADEMS)
Prof. Dr. J. Meijer
EU: FP7-ICT-2013.9.7 611143

Quantum Information with NV Centres (QINVC)
Prof. Dr. J. Meijer
EU/BMBF: CHIST-ERA VBP 01BQ1105

Diamond Materials for Quantum Application: Ultraprecise deterministic doping of diamond
Prof. Dr. J. Meijer
DFG: FOR1493

Functionalized Nanodiamonds for Biomedical Research and Therapy
Prof. Dr. J. Meijer
VolkswagenStiftung

EXMAD – Extreme Sensitive Magnetometry using Nitrogen–Vacancy Centers in Diamond
Prof. Dr. U.L. Andersen/Prof. Dr. J. Meijer
The Danish Council for Strategic Research

Utilization of Ion Accelerators for Studying and Modelling of Radiation Induced Defects in Semiconductors and Insulators
Prof. Dr. J. Meijer
IAEA: CRP F11016

Joint Lab "Einzelionenimplantation": "Sensorik mit einzelnen Atomen"
Prof. Dr. Dr. h.c. B. Rauschenbach/Prof. Dr. J. Meijer
Leibniz-Gemeinschaft/EU

ECR-Ionenquelle
Prof. Dr. J. Meijer
DFG: HBFG

Quanten und klassische Lichtquellen in Silizium: Verunreinigungen und komplexe Defekte für die Nanophotonik
Dr. S. Pezzagna, Prof. Dr. J. Meijer
DFG: ULYSSES

8.13 Organizational Duties

J. Meijer

- User Selction Panel for the Ion Beam Center: Helmholtz-Zentrum Dresden–Rossendorf
- Advisory Board: ISTAC Croatian Nuclear Science
- Referee: Several journals

J. Vogt

- Member of the Faculty Board

8.14 External Cooperations

Academic

- City University of New York, College of Staten Island, Department of Engineering Science and Physics, USA
  Assoc. Prof. Dr. A.M. Zaitsev
- Centre National de la Recherche Scientifique (CNRS), École normale supérieure (ENS), Laboratoire Aimé Cotton (LAC), Cachan, France
  Prof. Dr. J.-F. Roch
- Centre National de la Recherche Scientifique (CNRS), Laboratoire des Sciences des Procédés et des Matériaux (LSPM), Fabrication Processes of Advanced Materials (PEMA), Paris, France
  Prof. Dr. J. Achard
- Commissariat à l'énergie atomique et aux énergies alternatives (CEA), Institut Rayonnement Matière de Saclay (IRAMIS), Service de Physique de l'Etat Condensé (SPEC), Quantronique, Saclay, France
  Prof. Dr. D. Esteve
- ETH Zürich, Physikdepartement, Laboratorium für Festkörperphysik, Spin Physics and Imaging, Switzerland
  Prof. Dr. C. Degen
- Fraunhofer-Institut für Angewandte Festkörperphysik Freiburg, Mikro- und Nanosensoren
  Dr. C.E. Nebel
- Humboldt-Universität zu Berlin, Mathematisch-Naturwissenschaftliche Fakultät I, Institut für Physik, AG Nanooptik
  Prof. Dr. O. Benson

- Hungarian Academy of Sciences, Wigner Research Centre for Physics, Institute for Solid State Physics and Optics, Budapest, Hungaria
- Interuniversitair Micro-Electronica Centrum (imec) Leuven, Belgium
- Julius-Maximilians-Universität Würzburg, Fakultät für Chemie und Pharmazie, Institut für Organische Chemie
  Prof. Dr. A. Krüger
- Leibniz-Institut für Oberflächenmodifizierung e.V. Leipzig
  Prof. Dr. Dr. h.c. B. Rauschenbach, Prof. Dr. B. Abel
- Leibniz-Universität Hannover, Institut für Anorganische Chemie, AK Analytik
  Prof. Dr. C. Vogt
- Ludwig-Maximilians-Universität München, Fakultät für Physik, Experimentelle Quantenphysik
  Prof. Dr. H. Weinfurter
- Max-Planck-Institut für biophysikalische Chemie Göttingen, Karl-Friedrich-Bonhoeffer-Institut, Abt. NanoBiophotonik
  Prof. Dr. Dr. h.c. St.W. Hell
- Technische Universität München, Walter Schottky Institut, E25: Spins and Defects in Semiconductors
  Prof. Dr. M.S. Brandt
- Università di Torino, Dipartimento di Fisica Sperimentale, Gruppo di Fisica dello Stato Solido
  Prof. Dr. E. Vittone
- Universität Basel, Department of Physics, Quantum-Sensing Lab, Switzerland
  Prof. Dr. P. Maletinsky
- Universität Kassel
- Universität Konstanz, Mathematisch-Naturwissenschaftliche Sektion, Fachbereich Physik, Lehrstuhl für Ultrakurzzeitphysik und Photonik
  Prof. Dr. A. Leitenstorfer
- Universität Leipzig, Medizinische Fakultät, Institut für Medizinische Physik und Biophysik
  Prof. Dr. E. Donath, Dr. I. Estrela-Lopis, Dr. U. Reibetanz
- Universität Mainz, Fachbereich Physik, Mathematik und Informatik, Institut für Physik, Arbeitsgruppe Quanten-, Atom- & Neutronenphysik (QUANTUM)
  Prof. Dr. F. Schmidt-Kaler, Priv.-Doz. Dr. K. Singer
- Universität Stuttgart, Fakultät Mathematik und Physik, 3. Physikalisches Institut
  Prof. Dr. J. Wrachtrup
- Universität Ulm, Fakultät für Naturwissenschaften, Institut für Quantenoptik
  Prof. Dr. F. Jelezko
- Universität Ulm, Fakultät für Naturwissenschaften, Institut für Theoretische Physik, Controlled Quantum Dynamics Group
  Prof. Dr. M.B. Plenio

- University of Warwick, Department of Physics, Condensed Matter Physics, Magnetic Resonance Cluster, Coventry, UK
  Prof. Dr. M. Newton
- Universität Wien
- Westfälische Wilhelms-Universität Münster, Physikalisches Institut
  Prof. Dr. R. Bratschitsch

Industry

- ARTTIC Paris, France
- attocube systems AG München
- Element Six Ltd. Shannon, Co. Clare, Ireland
- THALES Research & Technology Palaiseau, France

8.15 Publications

Journals

J. Barzola-Quiquia, P. Esquinazi, M. Lindel, D. Spemann, M. Muallem, G.D. Nessim: *Magnetic order and superconductivity observed in bundles of double-wall carbon nanotubes*, Carbon **88**, 16 (2015), doi:10.1016/j.carbon.2015.02.062

J. Barzola-Quiquia, T. Lehmann, M. Stiller, D. Spemann, P. Esquinazi, P. Häussler: *Topological insulator thin films starting from the amorphous phase - Bi_2Se_3 as example*, J. Appl. Phys. **117**, 075301 (2015), doi:10.1063/1.4908007

R. Böttcher, M. Lorenz, A. Pöppl, D. Spemann, M. Grundmann: *Local zincblende coordination in heteroepitaxial wurtzite $Zn_{1-x}Mg_xO$: Mn thin films with $0.01 \leq x \leq 0.04$ identified by electron paramagnetic resonance*, J. Mater. Chem. C **3**, 11918 (2015), doi:10.1039/C5TC02720A

C. Bundesmann, R. Feder, R. Wunderlich, U. Teschner, M. Grundmann, H. Neumann: *Ion beam sputter deposition of* Ge *films: Influence of process parameters on film properties*, Thin Solid Films **589**, 487 (2015), doi:10.1016/j.tsf.2015.06.017

M. Chipaux, A. Tallaire, J. Achard, S. Pezzagna, J. Meijer, V. Jacques, J.-F. Roch, T. Debuisschert: *Magnetic imaging with an ensemble of Nitrogen Vacancy centers in diamond*, Eur. Phys. J. D **69**, 166 (2015), doi:10.1140/epjd/e2015-60080-1

M. Chipaux, L. Toraille, C. Larat, L. Morvan, S. Pezzagna, J. Meijer, T. Debuisschert: *Wide bandwidth instantaneous RF spectrum analyzer based on nitrogen vacancy centers in diamond*, Appl. Phys. Lett. **107**, 233502 (2015), doi:10.1063/1.4936758

M. Chipaux, S. Xavier, A. Tallaire, J. Achard, S. Pezzagna, J. Meijer, V. Jacques, J.-F. Roch, T. Debuisschert: *Nitrogen vacancies (*NV*) centers in diamond for magnetic sensors and quantum sensing*, Proc. SPIE **9370**, 93701V (2015), doi:10.1117/12.2084082

C. Eichhorn, D. Manova, R. Feder, R. Wunderlich, C. Nömayr, C.G. Zimmermann, H. Neumann: *Sputter yield measurements of thin foils using scanning transmission ion microscopy*, Eur. Phys. J. D **69**, 19 (2015), doi:10.1140/epjd/e2014-50552-1

I. Lorite, C. Zandalazini, P. Esquinazi, D. Spemann, S. Friedländer, A. Pöppl, T. Michalsky, M. Grundmann, J. Vogt, J. Meijer, S.P. Heluani, H. Ohldag, W.A. Adeagbo, S.K. Nayak, W. Hergert, A. Ernst, M. Hoffmann: *Study of the negative magneto-resistance of single proton-implanted lithium-doped* ZnO *microwires*, J. Phys.: Condens. Matter **27**, 256002 (2015), doi:10.1088/0953-8984/27/25/256002

J. Michels, J. Vogt, P. Simon, S.N. Gorb: *New insights into the complex architecture of siliceous copepod teeth*, Zoologie **118**, 141 (2015), doi:10.1016/j.zool.2014.11.001

J. Riedrich-Möller, S. Pezzagna, J. Meijer, C. Pauly, F. Mücklich, M. Markham, A.M. Edmonds, C. Becher: *Nanoimplantation and Purcell enhancement of single nitogen-vacancy centers in photonic crystal cavities in diamond*, Appl. Phys. Lett. **106**, 221103 (2015), doi:10.1063/1.4922117

Y. Romach, C. Müller, T. Unden, L.J. Rogers, T. Isoda, K.M. Itoh, M. Markham, A. Stacey, J. Meijer, S. Pezzagna, B. Naydenov, L.P. McGuinness, N. Bar-Gill, F. Jelezko: *Spectroscopy of surface-induced noise using shallow spins in diamond*, Phys. Rev. Lett. **114**, 017601 (2015), doi:10.1103/PhysRevLett.114.017601

R. Schirhagl, N. Raatz, J. Meijer, M. Markham, S.S.A. Gerstl, C.L. Degen: *Nanometer-scale isotope analysis of bulk diamond by atom probe tomography*, Diamond Relat. Mater. **60**, 60 (2015), doi:10.1016/j.diamond.2015.10.016

C. Schreyvogel, V. Polyakov, R. Wunderlich, J. Meijer, C.E. Nebel: *Active charge state control of single NV centres in diamond by in-plane Al-Schottky junctions*, Sci. Rep. **5**, 12160 (2015), doi:10.1038/srep12160

T. Staudacher, N. Raatz, S. Pezzagna, J. Meijer, F. Reinhard, C. A. Meriles, J. Wrachtrup: *Probing molecular dynamics at the nanoscale via an individual paramagnetic centre*, Nat. Commun. **6**, 8527 (2015), doi:10.1038/ncomms9527

A. Tallaire, M. Lesik, V. Jacques, S. Pezzagna, V. Mille, O. Brinza, J. Meijer, B. Abel, J.-F. Roch, A. Gicquel, J. Achard: *Temperature dependent creation of nitrogen-vacancy centers in single crystal CVD diamond layers*, Diam. Relat. Mat. **51**, 55 (2015), doi:10.1016/j.diamond.2014.11.010

Books

T. Butz: *Fourier Transformation for Pedestrians, 2nd ed.*, Springer, Cham (2015). doi:10.1007/978-3-319-16985-9

Talks

M. Chipaux, L. Toraille, C. Larat, L. Morvan, S. Pezzagna, J. Meijer, T. Debuisschert
Ensemble of NV *centers for instantaneous spectral analysis of microwave signals*
SBDD XX: Hasselt Diamond Workshop, Hasselt, Belgium, 25.–27.02.2015

M. Lorenz, A. Pöppl, S. Friedländer, D. Spemann, R. Böttcher, M. Grundmann
Nearest-neighbour Lattice Distortions in Oxygen-deficient ZnO *and* $Zn_{1-x}Mg_xO$ *Thin Films, probed by Electron Paramagnetic Resonance*
17th International Conference on II-VI Compounds and Related Materials, Paris, France, 13.–18.09.2015

J. Meijer
Status and novel concepts to implant countable single ions with high lateral resolution
MRS Spring Meetings & Exhibits, San Francisco, CA, USA, 06.–10.04.2015, invited

J. Meijer
Status of the countable single ion implantation with high lateral resolution and a new method to screen suitable new color centers
Seminar, Center for Beam Physics, LBNL, Berkeley, CA, USA, 13.04.2015, invited

J. Meijer
Functionalized single atoms by ion beam implantation
Workshop Ionenstrahlen & Nanostrukturen, Heidelberg, 22.–24.07.2015, invited

J. Meijer
Prospects and first results of the Leipzig screening program
Diamond Quantum Sensing Workshop, Takamatsu, Japan, 05.–07.08.2015, invited

J. Meijer
Functionalized single atoms for sensing and quantum information technology engineered by ion beam implantation
Physikalisches Kolloquium, Ruhr-Universität Bochum, 30.11.2015, invited

S. Pezzagna
Creation and engineering of optical centres in diamond for quantum information processing and magnetometry
Seminar, Spin Physics and Imaging Group, ETH Zurich, Switzerland, 02/2015, invited

S. Pezzagna
Defect engineering for determined production of NV centres in diamond
European Material Research Society: Spring Meeting, Lille, France, 11.–15.05.2015, invited

S. Pezzagna
Optical centres in diamond created and engineered by ion implantation: Status and prospects
26th International Conference on Diamond and Carbon Materials, Bad Homburg, 06.–10.09.2015, invited

D. Spemann, J.W. Gerlach, S. Rauschenbach, B. Rauschenbach, J. Meijer
Concept of single detector for deterministic ion implantation at the nanoscale
Workshop Ionenstrahlen & Nanostrukturen, Heidelberg, 22.–24.07.2015

8.16 Graduations

Master

- T. Lühmann
  3D-Ionenstrahlschreiben in Diamant zur Erzeugung von Graphitstrukturen und deren Charakterisierung
  June 2015
- M. Mensing
  Development of a python based ODMR software for the investigation of nitrogen-vacancy-center formation and outgrowths
  November 2015
- R. Staacke
  Magnetometrie nicht klassischer Leitungsmechanismen in amorphen Halbleitern mit Hilfe einzelner NV-*Zentren*
  September 2015
- J. Vogel
  Laserinduzierte Umladungseffekte von NV-Zentren in Diamant
  July 2015

Bachelor

- Chr. Eames
  Implanting on PMMA
  March 2015
- J. Helbig
  Untersuchung von NV-*Zentren mittels Photolumineszenz*
  January 2015
- J. Küpper
  Untersuchung von NV-*Zentren mittels Ionolumineszenz*
  January 2015
- M. Quaas
  Aufbau und Simulation eines Beschleunigers für mittlere Teilchenenergien
  July 2015

8.17 Guests

- Dr. G. Balasubramanian
  Max Planck Institute for Biophysical Chemistry Göttingen, Nanoscale Spin Imaging
  27.09.–01.10.2015
- P. Neumann
  Universität Stuttgart, 3. Physikalisches Institut
  28.09.–02.10.2015

- Dr. H. Fedder
  Universität Stuttgart, 3. Physikalisches Institut
  29.09.–02.10.2015
- Prof. Dr. B. Abel
  Leibniz-Institut für Oberflächenmodifizierung e.V. Leipzig
  30.09.2015
- Dr. B. Naydenov
  Universität Ulm, Institut für Quantenoptik
  30.09.–02.10.2015
- Prof. Dr. J.-F. Roch
  Centre national de la recherche scientifique (CNRS), École normale supérieure (ENS), Laboratoire Aimé Cotton (LAC), Cachan, France
  30.09.–04.10.2015
- Dr. F. Reinhard
  Technische Universität München, Walter-Schottky-Institut, Quantum Sensing
  01./02.10.2015
- Dr. Dr. M. Morawski
  Universität Leipzig, Medizinische Fakultät, Paul-Flechsig-Institut für Hirnforschung
  10./11.12.2015

9

Semiconductor Physics

9.1 Introduction

In the last year we could achieve tremendous progress in our core research areas. We are happy to present our latest results with this report and hope that you enjoying going through it. Our work has also been featured on a couple of covers.

Figure 9.1: Journal covers of 2015/16 publications of the semiconductor physics group

Most of our research is targeted towards *creating* – creating new nanostructures, new rectifying junctions, new devices for novel applications. Recently we have, however, solved a long-standing problem. Up to this work, Raman scattering intensities for arbitrarily oriented optically anisotropic crystals could not be explained. By combining our longstanding expertise in the dielectric function of anisotropic materials and our only recently established expertise in Raman spectroscopy, we introduced an effective Raman tensor which includes the effects due to birefringence, i.e. mode conversion and the peculiarities of extraordinary rays. In general, Raman scattering can be used to determine the orientation of a given crystal because the Raman intensity depends on the crystal orientation described by the Raman tensor. However, in the presence of birefringence, which affects six out of the seven crystal systems, the well-established formalism fails. The investigation of this phenomenon and the attempt to theoretically describe the experimentally observed intensities was object of many studies in the early

years of Raman scattering and concluded to be futile almost 50 years ago. Attempts to apply the established formalism anyhow required unphysical parameters and led to a misinterpretation of the results. Our results render these approaches obsolete. Besides enabling the determination of a crystal's orientation, they are a prerequisite for the excitation energy-dependent determination of the complete Raman tensor of low-symmetry crystals. Thereby, they open a new way to study the connection between electronic and structural properties. For further details see Section 9.18 "Raman tensor formalism for anisotropic crystals".

Monoclinic gallia (β-Ga_2O_3) has been in the focus regarding materials. The dielectric function has been determined in a wide spectral range and analyzed in terms of lattice and electronic oscillators. Also very good Schottky barrier diodes have been demonstrated, also on $(In_xGa_{1-x})_2O_3$ prepared by continuous composition spread pulsed laser deposition.

Another novel junction alloy thin films is the bipolar interface n-ZnO/p-NiO. It is a type-II heterostructure and has been used to fabricate transparent junction field effect transistors and a transparent solar cell. This cell absorbs only the UV part of the solar spectrum and delivers already several Watt per square meter under AM1.5. We are excited to further improve this disruptive invention.

We are largely indebted to our funding agencies in particular Deutsche Forschungsgemeinschaft (DFG). We are grateful for the continued funding of Sonderforschungsbereich SFB 762 "Functionality of Oxide Interfaces" that has been renewed (2016–2019) and our project on nanowire heterostructures in the Forschergruppe FOR 1616 "Nanowire Optoelectronics" which was extended for the second funding period (2015–2018). Also we thank Sächsische Aufbaubank to support our new work on Ga_2O_3 thin films and transparent oxide solar cells. A project on flexible oxide electronics has started in the new DFG SPP FFLexCom (SPP 1796). The work of our students and researchers together with our academic and industrial partners near and far was fruitful and enjoyable and thus it is with pleasure that the semiconductor physics group presents their progress report.

Marius Grundmann

9.2 Highly rectifying all-amorphous *pn*-heterojunction diodes

P. Schlupp, F.-L. Schein, H. von Wenckstern, M. Grundmann

Amorphous zinc tin oxide (ZTO) can be fabricated at room temperature (RT) and exhibits electron mobilities of more than 10 $cm^2V^{-1}s^{-1}$ [1, 2]. This makes its use interesting for channel layers in pixel driving thin film transistors for active matrix displays and for electronics on flexible substrates.

For active bipolar devices beside *n*-type semiconducting films also *p*-type films are neccessary. Zinc cobalt oxide (ZCO) is one the few *p*-type oxides for which bipolar heterodiodes have already been demonstrated [3]. Here, we discuss electrical properties of all amorphous n-ZTO/p-ZCO heterojunction diodes fabricated entirely at RT.
The oxide thin films were grown by pulsed laser deposition at room-temperature and

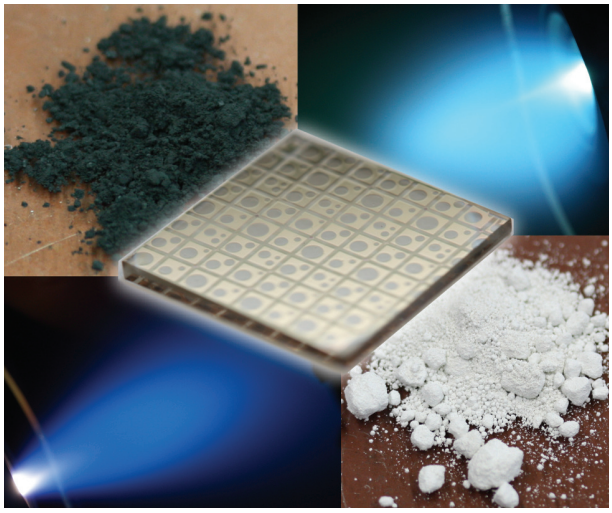

Figure 9.2: ZCO (dark) and ZTO (white) powders and PLD plasma plumes during deposition. The center shows a 10Å mm^2 sample with amorphous ZTO/ZCO diodes.

an 0.03 mbar oxygen atmosphere 9.2. To enhance the rectification of the diodes, an ultrathin semi-insulating ZTO layer was introduced at the heterointerface to spatially decouple electronic states possibly contribute to the leakage current. Figure 9.10 depicts the temperature-dependent *jU*-characteristics of (a) a *pn*-diode and (b) a *pin*-diode from room temperature to 100°C. They were modeled using the Shockley equation.

$$j = \frac{I_0}{A}\left[\exp\left(e\frac{U - R_s I}{\eta k_B T}\right) - 1\right] + \frac{U - R_s I}{A R_p} + \frac{I_C}{A}. \tag{9.1}$$

A is the contact area, R_s is the series resistance, R_p is the parallel resistance, η is the ideality factor, k_B is the Boltzmann constant and T the absolute temperature. The current rectifications obtained at RT j(1.5V)/j(-1.5V) are about 5×10^4 for the *pn*-diodes and 1.1×10^6 for the *pin*-diodes, respectively. Since the leakage current of the *pn*-diodes

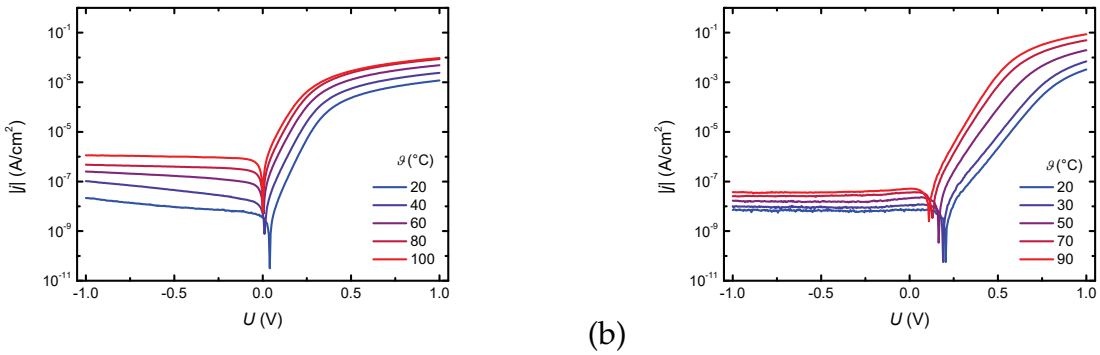

Figure 9.3: Temperature dependent *jU*-characteristics of a) a *pn*-diode and b) a *pin*-diode having an intrinsic insulating layer of about 5-10 nm at the heterointerface.

increases only slightly and less than the forward current with the temperature, the rectification is higher at elevated temperatures. The opposite holds true for the *pn*-diodes. The ideality factor of the *pn*-diode changes only slightly, from 1.27 to 1.17 with

increasing temperature. In comparison to that it decreases from 2.0 to below 1.2 with increasing temperature for the *pin*-diodes. We assume that this higher ideality factor obtained at room temperature is due to more interface trap states caused by the intrinsic insulating ZTO layer and a broader distribution of the barrier which can be overcome by charge carriers more easily at higher temperatures [4].
The work was supported by the ESF(SAB 100124929) and Leipzig School of Natural Science (BuildMoNa).

[1] M. K. Yajaraj, K. J. Saji, K. Nomura, T. Kamiya, H. Hosono: J. Vac. Sci. Technol. B **26**, 495 (2008)
[2] P. Schlupp, H. von Wenckstern, M. Grundmann: Mater. Res. Soc. Symp. Proc. **1633**, 101 (2014)
[3] F.-L. Schein, M. Winter, T. Böntgen, H. v. Wenckstern, M. Grundmann: Appl. Phys. Lett. **104**, 022104 (2014)
[4] P. Schlupp, F.-L. Schein,H. von Wenckstern,M. Grundmann: Adv. Electron. Mater. **1**, 1400023 (2015)

9.3 Semi-transparent NiO/ZnO UV Photovoltaic Cells

R. Karsthof, P. Räcke, H. von Wenckstern, M. Grundmann

Transparent photovoltaic cells open new fields of application for solar energy conversion, e.g. as 'photovoltaic windows' transmitting the entire visible spectral range of the solar radiation and, at the same time, converting the energy of UV and IR photons into electrical energy as efficiently as possible. By covering large glass surfaces with such devices, the otherwise unused energy of these photons can be used to generate extra electric power to supply low-power comsumers like charging units for mobile devices, but also air conditioning or artificial lighting of a building's interior.

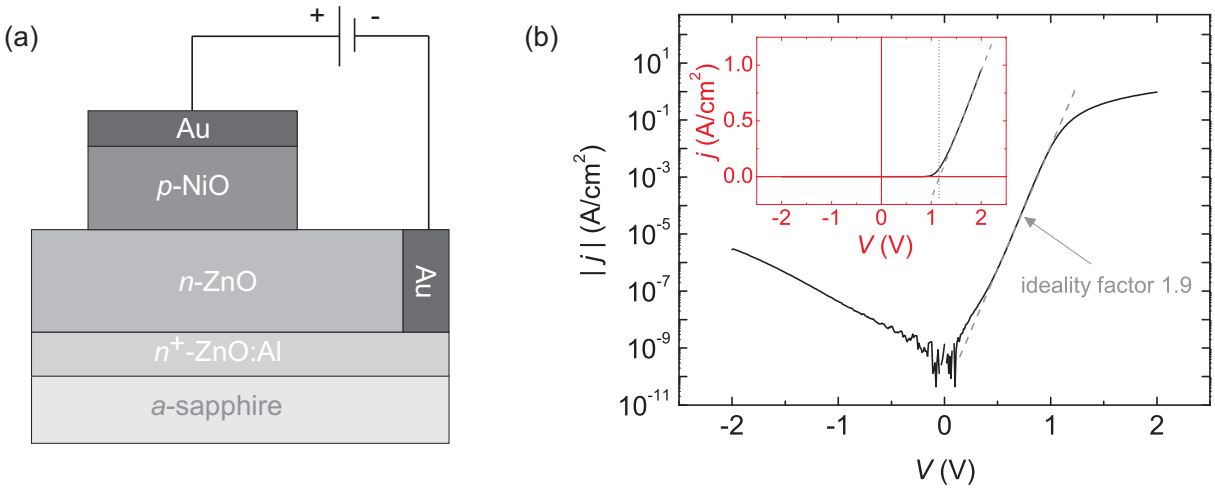

Figure 9.4: (a) schematic front view of sample structure, (b) jV characteristics of *p*-NiO/*n*-ZnO heterojunction diodes under dark conditions in log and lin (inset) scale.

In this work we focused on the fabrication of UV-active solar cells based on *p*-NiO/*n*-ZnO heterojunctions [1]. Using the pulsed laser deposition (PLD) technique, a

nominally undoped ZnO absorber layer was grown on top of *a*-plane sapphire substrates with a highly Al-doped ZnO layer beneath which serves as transparent back contact. During this step the substrate temperature was kept at 670 °C. Afterwards, we grew *p*-type NiO on top, using DC reactive sputtering in an Ar/O_2 atmosphere at room temperature (no intentional substrate heating) from a metallic Ni target. The NiO thickness was 16 nm. The NiO was covered with a 6 nm thin gold 'current-spreading layer' deposited by DC magnetron sputtering. Using standard UV photolithography, NiO/Au contacts with a circular shape were produced, enabling the characterization of individual sub-mm^2 cells. The average transmittance of the complete cell stack is 46 % in the visible spectral range (380 – 780 nm), dominated by absorption in the NiO and Au layers. We have shown by X-ray diffraction measurements that the NiO films are X-ray amorphous, possibly causing strong band tails and thereby optical absorption in the visible spectral range.

Electrical characterization was carried out by means of current-voltage measurements under dark conditions and under illumination with a Xe lamp simulating solar radiation. In dark, the contacts show highly rectifying behavior with recification ratios between six and eight orders of magnitude (see Fig. 9.4(b)). The diode ideality factor is close to 2, as predicted by theory for a type-II heterojunction [2]. Upon illumination, open-circuit voltages of around and above 500 mV and short-circuit current densities of around 0.5 mA/cm^2 have been measured. The fill factors of our devices were rather low (around 40 %), leading to total power conversion efficiencies of approximately 0.1 %. We also calculated a power conversion efficiency with respect to the UV spectral part of the solar spectrum, which amounts to 3.1 %. It is obvious that the absorption of light strongly deforms the current-voltage characteristics (Fig. 9.4(b)), leading to a strong voltage dependence of the current density in photovoltaic mode and thereby resulting in low fill factors.

To investigate the reasons for this behavior, we conducted an analysis of the collection efficiency of photo-generated charge carriers which can be responsible for a voltage dependence of the current under illumination. This was done by measuring *jV* characteristics at different levels of illumination; the details of the measurement principle can be found in the literature [3, 4]. We were able to fit our collection efficiency data with a model including recombination losses at the NiO/ZnO interface and within the depleted region of the junction (data and fit are shown in Fig. 9.5), and we conclude that the main reason for the observed low fill factors is fast recombination at the junction interface (recombination velocities of around 1×10^5 cm/s), enhanced by defect states energetically located in the interface gap. Optical emission of trapped charge carriers from these defects might be responsible for the deformation of the *jV* characteristics upon illumination, as it would increase the magnitude of the injected current.

To improve device performance, engineering of the interface properties is neccessary, e.g. by reduction of the interface defect density or by an optimization of the band alignment.

[1] R. Karsthof, H. von Wenckstern, M. Grundmann, Phys. Stat. Solidi A 213(1), 30 (2016)
[2] M. Grundmann, R. Karsthof, H. von Wenckstern, ACP Appl. Mater. Interfaces 6, 14785 (2014)
[3] K.W. Mitchell, A.L. Fahrenbruch, R.H. Bube, J. Appl. Phys. 48, 4365 (1977)

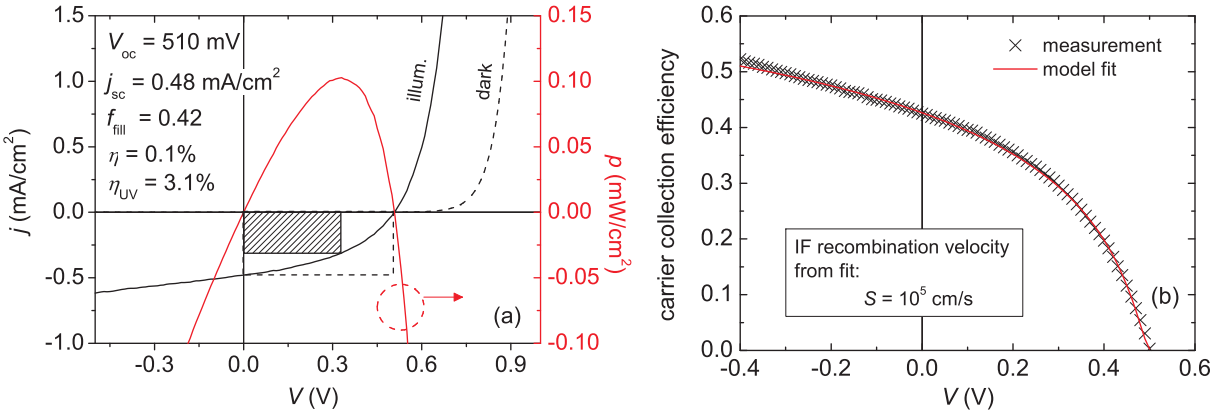

Figure 9.5: (a) comparison of jV characteristics in dark and under illumination and PV parameters, (b) charge carrier collection efficiency and respective fit

[4] S. Hegedus, D. Desai, C. Thompson, Prog. Photovolt.: Res. Appl. 15, 587 (2007)

9.4 Transparent JFETs based on NiO/ZnO heterojunctions

R. Karsthof, H. von Wenckstern, M. Grundmann

When compared to devices based on metal-insulator-semiconductor (MIS) or metal-semiconductor (MES) structures, junction field-effect transistors (JFETs) have advantages in certain fields of application. On one hand, in contrast to MISFETs, due to the absence of an insulating layer, high operating frequencies are possible. On the other hand, especially in the case of all-oxide devices, good performance also at elevated temperatures can be expected whereas ZnO-based MESFETs typically degrade when exposed to heat. Furthermore, the usage of large-band gap materials enables the fabrication of devices which are transparent for visible light. All-oxide JFETs based on p-$ZnCo_2O_4$(ZCO)/n-ZnO heterojunctions have already been demonstrated [1]. However, due to the band gap energy of ZCO being in the visible range, such devices are opaque. For this reason we chose NiO as gate material [2]. Its large band gap of around 3.7 eV enables the fabrication of devices with high optical transmittance in the visible range.

All oxide layers of the device were grown by pulsed laser deposition. UV photolithography was used to pattern the respective layers. First, a 20 nm thick ZnO layer was deposited on a-plane oriented sapphire substrate from which mesa structures were then produced by wet chemical etching. These structures were used as channels. Next, source and drain contacts were grown from Ga-doped ZnO (4 at. % Ga) and the gate contact from NiO, in both cases at room temperature. Again, source, drain and gate contacts were finally covered with a 6 nm thick Au current-spreading layer (structure schematically shown in Fig. 9.6(a)).

In Fig. 9.6(b) the transfer characteristic of the best device is shown. The typical current on/off-ratio was around 1×10^7 at ±2 V. Channel mobilities were approximately 4 cm^2/Vs and thus slightly lower than the values reported for our devices with ZCO gates. The best device showed a sub-threshold slope of 65 mV/dec which is only slightly

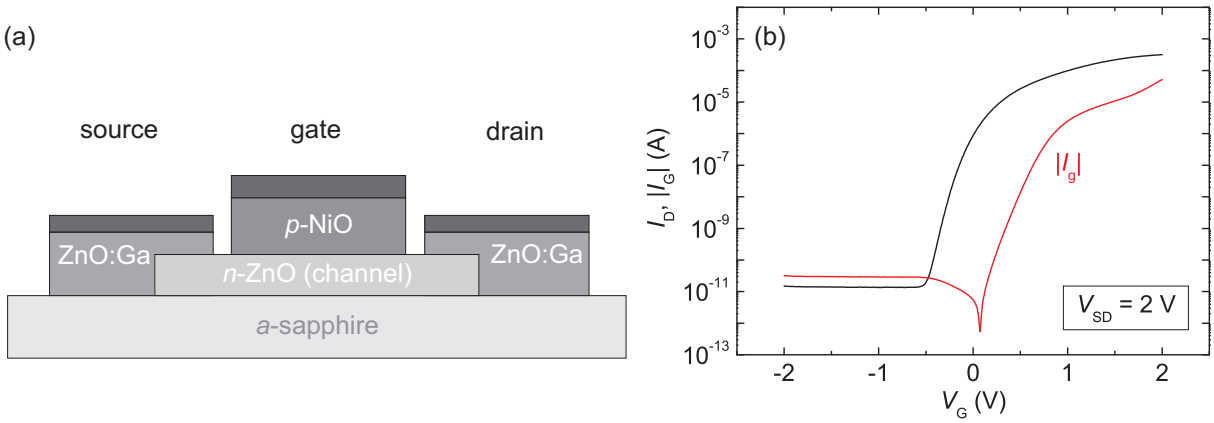

Figure 9.6: (a) schematic front view of transistor structure, (b) transfer characteristic and gate current of a selected device, measured at a drain voltage of 2 V

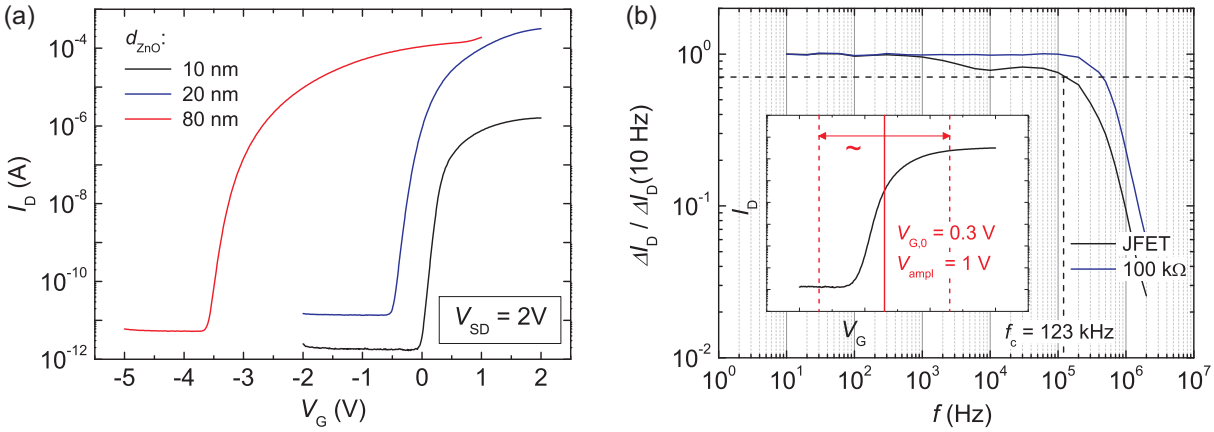

Figure 9.7: (a) transfer characteristics of devices with varying channel thickness, (b) drain current in dependence of gate operating frequency ('gate lag') and frequency response of a 100 kΩ resistor

above the theoretical minimum of 60 mV/dec. For the mentioned channel thickness of 20 nm, the on-voltage was around −0.5 V; by varying the thickness between 10 and 80 nm we could shift this value between approximately 0 V and −3.5 V (see Fig. 9.7(a)).

To check the high-frequency switching behavior of our transistors we investigated the so-called gate lag effect – i.e. the drain current was measured at a fixed drain voltage of 2 V while a sinusoidal signal of variable frequency was applied at the gate, quickly switching between the on- and off-state of the transistor. The frequency dependence of the drain current between 10 Hz and 20 MHz is shown in Fig. 9.7(b), together with the frequency response of the used amplifying circuit. A cutoff frequency of 123 kHz was determined for this device. We also investigated the temperature stability of the transistors in a range beween 10 ℃ and 100 ℃ (Fig. 9.8), and we could show that the devices are thermally stable in this temperature regime with regard to their transfer characterstics: even though a slight increase of the off-current was observed, full operationality is conserved at elevated temperatures, and the occurring changes were shown to be almost completely reversible after room temperature was restored.

[1] F.-L. Schein, H. von Wenckstern, H. Frenzel, M. Grundmann, IEEE Electron. Device

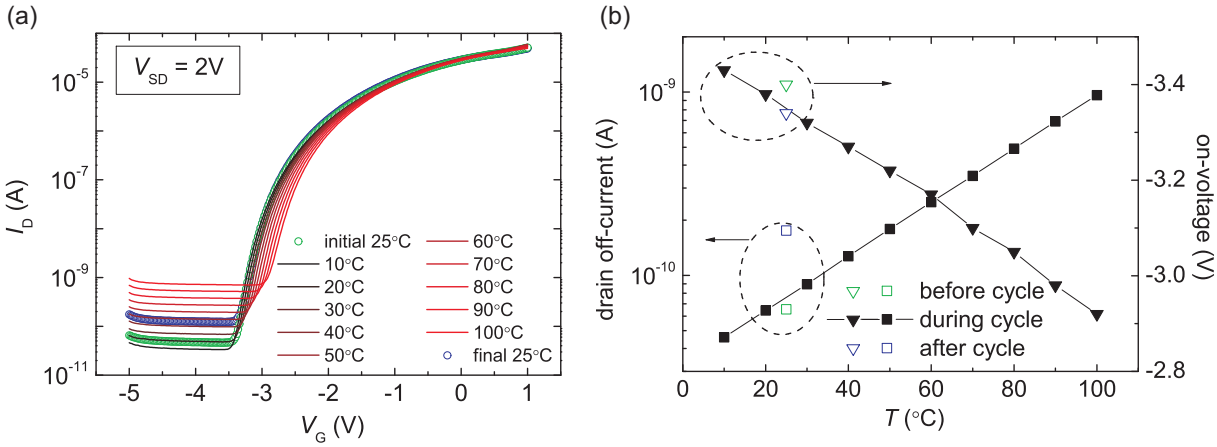

Figure 9.8: (a) Temperature dependence of the transfer characteristics of a NiO-gated JFET and (b) temperature dependence of the off-current and the on-voltage of the device

Letters 33, 676 (2014)
[2] R. Karsthof, H. von Wenckstern, M. Grundmann, IEEE Transactions On Electron Devices 62(12), 3999 (2015)

9.5 Eclipse pulsed laser deposition grown Schottky contacts on ZnO thin films

S. Müller, H. von Wenckstern, F. Schmidt, D. Splith, F.-L. Schein, H. Frenzel, M. Grundmann

In the last years $_\beta$-gallium Ga_2O_3 oxide has been investigated as semiconducting material with an increasing interest. Beside possible applications in opto-electronic devices like solar-blind UV-detectors, gallium oxide is due to its large band gap of about 4.9 eV interesting for high power electronics [1].

Here, we present a comparison of equally fabricated high quality PtO_x Schottky contacts (SCs) prepared by long-throw sputtering (LTS) on Ga_2O_3 thin films (TF) and bulk material (BM). The Ga_2O_3 TFs were grown by pulsed laser deposition on *c* - plane sapphire substrates at a temperature of 650 °C and an oxygen partial pressure of 1×10^{-3} mbar. The BM is commercially available from Tamura Corporation. The TF as well as the BM are ($\bar{2}$01) oriented. Circular SCs with diameters between 150 µm and 750 µm were defined using photolithography. The PtO_x SCs were fabricated in a 1/1 mixed Ar/O_2 atmosphere using LTS at room temperature and a pressure of 0.01 mbar. Subsequently after fabricating an approximately 50 nm thick layer of PtO_x a second layer of metallic Pt was deposited in Ar atmosphere to ensure an equipotential surface.

Fig. 9.9(a) shows the room temperature current density-voltage (*j*-*V*) characteristic of a PtO_x/Ga_2O_3 SC fabricated on TF and BM. In forward direction is for both characteristics a mono-exponential slope over several orders of magnitude visible, which allows to determine the effective barrier height and the ideality factor for the SCs using thermionic emission theory as dominant transport mechanism [2]. The effective barrier height of the SC on thin film is with 1.42 eV significantly smaller compared to the counterpart on bulk material (1.94 eV). The determined ideality factor of the SC on TF is with 1.28

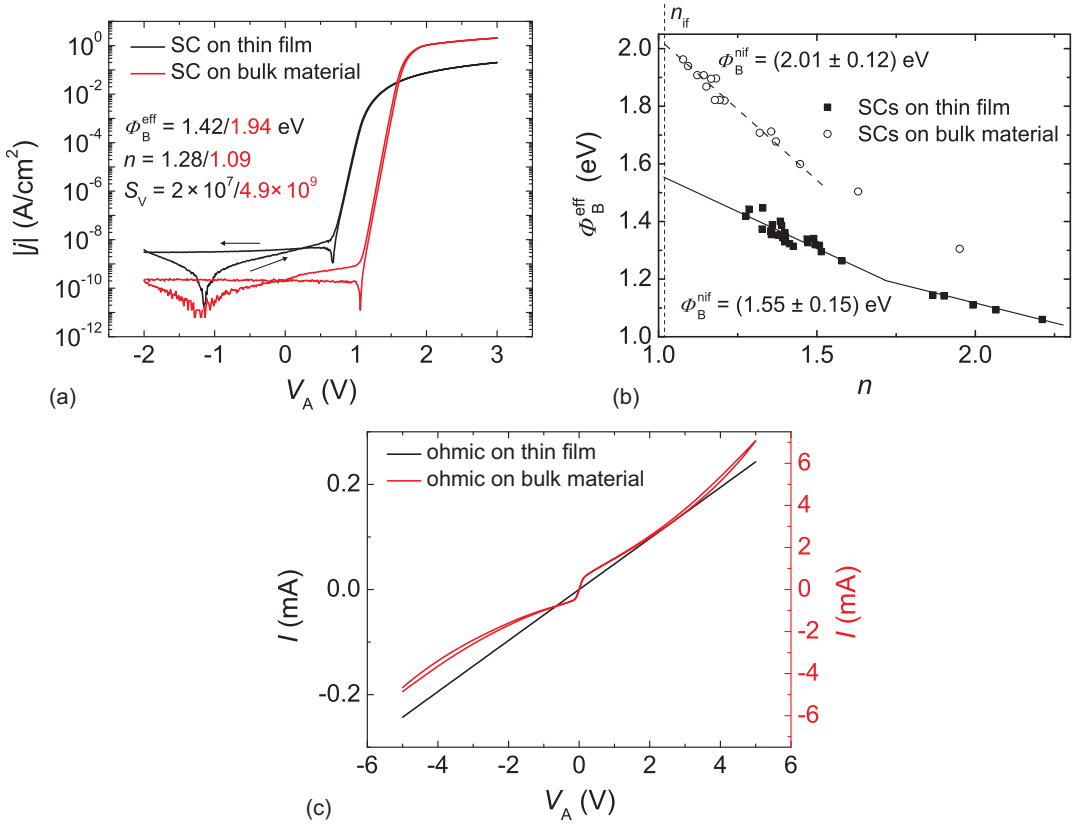

Figure 9.9: (a) Room temperature *j-V* characteristics of PtO_x/Ga_2O_3 SCs fabricated by long-throw sputtering on heteroepitaxial thin film and bulk material. The black arrow indicates the measurement direction. (b) Effective barrier height in dependence on the ideality factor of all PtO_x/Ga_2O_3 SCs on two samples. (c) Room temperature *I-V* characteristics measured between two nominally as ohmic contacts fabricated Ti/Al/Au contacts on heteroepitaxial thin film and bulk material.

larger than that of the SC on BM (1.09). That is caused by the inferior crystalline quality of the heteroepitaxial TF and the increased number of barrier height inhomogeneities. A sweep direction dependent splitting of the j-V characteristic is visible in Fig. 9.9(a) for the backward direction. This behavior can be explained in terms of a charging and discharging current of an additional parallel capacitance [2]. Depending on the sweep direction, the additional current increases or decreases the net carrier transport across the metal-semiconductor interface. Owing to this process, the zero crossing is shifted to positive voltages for one sweep direction and to negative voltages for the other. The additional current is for the SCs on TF approximately one order of magnitude larger. Therefore, and due to the larger series resistance (smaller electron mobility of the TF) of the SCs on TF the rectification ratio $S_V = |I(2\,V)/I(-2\,V)|$ of the SC on BM is with 4.9×10^9 more than two orders of magnitude larger compared to the SC on TF (2×10^7). For a comparison of the barrier height of the SCs on TF and BM it is necessary to determine the homogeneous barrier height like shown in Fig. 9.9(b). For the determination of the homogeneous barrier height a linear extrapolation of all data points with ideality factor smaller than 1.5 to the smallest ideality factor n_{if} = 1.02, which is given due to image force lowering effects at the metal-semiconductor interface, is used. The

homogeneous barrier height of the SCs fabricated on TF is with 1.55 eV approximately 0.4-0.5 eV smaller compared to that of the SCs on BM (2.01 eV). The large difference can be explained with an upward band bending for the BM in the as received state. In Fig. 9.9(c) are the *I-V* characteristics measured between two nominally as ohmic contacts fabricated Ti/Al/Au-contacts on TF and BM, respectively, is visualized. The characteristic measured for the TF exhibits an ohmic behavior. In contrast for the BM a slightly rectifying and non ohmic behavior, which clarifies the occurrence of such an upward band bending for the BM, is visible. The size of the upward band bending of the BM can be estimate to be 0.4-0.5 eV, which is the difference of the homogeneous barrier height of the SCs on TF and BM. This value is in very good agreement with recent reports determining the upward band bending using photoemission spectroscopy measurements to be 0.5 eV for BM [3, 4]. A more detailed discussion of the results presented here can be found in Ref. [7].

[1] M. Higashiwaki, K. Sasaki, A. Kuramata, T. Masui, and S. Yamakoshi, Appl. Phys. Lett. **100**, 013504 (2012), doi:10.1063/1.3674287
[2] D. Splith, S. Müller, F. Schmidt, H. von Wenckstern, J. J. van Rensburg, W. E. Meyer, and M. Grundmann, Phys. Status Solidi A **211**, 40 (2014), doi:10.1002/pssa.201330088
[3] T. C. Lovejoy, R. Chen, X. Zheng, E. G. Villora, K. Shimamura, H. Yoshikawa, Y. Yamashita, S. Ueda, K. Kobayashi, S. T. Dunham, F. S. Ohuchi, and M. A. Olmstead, Appl. Phys. Lett. **100**, 181602 (2012), doi:/10.1063/1.4711014
[4] A. Navarro-Quezada, Z. Galazka, S. Alamé, D. Skuridina, P. Vogt, and N. Esser, Appl. Surf. Sci. **349**, 368 (2015), doi:10.1016/j.apsusc.2015.04.225
[5] S. Müller, H. von Wenckstern, F. Schmidt, D. Splith, F.-L. Schein, H. Frenzel and M. Grundmann, Appl. Phys. Express **8**, 121102 (2015), doi:10.7567/APEX.8.121102

9.6 Ring oscillator circuits based on MESFETs and JFETs with ZnO channels

F.J. Klüpfel, H. von Wenckstern, M. Grundmann

Integrated circuits based on oxide semiconductors have been demonstrated mostly for field-effect transistors with insulated gate (MISFETs). For MISFET ring oscillators gate delays down to 31 ns have been demonstrated [1]. This indicates a maximum operation frequency in the range of 30 MHz for digital circuits. It has been shown by our group, that building blocks for integrated circuits, namely inverters and NOR gates, can be fabricated with ZnO based junction field-effect transistors (JFETS) and metal-semiconductor field-effect transistors (MESFETs) [2, 3]. Such circuits exhibit significantly reduced low frequency noise compared to other reported oxide semiconductor devices [4].

We demonstrated ring oscillators with JFETs and MESFETs based on crystalline ZnO thin films grown by pulsed laser deposition on a-plane sapphire substrates. Each ring oscillator consists of an odd number of inverters connected in a closed circuit, together with an additional inverter for signal outcoupling. The circuit fabrication needs a total of 10 lithographic processing steps. 5 steps are necessary to obtain the actual devices (front end of line, i.e. inverters), the remaining process provides for the wiring of

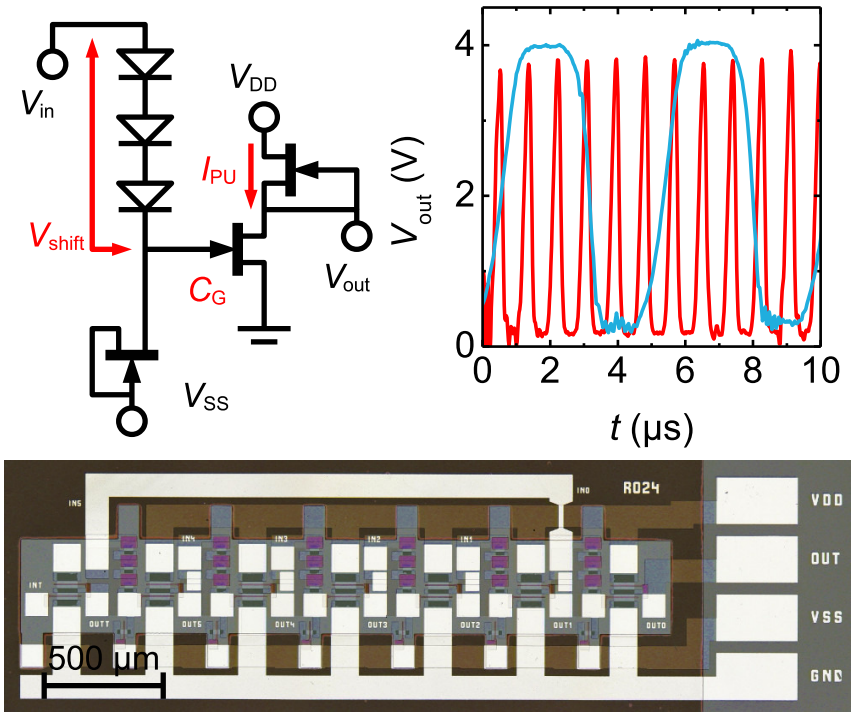

Figure 9.10: *Upper left*: circuit schematic of a full inverter using the Schottky diode FET logic (SDFL) technique. Device properties useful for estimation of the maximum switching speed are labelled red. *Upper right*: Measured output voltage of 3 stage ring oscillators based on two different ZnO samples. *Below*: Optical micrograph of a 5 stage ring oscillator featuring 6 identical full inverters.

the individual devices (back end of line). Fig. 9.10 shows the circuit schematic of a single inverter and an optical micrograph of a 5 stage inverter. We measure oscillation frequencies up to 1.1 MHz for 3 stage ring oscillators, which corresponds to a delay of 110 ns per stage. Typical time traces for the output voltage are depicted in Fig. 9.10.

The gate delay for a single stage can be estimated with the equation [5]

$$\tau_{D,calc} = \frac{C_G(V_{shift}/3 - V_{SS})}{I_{PU}}. \tag{9.2}$$

C_G is the gate capacitance of the input FET, I_{PU} the saturation current of the pull-up FET, and V_{shift} the voltage shift of the level shifter circuit (see Fig. 9.10). These quantities are readily measurable device properties. The calculated values are compared to measured delay times in Fig. 9.11, demonstrating a good agreement between theory and experiment.

We conclude that circuits with MESFETs and JFETs based on oxide semiconductors can reach bandwidths comparable to MISFET circuits. Furthermore, the presented technique has the advantage of significantly reduced noise levels in the low frequency regime.

[1] Sun *et al.*, IEEE Electron Device Letters, **29**, 721 (2008)
[2] Frenzel *et al.*, Applied Physics Letters, **96**, 113502 (2010)
[3] Klüpfel *et al.*, IEEE Transactions on Electron Devices, **62**, 4004 (2015)

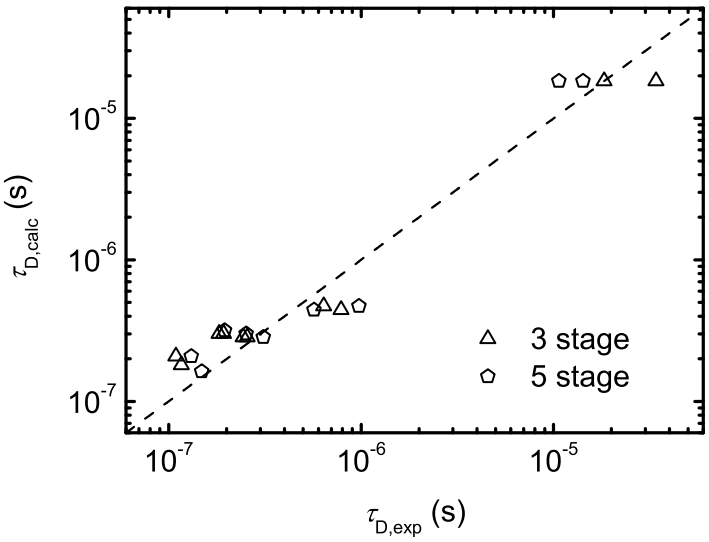

Figure 9.11: Delay times per stage calculated from Equation 9.2 compared to experimental values of 20 ring oscillators from 5 different samples.

[4] Klüpfel *et al.*, Applied Physics Letters, **106**, 033502 (2015)
[5] Klüpfel *et al.*, Advanced Electronic Materials, **2**, 1500431 (5 pages) (2016)

9.7 Properties of Schottky Barrier Diodes on $(In_xGa_{1-x})_2O_3$

D. Splith, H. von Wenckstern, A. Werner, S. Müller, M. Lorenz, M. Grundmann

Solar blind UV-photodetectors have a wide range of possible applications. Since they are insensitive to the terrestrial solar radiation background, they can be used for flame detection, monitoring of industrial processes, communication, UV-astronomy or even military purposes like missile plume detection. For the realisation of such devices, semiconductors with a wide band gap are needed. Additionally, in order to tailor the absorption edge of the photo detector to the particular purpose, alloying of two semiconductors with different band gaps can be used. A promising material system for this application are the group III sesquioxides Ga_2O_3, In_2O_3 and Al_2O_3. Since *p*-type conduction is not reported for such materials, the photodetectors must be realised by metal-semiconductor-metal (MSM) structures using two Schottky Barrier Diodes (SBDs). Therefore, the understanding of the influence of the alloying on the properties of such SBDs is crucial. Here, we report the properties of PtO_δ SBDs on an $(In_xGa_{1-x})_2O_3$ thin film having a lateral composition spread from $x = 0.01$ to $x = 0.8$ [1].

The thin film investigated was grown by pulsed laser deposition (PLD) on a two inch in diameter *c*-plane sapphire wafer. In order to achieve the lateral composition spread, a segmented target consisting of binary In_2O_3 and binary Ga_2O_3 was used, which was rotated synchronously with the wafer, as proposed by von Wenckstern *et al.* [2]. Additionally, 0.1 wt.% SiO_2 were admixed to both parts of the target in order to increase the conductivity. After the characterisation by energy-dispersive X-ray spectroscopy

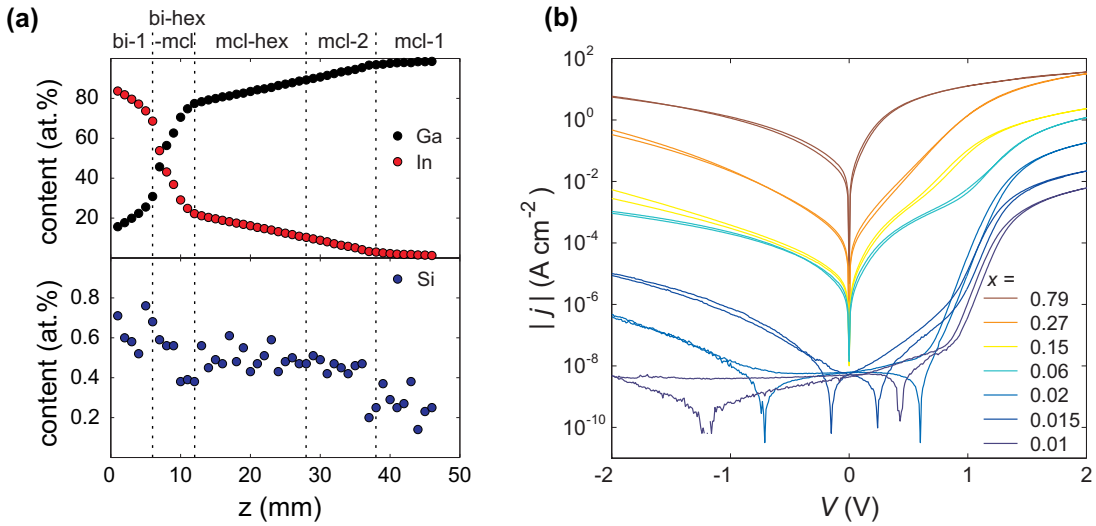

Figure 9.12: (a) In-, Ga- and Si content for different positions along the gradient determined from EDX measurements. The labels give the predominant phases for the different regions determined from the XRD measurements. (b) IV characteristics of selected diodes along the composition gradient.

(EDX) and X-ray diffraction (XRD) measurements, circular PtO_δ SBDs were fabricated on a 5 mm by 50 mm stripe along the gradient by a reactive sputtering process [3] and characterized by current-voltage (IV) measurements.

From the EDX measurements, the composition of the thin film in dependence on the position can be determined. In Fig. 9.12 (a), the In-, Ga- and Si-content are shown in dependence of the position along the gradient. Additionally, the predominant phases were determined by XRD measurements along the gradient. In the XRD scans, three different phases were found: the bixbyite In_2O_3 phase (bi), the hexagonal $InGaO_3$(II) phase (hex) and the monoclinic Ga_2O_3 phase (mcl). The regions in Fig. 9.12 (a) are labelled according to their predominant phases.

The IV characteristics of selected SBDs along the gradient can be seen in Fig. 9.12 (b). As the In content x increases, the series resistance decreases due to a higher conductivity, which can clearly be seen by the increasing current for voltages higher than 1.5 V. For further evaluation, the IV characteristics of all measured contacts along the gradient were fitted with the model of thermionic emission in order to determine the effective barrier heights and ideality factors. Additionally, the rectification ratios were calculated. The determined values of all contacts are shown in Fig. 9.13 (a), (b) and (c) in a false-color representation of the 5 mm by 50 mm stripe. From the mean values of these properties for similar In content, a clear trend is observable: For low x, the effective barrier heights are the highest with a mean value close to 1.2 eV. The incorporation of In leads to a decrease of the effective barrier heights down to mean values around 0.4 eV on the In-rich site. The ideality factors has its lowest mean values of around 2 for low and high In content. In the regions in between, the intermixing of different phases leads to barrier height inhomogeneity, which results in higher values for the ideality factor. Although the series resistance is the highest for low In content, the rectification is the highest here, due to the high barrier heights. Increasing x results in higher reverse currents, which lead to a drop of the rectification ratio from mean values around 5 orders of magnitude for low In content to below 10 for high In content.

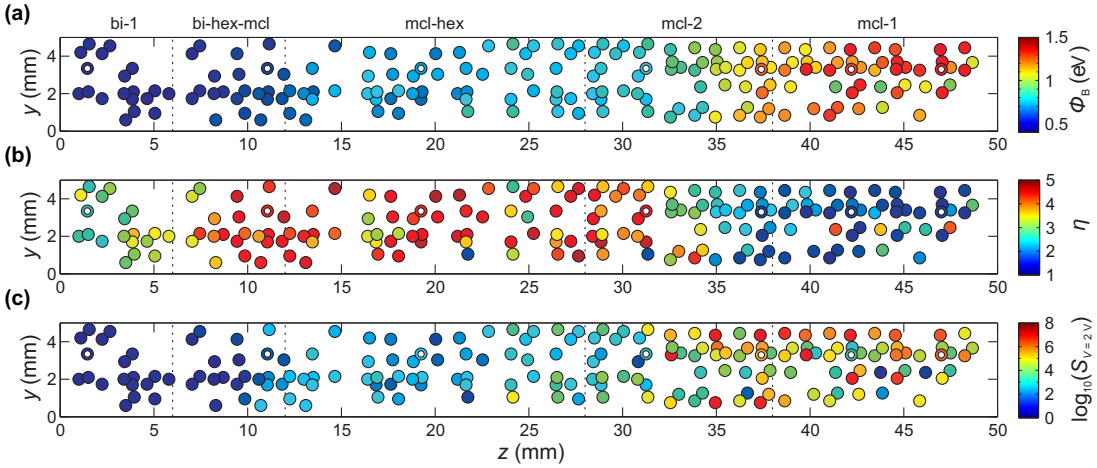

Figure 9.13: False-color representation of the (a) effective barrier heights Φ_B, (b) ideality factors η and (c) rectification ratios $S_{V=2\,V}$ of the contacts on a 5 mm by 50 mm stripe along the gradient. The contacts for which the IV characteristics are shown in Fig. 9.12 (b) are marked with a white dot. The labels give the predominant phases for the different regions determined from the XRD measurements.

[1] H. von Wenckstern *et al.*, ACS Comb. Sci. **17**, 710-715 (2015)
[2] H. von Wenckstern *et al.*, CrystEngComm **15**, 10020-10027 (2013)
[3] S. Müller *et al.*, Appl. Phys. Express **8**, 121102 (2015)

9.8 Rectifying *pn*-heterojunctions on In_2O_3

D. Splith, H. von Wenckstern, S. Lanzinger, F. Schmidt, S. Müller, P. Schlupp, R. Karsthof, M. Grundmann

In_2O_3 is a material well known in its highly tin doped form, which is used as an electrode in thin film solar cells, displays or as a contact layer in touch screens as a transparent conducting oxide. Recently, the interest in the semiconducting properties of nominally

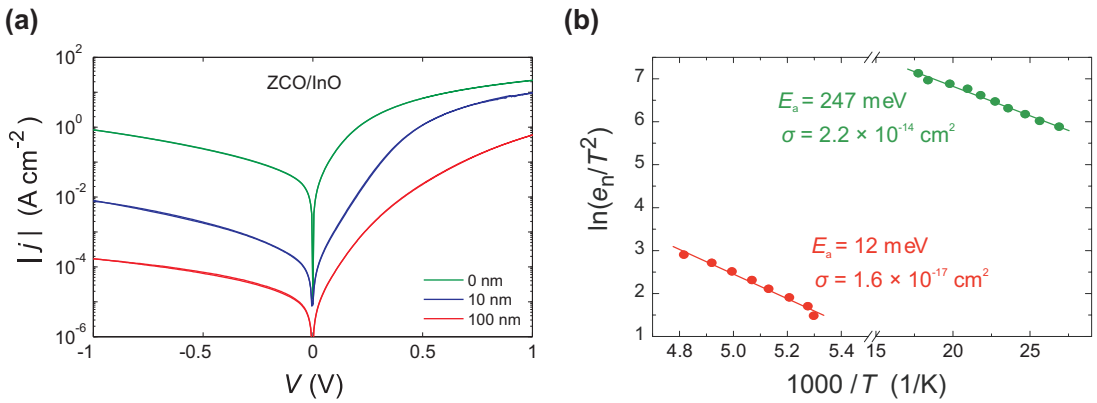

Figure 9.14: (a) *j-V* characteristics of ZCO/In_2O_3 *pn*-heterojunctions for different thicknesses *d* of the Mg-doped In_2O_3 layer. (b) Arrhenius plot of the two defects observable in the TAS measurement.

undoped or only slightly doped crystalline In_2O_3 arose for fundamental reasons as well as for potential application in transparent electronic devices. In order to fabricate devices like diodes or field-effect transistors and to perform defect spectroscopic measurements, rectifying contacts which create a space charge region inside the In_2O_3 are necessary. Since the branch point energy for In_2O_3 lies within the conduction band and therefore, In_2O_3 tends to form a surface electron accumulation layer (SEAL) [1], the realisation of such contacts on In_2O_3 is non-trivial. However, ZnO also tends to form a SEAL, but rectifying contacts can be fabricated by different methods. Recently, the realisation of Schottky contacts using a reactive sputtering process similar to Schottky contacts on ZnO was reported [2]. It was also recently shown that *p*-type amorphous oxide semiconductors like $ZnCo_2O_4$ (ZCO) or NiO form rectifying *pn*-heterojunctions on ZnO [3]. Here, we report how this approach can be used to fabricate *pn*-heterojunctions on In_2O_3 [4].

The In_2O_3 thin films used in this study were grown by pulsed laser deposition (PLD) from a nominally undoped target on YSZ substrate at a growth temperature of 600°C. Additionally, a thin Mg-doped In_2O_3 film was grown on top of the undoped film in order to reduce the net doping density and by that leakage currents. The thickness d of the Mg-doped layer was varied between 0, 10 and 100 nm. The *p*-type oxides ZCO and NiO were grown by PLD at room temperature. Here, only results for ZCO contacts will be discussed.

The *j-V* characteristics of ZCO contacts on the In_2O_3 thin film are shown in Fig. 9.14 (a) for different thicknesses d of the Mg-doped layer. Without the Mg-doped layer (d = 0 nm) the contacts show rectification ratios between 10 and 50. By introducing the Mg-doped layer, the rectification of the heterojunctions can be increased to values larger than 3 orders of magnitude for both the 10 and the 100 nm thick Mg-doped layer. The ideality factors for d = 10 nm and d = 100 nm were determined using the Shockley equation and bunch around 2 as expected for a type-II heterojunction with interface recombination being dominant [5].

Capacitance-Voltage (CV) and thermal admittance spectroscopy (TAS) measurements were performed on a ZCO/In_2O_3 heterojunction with a 10 nm thick Mg-doped layer, since the higher series resistance of the contacts with the 100 nm thick Mg-doped layer makes this sample structure unsuited for frequency dependent measurements due to the lower cut-off frequency. The net doping profile calculated from the CV measurement shows a decrease of the net doping from 3×10^{18} cm^{-3} to 2×10^{18} cm^{-3} at a distance of about 10 nm due to the 10 nm thick Mg-doped layer. From the TAS measurement, the Arrhenius plot of two defects shown in Fig. 9.14 (b) can be calculated. From the linear fit, defect levels energies of 247 meV and 12 meV with apparent capture cross-sections of 2.2×10^{-14} cm^2 and 1.6×10^{-17} cm^2 can be determined for the two defects, respectively.

[1] P. King *et al.*, Phys. Rev. Lett. **101**, 116808 (2008)
[2] H. von Wenckstern *et al.*, APL Mat. **2**, 046104 (2014)
[3] M. Grundmann *et al.*, Adv. Sci. Technol. **93**, (2014)
[4] H. von Wenckstern *et al.*, Adv. Electron. Mater. **1**, 1400026 (2015)
[5] M. Grundmann *et al.*, ACS Appl. Mater. Interfaces **6**, 14785 (2014)

9.9 Electron transport in rf-sputtered amorphous zinc oxynitride thin films

A. Reinhardt, H. Frenzel, H. von Wenckstern, D. Spemann, M. Grundmann

Electronic devices based on amorphous oxide semiconductors provide a variety of advantages such as low-temperature and large-scale fabrication. Intensive studies were conducted on multi-cation compounds such as amorphous indium-gallium-zinc-oxide (a-IGZO), which is currently integrated in LCD panels as channel material of the driving thin film transistors (TFTs). Nevertheless, the realization of future display electronics necessitates high performance TFTs based on semiconductors with even higher carrier mobility than in a-IGZO. Furthermore, the use of expensive metals such as indium is not preferable in terms of cost-effectiveness. A promising approach towards such next-generation displays provide amorphous multi-anion compounds. The incorporation of nitrogen into ZnO leads to the formation of amorphous zinc oxynitride (a-ZnON) with carrier mobilities of up to 100 $cm^2V^{-1}s^{-1}$ and an improved stability under illumination, as recently reported in [1–6].

Here, we discuss the carrier transport mechanism in as-deposited as well as annealed a-ZnON thin films using temperature dependent Hall effect measurements. The ZnON thin films were radio-frequency sputtered from a metallic zinc target in a reactive atmosphere consisting of N_2, O_2 and Ar. The electrical conductivity of the films was controlled via variation of the substrate temperature between room temperature (RT = 25 °C) and 200 °C. At substrate temperatures above 200 °C the formation of crystalline ZnO phases occurs. The annealing was performed on RT-deposited samples in N_2 atmosphere for 1 hour at 200 °C.

Figure 9.15(a) depicts the temperature dependence of the electrical conductivity (σ), the Hall mobility (μ_{Hall}) and the electron concentration (n) in an Arrhenius plot for a-ZnON films with different RT carrier concentrations. All films exhibit semiconducting behaviour. The electrical conductivity of the annealed film with $n \sim 10^{19}$ cm^{-3} is almost temperature independent, indicating quasi-metallic behaviour. However, the electrical conductivity of the as-deposited films with $n < 10^{19}$ cm^{-3} does not follow a simple thermally activated law ($\ln \sigma \propto T^{-1}$), as it would be expected for band conduction or nearest neighbour hopping. Figure 9.15 (b) confirm that the electrical conductivity σ of the as-deposited films obeys the relation $\ln \sigma \propto T^{\alpha}$ with temperature exponents of $\alpha = -1/2$ and $\alpha = -1/4$. For carrier densities $10^{18} < n < 10^{19}$ cm^{-3}, a linear dependence with two different slopes is observed in the corresponding plots. The observed kink suggests a transition between different conduction mechanisms occurring between 100 K and 125 K as the carrier density increases. The $T^{-1/4}$ dependence can be associated with Mott variable range hopping [7] as well as percolation conduction [8, 9]. As definite Hall voltage signals are obtained for temperatures above 130 K for all samples, variable range hopping is assumed not to be the dominant transport mechanism in this temperature regime. The observed behaviour can be explained by a percolation conduction model proposed by Adler *et al.* [10], who calculated the conductivity in terms of a percolation conduction in the absence of a sharp mobility edge. It is supposed that the electrons move through a random distribution of potential fluctuations with Gaussian distributed potential heights in the conduction band tail. Depending on the extent of the band tail, temperature exponents between − 1/2 and − 1/4 were calculated.

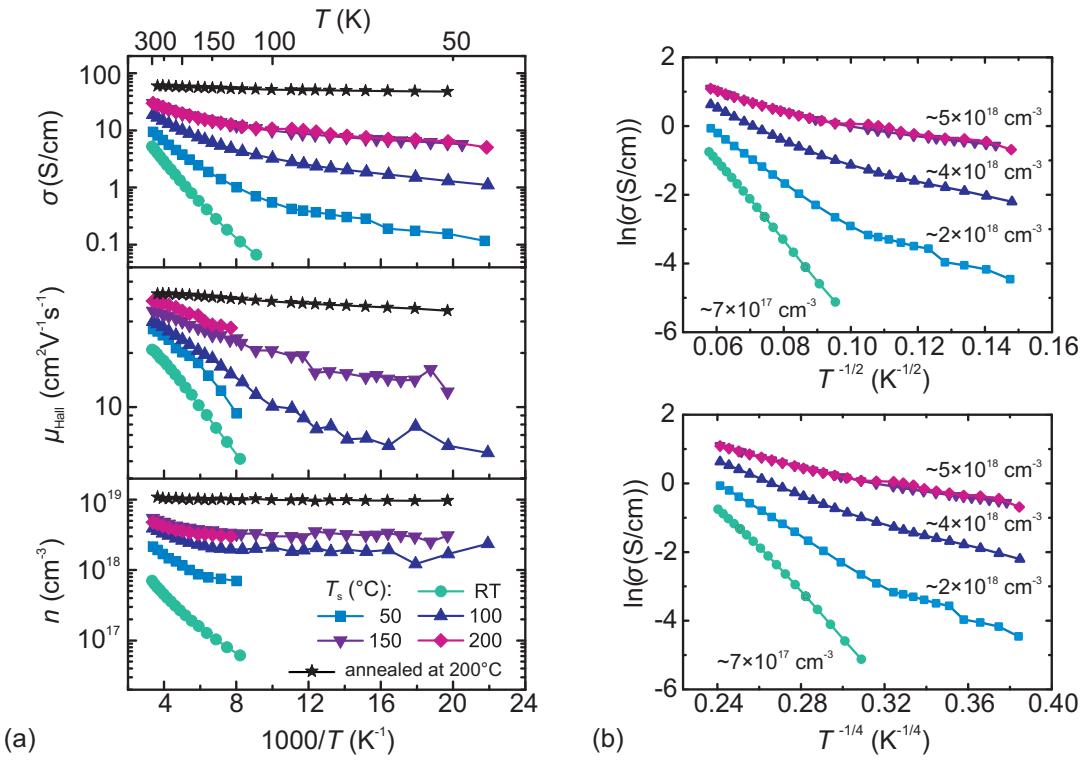

Figure 9.15: (a) Arrhenius plots of the electrical conductivity (σ), Hall mobility (μ_{Hall}) and carrier concentration (n) of a-ZnON thin films with different RT carrier densities. The films were sputtered at a total gas pressure of 0.4 Pa and at different substrate temperatures T_s as indicated. The annealing was performed at 200 °C in nitrogen atmosphere for 1 h on a RT-deposited sample. (b) $\ln\sigma$ vs. $T^{-1/2}$ plot and $\ln\sigma$ vs. $T^{-1/4}$ plot of the electrical conductivity σ of a-ZnON films.

The conduction band of ZnON is assumed to be composed of Zn 4s orbitals and N 2p orbitals similar to Zn_3N_2 [5, 11]. Therefore, the conduction band formed by the overlap of these orbitals is sensitive to bond angle disorder which results in band tailing [12]. This gives rise to the assumption of potential fluctuations or shallow trap states near the conduction band minima of ZnON, which provides a possible explanation for the observed temperature dependence of the electrical conductivity resembling a percolation controlled transport.

[1] Y. Ye, R. Lim, J. M. White, J. Appl. Phys. **106**, 074512 (2009)
[2] H. S. Kim, S. H. Jeon, J. S. Park, T. S. Kim, K. S. Son, J. B. Seon, S. J. Seo, S. J. Kim, E. Lee, J. G. Chung, H. Lee, S. Han, M. Ryu, S. Y. Lee, K. Kim, Sci. Rep. **3** , 1459 (2013)
[3] E. Lee, A. Benayad, T. Shin, H. Lee, D. S. Ko, T. S. Kim, K. S. Son, M. Ryu, S. Jeon, G. S. Park, Sci. Rep. **4**, 4948 (2014)
[4] E. Lee, T. Kim, A. Benayad, H. Kim, S. Jeon, G.-S. Park, Appl. Phys. Lett. **107**, 122105 (2015)
[5] S. Lee, A. Nathan, Y. Ye, Y. Guo, J. Robertson, Sci. Rep. **5**, 13467 (2015)
[6] K. C. Ok, H. J. Jeong, H. S. Kim, J. S. Park, IEEE Electr. Device L. **36**(1), 38–40 (2015)

[7] N. F. Mott, Philos. Mag. **19**(160), 835–852 (1969)
[8] V. Ambegaokar, Phys. Rev. B **4**(8), 2612–2620 (1971)
[9] M. Pollak, J. Non-Cryst. Solids **11**(1), 1–24 (1972)
[10] D. Adler, L. P. Laurence, S. D. Senturia, Solid State Commun. **12**(1), 9–12 (1973)
[11] R. Long, Y. Dai, L. Yu, M. Guo, B. Huang, J. Phys. Chem. B **111**(13), 3379–3383 (2007)
[12] J. Robertson, phys. status solidi (b) **245**(6), 1026–1032 (2008)

9.10 Doping efficiency and limits in (Mg,Zn)O:Al thin films grown by pulsed laser deposition

A. Mavlonov, H. von Wenckstern, M. Grundmann

The (Mg,Zn)O alloy is a suitable ternary compound for transparent electrode applications, i.e. for thin film solar cells, because of its tunable band gap, high transparency, and abundance of source materials [1]. Similar to binary ZnO thin films, the group III elements Al and Ga can be introduced to prepare highly conducting (Mg,Zn)O thin films. We investigated structural, electrical and optical properties of Al-doped (Mg,Zn)O thin films grown by PLD using a continuous composition spread method (CCS) [2, 3]. The samples on 2-inch in diameter $c-$plane sapphire substrates have two perpendicular, lateral composition gradients, i.e. the Mg composition is varied between 0 and 10 at. % in one direction, whereas the Al concentration is varied between $1 \times 10^{20}\,\mathrm{cm}^{-3}$ and $3 \times 10^{21}\,\mathrm{cm}^{-3}$ in a perpendicular direction. In order to obtain thin films with high crystalline quality, samples were grown at 600 °C. All investigated films have a thickness ranging from 120 to 200 nm. To facilitate electrical characterization, $(5 \times 5)\,\mathrm{mm}^2$ size pieces were cut from (Mg,Zn)O:Al thin films initially grown on 2-inch in diameter wafers.

For dopant content up to $2 \times 10^{21}\,\mathrm{cm}^{-3}$ all films have similar crystalline quality and similar grain size as depicted in Fig. 9.16 a). If the doping content exceeds $2 \times 10^{21}\,\mathrm{cm}^{-3}$ the crystalline quality deteriorates sharply as indicated by the increase (decrease) of the FWHM (grain size). With further increasing the dopant content, structural properties deteriorated. Fig. 9.16 b shows the dependence of the free electron concentration n versus the chemical dopant concentration, [Al] for different Mg admixtures. We observe an increase of n up to a dopant concentration of $1 \times 10^{21}\,\mathrm{cm}^{-3}$, a saturation and finally a decrease of n for $N_\mathrm{d} > 2 \times 10^{21}\,\mathrm{cm}^{-3}$. We further observe distinct dependencies of the free electron concentration on N_d. The trend described in the following holds for the Al doping series with 7 at.% Mg admixture. The two Al doping series with lower Mg content are considered below. For lower dopant concentration, i.e. $N_\mathrm{d} < 6 \times 10^{20}\,\mathrm{cm}^{-3}$, the free carrier concentration increases linearly with N_d ($n \propto N_\mathrm{d}$). For higher dopant concentration up to $N_\mathrm{d} \sim 1.4 \times 10^{21}\,\mathrm{cm}^{-3}$ the increase of n with increasing N_d becomes weaker and tends more to a $n \propto {N_\mathrm{d}}^{1/2}$ behavior. Different sources for doping limitations have been discussed in the literature such as the formation of secondary phases or defect complexes, or the formation of compensating intrinsic defects explained within the amphoteric defect model (ADM) [4, 5] and self-compensation by a doubly charged acceptor. For the case of ZnO or (Mg,Zn)O the main intrinsic defect forming at high

n-type doping is the zinc vacancy, indeed a doubly chargeable acceptor in ZnO [6] or other defects such as oxygen interstitials. For the $Mg_{0.04}Zn_{0.96}O$:Al series only the second regime, $n \propto {N_d}^{1/2}$ is visible and it is shifted to lower dopant density. For the $Mg_{0.03}Zn_{0.97}O$:Al series neither linear ($n \propto N_d$) nor square root ($n \propto {N_d}^{1/2}$) regimes are visible. Presumably, these regimes further shifted to lower dopant concentrations due to higher dopant activation for lower Mg content. This implies that also the dopant activation is highest for this series as can be seen in Fig. 9.16 d, showing $N_{d,act}$ as a function of N_d. As a general trend, the dopant activation decreases with increasing Mg-content. Further, it decreases strongly for all three Mg-contents for $N_d > 6 \times 10^{20}\,cm^{-3}$ where self-compensation becomes more and more important.

As depicted Fig. 9.16 c, the highest mobility exceeding $25\,cm^2/Vs$ is observed for low Mg-contents. A strong decrease of the mobility is found for dopant concentrations higher than $10^{21}\,cm^{-3}$. This coincides with the dopant concentration above which the incorporation of compensating acceptors, most likely zinc vacancies, is strongly enhanced. So it is reasonable to conclude a transition from grain boundary to ionized impurity scattering being the dominant scattering process. This is supported by taking a closer look to the samples with comparatively low free electron concentration, i.e. $Mg_{0.07}Zn_{0.93}O$:Al, for which the free carrier mobility increases or remains constant with increasing N_d in the lower doping regime. This is due to enhanced screening of and a decreased depletion region around the grain boundaries. If the dopant concentration is increased further, density of ionized impurities increases first linearly with it but as described above as soon as self-compensation starts to determine the free carrier concentration as the case for $N_d > 10^{21}\,cm^{-3}$ a strong decrease of the mobility is observed. This is also corresponding to the transition observed in the XRD data ($N_d \sim 10^{21}\,cm^{-3}$) the FWHM increases strongly which fits to the argument that more and more zinc vacancies are incorporated that are also responsible for the diminishing structural quality. For detailed discussion on this work as well as on Ga-doped (Mg,Zn)O alloys, the reader is referred to [3].

In summary, it has been found that the dopant efficiency tends to decrease with increasing Mg content x as well as Al concentration ($N_d > 6 \times 10^{20}\,cm^{-3}$), which can be explained with an increasing density of acceptor-like compensating defects and/or other defects such as oxygen interstitials. Compensation by intrinsic acceptors limits efficient doping to dopant concentrations of about $2 \times 10^{21}\,cm^{-3}$. Further, the electrical data suggest, that the compensating defect is doubly chargeable hinting to the zinc vacancy as microscopic origin. Increasing the dopant concentration above $2 \times 10^{21}\,cm^{-3}$ leads to a degradation of electrical and structural properties.

Funding: Islamic Development Bank (IDB), Merit Scholarship Programme for High Technology (A.M. Grant No. 91/UZB/P32).

[1] H. von Wenckstern *et al.*, The (Mg,Zn)O Alloy. Handbook of Zinc Oxide and Related Materials, Vol. 1 Materials. Taylor and Francis/CRC Press (2012).
[2] H. von Wenckstern *et al.*, CrystEngComm **15**, (2013) 10020-10027.
[3] A. Mavlonov *et al.*, PSS-A **212**, (2015) 2850-2855.
[4] W. Walukiewicz, Appl. Phys. Lett. **54**, (1989) 2094-2096.
[5] W. Walukiewicz, Physica B **302-303** (2001) 123-134.
[6] F. Oba *et al*. Phys. Rev. B **77**, (2008) 245202(6).

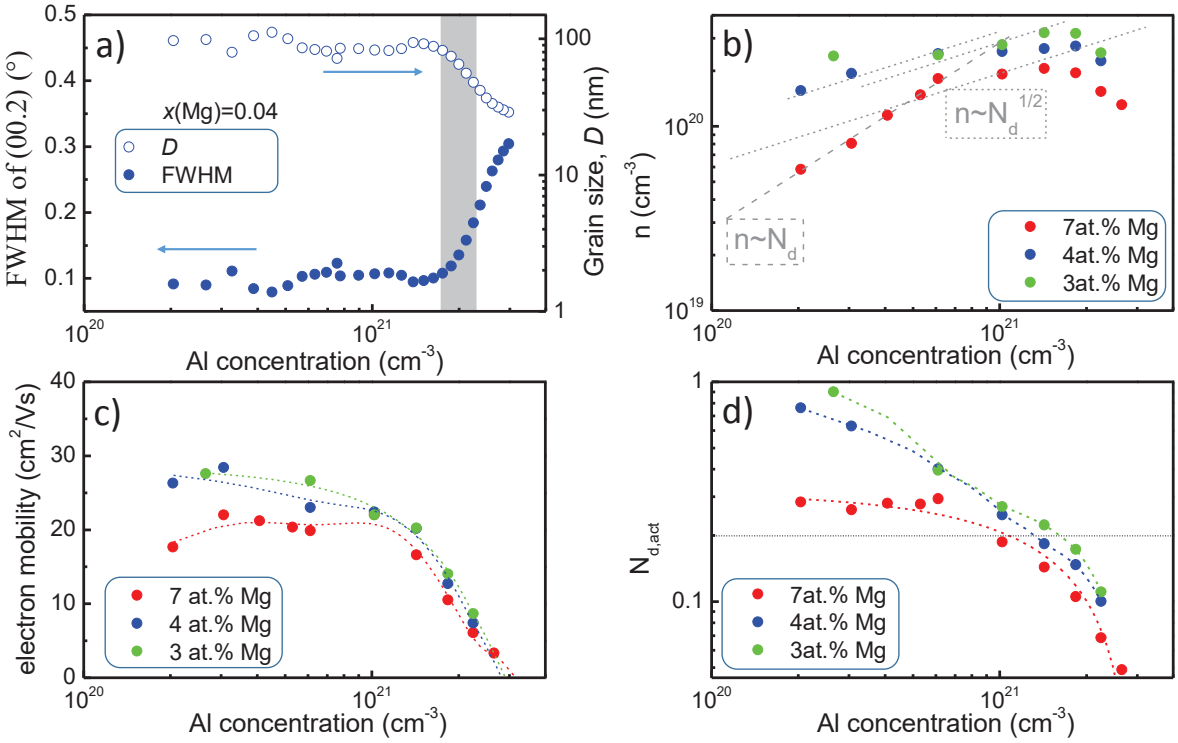

Figure 9.16: (a) The full-width at half-maximum of (00.2) peak and estimated grain size of the films (in vertical direction to the film surface), (b) the free charge carrier density, (c) Hall mobility, and (d) doping efficiency of Al-doped $Mg_xZn_{1-x}O$ thin films as a function Al concentration in the films. Dashed lines are guides to the eye.

9.11 Pseudomorphic, tilted wurtzite oxide heterostructures

M. Grundmann

Heterostructures from wurtzite semiconductors have been reported for the (Al,Ga)N/GaN, (In,Ga)N/GaN,(Mg,Zn)O/ZnO and (Cd,Zn)O/ZnO systems. They have technological relevance for a variety of photonic and electronic devices such as photodetectors, solar cells, intersubband detectors and cascade lasers, light emitting diodes as well as high mobility and power transistors. In the nitride system, all three binary materials InN, GaN and AlN (in the order of their band gap energy) exhibit the wurtzite structure. ZnO has also wurtzite structure, but MgO and CdO crystallize in the rocksalt structure. However, in thin film deposition $Mg_xZn_{1-x}O$ and $Cd_xZn_{1-x}O$ alloys can remain in the wurtzite phase for about $x < 0.55$ [1] and $x < 0.69$ [2], respectively.

We present a timely investigation of (Cd,Zn)O/ZnO and (Mg,Zn)O/ZnO heterostructures, in particular since we find that (Mg,Zn)O/ZnO behaves *qualitatively different* than (Cd,Zn)O/ZnO which itself is qualitatively similar to the well known nitride systems. MgO/ZnO is the only heterostructure for which ϵ_a and ϵ_c have different sign, i.e. $\mathrm{sgn}(\epsilon_a\,\epsilon_c) = -1$.

The geometry of the wurtzite unit cell with its [0001]-direction titled by the polar angle θ against the normal of the interface plane is depicted in Fig. 9.17. The coordinates

in the crystal system are denoted (x, y, z) with z being along the c-axis; the coordinates in the sample system are denoted (x', y', z') with z' being the epitaxial direction. The rotation of the crystal is around the $y = y'$-axis which is of $\langle 11\bar{2}0 \rangle$-type. The strain components for $Cd_{0.1}Zn_{0.9}O/ZnO$ are depicted in Fig. 9.19a.

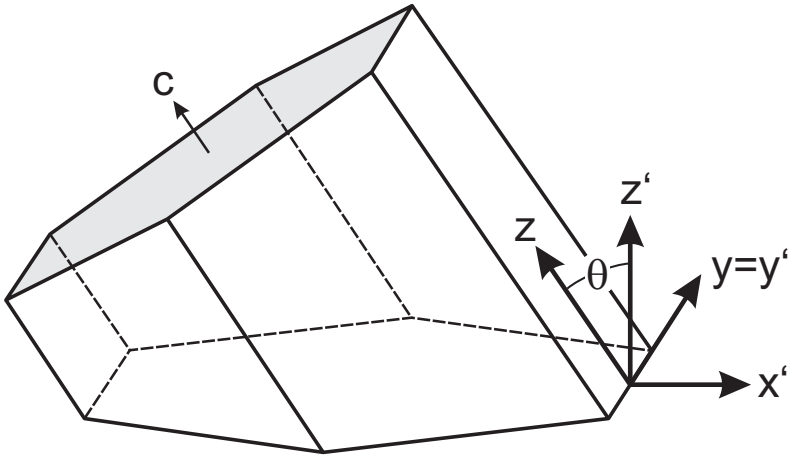

Figure 9.17: Geometry of wurtzite lattice rotated by the polar angle θ around the y-axis.

The in-plane strains are compressive (note that since $\epsilon'_{yy} = \epsilon_{yy}$ by construction, these two curves are superimposed), while the out-of-plane strain is tensile. All strains in the sample system (primed quantities, dashed lines in Fig. 9.19a are fairly similar for all angles. The shear strain ϵ'_{xz} is rather small and exhibits three zeros between 0 and 180°. The components with respect to the crystal system exhibit large changes and all change sign (except ϵ_{yy}). This is best followed for ϵ_{zz} which is tensile for $\theta = 0$ and compressive for $\theta = 90°$ since now the c-direction is an in-plane direction. These results are qualitatively similar to the strain in $In_xGa_{1-x}N/GaN$ and $Al_xGa_{1-x}N/GaN$ heterostructures.

The strain components for $Mg_{0.1}Zn_{0.9}O/ZnO$ are depicted in Fig. 9.19b. A very different situation arises since the signs of ϵ_a and ϵ_c are opposite. Already from eq. (**??**) it can be seen that these opposite signs can lead to small values of the out-of-plane strain ϵ'_{zz} at $\theta = 90°$: it depends on the material parameters how close its value gets to zero. ϵ'_{xx} changes sign from 0 to 90° as expected from (**??**) since it runs from ϵ_a (negative) for $\theta = 0°$ to ϵ_c (positive) for $\theta = 90°$.

Comparing the two materials systems (Mg,Zn)O and (Cd,Zn)O from a purely device-point of view, it turns out that whenever large polarization differences between materials are required, e.g. high electron mobility transistors, the (Zn,Cd)O/ZnO system is optimum, whereas (Mg,Zn)O/ZnO is preferred for devices where no or less internal electric field are beneficial, e.g. light emitting diodes for which the quantum confined Stark effect reduces their overall efficiency.

More generally, the larger lattice mismatch between the end components in the (Cd,Zn)O/ZnO system, combined with the particularity of the (Mg,Zn)O/ZnO system (i.e. $\mathrm{sgn}(\epsilon_a\,\epsilon_c) = -1$) render (Mg,Zn)/ZnO more attractive for the fabrication of heterostructures, given that strain, strain energy and stresses are systematically smaller (eventually zero). This should lead to larger critical thicknesses and, therefore, less constraints in terms of defect generation such as misfit dislocations.

More details can be found in [3].

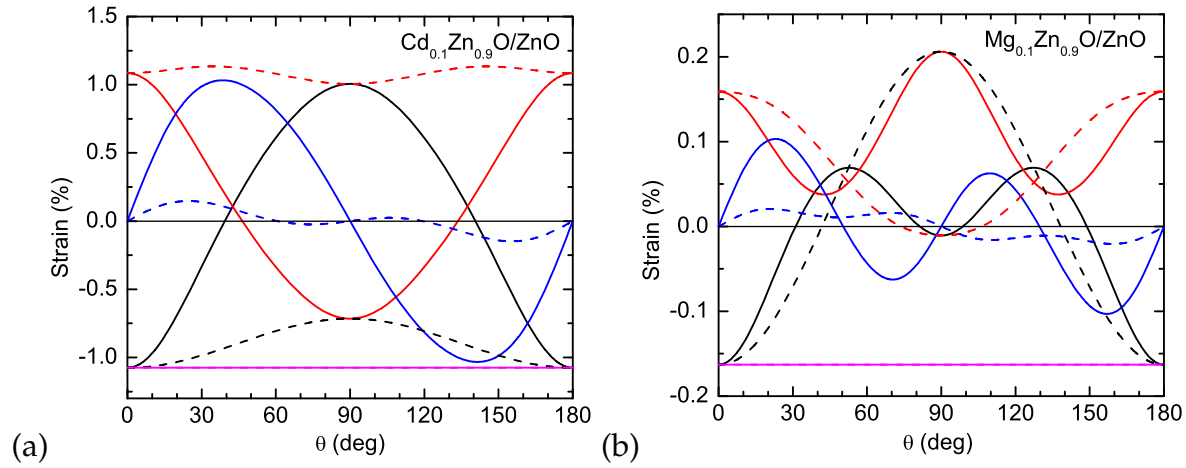

Figure 9.18: (a) Strain components for a pseudomorphic $Cd_{0.1}Zn_{0.9}O$/ZnO heterostructure as a function of the polar angle θ. The strain components ϵ_{ij} are depicted with *solid lines*, the components ϵ'_{ij} with *dashed lines* (*xx*: *black*, *yy*: *purple*, *zz*: *red*, *xz*: *blue*)

Figure 9.19: (b) Strain components for a pseudomorphic $Mg_{0.1}Zn_{0.9}O$/ZnO heterostructure as a function of the polar angle θ.

[1] H. von Wenckstern, R. Schmidt-Grund, C. Bundesmann, A. Müller, C.P. Dietrich, M. Stölzel, M. Lange, M. Grundmann, *The (Mg,Zn)O Alloy*, Handbook of Zinc Oxide and Related Materials, Vol. 1 Materials, p. 257-320 (2012), Z.C. Feng, ed. (Taylor and Francis/CRC Press, Florida, USA, 2012), ISBN 978-1439855706 doi:10.1201/b13072-14

[2] D.M. Detert, S.H.N. Lim, K. Tom, A.V. Luce, A. Anders, O.D. Dubon, K.M. Yu, W. Walukiewicz, *Crystal structure and properties of $Cd_xZn_{1-x}O$ alloys across the full composition range*, Appl. Phys. Lett. **102**, 232103 (2013)

[3] Marius Grundmann, Jesús Zúñiga-Pérez, *Pseudomorphic ZnO-based heterostructures: from polar through all semipolar to nonpolar orientations*, phys. stat. sol. (b) **253**, 351–360 (2016)

9.12 Local zincblende coordination in heteroepitaxial $Zn_{1-x}Mg_xO$:Mn thin films with $0.01 \leq x \leq 0.04$ identified by electron paramagnetic resonance

M. Lorenz, A. Pöppl*, R. Böttcher*, D. Spemann†, M. Grundmann

*Magnetic Resonance of Complex Quantum Solids group
†Nuclear Solid State Physics group

Oxide semiconductors such as $Zn_{1-x}Mg_xO$ are versatile functional materials. The atomic arrangement in the bulk and at the interfaces determines important properties of the oxides such as polarity of surfaces, and charge transfer processes to avoid polar discontinuities which are decisive for their device relevant electronic and optical performance. For the design of thin film heterostructures with advanced functionality such as

quantum emitters, and two-dimensional electron gases detailed knowledge about the crystallographic match of the materials at the interfaces is required [1] [2].

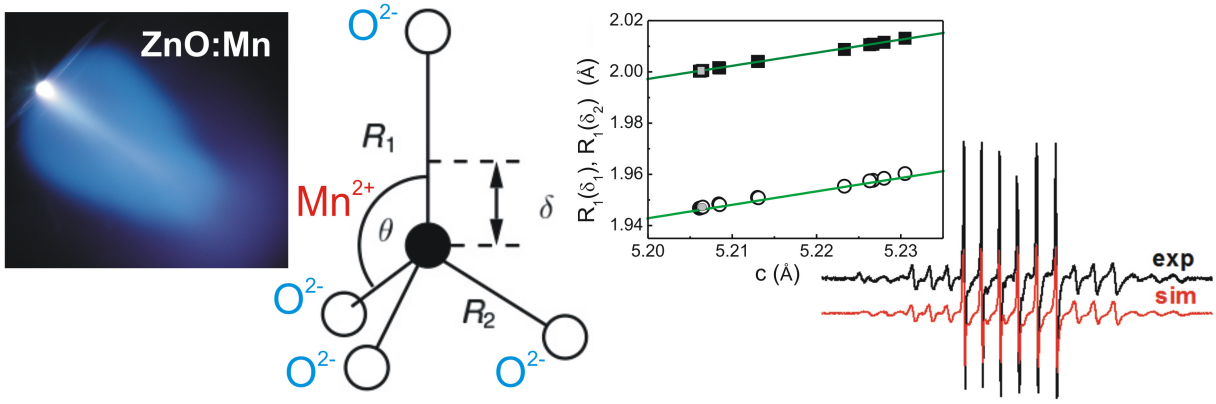

Figure 9.20: (a) Electron paramagnetic resonance of oxygen deficient ZnO:Mn thin films grown by pulsed laser deposition provides linear correlation of zero field splitting and displacement of Mn^{2+} in the MnO_4 tetrahedrons, and corresponding bond lengths. Images adopted from [1].

Recently, we explored the effect of oxygen vacancies on the local atomic structure of heteroepitaxial ZnO:Mn thin films and found the zero field splitting parameter D correlating linearly with displacement of Mn^{2+} ions along the c-axis in the MnO_4 tetrahedra and the corresponding bond lengths between the Mn^{2+} ions and the axial oxygen ion [1], see Figure 1. Now, the same methodology is applied to detect minor local structural phases in $Zn_{1-x}Mg_xO$:Mn with up to 4% Mg [2].

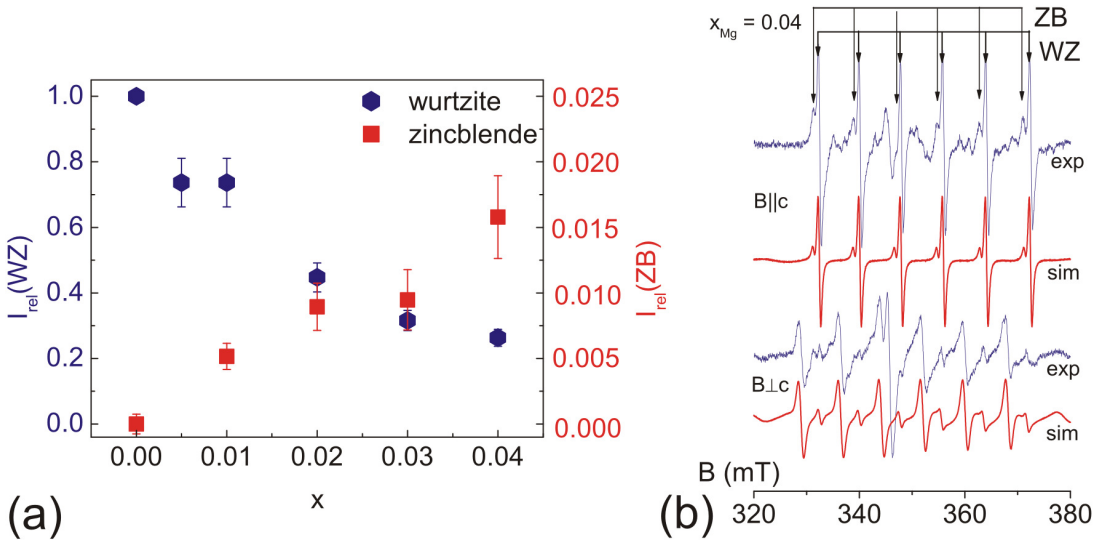

Figure 9.21: (a) Relative intensities I_{rel} of the EPR spectra of Mn^{2+} species wurtzite (WZ, blue hexagons) and zincblende (ZB, red squares) in $Zn_{1-x}Mg_xO$:Mn ($p(O_2)$ = 0.016 mbar, c_{MnO} = 0.05 %) thin film samples. (b) Experimental and simulated Mn^{2+} EPR spectra at 297 K of $Zn_{0.96}Mg_{0.04}O$:Mn thin film sample G5183 for different B-field orientations. Arrows indicate the ^{55}Mn HF lines of the central FS transition of Mn^{2+} species WZ and ZB, respectively. Images adopted from [2].

Besides the two stable crystalline phases wurtzite and rocksalt of ZnO, another

metastable cubic phase, namely zincblende, can be stabilized in ZnO by growth on cubic (001) oriented substrates, such as GaAs, Si, MgO and β-SiC. Actually, the correct term for the zincblende phase is sphalerite, since zincblende originates from ZnS. Both wurtzite and zincblende structures exhibit tetrahedral coordination of zinc and oxygen atoms. However, the lattice is cubic face centered (fcc) for zincblende, and hexagonal primitive for wurtzite. When considering the polytypes along (111) or (001), the zincblende fcc structure has a (bi)layer stacking sequence of ...ABC ABC..., while wurtzite shows ...AB AB AB..., analogous to a cubic or hexagonal closed packed atomic arrangement, respectively [2].

Because of the higher symmetry and lower ionicity in the zincblende structure possibly zincblende II-VI materials have advantages for applications such as lower carrier scattering, higher doping efficiency, and easier integration into 3C-SiC technology. Furthermore, zincblende ZnO shows a higher calculated dielectric constant of 6.0 in comparison to 4.7 for wurtzite ZnO, and a corresponding larger refractive index of 2.49 in relation to 2.0 for wurtzite [2].

We have shown that beginning with a chemical Mg content of already x = 0.01 in heteroepitaxial $Zn_{1-x}Mg_xO$:Mn thin films, a local cubic zincblende coordination of the Mn ion can be identified using electron paramagnetic resonance of Mn^{2+} ions, see Figure 2. The appearance of a cubic Mn^{2+} spectrum in the wurtzite (Zn,Mg)O films is attributed to an enhanced formation of stacking faults providing zincblende structure locally. The Mn^{2+} ions are incorporated at zinc lattice sites into the $Zn_{1-x}Mg_xO$ films and their zero field spitting allows to monitor even small structural changes in the MnO_4 tetrahedrons. Alloying with the smaller Mn^{2+} ions leads to a shrinking of the Mn-O bond length in dependence on the axial distortion of the parent ZnO_4. Our findings generally show that Mn^{2+} ions in low concentration represent a highly sensitive paramagnetic probe in group II-VI thin films [2].

We acknowledge financial support of the Deutsche Forschungsgemeinschaft (DFG) within the collaborative research center SFB 762 "Functionality of Oxide Interfaces".

[1] M. Lorenz, R. Böttcher, A. Pöppl et al., J. Mater. Chem. C **2**, 4947 (2014) doi:10.1039/C4TC00407H
[2] R. Böttcher, M. Lorenz, A. Pöppl et al., J. Mater. Chem. C **3**, 11918 (2015) doi:10.1039/C5TC02720A

9.13 Metal-insulator transition in (111)-oriented $LaNiO_3$/$LaAlO_3$ superlattices

H. M. Wei, M. Lorenz, M. Grundmann

$LaNiO_3$ (LNO)/$LaAlO_3$ (LAO) superlattices (SLs) have attracted significant attention as they may exhibit novel properties at interfaces that are not present in either of the bulk phases of the materials that make up the SLs. Our previous investigations demonstrated clear quantum confinement effect on the electronic properties of (100)-oriented [LNO/LAO] SLs [1]. Here we focus on the deposition and characterization of (111)-oriented [LNO/LAO] SLs which is a potential candidate for two-dimensional topological insulators [2].

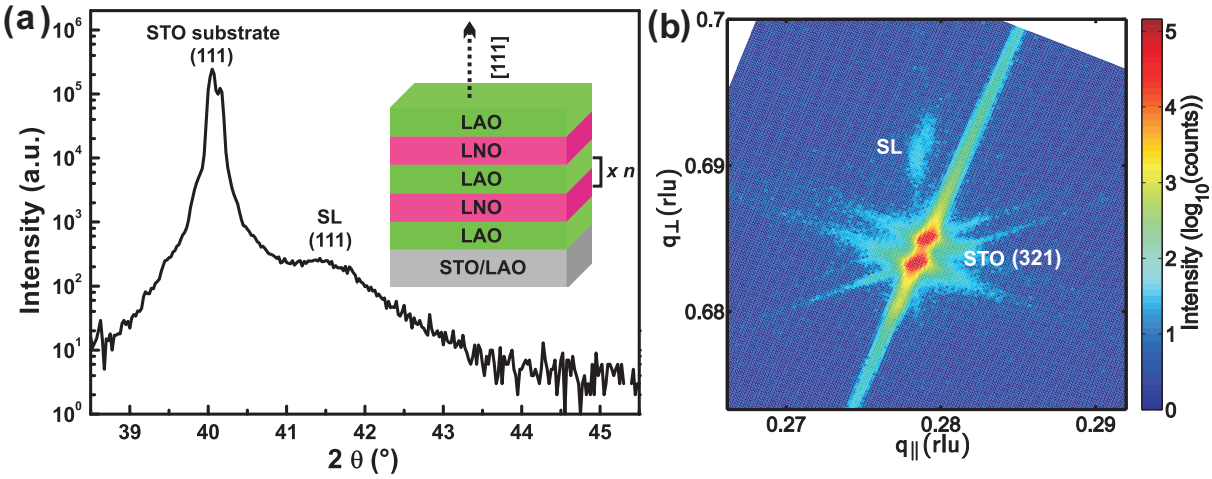

Figure 9.22: (a) XRD $2\theta - \omega$ scan of a $[9/7]_{10}$ SL on STO (111) substrate. The inset shows a structure scheme of the SL. (b) RSM of $[9/7]_{10}$ SL around the asymmetric STO (321) peak.

The $[LNO_l/LAO_m]_n$ SLs (l and m are the number of unit cells, respectively, therafter referred to as $[l/m]_n$) were deposited using pulsed laser deposition. The structure of SLs is schematically illustrated in the inset of Fig. 9.22 (a). The SL Bragg peak was observed near STO (111) substrate peak from X-ray diffraction (XRD) as indicated in Fig. 9.22 (a). The average distance between (111) layers of the SL was calculated as around 0.21 nm from the position of (111) peak. Fig. 9.22 (b) shows a representative XRD reciprocal space map (RSM) around (321) reflection of STO(111) substrate. The in-plane lattice match of $[9/7]_{10}$ SL and STO(111) substrate, that is, the strained, pseudomorphic growth mode is visually confirmed by the perfect vertical alignment of the (321) substrate and SL peak at indentical $q_{||}$ values. The epitaxial relation for out-of-plane direction is SL [111] || STO [111] and for in-plane SL [110] || STO [110] .

The scanning transmission electron microscopy (STEM), and energy dispersive X-Ray (EDX) mapping results of the $[94/96]_{10}$ SL are depicted in Fig. 9.23 (a). The STEM cross section and the corresponding EDX map of Ni confirm the presence of 10 double layers LNO/LAO with reasonably smooth interfaces. X-ray reflectivity (XRR), shown in Fig. 9.23 (b), was used to determine the SL thickness, and interfacial roughness. For all SLs, the strong Bragg reflections, arising from the difference in densities of LNO and LAO, are obtained indicating abrupt interfaces. Take $[9/7]_{10}$ SL for example, by fitting the XRR curve, the average thickness of each LNO and LAO single layer is 1.91 ± 0.01 nm and 1.51 ± 0.01 nm, respectively, that is in agreement with our design of 9 LNO unit cells and 7 LAO unit cells. The interfacial roughness is in between 0.56 and 0.58 nm.

In our SLs, we observe a clear dependence of the sheet resistance on the number of LNO unit cells in SLs. As shown in Fig. 9.24 (a), the thickness of each insulating layers is formed by 7 LAO unit cells. The thick insulating layers ensure that the electronic transport near the Fermi energy is effectively confined to the LNO layers. The SLs were deposited on STO and LAO substrates which induce tensile (1.74 %) and compressive (1.27 %) strain, respectively. The $[18/7]_{10}$ SLs show metallic behavior with positive resistivity temperature coefficient. With decreasing number of LNO unit cells in the SLs, insulating behavior appears. The $[7/6]_{10}$ SL on STO and $[7/4]_{10}$ SLs on both substrates are highly insulating hinting for a possible Mott behavior.

For the $[2/3]_{10}$ SL with thinner LNO layers, the transport can't be described by

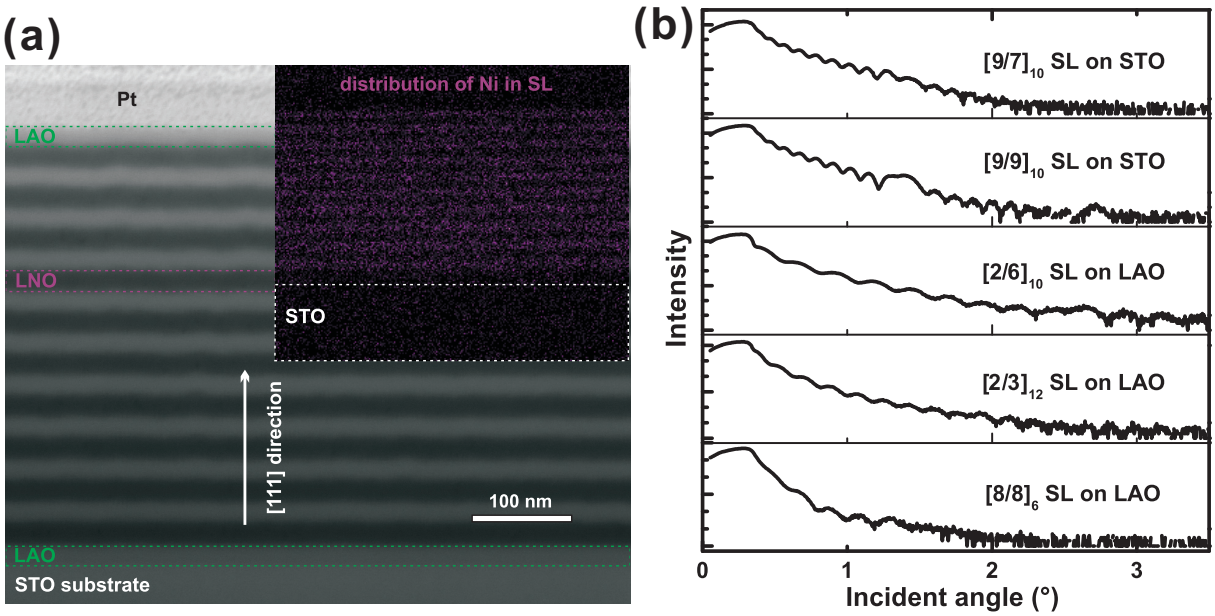

Figure 9.23: (a) STEM dark-filed image of $[94/96]_{10}$ SL grown on STO(111) substrate. The EDX map shows the distribution of Ni in the SL. (b) X-ray reflectivity of [LNO/LAO] SLs. The notation above the Bragg reflections refers to the structure of SLs on the indicated substrate materials.

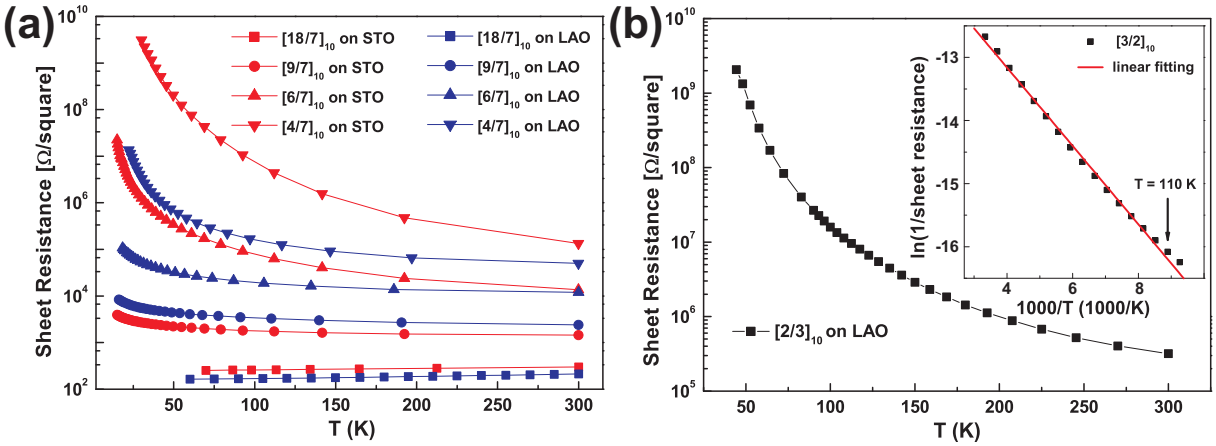

Figure 9.24: (a) Temperature-dependent sheet resistivity of SLs deposited on STO (red) and LAO (blue) substrate. (b) Sheet conductance as a function of 1000/T for the $[2/3]_{10}$ SL shows single exponentially activated gap behavior above 110 K. The red solid line is a linear fitting of data between 300 and 110 K.

Mott variable rang hopping (VRH) model because the calculated hopping distance is smaller than localization length. Instead, single activated gap model has been used to analyse the electronic transport in this kind of SLs [3]. The LAO layers with 3 unit cells isolates the Ni ions to a two-dimensional bilayer system. The buckled honeycomb lattice formed by the Ni ions of the (111) LNO bilayer. Allowing full lattice relaxation breaks "inversion" symmetry Z_2 and results in two inequivalent Ni sites which destroys the Dirac point by opening a gap at K and K' [4]. Fitting of the data from 300 to 110 K using the single activated gap model yields a gap energy of 106 ± 1 meV as shown in Fig. 9.24 (b), which is in good agreement with the published experimental value of 95 meV [3].

In summary, we have demonstrated epitaxial and lattice matched growth of (111)-oriented LNO/LAO SLs. The clear and smooth interfaces are demonstrated by STEM, EDX and XRR. The electric transport was studied using temperature-dependent resistivity measurement. A band gap of 106 meV was extracted for the $[2/3]_{10}$ SL which is, in theory, a potential candidate for two-dimensional topological insulators. More measurements will be done for the in-depth investigation of band structure by electron paramagnetic resonance and angle resolved photoemission spectroscopy.

We thank the Collaborative Research Center SFB 762 "Functionality of Oxide Interfaces" for financial support. We thank Jörg Lenzner for the STEM images and Gabriele Ramm for PLD target preparation.

[1] H. M. Wei et al.: Appl. Phys. Lett. **106**, 042103 (2015), doi:10.1063/1.4907011
[2] D. Xiao et al.: Nat. Commun. **2**, 596 (2011), doi:10.1038/ncomms1602
[3] S. Middey et al: Appl. Phys. Lett. **101**, 261602 (2012), doi:10.1063/1.4773375
[4] D. Doennig et al: Phys. Rev. B **89**, 121110(R) (2012), doi:10.1103/PhysRevB.89.121110

9.14 Oxygen vacancy superstructure in multiferroic $BaTiO_3$ - $BiFeO_3$ composite thin films with high magnetoelectric coupling

M. Lorenz, V. Lazenka*, G. Wagner†, O. Oeckler† M. Grundmann

*Instituut voor Kern- en Stralingsfysica, KU Leuven, B-3001 Leuven, Belgium
†Institut für Mineralogie, Kristallographie und Materialwissenschaft, Universität Leipzig

Multiferroic composites consisting of two different chemical compounds offer unique flexibility in geometrical and structural design. Correlations at the interfaces are essential to achieve high magnetoelectric (ME) coupling, for the state of the art and references see [2]. For our chemically-homogeneous $BaTiO_3$-$BiFeO_3$ composite thin films, we have chosen the source target composition for film growth by pulsed laser deposition (PLD) to be 67 wt % $BaTiO_3$ and 33 wt % $BiFeO_3$ [1]. The oxygen partial pressure during PLD was varied between 0.01 mbar and 0.5 mbar. We tried to compensate for the changing growth rate by using different total numbers of laser pulses for the growth, resulting in reduced thickness variation from 208 to 388 nm only. The substrate material of the films intended for X-ray diffraction (XRD) and ferroelectric and magnetoelectric measurements was $SrTiO_3$:Nb(001). For the STEM and SAED investigations only, films grown simultaneously on MgO(001) were used, see Figures 1 and 2 [2].

$BaTiO_3$-$BiFeO_3$ composite thin films show a clear dependence of magnetoelectric voltage coefficient α_{ME} on oxygen partial pressure during growth. Three composite films grown at 0.25 mbar show the highest α_{ME} values of 36 to 43 V/(cm*Oe) at 300 K [2]. α_{ME} decreases for both lower and higher growth pressure, due to increasing oxygen deficiency and increasing crystallite size, respectively. The composite films exhibit increasing out-of-plane strain with decreasing PLD growth pressure in the range from 0.5 mbar down to 0.01 mbar [2].

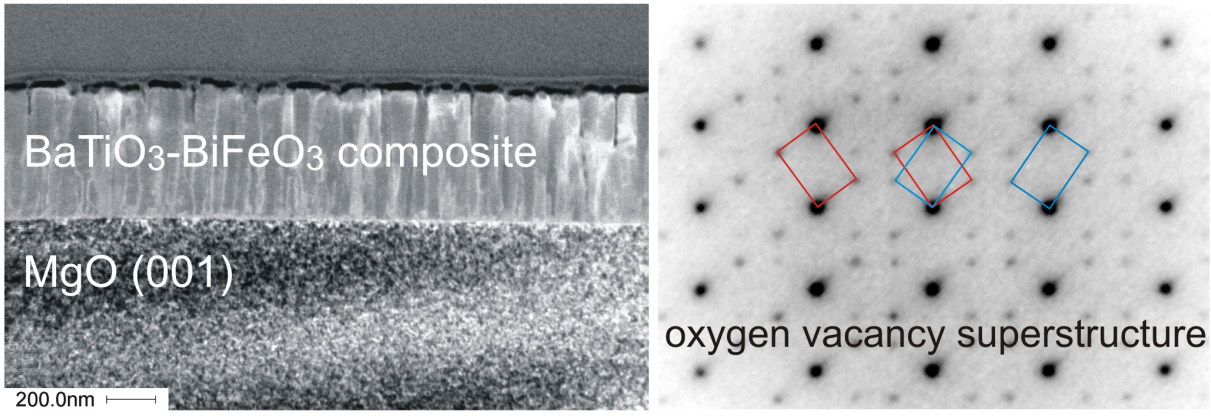

Figure 9.25: *left* Scanning TEM (STEM) dark-field image of the $BaTiO_3$-$BiFeO_3$ composite film grown at 0.25 mbar on MgO(001) taken from the (110) cross-section. *right* The selected area electron diffraction (SAED) pattern has been taken from the interface region of the composite. The main spots confirm the $BaTiO_3$-type structure of the composite film. The additional weak spots in the composite indicate superstructure reflections that are most probably due to oxygen vacancy ordering. The *red* and *blue* tilted rectangles demonstrate the two possible orientations of oxygen vacancy ordering. Images adopted from [2].

STEM micrographs and SAED patterns taken from different regions of cross-sections of the composite films indicate an oxygen vacancy superstructure, which arises from vacancy ordering on the {111} planes of the pseudocubic $BaTiO_3$-type structure of the composite films. The intensity of the additional superstructure reflections seems to correlate to the oxygen growth pressure of the two investigated samples. This means that the sample grown at lower (0.01 mbar) pressure seems to show a more pronounced oxygen vacancy superstructure in comparison to the sample grown at higher (0.25 mbar) oxygen pressure [2].

Contrary to our recently investigated ($BaTiO_3$-$BiFeO_3$) $\times$ 15 superlattices, α_{ME} shows an increasing behavior with decreasing temperature, which cannot be explained by strain-mediated ME coupling of piezoelectric and magnetostrictive phases in the composite films alone. Rather, charge-mediated ME coupling may play a role here. This work contributes to the understanding of magnetoelectric coupling as a complex and sensitive interplay of chemical, structural and geometrical issues of the $BaTiO_3$-$BiFeO_3$ composite system and, thus, paves the way to practical exploitation of magnetoelectric composites [2].

We acknowledge financial support of the Deutsche Forschungsgemeinschaft (DFG) within the collaborative research center SFB 762 "Functionality of Oxide Interfaces", and of the Fund for Scientific Research - Flandern (FWO) and the KU Leuven Concerted Action (GOA 14/007).

[1] M. Lorenz, V. Lazenka, P. Schwinkendorf et al., J. Phys. D: Appl. Phys. **47**, 135303 (2014) doi:10.1088/0022-3727/47/13/135303
[2] M. Lorenz, G. Wagner, V. Lazenka et al., Materials **9**, 44 (2016) doi:10.3390/ma9010044

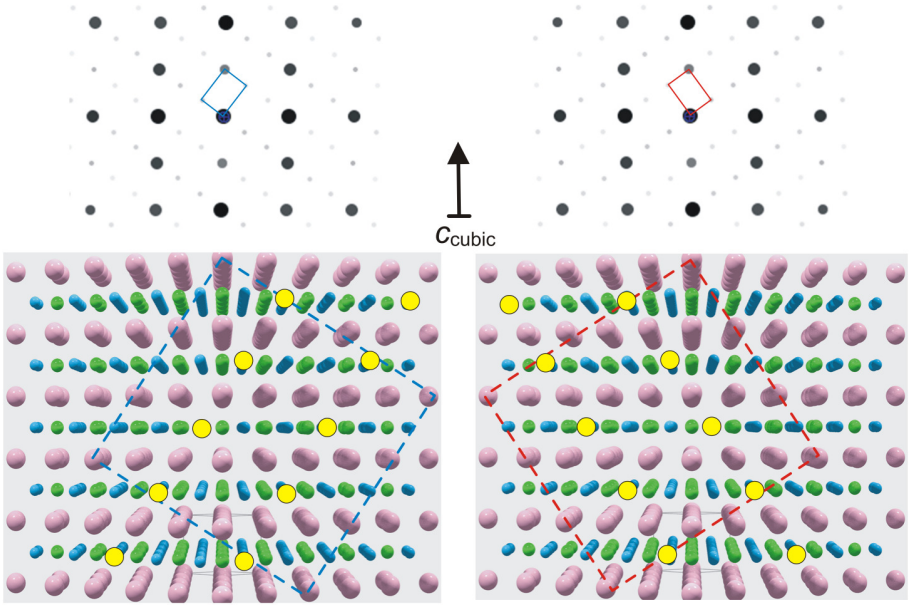

Figure 9.26: Structure model of oxygen vacancy ordering (*yellow*) in $BaTiO_3$-type composite film structures, in planes parallel (-111) (*left*) and (1-11) (*right*), respectively; projection along [110] (all directions according to cubic setting). The indication of atoms is as follows: *blue*, oxygen; *pink*, barium; *green*, titanium. Images adopted from [2].

9.15 Multiferroic $BaTiO_3$ - $BiFeO_3$ superlattices with epitaxial coherence at interfaces and high magnetoelectric coupling

M. Lorenz, V. Lazenka*, T. Höche†

*Instituut voor Kern- en Stralingsfysica, KU Leuven, B-3001 Leuven, Belgium
†Fraunhofer-Institut für Mikrostruktur von Werkstoffen und Systemen, D-06120 Halle

Magnetoelectric (ME) multiferroic composites are advantageous compared to single-phase magnetoelectrics in terms of value of magnetoelectric voltage coefficient α_{ME}, control of its temperature dependence, and design of tailored materials for applications for example in novel data storage devices. Elastic strain, charge, and exchange bias interactions all contribute to the ME coupling in an up to now not completely understood extend. In a fruitful colaboration with KU Leuven and the FhG IMWS in Halle we have investigated promising magnetoelectric composites with special emphasis on $BaTiO_3$-$BiFeO_3$ superlattices and the correlation of α_{ME} with microstructural features and the magnetic spin structure.

Pulsed laser deposition (PLD) [1] is used to grow $BaTiO_3$-$BiFeO_3$ superlattices with high flexibility and structural quality, as shown in Refs. [2–4]. Epitaxy and coherent interfaces are confirmed by X-ray diffraction scans, reciprocal space maps, and HR-TEM images, respectively, see Figures 1 and 2. The superlattices built from 15 double-layers $BaTiO_3$-$BiFeO_3$ show state-of-the-art magnetoelectric voltage coefficients α_{ME} up to about 50 $Vcm^{-1}Oe^{-1}$ at 300 K and zero DC-bias field, while single-phase $BiFeO_3$ films with similar thickness show a factor of 10 lower α_{ME} values.

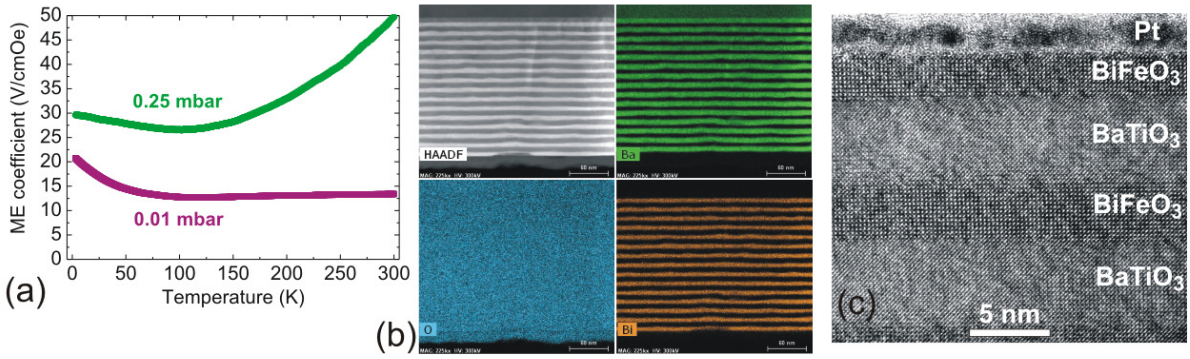

Figure 9.27: (a) Temperature dependent ME voltage coefficient α_{ME} of two ($BaTiO_3$-$BiFeO_3$)×15 superlattices grown at the indicated oxygen partial pressures with PLD on $SrTiO_3$(001). (b) HAADF and EDXS maps of Ba, O and Bi of a typical ($BaTiO_3$-$BiFeO_3$)×15 superlattice grown at 0.25 mbar with state-of-the-art ME coefficient. Note that the $SrTiO_3$ substrate is on top in the images in (b). The Ti and Fe maps (not shown) are similar to that of Ba and Bi, respectively. The scale bar is 60 nm. (c) HR-TEM image of the supperlattice from (b), demonstrating the coherent and strain-free growth of the layers near the surface of superlattice. Images adopted from [4].

We found clear correlation of ME coefficients with increasing oxygen partial pressure during growth, see Figure 1 (a). ME coupling is highest for lower density of oxygen vacancy-related defects (Figure 2). Detailed STEM and SAED microstructural investigations at 300 K revealed antiphase rotations of the oxygen octahedra in the BaTiO3 single layers of the superlattices, which are an additional correlated defect structure of the multilayers [3]. In conclusion, multiferroic superlattice composites can be fabricated with unique flexibility concerning dimensionality, phase coherence and separation of the included crystalline phases, to meet particular future application requirements.

We acknowledge financial support of the Deutsche Forschungsgemeinschaft (DFG) within the collaborative research center SFB 762 "Functionality of Oxide Interfaces", and of the Fund for Scientific Research - Flandern (FWO) and the KU Leuven Concerted Action (GOA 14/007).

[1] M. Lorenz and M. S. Ramachandra Rao, J. Phys. D: Appl. Phys. **47**, 030301 (2014) doi:10.1088/0022-3727/47/3/030301
[2] M. Lorenz, V. Lazenka, P. Schwinkendorf et al., J. Phys. D: Appl. Phys. **47**, 135303 (2014) doi:10.1088/0022-3727/47/13/135303
[3] M. Lorenz, G. Wagner, V. Lazenka et al., Appl. Phys. Lett. **106**, 012905 (2015) doi:10.1063/1.4905343
[4] M. Lorenz, V. Lazenka, T. Höche et al., Advanced Materials Interfaces (2016) accepted doi:10.1002/admi.201500822

9.16 Heteroepitaxial $YBiO_3$ thin films on $SrTiO_3$(100) prepared by pulsed laser deposition

M. Jenderka, J. Barzola-Quiquia, S. Richter, M. Grundmann, M. Lorenz

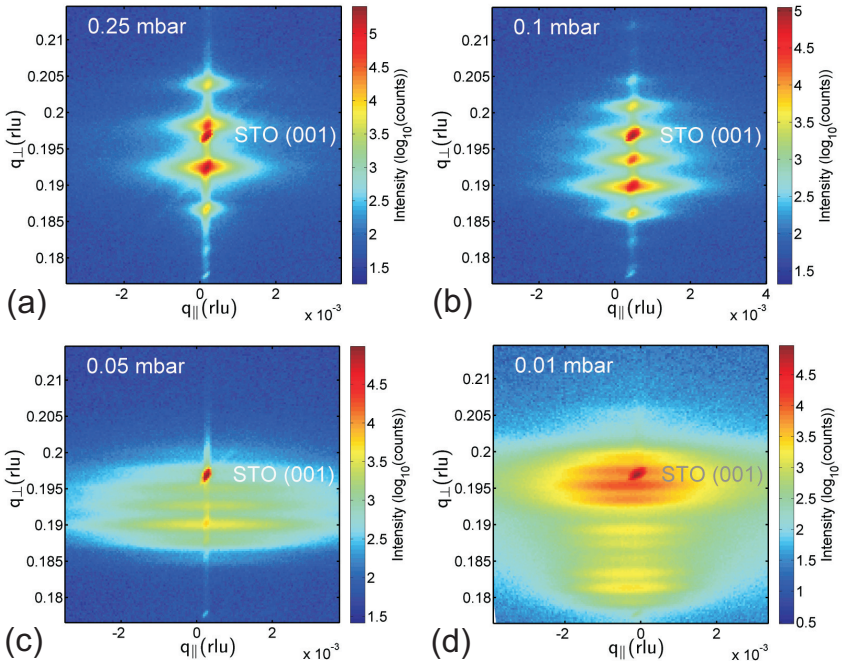

Figure 9.28: XRD reciprocal space maps around the symmetric $SrTiO_3$(001) peaks (i.e. K$\alpha_{1,2}$ splitted points with highest intensity in each RSM of ($BaTiO_3$-$BiFeO_3$)×15 multilayers grown at (a) 0.25, (b) 0.1, (c) 0.05, and (d) 0.01 mbar oxygen partial pressure. The increasing horizontal layer peak broadening indicates increasing multilayer mosaicity with decreasing growth pressure. This correlates clearly with increasing ME coefficient, see Fig. 1 (a). For more details see [3].

Cubic $YBiO_3$ was recently proposed to be a novel oxide topological insulator (TI) by first-principles band structure calculations of Jin et al. [1]. They argued that $YBiO_3$ with its high bulk resistivity (~ MΩm [2]) and large direct band gap of supposedly 300 meV promises the realization of truly surface-dominated transport and its direct measurement even at room-temperature. TIs are a rather newly discovered state of matter with potential relevance in spintronics, thermoelectricity and quantum computation [3, 4].

$YBiO_3$ has a cubic fluorite-type crystal structure with random distribution of Y^{3+} and Bi^{3+} at the 4a sites and lattice parameter a = 5.42 Å; its primitive cell is a pseudocubic perovskite with a_{per} = 3.83 Å [5]. Originally, $YBiO_3$ was deposited on $LaAlO_3$ (LAO) as a buffer layer for the high-temperature superconductor $YBa_2Cu_3O_{7-\delta}$ by aqueous chemical solution deposition [6]. After successful preparation of heteroepitaxial $YBiO_3$ films on top of LAO substrates employing pulsed laser deposition (PLD), we now report on heteroepitaxy of $YBiO_3$ on $SrTiO_3$ (STO) and $SrTiO_3$:Nb substrates. In contrast to LAO, STO substrates do not develop a micro-twin structure as introduced in LAO during PLD due to a structural phase transition around 540°C. In addition, conducting STO:Nb substrates are useful for future photoemission spectroscopy measurements, which allow direct investigation of possible topological surface states.

Using a polycrystalline $YBiO_3$ target, solid-state synthesized by sintering Y_2O_3 and Bi_2O_3 powders in a molar ratio of 1:1, single crystalline $YBiO_3$ films were prepared on STO(100) at an oxygen partial pressure of 0.05 mbar and a growth temperature of 650 °C. These growth parameters represent the optimum in the parameter range from

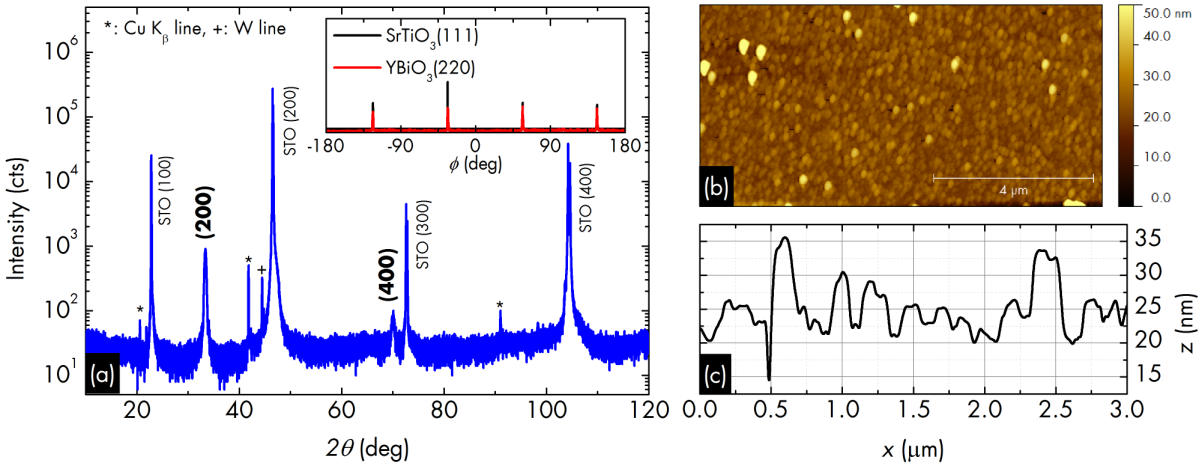

Figure 9.29: (a) XRD 2Θ-ω-scan confirming (100) preferential out-of-plane orientation of $YBiO_3$ on STO(100). Inset: The XRD ϕ-scans illustrate the in-plane epitaxial relationship, i.e., $YBiO_3$[110]||STO[111]. (b) Atomic force microscopy topographic image of a typical $YBiO_3$ film on STO(100). Root-mean-square surface roughness is about 3.5 nm. (c) Line profile taken from the topographic image in (b) suggests crystallite sizes from 50 to 150 nm.

3×10^{-4} to 0.2 mbar, and from 550 to 650 °C, respectively. X-ray diffraction 2Θ-ω measurements shown in Fig. 9.29(a) confirm a structural quality comparable with $YBiO_3$ films on LAO(001). Similarly, the epitaxial relationship is $YBiO_3$[100]||STO[100] and $YBiO_3$[110]||STO[111]. From atomic force microscopy, Frank-van der Merwe (layer-by-layer) growth can be excluded in our samples and the surface roughness is accordingly large with a root-mean-square (rms) value of about 3 nm, see Fig. 9.29(b,c). Sample annealing in a 700 mbar oxygen atmosphere and at temperatures from 850 to 905 °C could in average reduce the rms surface roughness by 22 %. However, energy-dispersive X-ray spectroscopy measurements showed a loss of Bi at these temperatures and a Y:Bi ratio of about 2.5. Hence, efforts are being made to achieve layer-by-layer growth via interval PLD. Layer-by-layer growth is expected to provide a considerably smoother film surface that is for example required for proper photoemission spectroscopy measurements.

A SQUID experiment measuring $M(H)$ and $M(T)$ confirmed that $YBiO_3$ is paramagnetic between 5 and 300 K. Paramagnetism is expected since both Y^{3+} and Bi^{3+} are non-magnetic ions, but also proves that samples are free of ferromagnetic impurities. Furthermore, thickness dependent (magneto-)resistance measurements are underway but are challenging due to the samples' high bulk resistivity. Observation of thickness-independent transport properties would be a strong indicator for topological surface states in $YBiO_3$. Preliminary results obtained from infrared spectroscopic ellipsometry performed at room-temperature found no evidence of either the indirect band gap at 0.183 eV or the non-trivial gap at 0.33 eV that were proposed in Ref. [1]. Hence, following experiments will instead focus on the energy range around 1 eV where a trivial band gap is expected according to [7].

As a matter of fact, results from infrared spectroscopic ellipsometry in particular could help to clear up the ongoing theoretical debate on the existence of topological surface states. Jin et al. [1] incorrectly performed band structure calculations using the perovskite primitive cell with the larger a = 5.42 Å. It was subsequently shown by

G. Trimarchi et al [7] that this structure is unstable. For the experimentally observed random fluorite-type structure their calculations instead favor a topologically trivial state. Consequently, observation of electronic excitations in infrared spectroscopic ellipsometry, as well as transport measurements will help to shed some light onto the band structure of $YBiO_3$ and its topology.

Financial support from the Deutsche Forschungsgemeinschaft (DFG) within the projects SFB 762 and DFG LO790 5-1 is gratefully acknowledged.

[1] H. Jin et al.: Scientific Reports **3**, 1651 (2013), doi:10.1038/srep01651
[2] Y. Zhao et al.: Physica C **463-465**, 574-579 (2007), doi:10.1016/j.physc.2007.05.022
[3] J.-H. Song et al.: Phys. Rev. Lett. **105**, 096493 (2010), doi:10.1103/PhysRevLett.105.096403
[4] C. Nayak et al.: Rev. Mod. Phys. **80**(3), 1083 (2008), doi:10.1103/RevModPhys.80.1083
[5] X.J. Zhang et al.: J. Supercond. Nov. Magn. **23**, 1011 (2010), doi:10.1007/s10948-009-0615-1
[6] G. Li et al.: J. Mater. Res. **22**, 2398 (2007), doi:10.1557/jmr.2007.0320
[7] G. Trimarchi et al.: Phys. Rev. B **90**, 161111(R) (2014), doi:10.1103/PhysRevB.90.161111

9.17 Growth of ultrathin ZnO nanowires at CMOS compatible temperature by pulsed laser deposition

A. Shkurmanov*, C. Sturm*, H. Hochmuth*, M. Grundmann*, G. Feuillet†, F. Tendille‡, P. DeMierry‡

*Institute for Experimental. Phys. II, Universität Leipzig, Linnéstrasse. 5, 04103 Leipzig, Germany
†CEA/LETI 17, rue des Martyrs, 38054 Grenoble Cedex 9, France
‡CNRS-CRHEA, rue Bernard Grégory, 06560 Valbonne, France

Nanowires (NWs) are promising to be used as building blocks for a wide variety of applications e.g. light emitters, sensors and resonators. For the integration of these NWs into devices, the growth process should be compatible with CMOS technology which requires process temperatures typically lower than than 500 ℃ [1] and therefore limits the possible growth techniques. Beside the application point of view, quantum confinement effects appear in NWs with diameter less than 10 nm which makes them interesting for quantum effects researches such as topological qubits [2]. However, the fabrication of such thin NWs is quite challenging and there are only few reports given in the literature.

By using Al and Ga doped ZnO seed layers we are able to control diameter, density and growth temperatures of the NWs. In the case of using pure ZnO seed layers,we obtain a low density growth of ZnO NWs (Fig. 9.30) with diameters typically in the range 200 – 600 nm at relatively high deposition temperatures ($T \approx 950$ ℃). In contrast to that by using $(Al, Ga)_xZn_{1-x}O$ seed layers ($x < 1\%$) we were able to reduce the deposition temperature and the diameter of the NWs down to 400 ℃ and to 7 nm, respectively. As can be seen the deposited NWs exhibit a well orientation perpendicular to the surface.

In order to change the orientation of the NWs in well defined way, as it is interesting for the fabrication of asymmetric hyperbolic media [4], we used pre-structured sapphire. For doing so, the r-plane sapphire wafer was etched by wet-chemical etching and presence of c-facet stays possible. Further ZnO deposition allows to grow NWs tilted to the surface normal with angle of 57° (Fig. 9.30c).

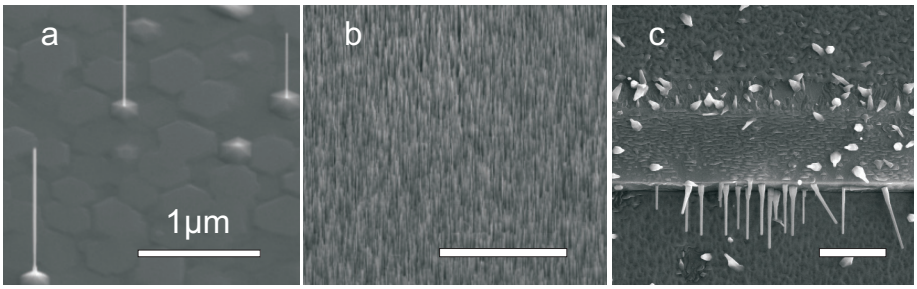

Figure 9.30: SEM image of the nanowire growth at $T = 950\,°C$ on (a) ZnO, (b) $Ga_{0.01}Zn_{0.99}O$ and (c) patterned sapphire seed layer.

[1] S. Sedky *et al.:* IEEE T Electron Dev. **48**, 377 (2001).
[2] S. Nadj-Perge *et al.:* Nature **48**, 1084 (2010).
[3] C.P. Dietrich, M. Grundmann in Wide Band Gap Semiconductor Nanowires: Low-Dimensionality Effects and Growth, V. Consonni, G. Feuillet eds., p. 303-323 (Wiley-ISTE, 2014)
[4] I. S. Nefedov *et al.:* Scientific Report **48**, 1 (2013).

9.18 Raman tensor formalism for anisotropic crystals

C. Kranert, C. Sturm, R. Schmidt-Grund, M. Grundmann

The Raman tensor is of central importance for the theoretical description of Raman scattering. It connects the scattering intensity I to the applied scattering geometry by the well-established equation [1]

$$I \propto \left|\vec{e}_1 \mathcal{R} \vec{e}_0\right|^2 , \tag{9.3}$$

where $\vec{e}_0$ and $\vec{e}_1$ are the polarization vectors of the incident and scattered light at the scattering event, respectively. However, due to mode conversion caused by birefringence in anisotropic crystals, these polarization vectors depend on the depth in the crystal where the scattering takes place. Thus, for a finite sample thickness these polarization vectors are in general unknown to the experimentalist. Beattie and Gilson concluded that the analysis of the Raman scattering intensity for polarization directions not parallel to the principal axes of the crystal's dielectric indicatrix is "pointless" [2].

We were successful in solving this problem for the very common case of normal-incident backscattering by taking into account the depth range over which the Raman scattering intensity is integrated [3]. The total Raman intensity can then be written as

$$I \propto \int \left|\vec{e}_s J(z) \mathcal{R} J(z) \vec{e}_i\right|^2 \mathrm{d}z = \vec{e}_s \int \left|J(z) \mathcal{R} J(z)\right|^2 \mathrm{d}z \, \vec{e}_i \tag{9.4}$$

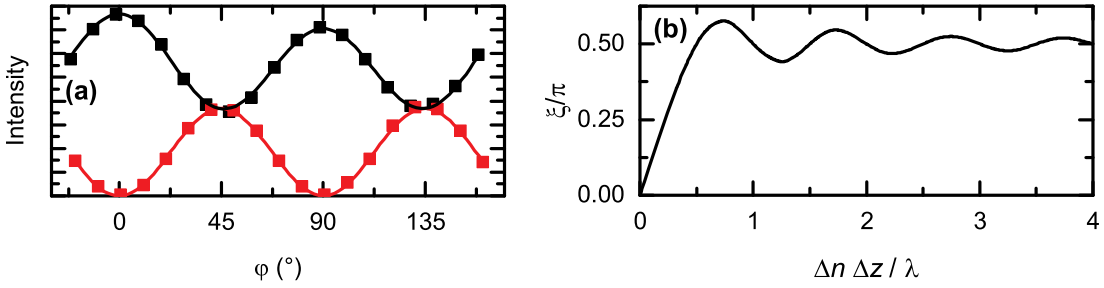

Figure 9.31: (a) Polarization-dependent Raman intensity of the A_1(TO) phonon mode for parallel (black) and cross polarization (red). Experimental data points (symbols) were modelled using the newly introduced formalism (lines). (b) Apparent angle ξ for a crystal with parallel surfaces in dependence on the magnitude of birefringence Δn, the thickness Δz and the excitation wavelength λ.

where $\vec{e}_i$ and $\vec{e}_s$ are the experimentally accessible polarization vectors of the incident and scattered light, respectively, outside the crystals and defined in the system of allowed polarizations for the respective sample orientation. The Jones matrix $J(z)$ describes the mode conversion of a birefringent material with thickness z. Obviously, the integral can be regarded as effective Raman tensor which only depends on the extension and shape of the depth profile contributing to the measured Raman spectrum.

We further found that the integral converges for integration over a sufficiently large scattering depth range, which is fulfilled for most combinations of bulk samples and experimental setups. This explains that, besides the expected dependence on experimental parameters such as excitation wavelength, depth resolution and focus point, experimental results can be routinely reproduced in different laboratories. In this case of convergence, the effective Raman tensor becomes a tensor of rank three with three orthogonal components $\mathcal{R}_0$, $\mathcal{R}_1$ and $\mathcal{R}_2$. For the general symmetric form of the Raman tensor for non-resonant excitation in the two dimensions of allowed polarization within the crystal,

$$\mathcal{R} = \begin{pmatrix} a & d \\ d & b \end{pmatrix}, \tag{9.5}$$

the components of the effective Raman tensor are

$$\mathcal{R}_0 = \begin{pmatrix} a & 0 \\ 0 & 0 \end{pmatrix}, \quad \mathcal{R}_1 = \begin{pmatrix} 0 & d \\ d & 0 \end{pmatrix}, \quad \text{and} \quad \mathcal{R}_2 = \begin{pmatrix} 0 & 0 \\ 0 & b \end{pmatrix}. \tag{9.6}$$

Due to the orthogonality of these components, the experimental Raman scattering intensity can be described using the simple equation

$$I \propto \left|\vec{e}_s \mathcal{R}_0 \vec{e}_i\right|^2 + \left|\vec{e}_s \mathcal{R}_1 \vec{e}_i\right|^2 + \left|\vec{e}_s \mathcal{R}_2 \vec{e}_i\right|^2 . \tag{9.7}$$

A great agreement to experimental data can be seen for example in Fig. 9.31a for uniaxial ZnO and was also demonstrated for biaxial β-Ga_2O_3 [4] (see Sec. 9.19.1).

If a smaller depth range is probed which does not yield convergence, both asymptotic descriptions, (9.3), which corresponds to a collinear case, and (9.7), presenting the orthogonal case, are not longer valid. Instead, the intensity for this intermediate range

has to be described using an apparent angle ξ resulting from numerical integration such that the numerical integration is not required when modelling the polarization-dependent intensity. This angle ξ is depicted in Fig. 9.31b for the case corresponding to a thin film. Considering an typical excitation wavelength of $\lambda = 500\,\mathrm{nm}$ and a moderate birefringence of $\Delta n = 0.02$, a value of 1 on the abscissa corresponds to a thickness of $\Delta z = 25\,\mu\mathrm{m}$. For bulk crystals, where the depth range is determined by the depth resolution and does not exhibit abrupt edges, the oscillations disappear and full convergence ($\xi \approx \pi/2$) is already achieved for a depth resolution in the order of $10\,\mu\mathrm{m}$ assuming the values from above.

[1] P. Y. Yu and M. Cardona, *Fundamentals of Semiconductors: Physics and Materials Properties* (Springer, 1996)
[2] I. R. Beattie and T. R. Gilson, Proc. Roy Soc. A **307**, 407 (1968) doi:10.1063/1.4915627
[3] C. Kranert, C. Sturm, R. Schmidt-Grund and M. Grundmann, Phys. Rev. Lett. **116**, 127401 (2016)
[4] C. Kranert, C. Sturm, R. Schmidt-Grund, M. Grundmann, arXiv:1606.07409 (2016)

9.19 Optical tensors of β-Ga_2O_3

C. Sturm, C. Kranert, R. Schmidt-Grund, J. Furthmüller*, F. Bechstedt*, M. Grundmann

* Institut für Festkörpertheorie und -optik, Friedrich-Schiller-Universität Jena, Max-Wien-Platz 1, 07743 Jena, Germany

Materials with low crystal symmetry of the classes orthorombic, monoclinic and triclinic have complex physical properties like for instance anisotropic phonon modes or electronic transitions. This manifests itself in tensorial character of the respective physical responses. On the one hand, this makes interpretation and modelling of experimental data challenging, but offers in turn deep insight into basic physical material properties which cannot be gained such way from simple isotropic materials.

We demonstrate exemplarily for monoclinic β-Ga_2O_3 [1–3] in the infrared to vacuum-ultraviolet spectral range, that treating the Raman and dielectric function tensor fully accounting for mode conversion and using a generalized oscillator model, which takes into account the actual spatial direction of the dipole moments, allows for very thorough understanding of properties of phonons and electronic transitions as detailed in the following sections. The results obtained from experiment agree excellently with theoretical findings.

The general Raman tensor formalism for anisotropic crystals is described in Sec. 9.18 [4]. The dielectric function (DF) of optically anisotropic materials is in general a symmetric tensor consisting of six independent components, which can be diagonalized independently for the real and imaginary part at each wavelength separately, leading to wavelength dependent directions of in general six independent dielectric axes. For monoclinic material the tensor reduces to

$$\varepsilon = \begin{pmatrix} \varepsilon_{xx} & 0 & \varepsilon_{xz} \\ 0 & \varepsilon_{yy} & 0 \\ \varepsilon_{xz} & 0 & \varepsilon_{zz} \end{pmatrix}. \tag{9.8}$$

Using generalized spectroscopic ellipsometry (SE), we have obtained these tensor elements numerically and indepently of each other as well as the directions of the dielectric axes for each photon energy [2]. For exploring the deeper nature of polarizabilities in the material, we have extended an existing model [5, 6] and applied it to model contributions of phonon modes, excitonic polarizabilities and electronic band-band transitions to the DF using individual oscillator functions contributing to all tensor elements according to the projection of the real space direction of their dipole moment within the crystal. In doing so, considering the monoclinic crystal symmetry with the symmetry axis $b \| y$ (y in the cartesian laboratory system), the dielectric function can be parametrised as follows [3]:

$$\varepsilon = \mathbf{1} + \sum_{i=0}^{N_\mathrm{y}} \varepsilon_{i,\mathrm{y}} + \sum_{j=0}^{N_\mathrm{xz}} R(\phi_j)\varepsilon'_{j,\mathrm{xz}}R(\phi_j)^{-1}\,, \tag{9.9}$$

where R are the rotation matrices for transfer of the dipole directions in the non-cartesian crystal system into the cartesian laboratory system (we choose our coordinate system in such way that $\hat{e}_x \parallel a$-axis, $\hat{e}_y \parallel b$-axis and $\hat{e}_z = \hat{e}_x \times \hat{e}_y$). N_y and N_xz represent the number of excitations with the corresponding polarization directions and ϕ the angle between the individual polarization direction and the x-axes within the x-z-plane.

For our studies, we investigated three differently cut β-Ga_2O_3 bulk single crystals with (010), ($\bar{2}$01) and (100) orientation (Tamura Corporation / IKZ Berlin) and a ($\bar{2}$01) oriented thin film grown by pulsed laser deposition (PLD).

Theoretical considerations have been applied for calculating properties of phonon modes by the ab-initio B3LYP hybrid functional approach implemented in the CRYSTAL14 code [1], as well as the electronic band-structure and the ultraviolet dielectric function by density functional theory combined with many-body perturbation theory including quasi-particle effects and excitonic correlations [2].

9.19.1 Phonon modes

Raman Tensor Elements

We successfully demonstrated the possibilities opened by our general Raman tensor formalism for anisotropic crystals (Ref. [4] and Sec. 9.18) by determining the Raman tensor elements of β-Ga_2O_3 bulk single crystals [1]. Before that, only Raman intensities for scattering geometries involving polarizations and propagation directions parallel to the principal axes of the crystal's dielectric axes at the excitation wavelength could be analyzed [7]. Within this restriction, it is only possible to determine the absolute values of the Raman tensor elements and that only if crystals with surfaces normal to principal axes are available which is not trivial for monoclinic or triclinic crystals. Using our approach, it is not only possible to determine these absolute values without this restriction, but also to obtain the signs of these numbers.

We measured the Raman spectra in normal-incidence backscattering geometry with an excitation wavelength of $\lambda = 532\,\mathrm{nm}$. The incident and scattered polarization were both rotated by means of the same $\lambda/2$ waveplate similar to rotating the sample, but without the problem of changing the position of the sample with respect to the focusing spot. Spectra were recorded in both parallel and cross polarized configuration.

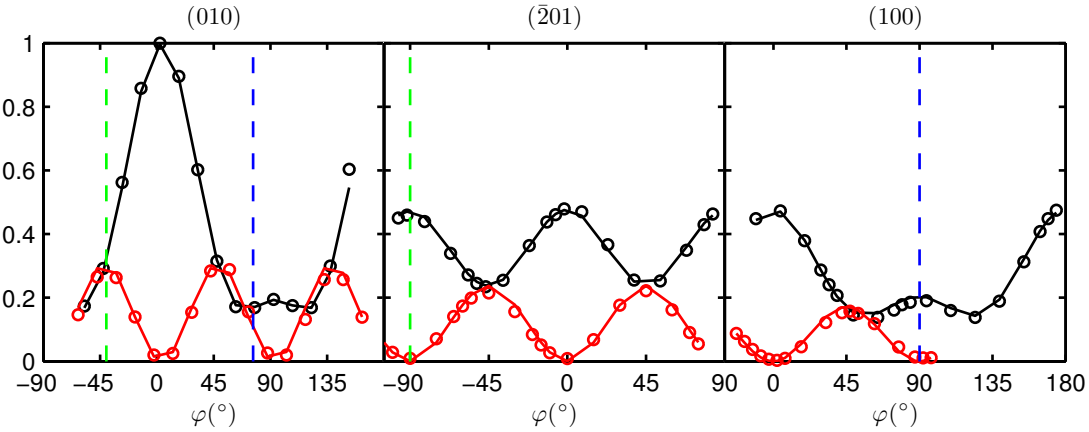

Figure 9.32: Experimental Raman scattering intensities (circles), model fits (solid lines) for the $A_g^{(3)}$-mode of β-Ga_2O_3 at 200 cm^{-1} in dependence on the direction of polarization φ. Excitation was carried out on the top facet of three differently oriented crystals as indicated on top of the spectra. The intensity was normalized to the maximum intensity. For the (010)-orientation, $\varphi = 0°$ is set such that it coincides with the [100]-direction, for the other two orientations 0° corresponds to the [010]-direction. The dashed green and blue lines indicate the [102]- and [001]-direction, respectively.

The areas of the peaks in the spectra were determined by means of a line shape analysis and then plotted in dependence on the polarization direction for the three crystal orientations. These were then modeled based on our Raman tensor formalism for anisotropic crystals [4], using only the real-valued Raman tensor elements as free parameters. However, also the parameters of the indicatrix at the excitation wavelength were required as input which were taken from ellipsometry measurements [2]. As can be seen representatively for the $A_g^{(3)}$ mode in Fig. 9.32, we achieved a very good agreement between model and experiment. This applies to all 13 out of 15 total Raman-active phonon modes which exhibited a sufficient intensity for this analysis. As can be seen from these plots, the intensities for polarization along the [102]- and [001]-direction, which are indicated by the colored dashed lines, vary between the different orientations. This results from birefringence and is in contradiction to the standard Raman tensor formalism, which requires the intensities to be the same, but is well described using our approach.

The phonon energies obtained by ab-initio calculations are in very good agreement with the experimental data. Further, by combining the Raman intensity option of the CRYSTAL14 code with the change in susceptibility under manually applied atomic shifts according to the individual phonon modes, we were able to extract the Raman tensor elements also from theoretical calculations. A convincingly good agreement to the experimental results was found which allowed to model the Raman intensity in dependence on the scattering geometry for the majority of the phonon modes. However, some deviations were found for other modes such that an experimental verification appears inevitable.

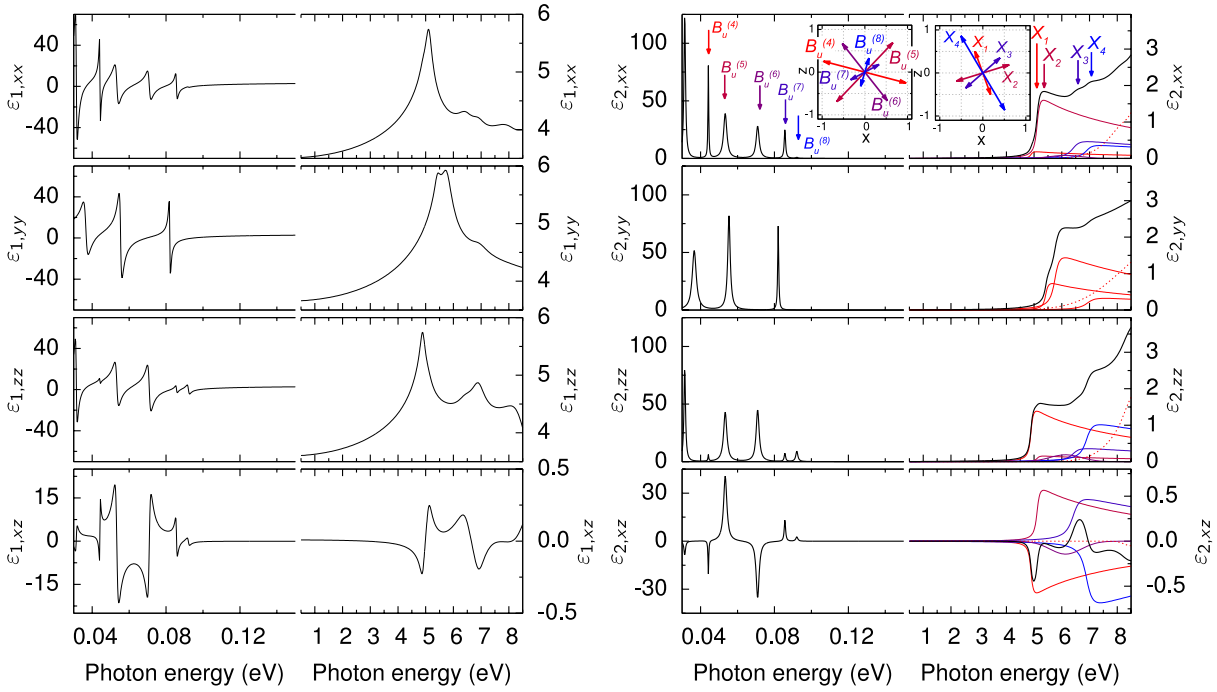

Figure 9.33: Dielectric function (black solid line) of a β-Ga_2O_3 bulk single crystal in the infrared and UV spectral range. The red . . . blue solid lines represent the excitonic contribution in the investigated UV spectral range whereas the red dashed lines represent the contribution of the high-energy contributions. The arrows in the insets depict the orientation of the corresponding dipole moment in the *a*-*c*-plane (*x*-*z*-plane) and their relative amplitude ratio.

Infrared dielectric function

The bulk single crystal's infrared dielectric function tensor elements ε_{xx}, ε_{yy}, ε_{zz} and ε_{xz} in the spectral range $250-1300\,\mathrm{cm}^{-1}$ are shown in Fig. 9.33. We observed 9 of the totally 12 infrared-active optical phonon modes. It can be clearly seen that some modes are purely polarized along the symmetry axis, i.e. *b*- / *y*-direction, and some solely within the *a*-*c*- (*x*-*z*-) plane. The first are modes with A_u and the latter modes with B_u-symmetry, as indicated in the figure. Their dipole moment's directions (expressed by the angle φ with respect to the *a*-axis – Eq. 9.9) differ for each phonon mode, whereby two of them are almost polarized along *x* / *a*, reflecting the crystal symmetry (cf. Fig. 9.34). The angle φ was found to excellently agree with the polarization directions obtained by the ab-initio calculations within a maximal deviation of about 7°. The very good agreement is also true for the phonon mode energies, amplitudes and the relative ratio of their oscillator strengths.

9.19.2 Electronic excitations

Bulk single crystal

The bulk single crystal's dielectric function tensor elements in the visible-to-ultraviolet spectral range are shown in Fig. 9.33 with their individual model contributions indicated by coloured lines. As we have shown by theoretical considerations [3], the DF in the spectral range from the fundamental absorption edge on up to some eV higher is dom-

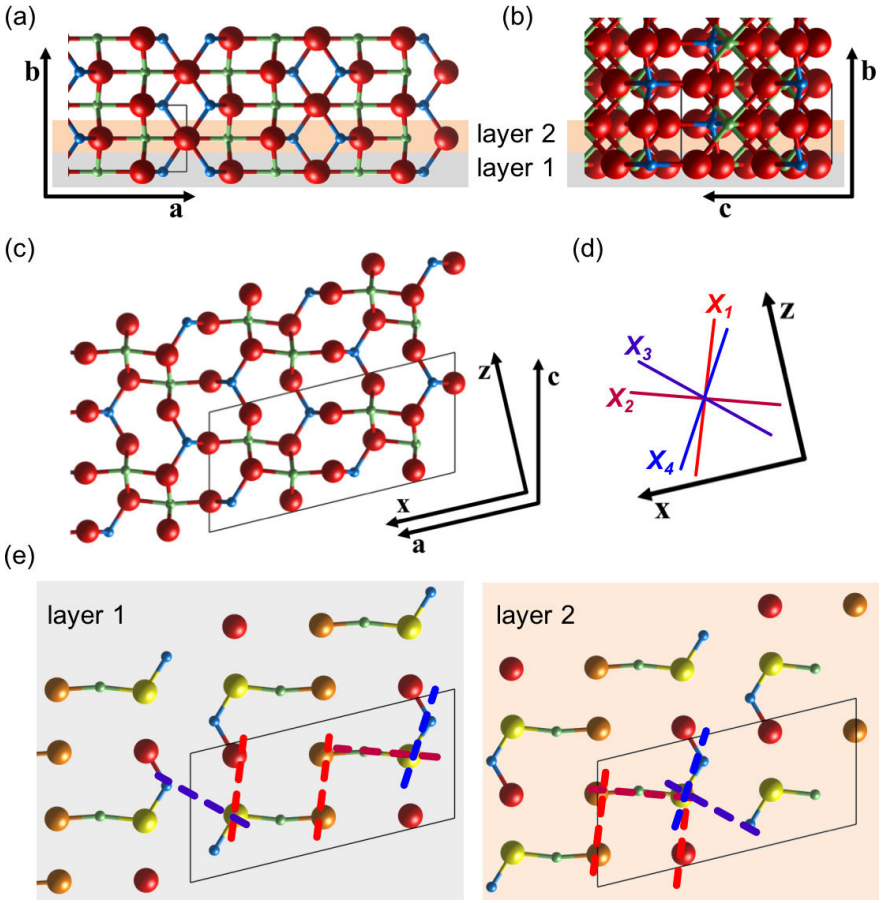

Figure 9.34: (a-c): Schematic representation of projections of the crystal structure of β-Ga_2O_3 into the *b*-*a*-plane (a), *b*-*c*-plane (b) and *c*-*a*-plane (c). The unit cell is indicated by the black framed boxes. Bonds are indicated by lines between the atoms. The respective Cartesian coordinates x and z are indicated, y points along b. The tetrahedrally coordinated Ga(I) atoms are shown in blue and the octahedrally coordinated Ga(II) are shown in green. The oxygen atoms are marked in red. (d) The directions of the dipole moments of the transitions $X_1 \ldots X_4$ within the *a*-*c*-plane (*x*-*z*-plane). (e) Sub-layers of the *c*-*a*-plane (left: layer 1, right: layer 2) as indicated also in (a) and (b). Here, the oxygen atoms at different lattice sites are highlighted by colours as O(I) red, O(II) orange and O(III) yellow. The dashed coloured lines relate the dipole directions of the transitions $X_1 \ldots X_4$ to atomic bonds within the crystal structure. Please note that only one example is shown for each transition. (Images created by VESTA (Ref. [8]).)

inated by excitonic correlation effects. Thus, several excitonic contributions have been considered in modeling. The contribution of weakly pronounced band-band-transitions where summarized by using a Gaussian oscillator. A further Gaussian oscillator and a pole function was included in each dielectric tensor component to account for contributions of transitions at energies higher than the investigated spectral range due to their spectral broadening. Note, that the experimental and theoretical calculated DF spectra agree with each other in great detail.

Analogously to the phonon modes, we were able to determine the direction of the dipole moments of the individual transitions, yielding purely y- / b-polarized transitions and those polarized within the x-z- (*a*-*c*) plane (labelled in Fig. 9.33). The directions of the latter one are indicated in the insets in Fig. 9.33 and are also indicated in the real

space crystal structure in Fig. 9.34. According to these directions and based on theoretical element- and orbital-resolved density-of-states data as well as charge carrier distribution within the crystal planes, we could assign the experimentally obtained transitions to individual atoms in the crystal. It is great to note that the experimentally determined directions of the exciton dipole moments agree excellently with the directions of the four dominating band-band transitions obtained by density functional calculations. This indicates that the respective excitons are mainly formed by these individual band-band transitions. This strong localization of the excitons and their large binding energy of about 270 meV clearly reveal their Frenkel-like nature.

These results nicely demonstrate the potential of the used model approach for the dielectric tensor to gain deep insight into electronic properties of highly anisotropic materials.

Thin film

The PLD-grown β-Ga_2O_3 thin film exhibits ($\bar{2}01$) out-of-plane orientation with 6 in-plane rotation domains, rotated by multiples of 60°. As their size is much smaller than the optically probed sample area of about $5\times8\,m^2$, the measured optical response is determined by an average over these domains. For uniform distribution of these rotation domains, the effective dielectric function is given by

$$\varepsilon = \frac{1}{6}\sum_{i=1}^{6} R(\phi_i)\varepsilon^{\text{mono}}R^{-1}(\phi_i) = \begin{pmatrix} 0.5(\varepsilon'_{xx}+\varepsilon_{yy}) & 0 & 0 \\ 0 & 0.5(\varepsilon_{xx}+\varepsilon_{yy}) & 0 \\ 0 & 0 & \varepsilon'_{zz} \end{pmatrix}, \tag{9.10}$$

with $\phi = (i-1)\pi/3$ the rotation angle of the i^{th} rotation domain and $R(\phi)$ being the rotation matrix around the surface normal. Equation (9.10) is similar to those of a uniaxial material with $\varepsilon_\perp = 0.5(\varepsilon'_{xx}+\varepsilon_{yy})$ and $\varepsilon_\parallel = \varepsilon'_{zz}$ ($\perp$ and $\parallel$: perpendicular and parallel to the optical axis) with orientation of the effective optical axis along the surface normal. Note that ε'_{xx} and ε'_{zz} are the tensor components for the coordinate system with the x- and z-axis parallel and perpendicular to the sample surface, respectively. In contrast to a homogeneous uniaxial material, those effective $\varepsilon_\perp$ and $\varepsilon_\parallel$ are not independent from each other. The components ε'_{xx} and ε'_{zz} reflect the same transitions and are determined by the projection $A'_{zz}/A'_{xx} = \sin^2\phi'/\cos^2\phi'$ of their amplitudes A.

For the parametric model of the DF of the thin film we used the same set of model DFs as for the bulk single crystal. The tensor components of the DF of the thin film are shown in Fig. 9.35. For comparison, the components calculated from the DF of the bulk single crystal by using Eq. (9.10) are shown as dashed lines. For the thin film, we needed to adjust energies and amplitudes of the transitions and even the dipoles' orientation angles ϕ within the x-z-plane (a-c-plane). Compared to the DF of the bulk single crystal, a blue-shift of the transition energies up to 100 meV and a lowering of the oscillator strengths is observed for the thin film. We relate these changes of the DF properties on the one hand to crystal imperfections typically lowering the oscillator strength of electronic transitions by dissipative processes. On the other hand, also strain is possibly present in the thin film, causing changes in the bond length and maybe also torsion of the unit cell causing different dipole moment orientations.

[1] C. Kranert, C. Sturm, R. Schmidt-Grund, M. Grundmann, arXiv:1606.07409 (2016)

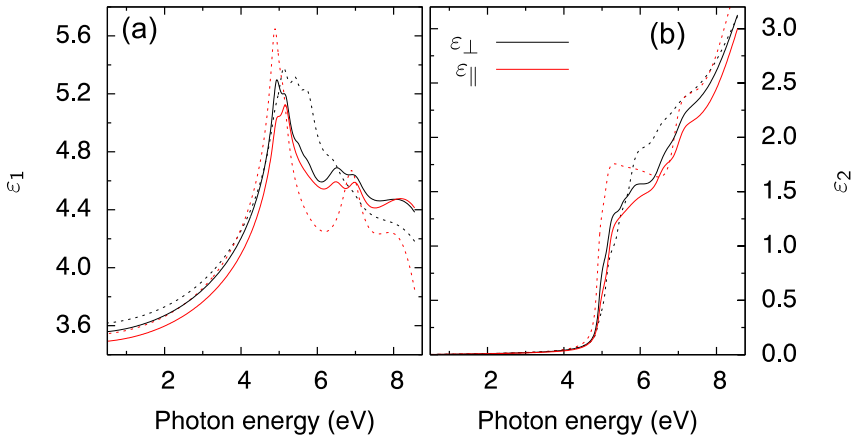

Figure 9.35: Real (a) and imaginary (b) part of the tensor components of the Ga_2O_3 thin film (solid lines). For comparison, the components calculated by Eq. (9.10) using the single crystal values are shown as dashed lines.

[2] C. Sturm *et al.*, APL Mater. **3**, 106106 (2015) doi:10.1063/1.4934705
[3] C. Sturm, R. Schmidt-Grund, C. Kranert, J. Furthmüller, F. Bechstedt, M. Grundmann, Phys. Rev. B **94**, 035148 (11 pages) (2016)
[4] C. Kranert, C. Sturm, R. Schmidt-Grund and M. Grundmann, Phys. Rev. Lett. **116**, 127401 (2016)
[5] A.G. Emslie and J.R. Aronson, J. Opt. Soc. Am. **73**, 916 (1983), doi:10.1364/JOSA.73.000916
[6] S. Höfer *et al.*, Vibrational Spectroscopy **67**, 44 (2013), doi:10.1016/j.vibspec.2013.04.003; and **72**, 111 (2014), doi:10.1016/j.vibspec.2014.03.003
[7] I.R. Beattie and T.R. Gilson, Proc. Roy Soc. A **307**, 407 (1968), doi:10.1098/rspa.1968.0199
[8] K. Momma and F. Izumi, J. Appl. Crystallogr. **44**, 1272 (2011), doi:10.1107/S0021889811038970

9.20 Spectroscopic ellipsometry as a unique method for investigating structural properties of spinel ferrite thin films

V. Zviagin, M. Bonholzer, Y. Kumar, I. Lorite, D. Spemann*, J. Meijer, P. Esquinazi, M. Grundmann, R. Schmidt-Grund.

*Leibniz Institute for Surface Modification, Physical Department, Permoserstr. 15, 04318 Leipzig, Germany.

Semitransparent spinel oxides continue to receive a considerable amount of attention due to their wide range of high-frequency and high-power applications, varying from detectors and sensors to magnetic recording media [1, 2]. Ideally they crystallize in either a normal or an inverse spinel structure, depending on the material. While Fe_3O_4 (FFO) is a ferromagnetic inverse spinel, normal spinel $ZnFe_2O_4$ (ZFO) is antiferromag-

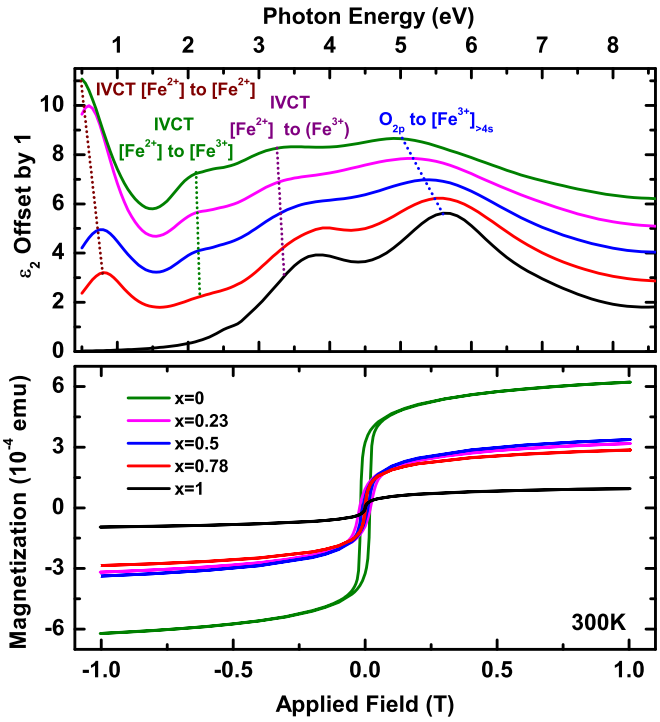

Figure 9.36: (Top) Model calculated imaginary part of the dielectric function (ε_2) for the $Zn_xFe_{3-x}O_4$ mixed crystals with the corresponding electronic transitions indicated. Square brackets correspond to octahedrally coordinated cations, while the parentheses correspond to cations located at tetrahedral lattice sites. (Bottom) Magnetization data for the same ZFO films measured at room temperature with composition values indicated.

netic with a Néel temperature of about 10 K, however their ferrimagnetic response at room temperature is not fully understood yet [3]. By varying the growth parameters, such as temperature and pressure, tunable electronic and magnetic properties are possible due to defects such as cation disorder, oxygen vacancies and a possible mixed crystallization state between normal and inverse spinel structures. The degree of disorder and its relation to electronic and magnetic properties of the spinel ferrites is still a controversial topic within the scientific community. We employ spectroscopic ellipsometry (SE) in a wide spectral range (0.5 – 8.5) eV to investigate structure properties of ZFO, $Zn_xFe_{3-x}O_4$ and FFO based on the transitions assigned from literature and previous studies [4]. We also relate the cation occupancy to the magnetic properties of the material, measured by superconducting quantum interference device (SQUID), and give a reasonable explanation for the observed magnetic response.

Composition dependence

A composite thin film, $Zn_xFe_{3-x}O_4$ with x varying from (0 – 1) , was grown by pulsed laser deposition (PLD) in Argon atmosphere on (100) $SrTiO_3$ substrate covered by a conducting TiN layer in order to optimise the magnetic tunneling junction application. The model dielectric function, obtained from SE data, (Fig. 9.36), shows a clear change for varying composition from ZFO to FFO. Since ideally ZFO crystallizes in a normal spinel structure and FFO in an inverse spinel structure, the transition between normal

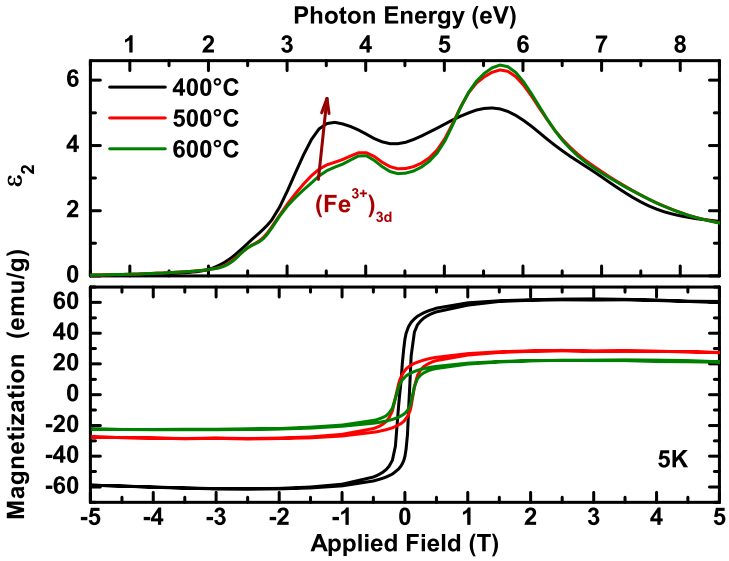

Figure 9.37: (Top) Model calculated imaginary part of the dielectric function (ε_2) for ZFO films grown at indicated temperatures. The amplitude increase of the transition involving Fe^{3+}, corresponding to disorder is indicated. (Bottom) Magnetization data for the same ZFO thin films recorded at 5 K.

and inverse spinel structures is clearly visible between x = 0.5 and 0.23 , observed from the drastic increase in amplitude of the inter-valence charge transfer transition (IVCT) involving octahedrally coordinated Fe^{2+} cations located below 1 eV. Figure 9.36 shows magnetization response for the composition, conducted at room temperature, which is highest for FFO and lowest for ZFO. However, the response is slightly higher for x = 0.5 than for x = 0.23 . This corresponds well to a previous study in which the overall magneto-optical response is greater for a disordered normal spinel than for a disordered inverse spinel crystal structure [4].

Influence of crystalline quality

The crystalline quality and thus the degree of cation disorder in the material is modified by varying the growth temperature [5] and by ion irradiation either inducing disorder in the crystal or causing cation relocation in already disordered material. Doing so, ZFO thin films (thickness of about 40 nm) were deposited by PLD on STO substrates at different temperatures and at highest O_2 pressure to minimize and have similar oxygen vacancy concentration, as determined from pressure dependent studies [6]. Inversion of the normal spinel structure was found to be one of the main mechanisms responsible for the highest magnetic response for the lowest growth temperature. The enhanced feature in the dielectric function located at 3.5 eV, related to a transition involving tetrahedrally coordinated Fe^{3+} cations (Fig. 9.37) corresponds to the dominating magnetic coupling between the octahedral and tetrahedral lattice sites, responsible for the overall ferrimagnetic behaviour of the film grown at the lowest temperature. Samples grown at lowest and highest temperatures were irradiated with Si ions. The shift in the transition energies in the dielectric function is due to a possible cation reordering in the disordered spinel and a relaxation mechanism in both disordered and normal spinel ZFO. The magnetization decreases in the irradiated disordered spinel structure, which

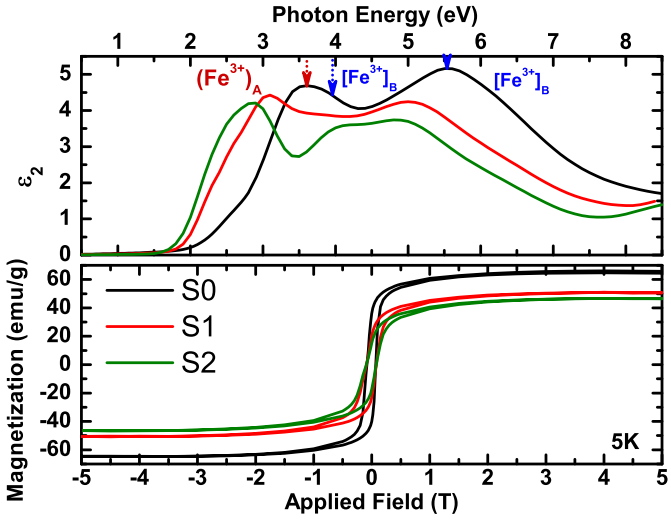

Figure 9.38: (Top) Model calculated imaginary part of the dielectric function (ε_2) for irradiated ZFO thin films grown at the lowest temperature, with transitions involving iron cations located at different lattice sites as indicated. The label S0, S1, and S2 corresponds to ZFO samples of no irradiation, one irradiation dose, and two irradiation doses, respectively. (Bottom) Magnetization data for the same samples recorded at 5 K.

corresponds well to the assumption of cation reordering (Fig. 9.38). In contrast, the magnetization signal increases with the increased dosage of Si radiation in the normal spinel ZFO, which is related to the introduction of disorder or inversion in the crystal structure [7].

[1] R. Valenzuela, Phys. Res. Int. **2012**, 591839 (2011), doi:10.1155/2012/591839
[2] M. Opel *et al.* Phys. Status Solidi (a) **208**, 232 (2011), doi:10.1002/pssa.201026403
[3] Y.F. Chen *et al.*, J. Phys. D: Appl. Phys. **41**, 205004 (2008), doi:10.1088/0022-3727/41/20/205004
[4] V. Zviagin *et al.*, Phys. Status Solidi (b) **253**, 429(2016), doi:10.1002/pssb.201552361
[5] V. Zviagin *et al.*, Appl. Phys. Lett. **108**, 131901 (2016), doi:10.1063/1.4944898
[6] C. E. Rodriguez Torres *et al.*, Phys. Rev. B **84**, 064404 (2011), doi:10.1103/PhysRevB.84.064404
[7] B. P. Uberuaga *et al.*, Nat. Commun. **6**, 8750 (2015), doi:10.1038/ncomms9750

9.21 Development of time-resolved spectroscopic ellipsometry with picosecond resolution

S. Richter, C. Sturm, H. Franke, O. Herrfurth, M. Grundmann, R. Schmidt-Grund

So far, time-resolved spectroscopic ellipsometry measurements are limited to rather low time-resolution in the order of microseconds. However, there is a need to explore dielectric functions of materials at smaller time-scales e.g. after excitation of free carriers by pumping. This gap is, so far, only filled by time-resolved reflectance or transmittance measurements which are generally inferior to ellipsometry if information about the electronic system shall be extracted.

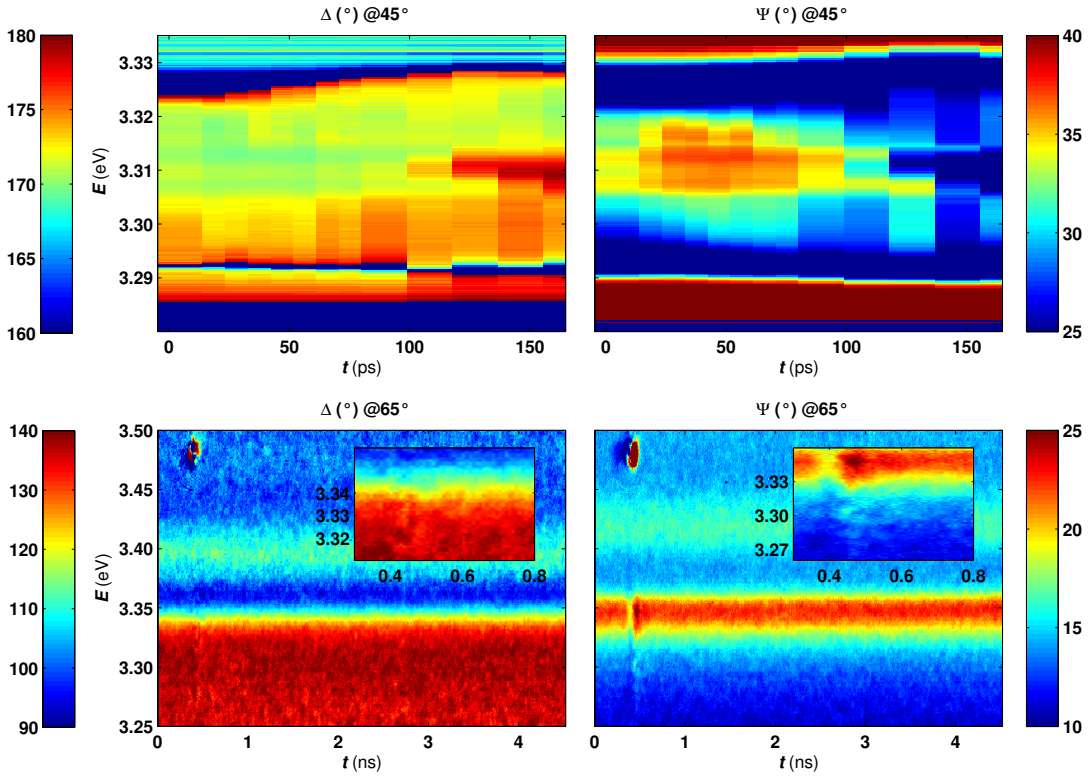

Figure 9.39: Time-resolved ellipsometric parameters Ψ and Δ of a ZnO single crystal upon excitation by a UV laser pulse for different setup schemes. Upper row: Pump-probe results using $\lambda_{\text{pump}} \approx 250$ nm and $\lambda_{\text{probe}} \approx 375$ nm. Bottom row: Results using a continuous broadband light source and streak camera detection with $\lambda_{\text{pump}} \approx 266$ nm. The insets shows a magnification of the time range directly after the pulse.

Two different schemes for faster spectroscopic ellipsometry measurements were developed. Both have been tested at ZnO single crystals which were pumped by a UV laser pulse.

One measurement scheme is based on a continuous light source which continuously probes the sample. The reflected light is then time-resolved detected by a streak camera which is triggered by the pulsed laser. The reflectance of different polarization states is measured consecutively and the ellipsometric quantities are calculated. Due to the available streak camera modules, the time-resolution is limited to roughly 50 ps. As can be seen in the bottom row of Fig. 9.39, this is still too low in order to observe free carrier effects in ZnO. Hence, another measurement scheme was developed, based on pump-probe-measurements. Here, the second and third harmonic of a seed pulse from a Ti:Sa laser is used for probing and pumping, respectively. Again, different polarization states are measured consecutively and the time-dependence is obtained by scanning a delay line. A time-integrating detector can be used and the time-resolution is only limited by the pump/probe pulse length to about 150 fs. However, the spectral range of the probing second harmonic is rather narrow. In order to measure a wider spectral range, scanning the wavelength of the seed laser pulse is necessary. Results of a pump-probe ellipsometry scan on a ZnO single crystal can be seen in the top row of Fig. 9.39. The data hints on exciton screening by excitation of free carriers by the pump pulse.

Besides finding a compromise between high time-resolution and wide spectral

range, remaining challenges are to obtain high pump densities and a proper overlay of pump and probe spots. Up to now all experiments were carried out using macroscopic spot sizes in the order of 100 μm. Future work aims for implementation of the method at a micro-spot setup. Otherwise, principal limitations to observable time-dependent processes are only their repeatability. For solid states, this demand means that switching processes have to be reversible within an appropriate time-scale.

9.22 ZnO-based microcavities

R. Schmidt-Grund, T. Michalsky, M. Wille, S. Richter, C. Sturm, E. Krüger, L. Fricke, H. Franke, M. Thunert, R. Buschlinger*, U. Peschel*, M. Grundmann

*Institut für Festkörpertheorie und -optik, Friedrich-Schiller-Universität Jena, Max-Wien-Platz 1, 07743 Jena, Germany

Like in the past years, also in 2015 we intensively investigated ZnO-based microcavities (MC). MC physics is in focus of current research because it still provides new facinating fundamental physical effects like quantum-optical properties in the strong light-matter coupling regime or even topological non-trivial states [1]. Further MC are of considerable interest for applications in quantum-information technology or optoelectronic devices like nanowire-based laser structures.

ZnO is an efficient emitter for ultraviolet light. Of major interest in the last few years research was the investigation of waveguiding and stimulated emission in nano- and microstructures with the goal to achieve 1D and 2D light emitting devices and laser diodes in the near UV spectral range. In fact semiconducting ZnO nano- and microwires (NW, MW) provide all components necessary for laser action intrinsically: under high excitation the semiconductor material acts as active gain medium and the resonator geometry is provided by either the end facets of the NW (Fabry-Pérot modes - FPM) or the hexagonal cross section of the MW represents a whispering gallery mode (WGM) type resonator due to total internal reflections (TIR) at the inner sidewalls.

We continued our investigations [2, 3] on nano- and microwire based structures yielding versatile optical mode properties enabling different regimes of light-matter interaction. Particularly, we investigated lasing in the weak coupling regime (WCR) due to Purcell enhancement by WGM of emission from electron-hole-plasma and exciton-scattering states as gain (cf. Sects. 9.22.2-9.22.5) and cavity exciton-polaritons in the strong coupling regime (SCR) (Sec. 9.22.5). By further developing our experimental setup and data analysis strategies we were able to prove for exciton-polariton Bose-Einstein condensates in planar MC [4] to show coherence times of up to 24 ps [5] and to exist more than 100 ps (Fig. 9.40). This is the longest existing BEC observed for this material class, comparable with such of farly developed GaAs-based MC. We have also theoretically investigated photonic and exciton-polariton modes in planar MC by means of 4×4-transfer-matrix calculations (Sec. 9.22.1). By that, we could on the one hand clarify a debate in literature regarding the correct quasi-particle approximation of exciton-polariton modes [6]. On the other hand, we have identified a non-trivial mode structure in pure photonic MC with an optical uniaxial cavity material with the optical axis not trivially aligned along the confinement direction. The eigenmodes reveal non-orthogonal polarization and also vortex like structures in the polarization-momentum

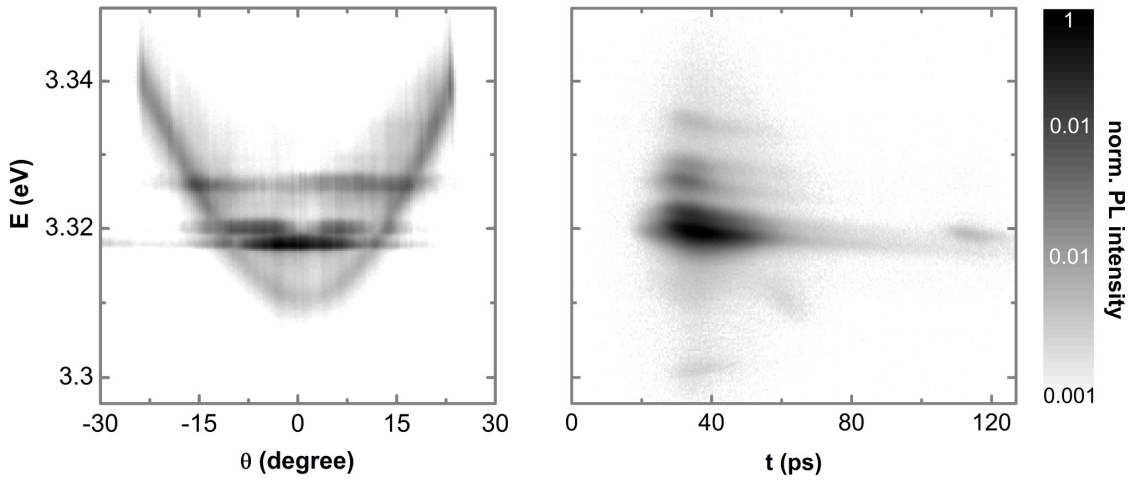

Figure 9.40: Gray scale image of the far-field emission (left) and time-resolved emission intensity (at $\theta = 0°$) in logarithmic scale of a exciton-polariton Bose-Einstein condensate in a planar ZnO-based MC.

space, which might be interesting for topological non-trivial photonics.

The MWs and some of the NWs are fabricated by carbothermal vapor phase transport at temperatures larger 1000 ℃ [7]. The nanowire cavity which is coated with a concentric shell distributed Bragg reflector (DBR) (Sec. 9.22.5) is produced by pulsed laser deposition (PLD) in three steps [8, 9]: on top of a planar nucleation layer bare NW are grown which then are coated at oblique incidence with DBR shells. The DBR of the nanowire cavity discussed here consists of 10.5 layer pairs Yttria stabilized zirconia (YSZ) and Al_2O_3. The planar MC is also grown by PLD using the same materials [4, 9].

9.22.1 Transfer matrix calculus for planar microcavities

Theoretical description of cavity photon and polariton modes is usually carried out by quasi-particle models. There, cavity photons are described by an effective mass associated to a parabolic dispersion relation and polariton dispersions result from coupling Hamiltonians between the cavity photons and excitons. However, this is only an approximation. Exact relations can be found by modeling the propagation of electromagnetic waves in a cavity in terms of Maxwell's theory.

Applying a complex 4×4 transfer matrix ($\hat{T}$) formalism [10] for isotropic planar MCs, we could explore the applicability of quasi-particle Hamiltonians and the dimension of the related Hilbert space in the case of exciton-polaritons in multi-level systems. Here, the excitonic resonance is represented by a Lorentzian oscillator function in an otherwise real-valued dielectric function (i.e. transparent media) and the eigenmodes of the system can be found by matrix singularities in a sub-matrix of $\hat{T}$. It could be shown for a polariton system with N photon modes and N_X excitons, that unambiguously the

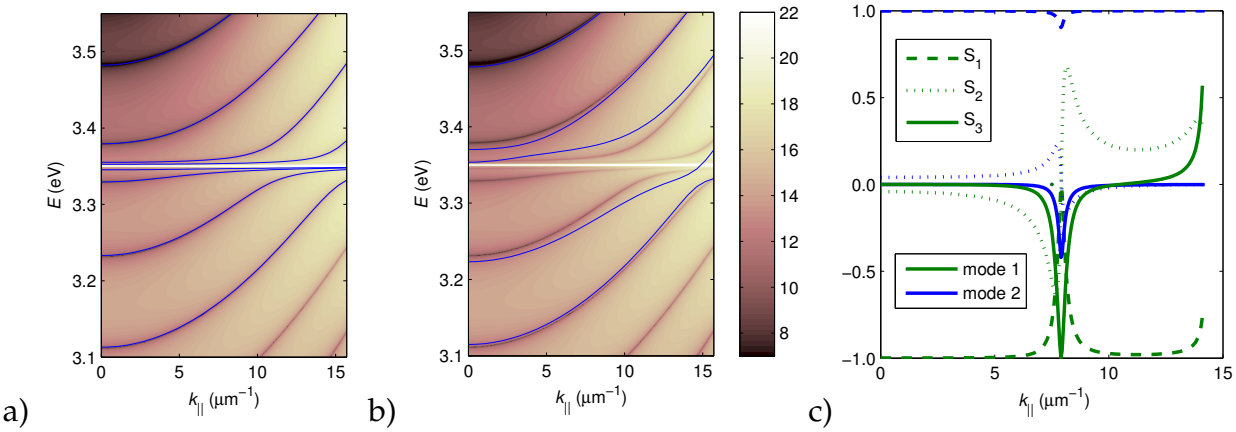

Figure 9.41: a), b): Logarithmic plot (color bar signifies decimal power) of $|T_{11}|$ [6] where minima represent *TE*-polarized modes. A thick MC reveals multiple photonic modes which couple to one exciton at 3.35 eV. In a) modeling with Eq. 9.11 is shown, in b) modeling with the wrong $N + N_X$-dimensional model, which can frequently be found in the literature. c): Numerically obtained polarization Stokes vector components for cavity photon modes of a uniaxial $\lambda/2$ cavity, the optical axis of which is oriented in the cavity plane. A clear circular polarization excess can be seen. The propagation direction is 1.2° off from the orientation of the optical axis.

system Hamiltonian is composed of N independent sub-systems according to [6]:

$$\mathcal{H} = \bigoplus_{j=1}^{N} \begin{pmatrix} E_{X1} & 0 & \dots & V_{1j} \\ 0 & E_{X2} & & V_{2j} \\ \vdots & & \ddots & \vdots \\ V_{1j} & V_{2j} & \dots & E_{Cj} \end{pmatrix} \tag{9.11}$$

with exciton and cavity photon energy E_{Xi} and E_{Cj}, respectively, and coupling strength V_{ij} ($i/j \in \{1, ..., N_X/N\}$). Hence, the dimension of the related Hilbert space is given by $N(N_X + 1)$. In the literature, contradicting model approaches can be found assuming dimensions of $N + N_X$ which is not true for such configurations. However, experimental data can often be modelled sufficiently well using such a wrong model. Figures 9.41 a) and b) show the dispersion of the polariton modes in a thick cavity where several photon modes couple to one exciton resonance. While a) depicts the correct modeling according to Eq. 9.11, the model based on the $N + N_X$-dimensional Hilbert space in b) is clearly wrong.

Applying the 4×4 transfer matrix formalism to MCs with optical anisotropic cavity material enables investigation of the eigenmodes without restricting the polarization beforehand. Hence, in contrast to approaches which separate the problem into transversal electric (*TE*) and transversal magnetic (*TM*) polarization, a general treatment is possible. Again, the eigenmodes are found rigorously as (sub-)matrix singularities. For a transparent $\lambda/2$-cavity surrounded by DBRs, it turns out that independent of the orientation of the cavity material's optical axis always two modes occur. This is known from the isotropic case but was not generally clear for the anisotropic one [11]. The modes generally carry elliptic polarizations which furthermore are generally not orthogonal to each other. Depending on the energy tuning between twice the optical cavity thickness and the central wavelength of the DBRs, the modes can even become circularly co-polarized as shown in Fig. 9.41 c) (Stokes vector component S_3). Those

circular polarization excesses are related to propagation nearly but not exactly along or perpendicular to the optical axis. Considering the two-dimensional in-plane momentum space around these "circular points" it turns out that they resemble pairs of half-vortices in the polarization space, which imply the presence of a non-trivial Berry phase and Chern number.

9.22.2 Lasing processes in ZnO microwires

We have observed different laser processes in a single ZnO microwire at room temperature [12]. Figure 9.42(a) depicts a scanning electron microscope image of a slightly tapered ZnO microwire with a diameter ranging from $8.7-12.3\,\mu m$ and a length of $L\sim 400\,\mu m$. It is clearly evident, that its hexagonal morphology is disturbed by several particles on the surface. When taking a closer look, these particles have partially tetrapod-like morphology with long and straight arms (lengths up to several μm and diameters of $100-400\,nm$). Using a fs-pulsed Ti:Sa laser, the microwire was excited at different lateral positions with variable excitation powers. Figure 9.42(b) shows typical lasing transition in microwires characterized by a regular WGM structure, which was observable at nearly all clean and particle-free positions along the microwire (e.g. Pos. 1 in Fig. 9.42(a)). The underlying electron-hole-plasma causes a gain profile which broadens to lower energies when the excitation power increases. This leads to the amplification of modes at the low energy side. However, when a tetrapod-like particle is on the surface of the microwire (see e.g. Pos. 2 in Fig. 9.42(a)), the lasing behavior changes drastically. Figure 9.42(c) shows the untypical laser transition, with only one dominating lasing mode at significantly higher energy. The energetic position as well as the lower lasing threshold power indicate, that the P-band, evoked by exciton-exciton scattering, may provide the underlying gain profile in this lasing case.

9.22.3 Strong enhancement of whispering gallery mode quality factors in hexagonal ZnO micro wires

The lasing processes discussed in the previous section are in the WCR, i.e. originating from highly dense charge carrier systems like electron-hole-plasma or exciton-exciton scattering states. To enter the SCR and reach Bose-Einstein condensation of exciton-polaritons and polariton lasing, the threshold charge carrier or rather exciton density for the non-linear phase transition have to be much lower. For that, optical losses and spontaneous emission of excitons have to be reduced considerably, for instance by increasing the quality factor and thus lifetime of the optical modes.

We present an approach to modify the optical mode properties of a hexagonal ZnO MW by placing it between two coplanar distributed Bragg reflectors (DBRs) as sketched in Fig. 9.43 a), thus combining a 1D hexagonal WGM cavitiy with a 2D planar FP cavity. It turned out that the spectral broadening δE of the resonant WGMs is by a factor of about 5 smaller compared to the bare wire. This implies that the quality factor $Q = E/\delta E$ and coherent lifetime [13] of the light in this cavity structure is increased by the same factor.

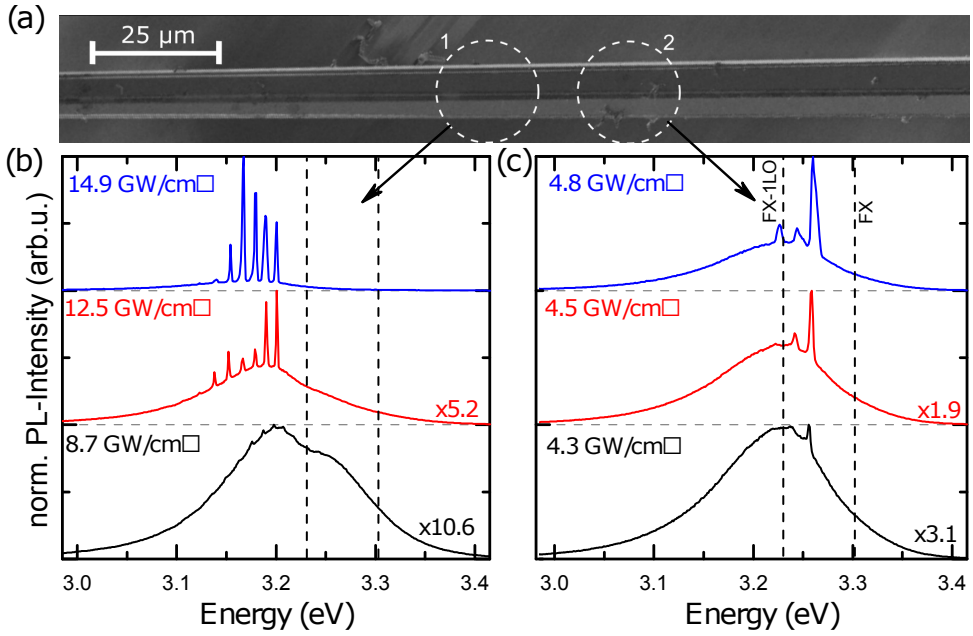

Figure 9.42: (a) Scanning electron microscope (SEM) image of a tapered ZnO microwire (dashed circles mark the investigation positions). Excitation power dependent µ-PL spectra from the clean and particle free position (b) and the particle covered position (c) at 300 K.

The microwire investigated here has a inner radius of $R \sim 0.6\,\mu m$ and a length of half a millimeter. It was placed on top of a bottom DBR, which was grown on a bulk sapphire substrate. Then, a top DBR was mechanically put onto this wire. In this special case, this DBR was priorly grown on a thin (100 µm) MgO substrate which was etched off with phosphoric acid before transferring it to the MW. The top DBR covers only half of the MW length, as shown in Fig. 9.43 b), to allow for investigation of the as grown wire as well as the influence of the coplanar DBR packaging, acting as planar optical cavity for the hexagonal wire.

We performed polarization resolved PL linescans along the wire, crossing the boundary between the region of the pure wire and the region with the wire within the external DBR cavity, as shown in Fig. 9.43 c). Two remarkable changes can be observed by entering the external DBR cavity. On the one hand there is a jump of the spectral position of the resonant modes. On the other hand the spectral width of the modes is reduced by a factor of about 5, as shown in Fig. 9.44 b). By measuring the angular distribution along and perpendicular to the wire axis inside the DBR cavity (cf. Fig. 9.44 a) it becomes clear that the resonant modes are still confined WGM-like. The dotted lines in Fig. 9.44 a) correspond to a WGM model [14] in a ZnO hexagon with an inner radius of $R = 0.601\,\mu m$. This proves that no FPMs are created by the planar external cavity. Furthermore the mode spacing does not change significantly which suggests that there is no change in the type of mode (WGM to FPM).

Bare hexagonal ZnO microwires naturally are good optical cavities as light is confined by total internal reflection (TIR) at the six hexagon facettes. The resulting modes, WGMs, in general exhibit low losses which are connected to corners [15]. Therefore the actual results are suprising at first glance because TIR inhibits by definition the most highest possible reflecivity and an additional mirror would only lower the reflectivity

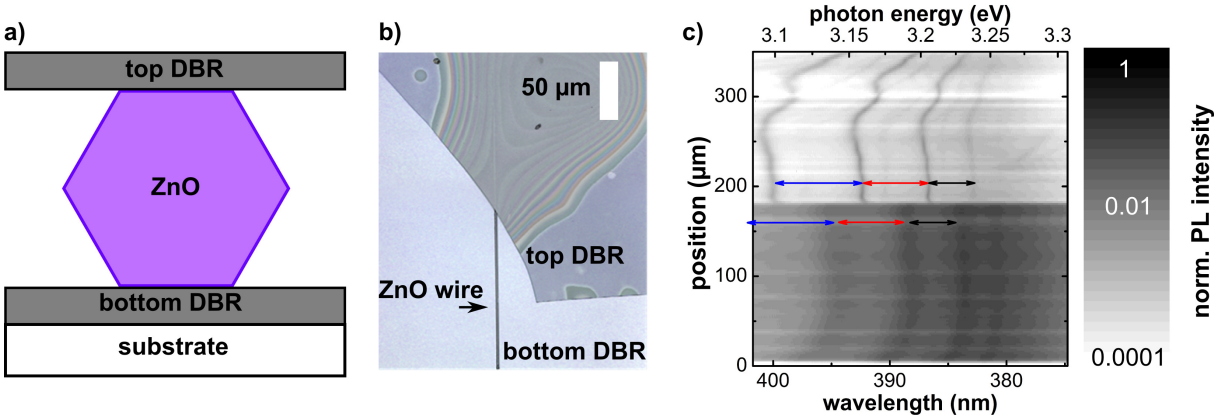

Figure 9.43: a) Cross sectional sketch of the DBR and wire structure. b) Optical top view of the real sample. c) Photoluminescence linescan along the ZnO microwire for TE polaritzation at room temperature displaying only the ground states of the modes. The light gray region represent the covered, the dark gray the uncovered part of the MW. The colored arrows symbolize the similar modespacing for the WGMs inside and outside the DBR cavity.

and therefore the quality factor. When we compare the measured spectral broadenings with the theoretical values, as shown in Fig. 9.44 c), we find for the WGMs outside the DBR cavity values comparable with theory, which is based on a passive cavity material.

An explanation for these extraordinary high quality factors may be found in the following: Excitons couple to the light field and can decay by stimulated (STE) or spontaneous emission (SPE). For SPE most of the photons will leave the wire incoherently through its surface accompanied with a low coherence time and quality factor. But when the wire is located between two DBRs the spontaneous excitonic surface recombination (leaky modes) is strongly reduced via the Purcell effect [16] and STE into the cavity modes (or cavity polariton modes) sets in which leads to a coherent state with high lifetime. Furthermore, this state is fed over a long time range by hot carriers slowly relaxing via incoherent particle-particle scattering processes, and thus photon losses determined by the pure ground state's lifetime are compensated and coherence remains. Therefore, due to the Purcell effect and STE, incoherently scattered polaritons can contribute to the coherent field and therefore increase temporal coherence and quality factor.

9.22.4 Lasing dynamics in ZnO nanowires

In NWs, optical modes are not confined as WGM within the cross section of MWs but are rather FPM confined between the end facets of the NW. As already reported in the last year [2], we have observed stimulated emission from distinct FPM in such ZnO NWs with gain from an electron-hole-plasma in a wide temperature range from 10 K to 300 K [17]. Figure 9.45(a) depicts a scanning electron microscope image of a slightly tapered ZnO nanowire with a diameter ranging from 165 – 190 nm and a length of $L = 7.9$ µm. Figure 9.45(b) shows the emission spectra obtained from a single facet of this ZnO nanowire for several excitation powers at 300 K. The temporal dynamics of the nano laser show a shift to lower energies in the course of time. In the considered time range of 100 ps it is noticeable that the absolute mode shift increases with increasing

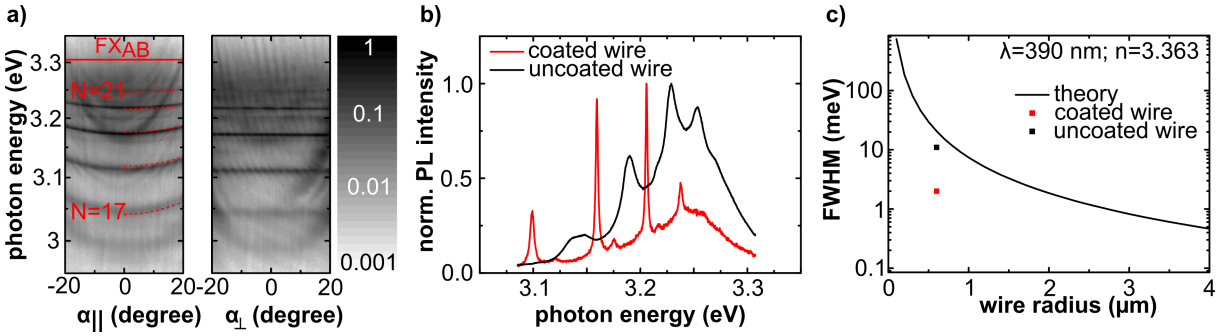

Figure 9.44: a) Angular resolved PL spectra along (left panel) and perpendicular (right panel) to the wire axis for TE polarization. The red line in the left panel shows the spectral position of the free A and B excitonic. The dotted lines represent fits based on a WGM model for a wire with inner radius of $R = 0.601\mu$m. b) Ground state PL spectra from the wire beeing inside (red) and outside (black) the DBR cavity. c) Extracted spectral broadenings compared to the theoretical model.

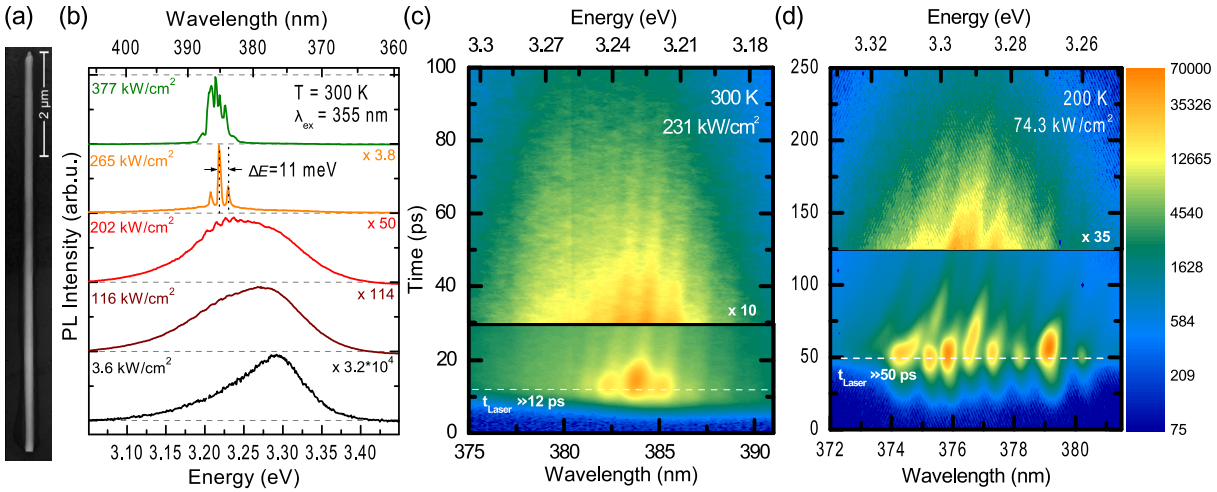

Figure 9.45: (a) Scanning electron microscope image (SEM) of a ZnO nanowire (length 7.9 μm, diameter 165 – 190 nm). (b) The excitation power dependent μ-PL end facet spectra of the respective nanowire at 300 K exhibit a transition from broad spontaneous emission to sharp Fabry-PÃ©rot mode (FPM) emission in the laser regime. Time-resolved PL images at the respective threshold power P_{th} at (c) 300 K and (d) 200 K in logarithmic color scale.

temperature (see Ref. [17]). Figures 9.45(c, d) show exemplary time-resolved images of the nanowire emission at the respective threshold power P_{th} at 300 K and 200 K.

Based on these findings, we have thoroughly investigated the observed temporal red shift of the resonator modes and found that it can be described by the carrier density driven change of the refractive index in time. Therefor we extended an existing model [18] for the calculation of the carrier density dependent complex refractive index for different temperatures. Figure 9.46(a, b) shows the complex refractive index at 300 K and 200 K for carrier densities from 1×10^{16} cm^{-3} to 4×10^{19} cm^{-3}. The model parameters were chosen in such a way, that the calculated data reproduce temperature dependent ellipsometry data [19] in the low carrier density case ($<1\times10^{16}$ cm^{-3}). Furthermore, we calculated the time dependent refractive index after the excitation laser pulse (see Fig. 9.46(c)). The middle graph in Fig. 9.46(c) shows that our model (solid lines) de-

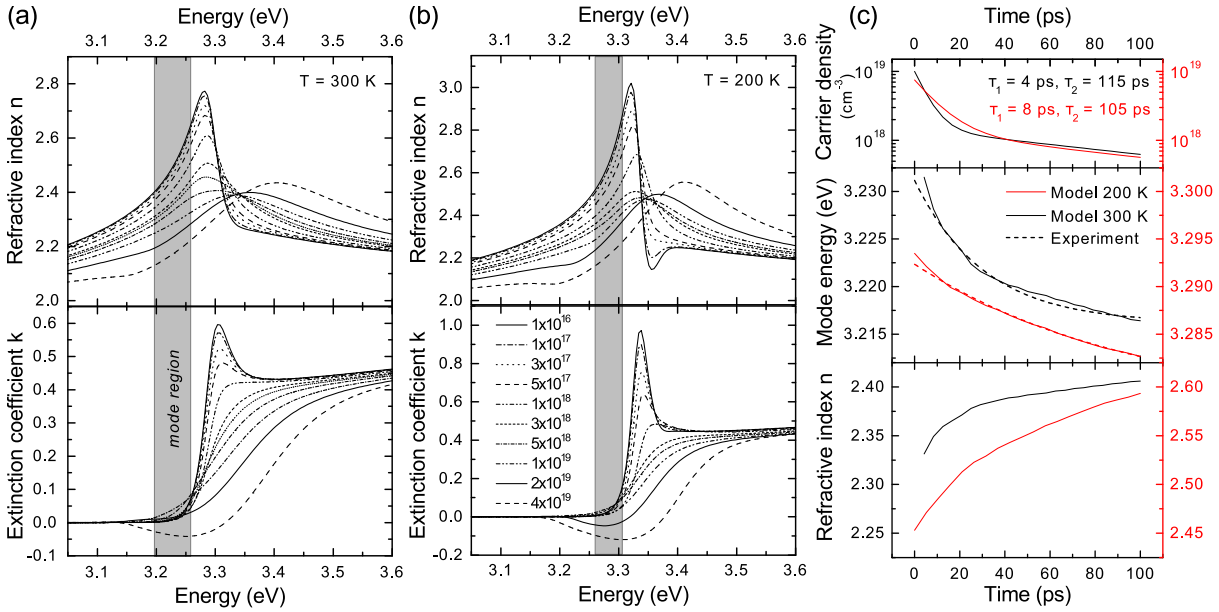

Figure 9.46: Simulation of the complex refractive index of ZnO for carrier densities in the range of $1\times10^{16}-4\times10^{19}$ cm^{-3} at (a) 300 K and (b) 200 K. The grey boxes mark the energy range where modes appear at and above the respective threshold power. (c) Time dependence of the carrier density, the calculated mode energy and the respective refractive index at 200 K (red) and 300 K (black).

scribes the experimentally observed temporal mode shift (dashed lines) quite well for 200 K and 300 K. In the considered time range of 100 ps the calculated refractive index exhibits a continuous increase (see lower graph in Fig. 9.46(c)), whereas the absolute increase of the refractive index at 200 K is larger compared to that at 300 K. At low temperatures the strong dispersion causes a strong change of the refractive index when the carrier density decreases. In this case the mode condition can only be fulfilled in a narrow spectral range resulting in a weakly pronounced mode shift. However, at room temperature the broadening of the exciton resonance causes a weaker change of the refractive index but in a wider spectral range.

9.22.5 Coexistence of strong and weak coupling in a ZnO nanowire cavity

As already reported in the last year [3], coating ZnO NWs with concentric DBR shells (Fig. 9.47) provides much higher optical confinement to enter the SCR as compared to the bare NWs discussed in the previous section and causes a very rich optical mode structure. Applying a simple exciton-photon coupling Hamiltonian taking into account only FPM confined laterally in this structure by the DBRs [8], we could prove the SCR to be present up to room temperature in this high quality two dimensional cavity structure [3]. But the nature of the appearing optical modes was not clear so far. Here we show that the spatial mode distribution allows for the simultaneous appearance of the WCR and SCR even at room temperature.

In order to gain insight into the spatial intensity distribution of resonant modes in our cavity structure, which is a priori not possible to conclude from optical meas-

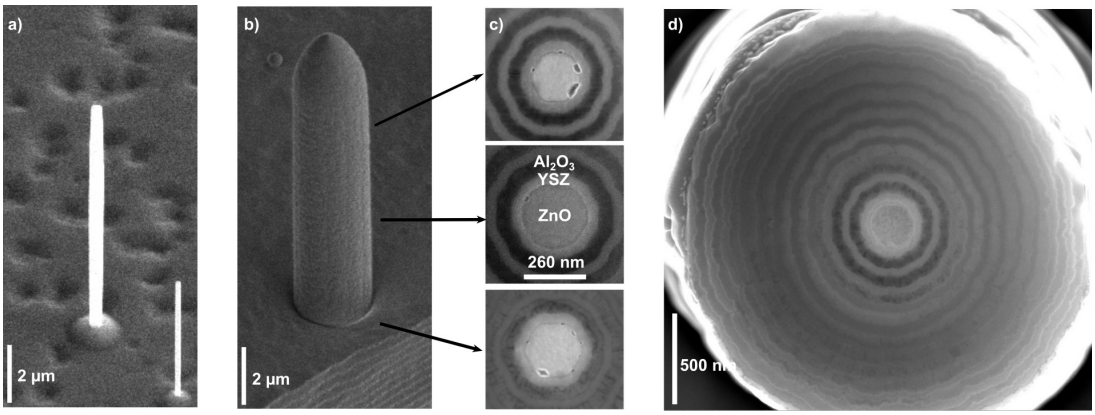

Figure 9.47: a) Scanning electron microscopy image of a bare ZnO nanowire and b) of the whole cavity structure. The images in c) show the center of the cavity and have been taken after cutting the cavity into slices with a focused ion beam. In d) the cross-sectional view of the whole cavity structure is shown.

urements alone, we performed two dimensional finite difference time domain (FDTD) simulations. The detuning between photonic and excitonic resonances, which gives access to their underlying coupling mechanisms, was thereby varied by changing the core wire diameter (~the cavity thickness, experimentally determined to be ~ 260 nm with an almost perfect circular geometry) in the range from 210 nm to 300 nm. As optical constants for our simulations we have chosen the material parameters from $T = 10$ K which were obtained by modelling spectroscopic ellipsometry and reflectivity data.

In the left panel of Fig. 9.48 the simulated resonant mode energies are shown as a function of the core wire diameter. Furthermore some selected field distributions of resonant modes are shown in Fig. 9.48 (right). It is obvious, that the modes do not resemble either WGM nor FPM type field distributions but show mixed character. From the simulated spectra one can clearly identify modes with different core wire thickness dispersions. Modes which cross the excitonic transitions have no spatial overlap with the core wire and its excitons. This defines that these modes are in the WCR [20]. In contrast to that there exist modes showing a clear anticrossing behaviour. These modes are in the SCR [20] and their simulated spatial intensity distribution shows overlap with the core wire. An important fact is, that for $T = 10$ K the simulations predict middle polariton branches (MPBs) between the excitonic A and B resonances. These MPBs are located around 3.38 eV and show almost no dispersion because of the small spectral spacing between the A and B excitons.

Photoluminescence (PL) measurements agree well with the results from the FDTD simulations. Especially, the theoretically predicted middle polariton branches between the A- and B-exciton ground state resonances in ZnO were observed experimentally benefiting from the high quality ZnO core NW. At $T = 10$ K for TE polarization, as shown in Fig. 9.49 b), we can clearly identify three different mode families by their angular dispersion properties. On the one hand, there are modes with a steep dispersion clearly crossing the A and B excitonic ground states. These modes have a energy spacing of $\delta E_{\mathrm{WCR}} \approx 10$ meV. On the other hand, there exist modes (for $\theta = 0°$ at 3.25 eV, 3.29 eV and 3.335 eV) whose dispersions tend to flatten by approaching the excitonic transitions at higher angles. Finally a bright emission band with a nearly flat angular dispersion

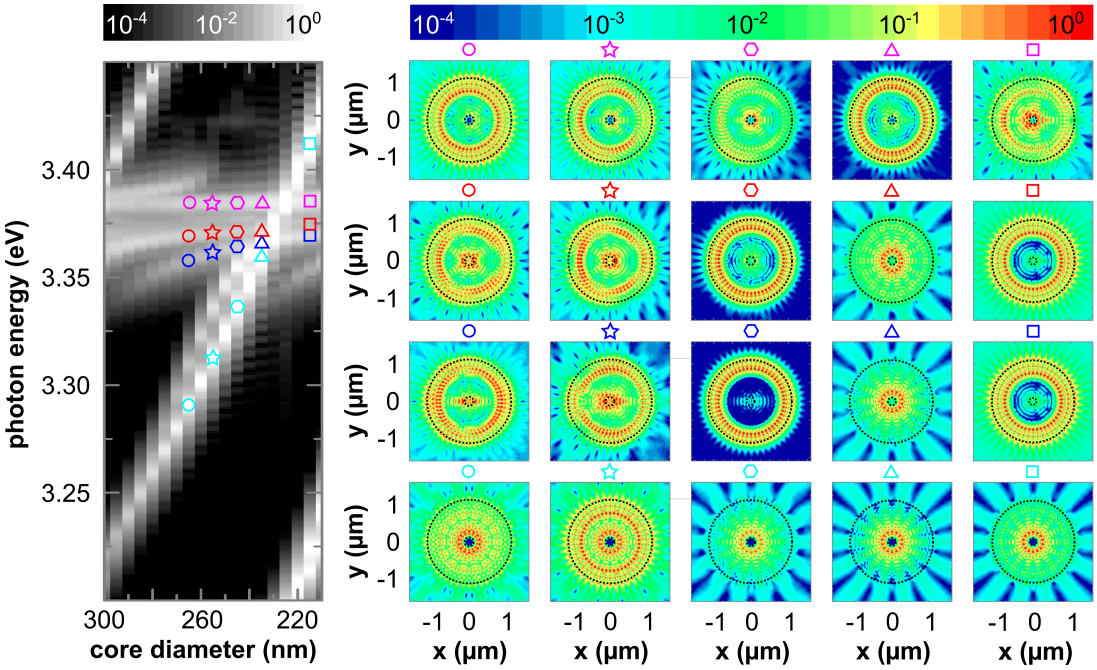

Figure 9.48: FDTD simulations: the left panel shows the resonant mode energies for different ZnO core wire diameters. The image array at the right side includes the spatial intensity distributions for a decreasing core wire diameter (left to right) and for the different modes (bottom to top). The colored symbols indicate the corresponding energy and core wire diameter in the left panel. Each spatial intensity image includes the core wire-DBR and the DBR-air interface as black dotted circles.

can be observed around 3.38 eV, corresponding to the spectral region of the A and B exciton ground state resonances at $T = 10\,\mathrm{K}$ and thus can be ascribed to the MPBs. Please note that the energy of this emission band differs from that of defect bound excitons typically present in ZnO as can be seen from Fig. 9.49 a).

As the dispersion behaviour shows immediately, and as shown by the FDTD simulations, we identify the mode family mentioned firstly to be in the WCR whereas the latter ones can be attributed to be in the SCR. By applying a coupled oscillator model [6] for the modes which are supposed to be in the SCR, including the A and B excitonic ground state energies FX_A and FX_B as well as three uncoupled photonic modes $E_{\mathrm{cav,i}}$ (i = 1, 2, 3), we can reproduce the experimental results very well (see Fig. 9.49 b). Furthermore the temperature evolution of these LPBs up to room temperature (see Fig. 9.49 c)) can be reproduced with the coupled oscillator model proving that the SCR is preserved even at room temperature.

Excitation dependent PL measurements at $T = 10\,\mathrm{K}$ and 10 K, as shown in Fig. 9.50, reveal nonlinear emission behavior. For low temperatures at a threshold power density of $P_\mathrm{th} \approx 100\,\mathrm{kW/cm^2}$ a superlinear increase in emission intensity can be observed in the spectral range below the A and B excitons in combination with the appearance of narrow modes having a spectral spacing of about 10 meV. These modes are almost purely TE polarized and extended over the full observable θ-range. The degree of polarization is $\Pi = (I_\mathrm{TE} - I_\mathrm{TM}) / (I_\mathrm{TE} + I_\mathrm{TM}) = 94\%$. The relatively high threshold power density in combination with the redshift of the underlying gain profile leads to the conclusion that the observed nonlinear phenomena can be explained with the formation of an

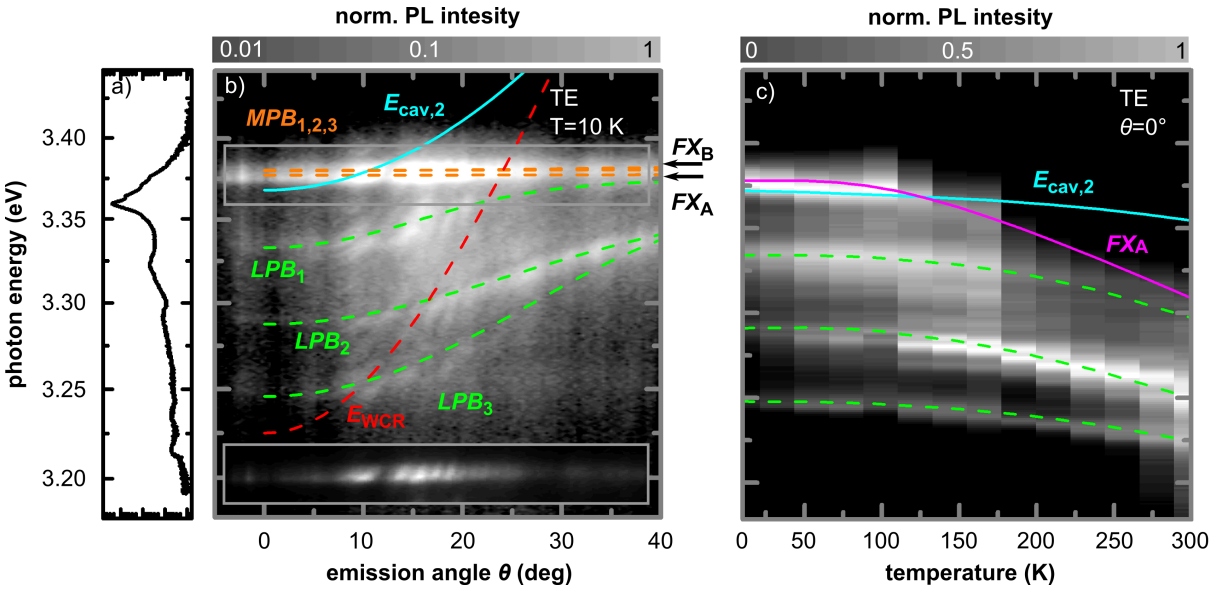

Figure 9.49: Panel a): TE polarized PL spectrum from an uncoated ZnO nanowire at $T = 10$ K. The emission maximum originates from defect bound excitons. In b) an angular resolved PL image at $T = 10$ K is shown. Lower (green lines) and middle (orange lines) polariton branches are modeled which result from the coupling of uncoupled cavity modes (e.g. blue line) with A and B excitons. The red dashed line follows one of the weakly coupled cavity modes. The inset in b) shows the spectral region of the excitons in a linear gray scale for a better visualization of the weakly coupled modes which cross the exciton resonances. Panel c) shows the measured temperature evolution of $\theta = 0°$ PL spectra for TE polarization including the thermal shift of the A exciton (magenta line) together with one uncoupled cavity mode and the modeled LPBs. For each temperature the spectrum was normalized to the maximum intensity for a better visibility.

electron-hole plasma providing gain for stimulated emission out of weakly coupled modes [21]. At room temperature single mode lasing can be observed in a cavity out of the same growing charge as the one described before. Here the threshold power density is found to be $P_{\text{th}} \approx 2000\,\text{kW/cm}^2$. At both temperatures the emission out of the LPBs can still be observed at or above the threshold. This coexistance is caused by the more or less Gaussian intensity distribution of the excitation laser spot profile on the sample. In its center, where the intensity is highest, lasing sets in firstly whereas at the rim of the excitation laser spot the critical density is not reached and polaritons can still exist.

[1] L. Lu *et al.*, Nat. Photonics **8**, 821 (2014), doi:10.1038/nphoton.2014.248
[2] M. Wille *et al.*, The Physics Institutes of Universität Leipzig, Report 2014, M. Grundmann (Ed.), p. 198, Leipzig, 2015, http://nbn-resolving.de/urn:nbn:de:bsz:15-qucosa-177125
[3] H. Franke *et al.*, The Physics Institutes of Universität Leipzig, Report 2014, M. Grundmann (Ed.), p. 199, Leipzig, 2015, http://nbn-resolving.de/urn:nbn:de:bsz:15-qucosa-177125
[4] H. Franke *et al.*, New J. Phys. **14**, 013037 (2012), doi:10.1088/1367-2630/14/1/013037
[5] M. Thunert *et al.*, Phys. Rev. B **93**, 064203 (2016), doi:10.1103/PhysRevB.93.064203
[6] S. Richter *et al.*, Appl. Phys. Lett. **107**, 231104 (2015), doi:10.1063/1.4937462

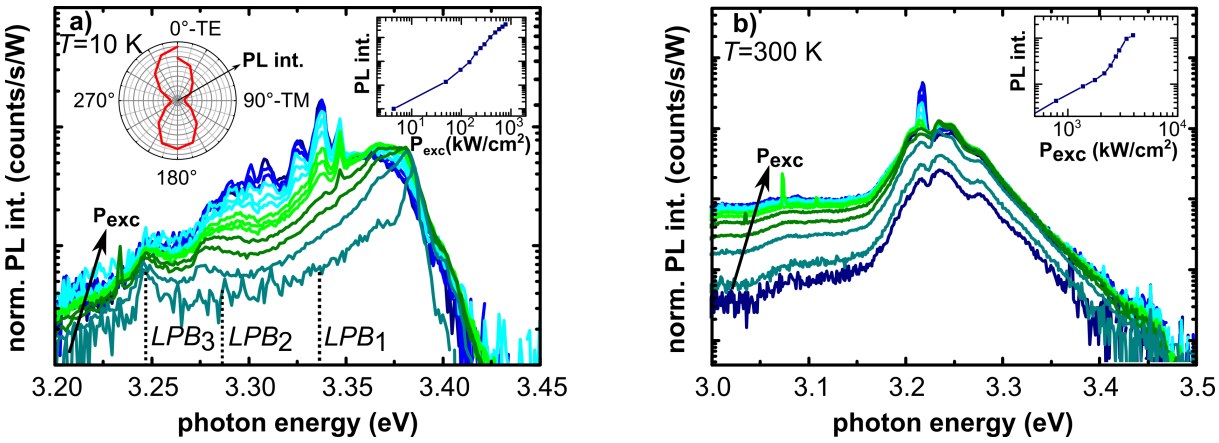

Figure 9.50: Panels a) and b) show excitation power dependent PL spectra for $\theta = 0°$ at10 K and 300 K, respectively. These spectra have been normalized to the applied excitation power density P_{exc} and integration time. The left inset in a) shows exemplarily the linear polarized emission intesity in dependence on the polarization angle. Both panels also include an inset showing the emitted PL intensity vs. excitation power density.

[7] C. Czekalla *et al.*, Phys. Status Solidi B **247**, 1351 (2010), doi:10.1002/pssb.200945527
[8] R. Schmidt-Grund *et al.*, Phys. Status Solidi B **247**, 1351 (2010), doi:10.1002/pssb.200945530
[9] H. Franke, PhD. thesis Uni Leipzig, http://nbn-resolving.de/urn:nbn:de:bsz:15-qucosa-98174
[10] M. Schubert, Phys. Rev. B **53**, 4265 (1996), doi:10.1103/PhysRevB.53.4265
[11] C. Sturm *et al.*, Phys. Rev. B **83**, 205301 (2011), doi:10.1103/PhysRevB.83.205301
[12] E. Krüger: *Lasingprozesse in ZnO Mikrodrähten bei Raumtemperatur*, Universität Leipzig, Bachelorarbeit (2014)
[13] N. Wiener *et al.*, Acta Mathematica **55**, 117 (1930), doi:10.1007/BF02546511
[14] T. Nobis *et al.*, Phys. Rev. Lett. **93**, 103903 (2004), doi:10.1103/PhysRevLett.93.103903
[15] J. Wiersig *et al.*, Phys. Rev. A **67**, 023807 (2003), doi:10.1103/PhysRevA.67.023807
[16] E. M. Purcell, Phys. Rev. **69**, 681 (1946), doi:10.1103/PhysRev.69.674
[17] M. Wille, T. Michalsky, E. Krüger, M. Grundmann, R. Schmidt-Grund, Appl. Phys. Lett. **109**, 061102 (4 pages) (2016)
[18] M. A. Versteegh *et al.* Phys. Rev. B **84**, 035207 (2011), doi:10.1103/PhysRevB.84.035207
[19] C. Bundesmann, R. Schmidt-Grund and M. Schubert, in *Transparent Conductive Zinc Oxide*, p. 79-124 (Springer 2008), doi:10.1007/978-3-540-73612-7
[20] V. Savona *et al.*, Solid State Commun. **93**, 733 (1995), doi:10.1016/0038-1098(94)00865-5
[21] A. Yamamoto *et al.*, State Commun. **122**, 29 (2002), doi:http://dx.doi.org/10.1016/S0038-1098(02)00077-7

9.23 Funding

Leipzig School of Natural Sciences - Building with Molecules and Nano-objects (BuildMoNa)
Prof. Dr. M. Grundmann
DFG GS 185/2

Polarisationswechselwirkung in Laser-MBE Wurtzit-Perowskit-Heterostrukturen
Prof. Dr. M. Lorenz
SFB 762/2-2012, TP A2 within SFB 762 *Funktionalität Oxidischer Grenzflächen*

Optische Untersuchungen zu magneto-elektro-optischen Wechselwirkungen in ihrer Dynamik in oxidischen Heterostrukturen
Dr. Rüdiger Schmidt-Grund
SFB 762/2-2012, TP B03 within SFB 762 *Funktionalität Oxidischer Grenzflächen*

Lateraler Transport in oxidischen Feldeffekt-Strukturen
Dr. H. von Wenckstern, Prof. Dr. M. Grundmann
SFB 762/2-2012, TP B04 within SFB 762 *Funktionalität Oxidischer Grenzflächen*

Spinabhängiges Tunneln in oxidischen Heterostrukturen
Prof. Dr. M. Grundmann, Prof. Dr. I. Mertig (Martin-Luther-Universität Halle-Wittenberg)
SFB 762/2-2012, TP B06 within SFB 762 *Funktionalität Oxidischer Grenzflächen*

Bose-Einstein-Kondensation und Supraflüssigkeit von Exziton-Polaritonen bei Raumtemperatur
Prof. Dr. M. Grundmann, Dr. R. Schmidt-Grund
DFG GR 1011/20-2

Extrem verzerrte Nano- und Mikrodrähte
Prof. Dr. M. Grundmann
DFG GR 1011/23-1

Quantum Gases and Liquids in Semiconductor Rods conformally coated with Bragg Mirrors
Dr. R. Schmidt-Grund, Prof. Dr. M. Grundmann
DFG SCHM 2710/2-1, SCHM 2710/2-2, TP P1 within FOR 1616 *Dynamics and Interactions of Semiconductor Nanowires for Optoelectronics*

Whispering Gallery Moden: Einfluss der Resonatorform auf Lasing-Eigenschaften
Prof. Dr. M. Grundmann
DFG GR 1011/26-1

Amorphe Spinelle als p-Typ Halbleiter
Prof. Dr. M. Grundmann
DFG GR 1011/27-1

Cupferiodid: Epitaxie, Dioden und Ferromagnetismus
Prof. Dr. M. Grundmann
DFG GR 1011/28-1

Dioden auf der Basis von MBE und MoVPE oxid-Dünnfilmen
Prof. Dr. M. Grundmann
DFG GR 1011/30-1

Flexible analoge und digitale Grundschaltungen in amorphen Metalloxiden
Prof. Dr. M. Grundmann
DFG GR 1011/31-1, within SPP *High Frequency Flexible Bendable Electronics for Wireless Communication Systems (FFLexCom)*

Graduiertenschule: Wolken, Aerosole und Strahlung am Beispiel des Mineralstaubes
Prof. Dr. M. Grundmann, Prof. Dr. A. Macke (Leibniz-Institut für Troposphärenforschung e. V.)
SAW-2012-IfT-4

3D in situ Ellipsometrie
Dr. R. Schmidt-Grund, Dr. C. Bundesmann (Leibniz-Institut für Oberflächenmodifizierung e. V.)
Forschungs- und Entwicklungsvertrag im Rahmen der Förderung aus dem Europäischen Sozialfonds

Transparente MESFET für digitale Anwendungen
Prof. Dr. M. Grundmann, Dr. H. Frenzel
BMBF 03V0509

SolarSens: Herstellung von wellenlängenselektiven DUV-Photoelektroden, Dr. H. von Wenckstern
BMBF 01DR15008

High-resolution fingerprint sensing with piezoelectric nanowire matrices: PiezoMat
Prof. Dr. M. Grundmann
European Union, Seventh Framework Programme 611019

LOMID - Large cost-effective OLED microdisplays and their applications
Prof. Dr. M. Grundmann, Dr. H. von Wenckstern
European Union, Horizon 2020 644101

PPP Spanien: Kohärenzeigenschaften kondensierter Exziton-Polaritonen
Dr. R. Schmidt-Grund
DAAD 57050448

9.24 Organizational Duties

M. Grundmann

- Prodekan Forschung der Fakultät für Physik und Geowissenschaften
- Direktor des Instituts für Experimentelle Physik II
- Stellvertretender Sprecher der Graduiertenschule "Leipzig School of Natural Sciences - Building with Molecules and Nano-objects" (BuildMoNa), http://www. buildmona.de

- Stellvertretender Sprecher des Sonderforschungsbereiches "Funktionalität Oxidischer Grenzflächen" (SFB762), http://www.physik.uni-halle.de/sfb762
- Stellvertretender Sprecher der Forschergruppe FOR 1616, http://www.for1616.uni-jena.de
- Sprecher der Fächerübergreifenden Arbeitsgemeinschaft Halbleiterforschung Leipzig (FAHL), http://www.uni-leipzig.de/~fahl
- Mitglied des wissenschaftlichen Beirats des Leibniz-Instituts für Oberflächenmodifizierung e. V., Leipzig (IOM)
- Organizer MRS Fall Meeting, Boston, Symposium "Oxide Semiconductors"
- Member Editorial Board: Physica Status Solidi (a), (b), RRL
- Member International Advising Board: Advanced Electronic Materials
- Project Reviewer: Deutsche Forschungsgemeinschaft (DFG), Alexander von Humboldt-Stiftung (AvH), Schweizerischer Nationalfonds zur Förderung der wissenschaftlichen Forschung (FNSNF), Fonds zur Förderung der Wissenschaften (FWF), EU, Österreichische Forschungsförderungsgesellschaft mbH (FFG), Agence Nationale de la Recherche (ANR, France)
- Referee: Applied PhysPhysics Letters, Electronics Letters, Journal of Applied Physics, Nature, Physica E, Physical Review B., Physical Review Letters, Physica Status Solidi, Advanced Materials, u.a.

M. Lorenz

- Editorial Board Member Journal of Physics D: Applied Physics (IOP, Bristol, U.K.)
- Project referee: Deutsche Forschungsgemeinschaft (DFG), Sächsisches Staatsministerium für Wissenschaft und Kunst (SMWK)
- Referee: ACS Applied Materials Interfaces, Advanced Materials, Advanced Functional Materials, Applied Physics Letters, Chemical Physics Letters, Crystal Growth and Design, IEEE Photonics Technology Letters, Journal of the American Ceramic Society, Journal of Applied Physics, Journal of Materials Chemistry C, Journal of Physical Chemistry, Journal of Physics D: Applied Physics, Journal of Solid State Chemistry, Journal of Vacuum Science and Technology A, Physica Status Solidi C, Physica Statur Solidi Rapid Research Letters, Thin Solid Films

H. von Wenckstern

- Project Reviewer: U.S. Department of Energy – Office of Science, National Research Fondation RSA
- Referee: Applied Physical Letters, Journal of Applied Physics, Thin Solid Films, Solid State Electronics, Physica Status Solidi, Journal of Electronic Materials, Turk. Journal of Physics, Journal of Material Sciences, u.a.

R. Schmidt-Grund

- Vice Chair of the German Association on Ellipsometry (Arbeitskreis Ellipsometrie – Paul Drude e.V.)
- Project Reviewer: Deutsche Forschungsgemeinschaft (DFG), US Department of Energy – Office of Science
- Referee: Thin Solid Films, Current Applied Physics, Physica Status Solidi C, Nature Communications, Applied Physics Letters, Optics Express, Journal of Electromagnetic Waves and Applications, Optical Materials, ACS Applied Materials & Interfaces

H. Frenzel

- Referee: IEEE Electronic Device Letters, Thin Solid Films, Applied Physics Letters, ETRI Journal, Journal of Applied Physics, Japanese Journal of Applied Physics, Advanced Materials, Physica Status Solidi (a)

9.25 External Cooperations

Academic

- Leibniz-Institut für Oberflächenmodifizierung e. V., Leipzig, Germany
  Prof. Dr. B. Rauschenbach, Prof. Dr. S. Mayr, Dr. J. Gerlach, Dr. C. Bundesmann, Dr. A. Lotnyk
- Universität Leipzig, Fakultät für Chemie und Mineralogie, Germany
  Prof. Dr. H. Krautscheid, Prof. Dr. R. Denecke
- Universität Halle-Wittenberg, Germany
  Prof. Dr. I. Mertig, Prof. Dr. W. Widdra, Prof. Dr. S.G. Ebbinghaus, Prof. Dr. W. Hergert
- Max-Planck-Institut für Mikrostrukturphysik, Halle/Saale, Germany
  Dr. O. Breitenstein, Dr. A. Ernst, Dr. P. Werner, Prof. Dr. D. Hesse
- Forschungszentrum Dresden-Rossendorf, Germany
  Prof. Dr. M. Helm, Dr. K. Potzger
- Technische Universität Berlin, Germany
  Prof. Dr. D. Bimberg, Prof. Dr. A. Hoffmann
- University of Aveiro, Portugal
  Prof. N. A. Sobolev
- Universität Magdeburg, Germany
  Dr. J. Bläsing, Prof. Dr. J. Christen
- Universität Jena, Germany
  Prof. Dr. C. Ronning
- University of Pretoria, South Africa
  Prof. F. D. Auret
- University of Canterbury, Christchurch, New Zealand
  Prof. Dr. M. Allen
- Centre de Recherche sur l' Hétéro-Epitaxie et ses Applications (CNRS-CRHEA), Valbonne, France
  Dr. J. Zúñiga-Pérez, Dr. G- Feuillet
- Western Michigan University, USA
  Prof. Dr. S. M. Durbin
- Katholieke Universiteit Leuven, Belgium
  Dr. V. Lazenka, Prof. Dr. K. Temst

Industry

- Freiberger Compound Materials GmbH, Freiberg, Germany
  Dr. G. Leibiger
- Volkswagen AG, Wolfsburg, Germany
  Matthias Overhoff

9.26 Publications

Journals

R. Böttcher, M. Lorenz, A. Pöppl, D. Spemann, M. Grundmann: *Local zinc blende coordination in heteroepitaxial wurtzite $Zn_{1-x}Mg_xO$: Mn thin films with $0.01 \leq x \leq 0.04$ identified by electron paramagnetic resonance*, J. Mat. Chem. C **3**, 11918-11929 (2015)

C. Bundesmann, R. Feder, R. Wunderlich, U. Teschner, M. Grundmann, B. Rauschenbach, H. Neumann: *Ion beam sputter deposition of Ge films: Influence of process parameters on film properties*, Thin Solid Films **589**, 487-492 (2015)

A. de Pablos-Martin, M. Ebert, C. Patzig, M. Krause, M. Dyrba, P. Miclea, M. Lorenz, M. Grundmann, Th. Höche: *Laser Welding of Sapphire Wafers Using a Thin-Film Fresnoite Glass Solder*, Microsyst. Technol. **21**(5), 1035-1045 (2015)

C.P. Dietrich, R. Johne, T. Michalsky, C. Sturm, P. Eastham, H. Franke, M. Lange, M. Grundmann, R. Schmidt-Grund: *Parametric relaxation in whispering-gallery mode exciton-polariton condensates*, Phys. Rev. B **91**, 041202(R) (6 pages) (2015)

C.P. Dietrich, R. Schmidt-Grund, T. Michalsky, M. Lange, M. Grundmann: *Room-temperature condensation in whispering gallery microresonators assisted by longitudinal optical phonons*, arxiv: **1501.01255** (11 pages) (2015)

S.F. Fischer, M. Grundmann: *Semiconductor Functional Oxides*, Semic. Sci. Technol. **30**(2), 020301 (2 pages) (2015)

H. Frenzel, T. Dörfler, P. Schlupp, H. von Wenckstern, M. Grundmann: *Long-throw magnetron sputtering of amorphous Zn-Sn-O-thin films at room temperature*, phys. stat. sol. (a) **212**(7), 1482-1486 (2015)

M. Grundmann: *Karl Bädeker (1877-1914) and the discovery of transparent conductive materials*, phys. stat. sol. (a) **212**(7), 1409-1426 (2015)

M. Grundmann: *Theory of Semiconductor Solid and Hollow Nano- and Microwires With Hexagonal Cross-Section Under Torsion*, phys. stat. sol. (b) **252**, 773-785 (2015)

M. Grundmann, A. Rahm, H. von Wenckstern: *Transparent Conductive Oxides – Preface*, phys. stat. sol. (a) **212**(7), 1408 (1 page) (2015)

M. Jenderka, R. Schmidt-Grund, M. Grundmann, M. Lorenz: *Electronic excitations and structure of Li_2IrO_3 thin films grown on ZrO_2:Y (001) substrates*, J. Appl. Phys. **117**, 025304 (5 pages) (2015)

R. Karsthof, H. von Wenckstern, M. Grundmann: *Transparent JFETs based on p-NiO/n-ZnO heterojunctions*, IEEE Transact. Electr. Dev. **62**(12), 3999-4003 (2015)

F.J. Klüpfel, H. von Wenckstern, M. Grundmann: *Low Frequency Noise of ZnO based MESFETs*, Appl. Phys. Lett. **106**, 033502 (4 pages) (2015)

F.J. Klüpfel, A. Holtz, F.-L. Schein, H. von Wenckstern, M. Grundmann: *All-Oxide Inverters Based On ZnO channel JFETs with amorphous $ZnCo_2O_4$ gates*, IEEE Transact. Electr. Dev. **62**(12), 4004-4008 (2015)

C. Kranert, R. Schmidt-Grund, M. Grundmann: *Free charge carriers as origin for redshift of LO modes in wurtzite semiconductors excited above the band gap*, J. Raman Spectr. **46**, 167-170 (2015)

C. Kranert, M. Jenderka, J. Lenzner, M. Lorenz, H. von Wenckstern, R. Schmidt-Grund, M. Grundmann: *Lattice parameters and Raman-active phonon modes of ß-$(Al_xGa_{1-x})_2O_3$*, J. Appl. Phys. **117**, 125703 (6 pages) (2015)

V. Lazenka, M. Lorenz, H. Modarresi, M. Bisht, R. Rüffer, M. Bonholzer, M. Grundmann, M.J. Van Bael, A. Vantomme, K. Temst: *Magnetic spin structure and magnetoelectric coupling in $BiFeO_3$-$BaTiO_3$ multilayer*, Appl. Phys. Lett. **106**, 082904 (4 pages) (2015)

M. Lorenz, H. Hochmuth, M. Kneiß, M. Bonholzer, M. Jenderka, M. Grundmann: *From high-T_C superconductors to highly correlated Mott insulators - 25 years of pulsed laser deposition of functional oxides in Leipzig*, Semic. Sci. Technol. **30**, 024003 (10 pages) (2015)

M. Lorenz, T. Weiss, F. Schmidt, H. von Wenckstern, M. Grundmann: *Aluminium- and gallium-doped homoepitaxial ZnO thin films: Strain-engineering and electrical performance*, phys. stat. sol. (a) **212**(7), 1440-1447 (2015)

M. Lorenz, G. Wagner, V. Lazenka, P. Schwinkendorf, H. Modarresi, M.J. Van Bael, A. Vantomme, K. Temst, O. Oeckler, M. Grundmann: *Correlation of magnetoelectric coupling in multiferroic $BaTiO_3$-$BiFeO_3$ superlattices with oxygen vacancies and antiphase octahedral rotations*, Appl. Phys. Lett. **106**, 012905 (5 pages) (2015)

I. Lorite, C. Zandalazini, P. Esquinazi, D. Spemann, S. Friedländer, A. Pöppl, T. Michalsky, M. Grundmann, J. Vogt, J. Meijer, S.P. Heluani, H. Ohldag, W.A. Adeagbo, S.K. Nayak, W. Hergert, A. Ernst, M. Hoffmann: *Study of the Negative Magneto-Resistance of Single Proton-Implanted Lithium-Doped ZnO Microwires*, J. Phys.: Condens. Matter **27**, 256002 (6 pages) (2015)

I. Lorite, C. Zandalazini, P. Esquinazi, D. Spemann, S. Friedländer, A. Pöppl, T. Michalsky, M. Grundmann, J. Vogt, J. Meijer, S.P. Heluani, H. Ohldag, W.A. Adeagbo, S.K. Nayak, W. Hergert, A. Ernst, M. Hoffmann: *Study of the Negative Magneto-Resistance of Single Proton-Implanted Lithium-Doped ZnO Microwires*, arxiv: **1504.08230** (2015)

T. Michalsky, H. Franke, C. Sturm, M. Grundmann, R. Schmidt-Grund: *Discrete relaxation of exciton-polaritons in an inhomogeneous potential*, arxiv: **1501.02644** (2015)

S. Müller, H. von Wenckstern, F. Schmidt, D. Splith, F.-L. Schein, H. Frenzel, M. Grundmann: *Comparison of Schottky contacts on β-gallium oxide thin films and bulk crystals*, Appl. Phys. Expr. **8**, 121102 (4 pages) (2015)

D. Poppitz, A. Lotnyk, J.W. Gerlach, J. Lenzner, M. Grundmann, B. Rauschenbach: *An aberration-corrected STEM study of structural defects in epitaxial GaN thin films grown by ion beam assisted MBE*, Micron **73**, 1-8 (2015)

S. Puttnins, M.S. Hammer, J. Neerken, I.Riedel, F. Daume, A. Rahm, A.Braun, M. Grundmann, T. Unold: *Impact of Sodium on the Device Characteristics of Low Temperature-Deposited CIGSe-Solar Cells*, Thin Solid Films **582**, 85-90 (2015)

S. Richter, S.G. Ebbinghaus, M. Grundmann, R. Schmidt-Grund: *Antiferromagnetic phase transition in the temperature-dependent NIR-VUV dielectric function of hexagonal $YMnO_3$*, arxiv: **1503.04043** (2015)

S. Richter, T. Michalsky, L. Fricke, C. Sturm, H. Franke, M. Grundmann, R. Schmidt-Grund: *Maxwell consideration of polaritonic quasi-particle Hamiltonians in multi-level systems*, Appl. Phys. Lett. **107**, 231104 (5 pages) (2015)

R. Schewski, G. Wagner, M. Baldini, D. Gogova, Z. Galazka, T. Schulz, T. Remmele, T. Markurt, H. von Wenckstern, M. Grundmann, O. Bierwagen, P. Vogt, M. Albrecht: *Epitaxial stabilization of pseudomorphic α-Ga_2O_3 on sapphire (0001)*, Appl. Phys. Expr. **8**, 011101 (4 pages) (2015)

P. Schlupp, F.-L. Schein, H. von Wenckstern, M. Grundmann: *All Amorphous Oxide Bipolar Heterojunction Diodes from Abundant Metals*, Adv. Electr. Mater. **1**(1-2), 1400023 (5 pages) (2015)

F. Schmidt, D. Splith, S. Müller, H. von Wenckstern, M. Grundmann: *Electronic defects in In_2O_3 and In_2O_3:Mg thin films on r-plane sapphire*, phys. stat. sol. (b) **252**(10), 2304-2308 (2015)

R. Schmidt-Grund, C. Kranert, H. von Wenckstern, V. Zviagin, M. Grundmann: *Dielectric function in the spectral range (0.5-8.5)eV of an $(Al_xGa_{1-x})_2O_3$ thin film with continuous composition spread*, J. Appl. Phys. **117**, 165307 (7 pages) (2015)

S. Schubert, F. Schmidt, H. von Wenckstern, M. Grundmann, K. Leo, L. Müller-Meskamp: *Eclipse Pulsed Laser Deposition for Damage-Free Preparation of Transparent ZnO Electrodes on Top of Organic Solar Cells*, Adv. Funct. Mater. **25**(27), 4321-4327 (2015)

C. Sturm, J. Furthmüller, F. Bechstedt, R. Schmidt-Grund, M. Grundmann: *Dielectric tensor of monoclinic Ga_2O_3 single crystals in the spectral range 0.5-8.5eV*, arxiv: **1507.05401** (2015)

C. Sturm, J. Furthmüller, F. Bechstedt, R. Schmidt-Grund, M. Grundmann: *Dielectric tensor of monoclinic Ga_2O_3 single crystals in the spectral range 0.5-8.5eV*, APL Mater. **3**, 106106 (9 pages) (2015)

H. von Wenckstern, D. Splith, M. Purfürst, Z. Zhang, C. Kranert, S. Müller, M. Lorenz, M. Grundmann: *Structural and optical properties of $(In,Ga)_2O_3$ thin films and characteristics of Schottky contacts thereon*, Semic. Sci. Technol. **30**, 024005 (7 pages) (2015)

H. von Wenckstern, D. Splith, S. Lanzinger, F. Schmidt, S. Müller, P. Schlupp, R. Karsthof, M. Grundmann: *pn-heterodiodes with n-type In_2O_3*, Adv. Electr. Mater. **1**(4), 1400026 (6 pages) (2015)

H. von Wenckstern, D. Splith, A. Werner, S. Müller, M. Lorenz, M. Grundmann: *Properties of Schottky barrier diodes on $(In_xGa_{1-x})_2O_3$ for $0.01 \leq x \leq 0.85$ determined by using a combinatorial approach*, ACS Comb. Sci. **17**(12), 710-715 (2015)

H. Wei, M. Jenderka, M. Grundmann, M. Lorenz: *$LaNiO_3$ films with tunable out-of-plane lattice parameter and their strain-related electrical properties*, phys. stat. sol. (a) **212**(9), 1925-1930 (2015)

H. Wei, M. Jenderka, M. Bonholzer, M. Grundmann, M. Lorenz: *Modeling the conductivity around the dimensionality-controlled metal-insulator transition in $LaNiO_3/LaAlO_3$ (100) superlattices*, Appl. Phys. Lett. **106**, 042103 (5 pages) (2015)

V. Zviagin, P. Richter, T. Böntgen, M. Lorenz, M. Ziese, D.R.T. Zahn, G. Salvan, M. Grundmann, R. Schmidt-Grund: *Comparative Study of Optical and Magneto-Optical Properties of Normal, Disordered and Inverse Spinel Type Oxides*, phys. stat. sol. (b), published online (2015)

V. Zviagin, P. Richter, T. Böntgen, M. Lorenz, M. Ziese, D.R.T. Zahn, G. Salvan, M. Grundmann, R. Schmidt-Grund: *Comparative Study of Optical and Magneto-Optical Properties of Normal, Disordered and Inverse Spinel Type Oxides*, arxiv: **1505.04664** (2015)

Talks

M. Grundmann: *Oxide Epitaxy, Transparent Electronics and Oxide Nanostructures*, Materials Seminar, CRHEA (CNRS), Valbonne, France, January 2015 (invited)

M. Grundmann: *The (non-Quantum) Hall-Effect: Well-Known Facts and (maybe) Surprises*, Materials Seminar, CRHEA (CNRS), Valbonne, France, May 2015 (invited)

M. Grundmann: *Oxide Diodes from Earth Abundant Materials*, 8th International Conference on Materials and Advanced Technologies of the Materials Research Society of Singapore (ICMAT 2015), Symposium "Earth Abundant Materials for Solar Energy Harvesting", Singapore, B3-3, July 2015 (invited)

M. Grundmann: *Realization of close-to-ideal pn-diodes using oxide semiconductors*, Binghamton University, Binghampton, NY, USA, July 2015 (invited)

O. Herrfurth, T. Michalsky, H. Franke, C. Sturm, R. Schmidt-Grund, M. Grundmann: *Excition-polariton relaxation in a* ZnO*-based microresonator*, DPG spring meeting, Berlin, Germany, March 2015

M. Jenderka, M. Lorenz: *Sodium and lithium iridate thin films grown by pulsed laser deposition*, Leibnitz Institute for Solid State Research (IWF), Dresden, Germany, June 2015

C. Kranert, M. Jenderka, J. Lenzner, M. Lorenz, H. v. Wenckstern, R. Schmidt-Grund, M. Grundmann: *Structural properties and phonon modes of* $(Al_xGa_{1-x})_2O_3$, DPG spring meeting, Berlin, Germany, March 2015

M. Lorenz, V. Lazenka: *Correlation of magnetoelectric coupling in multiferroic $BaTiO_3$-$BiFeO_3$ composite thin films with ordering of oxygen-related defects*, E-MRS Spring Meeting 2015 Lille, France, May 2015 (invited)

M. Lorenz, A. Pöppl, S. Friedländer, D. Spemann, R. Böttcher, M. Grundmann: *Nearest-neighbour Lattice Distortions in Oxygen-deficient ZnO and $Zn_{1-x}Mg_xO$ Thin Films, probed by Electron Paramagnetic Resonance*, 17th International Conference on II-VI Compounds and Related Materials, Paris, France, September 2015

A. Mavlonov, S. Richter, H. von Wenckstern, R. Schmidt-Grund, M. Lorenz, M. Grundmann: *The influence of Al and Ga dopants on the structural, electrical and optical properties of (Mg,Zn)O thin films grown by PLD*, DPG spring meeting, Berlin, Germany, March 2015

T. Michalsky, H. Franke, R. Schmidt-Grund, M. Grundmann: *Strong light-matter interaction in* ZnO *nanowires concentrically coated with Bragg reflectors*, DPG spring meeting, Berlin, Germany, March 2015

T. Michalsky, H. Franke, R. Buschlinger, R. Schmidt-Grund, U. Peschel, M. Grundmann: *Strong light-matter interaction in* ZnO *nanowires concentrically coated with Bragg reflectors*, Annual Conference of the Graduate School BuildMoNa, Leipzig, Germany, March 2015

T. Michalsky, M. Wille, R. Buschlinger, H. Franke, U. Peschel, M. Grundmann, R. Schmidt-Grund: *Light-matter interaction in* ZnO *based nano-and microwire cavities*, FOR1616 - project meeting, Jena, Germany, October 2015

A. Reinhardt, H. Frenzel, H. von Wenckstern, M. Grundmann: *Annealing efects on electrical properties of room-temperature deposited zinc oxynitride thin flms*, DPG spring meeting, Berlin, Germany, March 2015

A. Reinhardt, H. Frenzel, H. von Wenckstern, M. Grundmann: *Electrical and optical properties of long-throw magnetron sputtered zinc oxynitride thin films*, 26th International Conference on Amorphous and Nanocrystalline Semiconductors, Aachen, Germany, September 2015

S. Richter, R. Schmidt-Grund, C. Bundesmann, S.G. Ebbinghaus, M. Grundmann: *Temperature dependent dielectric function of hexagonal* $YMnO_3$, 9th Workshop Ellipsometry, Twente, Netherlands, March 2015

R. Schmidt-Grund: *Light-matter interaction in wire cavities – from Purcell effect to Bose-Einstein condensates*, DPG spring meeting, Berlin, Germany, March 2015 (invited)

P. Schlupp, H. von Wenckstern, M. Grundmann: *Room temperature fabricated amorphous oxide heterodiodes on glass and flexible substrates*, Annual BuildMoNa Conference, Leipzig, Germany, March 2015

P. Schlupp, H. von Wenckstern, M. Grundmann: *Room temperature fabricated amorphous oxide heterodiodes on glass and flexible substrates*, DPG spring meeting, Berlin, Germany, March 2015

P. Schlupp, H. von Wenckstern, M. Grundmann: *Room temperature fabricated amorphous oxide heterodiodes on glass and flexible substrates*, Electronic Materials Conference, Columbus (Ohio), USA, June 2015

P. Schlupp, S. Bitter, F.-L. Schein, H. von Wenckstern, M. Grundmann: *Room temperature fabricated unipolar and bipolar diodes comprising amorphous zinc tin oxide*, Conducting Oxide Semiconductors Workshop, Berlin, Germany, November 2015

R. Schmidt-Grund, C. Sturm, C. Kranert, H. Krauß, H. von Wenckstern, M. Bonholzer, J. Lenzner, M. Grundmann: *NIR-VUV dielectric function of* $(Al, In, Ga)_2O_3$ *thin films*, 9th Workshop Ellipsometry, Twente, Netherlands, March 2015

R. Schmidt-Grund: *Exciton-Polariton Bose-Einstein Condensates and Quantum Fluids - Fundamental Physics and Applications*, Lecture at DIADEMS Autumn School, Universität Leipzig, Germany, September 2015

R. Schmidt-Grund: *Halbleiter-Photonik - LEDs, Laser, Quantenemitter*, Lecture at 40. Fortbildungsveranstaltung für Physiklehrer/innen, Universität Bayreuth, Germany, October 2015

A Shkurmanov, C. Sturm, H. Franke, H. Hochmuth, M. Grundmann: *Low temperature PLD-growth of ZnO nanowires on* $Al_xZn_{1-x}O$ *films*, DPG spring meeting, Berlin, Germany, March 2015

D. Splith, F. Schmidt, S. Lanzinger, S. Müller, H. von Wenckstern, M. Grundmann: *Schottky contacts and pn-heterojunctions on heteroepitaxial* In_2O_3 *thin films grown by pulsed laser deposition*, DPG spring meeting, Berlin, Germany, March 2015

D. Splith, F. Schmidt, S. Lanzinger, S. Müller, H. von Wenckstern, M. Grundmann: *Schottky contacts and pn-heterojunctions on heteroepitaxial* In_2O_3 *thin films grown by pulsed laser deposition*, Annual Conference of the Graduate School BuildMoNa, Leipzig, Germany, March 2015

D. Splith, F. Schmidt, S. Lanzinger, S. Müller, H. von Wenckstern, M. Grundmann: *Schottky contacts and pn-heterojunctions on heteroepitaxial* In_2O_3 *thin films*, Graduate Student Workshop on Transparent Conducting Oxide Semiconductors, Berlin, Germany, November 2015

V. Zviagin, P. Richter, T. Böntgen, M. Lorenz, M. Ziese, D.R.T. Zahn, G. Salvan, R. Schmidt-Grund, M. Grundmann: *Optical and Magneto-Optical Investigation of Spinel Oxide Thin Films*, DPG spring meeting, Berlin, Germany, March 2015

Posters

S. Bitter, P. Schlupp, H. Frenzel, H. von Wenckstern, M. Grundmann: *Continuous composition spread method for amorphous zinc-tin-oxide*, DPG spring meeting, Berlin, Germany, March 2015

M. Bonholzer, K. Brachwitz, M. Lorenz, M. Grundmann: *Zinc ferrite based magnetic tunnel junctions*, DPG spring meeting, Berlin, Germany, March 2015

H. Frenzel, T. Dörfler, P. Schlupp, A. Reinhardt, H. von Wenckstern, M. Grundmann: *Long-throw magnetron sputtering of amorphous Zn-Sn-O thin films*, 11th International Thin-Film Transistor Conference, Rennes, Frankreich, February 2015

L. Fricke, C. Bundesmann, R. Fechner, M. Burkhardt, M. Helgert, A. Gatto, F. Frost, C. Sturm, R. Schmidt-Grund, M. Grundmann: *Mueller-Matrix-ellipsometry analysis of blazed gratings produced by reactive ion beam etching*, DPG spring meeting, Berlin, Germany, March 2015

L. Fricke, C. Bundesmann, R. Fechner, M. Burkhardt, M. Helgert, A. Gatto, F. Frost, C. Sturm, R. Schmidt-Grund, M. Grundmann: *Mueller-Matrix-ellipsometry analysis of blazed gratings produced by reactive ion beam etching*, 9th Workshop Ellipsometry, Twente, Netherlands, March 2015

A. Holm, M. Thunert, T. Michalsky, H. Franke, C. Sturm, M. Grundmann, R. Schmidt-Grund: *Interference measurements on exciton-polariton Bose-Einstein condensates*, DPG spring meeting, Berlin, Germany, March 2015

T. Jakubczyk, H. Franke, T. Smolenski, M. Sciesiek, W. Pacuski, A. Golnik, R. Schmidt-Grund, M. Grundmann, C. Kruse, D. Hommel, P. Kossacki: *Inhibition and enhancement of the spontaneous emission of quantum dots in micropillar cavities with radial Bragg reflectors*, Journées boites quantiques (French guantum dot days) 2015, Grenoble, France, June 2015

M. Jenderka, M. Grundmann, M. Lorenz: *Heteroepitaxial $YBiO_3$ thin films grown by pulsed laser deposition*, DPG spring meeting, Berlin, Germany, March 2015

M. Jenderka, M. Grundmann, M. Lorenz: *Heteroepitaxial $YBiO_3$ thin films grown by pulsed laser deposition*, International School of Oxide Electronics 2015, Cargése, France, October 2015

T. Michalsky, M. Wille, R. Buschlinger, H. Franke, U. Peschel, M. Grundmann, R. Schmidt-Grund: *Quantum Gases and Liquids in Semiconductor Rods*, BuildMoNa Minisymposium: Quantum Coherent Structures, Leipzig, Germany, September/October 2015

A. Reinhardt, H. Frenzel, H. von Wenckstern, M. Grundmann: *Room-temperature deposited zinc oxynitride thin films as active channel material for high-mobility thin-film transistors*, 11th International Thin-Film Transistor Conference, Rennes, France, February 2015

S. Richter, C. Sturm, H. Franke, R. Schmidt-Grund, M. Grundmann: *Exciton polariton modes of a planar resonator in magnetic fields*, DPG spring meeting, Berlin, Germany, March 2015

S. Richter, R. Schmidt-Grund, C. Bundesmann, S.G. Ebbinghaus, M. Grundmann: *Temperature dependent dielectric function of hexagonal* $YMnO_3$, DPG spring meeting, Berlin, Germany, March 2015

S. Richter, C. Sturm, H. Franke, R. Schmidt-Grund, M. Grundmann: *Towards time-resolved spectroscopic ellipsometry with ps-resolution*, 9th Workshop Ellipsometry, Twente, Netherlands, March 2015

S. Richter, C. Sturm, H. Franke, R. Schmidt-Grund, M. Grundmann: *Exciton-polariton modes of a planar resonator in magnetic fields*, Annual Conference of the Graduate School BuildMoNa, Leipzig, Germany, March 2015

S. Richter, C. Sturm, H. Franke, M. Grundmann, R. Schmidt-Grund: *Cavity photon and exciton-polariton modes with arbitrary cavity anisotropy*, BuildMoNa Minisymposium: Quantum Coherent Structures, Leipzig, Germany, September/October 2015

P. Schlupp, H. von Wenckstern, M. Grundmann: *Room temperature fabricated amorphous oxide heterodiodes on glass and flexible substrates*, International Confernece on Amorphous and Nanocrystalline Semiconductors, Aachen, Germany, September 2015

R. Schmidt-Grund, C. Sturm, C. Kranert, V. Zviagin, H. Krauß, H. von Wenckstern, M. Bonholzer, J. Lenzner, M. Grundmann: *NIR-VUV dielectric function of* $(Al, In, Ga)_2O_3$ *thin films*, DPG spring meeting, Berlin, Germany, March 2015

A. Shkurmanov, C. Sturm, H. Hochmuth, M. Grundmann: *Growth of ultrathin ZnO nanowires*, BuildMoNa Minisymposium: Quantum Coherent Structures, Leipzig, Germany, September/October 2015

D. Splith, S. Müller, H. von Wenckstern, M. Grundmann: *Schottky contacts on beta-*Ga_2O_3 *thin films grown by pulsed laser deposition*, International Workshop on Gallium Oxide and Related Materials, Kyoto, Japan, November 2015

D. Splith, F. Schmidt, S. Lanzinger, S. Müller, H von Wenckstern, M. Grundmann: *Schottky contacts and pn-heterojunctions on heteroepitaxial* In_2O_3 *thin films grown by pulsed laser deposition*, International Workshop on Gallium Oxide and Related Materials, Kyoto, Japan, November 2015

M. Thunert, S. Lange, H. Franke, C. Sturm, T. Michalsky, A. Janot, B. Rosenow, M.D. Martín, L. Viña, M. Grundmann, R. Schmidt-Grund: *Impact of disorder on the coherence of a polariton condensate in dependence on the temperature*, DPG spring meeting, Berlin, Germany, March 2015

M. Thunert, T. Michalsky, C. Sturm, H. Franke, R. Schmidt-Grund, M. Grundmann: *Coherence properties of disordered exciton-polariton Bose-Einstein-Condensates*, Annual Conference of the Graduate School BuildMoNa, Leipzig, Germany, March 2015

M. Thunert, A. Janot, T. Michalsky, H. Franke, C. Sturm, H. Franke, R. Schmidt-Grund, M. Grundmann: *Cavity polariton condensate in a disordered environment*, BuildMoNa Minisymposium: Quantum Coherent Structures, Leipzig, Germany, September/October 2015

M. Wille, T. Michalsky, R. Röder, C. Ronning, R. Schmidt-Grund, M. Grundmann: *Lasing Dynamics in ZnO and CdS Nanowires*, DPG spring meeting, Berlin, Germany, March 2015

M. Wille, T. Michalsky, R. Röder, C. Ronning, R. Schmidt-Grund, M. Grundmann: *Lasing dynamics in* ZnO *Nanowires*, Annual Conference of the Graduate School BuildMoNa, Leipzig, Germany, March 2015

M. Wille, T. Michalsky, R. Röder, C. Ronning, R. Schmidt-Grund, M. Grundmann: *Carrier density driven dynamics in* ZnO *Nanowires*, BuildMoNa Minisymposium: Quantum Coherent Structures, Leipzig, Germany, September/October 2015

V. Zviagin, P. Richter, C. Kranert, T. Böntgen, M. Lorenz, D.R.T. Zahn, G. Salvan, R. Schmidt-Grund, M. Grundmann: *Spectroscopic and Magneto-Optical Study of Spinel Oxide Thin Films*, 9th Workshop Ellipsometry, Twente, Netherlands, March 2015

9.27 Graduations

Doctorate

- Felix Daume
  Degradation of Flexible Cu(In,Ga)Se_2 Solar cells
  December 2015
- Fabian Klüpfel
  Transparent semiconducting ocides for active multi-electrode arrays
  February 2015
- Stefan Puttnins
  Der Einfluss von Natrium auf Rekombinationsprozesse in Cu(In,Ga)Se_2 Solarzellen
  December 2015
- Friedrich-Leonhard Schein
  Herstellung und Charakterisierung von bipolaren Heterostrukturen mit oxidischen Halbleitern
  September 2015

Master

- Sofie Bitter
  Electrical and optical characterization of amorphous zinc-tin-oxide thin films having a continuous composition spread
  March 2015
- Tobias Lühmann
  3D Ionenstrahlschreiben in Diamant zur Erzeugung von Graphitstrukturen un deren Charakterisierung
  April 2015
- Ahsan Rasheed
  Growth, Structural and Electrical characterization of Yttrium-doped homoepitaxial ZnO thin films
  December 2015
- Michael Scheibe
  Defekte in (Mg,Zn)O Dünnfilmen: Einfluss der Pufferschicht und des Substratschnitts
  December 2015

Bachelor

- Sören Herath
  Struktur und elektrische Eigenschaften von homoepitaktischen ZnO:IN Dünnfilmen
  January 2015
- Rebecca Hölldobler
  Ramanspektroskopie an Seltenerd-Platin-Verindungen
  September 2015

- Julian Pohl
  Herstellung und elektrische Charakterisierung von Galliumoxid-Transistoren
  October 2015
- Laurenz Thyen
  Untersuchung der Spannungsfestigkeit von Schottky-Kontakten auf β-Galliumoxid
  November 2015
- Tim Wolter
  Untersuchung von MSM-Photodetektiren auf Magnesiumzinkoxid-Basis
  February 2015

9.28 Guests

- Francesco Boschi
  University of Parma, Italy
  May 2015 – August 2015
- Yangqing Wu
  Nanjing University, China
  August 2015 – September 2015

10

Superconductivity and Magnetism

10.1 Introduction

The main interests of the group at the division are phenomena related to superconductivity and magnetism in solids. In the last few years the research activities in superconductivity have been mainly concentrated in searching for its existence in graphite, especially at graphite interfaces between Bernal-like crystalline regions. This research issue started in our division in Leipzig in the year 2000 and became supporting experimental evidence quite recently, indicating the existence of superconductivity at temperatures above 100 K. Future work will be concentrated in the localization of the superconducting phases and the increase of the superconducting yield.

Our division was the first to show that atomic lattice defects can produce magnetic order in graphite without the need of magnetic ions. This phenomenon is known nowadays as Defect-Induced Magnetism and it is found in a broad spectrum of different materials. We are involved in a collaborative research project with the aim of triggering this phenomenon in nominally non-magnetic oxides, via vacancies and/or hydrogen doping. Further research topic is the study of the electrical and magnetic properties of oxide multilayers of thickness starting from a few unit cells. Main research issues are related to the magnetic coupling at the interfaces of oxide layers, i.e. exchange bias phenomena, as well as to interfacial conductivity.

Pablo Esquinazi

10.2 Persistent circular currents around holes in graphite interfaces

B. Semenenko, A. Setzer, W. Böhlmann, P. Esquinazi

The aim of this work is to prove the existence of persistent circular currents around artificially made holes in graphite flakes with embedded interfaces. For the experiment we used highly oriented pyrolytic graphite (HOPG) produced by Union Carbide company with highest quality ZYA, which has a large density of interfaces. As it is known from previous investigations [1, 2], the presence of interfaces in HOPG is responsible for the metallic-like behavior as well as for the superconductivity found in some graphite

materials. We decided to prove it with high precision magnetic measurements using a Superconducting Quantum Interference Device (SQUID) at temperatures ranging from 5 K to 300 K and maximum magnetic fields between 0.05 T and 5 T applied normal to the holes area. The holes of $\sim 2\ \mu$m diameter were produced using a focused gallium ions beam microscope, see Fig. 10.1. The rest of the graphite surface was protected by a thick layer of PMMA. The measurements show that if we drill holes in the HOPG, then it is possible to see a relatively large magnetic field signal, which remains persistent after removing the applied field. We speculate that this signal originates from circular currents around the holes that flow at the different interfaces (about 100 within the thickness of the graphite flake used). The presence of interfaces in graphite allows the formation of a plurality of circular currents along the hole axis, which results in a significant persistent magnetic moment.

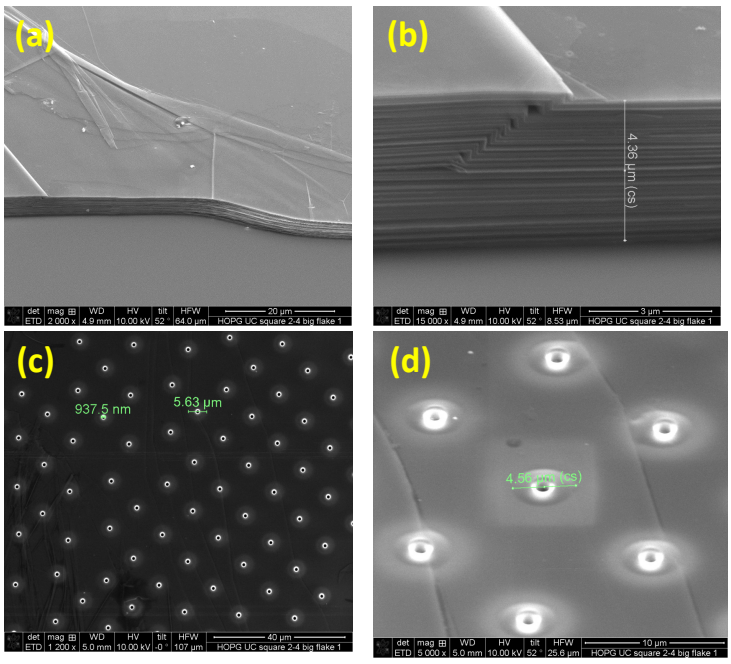

Figure 10.1: Transmission electron microscopy images of (a), (b) the HOPG flake and (c), (d) the holes produced by focused ion beam etching.

[1] P. Esquinazi, T. T. Heikkilä, Y. V. Lysogoskiy, D. A. Tayurskii, and G. E. Volovik, JETP Lett. **100**, 336 (2014).
[2] A. Ballestar et al., New J. Phys. **15**, 023024 (2013).

10.3 Substrate temperature dependent structural and magnetic properties of $ZnFe_2O_4$ thin films

Y. Kumar, V. Zviagin*, I. Lorite, P. Esquinazi, M. Grundmann*, R. Schmidt-Grund*

*Semiconductor Physics Group, Faculty of Physics and Geosciences, Leipzig University

We have studied the variation in the structural and magnetic properties of zinc ferrite thin films, grown by pulsed laser ablation, with the substrate temperature used during deposition. Thin films were grown on *c*-axis oriented $SrTiO_3$ single crystals kept at 400, 500 and 600°C and under partial oxygen pressure of 0.016 mbar. X-ray diffraction (XRD) measurements confirm the epitaxial growth of all the films and display a reduction in lattice parameter with the rise in the growth temperature. It is clear from the magnetization measurements at 5 K, shown in Fig. 10.2, that films exhibit ferrimagnetic order. However, there is a reduction in magnetization, both saturation and remanence, with increase in the deposition temperature. It matches with the variation in lattice parameter observed in XRD. Ellipsometric investigations suggest that main mechanism responsible for the increase in magnetic response at lowest growth temperature is the inversion of the normal spinel structure [1].

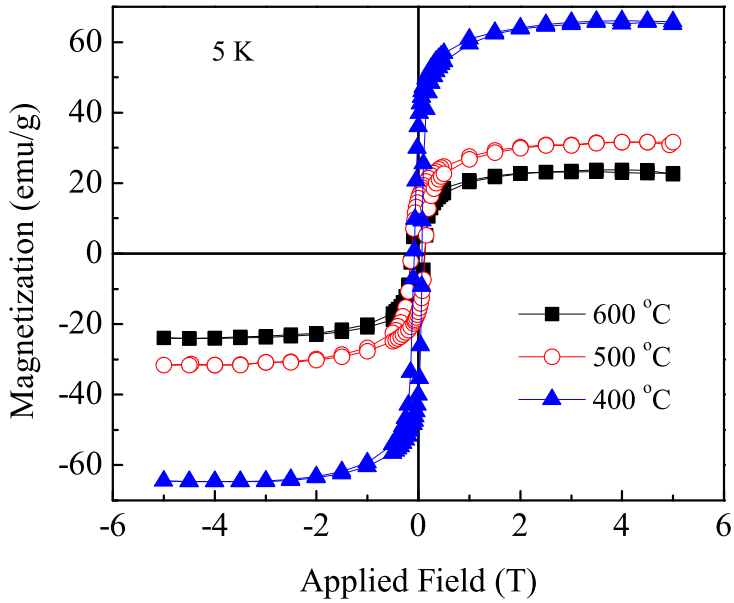

Figure 10.2: Magnetization as a function of applied magnetic field at 5 K for zinc ferrite thin films grown at different substrate temperatures.

[1] V. Zviagin et al.: Appl. Phys. Lett. **108**, 131901 (2016), doi:10.1063/1.4944898

10.4 Electrical Properties of Single ZnO Nanowires

M. Stiller, J. Barzola-Quiquia, M. Zoraghi, P. Esquinazi

We have investigated the electrical resistance $R(T)$ of ZnO nanowires of $\approx$ 400 nm diameter as a function of temperature, between 30 K and 300 K, and frequency in the range 40 Hz to 30 MHz. The measurements were done on the as-prepared and after low-energy proton implantation at room temperature. The temperature dependence of the resistance of the wire, before proton implantation, can be well described by two processes in parallel. One process is the fluctuation induced tunneling conductance (FITC) and the other the usual thermally activated process. The existence of

a tunneling conductance was also observed in the current-voltage $I - V$ results, and can be well described by the FITC model. Impedance spectroscopy measurements in the as-prepared state and at room temperature, indicate and support the idea of two contributions of these two transport processes in the nanowires. Electron backscatter diffraction confirms that the ZnO NW is not a single crystal, but it is composed of crystalline regions having different orientations. This is compatible with the impedance spectroscopy results and supports the application of the FITC model. After the implantation of H^+ a third thermally activated process is found and can be explained by taking into account the impurity band splitting due to proton implantation. This provides the possibility of tailoring the transport properties of single ZnO nanowires through modifying the surface by means of a controlled implantation of H^+.

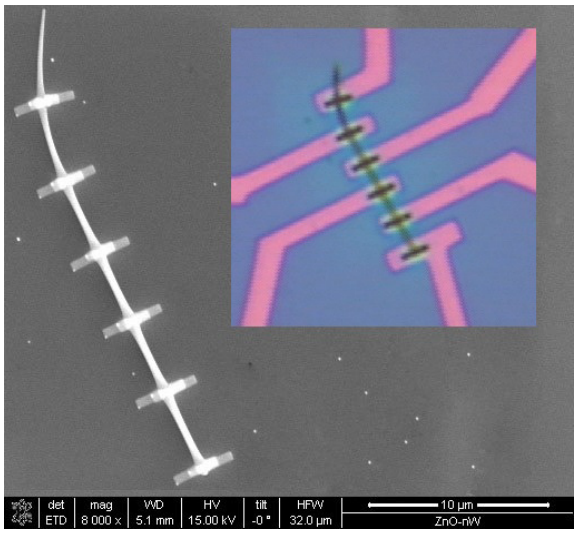

Figure 10.3: ZnO nanowire fixed with EBID prepared WC_x structures. The inset shows the NW with Cr/Au contacs.

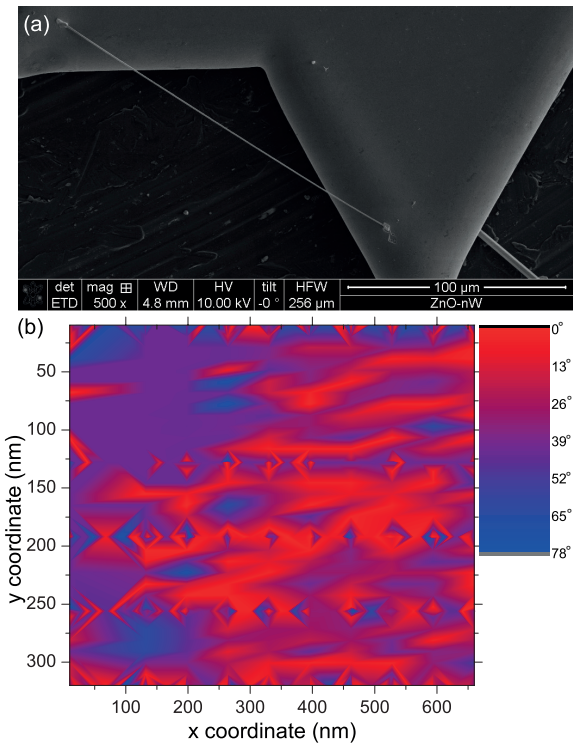

Figure 10.4: (a) shows the ZnO NW fixed on both ends to the sample holder. EBID of Platinum was used to attach the wire. In (b) the results of EBSD measurements are shown for a scanned area of (660×320) nm. Taking the main axis of the wire as reference (x-axis in the figure), the colors show the deviation of the c-axis from this vector, with a maxima of 78°.

10.5 Funding

Defect-induced Magnetism in Oxides
Prof. Dr. Pablo Esquinazi

DFG SFB 762/3, B1

Magnetic and electric properties of ultrathin oxide films
Prof. Dr. Pablo Esquinazi and Prof. Dr. Michael Ziese
DFG SFB 762/3, B5

10.6 Organizational Duties

P. Esquinazi

- Project Reviewer: Deutsche Forschungsgemeinschaft (DFG), National Science Foundation (USA), German-Israeli Foundation (GIF), Israel Science Foundation, Department of Energy (Washington), DAAD
- Referee: Phys. Rev. Lett, Phys. Rev. B., Appl. Phys. Lett., Chem. Phys. Lett., Nature Physics, Nature Materials, Physica C, Phys. Lett. A, phys. stat. sol., J. Low Temp. Phys., Carbon, J. Chem. Phys., Eur. J. Phys. B, J. Magn. Magn. Mater.

M. Ziese

- Head of the Undergraduate Physics Laboratory
- Dean of Studies
- Referee: Phys. Rev. Lett., Phys. Rev. B., Adv. Mater., Appl. Phys. A, Current Nanoscience, Eur. Phys. J. B, IEEE Trans. Magn., J. Phys.: Condens. Matter, J. Phys. D: Appl. Phys., J. Alloys Comp., J. Appl. Phys., J. Am. Ceram. Soc., J. Magn. Magn. Mater., J. Mater. Research, J. Mater. Science, Materials Science and Engineering B, Nanotechnology, phys. stat. sol., Thin Solid Films

W. Böhlmann

- Referee: J. Physical Chemistry, J. of American Chemical Society, Microporous and Mesoporous Materials

10.7 External Cooperations

Academic

- State University of Campinas, Campinas, Brazil
  Prof. Dr. Yakov Kopelevich
- Universität zu Köln, Cologne, Germany
  Dr. Ionela Vrejoiu
- Max-Planck Institute of Microstructure Physics, Halle, Germany
  Prof. Dietrich Hesse
- Max-Planck Institute of Microstructure Physics, Halle, Germany
  Dr. Arthur Ernst
- Martin-Luther Universität Halle-Wittenberg, Halle, Germany
  Prof. Ingrid Mertig
- Martin-Luther Universität Halle-Wittenberg, Halle, Germany
  Prof. Wolfram Hergert

- Martin-Luther Universität Halle-Wittenberg, Halle, Germany
  Dr. Angelika Chassé
- Martin-Luther Universität Halle-Wittenberg, Halle, Germany
  Dr. Manfred Dubiel
- Stanford Synchrotron Radiation Laboratory, USA
  Dr. Hendrik Ohldag
- Laboratorio de Física de Sistemas Pequeños y Nanotecnologíia, Consejo Superior de Investigaciones Científicas, Madrid, Spain
  Prof. N. García (Madrid)
- Forschungszentrum Dresden-Rossendorf e.V., Institut für Ionenstrahlphysik und Materialforschung, Germany
  Dr. W. Anwand
- Forschungszentrum Dresden-Rossendorf e.V., Institut für Ionenstrahlphysik und Materialforschung, Germany
  Dr. G. Brauer
- Tucuman University, Argentina
  Prof. S. P. de Heluani
- University of La Plata, Argentina
  Dr. C. E. Rodriguez Torres
- Universidad Autónoma de Madrid, Spain
  Prof. Dr. Miguel Angel Ramos
- Bar Ilan University, Israel
  Dr. G. D. Nessim

10.8 Publications

Journals

A. Ballestar, and P. Esquinazi:
Transport characteristics of focused beam deposited nanostructures
Nanofabrication **2**, 1 (2015)

A. Ballestar, P. Esquinazi, and W. Böhlmann:
Granular superconductivity below 5 K in SPI-II pyrolytic graphite
Phys. Rev. B **91**, 014502 (2015)

J. Barzola-Quiquia, T. Lehmann, M. Stiller, D. Spemann, P. Esquinazi, and P. Häussler:
Topological insulator thin films starting from the amorphous phase-Bi_2Se_3 as sample
J. Appl. Phys. **117**, 075301 (2015)

J. Barzola-Quiquia, P. Esquinazi, M. Lindel, D. Spemann, M. Muallem, and G. D. Nessim:
Magnetic order and superconductivity observed in bundles of Double-Wall Carbon Nanotubes
Carbon **88**, 16 (2015)

I. Lorite, B. Straube, H. Ohldag, P. Kumar, M. Villafuerte, P. Esquianzi, C. E. Rodríguez Torres, S. Perez de Heluani, V. N. Antonov, L. V. Bekenov, A. Ernst, N. M. Hoffmann, S. K. Nayak, W. A. Adeagbo, G. Fischer, and W. Hergert:
Advances in methods to obtain and characterise room temperature magnetic ZnO
Appl. Phys. Lett. **106**, 082406 (2015)

I. Lorite, C. Zandalazini, P. Esquinazi, D. Spemann, S. Friedländer, A. Pöppl, T. Michalsky, M. Grundmann, J. Vogt, J. Meijer, S. Perez de Heluani, H. Ohldag, W. A. Adeagbo, S. K. Nayak, W. Hergert, A. Ernst, and M. Hoffmann:
Study of the negative magneto-resistance of single proton-inplanted lithium-doped ZnO microwires
J. Phys.: Condens. Matter **27**, 256002 (2015)

Y. Kumar, F. Bern, J. Barzola-Quiquia, I. Lorite, and P. Esquinazi:
Study of non-linear Hall effect in nitrogen-grown ZnO microstructure and the effect of H^+-implantation
Appl. Phys. Lett. **107**, 022403 (2015)

M. Stiller, J. Barzola-Quiquia, M. Zoraghi, and P. Esquinazi:
Electrical properties of ZnO single nanowires
Nanotechnology **26**, 395703 (2015)

J. Barzola-Quiquia, M. Stiller, M. Stiehler, P. Esquinazi, and P. Häussler Structural, magnetic and electronic transport properties of amorphous and quasicrystalline $Al_{70}Pd_{20}Fe_{10}$ thin films
Mater. Res. Express **2**, 096403 (2015)

I.Lorite, Y. Kumar, P. Esquinazi, C. Zandalazini, and S. Perez de Heluani:
Detection of Defect-Induced Magnetism in Low-Dimensional ZnO Structures by Magnetophotocurrent
Small **11**, 4403 (2015)

Talks

Structural, Magnetic and Magnetotransport Properties of $La_{0.7}Sr_{0.3}MnO_3/SrRuO_3$ Superlattices and Embedded Films
M. Ziese
State Key Laboratory of Electronic Thin Films and Integrated Devices, University of Electronic Science and Technology of China, Chengdu, China

Transient photocurrent studies on ZnO based materials under the effect of magnetic field
Y. Kumar
DPG Konferenz 2015 Berlin

Umkehr effect observed in the magnetothermoelectric power of graphite
S. Muiños Landín
DPG Konferenz 2015 Berlin

Posters

Persistent circular currents around holes in graphite interfaces
B. Semenenko
DPG Konferenz 2015 Berlin

10.9 Graduations

Master

- Markus Stiller
  The Electrical Transport Properties of TiO_2 Nanotubes, ZnO Nanowires and the Magnetic Properties of TiO_2 Thin Films
  05.10.2015

Bachelor

- Tiago Rafael da Silva Cordeiro
  Magnetization Measurements in Granular YBaCuO
  09.01.2015
- Lukas Botsch
  On the effect of polorized light on the photoresistonce of mognetic ZnO somples
  08.06.2015
- Artiom Zaitev
  Magnetotransport und Charakterisierung von Wolframditellurid
  21.09.2015

10.10 Guests

- Prof. Dr. Iokov Veniominovith Kopelevitch
  Universidade Estadual de Campinas-UNICAMP, Bairro Barão Geraldo, Brasilien
  02.07.2014 - 17.02.2015
- Dr. Bruno Camargo
  Universidade Estadual de Campinas-UNICAMP, Bairro Barão Geraldo, Brasilien
  10.08.2014 - 31.07.2015
- Karen Lizeth Salcedo Rodríguez
  Instituto de Fisica La Plata, Universidad de La Plata, Argentinien
  02.03.2015 - 30.04.2015
- Artur Gabdullin
  National Research Nuclear University “MEPhI” Moskau, Russland
  09.06.2015 - 30.08.2015
- Dr. Marcelo Jaime
  Los Alamos National Laboratory, USA
  06.07.2015 - 08.07.2015

- Soumyadeep Ghosh
  Manipal Institute of Technology, Karnataka/Indien
  13.07.2015 - 30.09.2015
- Benjamin Straube
  Facultad de Ciencias Exactas y Tecnología, Universidad Nacional de Tucumán, Argentinien
  08.07.2015 - 30.09.2015
- Fernando Meneses
  Lic. en Física - FaMAF - UNC, Argentinien
  02.11.2015 - 31.12.2015
- Dr. Vincent Jacques
  Laboratoire Charles Coulomb, Université de Montpellier, Frankreich
  01.12.2015 - 03.12.2015

III

Institute for Theoretical Physics

11

Computational Quantum Field Theory

11.1 Introduction

The Computational Physics Group performs basic research into classical and quantum statistical physics with special emphasis on phase transitions and critical phenomena. In the centre of interest are the physics of spin glasses, diluted magnets and other materials with quenched, random disorder, soft condensed matter physics with focus on fluctuating paths and interfaces, biologically motivated problems such as protein folding, aggregation and adsorption as well as related properties of homopolymers, and the intriguing physics of low-dimensional quantum spin systems.

The methodology is a combination of numerical and analytical techniques. The numerical tools are mainly Monte Carlo and Molecular Dynamics computer simulations as well as exact enumeration techniques. The computational approach to theoretical physics is expected to gain more and more importance with the future advances of computer technology, and is likely to become the third cornerstone of physics besides experiment and analytical theory as sketched in Fig. 11.1. Already now it often helps to bridge the gap between experiments and the often necessarily approximate calculations in analytic approaches. To achieve the desired high efficiency of the numerical studies we develop new algorithms and, to guarantee the flexibility required by basic research, all computer codes are implemented by ourselves. The technical tools are Fortran, C, C++, and Python programs running under Unix or Linux operating systems and computer algebra using Maple or Mathematica. The software is developed and tested at the Institute on a cluster of PCs and workstations, where also most of the numerical analyses are performed. Currently we are also exploring the possibilities of the rapidly developing graphics card computing, that is computer simulations on graphics processing units (GPUs) with many cores. Large-scale simulations requiring vast amounts of computer time are carried out at the Institute on quite powerful compute servers, at the parallel computers of the Saxon computing centre in Dresden, and, upon successful grant application, at the national supercomputing centres in Jülich, Stuttgart and München on parallel high-capability computers. This hierarchy of various platforms gives good training and qualification opportunities for the students, which offers promising job perspectives in many different fields for their future careers.

Our research activities are closely integrated into the Graduate School "BuildMoNa": Leipzig School of Natural Sciences – *Building with Molecules and Nano-objects*, the International Max Planck Research School (IMPRS) *Mathematics in the Sci-*

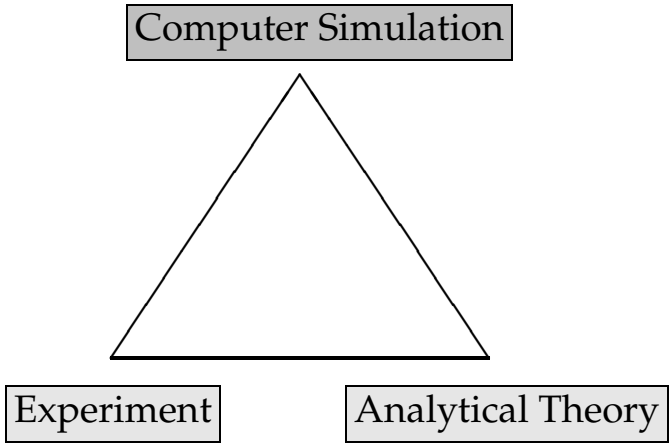

Figure 11.1: Sketch of the "triangular" relationship between experiment, analytical theory and computer simulation.

ences, and the International Graduate School *Statistical Physics of Complex Systems* with Université de Lorraine in Nancy, France, supported by the Deutsch-Französische Hochschule (DFH-UFA). In the second funding period 2011–2013, Coventry University in England has been integrated as an associated partner, and in the current third funding period 2014–2016, also the National Academy of Sciences of Ukraine in Lviv has joined as another associated partner institution, offering our PhD students now several interesting options for secondments. For instance, in 2014, one PhD student started a "co-tutelle de thèse" jointly supervised with a colleague from Coventry University. The three Graduate Schools are all "Classes" of the Research Academy Leipzig (RALeipzig), providing the organizational frame for hosting visiting students and senior scientists, offering language courses, organizing childcare and for many other practical matters.

At a more post-graduate level our research projects are embedded into the "Sächsische DFG-Forschergruppe" FOR877 *From Local Constraints to Macroscopic Transport* jointly with the universities in Chemnitz and Dresden, and the Sonderforschungsbereich/Transregio SFB/TRR 102 *Polymers under Multiple Constraints: Restricted and Controlled Molecular Order and Mobility* together with Halle University. Our group also actively contributes to two of the top level research areas ("Profillinien") and the Centre for Theoretical Sciences (NTZ) of the University. Beside "BuildMoNa" the latter structures are particularly instrumental for our cooperations with research groups in experimental physics and biochemistry on the one hand and with mathematics and computer science on the other.

On an international scale, our research projects are carried out in a wide net of collaborations which are currently mainly funded by the Alexander von Humboldt Foundation through an Institute Partnership with the National Academy of Sciences in Lviv, Ukraine, on *Polymers in Porous Environments and on Disordered Substrates* and the EU IRSES Network DIONICOS: *Dynamics of and in Complex Systems*, a consortium of 6 European and 12 non-European partners, including sites in England, France and Germany as well as in Armenia, Russia, Ukraine, India, the United States and Venezuela, which commenced work in 2014. Further close contacts and collaborations are established with research groups in Armenia, Austria, China, France, Great Bri-

tain, India, Israel, Italy, Japan, Poland, Russia, Spain, Sweden, Taiwan, Turkey, Ukraine, and the United States. These contacts are refreshed and furthered through topical Workshops, Advanced Training Modules and Tutorials, and our International Workshop series *CompPhys: New Developments in Computational Physics*, taking annually place at the end of November just before the first advent weekend.

Wolfhard Janke

11.2 Finite-size scaling of droplet condensation

J. Zierenberg, W. Janke

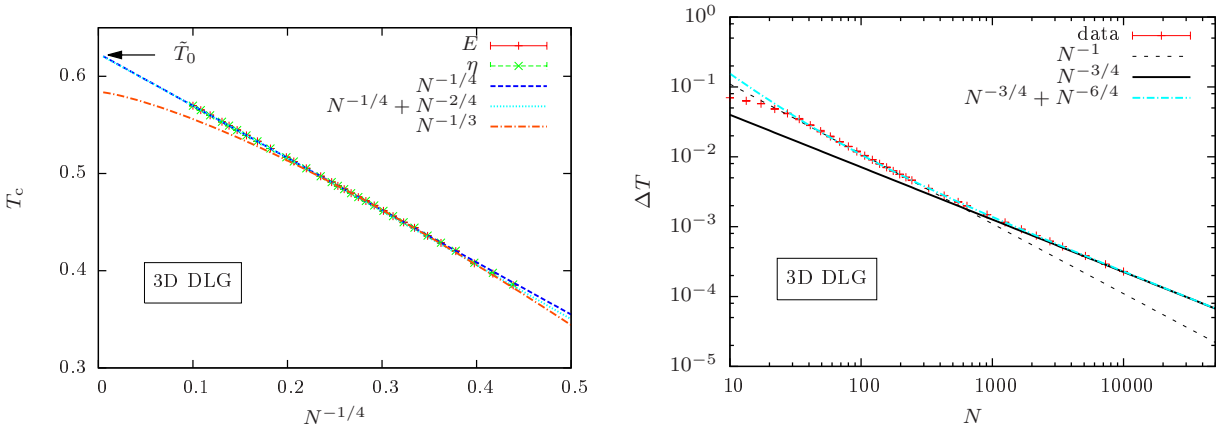

(a) (b)

Figure 11.2: Finite-size scaling of (a) the transition temperature and (b) the transition rounding of a three-dimensional lattice gas at fixed density $\rho = 10^{-2}$.

We investigated the finite-size scaling behaviour of the droplet condensation-evaporation transition for the two- and three-dimensional Ising lattice gas as well as the three-dimensional Lennard-Jones gas [1]. The lattice models allow us to exploit the equivalence to the Ising model, comparing to exact results in two dimensions and low-temperature series expansions in three dimensions. The Lennard-Jones model ensured the generality of our results. Opposed to the consideration at fixed temperature [2], for which leading-order predictions exist [3], we consider an orthogonal setup at fixed density. Applying Taylor expansions around the infinite-system limit, we obtain the same leading-order scaling behaviour for the finite-size transition temperature $T_c(N)$ and rounding ΔT of a D-dimensional system with N particles:

$$T_c(N) - T_0 \propto N^{-1/(D+1)}, \tag{11.1}$$

$$\Delta T \propto N^{-d/(D+1)}. \tag{11.2}$$

This is not the standard $1/V$ finite-size scaling of a first-order phase transition, because droplet evaporation-condensation describes a transition between a homogenous gas phase and an inhomogeneous or mixed phase where a single droplet is in equilibrium

with surrounding vapor. A comparison with our numerical results from parallel multicanonical simulations [4] is shown in Fig. 11.2 for the case of the three-dimensional lattice gas.

For intermediate system sizes, we observe a non-expected scaling regime where the system behaves as for homogeneous phase transitions, i.e., $T_c(N) - T_0 \propto N^{-1/D}$ and $\Delta T \propto N^{-1}$. For the three-dimensional lattice gas we can compare to low-temperature series expansion estimates of the transition temperature $\tilde{T}_0(\rho)$ and the agreement is very good. With our approach, we were able to reach up to $N = 10\,000$ lattice particles and the finite-size scaling analysis suggests that we are in fact quite close to the asymptotic scaling regime.

[1] J. Zierenberg, W. Janke: Phys. Rev. E **92**, 012134 (2015)
[2] J. Zierenberg et al.: J. Phys: Conf. Ser. **510**, 012017 (2014)
[3] M. Biskup et al.: Europhys. Lett. **60**, 21 (2002); Commun. Math. Phys. **242**, 137 (2003)
[4] J. Zierenberg et al.: Comput. Phys. Comm. **184**, 1155 (2013)

11.3 Aggregation of θ-polymers in spherical confinement

J. Zierenberg, M. Müller, P. Schierz, M. Marenz, W. Janke

This project aims for a better understanding of the influence of external confinement onto the physical properties of a small number of polymers [1]. We therefore investigated the change of the aggregation temperature for few polymers enclosed in a sphere. This enables a systematic variation of the available space by only one parameter, the radius of the sphere. The enclosing sphere is steric, leading at most to an effective repulsion, without introducing technical difficulties with self-interactions imposed by periodic boundaries.

We are thus able to explore the influence of the density onto the aggregation transition temperature of this system of θ-polymers (which means they are parametrized by a model that allows a single polymer to undergo a collapse transition), whose parametrization is summarized in Fig 11.3(a). This allows us to reweight our data to a whole range of different temperatures of the surrounding heat bath, hence the notion of *multi*-canonical simulations. We conducted such simulations in a highly parallelized way [2, 3] for several different radii of the sphere and with that we vary the volume accessible to the system. In the canonical picture we find that the aggregation temperature shifts in dependence of the radii.

To gain a quantitative understanding of this shift, we note that the spatial entropy available to the *aggregate* is in a first approximation independent from the radius of the surrounding sphere. In the separated regime the polymers can be treated similar to an ideal gas. Here, we can thus relate the entropy to the volume of the system, and with that to the radius of the sphere and the system's density. With the Gibbs construction we relate then the entropy difference of the two regimes to the microcanonical temperature T_{agg}, allowing the derivation of an explicit relation of the inverse transition temperature to the logarithm of the density,

$$1/T_{\mathrm{agg}}(\rho) = \frac{S(E_{\mathrm{sep}},\rho) - S(E_{\mathrm{agg}},\rho)}{\Delta E} \sim \frac{S(E_{\mathrm{sep}},\rho)}{\Delta E} = \frac{S(E_{\mathrm{sep}},\rho)}{M\Delta e} \sim -\ln\rho + \mathrm{const}\,, \quad (11.3)$$

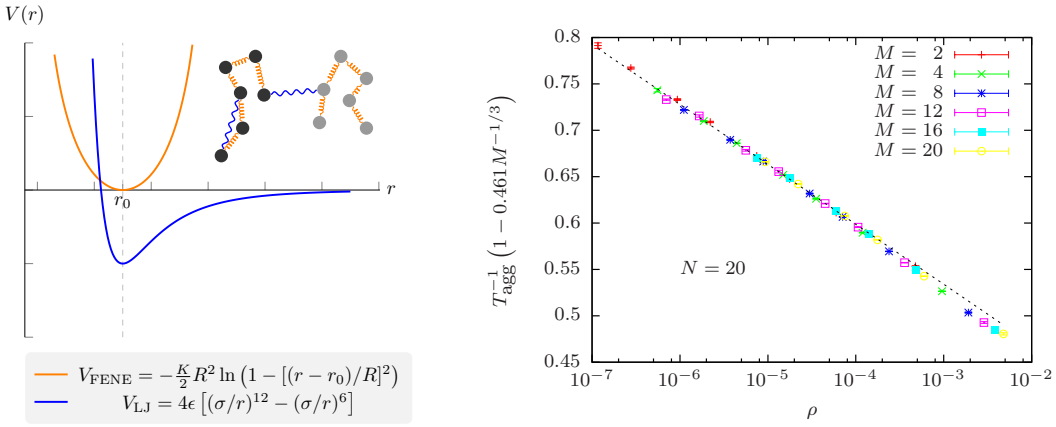

Figure 11.3: (a) The different interaction potentials that characterize a small number M of θ-polymers, which are enclosed in a sphere whose radius is varied, watching closely the aggregation transition temperature. (b) Combining entropic and energetic arguments, and respecting the typical length scale of the aggregate, we find an empirical data collapse of the inverse transitions temperatures over a broad range of densities.

with $\Delta E = E_{\text{sep}} - E_{\text{agg}} = M\Delta e$ under the assumption that, for fixed M and N, the latent heat Δe is almost constant.

For *flexible* polymers, the aggregate of M polymers with N monomers can be approximated by a single polymer with length $M \times N$, and this defines a "typical" length scale $R \sim (NM)^{-1/3}$ of the polymer aggregate, which may be exploited to derive an empirical scaling law for the inverse temperature in Eq. (11.3) in dependence of the *number of polymers*. With this we gain some insight into the nature of the finite-size effects in such a system enabling the empirical data collapse for a broad range of densities for different numbers of polymers shown in Fig. 11.3(b).

For *stiffer* polymers this typical length scale is not as easy to determine. Here, we found interesting structural properties that are already visible in a very intuitive order parameter [4], the so-called phase-separation parameter. This is essentially the average center-of-mass distance of the different polymers, and for the aggregate, it becomes smaller the stiffer the polymers are. This is at first sight counter-intuitive, but can be traced back to the formation of polymer bundles [5] which allow the polymers' center-of-masses to get closer as the polymers align.

[1] J. Zierenberg et al.: J. Chem. Phys. **141**, 114908 (2014)
[2] J. Zierenberg et al.: Comput. Phys. Comm. **184**, 1155 (2013)
[3] J. Zierenberg et al.: in *Computer Simulation Studies in Condensed-Matter Physics XXVI*, eds. D.P. Landau, H.-B. Schüttler, S. Lewis, M. Bachmann, Physics Procedia **53**, 55 (2014)
[4] M. Mueller et al.: in *Computer Simulation Studies in Condensed-Matter Physics XXVIII*, eds. D.P. Landau, H.-B. Schüttler, S. Lewis, M. Bachmann, Physics Procedia **68**, 95 (2015)
[5] J. Zierenberg, W. Janke: Europhys. Lett. **109**, 28002 (2015)

11.4 Aggregation of semiflexible polymers

J. Zierenberg, W. Janke

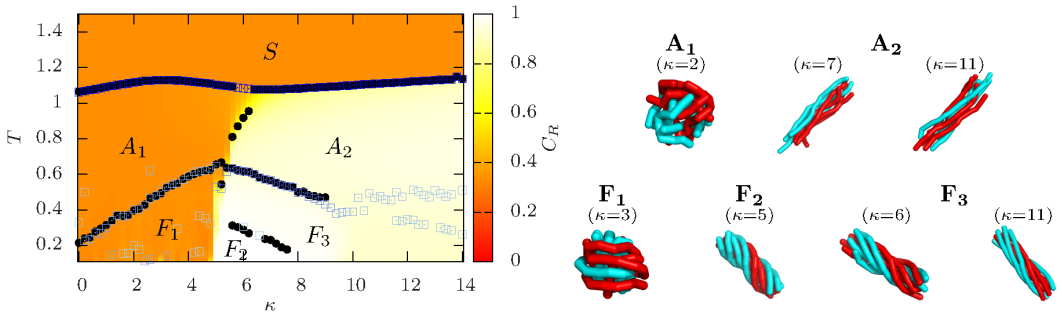

Figure 11.4: Full temperature-stiffness structural phase diagram of 8 polymers with 13 monomers each, combining the surface plot of a correlation parameter (1 = correlated; 1/3 = uncorrelated) with the peak locations of the heat capacity (black) and the thermal derivative of the phase separation parameter (blue). Representative conformations are presented next to the phase diagram. Figure taken from Ref. [2].

The effect of solvent salt concentration was shown to influence the dynamics and emerging structures in amyloid fibrils ranging from rapid formation of amorphous structures at high salt concentration to long-time relaxation of amyloid fibrils at low salt concentration [1]. It may be argued that the salt concentration influences the effective stiffness of a coarse-grained description of biopolymers. Therefore, we investigated the role of stiffness on the structural motifs of polymer aggregation, leading from amorphous aggregates for rather flexible polymers to polymer bundles for stiffer polymers [2]. Employing parallel multicanonical simulations [3], we were able to map out generic T-κ structural phase diagrams describing an entire class of coarse-grained semiflexible polymers. In Fig. 11.4 we present such a diagram for 8 polymers of length $N = 13$, including both amorphous aggregates and polymer bundles well described by an end-to-end correlation parameter $C_R \approx 1/3$ and $C_R \approx 1$, respectively. Low-temperature conformations even include twisted bundles known also from biopolymer networks.

The numerical data was generated on the supercomputer JUROPA at Jülich Supercomputing Centre (JSC).

[1] Y. Yoshimura et al.: Proc. Natl. Acad. Sci. USA **109**, 14446 (2012)
[2] J. Zierenberg, W. Janke: Europhys. Lett. **109**, 28002 (2015)
[3] J. Zierenberg et al.: Comput. Phys. Comm. **184**, 1155 (2013)

11.5 Polymer knots as topological order parameter

M. Marenz, W. Janke

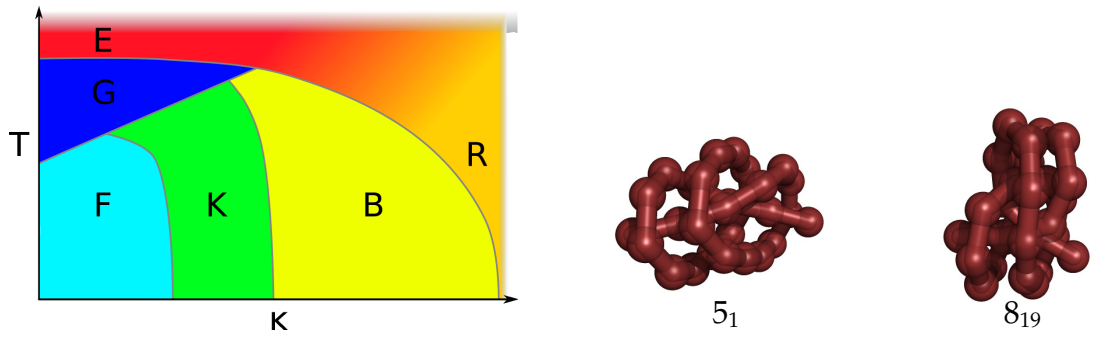

Figure 11.5: Sketch of the phase diagram for a semiflexible bead-stick model exhibiting several phases: E – elongated, R – rod-like, G – globular, F – frozen, K – knotted, B – bent. Next to the phase diagram two typical knots of types 5_1 and 8_{19} for a 28mer are shown.

To investigate the generic behaviour of polymers and proteins with computer simulations, it is common to use minimalistic, coarse-grained models since this is the only possibility to investigate large time scales, length scales or parameter ranges. In this study we used a bead-stick model for a semiflexible polymer defined by the Hamiltonian

$$H = E_{\mathrm{LJ}} + \kappa E_{\mathrm{Bend}} = 4 \sum_{i=1}^{N-2} \sum_{j=i+2}^{N} \left(\frac{1}{r_{ij}^{12}} - \frac{1}{r_{ij}^{6}} \right) + \kappa \sum_{i} (1 - \cos \theta_i) \ , \tag{11.4}$$

where r_{ij} is the distance between non-adjacent monomers, and θ_i is the angle of two adjacent bonds. The parameter κ allows to vary the bending stiffness of the polymer from flexible over semiflexible to stiff.

To simulate the system in the complete (T, κ)-plane we used two advanced Monte Carlo algorithms. A parallel multicanonical algorithm [1] combined with a one-dimensional replica exchange in the κ direction and a two-dimensional replica-exchange method, which simulates the system in parallel in the T and κ direction. Employing both algorithms, we calculated surface plots of various observables (energy, end-to-end distance, radius of gyration, eigenvalues of gyration tensor) to construct the full pseudo-phase diagram for several polymer lengths ($N = 14, 28, 42$) [2, 3].

Despite the simplicity of the model, the phase diagram sketched in Fig. 11.5 is remarkably rich. Compared to former work simulating similar coarse-grained models [4], we observed a novel type of phases labeled by "K", which are characterized by thermodynamically stable knots [5], which may be considered as topological order parameters. The transitions into these knot phases exhibit some intriguing characteristics. Although we observed clear signals of a first-order transition between the knotted and unknotted phases, the transition apparently shows no latent heat [2, 3]. Instead the two sub-energies, the Lennard-Jones energy and the bending energy, are transformed into each other while the polymer knots itself, see Fig. 11.6.

[1] J. Zierenberg et al.: Comput. Phys. Comm. **184**, 1155 (2013)
[2] M. Marenz, W. Janke: Phys. Rev. Lett. **116**, 128301 (2016)
[3] M. Marenz, W. Janke: *Stable knots in the phase diagram of semiflexible polymers: A topological order parameter?*, to appear in *Computer Simulation Studies in*

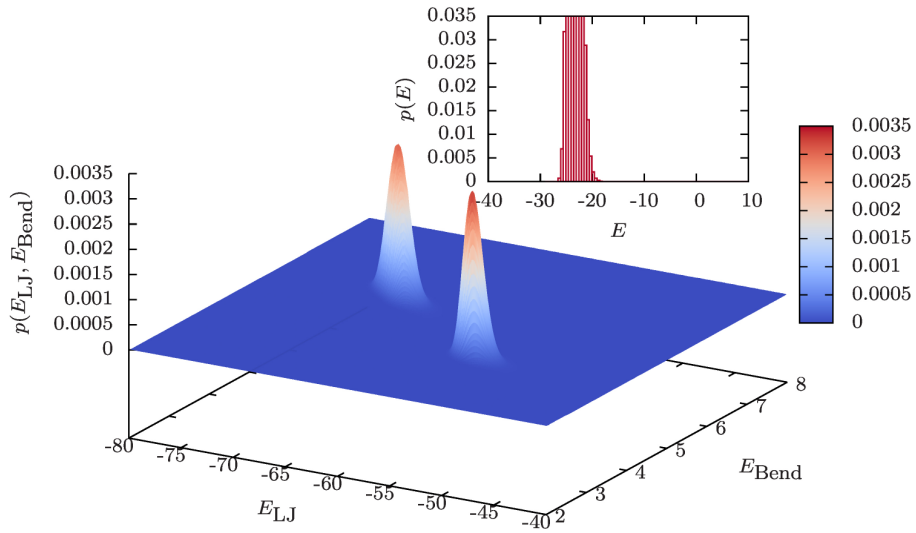

Figure 11.6: Two-dimensional energy histogram $p(E_{\mathrm{LJ}}, E_{\mathrm{Bend}})$ of a 28mer at the transition into the knot phase signaling clear phase coexistence. The inset shows the one-dimensional energy histogram $p(E)$ of the total energy $E = E_{\mathrm{LJ}} + \kappa E_{\mathrm{Bend}}$, which corresponds to a projection along the diagonal of the two-dimensional histogram. In this projection, the two peaks fall on top of each other, so only a single peak is visible in $p(E)$.

Condensed-Matter Physics XXIX, eds. D.P. Landau, H.-B. Schüttler, S. Lewis, M. Bachmann, J. Phys.: Conf. Ser. (2016), in print
[4] D.T. Seaton et al.: Phys. Rev. Lett. **110**, 028103 (2013)
[5] L.H. Kauffman: *Knots and Physics*, 2nd ed. (World Scientific, Singapore, 1991)

11.6 Polymer adsorption to a nano-sphere

H. Arkın*, W. Janke

*Department of Physics Engineering, Faculty of Engineering, Ankara University, Tandogan, 06100 Ankara, Turkey

The interaction of macromolecules with differently shaped substrates is particularly important for interdisciplinary research and nano-technological applications including, e.g., the fabrication of biosensors and peptide adhesion to metals or semiconductors. The knowledge of structure formation for a variety of interfaces has therefore been a challenging subject of numerous experimental and computational studies.

Recently we have investigated the purely steric confinement effect of a spherical cage enclosing a simple flexible polymer chain to determine its influence on the location of the collapse and freezing transitions [1]. Another hybrid system under consideration was a polymer chain inside an attractive spherical cage for which we have constructed the finite-temperature phase diagram depending on the attraction strength of the sphere inner wall and the temperature [2, 3] and investigated the ground-state properties [4].

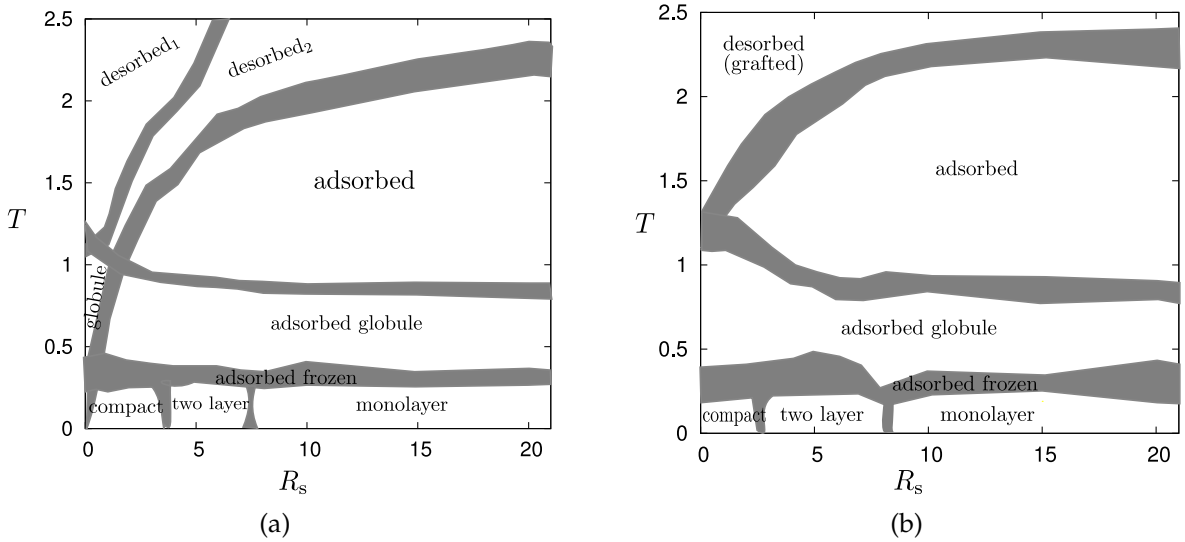

Figure 11.7: The phase diagram of a homopolymer interacting with an attractive spherical surface of radius R_s for (a) a non-grafted and (b) an end-grafted 20mer.

We have also compared the results with an attractive flat surface [5, 6]. These systems exhibit a rich phase behaviour ranging from highly ordered, compact to extended, random coil structures.

Here, we consider the opposite situation: A nano-sphere whose attractive outer spherical surface is the target for the adsorbing polymer. This problem could have practical implications for a broad variety of applications ranging from protein-ligand binding, designing smart sensors to molecular pattern recognition and for the discovery of new drugs that bind to specific receptors. Therefore it is interesting to study the adsorption of macromolecules on different types of substrates and identify the conformational changes that a polymer can experience at the interface.

In this project we investigate a simple coarse-grained polymer model interacting with a spherical surface of varying radius (and consequently curvature) by means of extensive generalized-ensemble Monte Carlo computer simulations [7]. The employed multicanonical method enables us to describe the different phases of the finite chain over a wide range of sphere radius and temperature. In a comparative study, we determined how the structural phase diagram changes with the sphere radius and temperature, both for non-grafted and end-grafted polymer chains. The band widths of the boundaries separating the individual conformational phases in Fig. 11.7 indicate the variation of the peak locations of temperature derivatives of different structural observables which we have analyzed simultaneously [7]. Typical conformation for the case of a non-grafted polymer are shown in Fig. 11.8.

[1] M. Marenz et al.: Condens. Matter Phys. **15**, 43008 (2012)
[2] H. Arkın, W. Janke: Phys. Rev. E **85**, 051802 (2012)
[3] H. Arkın, W. Janke: J. Chem. Phys. **138**, 054904 (2013)
[4] H. Arkın, W. Janke: J. Phys. Chem. B **116**, 10379 (2012)
[5] M. Möddel et al.: J. Phys. Chem. B **113**, 3314 (2009); Phys. Chem. Chem. Phys. **12**, 11548 (2010); Macromolecules **44**, 9013 (2011)

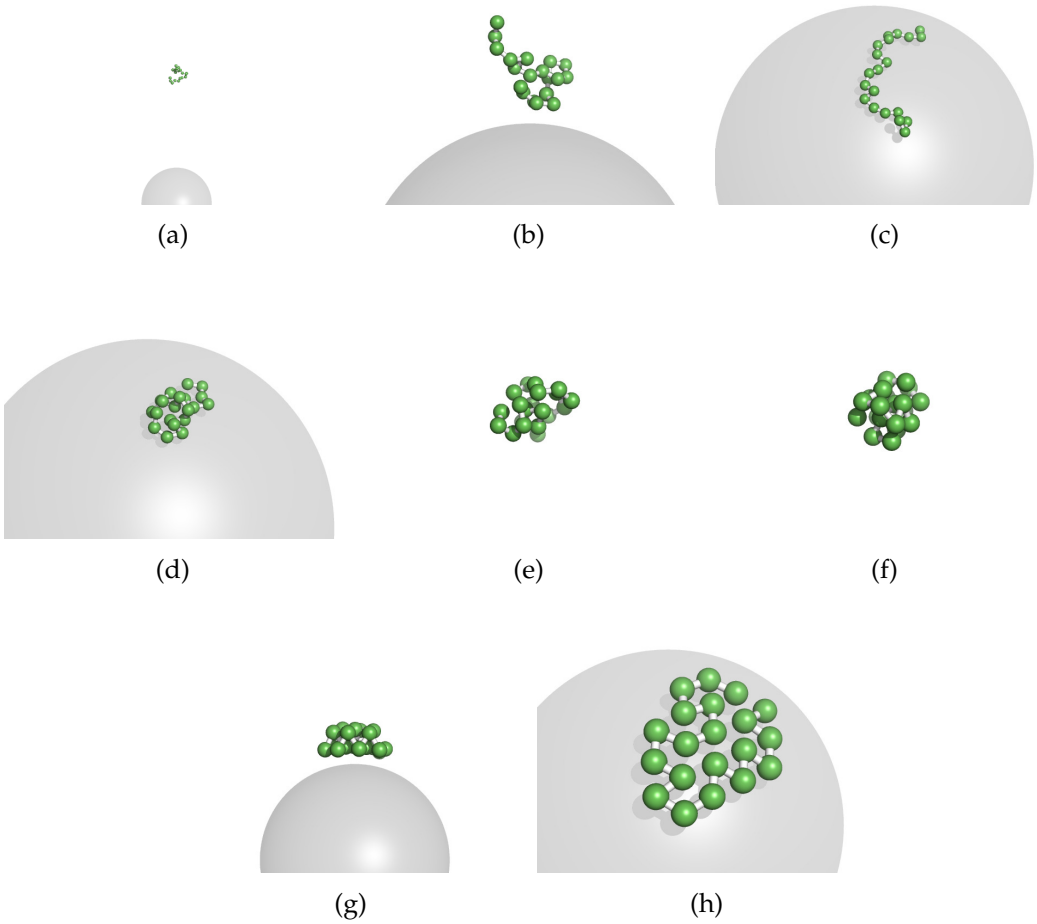

Figure 11.8: Typical conformations for the regions (a) desorbed$_1$, (b) desorbed$_2$, (c) adsorbed, (d) adsorbed globule, (e) globule, (f) compact, (g) two layer, and (h) monolayer in the phase diagram of a non-grafted polymer.

[6] H. Arkın, W. Janke: Eur. Phys. J. – Special Topics **216**, 181 (2013)
[7] H. Arkın, W. Janke: *Polymer adsorption on curved surfaces*, Ankara/Leipzig preprint `arXiv:1512.06990` [cond-mat.soft] (2015), submitted

11.7 Comparative simulations of poly(3-hexylthiophene) models

J. Gross, M. Ivanov, W. Janke

Regioregular poly(3-hexylthiophene) (P3HT) is a very interesting conjugated polymer due to its electronic and optical properties [1]. One of its applications is the use as semiconducting layer in organic photovoltaics [2–4]. Studies of P3HT on the microscopic level are of great importance for a fundamental understanding of the tuneability of electronic properties and their dependence on external constraints, e.g., the adsorption on electrode surfaces. Hence a number of experimental studies addressed for example

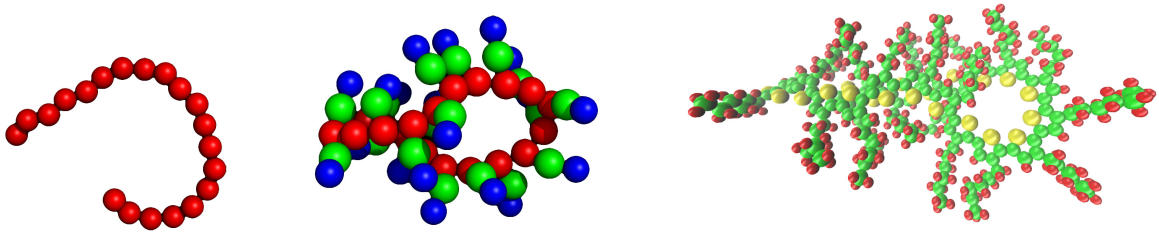

Figure 11.9: Hairpin conformations of Poly(3-hexylthiophene) for a degree of polymerization $DP_n = 20$ in three different models. (Left) One-particle coarse-grained model (one bead per monomer), (middle) three-particle coarse-grained model, and fully atomistic model (right).

the influence of structure formation by polymer self-assembly on ideal surfaces on the electronic properties of oligo- and polythiophenes [5]. Due to the complexity of these macromolecules many of the experimental findings have not been supported with simulations so far, which in contrast is well-established for studies of small organic molecules. Our pervious study [6] reported on an collaborative effort within the DFG SFB/TRR 102 project to combine the experimental observation of polymer chain conformations adsorbed on a metal surface with Monte Carlo simulations of a coarse-grained P3HT model developed by Huang *et al.* [7]. Based on our previous work on a three beads per monomer coarse-grained model, we expanded our studies in two directions. We focused our interest on the polymer itself and, firstly, investigated an even coarser model with one bead per monomer [8] using Monte Carlo simulations. Secondly, we simulated a fully atomistic representation of P3HT using molecular dynamics. We pursue these two routes to gauge the level of detail that is necessary to reproduce experimental findings more accurately. Another interest is the development of our own simplified model by systematically performing the coarse-grain procedure ourselves. For this we looked at the iterative Boltzmann inversion method [9]. The comparative analysis of all three models regarding structural observables, but also computational effort are discussed in Ref. [10].

[1] X. Bai, S. Holdcroft: Macromolecules **26**, 4457 (1993); Z. Bao et al.: Appl. Phys. Lett. **69**, 4108 (1996); M.R. Andersson et al.: J. Mater. Chem. **9**, 1933 (1999); B.W. Boudouris et al.: Macromolecules **44**, 6653 (2011)
[2] J.M. Frost et al.: Nano Letters **6**, 1674 (2006)
[3] M. Campoy-Quiles et al.: Nat. Mater. **7**, 158 (2008)
[4] A.M. Ballantyne et al.: Adv. Funct. Mater. **18**, 2373 (2008)
[5] Z.Y. Yang et al.: ACS Nano **2**, 743 (2008); Y.F. Liu et al.: Nanoscale **5**, 7936 (2013)
[6] S. Förster et al.: J. Chem. Phys. **141**, 164701 (2014)
[7] D.M. Huang et al.: J. Chem. Theory Comput. **6**, 526 (2010)
[8] C.K. Lee et al.: Energy Environ. Sci. **4**, 4124 (2011)
[9] D. Reith et al.: J. Comput. Phys. **24**, 1624 (2003); Macromolecules **36**, 5406 (2003)
[10] J. Gross et al.: *Comparing atomistic and coarse-grained simulations of P3HT*, to appear in J. Phys.: Conf. Ser. (2016), in print

11.8 Kinetics of cluster formation and growth during collpase of a polymer

S. Majumder, W. Janke

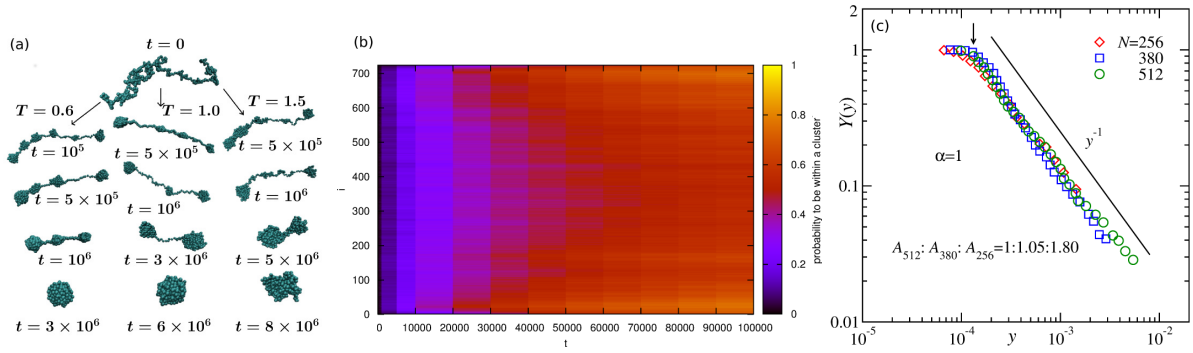

Figure 11.10: (a) Time evolution showing the sequence of events occurring during the collapse of a polymer upon being quenched from an expanded state (at high temperature) into the globular phase (at low temperatures). (b) Probability of formation of clusters at a site i along the polymer chain during the nucleation stage of the collapse. (c) Finite-size scaling plots showing the collapse of data for different chain lengths confirming the linear growth of the average cluster size [1].

A polymer undergoes a collapse transition when it is quenched from a high-temperature expanded coil state (or in good solvent) to a low-temperature compact globule (in poor solvent). Understanding the kinetics of the collapse of a polymer is an important physical problem considering its potential connections to many biological phenomena such as protein folding. A polymer collapses via nucleation, growth and subsequent coarsening or coalescence of clusters of monomers to form a single compact globule [2], as shown in Fig. 11.10(a). During the coarsening stage the average cluster size (average number of monomers within a cluster), $C_s(t)$, is expected to follow a power law. In spite of the fact that the relaxation dynamics during the collapse has been studied in previous works [2], there exist no simulation studies which quantify the growth exponent unambiguously.

In this work we have addressed this issue by state-of-the-art Monte Carlo simulations of a model polymer with the aim to understand the kinetics of cluster formation and growth exponent related to the coarsening stage of the collapse. In Fig. 11.10(b) we show the probability of nucleation of clusters at a site i during the first stage of the collpase [3]. By drawing analogy with standard coarsening systems we analyze our results via the application of finite-size scaling technique in the nonequilibrium context [4]. Figure 11.10(c) shows such a scaling plot where in contradiction to previous theoretical and simulation results [5], the decay of the master curve shows a linear growth of the average cluster size, as known from the Lifshitz-Slyozov mechanism of cluster growth.

[1] S. Majumder, W. Janke: Europhys. Lett. **110**, 58001 (2015)
[2] A. Halperin, P. Goldbart: Phys. Rev. E **61**, 565 (2000)
[3] S. Majumder et al.: In preparation

[4] S. Majumder, S.K. Das: Phys. Rev. E **81**, 050102(R) (2010); Phys. Rev. E **84**, 021110 (2011)
[5] Yu.A. Kuznetsov et al.: J. Chem. Phys. **103**, 4807 (1995); J. Chem. Phys. **104**, 3338 (1996)

11.9 Aging and related scaling during collapse of a polymer

S. Majumder, W. Janke

Aging, a phenomenon characterized by faster relaxation of younger systems than older ones is quite popular for systems with slow dynamics, e.g., glasses (both spin glass and structural glass), and especially for ordering kinetics or coarsening the theoretical understanding is richly developed [1, 2]. On the other hand, in spite of phenomenological similarities with standard coarsening systems there have been only few efforts to explore this aging during the collapse of a polymer chain when it is quenched from its extended state in a good solvent (above the collapse transition temperature) to the globular phase in a poor solvent (below the collapse transition temperature). This motivates us to look into aging during the collapse of a polymer seeking the presence of any dynamical scaling.

Aging is probed by multiple time quantities, e.g., the two-time autocorrelation of a microscopic variable O_i as

$$C(t, t_w) = \langle O_i(t) O_i(t_w) \rangle - \langle O_i(t) \rangle \langle O_i(t_w) \rangle, \tag{11.5}$$

where t and t_w ($\ll t$) are the observation and waiting times, respectively. Slower decay of $C(t, t_w)$ with an increase of t_w is the signature of aging phenomena. For a nonequilibrium process, $O_i(t)$ is generally a quantity reflecting the time evolution of the system and here we judicially choose this parameter to be ± 1 depending on whether the monomer is inside (+1) or outside (-1) a cluster formed during the collapse, thus constructing an analogue to the ususal density-density autocorrelation used in glassy systems or the order-parameter autocorrelation used in coarsening kinetics. In Fig. 11.11(a) we show plots of such autocorrelations which decay slower as the age of the system increases, the signature of aging. In the inset we show the scaling of the autocorrelation as a function of t/t_w [3]. Our data not only shows scaling with respect to t/t_w but also with respect to the ratio of cluster size $C_s(t)/C_s(t_w)$ as

$$C(t, t_w) \sim [C_s(t)/C_s(t_w)]^{-\lambda_c} \tag{11.6}$$

For the exponent λ_c governing the decay, we provide a simple scaling argument to predict the bound (11.7)

$$(\nu d - 1) \leq \lambda_c \leq 2(\nu d - 1) \tag{11.7}$$

in relation to the universal Flory exponent ν. Numerical estimate of λ_c via finite-size scaling analysis gives $\lambda_c = 1.25(5)$ which obeys the predicted bound. In Fig. 11.11(b) we show a scaling plot of the autocorrelation as a function of $C_s(t)/C_s(t_w)$ for different

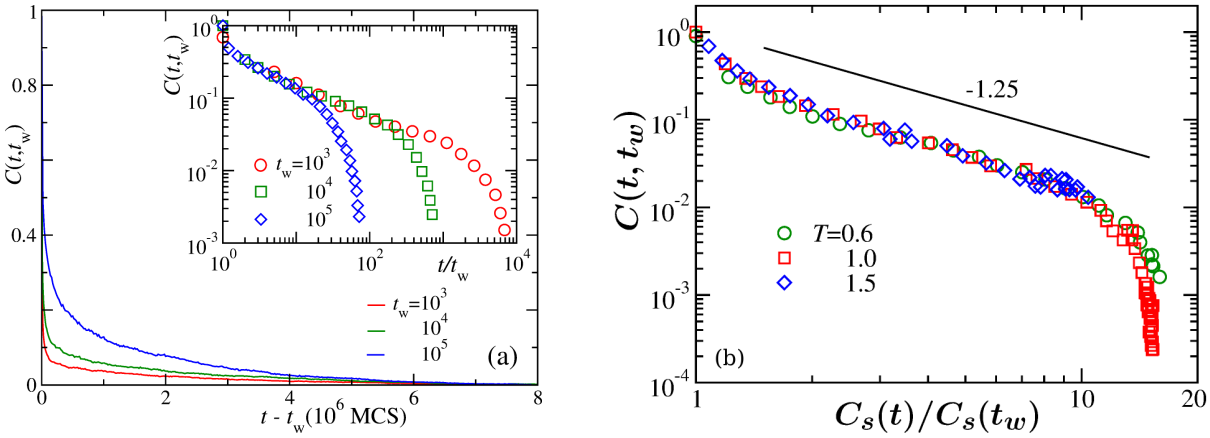

Figure 11.11: (a) Plot of the autocorrelation function $C(t, t_w)$ of a polymer with $N = 724$ for three different values of t_w at $T = 1$. The inset shows the scaling with respect to t/t_w. (b) Scaling plot of $C(t, t_w)$ as a function of $C_s(t)/C_s(t_w)$ for collapse at three different temperatures as indicated in the legend.

temperatures [4]. The consistency of our data with the power-law decay having an exponent -1.25 obeying the bound (11.7) confirms that the observed dynamical scaling is independent of temperature.

[1] M. Zannetti: *Aging in domain growth*, in *Kinetics of Phase Transitions*, eds. S. Puri, V. Wadhawan (CRC Press, Boca Raton, 2009), p. 153
[2] M. Henkel, M. Pleimling: *Non-Equilibrium Phase Transitions, Vol 2: Ageing and Dynamical Scaling far from Equilibrium* (Springer, Heidelberg, 2010)
[3] S. Majumder, W. Janke: Phys. Rev. E **93**, 032506 (2016)
[4] S. Majumder, W. Janke: *Aging and related scaling during the collapse of a polymer*, to appear in *Computer Simulation Studies in Condensed-Matter Physics XXIX*, eds. D.P. Landau, H.-B. Schüttler, S. Lewis, M. Bachmann, J. Phys.: Conf. Ser. (2016), in print

11.10 Periodically driven DNA: A comparative study of Langevin and Brownian dynamics

R. Kumar, S. Kumar*, W. Janke

*Department of Physics, Banaras Hindu University, Varanasi 221 005, India

DNA replication is one of the most important biological processes in living organisms. Under the influence of special enzymes, two strands of the DNA double helix can separate themselves like a zip. The first step in the process of DNA replication is to unzip the double-helix structure of the DNA molecule. Therefore, it is very important to study the unzipping of DNA. There has been some experimental studies at a constant force or loading rate used in SMFS experiments to unzip the DNA *in vitro*. In these experiments one end of the DNA was fixed and a constant force was applied on its other end. However, such processes are driven by different types of molecular motors

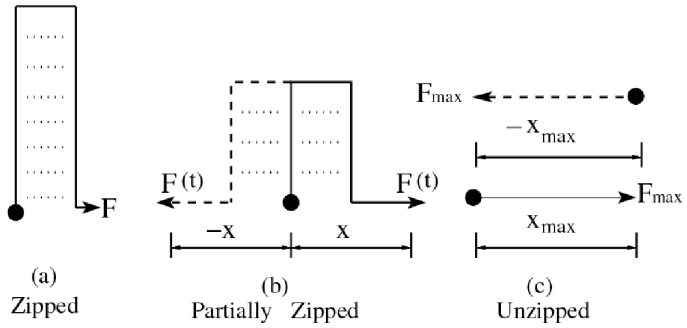

Figure 11.12: Schematic representations of DNA: (a) zipped, (b) partially zipped, and (c) unzipped state. One end is kept fixed (indicated by a solid circle), while the other end may move.

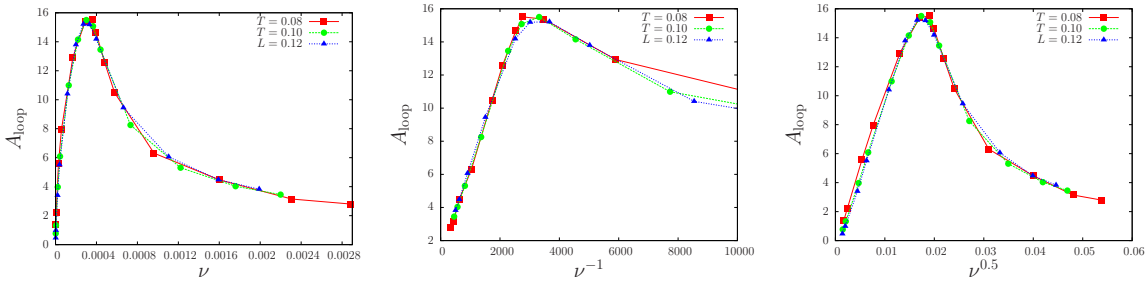

Figure 11.13: Effect of temperature on the area of the hysteresis loop for the model with parameters $L = 32$, $F = 1.0$, and $\gamma = 0.4$ for (a) loop area $A_{\rm loop}$ vs. ν, (b) area vs. ν^{-1} in the higher frequency regime, and (c) area vs. $\nu^{0.5}$ in the lower frequency regime. Here the x-axis is rescaled in order to show the data collapse for all temperatures.

in vivo [1]. Hence, the picture provided by constant force unzipping is not complete. In some recent theoretical studies it was suggested [2–5] that the application of a periodic force shows a force-driven transition in contrast to the case of a steady force.

This model was further simplified in [6, 7] by reducing the degrees of freedom and studying the overdamped limit using Brownian dynamics. This simplified model was investigated only at zero temperature. Therefore, it became crucial to further investigate how the temperature effects the dynamics of such system using the detailed model described in [3]. Emphasis was placed on the effect of different temperatures on the scaling properties. Moreover, we compared results of the Langevin dynamics for the detailed model and Brownian dynamics for the simplified model. We observed that the temperature and over-damped limit does not effect the scaling exponents. Hence, the model proposed by us is good enough to study the scaling properties and provides a possibility of analytic studies within certain limits.

[1] B. Alberts et al.: *Molecular Biology of the Cell* (Garland Publishing, New York, 1994)
[2] S. Kumar, M. S. Li: Phys. Rep. **486**, 1 (2010)
[3] S. Kumar, G. Mishra: Phys. Rev. Lett. **110**, 258102 (2013)
[4] G. Mishra et al.: Phys. Rev. E **87**, 022718 (2013)
[5] R.K. Mishra et al.: J. Chem. Phys. **138**, 244905 (2013)
[6] S. Kumar et al.: Phys. Rev. E **93**, 010402(R) (2016)

[7] R. Kumar et al.: Leipzig/Varanasi preprint (2015), to be published

11.11 Computer simulations of semiflexible polymers in disordered environments

J. Bock, W. Janke

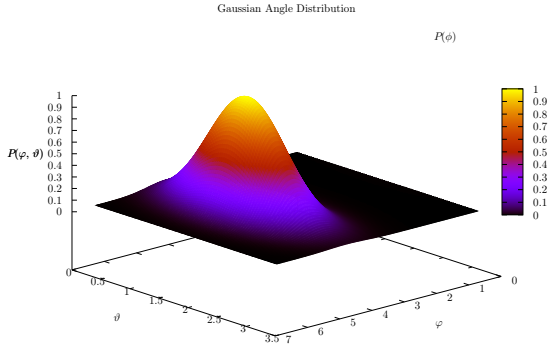

(a) Weighting histogram

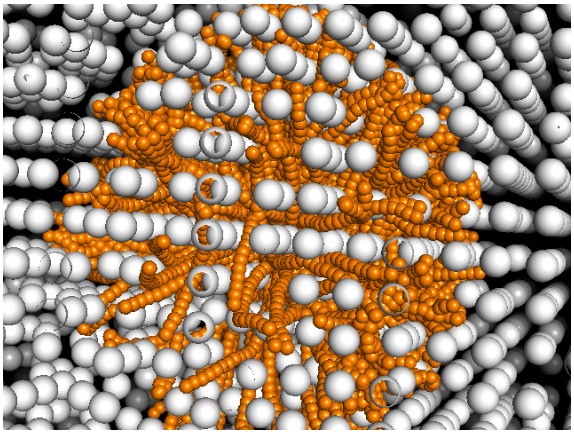

(b) Semiflexible polymer in 3D disorder

Figure 11.14: (a) Histogram used for the guiding field in 3D and (b) an examplary configuration of a polymer with $N = 30$ and $\xi = 1$.

Single-molecule experiments have established the wormlike chain (WLC) as a standard model for semiflexible polymers [1]. Exploiting the analogy of the WLC with a one-dimensional Heisenberg ferromagnet, it can be shown that the equilibrium tangent-tangent correlation function decays exponentially. The decay rate defines the thermal persistence length l_p. When the same polymer is embedded in a quenched, disordered environment in three dimensions, this property may change quantitatively or even qualitatively. We addressed this problem by performing extensive numerical simulations of semiflexible polymers in a simple lattice disorder and in a gaseous disorder constructed by microcanonical Lennard-Jones gas simulation which represents the disordered environment. Further plans are to simulate the polymers in algebraically correlated disorder. Only the space between the spheres is accessible to the polymer. The extreme strength and density of the environmental constraints are a great challenge to conventional Monte Carlo simulation schemes, which we found hard to overcome even with a sophisticated multicanonical histogram reweighting procedure [2]. We have therefore adopted a breadth-first chain-growth algorithm [3] that resolves this difficulty by circumventing energy barriers instead of trying to cross them [2, 4], see examples in Fig. 11.14. Therefore the already existing procedures in two dimensions were expanded to the third dimension to investigate the behaviour of the tangent-tangent correlation length, the mean squared end-to-end distance and the end-to-end probability distribution function, see Fig. 11.15. A difference in behaviour is clear and the task now is to

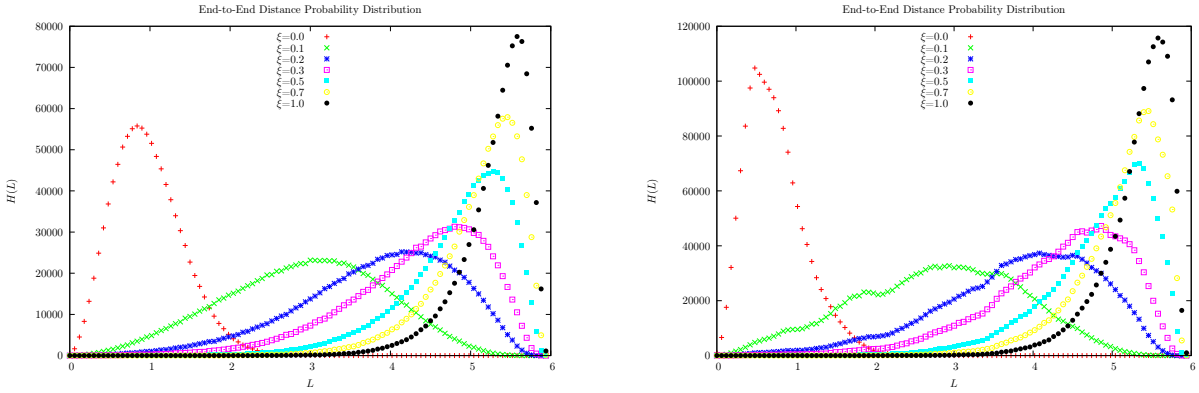

(a) Free polymers (b) Polymers in disorder

Figure 11.15: End-to-end distance distributions for (a) free polymers and (b) polymers in gaseous disorder, both in 3D.

check wether the differences scale similarly as in two dimensions, where the disorder renormalization is claimed to be [5]:

$$\frac{1}{l_p^*} = \frac{1}{l_p} + \frac{1}{l_p^D},$$

with l_p^* the renormalized persistence length, l_p the persistence length given as simulation parameter and l_p^D the measured disorder persistence length.

[1] O. Otto et al.: Nature Comm. **4**, 1780 (2013)
[2] S. Schöbl et al.: Phys. Rev. E **84**, 051805 (2011)
[3] T. Garel, H. Orland: J. Phys. A: Math. Gen. **23**, L621 (1999)
[4] S. Schöbl et al.: J. Phys. A: Math. Theor. **45**, 475002 (2012)
[5] S. Schöbl et al.: Phys. Rev. Lett. **113**, 238302 (2014)

11.12 Low-temperature behaviour of polymers in fractal disorder

N. Fricke, W. Janke

The asymptotic scaling behaviour of flexible polymers with short-range interactions is well described by the model of discrete self-avoiding walks with nearest-neighbor attractions, see [1]. For these so-called self-attracting self-avoiding walks (SASAWs), the canonical average of an observable such as the squared end-to-end distance, $\langle R^2 \rangle$, is given by

$$\langle R^2 \rangle_T = \frac{\sum_\omega R_\omega^2 e^{-m_\omega \epsilon/(k_B T)}}{\sum_\omega e^{-m_\omega \epsilon/(k_B T)}}, \tag{11.8}$$

where the sums go over all possible chain conformations ω, m_ω is the number of neighboring monomer pairs, ϵ gives the strength of attraction (set to $\epsilon = k_B$ for convenience),

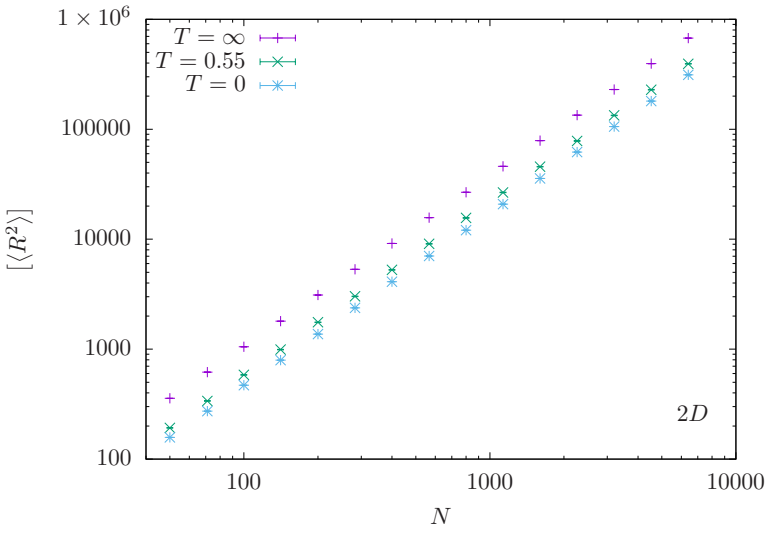

Figure 11.16: Quenched averages of the mean-squared end-to-and distances vs. number of steps for self-attracting self-avoiding walks on critical percolation clusters at different temperatures. Each data point was obtained by averaging over all walk conformations on 10^4 randomly generated clusters.

and T denotes the temperature. On regular lattices, this system undergoes a phase transition from an entropy-dominated *coiled* phase to an energy-dominated *globular* phase when the temperature is lowered. This so-called Θ-transition manifests itself through a change of the exponent describing the scaling of the average end-to-end distance with the number of steps, $\langle R^2 \rangle \sim N^{2\nu_T}$: above the transition temperature the value of ν_T is the same as for non-interacting self-avoiding walks, while below it is given by the inverse of the system's dimension.

We investigated SASAWs in the presence of fractal disorder. Specifically, we looked at the quenched averages on critical percolation clusters for square and cubic lattices. This has been considered in several previous studies where evidence for a Θ-transition had been reported [2, 3]. However, these works had relied on numerical methods that only allowed for rather small systems, so that the conclusiveness of the results was limited. We could study the system in much greater detail thanks to a new exact enumeration technique [4, 5], which makes use of the system's fractal geometry and can thus easily handle walks of several thousand steps. This revealed that the asymptotic scaling behaviour of SASAWs on critical percolation clusters is actually independent of the temperature as can be seen in Fig. 11.16 where the quenched averages of $\langle R^2 \rangle$ for SASAWs at different temperatures are plotted against the number of steps N. Indeed, our estimates for the exponents ν_T all agree within the errors of the fits. This unusual absence of a temperature-driven collapse transition might be explained by the fact that – unlike for the undiluted system – energy and entropy do not compete: At both high and low temperatures, the average on a critical percolation cluster is dominated by a few highly interconnected cluster regions, which are entropically favorable while at the same time allowing for most nearest-neighbour contacts.

[1] B. Duplantier, H. Saleur: Phys. Rev. Lett. **59**, 539 (1987)
[2] B. Barat, B.K. Chakrabarti: Phys. Rep. **258**, 377 (1995)

[3] V. Blavatska, W. Janke: Phys. Rev. E **80**, 051805 (2009)
[4] N. Fricke, W. Janke: Europhys. Lett. **99**, 56005 (2012)
[5] N. Fricke, W. Janke: Phys. Rev. Lett. **113**, 255701 (2014)

11.13 Dynamical greedy algorithm for the Edwards-Anderson model

S. Schnabel, W. Janke

One of the most intuitive and natural approaches to optimization problems is realized by the so-called greedy algorithms. These methods create trajectories in the space of possible solution by always choosing the next step such that the energy is maximally reduced (or a fitness function maximally increased). Naturally, this will usually not find the global optimum, just as starting at a random spot and always walking uphill will usually not lead a wanderer to the summit of Mt. Everest. Therefore, in practice many attempts with randomly created starting points are made and if the problem is not too difficult the global optimum may be found this way.

On the other hand, there is practically no chance of success if the energy landscape is as complicated and possesses as many local minima as in the case of the Edwards-Anderson spin-glass model [1], whose Hamiltonian is given by

$$\mathcal{H} = \sum_{\langle ij \rangle} J_{ij} S_i S_j,$$

where the spins can take two values $S_i \in \{-1, 1\}$ and adjacent spins interact via normally distributed random couplings J_{ij}. If such a model on a three-dimensional cubic lattice of 1000 spins is considered, about 10^{30} attempts were necessary in order to find the ground state this way.

However, the greedy algorithm can still be a very helpful tool, since it is a comparatively simple and reliable method to reach states of low energy. We devised a method to efficiently update the greedy algorithm, i.e., to reuse the data created during a minimization from a configuration $\mathbf{S}$ to the configuration $\mathbf{S}_{\min}$ to obtain the result $\mathbf{S}'_{\min}$ of the minimization from a configuration $\mathbf{S}'$ which differs from $\mathbf{S}$ only in the values of one or very few spins. If furthermore, both, the terminal configuration, delivered by the greedy algorithm, and its energy are understood as attributes of the starting configuration, it is possible to use the energy of the minimized configurations $\mathbf{S}_{\min,t}$ to steer a path in the space of starting configurations $\mathbf{S}_t$.

A simple application is to apply the greedy algorithm again: It is tested which alteration (e.g, which single spin flip) of the starting configuration will reduce the energy of the *minimized* configuration by the largest amount and this locally optimal step is performed. Repeating this simple procedure as long as viable as a "second order greedy algorithm" will lead to much lower energies albeit not the ground state.

Alternatively, the energy of the minimized configuration can be used as argument for the occupation probability for a generalized ensemble [2]:

$$P(\mathbf{S}) = P(\mathbf{S}_{\min}),$$

which can then be sampled using Monte Carlo techniques. All states in the same "valley" in the energy landscape, i.e., all configuration which minimize to the same local energy minimum, now occur with the same probability and the barriers of high energy which greatly hamper standard Monte Carlo simulations simply vanish. In consequence, the configuration space is sampled much more easily and the performance of ground-state search is greatly improved.

[1] S.F. Edwards, P.W. Anderson: J. Phys. F **5**, 965 (1975)
[2] D.J. Wales: J. Phys. Chem. A **101**, 5111 (1997)

11.14 Spin glasses with variable frustration

R. Kumar, M. Weigel*, W. Janke

*Applied Mathematics Research Centre, Coventry University, Coventry, England, UK

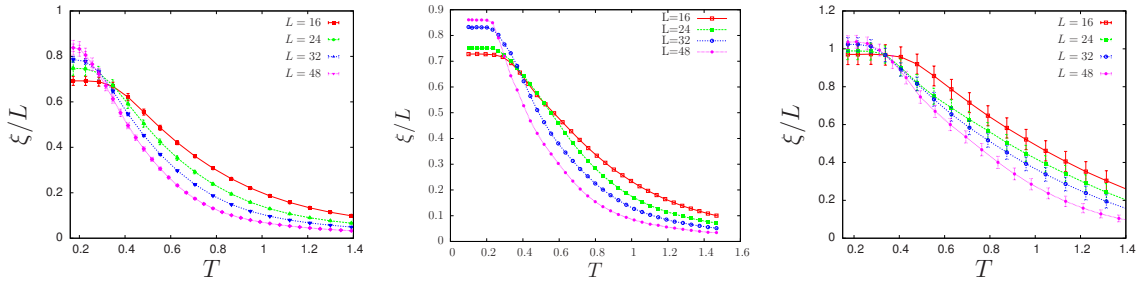

Figure 11.17: Correlation length as a function of temperature for (a) stochastic frustrated system, (b) a system with 46% frustration, and (c) a system with 20% frustration.

Together with randomness, frustration is believed to be a crucial prerequisite for the occurrence of glassy behaviour in spin systems. The degree of frustration is normally the result of a chosen distribution of exchange couplings in combination with the structure of the lattice under consideration. Here, however, we discuss a process for tuning the frustration content of the Edwards-Anderson model on arbitrary lattices. With the help of extensive parallel-tempering Monte Carlo simulations we study such systems on the square lattice and compare the outcomes to the predictions of a recent study employing the Migdal-Kadanoff real-space renormalization procedure [1]. We use a cluster algorithm proposed in [2] in order to reduce the equilibration time. The phase transition studies are done by looking at the divergence of the correlation length, see Fig. 11.17. The results are benchmarked by comparing to the stochastic case described in [3].

We find that the divergence of the correlation length occurs at non-zero finite temperature for the 2D Ising spin glass. This gives hints of a phase transition, but such transitions have to be studied carefully in order to fully understand the phases [4].

[1] E. Ilker, A.N. Berker: Phys. Rev. E **89**, 042139 (2014)

[2] J. Houdayer: Eur. Phys. J. B **22**, 479 (2001)
[3] H.G. Katzgraber, L.W. Lee: Phys. Rev. B **71**, 134404 (2005)
[4] A. Hartmann: Phys. Rev. B **67**, 214404 (2003)

11.15 Equilibrium properties of the plaquette model

M. Müller, W. Janke, D.A. Johnston*

*Department of Mathematics and the Maxwell Institute for Mathematical Sciences, Heriot-Watt University, Edinburgh, UK

A family of Hamiltonians, called gonihedric Ising model, originates from high-energy physics as a possible discretization of the area swept out by a string worldsheet moving through spacetime. The name comprises the greek words gonia (angle) and hedra (face) as a reminder of the origin, see [1] for a review.

The plaquette model is a special case of this gonihedric Ising model which looks unobtrusive,

$$H = \sum_{[i,j,k,l]} \sigma_i \sigma_j \sigma_k \sigma_l \ , \tag{11.9}$$

but features very interesting properties. The first-order phase transition apparent in the system [2] is a very strong one and thus canonical simulations get easily trapped in one of the phases, potentially spoiling estimators for the transition temperature and latent heat. In addition, we found that the finite-size scaling behaviour for this model is changed due to the exponential degeneracy in the low-temperature phase [3]. Taking that into account, we found an overall consistent inverse transition temperature of the infinite system $\beta = 0.551\,334(8)$ that incorporates estimators from both periodic and fixed boundary simulations as well as an estimator coming from a dual representation of the model [4, 5]. The puzzling effect of obtaining different latent heats for different boundary conditions could be traced back to extraordinary huge boundary effects [6].

To gain a deeper understanding of the properties of the transition, we investigated a recent suggestion in [7, 8] for a candidate order parameter coming from an anisotropic limit of the model. Indeed, we found that this planar order parameter is well suited to distinguish between the different phases [9]. Also, this parameter is subject to the non-standard finite-size effects, as depicted in Fig. 11.18(b). We also showed that the order parameter like behaviour of the susceptibility seen earlier in Metropolis simulations was an artefact of the algorithm failing to explore the phase space of the macroscopic degenerate low-temperature phase. Our multicanonical simulations were able to alleviate this to some extent, but we suggest to incorporate non-local plane-flips into simulations to improve ergodicity properties and measurements of (standard) magnetic properties.

With our multicanonical simulations combined with the nonstandard finite-size scaling, the equilibrium properties of both energetic and magnetic quantities of the $3D$ plaquette gonihedric Ising model are now under good numerical control and the order parameter has been clearly identified. The *non*-equilibrium properties, in particular earlier suggestions that the model might serve as a generic example of glassy behaviour, even in the absence of quenched disorder, still pose open questions.

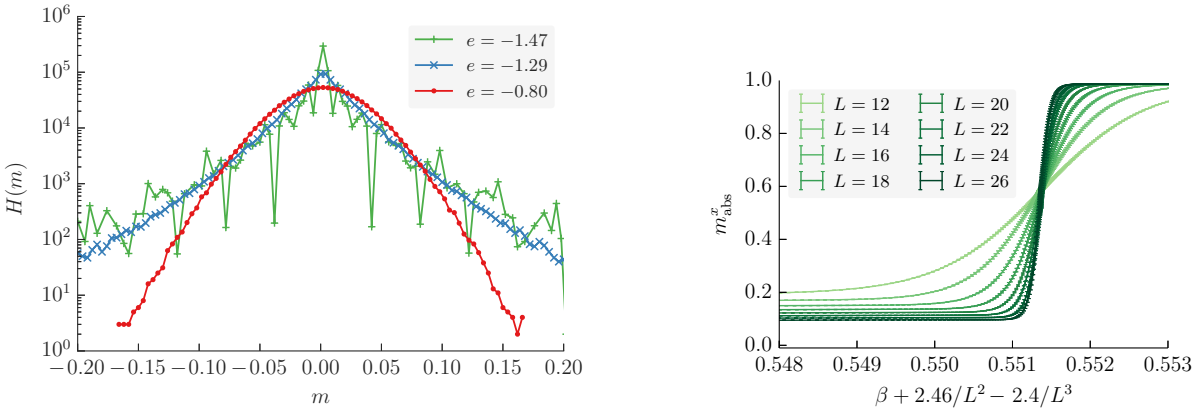

(a) (b)

Figure 11.18: (a) Conducting 10^6 random plane-flips in three configurations that are fixed in the different phases reveals the symmetry of the magnetic probability density. The ensemble average of the magnetization is equal to zero for both phases. (b) One of the planar order-parameters as a function of inverse temperature, showing a sharp jump at the phase transition point.

[1] D.A. Johnston et al.: in *Rugged Free Energy Landscapes: Common Computational Approaches to Spin Glasses, Structural Glasses and Biological Macromolecules*, ed. W. Janke, Lecture Notes in Physics **736** (Springer, Berlin, 2008), p. 173
[2] D. Espriu et al.: J. Phys. A: Math. Gen. **30**, 405 (1997)
[3] M. Mueller et al.: Phys. Rev. Lett. **112**, 200601 (2014)
[4] M. Mueller et al.: Nucl. Phys. B **888**, 214 (2014)
[5] M. Mueller et al.: in *Computer Simulation Studies in Condensed-Matter Physics XXVII*, eds. H.-B. Schüttler, S. Lewis, M. Bachmann, D.P. Landau, Physics Procedia **57**, 68 (2014)
[6] W. Janke et al.: J. Phys.: Conf. Ser. **640**, 012002 (2015)
[7] D.A. Johnston: J. Phys. A: Math. Theor. **45**, 405001 (2012)
[8] Y. Hashizume, M. Suzuki: Int. J. Mod. Phys. B **25**, 73 (2011); *ibid.* **25**, 3529 (2011)
[9] M. Mueller et al.: Nucl. Phys. B **894**, 1 (2015); D.A. Johnston et al.: Mod. Phys. Lett. B **29**, 1550109 (2015)

11.16 Boundary conditions and non-local constraints in plaquette models

M. Müller, W. Janke, D.A. Johnston*

*Department of Mathematics and the Maxwell Institute for Mathematical Sciences, Heriot-Watt University, Edinburgh, UK

An anisotropic limit of the 3*D* plaquette Ising model, in which the plaquette couplings in one direction were set to zero, was solved for free boundary conditions by Suzuki [1], who later dubbed it the fuki-nuke, or “no-ceiling”, model. Defining new

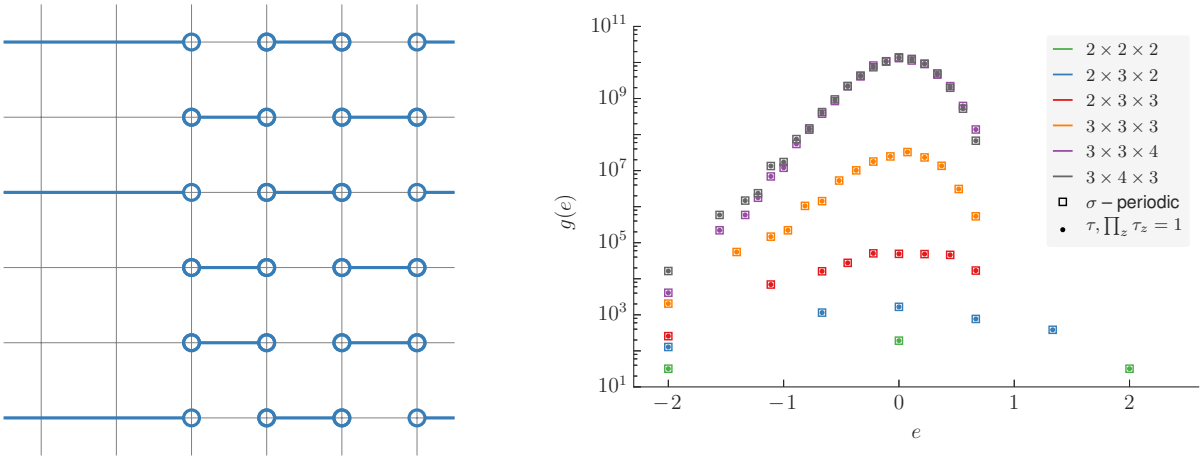

(a) (b)

Figure 11.19: (a) Graphical dimer-representation of one term that contributes to the partition function in the 2*D* plaquette models. (b) Using exact enumerations to get the number of states $g(E)$ with given energy E, we ensure that no trivial errors enter the calculation of the partition function in the product-spin representation that leads to non-local constraints.

spin variables as the product of nearest-neighbour spins transforms the Hamiltonian into that of a stack of (standard) 2*D* Ising models and reveals the planar nature of the magnetic order, which is also present in the fully isotropic 3*D* plaquette model [2]. More recently, the solution of the fuki-nuke model was discussed for periodic boundary conditions applied to the spin lattice, which require a slightly different approach to defining the product spin transformation, by Castelnovo *et al.* [3].

We find that the essential features of the differences between free and periodic boundary conditions when using a product spin transformation are already present in the 1*D* Ising model [4], which thus provides an illuminating test case for its use in solving plaquette spin models and an alternative method for solving the 1*D* Ising model with periodic boundary conditions.

We clarify the exact relation between partition functions expressed in terms of the original and product spin variables for the 1*D* Ising model, 2*D* plaquette and 3*D* fuki-nuke models with free and periodic boundary conditions. Representing graphically the combinatorial factors that contribute to the partition function, we are able to solve the 2*D* plaquette model with free, periodic and helical boundary conditions and various combination of these in x- and y-directions, see Fig. 11.19. The various exactly solved examples illustrate how correlations can be induced in finite systems as a consequence of the choice of boundary conditions.

The similarities between the 2*D* plaquette model with periodic boundaries, when expressed in terms of the product spin variables and a "ladder" of interaction-free 1*D* Ising models that are coupled by non-local constraints is subject to further studies and might give even deeper (pedagogical) insight into the interplay between boundary conditions and non-local constraints that directly influence correlations between spins.

[1] M. Suzuki: Phys. Rev. Lett. **28**, 507 (1972)
[2] M. Mueller et al.: Nucl. Phys. B **894**, 1 (2015); D.A. Johnston et al.: Mod. Phys. Lett. B **29**, 1550109 (2015)

[3] C. Castelnovo et al.: Phys. Rev. B **81**, 184303 (2010)
[4] M. Mueller et al.: *Boundary conditions subtleties in plaquette models (and the 1d Ising model)*, Leipzig/Edinburgh preprint (January 2016), submitted

11.17 First-order directional ordering transition in the three-dimensional compass model

M.H. Gerlach*, W. Janke

*Institut für Theoretische Physik, Universität zu Köln, Germany

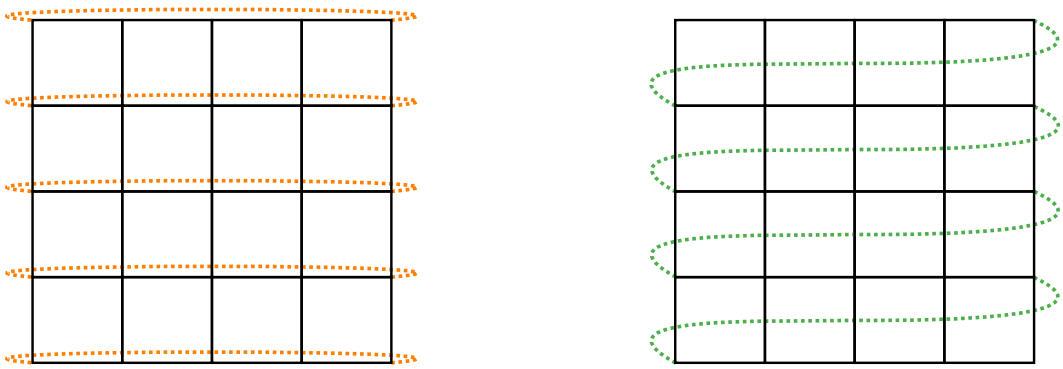

(a) PBC (b) SBC

Figure 11.20: Sketch of (a) periodic (PBC) and (b) screw-periodic boundary conditions (SBC) along the x-axis of a two-dimensional lattice. In the SBC picture the link between the lower right and the upper left corner is not shown. Equivalent boundary conditions are applied to the y-direction. Here a screw parameter of $S = 1$ is used.

Both the classical and the quantum version of the compass model have recently attracted much interest in the literature. The resaon is its connection to interesting quantum phenomena ranging from orbital order in transition metal compounds to topologically protected qbits [1–3]. In three dimensions the classical model is defined by the Hamiltonian

$$\mathcal{H} = J \sum_{i=1}^{N} \left(\sigma_i^x \sigma_{i+e_x}^x + \sigma_i^y \sigma_{i+e_y}^y + \sigma_i^z \sigma_{i+e_z}^z \right) , \tag{11.10}$$

where $\sigma = (\sigma^x, \sigma^y, \sigma^z)$ are three-dimensional unit spin vectors, e_x, e_y, and e_z are unit vectors in x, y, and z direction, and J is a coupling constant. Although simple looking at first sight, surprisingly little is known about this model in three dimensions. Most studies so far focused on the two-dimensional analogue which still turned out to be rather hard to study numerically. It was shown to possess rich physics ranging from highly degenerate ground states to quantum phase transitions to an exciting thermal phase transition [4, 5].

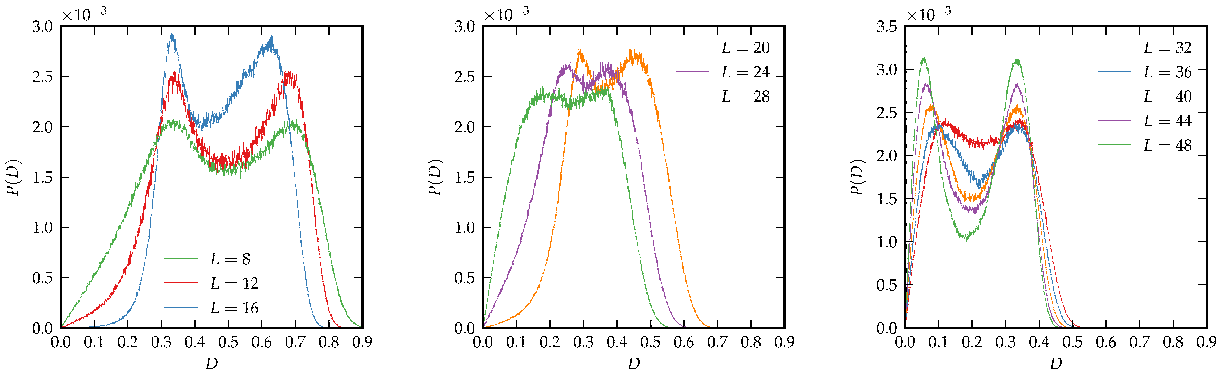

Figure 11.21: Histograms of the directional order parameter D in the three-dimensional compass model with screw-periodic boundary conditions for various lattice sizes L.

In recent analyses of high-temperature series expansions of the three-dimensional quantum model (where the classical spins are replaced by Pauli matrices) it was claimed that this model does not exhibit a phase transition at any finite temperature [6]. This motivated us to consider first the three-dimensional classical model and to investigate whether this model exhibits a phase transition [7]. To this end we employed state-of-the-art Monte Carlo computer simulations using Metropolis, cluster, and parallel tempering (PT) techniques. From our previous studies in two dimensions [5] we knew that employing so-called screw-periodic boundary conditions [8] sketched in Fig. 11.20 considerably improves the finite-size scaling behaviour of this model. As a result we obtained convincing numerical evidence for a phase transition of first-order at the temperature $T_0 = 0.098328 \pm 0.000003$. This value is in good agreement with a brief remark in Ref. [9]. The nature of the phase transition can be read off from the histograms of the directional order parameter D of the model in Fig. 11.21 which exhibit for large lattice sizes L a characteristic double-peak structure. Note the nonmonotonic behaviour as function of lattice size: Initially, the double peak becomes *less* pronounced until $L \approx 28-32$, and only from then on it becomes more pronounced with further increasing L. By analyzing the ratio of peak maximum to peak minimum, we arrive at a definitely nonzero, albeit small value for the associated interface tension, $\sigma_{\mathrm{od}} \approx 3 \times 10^{-4}$.

[1] K.I. Kugel, D.I. Khomskii: Sov. Phys. Usp. **25**, 231 (1982)
[2] B. Douçot et al.: Phys. Rev. B **71**, 024505 (2005)
[3] A. Kitaev: Ann. Phys. **321**, 2 (2006)
[4] S. Wenzel, W. Janke: Phys. Rev. B **78**, 064402 (2008); see also "Publisher's Note" in Phys. Rev. B **78**, 099902(E) (2008) [Fig. 1 selected for Phys. Rev. B "Kaleidoscope" August 2008]
[5] S. Wenzel et al.: Phys. Rev. E **81**, 066702 (2010)
[6] J. Oitmaa, C.J. Hamer: Phys. Rev. B **83**, 094437 (2011)
[7] M.H. Gerlach, W. Janke: Phys. Rev. B **91**, 045119 (2015)
[8] E. Bittner et al.: Nucl. Phys. B **820**, 694 (2009)
[9] S. Wenzel, A.M. Läuchli: Phys. Rev. Lett. **106**, 197201 (2011)

11.18 Transition barriers in the three-dimensional Blume-Capel model

J. Zierenberg, N.G. Fytas*, W. Janke

*Applied Mathematics Research Centre, Coventry University, Coventry, England, UK

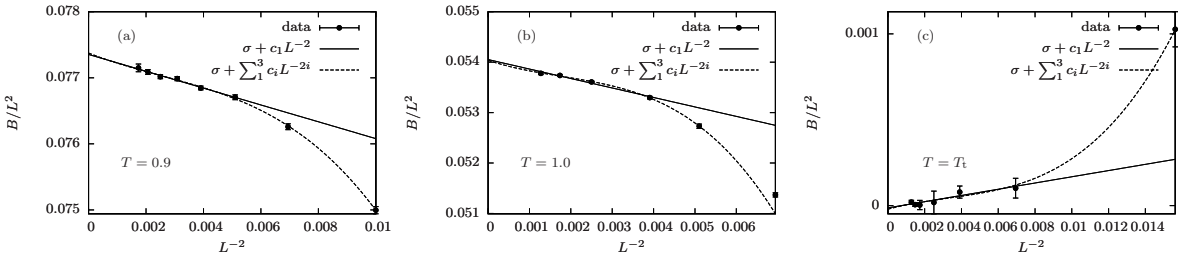

(a) (b) (c)

Figure 11.22: Finite-size scaling of the transition barrier in the 3D Blume-Capel model at fixed temperature under variation of the crystal field for (a) $T = 0.9$, (b) $T = 1.0$, and (c) $T = 1.4182$ (close to the tricritical point).

The Blume-Capel model [1, 2] is a perfect test model for studies of phase transitions. We consider this spin-one Ising model in a crystal field on a cubic lattice in three dimension (3D), described by the Hamiltonian

$$\mathcal{H} = -J \sum_{\langle ij \rangle} \sigma_i \sigma_j + \Delta \sum_i \sigma_i^2 = E_J + \Delta E_\Delta \,. \tag{11.11}$$

Using a multicanonical based approach, we study the first- and second-order phase transitions at fixed temperature along the crystal field axis [3]. This allows us to directly estimate the barrier associated with the suppression of states during a first-order phase transition as

$$B = \frac{1}{2\beta\Delta} \ln\left(\frac{P_{\max}}{P_{\min}}\right)_{\text{eqh}} , \tag{11.12}$$

where $P_{\max}$ and $P_{\min}$ are the maximum and the local minimum of the distribution $P(E_\Delta)$, respectively. The resulting barrier connects a spin-0 dominated regime (E_Δ small) and a spin-±1 dominated regime (E_Δ large), which may be associated with condensation and strip formation of spin-0 clusters and thus shows analogies to Ising (lattice gas) droplet/strip transitions [4, 5]. Consequently, we expect a scaling behaviour in three dimensions as $B/L^2 = \sigma + c_1/L^2 + \mathcal{O}\left(1/L^4\right)$, see Fig. 11.22. A higher-order fit yields $\sigma_3 = 0.0774(1)$ and $\sigma_2 = 0.0540(2)$ for $T_3 = 0.9$ and $T_2 = 1.0$, respectively. In the vicinity of the tricritial point [6], at $T_t = 1.4182$, the extrapolation yields $\sigma \approx 0$, indicating as expected that the interface tension vanishes in the thermodynamic limit.

[1] M. Blume: Phys. Rev. **141**, 517 (1966)
[2] H.W. Capel: Physica (Utr.) **32**, 966 (1966)

[3] J. Zierenberg et al.: Phys. Rev. E **91**, 032126 (2015)
[4] A. Nußbaumer et al.: Europhys. Lett. **75**, 716 (2006)
[5] A. Nußbaumer et al.: Phys. Rev. E **77**, 041109 (2008)
[6] M. Deserno: Phys. Rev. E **56**, 5204 (1997)

11.19 Boundary drive induced phase transitions in stochastic transport condensation models

H. Nagel, H. Christiansen, W. Janke

Stochastic mass transport processes such as the asymmetric simple exclusion process (ASEP) or the zero-range process (ZRP) are simple transport models for particle hopping aiming to improve the understanding of basic phenomena in the dynamics of particles in driven diffusive systems. An important class of such phenomena that can be studied and understood on an abstract level is the emergence of generic condensates. In this project we considered such a transport processes under driven particle exchange through open boundaries and systematically studied the emerging phase diagrams. While boundary drive induced phase transitions are known since long for the ASEP, the research for the ZRP with condensation dynamics is more recent [1].

More precisely we investigated transport processes with tunable weights [2] as well as various types of interactions at the boundaries to study these effects on a much broader scale. The tunable model allowed us to effectively interpolate between ZRP-type as well as strong short-range interactions. At the boundaries we considered the existence of fixed versus loose couplings as well as different approaches to particle injection and removal rates. For the generated cases we produced the phase diagrams under differing strengths of the driven particle exchange at the boundaries for symmetric and totally asymmetric dynamics [3–5]. The main phases, as shown in Fig. 11.23, are: a thin particle gas (G), formation of aggregate condensates (A) and the spanning bulk condensate (SC). While the phase diagrams with vanishing as well as stronger short-range interactions are very similar except for the SC phase, we observed a qualitatively different mechanism for aggregate condensate formation with short-range interactions.

[1] E. Levine et al.: J. Stat. Phys. **120**, 759 (2005)
[2] B. Wacław et al.: Phys. Rev. Lett. **103**, 080602 (2009)
[3] H. Nagel et al.: in *Computer Simulation Studies in Condensed-Matter Physics XXVII*, eds. H.-B. Schüttler, S. Lewis, M. Bachmann, D.P. Landau, Physics Procedia **57**, 77 (2014)
[4] H. Nagel et al.: Europhys. Lett. **111**, 30001 (2015)
[5] H. Nagel, W. Janke: J. Stat. Mech.: Theor. Exp., 013207 (2016)

11.20 A simple non-equilibrium model for Stranski-Krastanov growth

J.K. Ochab*, H. Nagel, W. Janke, B. Wacław†

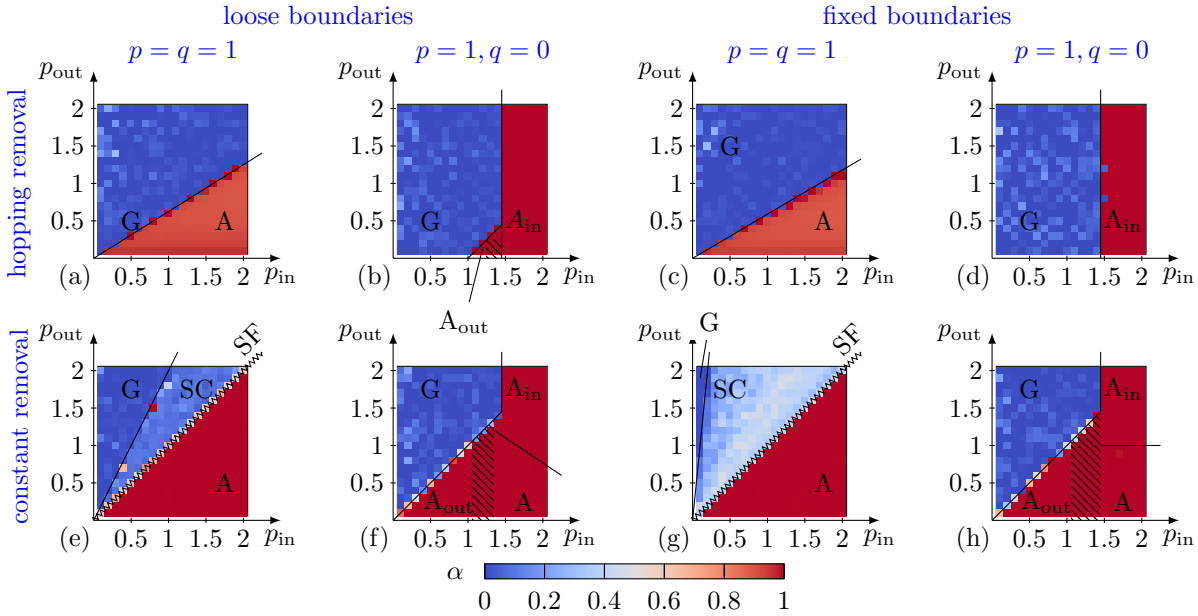

Figure 11.23: Phases induced by driven particle exchange through open boundary conditions of the system [5]. With respect to the specific implementation of the interaction at the boundary, different phase diagrams are observed.

*Marian Smoluchowski Institute of Physics and Mark Kac Complex Systems Research Center, Kraków, Poland
†School of Physics and Astronomy, University of Edinburgh, Scotland, UK

We consider a simple non-equilibrium model of mass condensation with Lennard-Jones interactions between particles and a substrate. This model is an extension of the zero-range process to nearest-neighbour interactions, similar to that of Refs. [1–3], where particles interact when they are at the same site or at neighbouring sites. Although the model can be driven far from equilibrium, it is closely related to the equilibrium solid-on-solid (SOS) model [4]. A remarkable feature of this stochastic process is that the steady state factorises over pairs of neighbouring sites, also in dimensions higher than one, and thus it is called the pair-factorised steady state (PFSS) process. This property facilitates analytical calculations in the one-dimensional version of the model and, in certain cases, also in more than one dimension [5].

We show that when some number of particles is deposited onto the surface and the system is left to equilibrate, particles condense into an island if the density of particles becomes higher than some critical density [6]. We illustrate this with numerically obtained phase diagrams for (2+1)-dimensional systems. We also solve a (1+1)-dimensional counterpart of this model analytically and show that not only the phase diagram but also the shape of the cross-sections of (2+1)-dimensional condensates qualitatively matches the (1+1)-dimensional predictions [2, 3, 7]. Furthermore, when particles are being deposited with a constant rate, we demonstrate that the system has two phases: a single condensate for low deposition rates, and multiple condensates for fast deposition [6]. The behaviour of our model is thus similar to that of thin film growth processes, and in particular to Stranski-Krastanov growth.

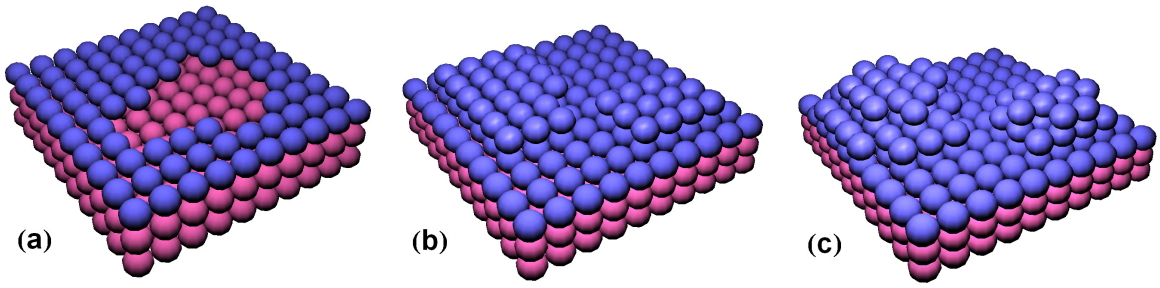

Figure 11.24: Schematic stages of Stranski-Krastanov growth. (a) The substrate (purple spheres) is covered with an increasing number of adatoms (blue spheres), starting from an incomplete monolayer. (b) As the density of adatoms increases, the adatoms form a complete monolayer and a partially filled second layer. (c) Upon further density increase, islands of variable height begin to form on the monolayer. Here the critical density of adatoms above which islands occur equals one adatom per one substrate site.

[1] M. Evans et al.: Phys. Rev. Lett. **97**, 010602 (2006)
[2] B. Wacław et al.: Phys. Rev. Lett. **103**, 080602 (2009)
[3] B. Wacław et al.: J. Stat. Mech.: Theor. Exp., P10021 (2009)
[4] S.T. Chui, J.D. Weeks: Phys. Rev. B **23**, 2438 (1981)
[5] B. Wacław et al.: J. Phys. A: Math. Theor. **42**, 315003 (2009)
[6] J.K. Ochab et al.: J. Stat. Mech.: Theor. Exp., P09013 (2015)
[7] E. Ehrenpreis et al.: J. Phys. A: Math. Theor. **47**, 125001 (2014)

11.21 Molecular dynamics simulations of hydrogen diffusion in ZIF-11

P. Schierz, S. Fritzsche, W. Janke, S. Hannongbua[*], O. Saengsawang[†], C. Chmelik[‡], J. Kärger[‡]

[*]Chulalongkorn University, Computational Chemistry Unit Cell (CCUC), Department of Chemistry, Faculty of Science, Bangkok 10330, Thailand
[†]Office of Corporate R&D, IRPC Public Company Limited, Rayong, Thailand
[‡]Institute for Experimental Physics I

The properties of porous materials have become a topic of great interest for basic research as well as for practical applications. Two of the most common aims are to improve selectivity and storage properties for sorbent applications. In recent years, metal organic frameworks (MOFs) have become porous materials of great interest because of their promising properties and because of the big variety of structures that can be obtained from the combinations of metal knots and organic linkers [1]. ZIFs (zeolitic imidazolate frameworks), as one subgroup of MOFs, have attracted attention due to their exceptional chemical and thermal stability [2].

In this project [3] the crystallographic structure of ZIF-11 was investigated with the conclusion that different linkers should be described with different MD parameters to reproduce the structure as it was determined by X-ray diffraction, see Fig. 11.25.

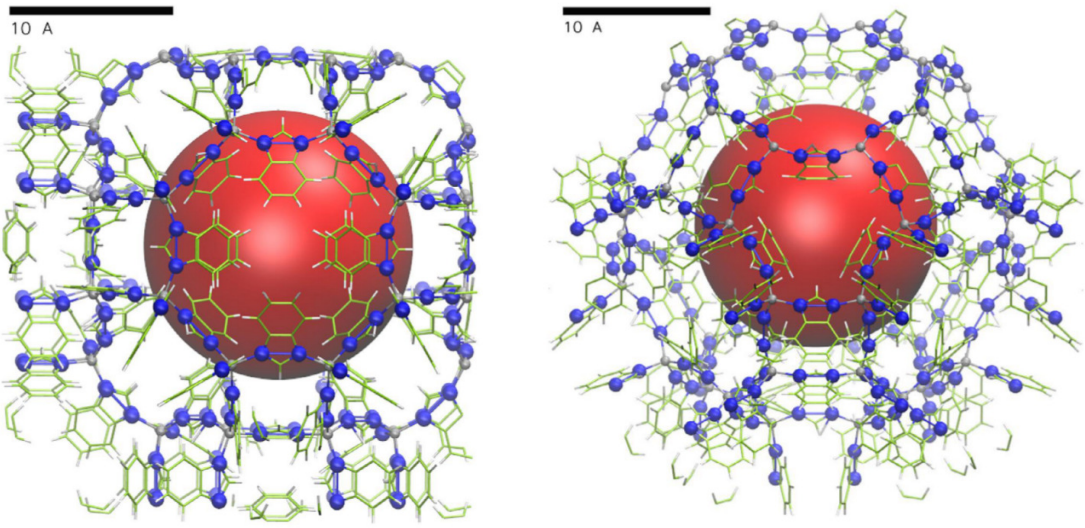

(a) (b)

Figure 11.25: ZIF-11 structure viewed (a) through the 8-membered ring and (b) through the 6-membered ring window.

It turned out that in ZIF-11, up to room temperature, there is essentially only one type of connections between adjacent cavities. The crystallographic structure of ZIF-11 was reproduced with a high accuracy and the lattice parameters (physical dimension of the unit cell) were shown to be reproduced in NPT test simulations. The force field presented in this work leads to good agreement with the complete experimental adsorption isotherm of hydrogen in ZIF-11, by fitting only the hydrogen-hydrogen Lennard-Jones parameters. For this type of material it is therefore possible to describe experimental values with the used type of force field for at least one temperature. This is encouraging since the used types of force fields are, in some cases, rather simple. The flexibility of the lattice had a small, but noticeable, influence on the adsorption data. To get full accuracy it is advisable to take account of the lattice flexibility of ZIF-11. The good agreement obtained between the simulated and measured adsorption properties is referred to the high accuracy of the ZIF-11 structure ensured in our simulations.

[1] L. James: Chem. Soc. Rev. **32**, 276 (2003)
[2] K.S. Park et al.: Proc. Natl. Acad. Sci. USA **103**, 10186 (2006)
[3] P. Schierz et al.: Microporous Mesoporous Mater. **203**, 132 (2015)

11.22 The NVE ensemble as the bridge between molecular dynamics and Monte Carlo simulations for liquid-gas like phase transitions

P. Schierz, J. Zierenberg, W. Janke

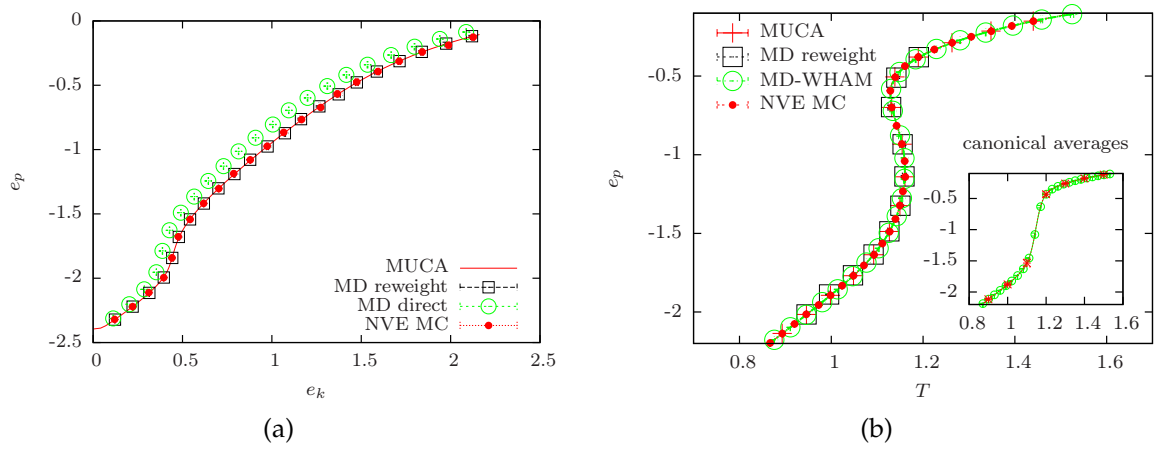

Figure 11.26: (a) The potential energy e_p vs kinetic energy e_k for a single polymer with 13 monomers. The MD data is once evaluated directly (NVEPJ ensemble) and once reweighted to the NVE ensemble. (b) The potential energy vs. temperature for 8 polymers with 13 monomers each, simulated with two MC techniques and MD.

Molecular dynamics (MD) and Monte Carlo (MC) simulations are starting from two distinct physical points of view. While MD numerically integrates Newton's equations of motion, MC samples according to known ensemble probabilities from statistical physics. The ergodic hypothesis states that both approaches should give the same results in equilibrium, which is the basis for the formulation of the microcanonical ensemble.

Energy conserving MD simulations are normally considered to sample the NVE ensemble which is, as we recover, not entirely correct [1]. Since energy conserving MD simulations encounter total angular momentum J and total linear momentum P conservation, the available phase space for an MD simulation is restricted. The resulting ensemble is either the NVEPJ or NVEP ensemble depending on the conserved quantities. Hence we obtain in Fig. 11.26(a) a deviating behaviour in comparison to simulations in the pure NVE ensemble which were obtained with Monte Carlo techniques [2, 3] for a small number of degrees of freedom. MD simulations for a liquid-gas like phase transition encounter a transition between NVEPJ and NVEP ensemble behaviour. The reason are the periodic boundary conditions which lead to a violation of angular momentum conservations whenever they are used. If a system stays within a droplet phase it will not be influenced by the boundaries and hence the angular momentum remains conserved (NVEPJ behaviour [4]). For the gas phase, however, the angular momentum fluctuates and we encounter NVEP [5] behaviour.

With the exact knowledge of the ensemble which is sampled by MD it was possible to develop a method which allows to estimate the density of states of the simulated systems. In a first step we reweighted the obtained data from MD to the NVE ensemble. For the NVE ensemble we adapted the known "Weighted Histogram Analysis Method" (WHAM) [6], which allows one to estimate the density of states.

Afterwards, the density of states can be used to calculate the behaviour in the NVT ensemble [see Fig. 11.26(b)] and therefore to investigate phase transitions with varying temperature without the use of any thermostat in MD. Since the NVE ensemble shows very good sampling behaviour in the potential-energy range of canonical first-order

phase transitions it is possible to estimate NVT phase transition behaviour by performing many NVE simulations at various total energies. Since this method estimates the density of states it is also a promising approach for the estimation of free-energy barriers for first-order phase transitions with MD.

[1] P. Schierz et al.: J. Chem. Phys. **143**, 134114 (2015)
[2] J.R. Ray: Phys. Rev. A **44**, 4061 (1991)
[3] R. Lustig: J. Chem. Phys. **109**, 8816 (1998)
[4] F. Calvo et al.: J. Chem. Phys. **112**, 10350 (2000)
[5] R. Lustig: J. Chem. Phys. **100**, 3048 (1994)
[6] A.M. Ferrenberg, R.H. Swendsen: Phys. Rev. Lett. **63**, 1195 (1989)

11.23 The real microcanonical ensemble and its advantageous behaviour for first-order phase transitions

P. Schierz, J. Zierenberg, W. Janke

The microcanonical ensemble can be found in any standard text book on statistical physics. In almost all cases this ensemble is quickly dismissed in favor of the canonical ensemble since it is quite unrealistic for most physical systems in a laboratory. In the literature on phase transitions, however, this ensemble gained some interest also due to the development of the generalized ensemble methods MUCA [1, 2] and Wang-Landau [3]. Here, however, one refers to the microcanonical ensemble at constant potential energy while the "real" microcanonical ensemble was originally defined at constant total energy. We previously investigated the behaviour of molecular dynamics and Monte Carlo simulations within this ensemble and made the interesting observation that a Monte Carlo simulation in this ensemble sampled the first-order aggregation transition in a very efficient way [4]. We found that this behaviour was previously described by Martin-Mayor [5] for the temperature-driven first-order phase transition in the Potts model. We further investigated this simulation technique in the real microcanonical ensemble for a continuous Lennard-Jones system and found the same sampling advantage. We reached the same amount of particles with these simulations as for the sophisticated MUCA simulation technique.

In Ref. [6] we were able to develop a framework based on the generalization of the equal-area rule which allowed us to explain the obtained simulation behaviour of the real microcanonical ensemble. For comparisons we introduced the transition barrier of an ensemble as

$$B = \ln\left[P^{\mathrm{eqh}}\left(E_p^{\pm}\right)/P^{\mathrm{eqh}}\left(E_p^{0}\right)\right], \tag{11.13}$$

where $P^{\mathrm{eqh}}\left(E_p^{\pm}/E_p^{0}\right)$ denotes the equal-height histogram emerging due to phase coexistence, $E_p^{\pm}$ the positions of the two maxima and E_p^{0} the position of the minimum. This quantity hence allows one to evaluate how "hard" the first-order transition between two phases is within an ensemble. This framework allowed the conclusion that the

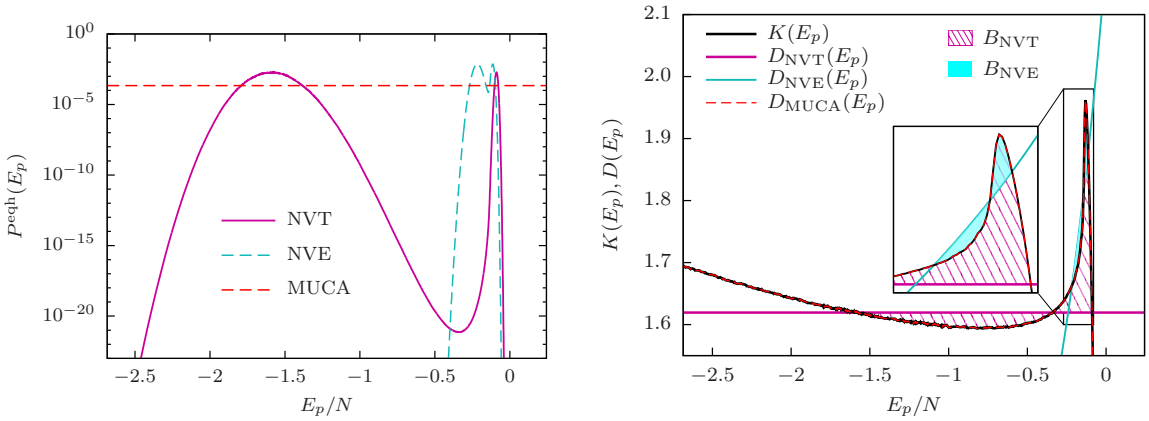

Figure 11.27: (a) The potential-energy histogram at equal height for three different ensembles for the $N = 2048$ Lennard-Jones system [6]. (b) The system dependent quantity $K(E_p)$ and the ensemble dependent $D(E_p)$ for the considered ensembles as defined in [6].

barrier in the canonical ensemble is always larger than in the microcanonical ensemble, $B_{\mathrm{NVT}} > B_{\mathrm{NVE}}$. In the microcanonical ensemble the transition barrier can even vanish as it was observed in [4] for polymer aggregation and by reproducing the data from Ref. [5]. For the example of the Lennard-Jones system with $N = 2048$ particles we discovered that the sampling with the microcanonical ensemble is of the order of $\exp(B_{\mathrm{NVT}} - B_{\mathrm{NVE}}) \approx 10^{16}$ more efficient than simulations in the canonical ensemble due to the difference of the barriers.

[1] B.A. Berg, T. Neuhaus: Phys. Lett. B **267**, 249 (1991); Phys. Rev. Lett. **68**, 9 (1992)
[2] W. Janke: Int. J. Mod. Phys. C **03**, 1137 (1992); Physica A **254**, 164 (1998)
[3] F. Wang, D.P. Landau: Phys. Rev. Lett. **86**, 2050 (2001); Phys. Rev. E **64**, 056101 (2001)
[4] P. Schierz et al.: J. Chem. Phys. **143**, 134114 (2015)
[5] V. Martin-Mayor: Phys. Rev. Lett. **98**, 137207 (2007)
[6] P. Schierz et al.: Phys. Rev. E **94**, 021301(R) (2016)

11.24 Framework for programming Monte Carlo simulations (βMC)

M. Marenz, J. Zierenberg, W. Janke

Monte Carlo (MC) computer simulations are a very powerful tool for investigating and understanding the thermodynamic behaviour of a wide variety of physical systems. These systems range from such simple ones like the Ising spin model to complex ones like the adsorption properties of proteins on surfaces [1]. In contrast to Molecular Dynamics (MD) simulations, the other important class of algorithm to simulate microscopic systems, MC simulations are not suitable to investigate dynamical properties. On the other hand, the ability of modern MC methods to explore efficiently the phase space of physical systems, especially those with a phase transition, makes them a very powerful and indispensable tool.

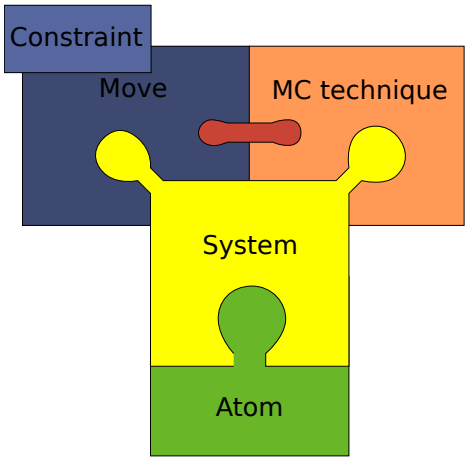

Figure 11.28: The 5 basic building blocks.

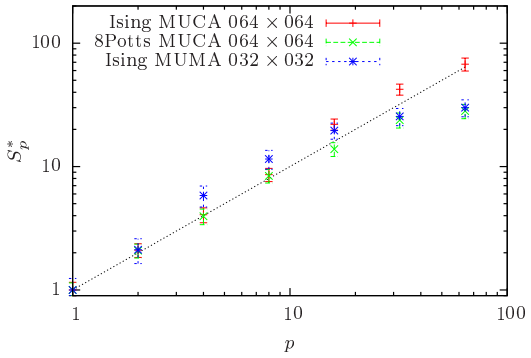

Figure 11.29: Scaling properties of the parallel multicanonical algorithm as a function of the number of processors p.

Another difference to MD simulations is the lack of a widely used program package for generic MC simulations. One reason for this lack is the versatility of modern MC algorithms – there are various different algorithm and many different possibilities to adjust a MC simulation to a specific problem. This was the starting point for the development of our framework for advanced MC algorithms. The aim of the framework is to enable the programmer to implement specific simulations in an easy and efficient way, without the need to implement all the tricky details for every new problem. The framework is implemented in the C++ programming language and is designed such that it separates basics parts of a MC algorithm in separate building blocks. These building blocks can be used by the programmer to implement a specific simulation.

There are 5 basic building blocks as illustrated in Fig. 11.28: The first one is the "system", which defines the Hamiltonian and the structure of the physical system. This means that the "system" building block encapsulates the energy calculation and the structure of the considered physical problem. For off-lattice systems this block contains a smaller subpart, the "atom" block, which encodes the geometry of the system (e.g., boundary conditions). As systems we have implemented so far different kinds of coarse-grained homopolymers, the Lennard-Jones gas, the TIP4P water model, lattice polymers and the Potts model in different dimensions. On top of the "system" are the last two other building blocks, the "move" and the "MC technique". A "move" defines a single update proposal, propagating the system from the current state to the next one. Additionally a "constraint" can be added to every "move" in order to simulate efficiently systems with geometrical confinements. The "MC technique" implements the Monte Carlo algorithm itself. At the moment we have implemented various algorithms such as Metropolis MC, parallel tempering, multicanonical MC, multimagnetic MC and the Wang-Landau MC algorithm. One of the most advanced MC algorithms we have implemented is a parallel version of the multicanonical algorithm [2], see Fig. 11.29.

The boundaries between these blocks are well defined, so that one can easily exchange one of them. For example one can use two different algorithm to simulate a specific system without implementing a completely new program. The framework is already in practical use for different studies, for example the investigation of the influence of bending stiffness on a coarse-grained homopolymer, the influence of a spherical

confinement to pseudo-phase transitions of homopolymers, and the study of polymer aggregation of several polymers for a large set of parameters (temperature, bending stiffness). Thus, the framework is very useful and has led already to several publications [2–8].

[1] M. Bachmann et al.: Angew. Chem. Int. Ed. **49**, 9530 (2010) [Angew. Chem. **122**, 9721 (2010), in German]
[2] J. Zierenberg et al.: Comput. Phys. Comm. **184**, 1155 (2013)
[3] M. Marenz et al.: Condens. Matter Phys. **15**, 43008 (2012)
[4] J. Zierenberg et al.: J. Phys.: Conf. Ser. **510**, 012017 (2014)
[5] J. Zierenberg et al.: J. Chem. Phys. **141**, 114908 (2014)
[6] J. Zierenberg, W. Janke: Europhys. Lett. **109**, 28002 (2015)
[7] M. Mueller et al.: in *Computer Simulation Studies in Condensed-Matter Physics XXVIII*, eds. D.P. Landau, H.-B. Schüttler, S. Lewis, M. Bachmann, Physics Procedia **68**, 95 (2015)
[8] M. Marenz, W. Janke: Phys. Rev. Lett. **116**, 128301 (2016)

11.25 Funding

Graduate School *"BuildMoNa": Leipzig School of Natural Sciences – Building with Molecules and Nano-objects*
W. Janke (Principal Investigator)

Graduate School *Statistical Physics of Complex Systems*
W. Janke (with B. Berche, Nancy)
Deutsch-Französisches Doktorandenkollegium (DFDK) with "Co-tutelle de Thèse", jointly with Université de Lorraine, Nancy, France, and Coventry University, UK, and National Academy of Sciences of Ukraine, Lviv, Ukraine, as associated partners
Deutsch-Französische Hochschule (DFH-UFA), Grant No. CDFA-02-07

International Max Planck Research School (IMPRS) *Mathematics in the Sciences*
W. Janke (Scientific Member)
Max Planck Society and Klaus Tschira Foundation

Forschergruppe 877 *From Local Constraints to Macroscopic Transport*
W. Janke (Principal Investigator, project P9 in collaboration with K. Kroy, Research Unit "Theory of Condensed Matter (TKM)")
Deutsche Forschungsgemeinschaft (DFG), Grant No. JA 483/29-1

Sonderforschungsbereich/Transregio SFB/TRR 102 *Polymers under Multiple Constraints: Restricted and Controlled Molecular Order and Mobility*
W. Janke (Principal Investigator, project B04)
Deutsche Forschungsgemeinschaft (DFG)

Molecular Conformation Mechanics of Proteins and Polymers
W. Janke
Deutsche Forschungsgemeinschaft (DFG), Grant No. JA 483/24-3

Mass Transport Models on Networks
W. Janke (twin project with H. Meyer-Ortmanns, Jacobs University Bremen)
Deutsche Forschungsgemeinschaft (DFG), Grant No. JA 483/27-1

Free-Energy Landscapes of Semiflexible Theta-Polymer Aggregation with and without External Force
W. Janke
Deutsche Forschungsgemeinschaft (DFG), Grant No. JA 483/31-1

Stable Knotted Phases in Semiflexible Polymers
W. Janke
Deutsche Forschungsgemeinschaft (DFG), Grant No. JA 483/33-1

Institute Partnership with the Institute for Condensed Matter Physics of the National Academy of Sciences of Ukraine, Lviv, Ukraine, *Polymers in Porous Environments and on Disordered Substrates*
W. Janke (with V. Blavatska, Lviv)
Alexander von Humboldt Foundation (AvH)

Marie Curie IRSES Network *DIONICOS: Dynamics of and in Complex Systems*
W. Janke (Principal Investigator, Head of Leipzig node)
European Union (EU), Contract No. PIRSES-GA-2013-612707.

Aggregation and Collapse of Polymers in Confinement
W. Janke, M. Marenz, J. Zierenberg
NIC Jülich (computer time grant for "JUROPA"), Grant No. HLZ21

Free-Energy Landscapes of Semiflexible Polymer Aggregation
W. Janke, J. Zierenberg
NIC Jülich (computer time grant for "JURECA"), Grant No. HLZ24

11.26 Organizational Duties

Wolfhard Janke

- Director, Institute for Theoretical Physics (ITP), Universität Leipzig
- Director, Naturwissenschaftlich-Theoretisches Zentrum (NTZ), Universität Leipzig
- Member of Department Council ("Fakultätsrat"), Faculty for Physics and Earth Sciences, Universität Leipzig
- Member of the Steering Committee ("Direktorium") of the Graduate Centre *Mathematics/Computer Science and Natural Sciences*, Research Academy Leipzig
- Principal Investigator of the Graduate School "BuildMoNa"
- Scientific Member of the International Max Planck Research School (IMPRS) *Mathematics in the Sciences*
- Principal Investigator of the DFG Sonderforschungsbereich/Transregio SFB/TRR 102 *Polymers under Multiple Constraints: Restricted and Controlled Molecular Order and Mobility*
- Principal Investigator of the DFG Forschergruppe FOR877 *From Local Constraints to Macroscopic Transport*

- Principal Investigator of "Profillinie" *Complex Matter*, Universität Leipzig
- Principal Investigator of "Profillinie" *Mathematical and Computational Sciences*, Universität Leipzig
- Spokesperson of the German-French Graduate College *Statistical Physics of Complex Systems* with Nancy (France), and associated partners in Coventry (England, UK) and Lviv (Ukraine), of the Deutsch-Französische Hochschule (DFH-UFA)
- Spokesperson of the German-Ukrainian Institute Partnership Leipzig-Lviv of the Alexander von Humboldt Foundation (AvH)
- External Member of the Jagiellonian University Graduate School *International Ph.D. Studies in Physics of Complex Systems*, Krakow, Poland
- *International Visiting Professor* of Coventry University, England, UK
- *Adjunct Professor* of The University of Georgia, Athens, Georgia, USA
- Permanent Member of the International Advisory Board for the Annual *Conference of the Middle European Cooperation in Statistical Physics (MECO)*
- Member of the Program Committee of the *International Conference on Computer Simulation in Physics and beyond*, Moscow, Russia, September 06.–10. September 2015
- Organizer of the Workshop *CompPhys15* – 16th International NTZ Workshop on *New Developments in Computational Physics*, ITP, Universität Leipzig, 26.–28. November 2015
- Organizer of the Workshop *CompPhys16* – 17th International NTZ Workshop on *New Developments in Computational Physics*, ITP, Universität Leipzig, 24.–26. November 2016
- Editor "Computational Physics", Central European Journal of Physics, Krakow, Poland
- Member of Editorial Board, Condens. Matter Phys., Lviv, Ukraine
- External Reviewer for Deutsche Forschungsgemeinschaft (DFG), Humboldt-Stiftung (AvH), Studienstiftung des deutschen Volkes, Fond zur Förderung der wissenschaftlichen Forschung (FWF), Österreich, The Royal Society, UK, The Engineering and Physical Sciences Research Council (EPSRC), UK, Israel Science Foundation, Israel, National Science Foundation (NSF), USA, Natural Sciences and Engineering Research Council of Canada (NSERC), Canada, The Jeffress Memorial Trust, Bank of America, Virginia, USA, Universität Mainz, Germany, The University of Warwick, England, UK, Coventry University, England, UK, CECAM, Lyon, France
- Referee for Physical Review Letters, Physical Review B, Physical Review E, Journal of Chemical Physics, Europhysics Letters, Physics Letters A, Physics Letters B, The European Physical Journal B, Physica A, Proceedings of the Royal Physical Society, Journal of Physics A, Computer Physics Communications, JSTAT, Condens. Matter Phys., PLOS ONE, New Journal of Physics, International Journal of Modern Physics C

11.27 External Cooperations

Academic

- Institute of Physics, Jagiellonian University, Kraków, Poland

Prof. Dr. Piotr Białas, Dr. Leszek Bogacz, Prof. Dr. Zdzisław Burda

- CEA/Saclay, Service de Physique Théorique, France
  Dr. Alain Billoire
- Institut für Physik, Universität Mainz, Germany
  Prof. Dr. Kurt Binder, Andreas Nußbaumer, Prof. Dr. Friderike Schmid
- Max Planck Institute for Polymer Research, Mainz, Germany
  Dr. Hsiao-Ping Hsu, Prof. Dr. Kurt Kremer
- Institut für Theoretische Physik, Universität Heidelberg, Germany
  Dr. Elmar Bittner
- Laboratoire de Physique des Matériaux (UMR CNRS No 7556), Université de Lorraine, Nancy, France
  Prof. Dr. Bertrand Berche, Dr. Christophe Chatelain, Dr. Olivier Collet, Prof. Dr. Malte Henkel, Prof. Dr. Dragi Karevski
- Groupe de Physique des Matériaux (UMR CNRS No 6634), Université de Rouen, France
  Dr. Pierre-Emmanuel Berche
- SUPA, School of Physics and Astronomy, University of Edinburgh, Scotland, UK
  Dr. Richard A. Blythe, Prof. Dr. Martin R. Evans, Dr. Bartłomiej Wacław
- Istituto Nazionale di Fisica Nucleare, Sezione di Milano-Bicocca, Milano, Italy
  Prof. Dr. Pablo Butera
- Jülich Supercomputing Centre (JSC), Forschungszentrum Jülich, Germany
  Prof. Dr. Peter Grassberger, PD Dr. Thomas Neuhaus
- IAC-1, Universität Stuttgart, Germany
  Prof. Dr. Rudolf Hilfer, Prof. Dr. Christian Holm
- Complex Systems Division, Department of Theoretical Physics, Lunds Universitet, Lund, Sweden
  Prof. Dr. Anders Irbäck
- Department of Mathematics and the Maxwell Institute for Mathematical Sciences, Heriot-Watt University, Edinburgh, Scotland, UK
  Prof. Dr. Desmond A. Johnston
- Applied Mathematics Research Centre, Coventry University, England, UK
  PD Dr. Christian von Ferber, Dr. Nikolaos G. Fytas, Prof. Dr. Ralph Kenna, Dr. Thierry Platini, Dr. Martin Weigel
- Inst. für Theoretische Physik, FU Berlin, Germany
  Prof. Dr. Hagen Kleinert
- Atominstitut, TU Wien, Austria
  Prof. Dr. Harald Markum
- Jacobs Universität Bremen, Germany
  Prof. Dr. Hildegard Meyer-Ortmanns, Darka Labavić
- Applied Mathematics, Universitat Pompeu Fabra, Barcelona, Spain
  Dr. Ramon Villanova

- CERN (PH-SFT), Geneva, Switzerland
  Dr. Sandro Wenzel
- Department of Engineering of Physics, Ankara University, Ankara, Turkey
  Prof. Dr. Handan Arkın (Olgar), Mustafa Bilsel, Buket Taşdizen
- Dept. of Physics, Hacettepe University, Ankara, Turkey
  Prof. Dr. Tarik Çelik, Gökhan Gökoğlu
- Dept. of Physics Engineering, Hacettepe University, Ankara, Turkey
  Prof. Dr. Fatih Yaşar
- Institute for Condensed Matter Physics, National Academy of Sciences, Lviv, Ukraine
  Dr. Viktoria Blavatska, Prof. Dr. Yurij Holovatch
- Yerevan Physics Institute, Yerevan, Armenia
  Prof. Dr. David B. Saakian
- Alikhanyan National Science Laboratory, Yerevan, Armenia
  Prof. Dr. Nerses Ananikyan, Dr. Nikolay Izmailyan
- Landau Institute for Theoretical Physics, Chernogolovka, Russia
  Dr. Lev Barash, Prof. Dr. Lev N. Shchur
- Center for Simulational Physics, The University of Georgia, Athens, USA
  Prof. Dr. Michael Bachmann, Prof. Dr. David P. Landau
- Dept. of Physics, Florida State University, Tallahassee, USA
  Prof. Dr. Bernd A. Berg
- Dept. of Chemistry and Biochemistry, University of Oklahoma, Norman, USA
  Prof. Dr. Ulrich H.E. Hansmann
- Los Alamos National Laboratory, Los Alamos, USA
  Dr. Christoph Junghans
- Dept. of Physics and Astronomy, Texas A&M, College Station, USA
  Prof. Dr. Helmut G. Katzgraber
- Dept. of Physics, Virginia Tech, Blacksburg, USA
  Prof. Dr. Michel Pleimling, Prof. Dr. Royce K.P. Zia
- Physics Department, Carnegie Mellon University, Pittsburgh, USA
  Prof. Dr. Robert H. Swendsen
- Stetson University, DeLand, USA
  Dr. Thomas Vogel
- Jawaharlal Nehru Centre for Advanced Scientific Research (JNCASR), Jakkur, India
  Prof. Dr. Subir K. Das
- Computational Chemistry Unit Cell (CCUC), Department of Chemistry, Chulalongkorn University, Bangkok, Thailand
  Prof. Dr. Supot Hannongbua, Dr. Oraphan Saengsawang
- Ramkhamhaeng University, Department of Chemistry, Faculty of Science, Bangkok, Thailand
  Dr. Tatiya Chokbunpiam

- Laboratory of Statistical and Computational Physics, Institute of Physics, Academia Sinica, Nankang, Taipei, Taiwan
  Prof. Dr. Chin-Kun Hu
- The University of Tokyo, Tokyo, Japan
  Prof. Dr. Nobuyasu Ito
- Banaras Hindu University, Varanasi, India
  Prof. Dr. Sanjay Kumar
- Nagoya University, Nagoya, Japan
  Dr. Tetsuro Nagai, Prof. Dr. Yuko Okamoto
- Zhejiang Institute of Modern Physics, Zhejiang University, Hangzhou, P.R. China
  Prof. Dr. He-Ping Ying, Prof. Dr. Bo Zheng

11.28 Publications

Journals

N. Fricke, S. Sturm, M. Lämmel, S. Schöbl, K. Kroy, W. Janke: *Polymers in Disordered Environments*, Diff. Fundam. (diffusion-fundamentals.org) **23**, 7-1–12 (2015)

M.H. Gerlach, W. Janke: *First-Order Directional Ordering Transition in the Three-Dimensional Compass Model*, Phys. Rev. B **91**, 045119-1–8 (2015)

J. Gross, T. Vogel, M. Bachmann: *Structural Phases of Adsorption for Flexible Polymers on Nanocylinder Surfaces*, Phys. Chem. Chem. Phys. **17**, 30702–30711 (2015)

W. Janke: *Computer Simulation Studies of Polymer Adsorption and Aggregation – From Flexible to Stiff*, in *Computer Simulation Studies in Condensed-Matter Physics XXVIII*, eds. D.P. Landau, H.-B. Schüttler, S. Lewis, M. Bachmann, Physics Procedia **68**, 69–79 (2015)

W. Janke, M. Mueller, D.A. Johnston: *Finite-Size Scaling and Latent Heat at the Gonihedric First-Order Phase Transition*, J. Phys.: Conf. Ser. **640**, 012002-1–6 (2015)

D.A. Johnston, M. Mueller, W. Janke: *Macroscopic Degeneracy and Order in the* $3d$ *Plaquette Ising Model*, Mod. Phys. Lett. B **29**, 1550109-1–10 (2015)

S. Majumder, W. Janke: *Cluster Coarsening During Polymer Collapse: Finite-Size Scaling Analysis*, Europhys. Lett. **110**, 58001-1–6 (2015)

M. Mueller, W. Janke, D.A. Johnston: *Planar Ordering in the Plaquette-Only Gonihedric Ising Model*, Nucl. Phys. B **894**, 1–14 (2015)

M. Mueller, J. Zierenberg, M. Marenz, P. Schierz, W. Janke: *Probing the Effect of Density on the Aggregation Temperature of Semi-Flexible Polymers in Spherical Confinement*, in *Computer Simulation Studies in Condensed-Matter Physics XXVIII*, eds. D.P. Landau, H.-B. Schüttler, S. Lewis, M. Bachmann, Physics Procedia **68**, 95–99 (2015)

H. Nagel, H. Meyer-Ortmanns, W. Janke: *Boundary Drive Induced Formation of Aggregate Condensates in Stochastic Transport with Short-Range Interactions*, Europhys. Lett. **111**, 30001-1–6 (2015)

J.K. Ochab, H. Nagel, W. Janke, B. Wacław: *A Simple Non-Equilibrium, Statistical-Physics Toy Model of Thin-Film Growth*, J. Stat. Mech.: Theor. Exp., P09013-1–25 (2015)

P. Schierz, S. Fritzsche, W. Janke, S. Hannongbua, O. Saengsawang, C. Chmelik, J. Kärger: *MD Simulations of Hydrogen Diffusion in ZIF-11 with a Force Field Fitted to Experimental Adsorption Data*, Microporous Mesoporous Mater. **203**, 132–138 (2015)

P. Schierz, J. Zierenberg, W. Janke: *Molecular Dynamics and Monte Carlo Simulations in the Microcanonical Ensemble: Quantitative Comparison and Reweighting Techniques*, J. Chem. Phys. **143**, 134114-1–11 (2015)

T. Vogel, J. Gross, M. Bachmann: *Thermodynamics of the Adsorption of Flexible Polymers on Nanowires*, J. Chem. Phys. **142**, 104901-1–8 (2015)

J. Zierenberg, N.G. Fytas, W. Janke: *Parallel Multicanonical Study of the Three-Dimensional Blume-Capel Model*, Phys. Rev. E **91**, 032126-1–8 (2015)

J. Zierenberg, W. Janke: *From Amorphous Aggregates to Polymer Bundles: The Role of Stiffness on Structural Phases in Polymer Aggregation*, Europhys. Lett. **109**, 28002-1–6 (2015)

J. Zierenberg, W. Janke: *Exploring Different Regimes in Finite-Size Scaling of the Droplet Condensation-Evaporation Transition*, Phys. Rev. E **92**, 012134-1–11 (2015)

in press

T. Chokbunpiam, S. Fritzsche, C. Chmelik, J. Caro, W. Janke, S. Hannongbua: *Gate Opening Effect for Carbon Dioxide in ZIF-8 by Molecular Dynamics – Confirmed, but at High CO_2 Pressure*, Chem. Phys. Lett. **648**, 178–181 (2016)

W. Janke, W. Paul: *Thermodynamics and Structure of Macromolecules from Flat-Histogram Monte Carlo Simulations*, invited review, Soft Matter **12**, 642–657 (2016)

S. Kumar, R. Kumar, W. Janke: *Periodically Driven DNA: Theory and Simulation*, Phys. Rev. E **93**, 010402(R)-1–5 (2016)

S. Majumder, W. Janke: *Evidence of Aging and Dynamic Scaling in Collapse of a Polymer*, Phys. Rev. E **93**, 032506-1–6 (2016)

M. Marenz, W. Janke: *Knots as a Topological Order Parameter for Semiflexible Polymers*, Phys. Rev. Lett. **116**, 128301-1–6 (2016)

H. Nagel, W. Janke: *Emergence of Dynamic Phases in the Presence of Different Kinds of Open Boundaries in Stochastic Transport with Short-Range Interactions*, J. Stat. Mech.: Theor. Exp., 013207-1–19 (2016)

H. Nagel, W. Janke: *Dynamics of Condensate Formation in Stochastic Transport with Pair-Factorized Steady States: Nucleation and Coarsening Time Scales*, Phys. Rev. E **93**, 052112-1–12 (2016)

Z. Zhu, A.J. Ochoa, S. Schnabel, F. Hamze, H.G. Katzgraber: *Best-Case Performance of Quantum Annealers on Native Spin-Glass Benchmarks: How Chaos can Affect Success Probabilities*, Phys. Rev. A **93**, 012317-1–8 (2016)

P. Schierz, J. Zierenberg, W. Janke: *First-Order Phase Transitions in the Real Microcanonical Ensemble*, Phys. Rev. E **94**, 021301(R)-1–5 (2016).

J. Gross, M. Ivanov, W. Janke: *Comparing Atomistic and Coarse-Grained Simulations of P3HT*, to appear in *Computer Simulation Studies in Condensed-Matter Physics XXIX*, eds. D.P. Landau, H.-B. Schüttler, S. Lewis, M. Bachmann, J. Phys.: Conf. Ser. (2016), in print

W. Janke, M. Marenz: *Stable Knots in the Phase Diagram of Semiflexible Polymers: A Topological Order Parameter?*, to appear in *Computer Simulation Studies in Condensed-Matter Physics XXIX*, eds. D.P. Landau, H.-B. Schüttler, S. Lewis, M. Bachmann, J. Phys.: Conf. Ser. (2016), in print

S. Majumder, W. Janke: *Aging and Related Scaling During the Collapse of a Polymer*, to appear in *Computer Simulation Studies in Condensed-Matter Physics XXIX*, eds. D.P. Landau, H.-B. Schüttler, S. Lewis, M. Bachmann, J. Phys.: Conf. Ser. (2016), in print

A. Nußbaumer, J. Zierenberg, E. Bittner, W. Janke: *Numerical Test of Finite-Size Scaling Predictions for the Droplet Condensation-Evaporation Transition*, invited talk, Conference Proceedings *CCP2015*, 2 – 5 December 2015, IIT Guwahati, India, to appear in J. Phys.: Conf. Ser. (2016), in print

J. Zierenberg, W. Janke: *Finite-Size Scaling of Lennard-Jones Droplet Formation at Fixed Density*, to appear in *Computer Simulation Studies in Condensed-Matter Physics XXIX*, eds. D.P. Landau, H.-B. Schüttler, S. Lewis, M. Bachmann, J. Phys.: Conf. Ser. (2016), in print

J. Zierenberg, M. Marenz, W.Janke: *Dilute Semiflexible Polymers with Attraction: Collapse, Folding and Aggregation*, to appear in Polymers **8** (2016), in print

Talks

J. Gross, M. Ivanov, W. Janke: *Comparing Atomistic and Coarse-Grained Simulations of P3HT*, 16th International NTZ-Workshop on New Developments in Computational Physics – CompPhys15, Leipzig, Germany, 26. November 2015

W. Janke: *Computer Simulation Studies of Polymer Adsorption and Aggregation – From Flexible to Stiff*, invited talk, Departmental Colloquium and 28th Annual CSP Workshop on *Recent Developments in Computer Simulation Studies in Condensed Matter Physics*, The University of Georgia, Athens, USA, 23.–27. February 2015

W. Janke: *Nonstandard Finite-Size Scaling at First-Order Phase Transitions*, APS March Meeting 2015, San Antonio, Texas, USA, 02.–06. March 2015

W. Janke: *Nonstandard Finite-Size Scaling at First-Order Phase Transitions with Macroscopic Low-Temperature Phase Degeneracy*, DPG Frühjahrstagung 2015, TU Berlin, Germany, 15.–20. March 2015

W. Janke: *Asymptotic Scaling Behavior of Self-Avoiding Walks on Critical Percolation Clusters*, MECO 40 Conference, Esztergom, Hungary, 23.–25. March 2015

W. Janke: *Asymptotic Scaling Behavior of Self-Avoiding Walks on Critical Percolation Clusters*, Workshop *Statistical Physics and Low Dimensional Systems – SPLDS*, Abbaye des Prémontrés, Pont-à-Mousson, France, 20.–22. May 2015

W. Janke: *Computersimulationen in der statistischen Physik*, DPG Schülertagung 2015, Max-Planck-Institut für *Mathematik in den Naturwissenschaften*, Leipzig, Germany, 25. June 2015

W. Janke: *Self-Avoiding Walks on Critical Percolation Clusters – A Paradigm for Polymers in Disordered Environments*, invited talk, 4th International Workshop on *Theory and Computer Simulations of Polymers: New Developments*, Martin-Luther Universität Halle (Saale), Germany, 28. June – 01. July 2015

W. Janke: *Computer Simulation Studies of Polymer Adsorption and Aggregation*, invited plenary talk, International Conference on *Computer Simulation in Physics and Beyond*, Moscow, Russia, 06.–10. September 2015

W. Janke: *Stable Knot Phases of Semiflexible Polymers*, Conference *shape up 2015 – Exercises in Materials Geometry and Topology*, TU Berlin, Germany, 14.–18. September 2015

W. Janke: *Finite-Size Scaling of Particle and Polymer Nucleation*, invited talk, International Conference on *Growing Length Scale Phenomena in Condensed Matter Physics*, Jawaharlal Nehru Centre for Advanced Scientific Research, Bangalore, India, 08.–10. October 2015

W. Janke: *Finite-Size Scaling of Particle and Polymer Nucleation*, invited talk, XXVII IUPAP Conference on *Computational Physics – CCP2015*, Indian Institute of Technology, Guwahati, Assam, India 02.–05. December 2015

S. Majumder, W. Janke: *Nonequilibrium Dynamics in Polymer Collapse* Conference on *Growing Length Scale Phenomena in Condensed Matter Physics*, Bangalore, India, 08. October 2015

S. Majumder, W. Janke: *Evidence of Aging and Dynamical Scaling During Collapse of a Polymer*, 16th International NTZ-Workshop on *New Developments in Computational Physics – CompPhys15*, Leipzig, Germany, 26. November 2015

M. Mueller: *Aggregation of Flexible Polymers under Spherical Constraints*, 28th Workshop on *Computer Simulation Studies in Condensed Matter Physics (CSP2015)*, Athens, Georgia, USA, 23. February 2015

H. Nagel, W. Janke: *Boundary Induced Phase Transitions in Stochastic Transport with Short-Range Interactions*, 16th International NTZ-Workshop on *New Developments in Computational Physics – CompPhys15*, Leipzig, Germany, 27. November 2015

P. Schierz, J. Zierenberg, W. Janke: *Computational Investigation of Polymers*, Seminar of the cdfa-dfdk, Coventry, England, UK, 04. February 2015

P. Schierz, J. Zierenberg, W. Janke: *Interesting Properties of the Microcanonical Ensemble with Constant Total Energy*, Seminar of the cdfa-dfdk, Nancy, France, 16. September 2015

P. Schierz, J. Zierenberg, W. Janke: *First-Order Phase Transitions in the Advantageous Full Microcanonical Ensemble*, 16th International NTZ-Workshop on *New Developments in Computational Physics – CompPhys15*, Leipzig, Germany, 26. November 2015

S. Schnabel, W. Janke: *Where to go in a Rough Free-Energy Landscape?*, Annual Conference of the German Physical Society (DPG), TU Berlin, Germany, 15.–20. March 2015

S. Schnabel, W. Janke: *Greedy Monte Carlo for Spin Glass Ground-State Search*, 16th International NTZ-Workshop on *New Developments in Computational Physics – CompPhys15*, Leipzig, Germany, 26.–28. November 2015

J. Zierenberg, W. Janke: *The Role of Stiffness in Polymer Aggregation: Leading from Amorphous Aggregates to Polymer Bundles*, DPG Frühjahrstagung, TU Berlin, Germany, 18. March 2015

J. Zierenberg: *From Particle Condensation to Polymer Aggregation: Phase Transitions and Structural Phases in Mesoscopic Systems*, Seminar of the cdfa-dfdk, Coventry, England, UK, 22. October 2015

J. Zierenberg, W. Janke: *Exploring Different Regimes in Finite-Size Scaling of the Droplet Condensation-Evaporation Transition*, 16th International NTZ-Workshop on *New Developments in Computational Physics – CompPhys15*, Leipzig, Germany, 26. November 2015

J. Zierenberg, M. Mueller, M. Marenz, P. Schierz, W. Janke: *Aggregation of Flexible Polymers under Spherical Constraints*, DPG Frühjahrstagung, Berlin, Germany, 18. March 2015

Posters

J. Bock, W. Janke: *Computer Simulations of Semiflexible Polymers in Disordered Media*, 79th Annual Meeting of the DPG and DPG Spring Meeting, TU Berlin, Germany, 15.–20. March 2015

J. Bock, W. Janke: *Computer Simulations of Semiflexible Polymers in Disordered Media*, 16th International NTZ-Workshop on *New Developments in Computational Physics – CompPhys15*, Leipzig, Germany, 26.–28. November 2015

M. Ivanov, J. Gross, W. Janke: *Poly(3-hexylthiophene) (P3HT) Molecules Interacting with Au(001) Substrates*, 79th Annual Meeting of the DPG and DPG Spring Meeting, TU Berlin, Germany, 15.–20. March 2015

M. Ivanov, J. Gross, W. Janke: *Poly(3-hexylthiophene) (P3HT) Molecules Interacting with Au(001) Substrates*, 4th International Workshop on *Theory and Computer Simulations of Polymers: New Developments*, Martin-Luther Universität Halle (Saale), Germany, 29. June – 01. July 2015

M. Ivanov, J. Gross, M. Mueller, W. Janke: *Computer Simulations of P3HT*, SFB TRR/102 3rd Mini-Workshop, Martin-Luther Universität Halle (Saale), Germany, 02. October 2015

M. Ivanov, P. Schierz, J. Gross, W. Janke: *Boltzmann Inversion of Harmonic Oscillators*, 16th International NTZ-Workshop on New Developments in Computational Physics – CompPhys15, Leipzig, Germany, 26.–28. November 2015

R. Kumar, S. Kumar, W. Janke: *Driven DNA: Does Dynamic Transition Exist in the Thermodynamic Limit?* Bad Honnef Physics School on *Computational Physics of Complex and Disordered Systems*, Physikzentrum Bad Honnef, Germany, 20.–25. September 2015

R. Kumar, S. Kumar, W. Janke: *Driven DNA: Does Dynamic Transition Exist in the Thermodynamic Limit?* 16th International NTZ-Workshop on *New Developments in Computational Physics – CompPhys15*, Leipzig, Germany, 26.–28. November 2015

S. Majumder, W. Janke: *Cluster Growth During a Polymer Collapse*, 4th International Workshop on *Theory and Computer Simulations of Polymers: New Developments*, Martin-Luther Universität Halle (Saale), Germany, 29. June – 01. July 2015

M. Mueller, D.A. Johnston, W. Janke: *Planar ("Fuki-Nuke") Ordering and Finite-Size Effects for a Model with Four-Spin Interactions*, 16th International NTZ-Workshop on *New Developments in Computational Physics – CompPhys15*, Leipzig, Germany, 26.–28. November 2015

H. Nagel, W. Janke: *Boundary Induced Phase Transitions in Stochastic Transport with Short-Range Interactions*, Conference of the Middle European Cooperation in Statistical Physics, Esztergom, Hungary, 23.–25. March 2015

P. Schierz, J. Zierenberg, W. Janke: *Comparability of Microcanonical Data sampled by Molecular Dynamics and Monte Carlo Simulations*, 79th Annual Meeting of the DPG and DPG Spring Meeting, TU Berlin, Germany, 15.–20. March 2015

P. Schierz, J. Zierenberg, W. Janke: *Theta-Polymers in Spherical Confinement: Investigation of the Aggregation Behaviour*, Annual BuildMoNa Conference, Leipzig, Germany, 23.–24. March 2015

P. Schierz, J. Zierenberg, W. Janke: *3D-Visualisierung von Polymeren – oder wie verkleben Spaghetti*, Dies Academicus, Leipzig, Germany, 02. Dezember 2015

J. Zierenberg, W. Janke: *Aggregation of Semiflexible Polymers*, 4th International Workshop on *Theory and Computer Simulations of Polymers: New Developments*, Martin-Luther Universität Halle (Saale), Germany, 29. June – 01. July 2015

11.29 Graduations

Doctorate

- Johannes Zierenberg
  From Particle Condensation to Polymer Aggregation: Phase Transitions and Structural Phases in Mesoscopic Systems
  17. December 2015

Master

- Kieran Austin
  Adsorption and Stiffness of a Grafted Polymer
  23. September 2015

Bachelor

- Simon Schneider
  Stochastic Approximation Monte Carlo Simulations: Applications and Performance Test for the Ising Model
  29. April 2015
- Felix Neduck
  Population Annealing für Spinsysteme
  28. Juli 2015

11.30 Guests

- M.Sc. Hamid Khoshbakht
  Coventry University, England, UK
  DFH-UFA Colloquium (10. February 2015)
  On the Uniform Sampling of Ground States in the 2D ±J Ising Spin-Glass Model
  02.–15. February 2015
- M.Sc. Eren Metin Elçi
  Coventry University, England, UK
  DFH-UFA Colloquium (12. March 2015)
  Perfect Sampling, Relaxation and Extreme Value Theory – An Intriguing Interplay
  13. February – 16. March 2015
- Prof. Dr. Sanjay Kumar
  Banaras Hindu University, Varanasi, India
  SFB/TRR 102 Colloquium (07. May 2015)
  DNA under Force: New Insights from Simulations
  27. April – 20. May 2015
- Dr. Lev Barash
  Landau Institute, Chernogolovka, Russia
  NTZ/DFH-UFA and DIONICOS Colloquium (28. May 2015)
  Population Annealing on GPUs
  26. May – 25. June 2015

- Prof. Dr. Ulrich H.E. Hansmann
  University of Oklahoma, Norman, USA
  SFB/TRR 102 Polymer and Soft-Matter Seminar (02. June 2015)
  Simulations of Folding and Aggregation of Proteins
  28. May – 11. June 2015
- Dr. Christoph Junghans
  Los Alamos National Laboratory, New Mexico, USA
  02. July 2015
- Prof. Dr. Subir K. Das
  Jawaharlal Nehru Centre for Advanced Scientific Research, India
  TKM/DFH-UFA and DIONICOS Colloquium (03. July 2015)
  Aging in Kinetics of Phase Transitions
  02.–04. July 2015
- M.Sc. Ati Moncef
  University of Sciences and Technology of Oran, Algeria
  13. October – 12. November 2015
- Dr. Nikolaos G. Fytas
  Coventry University, England, UK
  DFH-UFA Colloquium (03. December 2015)
  Critical Phenomena in Disordered Systems
  24. November – 04. December 2015
- Prof. Dr. Michael Bachmann
  Center for Simulational Physics, The University of Georgia, Athens, USA
  Stabilization of Helical Structures by Bending Restraints
  25.–27. November 2015
- Prof. Dr. Alexander Hartmann
  Univ. Oldenburg, Germany
  Distribution of Convex Hulls for Single and Multiple Random Walks
  25.–27. November 2015
- Dr. Martin Thomas Horsch
  TU Kaiserslautern, Germany
  Multicriteria Optimization of Molecular Force Field Models
  25.–27. November 2015
- Dr. Francesco Parisen Toldin
  Universität Würzburg, Germany
  Line Contribution to the Critical Casimir Force between a Homogeneous and a Chemically Stepped Surface
  25.–27. November 2015
- Dr. Hsiao-Ping Hsu
  MPI für Polymerforschung, Mainz, Germany
  Static and Dynamic Properties of Large Polymer Melts in Equilibrium
  25.–28. November 2015
- Miriam Klopotek
  Institut für Angewandte Physik, Universität Tübingen, Germany

Monolayer Growth in a Hard-Rod Lattice Model
25.–28. November 2015

- Prof. Dr. Ezequiel Albano
IFLYSIB, La Plata, Argentina
Multicriticality in Confined Ferromagnets with Impurities
25.–29. November 2015

- Dr. Ewa Gajda-Zagórska
AGH University, Krakow, Poland
Multi-Objective Solver for Inverse Parametric Problems
25.–29. November 2015

- Prof. Dr. Dennis C. Rapaport
Bar-Ilan University, Ramat-Gan, Israel
Joint NTZ–SFB/TRR 102 Colloquium (26. November 2015)
Simulating Emergent Phenomena (with GPU-based Molecular Dynamics)
25.–29. November 2015

- Prof. Dr. George Savvidy
Demokritos NRC, Athens, Greece
Kolmogorov-Anosov C-Systems and MIXMAX Random Number Generator
25.–29. November 2015

- Prof. Dr. Lev Shchur
Landau Institute, Chernogolovka, Moscow Region, Russia
Current State-of-the-Art in Kinetic Monte Carlo Simulations
25.–29. November 2015

- Dr. Martin Weigel
Coventry University, England, UK
Regular Packings on Periodic Lattices
25.–29. November 2015

- Dr. Marcin Zagórski
IST Klosterneuburg/Wien, Austria
Evolutionary Accessibility of Fitness Landscapes with Multiple Alleles
25.–29. November 2015

- Prof. Dr. Jürgen Vollmer
MPI Dynamik und Selbstorganisation, Göttingen, Germany
Ostwald Ripening, Scaling and Size Focussing in the Evolution of Droplet Size Distributions
25.–30. November 2015

- Dr. Elmar Bittner
Universität Heidelberg, Germany
26.–27. November 2015

- Prof. Dr. Stefan Boettcher
Emory University, Atlanta, USA
Ground States of Edwards-Anderson Spin Glasses
26.–28. November 2015

12

Statistical Physics

12.1 Introduction

The focus of research in the STP group is on low-dimensional and mesoscopic interacting systems. These systems are fascinating because on the one hand they allow to study fundamental questions of quantum statistical mechanics, and on the other hand they have a great potential for technological applications. The interplay of a reduced dimensionality with enchanced interaction effects, non-equilibrium physics, and possibly disorder allows the observation of many interesting phenomena, which pose a stimulating challenge for theoretical analysis. The mathematical language used for the description of these systems is quantum field theory, including techniques like functional integrals, renormalization group, instanton calculus, the Keldysh technique for non-equilibrium situations, and the replica method for disordered systems. These analytical tools are suplemented by the use of computer algebra (Mathematica) and numerical calculations (Matlab, Perl, C++). We try to combine the analysis of theoretically interesting problems with relevance to experiments on nanostructures.
Fractional quantum hall (QH) systems display perhaps the richest and most beautiful physics of all condensed matter systems. They are a prime example for the idea that the whole is more than the sum of its parts, as low lying excitations of a fractional QH fluid carry only a faction of the electron charge and are thus qualitatively different from the system constituents. Recently, interest in fractional QH physics has been reinvigorated by the prospect that quasiparticles (QPs) of the fractional QH state at filling fraction 5/2 may be non-abelian anyons, i.e. their braiding may not only give rise to a multiplication of the wave function with a complex phase, but in addition corresponds to a unitary transformation of the highly degenerate ground state. Due to the topological nature of braiding, these unitary transformations are robust against local perturbations and guarantee a high degree of stability of the quantum weave of braids, lending it to the construction of topological quantum bits. Future research in this field will concentrate on both the analysis of qualitative properties of topologically ordered systems and the description of experimentally relevant consequences in nanostructured systems.
Similarly to the edge states of QH systems, in single channel nanowires interactions strongly modify the dynamics of electrons. In the presence of strong spin-orbit coupling and in proximity to a superconductor, nanowires can support a topologically ordered state suitable for the formation of topological quantum bits. In multimode nanowires, a quantum phase transition between superconductor and diffusive metal can occur,

which is tuned by an external magnetic field and is experimentally realized in niobium and molybdenum-germanium systems. Comparatively small changes in the external magnetic field can give rise to a large change in conductivity. Quantum mechanical fluctuations of the superconducting phase can restore part of the density of states, which is reduced due to scattering of electrons off the superconducting order parameter.

B. Rosenow

12.2 Enhanced Bulk-Edge Coulomb Coupling in Fractional Fabry-Perot Interferometers

CW. von Keyserlingk [*] [†], S.H. Simon[†], B. Rosenow

[*]Princeton Center for Theoretical Science, Princeton University, Princeton, New Jersey 08544, USA
[†]Rudolf Peierls Centre for Theoretical Physics, 1 Keble Road, Oxford, OX1 3NP, United Kingdom

A Fabry-Perot (FP) interferometer is a Hall bar perturbed by two constrictions, which introduce amplitudes for interedge tunneling of quasiparticles (QPs) and thus give rise to interference [1]. The probability of backscattering is a function of magnetic field and the interferometer's area. For idealized devices the interference measurements contain information about the (potentially fractional) charges of interfering QPs, and their braiding with localized quasiparticles in the bulk.
FP devices have been used to test the theoretical prediction [3–5] that the $\nu = 5/2$ fractional Quantum Hall effect (FQHE) plateau is a Moore-Read (MR) Pfaffian (PF) or anti-Pfaffian (PF) state. Both candidate states support non-Abelian QP excitations. While this putative MR state cannot be used for universal quantum computation, it could well be the first experimentally realized non-Abelian topological phase, and verifying this is an important proof of concept step on the road to topological quantum computation. We note that the experiments appear inconsistent with a model neglecting bulk-edge Coulomb coupling and Majorana tunneling, so we reexamine the theory of FP devices. Even a moderate Coulomb coupling may strongly affect some fractional plateaus, but very weakly affect others, allowing us to model the data over a wide range of plateaus. While the recent experiment [5] is consistent with the $\nu = 5/2$ state harboring MR topological order, they may have measured Coulomb effects rather than an even-odd effect due to non-Abelian braiding. We proposed a correction to the orthodox picture, namely, the parity of neutral fermions in the interferometer cell is random over the measurement time scale. Further assuming moderate bulk-edge Coulomb coupling, we can largely fit the data from experiments for $\nu = 5/2$ and a wide range of other plateaus.

[1] C. de. Chamon, D. E. Freed, S. A. Kivelson, S. L. Sondhi, and X. G. Wen, Phys. Rev. B **55**, 2331 (1997),
[2] G. Moore and N. Read, Nucl. Phys. **B360**, 362 (1991),
[3] S.-S. Lee, S. Ryu, C. Nayak, and M. P. A. Fisher, Phys. Rev. Lett. **99**, 236807 (2007),
[4] M. Levin, B. I. Halperin, and B. Rosenow, Phys. Rev. Lett. **99**, 236806 (2007),

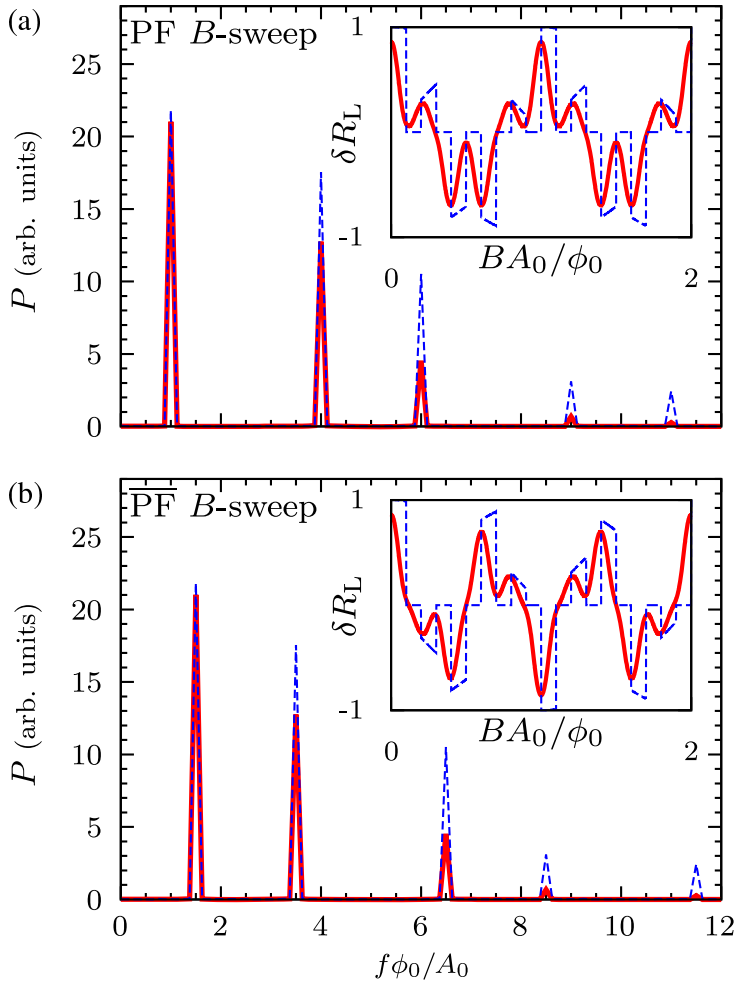

Figure 12.1: Power spectrum for the variation of $\langle \delta R_L \rangle$ with magnetic field at $\nu = 5/2$, with fixed fermion parity (orthodox theory). The number of QPs was thermally averaged, with a ratio of charging energy K to temperature T of $T/K = 1/5$ for the red curve, and $T/K = 0$ for the blue dotted curve. (a) and (b) label the $PF/\bar{P}F$ cases, respectively. The dominant peaks at $1, 1.5\phi_0^{-1}$, respectively, disagree with the experimentally observed [17] frequencies near $5\phi_0^{-1}$. Insets show corresponding plots of $\langle \delta R_L \rangle$ against BA_0/ϕ_0.

[5] R. L. Willett, C. Nayak, K. Shtengel, L. N. Pfeiffer, and K. W. West, Phys. Rev. Lett. **111**, 186401 (2013).

12.3 Intermediate fixed point in a Luttinger liquid with elastic and dissipative backscattering

A. Altland*, Y. Gefen†, B. Rosenow

*Institut für Theoretische Physik, Universität zu Köln, Köln, 50937, Germany
†Department of Condensed Matter Physics, The Weizmann Institute of Science, Rehovot 76100, Israel

The concept of a Luttinger liquid (LL) provides a very general framework to deal with a strongly interacting electron gas confined to one spatial dimension (1D). Contrary to higher-dimensional situations, where the quasiparticle (qp) concept describes low-energy excitations, in an LL only collective excitations are long lived and stable. Particlelike excitations of an LL have an energy dependent density of states and can relax in energy in the presence of backscattering. Hitherto there have been two paradigmatic models that addressed impurity scattering in the context of LL: a purely elastic impurity as discussed by Kane and Fisher [1] (KF), and totally inelastic scattering described by Furusaki and Matveev [1] (FM). In a recent publication [2], we have introduced and studied a model which is a hybrid between the two. We have addressed interacting electrons in one dimension described by a Luttinger model, which includes a scatterer that may give rise to elastic coherent tunneling, and at the same time may accommodate inelastic modes. Our analysis has led to predictions that are qualitatively different from the KF and the FM pictures, and in this sense can be considered as a new paradigmatic scheme of impurity scattering in the context of LL.
Here we present an extensive study of the renormalization group flows for this problem, the fixed point landscape, and scaling near those fixed points. Our analysis is nonperturbative in the elastic tunneling amplitudes, employing an instanton calculation in one or two of the available elastic tunneling channels. Our analysis accounts for nontrivial Klein factors, which represent anyonic or fermionic statistics. These Klein factors need to be taken into account due to the fact that higher-order tunneling processes take place. We have found that the combination of inelastic and elastic scattering channels can stabilize a new $\frac{1}{2} - \frac{1}{2}$ fixed point, with probability 1/2 for the transmission and probability 1/2 for the reflection of an incoming particle. This fixed point is intermediate between the $1 - 0$ and $0 - 1$ fixed points in the presence of only elastic scattering channels. Our main result is that the intermediate fixed point is stable for Luttinger parameters $g < 1$ in the leads. This conclusion is backed up by a refermionization analysis for the special value $g = 1$. For noninteracting fermions with $g = 1$, we recover the well-known marginal relevance of scattering.

[1] C. L. Kane and M. P. A. Fisher, Phys. Rev. B. **46**, 15233 (1992),
[2] A. Furusaki and K. A. Matveev, Phys. Rev. Lett. **75**, 709 (1995); Phys. Rev. B **52**, 16676 (1995),
[3] A. Altland, Y. Gefen, and B. Rosenow, Phys. Rev. Lett. **108**, 136401 (2012).

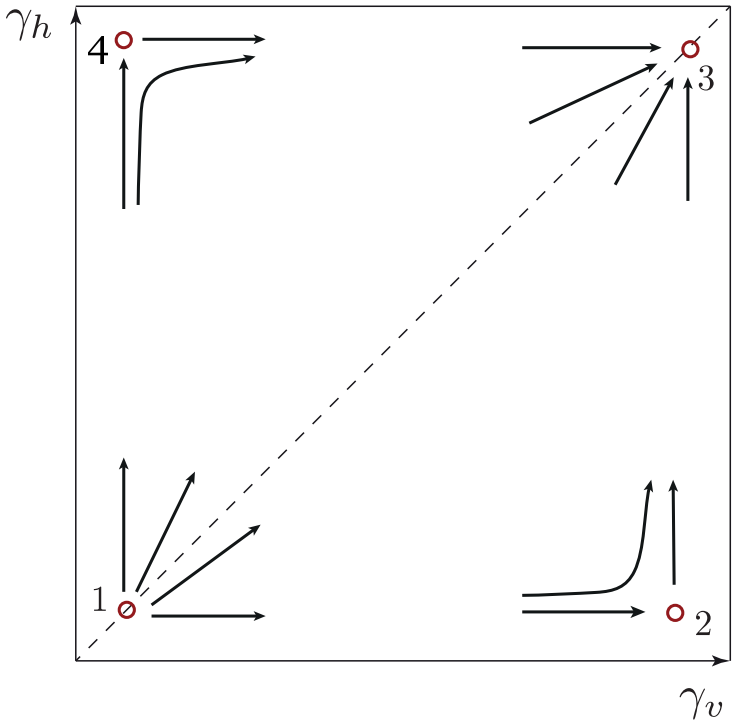

Figure 12.2: Description of the RG flow in terms of masses γ_h and γ_v , which denote the strength of elating tunneling in horizontal and vertical direction, respectively. Near the RG-unstable weak-weak fixed point 1, there are perturbative corrections to the Gaussian $(1/2, 1/2)$ conductance in both γ_h and γ_v, which grow under the RG. In the vicinity of the weak-strong fixed point 2, instantons in the strong scattering term γ_v are irrelevant, constituting a stable direction in parameter space, while the weak scattering amplitude γ_h grows under the RG and thus constitutes an unstable direction. The conductance is close to unity in the vertical direction, and perturbatively small in the horizontal direction. In the vicinity of the strong-strong fixed point 3, both vertical and horizontal tunnelings are strong, with RG irrelevant instanton corrections. The conductance is $(1/2, 1/2)$, and the fixed point is stable under RG scaling.

12.4 Noise due to neutral modes in the $\nu = 2/3$ fractional quantum Hall state

S. Takei*, B. Rosenow, A. Stern†

*Department of Physics and Astronomy, University of California, Los Angeles, California 90095, USA
†Department of Condensed Matter Physics, The Weizmann Institute of Science, Rehovot 76100, Israel

The behavior of two-dimensional (2D) electron gases in the fractional quantum Hall (FQH) regime has garnered much attention ever since its discovery [1]. While FQH liquids are incompressible with finite energy gaps to all bulk excitations, they support one or more 1D gapless conducting channels along their boundaries [2]. The edges of some FQH states, such as the spin-polarized $\nu = 2/3$ and the $\nu = 5/2$ Pfaffian and anti-Pfaffian non-Abelian states [3, 4], are predicted to possess neutral modes that can carry heat but no charge. The Majorana degree of freedom in the (anti-)Pfaffian neutral

mode is essential for the non-Abelian statistics of these states. For the case of $\nu = 2/3$ (the focus of this work), the neutral mode flows opposite to the charge mode.
We address the question of how neutral mode dipole fermion (DF) excitations and their interaction with a quantum point contact (QPC) can be described theoretically, and we identify signatures of their quantum statistics in a setup where two biased neutral modes collide at a QPC. By drawing on an analogy with the effect of a current bias on edge correlation functions of the charge mode, we associate an oscillatory behavior of neutral mode edge correlation functions with a biased neutral mode. We find that for biased neutral modes, the ratio between the current noise at a QPC due to two colliding neutral modes and that due to only one impinging neutral mode, γ is not only smaller than two, but it is also much smaller than the case of colliding thermally excited neutral modes. This result is a fingerprint of quantum statistics. It originates from a partial Pauli blockade of occupied states, and also allows one to experimentally distinguish DF excitations from thermally excited neutral modes. Our heuristic description of biased neutral modes is backed up by a full-fledged Keldysh calculation, and a comparison of our results with the recent experiment [5] suggests that the collision of thermally excited neutral modes was observed there. In the case of two neutral modes impinging on a QPC the noise power reflects the quantum statistics of bosonic thermal excitations vs DFs, thus allowing one to detect a fingerprint of the quantum statistics of neutral edge excitations.

[1] D. C. Tsui, H. L. Stormer, and A. C. Gossard, Phys. Rev. Lett. **48**, 1559 (1982),
[2] X. G. Wen, Phys. Rev. B **43**, 11025 (1991),
[3] M. Levin, B. I. Halperin, and B. Rosenow, Phys. Rev. Lett. **99**, 236806 (2007),
[4] S.-S. Lee, S. Ryu, C. Nayak, and M. P. A. Fisher, Phys. Rev. Lett. **99**, 236807 (2007),
[5] Y. Gross, M. Dolev, M. Heiblum, V. Umansky, and D. Mahalu, Phys. Rev. Lett. **108**, 226801 (2012).

12.5 Symmetry-protected topological invariant and Majorana impurity states in time-reversal-invariant superconductors

L. Kimme, T. Hyart*, B. Rosenow

*Instituut-Lorentz, Universiteit Leiden, Post Office Box 9506, 2300 RA Leiden, The Netherlands

Local impurities in superconductors (SCs) give rise to astonishing physics. Magnetic impurities in s-wave SCs lead to pair breaking, and can induce a quantum phase transition to a metallic state with gapless superconductivity near the transition point. Due to Anderson's theorem, nonmagnetic impurities have little influence on s-wave SCs. However, in unconventional SCs, where the sign of the order parameter depends on the direction of momentum, scattering by impurities leads to pair breaking since the momentum direction of the paired electrons is changed without changing the phase. Thus, impurities give rise to subgap states and can be used to probe high-Tc superconductivity.

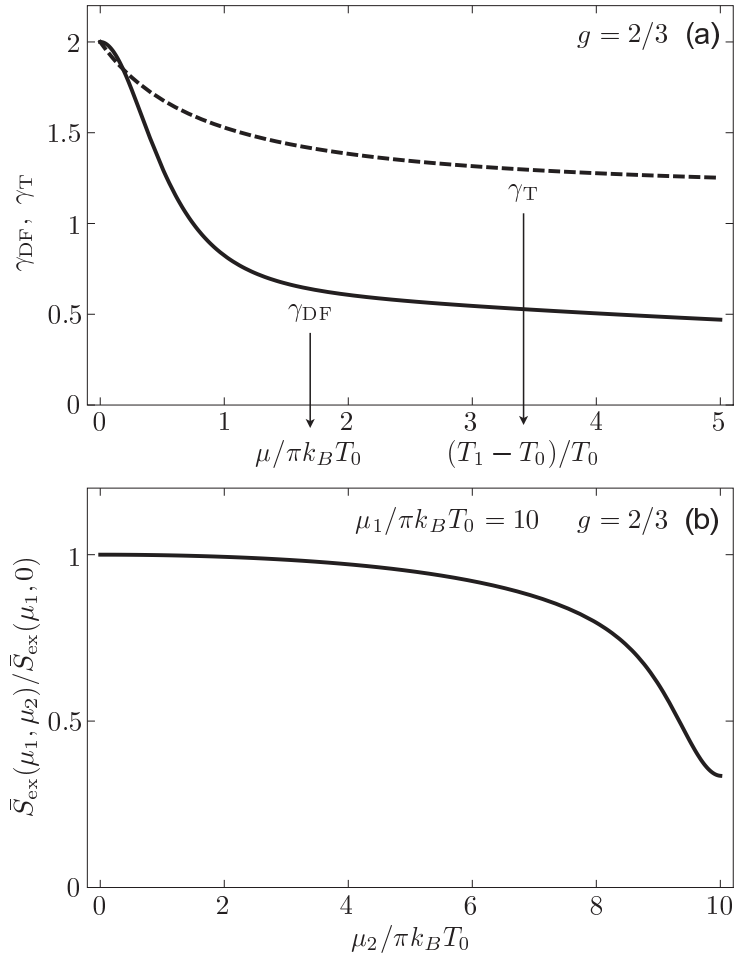

Figure 12.3: (a) Excess noise ratio for one and two excited neutral modes within the dipole picture $\gamma_{\rm DF}$ (solid line) and the thermal picture γ_T (dashed line). (b) Excess noise ratio for one and two excited neutral modes within the dipole picture while fixing the edge 1 bias in the asymptotically large regime, $\mu_1/\pi k_B T_0 = 10$, and varying the edge 2 bias, μ_2.

We focus on impurity bound states in time-reversal (TR) invariant odd-parity SCs. These SCs belong to symmetry class DIII of the Altland-Zirnbauer classification [1] and come in two variants, characterized by a $\mathbb{Z}_2$ topological invariant Q. The topologically nontrivial SC has protected Majorana boundary modes. We described symmetries which guarantee the existence of zero-energy impurity bound states in these TR-invariant SCs for a critical value of the impurity strength. The same symmetries allow the definition of the position-space topological $\mathbb{Z}_2$ invariant Q_{DIII} which we related to the bulk $\mathbb{Z}_2$ invariant Q. The relevance of our findings was demonstrated for the TR-invariant p-wave phase of the doped Kitaev-Heisenberg model, where symmetries protect the zero-energy crossings and a lattice of impurities can change the bulk topological order of the system. Finally, we have shown that TR-invariant topologically nontrivial SCs can be made robust against low-energy impurity states by strongly breaking all additional symmetries. This improves prospects for protocols utilizing topologically protected Majorana zero-energy states.

[1] A. Altland and M. R. Zirnbauer, Phys. Rev. B **55**, 1142 (1997); M. R. Zirnbauer, J. Math. Phys. **37**, 4986 (1996),

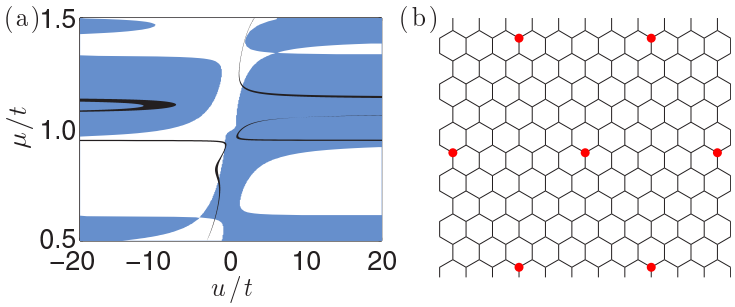

Figure 12.4: (a) Phase diagram of Q for an impurity lattice with impurity distance $a_{\text{imp}} = 5$ in the TR-invariant p-wave phase of the doped KH model as a function of the impurity strength u and the chemical potential μ. Blue denotes the topologically trivial phase $Q = +1$ whereas white denotes the nontrivial phase $Q = -1$. Black denotes regions where the system is gapless. (b) Impurity lattice for $a_{\text{imp}} = 5$; red dots mark impurity sites.

12.6 Critical flow and dissipation in a quasi one-dimensional superfluid

P-F. Duc*, M. Savard*, M. Petrescu*, B. Rosenow, A.D. Maestro†, G. Gervais*,‡

*Department of Physics, McGill University, Montreal, Quebec H3A 2T8, Canada
†Department of Physics, University of Vermont, Burlington, VT 05405, USA
‡Canadian Institute for Advanced Research, Toronto, Ontario M5G 1Z8, Canada

In one of the most celebrated examples of the theory of universal critical phenomena, the phase transition to the superfluid state of ^{4}He belongs to the same three-dimensional (3D) $O(2)$ universality class as the onset of ferromagnetism in a lattice of classical spins with XY symmetry. Below the transition, the superfluid density ρ_s and superfluid velocity v_s increase as a power law of temperature described by a universal critical exponent that is constrained to be identical by scale invariance. As the dimensionality is reduced toward 1D, it is expected that enhanced thermal and quantum fluctuations preclude long-range order, thereby inhibiting superfluidity. We have measured the flow rate of liquid helium and deduced its superfluid velocity in a capillary flow experiment occurring in single 30-nm-long nanopores with radii ranging down from 20 to 3 nm. As the pore size is reduced toward the 1D limit, we observe the following: (i) a suppression of the pressure dependence of the superfluid velocity; (ii) a temperature dependence of vs that surprisingly can be well-fitted by a power law with a single exponent over a broad range of temperatures; and (iii) decreasing critical velocities as a function of decreasing radius for channel sizes below $R \simeq 20nm$, in stark contrast with what is observed in micrometer-sized channels. We interpret these deviations from bulk behavior as signaling the crossover to a quasi-1D state, whereby the size of a critical topological defect is cut off by the channel radius.

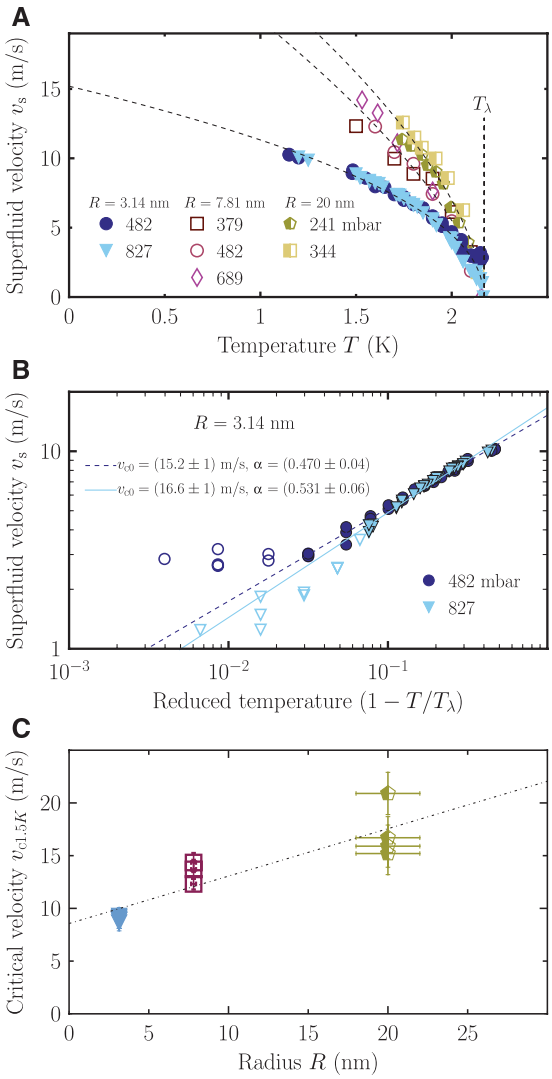

Figure 12.5: . (A) The superfluid velocities are shown at several pressures below 1 bar for three different nanopore radii. The filled symbols refer to the 3.14-nm pore, the open symbols to the 7.81-nm pore, and the half-filled symbols to a 20-nm pore from a previous study (21). The dashed lines are fits using the power law $v_s(T) = v_{c0}\left(1 - \frac{T}{T\lambda}\right)^{\alpha}$, where T_λ is the λ-transition temperature and v_{c0} is the superfluid critical velocity at zero temperature. (B) Log-log plot of the superfluid velocity versus the reduced temperature for the 3.14-nm pore data. The data used for the power law fit are highlighted with filled symbols. The fits are shown by a dashed line (482 mbar) and a solid line (827 mbar). (C) Critical velocity in the nanopores extracted at 1.5 K temperature (plotted at several pressures less than 1 bar) to compare with previous work in much larger channels. The superfluid velocities are assumed to be reaching the critical velocity. The dotted line is a blind linear fit shown here only as a guide to the eye.

12.7 International Workshop on Non-equilibrium Dynamics of Low-dimensional Electronic Systems

N. Andrei*, Y. Gefen†, B. Rosenow

*Deparmtent of Physics and Astronomy, Rutgers University, Piscataway, New Jersey 08854, USA

[†]Department of Condensed Matter Physics, The Weizmann Institute of Science, Rehovot 76100, Israel

The workshop was motivated by recent experimental and theoretical progress providing new insights into the non-equilibrium dynamics of low-dimensional electronic systems. For instance, the development of new spectroscopic methods involving localized resonant levels has made possible the measurement of non-equilibrium electron distribution functions in Luttinger liquids. Recent progress in terahertz technology has made the creation of intense pulses with high peak electric fields feasible, allowing for the observation of the Higgs (amplitude) mode in a BCS superconductor. The preparation of molecules in an optical lattice in the quantum regime has recently allowed to study coherence in melting Mott insulators. On the theoretical side, these experimental advances are complemented by the development of the non-perturbative method of non-equilibrium bosonization, and progress in treating the equilibration of isolated systems.

The first workshop day January 12 was organized as a Winter School, bringing junior scientists up to speed for following the lectures during the next days. The pedagogically outstanding and internationally recognized lecturers Prof. Thierry Giamarchi (Geneva), Prof. Amir Yacoby (Harvard), and Prof. Alex Kamenev (Minnesota) discussed in two lectures each Low-dimensional electrons and non-equilibrium, Exploring 1d electrons, and Many-body systems out of equilibrium.

Topics covered by the 29 invited speakers include: Non-equilibrium physics and equilibration of edge modes and one-dimensional conductors, non-equilibrium superconductivity, relaxation and thermalization in Mott insulators, quantum quenches and equilibration in cold atomic gases, non-equilibrium spin systems. This list makes it clear that the goal of covering the workshop topic in its full width has been achieved, and that different sub-communities of condensed matter physics had the opportunity to exchange ideas, learn from each other, and initiate novel research. A poster session provided students with an opportunity to present their research. A detailed list of talks and conference participants can be found under http://conference.uni-leipzig.de/neqdyn/program.pdf

The impact of this workshop can be judged from three different perspectives.

1. Impact on young researchers. The structure of this workshop has guaranteed that young researchers (students, post- docs, who take their first steps in this field or are about to enter it) have been exposed to one day of pedagogical talks. The latter emphasized the foundations of non- equilibrium many- body physics, and pointed out to some major outstanding problems in the field. This has facilitated the active involvement of those young researchers in the follow-up intensive program.

2. Exposure of junior faculty. A significant fraction of the speakers were young faculty members, who presented exciting results and had the opportunity to be exposed to the community at large, including senior researchers.

3. Integration. The fact that disparate niches of the huge field of non-equilibrium were represented, provided a rare opportunity for researchers coming from dif-

ferent directions to compare knowledge and exchange ideas, leading to mutual fertilization.

In summary, the workshop was valuable in bringing together researchers from different directions, giving junior scientists exposure to current research and allowing them to present themselves to the community, and in initiating new collaborations. The organizers are grateful to ICAM and NSF for the generous support, without which the workshop would not have been possible. Additional support by DFG as well as Research Profile Area Complex Matter and the Leibniz program of Leipzig University are gratefully acknowledged.

12.8 Funding

Engineering the coherency of fractional and non-abelian electronic interferometers
B. Rosenow
DFG grant RO 2247/8-1

12.9 Organizational Duties

B. Rosenow

- Member of the Qualitätssicherungskommission of the Faculty of Physics and Earth Sciences
- Referee for Science, Phys. Rev. Lett., Phys. Rev. B, Europhys. Lett. Adv. Con. Matter, JSTAT, Physica A, NSF, Studienstiftung des Deutschen Volkes

12.10 External Cooperations

Academic

- University of Vermont, USA
  Adrien Del Maestro
- Max-Planck-Institut für Festkörperforschung, Stuttgart, Germany
  G. Khaliullin
- Universiteit Leiden, Netherlands
  Dr. Timo Hyart
- School of Physics and CRANN, Trinity College, Ireland
  Prof. Paul Eastham
- Weizmann Institute for Science, Israel
  Prof. Yuval Gefen, Prof. Ady Stern
- Harvard University, USA
  Prof. Bert Halperin
- McGill University, Canada
  Pierre/Francois Duc, Michel Savard, Matei Petrescu, Guillaume Gervais

- University of California, Los Angeles, USA
  So Takei
- Universität zu Köln, Germany
  Prof. Dr. Alexander Altland
- Princeton University, USA
  Curt von Keyserlingk
- University of Oxford, United Kingdom
  Steve Simon

12.11 Publications

Journals

C.W. von Keyserlingk, S.H. Simon, and B. Rosenow, Enhanced bulk-edge Coulomb coupling in Fractional Fabry-Perot interferometers, Phys. Rev. Lett. **115**, 126807 (2015)

A. Altland, Y. Gefen, and B. Rosenow, Intermediate fixed point in a Luttinger liquid with elastic and dissipative backscattering, Phys. Rev. B **92**, 085124 (2015)

P.-F. Duc, M. Savard, M. Petrescu, B. Rosenow, A. Del Maestro, and G. Gervais, Critical Flow and Dissipation in a Quasi-One-Dimensional Superfluid, Science Advances **1**, e1400222 (2015)

S. Takei, B. Rosenow, and A. Stern, Noise due to neutral modes in the $\nu = 2/3$ fractional quantum Hall state, Phys. Rev. B **91**, 241104(R) (2015)

L. Kimme, T. Hyart, and B. Rosenow, Symmetry-protected topological invariant and Majorana impurity states in time-reversal invariant superconductors, Phys. Rev. B **91**, 220501(R) (2015)

in press

M. Horsdal, G. Khaliullin, T. Hyart, and B. Rosenow, Enhancing Triplet Superconductivity by the Proximity to a Singlet Superconductor in Oxide Heterostructures

P. R. Eastham and B. Rosenow, Universal themes of Bose-Einstein condensation

B. Zocher and B. Rosenow, Topological superconductivity in Quantum Hall-superconductor hybrid systems

B. Rosenow, I. P. Levkivskyi, and B. I. Halperin, Current Correlations from a Mesoscopic Anyon Collider

A. Janot, B. Rosenow, and G. Refael, Topological Polaritons in a Quantum Spin Hall Cavity

S. Hennel, B. A. Braem, S. Baer, L. Tiemann, P. Sohi, D. Wehrli, A. Hofmann, C. Reichl, W. Wegscheider, C. Rössler, T. Ihn, K. Ensslin, M. S. Rudner, and B. Rosenow, Nonlocal Polarization Feedback in a Fractional Quantum Hall Ferromagnet

L. Kimme, B. Rosenow, A. Brataas, Backscattering in helical edge states from a magnetic impurity and Rashba disorder

M. Thunert, A. Janot, H. Franke, C. Sturm, T. Michalsky, M. Martin, L. Vina, B. Rosenow, M. Grundmann, and R. Schmidt-Grund, Cavity Polariton Condensate in a Disordered Environment

S. L. Schreier, A. Stern, B. Rosenow, and B. I. Halperin, Thermodynamic properties of a quantum Hall anti-dot interferometer

Talks

B. Rosenow, Interferometry with Anyons, Winter School Topological Quantum Matter, Harish-Chandra Research Institute at Allahabad, February 2015

B. Rosenow, Transient Features in Charge Fractionalization and Non-equilibrium Bosonization, APS March Meeting San Antonio, March 2015

B. Rosenow, Exotic particles in two dimensions: interferometry with anyons, Physics Colloqium, University of Vermont, Burlington, October 2015

B. Rosenow, Enhanced Bulk-Edge Coulomb Coupling in Fractional Fabry-Perot Interferometers, Condensed Matter Seminar, McGill University, Montreal, October 2015

B. Rosenow, Coulomb Effects in Fractional Quantum Hall Interferometers, Condensed Matter Theory Seminar, Harvard University, October 2015

D. D. Scherer, Correlated fermions and spin-orbit effects: the doped Kitaev-Heisenberg model, Niels Bohr Institute, Copenhagen, March 2015

L. Kimme, Effects of random Rashba spin-orbit coupling and magnetic impurities on edge state transport in topological insulators, DPG Frühjahrstagung, Berlin, April 2015

Posters

M. Treffkorn, B. Zocher, and B. Rosenow, Current Distribution in Quantum Hall Systems, Minisymposium on Unconventional Superconductivity, Leipzig, September 2015

M. Treffkorn, B. Zocher, and B. Rosenow, Towards non-equilibrium transport in quantum Hall point contacts, International Workshop on Non-equilibrium Dynamics of Low-dimensional Electronic Systems, Leipzig, January 2015

12.12 Graduations

Master

- Alexander Schneider
  Transient Features in Charge Fractionalization and Non-equilibrium Bosonization
  03.02.2015

12.13 Guests

- Prof. Mark Rudner
  University of Copenhagen
  14. – 17. March 2015
- Giovanni Frigeri
  University of Milan
  7. – 10. May 2015
- Dr. Giandomenico Palumbo
  University of Leeds
  11. –13. May 2015
- Dr. Erwand Kandelaki
  2. June 2015
- Prof. Adrian Del Maestro
  University of Vermont at Burlington
  18.July – 7.August 2015
- Dr. Casper Drukier
  Universität Frankfurt
  26. – 27. May 2015
- Prof. Johannes Reuther
  FU Berlin
  29.5 May 2015
- Prof. Yuval Gefen
  Weizmann Institute for Science
  17. – 19. September 2015

13

Theory of Condensed Matter

13.1 Introduction

Major research topics of our groups include nonequilibrium phenomena and pattern formation in systems of various nature, e.g. in soft condensed matter and in biological systems. Modern analytic methods of statistical physics and computer simulations complement and stimulate each other. Cooperations with mathematicians, theoretical and experimental physicists, biologists and medical researchers in Germany, Europe and around the world are well established.

Stochastics and pattern formation (Behn). Noise induced phenomena like nonequilibrium phase transitions are studied with analytical and cumputational methods in stochastically driven nonlinear systems with many degrees of freedom. Methods of nonlinear dynamics and statistical physics are used to formulate and investigate mathematical models of the adaptive immune system. We describe the randomly driven evolution of idiotypic networks of the B-lymphocyte subsystem and its role in self tolerance and autoimmunity. The lineage committment and plasticity of $CD4^+$ T cells is modeled using a minimal Boolean network to describe the intracellular signal transduction.

Non-equilibrium dynamics in soft-condensed-matter systems (Kroy). The group's activities can be subsumed under the name of "Soft Mesoscopics", the study of of emerging properties in soft and biological matter. Studied phenomena range from structure formation by wind-blown sand resulting in ripples and dunes, through nonequilibrium dynamics of hot nanoparticles, proteins and polymers, the viscoelastic and inelastic mechanics of the cytoskeleton, to the tension propagation in single DNA molecules under strong external fields. (Related experimental work is currently in progress at EXP1: MON, MOP, PWM.) A common theme is the presence of strong fluctuations and stochastic dynamics on the microscale. The emergence of the mesoscopic structure and transport is to be understood. The applied methods comprise a broad statistical mechanics toolbox including stochastic (integro-)differential equations, liquid-state theories, effective hydrodynamic equations, various systematic coarse-graining techniques, and massively parallel numerical simulations on GPUs.

Ulrich Behn, Klaus Kroy

13.2 Stochastic Phenomena in Systems with Many Degrees of Freedom

U. Behn, R. Kürsten

Arrays of coupled nonlinear dynamical systems driven by multiplicative or additive noise show close analogies to phase transitions in equilibrium [1].

For an infinite array of globally coupled overdamped anharmonic oscillators subject to additive Gaussian white noise a mean-field like description is exact. We have proved the existence of a well-behaved critical manifold in the parameter space which separates a symmetric phase from a symmetry broken phase and calculated exact, optimal bounds of the critical value of the control parameter [2]. The method can be extended to models with higher order saturation and with competing interactions which exhibit discontinuous phase transitions. For the latter, optimal bounds for the tricritical point are derived [3].

We further developed a method, the patchwork sampling, which allows by a suitable decomposition of the state space an efficient computer simulation of nonlinear stochastic differential equations to sample probability densities also in sparsely visited regions of the support [4]. The method is based on the concept of truncated Markov chains for reversible processes, cf. Fig. 13.1, and can be extended to the non-reversible case.

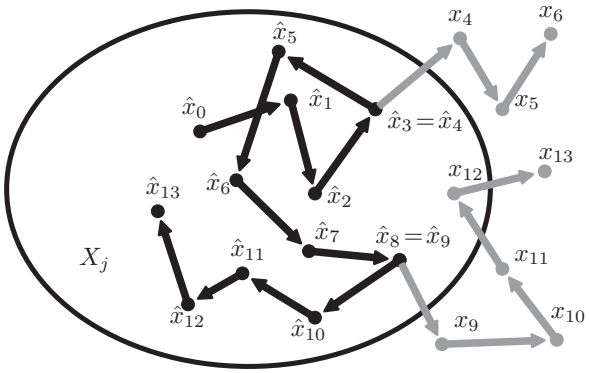

Figure 13.1: Construction of the process $\hat{x}_t$ (black) which is truncated to the patch X_j. Inside the patch the truncated process follows the realizations of the original process x_t. Each time x_t leaves X_j (gray) the truncated process is set back to its previous position and follows a new realization of x_t. The correct weight for each patch is obtained by counting the attempted transitions between all different patches. >From [4].

[1] F. Sagués, J. García-Ojalvo, J.M. Sancho: Rev. Mod. Phys. **79**, 829 (2007)
[2] R. Kürsten, S. Gütter, U. Behn: Phys. Rev. E **88**, 022114 (2013)
[3] R. Kürsten, U. Behn: *Critical Manifold and Tricritical Point of Nonlinear Globally Coupled Systems with Additive Noise*, in preparation
[4] R. Kürsten, U. Behn: Phys. Rev. E **93**, 033307 (2016)

13.3 Random Recursive Trees and the Elephant Random Walk

R. Kürsten

One class of random walks with infinite memory, so called elephant random walks [1], see Fig. 13.2, are simple models describing anomalous diffusion [2]. We present a surprising connection between these models and bond percolation on random recursive trees which is exploited to translate results from elephant random walks to the percolation process. We calculate, besides other quantities, exact expressions for the first and the second moment of the root cluster size and of the number of nodes in child clusters of the first generation. We further introduce a new model, the skew elephant random walk, and calculate the first and second moment of this process [3].

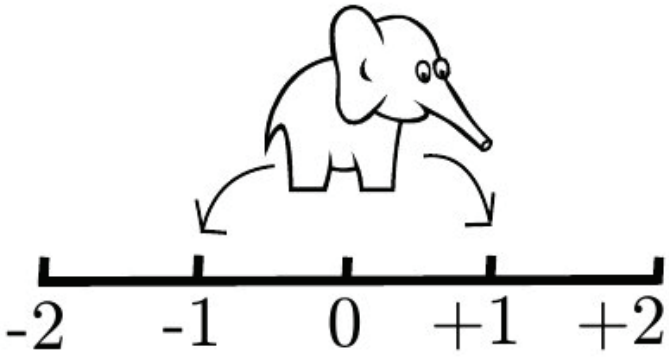

Figure 13.2: In the simplest version the elephant can perform steps of unit length to the left or to the right and has a long memory. After the first step he choses a random instant in the past and is doing the same step as in that instant with probability $\tilde{p}$ or the opposite with probability $1 - \tilde{p}$.

[1] G. M. Schütz, S. Trimper: Phys. Rev. E **70**, 045101 (2004)
[2] R. Kürsten: "Comment on 'Anomalous diffusion induced by enhancement of memory' ", arXiv:1503.03302
[3] R. Kürsten: Phys. Rev. E **93**, 032111 (2016)

13.4 Randomly Driven Evolution of Idiotypic Networks

U. Behn, S. Landmann, J. Müller

The paradigm of idiotypic networks conceptualized a few decades ago by Niels Jerne [1] finds today a renewed interest mainly from the side of systems biology and from clinical research, see e.g. [2, 3].

We have considered the problem of self tolerance and its failure –autoimmunity– in the frame of a minimal model of the idiotypic network developed in our group

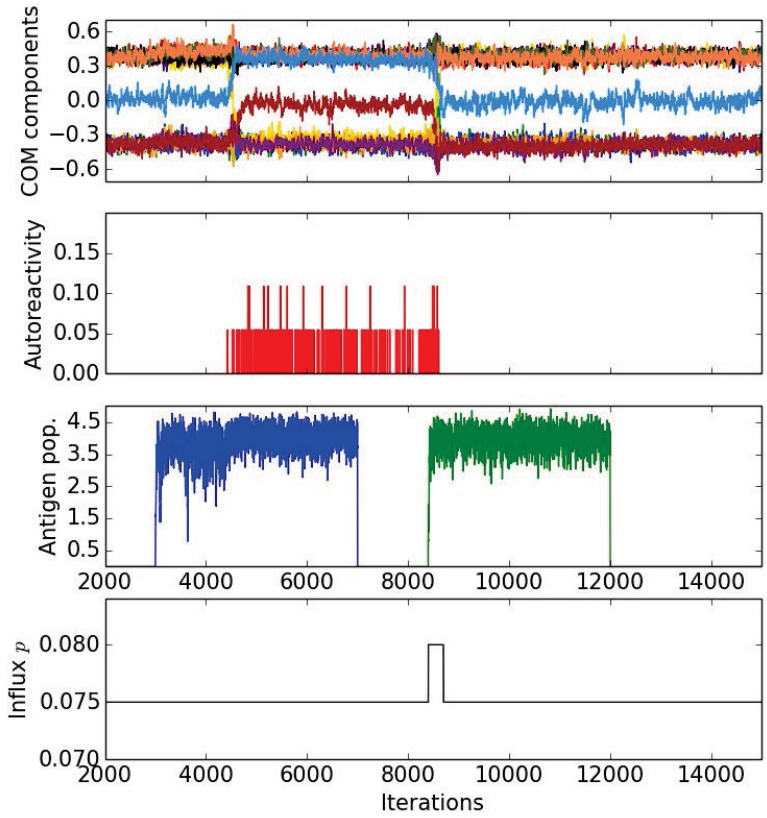

Figure 13.3: Induction of an autoreactive state by an infection and restitution of self tolerance by a second infection with a different antigen. The figure shows time series of the center of mass (COM) vector components which indicate structural changes in the networks architecture (top panel), of the autoreactivity (second panel), of the two antigen populations (third panel) of the first infection (blue) and the second one (green). The protocol includes an enhancement of the influx of new B lymphocytes of random idiotype (bottom panel) which should accompany the begin of the second infection.

[4–7]. In this model a node represents a clone of B lymphocytes with certain idiotype. The model network evolves, driven by the random influx of new idiotypes, towards a highly organized modular architecture where groups of nodes which share statistical characteristics can be identified. Self is modeled by permanently occupied nodes. We found in simulations that in the presence of self the architecture organizes in a way that the neighbors of self are only weakly occupied, such that self is tolerated [8]. This self-tolerant state has a lower entropy than the initial autoreactive state. We investigated the effect of infections which can induce a reorganization of the network to an autoreactive state and devised protocols which restore the self-tolerant state, see Fig. 13.3. The simulation results are corroborated by an analytical modular mean field theory which includes correlations [9].

Furthermore, the response of the network in an established architecture to perturbations of various kinds and the relative stability of different architectures is studied using numerical simulations and analytical methods (Müller).

[1] N.K. Jerne: Ann. Inst. Pasteur Immunol. **125C**, 373 (1974)
[2] U. Behn: Immunol. Rev. **216** 142 (2007)
[3] U. Behn: *Idiotype Network*, in: Encyclopedia of Life Sciences, John Wiley & Sons, Ltd, Chichester, doi:10.1002/9780470015902.a0000954.pub2 (2011)
[4] M. Brede, U. Behn: Phys. Rev. E **67**, 031920 (2003)
[5] H. Schmidtchen, M. Thüne, U. Behn: Phys. Rev. E **86**, 011930 (2012)
[6] H. Schmidtchen, U. Behn: Phys. Rev. E **86**, 011931 (2012)
[7] H. Schmidtchen: Dissertation, Universität Leipzig, 2015
[8] R. Schulz, B. Werner, U. Behn: Frontiers in Immunology **5**, 00086 (2014), doi: 10.3389/fimmu.2014.00086
[9] S. Landmann, N. Preuss, U. Behn: *Self tolerance and autoimmunity in a minimal model of the idiotypic network*, in preparation

13.5 T Cell Regulation, Differentiation, and Plasticity

U. Behn, C. Schöller

T helper cells play a significant role in immune responses to allergenic substances. There are several subtypes which differ in function according to their cytokine profiles. Immunologists distinguish four major lineages: Th1, Th2, Th17 and regulatory T cells (Treg). Among these, mainly specific Th2cells are responsible for allergic reactions since they activate the production of IgE antibodies which provoke the well-known allergic symptoms.

We developed a mathematical model describing the nonlinear dynamics of Tregs, naive T helper cells, Th1 and Th2 subsets, and their major cytokines [1]. Administration of allergen according to empirical protocols is targeting the model to a tolerant state. There are other systems with a skewed T-cell balance where the novel Th-subtype Th17 is suspected to play a decisive role. They include allergic asthma, Crohn's disease and ulcerative colitis, rheumatoid arthritis, and many others. Th17 cells have a much higher plasticity compared to Th1 and Th2 cells.

To describe the lineage committment and the plasticity of CD4+ T cells we developed a minimalistic model of the network of intracellular signal transduction [2] based on Boolean cellular automata. Already in its simplest version the Boolean network has attractors which describe Th1, Th2, Treg, and Th17 phenotypes and hybrids such as Th1/Th17, Th2/Th17, and Treg/Th17 and reproduces, for example, the high plasticity of Th17 cells [3]. We continue the research studying properties of the model in variant architectures and aim to develop a multi-scale description of T-cell regulation.

[1] F. Groß, G. Metzner, U. Behn: J. Theor. Biol. **269**, 70-78 (2011)
[2] J. Zhu, W.E. Paul: Immunol. Rev. **238**, 247-262 (2010)
[3] D. Kröber: Master thesis, Universität Leipzig, 2011

13.6 Computational high-speed force spectroscopy

J. T. Bullerjahn, S. Sturm, K. Kroy

Dynamic force spectroscopy (DFS) is a well-established technique that allows the experimentalist to determine the free-energy landscape of single molecules by probing their rupture behavior under external force. Conventional theories of DFS rely on a quasistatic model of bond breaking [1] that is well justified for current experimental setups, but fails to cover the high loading rates amenable to full-scale molecular dynamics simulations and, possibly, future high-speed force spectroscopy assays [2]. We have successfully extended these theories to rapid force spectroscopy protocols by explicitly resolving the non-equilibrium internal bond dynamics [3]. Our analytical predictions are exact for fast loading protocols and reduce to established quasistatic results in the limit of slow external loading.

In a collaboration with the group of Frauke Gräter from the Heidelberg Institute of Theoretical Studies, we used our model to analyze DFS data from a molecular dynamics simulation, where the role of focal adhesion kinase as a mechano-sensor was investigated [4]. A fit by our model, using Bayesian methods of data analysis, provided parameter values that characterize the underlying free-energy landscape of the protein and predict its dynamical behaviour under external load.

[1] O. K. Dudko, G. Hummer, A. Szabo: Phys. Rev. Lett. **96**, 108101 (2006)
[2] M. Rief, H. Grubmüller: ChemPhysChem **3**, 255-261 (2002)
[3] J. T. Bullerjahn, S. Sturm, K. Kroy: Nat. Commun. **5**, 4463 (2014)
[4] J. Zhou, C. Aponte-Santamaría, S. Sturm, J. T. Bullerjahn, A. Bronowska, F. Gräter: PLoS Comput. Biol. **11**, e1004593 (2015)

13.7 Viscoelastic response of stiff polymer solutions

M. Lämmel, K. Kroy

A central task in biomechanics is to establish a physical understanding of the unique mechanical properties of living cells and tissues in terms of the material properties of their polymeric constituents. We propose an analytical model for the linear and nonlinear viscoelastic shear response of solutions of stiff polymers. It integrates locally non-affine bending deformations as captured by an effective-medium theory based on the tube model of semiflexible polymers [1] with transient non-affine polymer stretching [2] and elucidates the crucial role of the contour length for the macroscopic mechanical response.

[1] H. Isambert, A.C. Maggs: Macromolecules **29**, 1036–1040 (1996)
[2] F. Gittes, F. MacKintosh: Phys. Rev. E **58**, R1241–R1244 (1998)

13.8 Linear and nonlinear microrheology of shear-thinning fluids

T. Herpich, K. Kroy

We first review a recently published active microrheology experiment [1] employing a circular trajectory in a viscoelastic wormlike micellar solution allegedly probing nonlinear fluid response and demonstrate, starting from a linear fluid-response assumption and using an exact yet simple model, that it is the specific trajectory chosen in this experiment giving rise to the apparent nonlinear fluid response. As a complement to the foregoing discussion, we furthermore propose approximate models for both the rotational and translational microrheology in generalized power-law shear-thinning fluids by partitioning the system into (deformed) shells according to the different regimes of the constitutive generalized power-law equation characterizing the shear-thinning fluid.

[1] J. R. Gomez-Solano and C. Bechinger: Europhysics Letters **108**, 54008 (2014)

13.9 Nonequilibrium statistical mechanics: from energy partition to state equations

G. Falasco, F. Baldovin*, K. Kroy, M. Baiesi*

*University of Padova

From equilibrium statistical mechanics we are accustomed to the idea that there is energy equipartition among all quadratic degrees of freedom of classical systems, and that the "energy bit" corresponds to $k_BT/2$. >From this fundamental result, the mechanical equation of state —i.e. the relation between pressure and the other relevant thermodynamic variables— of a many-body system can be obtain through the virial theorem. Since equipartition is not granted for dissipative driven systems, one may wonder to what extent such framework carries over to non-equilibrium conditions. For a wide class of non-equilibrium steady states, both stochastic (Langevin) and deterministic (Nose-Hoover), we have derived a mesoscopic virial equation governing energy partition between conjugate position and momentum variables of individual degrees of freedom. Upon summation over all degrees of freedom, a generalized macroscopic virial theorem is obtained which involves dissipative heat flows on the same footing with state variables. As much as in equilibrium, it allows for the derivation of non-equilibrium mechanical equations of states. We have applied these results to a variety of model systems, e.g. studying the energy distribution between modes of heat-conducting lattices (13.4) and deriving the pressure equation for self-propelled Brownian particles [2].

[1] G. Falasco, F. Baldovin, K. Kroy, M. Baiesi: arXiv:1512.01687 (2015)
[2] M. C. Marchetti *et al.*: Rev. Mod. Phys., **85**(3), 1143 (2013)

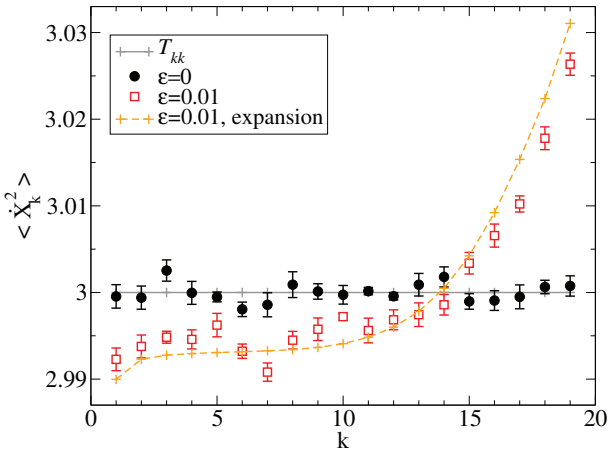

Figure 13.4: Kinetic energy of the normal modes for a chain of $N = 20$ unit masses coupled via quadratic-quartic potential (harmonic constant $\kappa = 1$, quartic $\epsilon = 0, \ldots, 10$) and immersed in heat baths characterised by the (global) friction constant $\gamma = 0.1$ and the local temperatures T_i, which grow linearly with i from $T_0 = 1$ to $T_{N-1} = 5$ (in natural dimensionless units). Comparison between the analytic expansion of the mesoscopic virial equation (+) and the numerically estimated kinetic energy (□) obtained by integration of the oscillators' stochastic dynamics.

13.10 Hot Brownian motion

G. Falasco, K. Kroy

The theory of isothermal Brownian motion relies on fundamental principles of equilibrium classical statistical mechanics, such as the equipartition theorem, embedded in the stochastic framework of the Langevin equation. In the presence of a non-isothermal solvent it becomes questionable whether a Langevin-like description still applies and, if so, no general criterion exists which uniquely determines friction and thermal fluctuations. Starting from the fluctuating hydrodynamics of a solvent in local equilibrium, we have constructively showed that a generalized Langevin description does hold and derive the statistics of the corresponding thermal noise [2]. The coupling between the hydrodynamic modes excited by the particle itself and the solvent temperature gradient turns the Langevin noise energy spectrum into a frequency-dependent tensor. We have derived an explicit expression for this energy spectrum in the analytically tractable case of hot Brownian motion, i.e. a constantly heated particle generating a co-moving radial temperature field. This allows us to explain the break of energy equipartition and express the energy content of the particle velocity and position in terms of effective temperatures [1].

[1] G. Falasco, M. V. Gnann, D. Rings and K. Kroy: Phys. Rev. E **90**(3), 032131 (2014)
[2] G. Falasco and K. Kroy: Phys. Rev. E **93**(3), 032150 (2016)

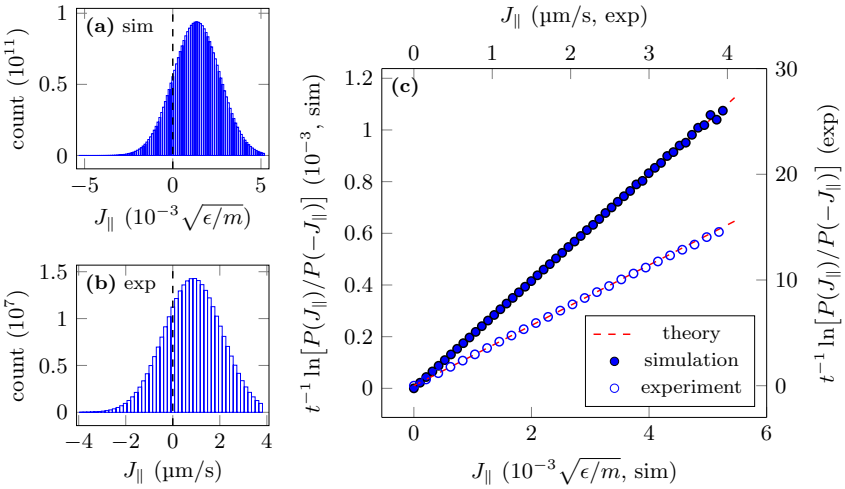

Figure 13.5: *Upper panel:* histograms of the longitudinal particle current $J_\parallel$ as measured in simulation (a) and experiment (b). *Lower panel:* test of the fluctuation theorem, using these histograms as proxies for $P(J_\parallel)$. The parallel particle current $J_\parallel$ can be related to the entropy production S by the theory

13.11 Fluctuation theorems for a hot Brownian swimmer

G. Falasco, R. Pfaller A. P. Bregulla F. Cichos K. Kroy

Artificial self-propelled colloidal particles are peculiar examples of non-equilibrium systems. They rely on the creation of asymmetric gradients of a thermodynamic field (e.g. temperature) in the solvent to attain a systematic drift through classical interfacial phoretic processes [1]. The directed autonomous motion of such "Brownian swimmers", achieved by a constant energy input on the particle scale (e.g. laser light absorption), is limited by Brownian motion though. The competition between propulsion and diffusion, both non-equilibrium in nature, results in atypical transient fluctuations that depart from the expected thermodynamic behavior —i.e. the average motion along the direction of propulsion. Such fluctuations are expected to be not completely chaotic, but rather to be characterized by universal symmetry relations, called fluctuation theorems. They quantify the irreversibility of generic non-equilibrium processes by the total entropy production S, saying that the probability $P(S)$ for positive S is exponentially larger than for negative S: $P(S) = P(-S)\exp(S/k_B)$ (see 13.5). By means of experiments (conducted in the nanophotonic group of Prof. Cichos) and molecular dynamics simulations, we test this fundamental relation for a heated Janus particle, together with a similar recently discovered relation for the particle current [2].

Using modern GPUs and our own source code, we perfomed large-scale MD simulations on Brownian motion and in particular on Brownian swimmers. We were able to successfully test fluctuation theorems and a thermodynamic uncertainty relation that link the fluctuating particle current to its entropy production at an effective temperature.

[1] H. R. Jiang, N. Yoshinaga, M. Sano: Phys. Rev. Lett., **105**(26), 268302 (2010)
[2] G. Falasco *et al.*: arXiv:1602.08890 (2016)

13.12 Pressure of active particles

S. Steffenoni, G. Falasco K. Kroy

Active particles, i.e. colloids provided with internal propulsion engine able to convert chemical energy in kinetic energy, continue to surprise physicists. It is not straightforward how to conciliate the propulsion force with the mechanical interaction they could afford, from the inter-particles forces to the interaction with a wall. In particular, the latter is still an open and debated topic. The pressure that active particles are able to exert on a wall, seems to be a boundary problem since most of the peculiar properties appears close to boundaries where many symmetries are broken. Many works have appeared recently which consider global average approaches in which the boundary effects are flattened and hidden. Furthermore, it is still not clear how to conciliate the propulsion force with the overdamped limit. Therefore we are developing a local approach, sensitive to localised correlation and fluctuation. Starting from an underdamped Langevin equation we take both overdamped and hydrodynamic limit, in order to obtain a local continuum momentum equation.

[1] G. Falasco, F. Baldovin, K. Kroy, and M. Baiesi: arXiv 1512.01687v1 (2015)

13.13 Polarization of thermophoretic microswimmers in external gradients

G. Zecua, S. Auschra, K. Kroy

We considered a spherical Janus particle undergoing Brownian and passive thermophoretic motion as it is exposed to an external temperature gradient stemming from a hot spot in the vicinity of the microswimmer. Finding a rigorous definition of a so-called phoretic center where the phoretic force exerted on the particle effectively acts and causes a translation as well as rotation was the main goal of our theoretical work. Moreover, we set up a GPU-supported extensive molecular dynamics code[1] in order to simulate the abovementioned situation and to verify theoretical predictions [1] as well as experimental results.

[1] T. Bickel, G. Zecua, A. Würger: Phys. Rev. E. **89**, 050303(R) (2014)

[1] We used the Lammps Molecular Dynamics Simulator http://lammps.sandia.gov/

13.14 Shape, size and stability of sand dunes

S. Auschra, M. Lämmel, M. Guthardt, K. Kroy

Based on a well-established model for two-dimensional slices of isolated dunes [1], we derived a coarse-grained description of the three-dimensional barchan's shape and mass and investigate its complex response to heterogeneous sand supply. For homogeneous flux fields, we recover two major predictions of the original model, mass instability and the shape transition from heaps to dunes, as illustrated in Fig. 13.6.

As a consequence of the sensitivity of barchans to sand influx inhomogeneities within our model, we were able to explain asymmetric dune shapes as observed in the desert [2]. Moreover, we performed a mass stability analysis for a pair of consecutive dunes in a barchan field in order to uncover the underlying stabilization mechanism of the inherently unstable barchan dunes [3].

To investigate the consequences of our model equations for extended dune corridors, we started to develop a coarse-grained dune field simulation that is currently tested against our analytical predictions. In the future, it shall help to unravel the conundrum of barchan field stabilization.

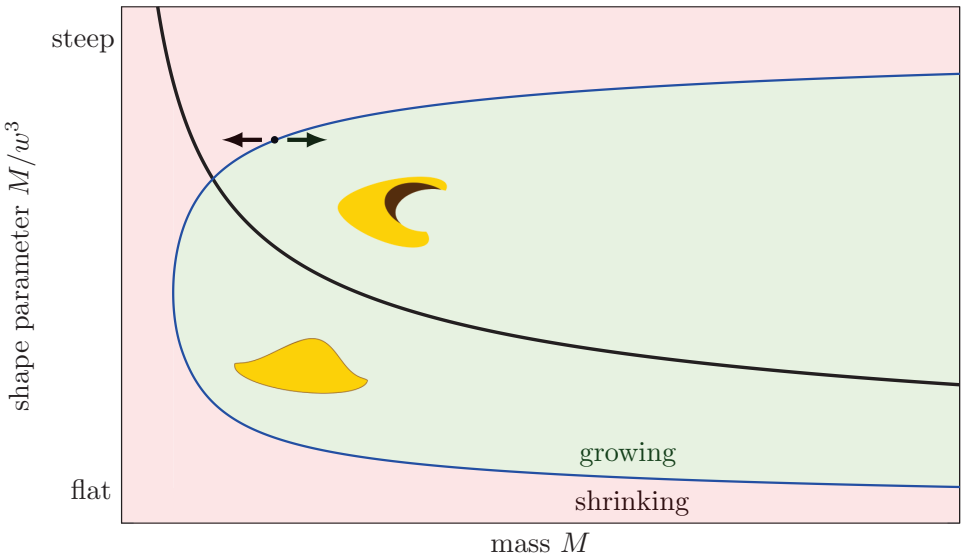

Figure 13.6: Mass instability and shape transition. The blue curve indicates unstable fixed points to a given constant sand influx and separates shrinking from growing dunes (red or green area respectively). All dunes above the black curve exhibit the typical slip face whereas below that curve barchans have transformed into sand heaps.

[1] E. Fischer, M. E. Cates, K. Kroy: Phys. Rev. E **77**, 031302 (2008)
[2] G. Sauermann *et al.*: Geomorphology **36**, 47-62 (2000)
[3] O. Duran *et al.*: Nonlin. Processes Geophys. **69**, 455-467 (2011)

13.15 Analytical mesoscale modeling of aeolian sand transport

M. Lämmel, A. Meiwald, K. Kroy

The mesoscale structure of aeolian sand transport plays a crucial role for the understanding and control of a variety of natural phenomena in planetary and Earth science. We analyze it beyond the mean-field level, using a refined version of our previously proposed two-species transport model [1] that is based on the conservation laws and kinematics governing the grain-scale physics. Analytical predictions for the height-resolved sand flux and other important mesoscale characteristics of the aeolian transport layer are derived. Their remarkable agreement with a comprehensive compilation of field and wind tunnel data suggests that the essential mesoscale physics is robustly captured by the coarse-grained analytical model. It also reveals that certain widely accepted experimental procedures are prone to systematic measurement errors, and new ways to avoid them.

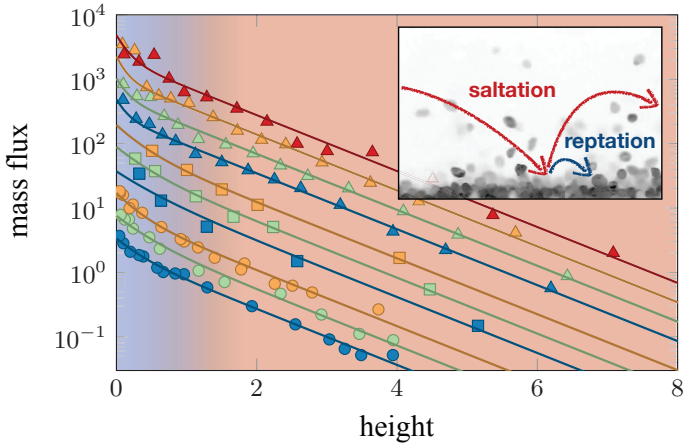

Figure 13.7: Height-dependent two-species mass flux (solid lines) compared with wind tunnel measurements (dots [2], squares [3]), and field data (triangles [4]) for various wind strengths. The pronounced flux close to the ground reflects the dense repton layer (blue background); the faster but fewer saltating grains yield the exponential decay in the upper region (red background). *Inset:* Within our formalism, reptating grains represent passive ejecta created by impacting saltating grains. The background shows a snapshot taken in a wind tunnel. Source: BBC/A. Valance (Université de Rennes 1, France).

[1] M. Lämmel, D. Rings, K. Kroy: New J. Phys. **14**, 093037 (2012)
[2] K. R. Rasmussen, H. E. Mikkelsen: Sedimentology **45**, 789–800 (1998)
[3] K. R. Rasmussen, M. Sørensen: J. Geophys. Res. **113**, F02S12 (2008)
[4] S. L. Namikas: Sedimentology **50**, 303–326, (2003)

13.16 Aeolian sand sorting and megaripple formation

M. Lämmel, A. Meiwald, K. Kroy

Turbulent flows drive sand along riverbeds or blow it across beaches and deserts. This seemingly chaotic process creates a whole hierarchy of structures ranging from ripple patterns over dunes to vast wavy sand seas. Moreover, by the very same process, grains are constantly being sorted, because smaller grains advance faster while their heavier companions trail behind. Starting from the grain-scale physics, we model the sorting dynamics by erosion and show how it creates the characteristic bimodal grain size distribution that we predict to be a necessary prerequisite for the formation of so-called megaripples. Due to the separation into small and big grains, these structures have a lot in common with their bigger relatives, aeolian sand dunes, whose physics is much better understood. This enables us to adapt a well established dune model [1] to predict formation, morphology, and dynamics of the megaripples. Preliminary tests against field data strongly support our approach, which, moreover, provides a roadmap for future systematic field and laboratory measurements.

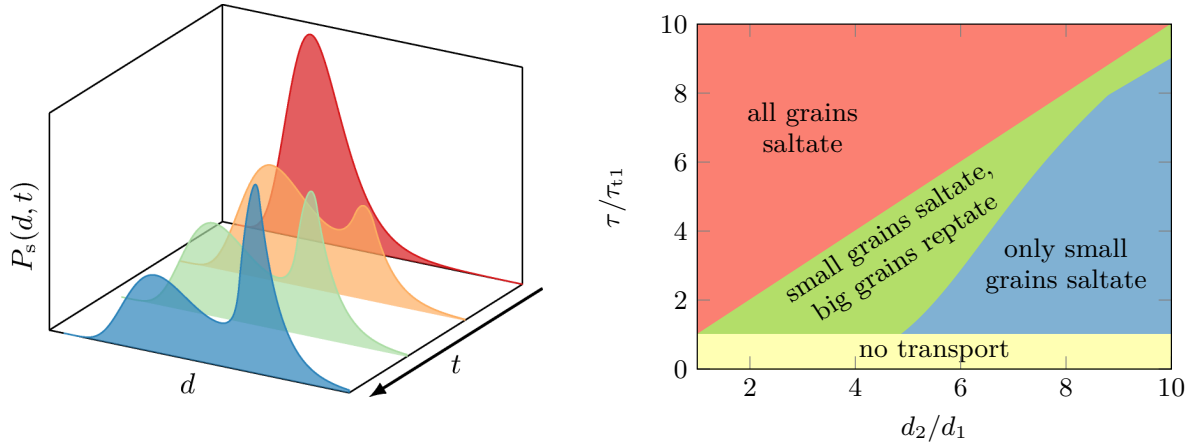

Figure 13.8: Wind-driven sand sorting as predicted by the erosion model. The left panel illustrates how the initially unimodal surface grain size distribution (GSD) $P_s(d, t = 0)$, given by the bulk GSD, evolves towards a bimodal distribution. This time series is obtained by numerically integrating our erosion model with a log-normal bulk GSD and an erosion kernel $\propto d/d^* - 1$, with a threshold grain size d^* above which grains are too big to be transported. The right diagram shows the transport regimes of sorted bidisperse sand as function of wind strength, given by the shear stress τ, and grain size ratio d_2/d_1. In the green corridor, sand structures can develop; in the blue and yellow region, they are frozen; in the upper red region, the surface layer is reshuffled and the ripple pattern destroyed.

[1] K. Kroy, G. Sauermann, H. J. Herrmann: Phys. Rev. Lett. **88**, 054301 (2002)

13.17 Funding

German-Israeli Foundation for Scientific Research and Development
K. Kroy (Principle Investigator), A. Meiwald
4411-1.02/8.44

DFG "Non-isothermal Brownian Motion"
K. Kroy
DFG, KR 3381/4-1

DFG SPP 1726 " TP Propulsion and Interaction of Hot Brownian Swimmers"
K. Kroy in collaboration with F. Cichos
DFG, KR 3381/5-1

FOR 877 "From Local Constraints to Macroscopic Transport"
K. Kroy (Principal Investigator) Project P9, in collaboration with W. Janke
DFG, KR 3381/3-1

FOR 877 "From Local Constraints to Macroscopic Transport"
K. Kroy (Principal Investigator), project P1 in collaboration with F. Cichos, M. Mertig
DFG, KR 3381/2-2

The European Union and the Free State of Saxony
J. Bullerjahn, S. Sturm

Leipzig School of Natural Sciences – Building with Molecules and Nano-objects
J. Bullerjahn, S. Sturm, G. Falasco

H-ITS, Universität Heidelberg
S. Sturm

Nonlinear Stochastically Driven Systems with Many Degrees of Freedom
R. Kürsten, M.Sc.
IMPRS Fellowship (April-October 2015)

13.18 Organizational Duties

Ulrich Behn

- Speaker of the Condensed Matter Theory Group
- Vertrauensdozent für die Nobelpreisträgertagungen in Lindau
- Bibliotheksbeauftragter of the Faculty
- Member of the Library Commission of the university
- Member of Research Profile Area "Mathematical and Computational Sciences"
- Scientific Member of the International Max Planck Research School "Mathematics in the Sciences"
- Referee: Discrete and Continuous Dynamical Systems B
- Reviewer: U Manchester

K. Kroy

- Member of the graduation grants committee of the University
- Study counselor for physics
- Scientific Member of the International Max Planck Research School "mathematics in the Sciences"
- Referee for Nature Commun., Proc. Natl. Acad. Sci. (USA), Phys. Rev. Lett., Phys. Rev. E, J. Chem. Phys., Biophysical Journal, Soft Matter, Physica A, J. Phys. Cond. Mat., and various funding organizations (e.g. DFG)

13.19 External Cooperations

Academic

- Universität Heidelberg
  Prof. Frauke Gräter
- University of Padova
  Dr. F. Baldovin, Prof. Dr. M. Baiesi
- Forschungszentrum Jülich
  Prof. Dr. R. Merkel, Dipl. E. Jaschinski
- University of Minnesota, USA
  Prof. Dr. David C. Morse
- Ben-Gurion University of the Negev, Israel
  H. Yizhaq, I. Katra, H. Tsoar
- Université de Rennes, France
  A. Valance
- Joint Institute for Nuclear Research, Dubna, Russia
  Prof. Dr. N. M. Plakida

13.20 Awards

- BuildMoNa award for outstanding scientific results (2015), 3rd prize,
  J. T. Bullerjahn
  Leipzig School of Natural Sciences "Building with molecules and nano-objects"
- EPL Poster Awards of the DPG Biological Physics Division (2015), 1st prize,
  J. T. Bullerjahn
  DPG biological physics division

13.21 Publications

Journals

K. Kroy, E. Frey, "Focus on soft mesoscopics: physics for biology at a mesoscopic scale", New Journal of Physics **17** (11), 110203, 2015

J. Zhou *et al.*: "Mechanism of Focal Adhesion Kinase Mechanosensing", PLoS Comput Biol, **11**, 1-16, 2015

N. Fricke *et al.*: "Polymers in disordered environments", Diffusion Fundamentals, **23**, 7, 2015

R. Schachoff *et al.*:"Hot Brownian motion and photophoretic self-propulsion", diffusion-fundamentals.org, **23** (1), 1-19, 2015

M. Gralka, K. Kroy: "Inelastic mechanics: A unifying principle in biomechanics", Biochimica et Biophysica Acta (BBA)-Molecular Cell Research **1853** (11), 3025-3037, 2015

A. A. Vladimirov, D. Ihle, N. M. Plakida: "Magnetic order in the two-dimensional compass-Heisenberg model", Eur. Phys. J. B **88**, 148, 2015

P. Müller, J. Richter, A. Hauser, D. Ihle: "Thermodynamics of the frustrated J_1-J_2 Heisenberg ferromagnet on the body-centered cubic lattice with arbitrary spin, Eur. Phys. J. B **88**, 159, 2015

Preprints

G. Falasco, F. Baldovin, K. Kroy and M. Baiesi: "Mesoscopic virial equation for nonequilibrium statistical mechanics", arXiv:1512.01687

G. Falasco, K. Kroy: "Non-isothermal fluctuating hydrodynamics and Brownian motion", arXiv:1503.04025

G. Falasco, M. Baiesi: "Temperature response in nonequilibrium stochastic systems", arXiv:1509.03139

G. Falasco, M. Baiesi: "Inflow rate, a time-symmetric observable obeying fluctuation relations", arXiv:1506.07286

G. Falasco *et al.*: "Energy repartition for a harmonic chain with local reservoirs", arXiv:1505.05088

R. Kürsten, U. Behn: "Patchwork Sampling of Stochastic Differential Equations", arXiv:1510.00597, to appear in: Phys. Rev. E **93**, 033307, 2016

R. Kürsten: "Comment on 'Anomalous diffusion induced by enhancement of memory"', arXiv:1503.03302

R. Kürsten: "Random Recursive Trees and the Elephant Random Walk", arXiv:1512.05275, to appear in Phys. Rev. E 93, 032111, 2016

Talks

U. Behn: *Komplexe Systeme: Das Netzwerk-Paradigma*, Physik am Samstag, Leipzig, January 10, 2015

K. Kroy: *Coarse-graining non-isothermal complex fluids*, CECAM-Workshop Saragossa, May 20-22, 2015

K. Kroy: *Hot Brownian Motion*, 8th International Conference Engineering of Chemical Complexity, Garching, June 22-26, 2015

K. Kroy: *Hot Brownian Motion*, Diffusion Fundamentals, Dresden, August 24-27 2015

K. Kroy: *Thermophoretic Swimmers*, School on Microswimmers, Jülich, September 21-25, 2015

K. Kroy: *Hot Brownian Motion*, Theory Seminar, Göteborg, October 15, 2015

K. Kroy: *Warum ist die Wüste nicht flach. Die Physik der Wanderdünen*, Wissenschaft für Jedermann, Deutsches Museum in München, November 11, 2015

K. Kroy: *Inelastic Biomechanics*, SFB Seminar, Universität des Saarlandes, November 17, 2015

M. Lämmel: *Aeolian sand sorting and megaripple formation*, 79. DPG annual conference, Berlin, March 15-20th 2015

S. Auschra: *Mutual Stabilization of Barchan Dunes*, 79. DPG annual conference, Berlin, March 15-20th 2015

R. Kürsten, U. Behn: *Simulating stochastic differential equations using truncated Markov chains*, 79. DPG annual conference, Berlin, March 15-20th 2015

G. Falasco "Non-isothermal Brownian motion", Italian National Conference on Condensed Matter Physics, Palermo, November 28 - October 2, 2015

Posters

J. T. Bullerjahn, S. Sturm, K. Kroy: *Theory of rapid force spectroscopy*, 79. DPG annual conference, Berlin, March 15-20th 2015

G. Falasco, K. Kroy "Non-isothermal Brownian motion", Italian National Conference on Statistical Physics and Complex Systems, Parma, June 29 - July 1, 2015

R. Kürsten: *Bernoulli bond percolation on random recursive trees*. 79. DPG annual conference, Berlin, March 15-20th 2015

R. Kürsten, U. Behn: *Optimal Bounds on Critical or Tricritical Points of Nonlinear Globally Coupled Systems with Additive Noise*, IMPRS Evaluation, MPI MIS, Leipzig, April 22, 2015

13.22 Graduations

Doctorate

- H. Schmidtchen
  Randomly Evolving Idiotypic Networks: Architecture, Statistical Properties, and Model Experiments
  February 6, 2015

Master

- T. Herpich
  Linear and nonlinear microrheology
  December 15, 2015
- F. Schramm
  Solutions of adhesive Biopolymers
  October 10, 2015

13.23 Guests

- Prof. Dr. L. Schimansky-Geier
  Humboldt-University Berlin
  January 16, 2015
- Dr. M. Polettini
  University of Luxembourg
  January 20, 2015
- Prof. Dr. D. Chakraborty
  IISER Mohali
- Prof. Dr. M. von Renesse
  University of Leipzig
- Dr. I. Goychuk
  University of Augsburg
  April 16, 2015
- Prof. Dr. C. Maes
  KU Leuven
  April 21, 2015
- Dr. F. Höfling
  Freie Universität Berlin
  April 23, 2015
- Prof. Dr. J. Kierfeld
  TU Dortmund
  May 13, 2015

DAAD Rise exchange students

- K. Dzikovski
  Lancaster University
  June 15 - August 21, 2015
- A. Abdullahi
  University College London
  July 16 - September 9, 2015

14

Theory of Elementary Particles

14.1 Introduction

Our group is interested in the properties of matter at very high energies (small scales) or under other extreme conditions, covering a broad variety of research topics ranging from the study of elementary particles and their properties to the study of quantized matter fields in the presence of strong gravitational fields. The underlying theme of our research and teaching activity is the theory of such quantized fields in its various manifestations, and applications, including:

1. Quantum fields on discrete spacetimes (lattices) and their numerical and theoretical study
2. Quantum fields on curved spacetimes
3. Applications of ideas from integrable systems to the study of quantum gauge theories
4. Dualities and relation with classical General Relativity

Quantum field theories on lattices are discretized counterparts of continuum models describing elementary particles in quantum field theoretic models such as the standard model of particle physics. They were introduced in order to investigate certain non-perturbative features of these models in a controlled approximation. A substantial fraction of the current work being done in this area are numerical simulations and the development of new theoretical methods leading to improved numerical schemes. Our group is participating in this endeavor.

Quantum gauge theories such as the standard model can also be treated as continuum field theories, and can thereby be studied using for instance by perturbative methods. The task of finding improved ways of handling perturbative calculations is an important aspect of quantum field theory and is actively pursued in our group from a variety of different viewpoints, including operator product expansion techniques, methods from integrability, renormalization group methods, holographic ideas, and more.

We also pursue the quest to generalize quantum field theory to curved spacetime (QFTCS), which is inspired by the ideas and principles of General Relativity. On account

of its classical treatment of the metric, QFTCS cannot be a fundamental theory of nature. However, QFTCS is expected to provide an accurate description of quantum phenomena in a regime where the effects of curved spacetime may be significant, but effects of quantum gravity itself may be neglected. In particular, it is expected that QFTCS should be applicable to the description of quantum phenomena occurring in the early universe and near (and inside of) black holes, provided that one does not attempt to describe phenomena occurring so near to singularities that curvatures reach Planckian scales and the quantum nature of the spacetime metric would have to be taken into account. Quantum field theory in curved spacetimes has provided important physical insights into the quantum nature of black holes, indicating that they should, if left alone, gradually evaporate due to the emission of quanta whose energies are distributed thermally at the famous Hawking temperature.

In parallel to direct approaches to quantum field theory via perturbative, or numerical, techniques, there are now also more indirect approaches via so-called "holographic dualities". Such dualities typically establish a connection with a quantum field theory living on some sort of boundary of a space and a classical, gravitational, theory living in the higher dimensional space itself. This type of duality is believed to probe rather different regimes of quantum field theory (strong coupling, "large N"), and is hence complementary to other methods. At the technical level, it motivates studies into higher dimensional gravity theories, which turn out to have a rather rich mathematical structure. The study of such structures is another research topic in our group.

More information may be found on the group's webpages, www.uni-leipzig.de/~tet

Group Leader: Prof. S. Hollands

14.2 Stability of higher dimensional black holes

S. Hollands

Black holes are a key feature of Einstein's theory of General Relativity, as well as cousins of this theory in higher dimensions or with a more elaborate field content inspired by holographic ideas. A central question is the stability of such objects under perturbations. For the Schwarzschild and Kerr-spacetimes in four spacetime dimension, this question appears more or less settled, but remains wide open e.g. in higher dimensions, or as soon as more elaborate field content is considered. In a work with Wald [1], we have established a novel method that makes use of ideas from black hole thermodynamic. We have applied these ideas to a variety of interesting situations, most recently for a thorough investigation of so-called "super-radiant" instabilities of fast rotating black holes in AdS-type spacetimes [2]. Such investigations are of interest in their own right as well as for holographic descriptions of field theories within the gauge-gravity duality.

[1] S. Hollands and R. M. Wald, "Stability of Black Holes and Black Branes," Commun. Math. Phys. **321** (2013) 629 [arXiv:1201.0463 [gr-qc]].

[2] S. R. Green, S. Hollands, A. Ishibashi and R. M. Wald, "Superradiant instabilities of asymptotically anti-de Sitter black holes," Class. Quant. Grav. **33**, no. 12, 125022 (2016) doi:10.1088/0264-9381/33/12/125022 [arXiv:1512.02644 [gr-qc]].

14.3 Operator product expansions in quantum field theory

S. Hollands, J.W. Holland, M.B. Fröb, Y. Honma

All quantum field theories with well-behaved ultra violet behavior are believed to have an operator product expansion (OPE) [1]. This means that the product of any two local fields located at nearby points x and y in spacetime can be expanded in the form

$$O_A(x)O_B(y) \sim \sum_C C_{AB}^C(x-y)\, O_C(y), \tag{14.1}$$

where A, B, C are labels for the various local fields in the given theory (incorporating also their tensor character/spin), and where C_{AB}^C are certain numerical coefficient functions—or rather distributions—that depend on the theory under consideration, the coupling constants, etc. The sign "$\sim$" indicates that this can be understood as an asymptotic expansion: If the sum on the right side is carried out to a sufficiently large but finite order, then the remainder goes to zero fast as $x \to y$ in the sense of operator insertions into a quantum state, or into a correlation function. The operator product expansion is on the one hand an important tool for calculations in asymptotically free quantum field theories (such as Quantum Chromo Dynamics, QCD). At a conceptual level, the OPE may be viewed as a kind of algebraic skeleton of quantum field theory, and its understanding may shed some light on fundamental open questions in this theory. Our work has been directed in the following directions:

1. Algebraic aspects of the expansion ("associativity", "crossing symmetry")
2. Recursive procedures for calculating the OPE coefficients in perturbation theory, functional equations for the OPE coefficients.
3. Ways to construct the OPE beyond perturbation theory.
4. Understanding the role of gauge invariance with in the OPE in non-abelian gauge theories.

This is a longer term research project funded by an ERC grant.

[1] K. G. Wilson and W. Zimmermann, "Operator product expansions and composite field operators in the general framework of quantum field theory," Commun. Math. Phys. **24**, 87 (1972).
[2] M. B. Fröb and J. Holland, "All-order existence of and recursion relations for the operator product expansion in Yang-Mills theory," arXiv:1603.08012 [math-ph].
[3] J. Holland and S. Hollands, "Associativity of the operator product expansion," J. Math. Phys. **56**, no. 12, 122303 (2015). doi:10.1063/1.4937811
[4] S. Hollands and C. Kopper, "The operator product expansion converges in massless φ_4^4 theory," Commun. Math. Phys. **313** (2012) 257 [arXiv:1411.1785 [hep-th]].
[5] J. Holland and S. Hollands, "Recursive construction of operator product expansion coefficients," arXiv:1401.3144 [math-ph].
[6] J. Holland and S. Hollands, "A small cosmological constant due to non-perturbative quantum effects," Class. Quant. Grav. **31** (2014) 125006 [arXiv:1305.5191 [gr-qc]].

14.4 Orthogonal and symplectic Yangians

R. Kirschner, A.P. Isaev, D. Karakhanyan

We have studied Yang-Baxter relations with symmetry based on orthogonal and symplectic Lie algebras, in particular the RLL relations involving the fundamental R-matrix. The generators of the related Yangian algebra are obtained from the expansion of the L-operator in inverse powers of the spectral parameter. In the case when this expansion is truncated the involved algebra generators have to obey additional conditions which can be fulfilled in distinguished representations only. The spinor representation in the orthogonal case and the metaplectic representation in the symplectic case allow L-operators with only one non-trivial term in the expansion. The generator matrix obeys a quadratic relation. Second order L-operators can be constructed for Jordan-Schwinger type representations. The generator matrix obeys a cubic relation. The Yangian algebra concept provides a deeper understanding of the classical results [1–3]. Our work continues recent work [4].

[1] A.B. Zamolodchikov and Al.B. Zamolodchikov, "Factorized S Matrices in Two-Dimensions as the Exact Solutions of Certain Relativistic Quantum Field Models," Annals Phys. **120** (1979) 253.
[2] B. Berg, M. Karowski, P. Weisz and V. Kurak, "Factorized U(n) Symmetric s Matrices in Two-Dimensions," Nucl. Phys. B **134** (1978) 125.
[3] N.Yu. Reshetikhin, Integrable models of quantum one-dimensional models with $O(n)$ and $Sp(2k)$ symmetry, Theor. Math. Fiz. **63** (1985) 347-366.
[4] D. Chicherin, S. Derkachov and A. P. Isaev, "The spinorial R-matrix," J. Phys. A **46** (2013) 485201. arXiv:1303.4929 [math-ph].

14.5 Entanglement entropy of quantum fields

K. Sanders, S. Hollands

A typical state of a quantum field theory (QFT) may exhibit a lot of entanglement between spacelike separated regions. In Minkowski space this is due to the Reeh-Schlieder theorem, which has partial extensions to curved spacetimes [2]. In order to quantify the amount of entanglement of a state between two given regions, one may adopt the notion of entanglement entropy as used in quantum mechanics (QM). Computing entanglement entropies is difficult, even for free fields [3], but the results show some interesting features. E.g., when space is divided into two regions by a boundary surface S, the entanglement entropy of the vacuum is divergent and the coefficient of the leading divergent order is proportional to the area of S ("area law").

Unfortunately, the existing computations have a number of drawbacks: they often only work for ground states (using path integrals), and they introduce regulators and subtle computational tricks whose physical meaning is unclear (e.g. the replica method). In this project we endeavour to provide an alternative approach to entanglement entropy, with a better physical motivation, and compare with the existing results. We focus on the following questions:

- The definition of entanglement entropy in terms of density matrices, familiar from QM, requires modification, due to the existence of inequivalent Hilbert space representations in QFT. For this reason we resort to the relative entropy of Araki [1], leading to a well-defined entanglement entropy in a very general setting, taking values in $[0, \infty]$.

- For two quasi-free states in QM, we obtained an explicit formula for their relative entropy, relying heavily on literature from quantum information theory [4]. This general result allows us to find upper and lower bounds for entanglement entropies.

- For quasi-free states of a free scalar QFT, we expect to find their relative entropy as a generalisation of the formula from QM, and the upper and lower bounds should generalise as well.

- In simple explicit cases, such as the Minkowski vacuum and spacelike separated regions with sufficiently simple geometry, it may be possible to evaluate or approximate the bounds on the entanglement entropy. This allows for a comparison of computational methods and results with the existing literature (e.g. the area law).

[1] H. Araki, Publ. Res. Inst. Math. Sci. **11** (1975/76), 809–833
[2] K. Sanders, Commun. Math. Phys. **288** (2009), no.1, 271–285
[3] S.N. Solodukhin, Living Rev. Relativity **14** (2011), no.8
[4] C. Weedbrook, S. Pirandola, R. García-Patrón, N.J. Cerf, T.C. Ralph, J.H. Shapiro and S. Lloyd, Rev. Mod. Phys. **84** (2012), no.2, 621–669

14.6 Modular nuclearity in curved spacetimes

K. Sanders, G. Lechner

Nuclearity conditions were introduced in quantum field theory by [1], and modular nuclearity, which makes use of Tomita-Takesaki theory, has recently played an important role in certain integrable interacting algebraic QFTs in two dimensional Minkowski space [2]. Although conditions of this sort are physically desirable, mathematically useful, and expected to hold quite generally, they have only been verified in very few cases, even for free fields.

The general formulation of a nuclearity condition requires a reference Hilbert space (obtained from a reference state), a (bounded) region of spacetime, and an operator representing the energy. For free scalar fields, the condition has been verified e.g.

- For the Hamilton operator in the ground state on an ultrastatic spacetime, using localisation in arbitrary bounded regions [3].

- For the modular operator of a wedge region in the Minkowski vacuum, using localisation in any smaller wedge region [2].

In this project we have exploited modular operators to formulate a modular nuclearity condition for generally covariant quantum field theories, formulated in terms of C^*-algebras. At this level of generality we have established that this condition is preserved under pull-backs and under mixing of states, and that it behaves well under space-time deformations. For free scalar fields (with arbitrary potential energy functions, including all masses and scalar curvature couplings) we were able to verify this condition for all quasi-free Hadamard states, both at the one-particle and at the second quantised levels, making use of results of Verch [4].

[1] D. Buchholz and E. Wichmann, Commun. Math. Phys. **106** (1986), no.2, 321–344
[2] D. Buchholz and G. Lechner, Ann. Henri Poincaré **5** (2004), no.6, 1065–1080
[3] R. Verch, Lett. Math. Phys. **29** (1993), no.4, 297–310
[4] R. Verch, Commun. Math. Phys. **160** (1994), no.3, 507–536

14.7 Categories and space-time

K. Sanders

The classical concept of space-time is generally believed to be an approximation, which should arise as an emergent concept in theories of quantum gravity. In order to understand what requirements this imposes on quantum gravity theories, it is necessary to have a good understanding of the classical structure of space-time.

The most advanced in which space-time is treated classically are quantum field theories (QFTs) in curved space-times. Such theories can be discussed in the language of locally covariant QFT (LCQFT), which provides a general, precise and flexible framework [1]. A key aspect of this language is its use of category theory to implement locality and general covariance in a unified way.

In this project we review an interpretation of the categorical language used in LCQFT [3], linking it to modal logic and to an implicit notion of space-time. We consider the importance of the categorical language for the studies of Fewster and Verch on doing the "same physics in all space-times" [2], and we consider its repercussions for the notion of space-time in general and for theories of quantum gravity.

[1] R. Brunetti, K. Fredenhagen and R. Verch, Commun. Math. Phys. **237**, 31–68 (2003)
[2] C. Fewster and R. Verch, Ann. Henri Poincaré **13** (2012), 1613–1674
[3] K. Sanders, PhD Thesis, University of York (2009), arXiv:0809.4828v1 [math-ph]

14.8 Local vs. global temperature

K. Sanders

A state of a quantum field theory can be said to be in thermodynamic equilibrium when it satisfies the KMS-condition [1]. This condition is motivated by strong analogies to quantum statistical mechanics, but it has some drawbacks. In general curved

space-times, the analogies used are questionable (see e.g. [3] for the case of accelerated observers). Furthermore, the KMS condition is a global condition, and its relation to a locally measured temperature is unclear.

For a massless free scalar field, a mathematical model of a local thermometer was proposed in [2]. The local temperature is defined in terms of the expectation value of a generally covariant Wick square, assuming that this expectation value is non-negative. This definition is local, generally covariant and reduces to global temperature for KMS states in Minkowski space. However, its usefulness in general curved space-times is unclear, because the local temperature may be ill-defined even for many KMS states in stationary space-times. One known cause for this lies in the acceleration of the stationary observers.

In this project we compare the global and local definitions of temperature. We will show that the local temperature can also be ill-defined for ground states in ultra-static space-times, when the space-time violates the weak energy condition. However, in ultra-static space-times with non-negative scalar curvature, compact Cauchy surface, and minor other conditions, we will show that the local temperature is well-defined for all stationary states in any flat region. Furthermore, when both local and global temperature are well-defined, we show that both notions give qualitatively similar behaviour.

[1] O. Bratteli and D.W. Robinson, "Operator Algebras and Quantum Statistical Mechanics 2," Springer, Berlin (1997)
[2] D. Buchholz and J. Schlemmer, Class. Quantum Grav. **24**, F25–F31 (2007)
[3] J. Earman, Stud. Hist. Philos. Sci. B Stud. Hist. Philos. Mod. Phys. **42** (2011), no.2, 81–97
[4] R. Schoen and S.-T. Yau, Phys. Rev. Lett. **42**, 547–548 (1979)
[5] R. Schoen, J. Differential Geom. **20** (1984), no.2, 479–495

14.9 Applications of numerical stochastic perturbation theory to lattice QCD

H. Perlt, A. Schiller

In collaboration with authors from different locations we have continued our research program using numerical stochastic perturbation theory (NSPT).

It is well known that lattice perturbation theory (LPT) is much more involved compared to its continuum QCD counterpart. The complexity of diagrammatic approaches increases rapidly beyond the one-loop approximation. By now only a limited number of results up to two-loop accuracy have been obtained.

Applying the standard Langevin dynamics [1, 2] to the problem of weak coupling expansions for lattice QCD, a powerful numerical approach for higher loop calculations – called numerical stochastic perturbation theory (NSPT) – has been proposed in [3].

With colleagues from the QCDSF collaboration we have calculated Wilson loops of various sizes up to 20 loops in SU(3) pure lattice gauge theory at different lattice sizes for Wilson gauge action using the technique of numerical stochastic perturbation

theory [4]. This allowed us to investigate the perturbative series for various Wilson loops at high loop orders. In we have calculated [5] the SU(3) beta function from Wilson loops to 20th order numerical stochastic perturbation theory. An attempt has been made to include massless fermions, whose contribution is known analytically to 4th order. The question whether the theory admits an infrared stable fixed point is addressed.

The subtraction of hypercubic lattice corrections, calculated at one-loop order in lattice perturbation theory, is common practice, e.g., for determinations of renormalization constants in lattice hadron physics (see the next project). One may overcome the limitation to one-loop and calculate hypercubic corrections for any operator and action beyond the one-loop order using Numerical Stochastic Perturbation Theory (NSPT). Together with colleagues from Regensburg and Dubna we started [6] a first check whether NSPT can by used to subtract hypercubic lattice corrections and provide (in a parametrization valid for arbitrary lattice couplings) the lattice corrections up to three-loop order for the SU(3) gluon and ghost propagators in Landau gauge. In [7] we explored the practicability of such an approach to operators including fermions and considered, as a first test, the case of Wilson fermion bilinear operators in a quenched theory. Our results allow us to compare boosted and unboosted perturbative corrections up to three-loop order.

[1] G. Parisi and Y. s. Wu, Sci. Sin. **24** (1981) 483.
[2] G. G. Batrouni, G. R. Katz, A. S. Kronfeld, G. P. Lepage, B. Svetitsky and K. G. Wilson, Phys. Rev. D **32** (1985) 2736.
[3] F. Di Renzo, E. Onofri, G. Marchesini and P. Marenzoni, Nucl. Phys. B **426** (1994) 675 [arXiv:hep-lat/9405019].
[4] R. Horsley, G. Hotzel, E.-M. Ilgenfritz, R. Millo, Y. Nakamura, H. Perlt, P. E. L. Rakow, G. Schierholz and A. Schiller, Phys. Rev. D **86** (2012) 054502 [arXiv:1205.1659 [hep-lat]].
[5] R. Horsley, H. Perlt, P. E. L. Rakow, G. Schierholz and A. Schiller, Phys. Lett. B **728** (2014) 1 [arXiv:1309.4311 [hep-lat]].
[6] J. Simeth, A. Sternbeck, E. -M. Ilgenfritz, H. Perlt and A. Schiller, PoS LATTICE **2013** (2014) 459 [arXiv:1311.1934 [hep-lat]].
[7] J. Simeth, A. Sternbeck, M. Göckeler, H. Perlt and A. Schiller, arXiv:1501.06322 [hep-lat].

14.10 Aspects in the determination of renormalization constants on the lattice

H. Perlt, A. Schiller

Renormalization factors in lattice Quantum Chromodynamics (QCD) relate observables computed on finite lattices to their continuum counterparts in specific renormalization schemes. Therefore, their determination should be as precise as possible in order to allow for a reliable comparison with experimental results. One approach is based on lattice perturbation theory [1]. However, it suffers from its intrinsic complexity, slow

convergence and the impossibility to handle mixing with lower-dimensional operators. Therefore, nonperturbative methods have been developed and applied. Among them the so-called regularization-invariant momentum (RI-MOM) scheme [2] is widely used because of its simple implementation.

Like (almost) all quantities evaluated in lattice QCD also renormalization factors suffer from discretization effects. One can attempt to cope with these lattice artifacts by extrapolating the nonperturbative scale dependence to the continuum (see Ref. [3]) or one can try to suppress them by a subtraction procedure based on perturbation theory. Here we were dealing with the latter approach.

In a recent paper of the QCDSF/UKQCD collaboration [4] a comprehensive discussion and comparison of perturbative and nonperturbative renormalization have been given. Particular emphasis was placed on the perturbative subtraction of the unavoidable lattice artifacts. For the simplest operators and lattice actions this can be done with reasonable effort in one-loop order completely by computing the corresponding diagrams for finite lattice spacing numerically. An alternative approach can be based on the subtraction of one-loop terms of order a^2 with a being the lattice spacing. The computation of those terms has been developed by the Cyprus group [6] and applied to various operators for different actions.

In collaboration with colleagues from QCDSF and Cyprus university we have used in works [7] and [8] some of those results for the analysis of lattice Monte Carlo data of the QCDSF collaboration to determine as precisely as possible the renormalization constants in the so-called renormalization group invariant (RGI) scheme Z^{RGI}.

A novel method for nonperturbative renormalization of lattice nonsinglet as well as singlet operators has been introduced by our lattice collaboration [9], which is based on the Feynman-Hellmann relation (for more details see [10]). The Feynman-Hellmann technique offers a promising alternative for calculations of quark line disconnected contributions to hadronic matrix elements. The method involves computing two-point correlators in the presence of generalized background fields arising from introducing additional operators into the action. As a first application, and test of the method, we computed the renormalization factors of the axial vector current and the scalar densityfor both nonsinglet and singlet operators for three quark flavors of SLiNC fermions. For nonsinglet operators, where a meaningful comparison is possible, perfect agreement with recent calculations using standard three-point function techniques has been found.

[1] S. Capitani, Phys. Rept. **382** (2003) 113 [arXiv:hep-lat/0211036]
[2] G. Martinelli, C. Pittori, C. T. Sachrajda, M. Testa and A. Vladikas, Nucl. Phys. B **445** (1995) 81 [arXiv:hep-lat/9411010]
[3] R. Arthur and P. A. Boyle (RBC and UKQCD Collaborations), Phys. Rev. D **83** (2011) 114511 [arXiv:1006.0422 [hep-lat]].
[4] M. Göckeler, R. Horsley, Y. Nakamura, H. Perlt, D. Pleiter, P. E. L. Rakow, A. Schäfer, G. Schierholz, A. Schiller, H. Stüben and J. M. Zanotti, (QCDSF/UKQCD Collaboration) Phys. Rev. D **82** (2010) 114511 [Erratum-ibid. D **86** (2012) 099903] [arXiv:1003.5756 [hep-lat]].
[5] M. Göckeler, R. Horsley, E.-M. Ilgenfritz, H. Perlt, P. E. L. Rakow, G. Schierholz and A. Schiller, Phys. Rev. D **54** (1996) 5705 [arXiv:hep-lat/9602029].

[6] M. Constantinou, V. Lubicz, H. Panagopoulos and F. Stylianou, JHEP **0910** (2009) 064 [arXiv:0907.0381 [hep-lat]].
[7] M. Constantinou, M. Costa, M. Göckeler, R. Horsley, H. Panagopoulos, H. Perlt, P. E. L. Rakow, G. Schierholz and A. Schiller, Phys. Rev. D **87** (2013) 9, 096019 [arXiv:1303.6776 [hep-lat]].
[8] M. Constantinou, R. Horsley, H. Panagopoulos, H. Perlt, P. E. L. Rakow, G. Schierholz, A. Schiller and J. M. Zanotti, Phys. Rev. D **91** (2015) 1, 014502 [arXiv:1408.6047 [hep-lat]].
[9] A. J. Chambers *et al.* [QCDSF Collaboration], Phys. Lett. B **740** (2015) 30 [arXiv:1410.3078 [hep-lat]].
[10] A. J. Chambers *et al.* [CSSM and QCDSF/UKQCD Collaborations], Phys. Rev. D **90** (2014) 1, 014510 [arXiv:1405.3019 [hep-lat]].

14.11 Fuzzy extra dimensions in $\mathcal{N} = 4$ super Yang-Mills theory and matrix models

H. Steinacker*, J. Zahn

*Faculty of Physics, University of Vienna, Austria

The maximally supersymmetric $\mathcal{N} = 4$ $SU(N)$ super-Yang-Mills theory takes a special role among all 4-dimensional quantum field theories. It is arguably the most symmetric 4-dimensional gauge theory, it is perturbatively finite, and much research effort has been devoted in recent years to study various aspects of this model. Its 6 scalar fields are $N \times N$ matrix valued, and non-trivial configurations of these can be interpreted as fuzzy geometries embedded in $\mathbb{R}^6$ (with the eigenvalues of the matrices indicating the embedding coordinates). Such non-trivial vacua can be obtained by adding soft supersymmetry breaking terms to the potential. In particular, it is well-known that fuzzy spheres S^2_N [1] can arise in this way. These can be understood as quantized coadjoint orbits of $SU(2)$, i.e., quantized spheres S^2.

In our project [2], we found a new type of solutions, which can geometrically be understood as projections of quantized coadjoint orbits of $SU(3)$. These coadjoint orbits would naturally be embedded in $\mathbb{R}^8$, but the projection to $\mathbb{R}^6$ leads to singularities and self-intersections. This is illustrated in Figure 14.1 for one such coadjoint orbit, the projective space $\mathbb{C}P^2$.

We confirmed that our new solutions are stable in the sense that the spectrum of perturbations does not contain imaginary frequency modes. On the other hand, there are fermionic zero modes which link sheets with opposite orientation and carry a definite chirality. This may pave the way to constructing more realistic (chiral) models out of the highly symmetric $\mathcal{N} = 4$ super-Yang-Mills theory. Also the fact that the fermionic zero modes naturally organize in a $\mathbb{Z}_3$ family structure is reminiscent of the standard model.

[1] J. Madore, "The Fuzzy sphere," Class. Quant. Grav. **9**, 69 (1992).

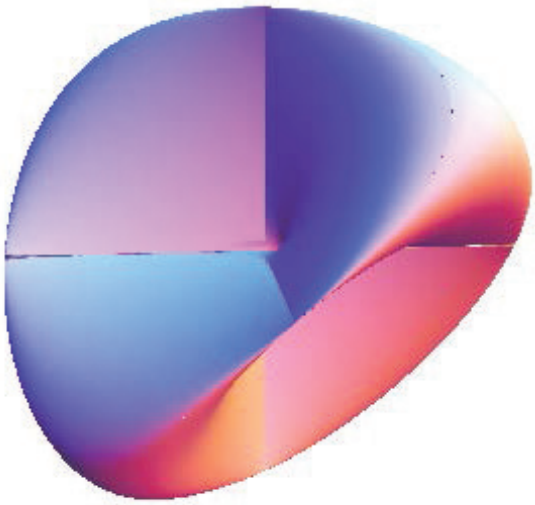

Figure 14.1: Three-dimensional section through the projected $\mathbb{C}P^2$.

[2] H. C. Steinacker and J. Zahn, "Self-intersecting fuzzy extra dimensions from squashed coadjoint orbits in $\mathcal{N} = 4$ SYM and matrix models," JHEP **1502**, 027 (2015).

14.12 Quantum electrodynamics in external potentials

J. Zahn

Quantum electrodynamics in external potentials (QEDext) has received increasing interest in recent years, triggered in particular by the envisioned high intensity laser sources, c.f. [1] for a review. These may allow to experimentally study the creation of electron-positron pairs in strong external fields, the so-called Schwinger effect. As this is a non-perturbative effect, this opens the exciting possibility to experimentally probe quantum field theory in such a regime. On the other hand, the effect depends highly non-linearly on the external potential, so for interpretations of the experiments it is important to have reliable theoretical and computational tools at disposal.

The theory of quantum fields on curved spacetimes (QFTCS) has much in common with QEDext: For generic external potentials, tools such as Wick rotation or Fourier transformation, which are heavily exploited in quantum field theory on Minkowski space, are not available. QFTCS has witnessed tremendous progress during the last two decades, c.f. the review [2], so it is natural to revisit QEDext from this point of view. This already led to a new formula for the non-perturbative evaluation of vacuum polarization in static potentials [3] and of the vacuum current in time-dependent homogenous electric fields [4].

We plan to continue this line of research by further developing a method, already sketched in [4], to compute particle creation, i.e., the Schwinger effect, in time-dependent

external potentials. In contrast to other schemes, it is in principle applicable to generic external potentials. Due to a different treatment of the inherent renormalization ambiguities, the method also circumvents some difficulties that are present in other schemes.

[1] G.V. Dunne, *New Strong-Field QED Effects at ELI: Nonperturbative Vacuum Pair Production*, Eur. Phys. J. D55 (2009) 327.
[2] S. Hollands and R.M. Wald, *Quantum fields in curved spacetime*, Phys. Rept. 574 (2015) 1.
[3] J. Schlemmer and J. Zahn, *The current density in quantum electrodynamics in external potentials*, Annals Phys. 359 (2015) 31.
[4] J. Zahn, *The current density in quantum electrodynamics in time-dependent external potentials and the Schwinger effect*, J. Phys. A 48, no. 47 (2015) 475402.

14.13 Funding

ERC Starting Grant
Prof. S. Hollands
QC & C 259562

DFG Grant
Dr. A Schiller
SCHI 422/9-1

14.14 Organizational Duties

Prof. S. Hollands

- Group leader
- Group speaker
- Erasmus coordinator
- Kolloquium organizer
- Associate editor: General Relativity and Gravitation

Dr. A. Schiller

- Referee Phys. Rev. D
- Referee Europhysics Journal C

14.15 External Cooperations

Academic

- DESY Hamburg
  Prof. G. Schierholz (QCDSF collaboration)
- Edinburgh U., UK
  Dr. R. Horsley (QCDSF collaboration)

- Liverpool U., UK
  Dr. P.E.L. Rakow (QCDSF collaboration)
- Adelaide U., Australia
  Dr. J. Zanotti (QCDSF collaboration)
- Cyprus U. Nikosia
  Prof. H. Panagopoulos and collaborators
- Jena U.
  Dr. A. Sternbeck
- Dubna, Russia
  Dr. E.-M. Ilgenfritz
- U. Chicago, USA
  Prof. R. M. Wald
- Kinki U., Japan
  Prof. A. Ishibashi
- Perimeter Institute, Canada
  Dr. S. Greene
- Grenoble U., France
  Dr. M. Wrochna
- Vienna U., Austria
  Dr. J. Schlemmer, Dr. H. Steinacker
- Dubna, Russia
  Prof. A. Isaev (Heisenberg-Landau grant)
- St. Petersburg, Steklov Inst., Russia
  Dr. S.E Derkachov
- Yerevan Phys. Inst., Armenia
  Dr. D. Karakhanyan
- Heriot-Watt U. Edinburgh, UK
  Dr. A. Schenkel
- CBPF Rio de Janeiro, Brazil
  Prof. M. Casals

14.16 Publications

Journals

S. Hollands and A. Thorne, "Bondi mass cannot become negative in higher dimensions," Commun. Math. Phys. **333**, no. 2, 1037 (2015).

S. Hollands and R. M. Wald, "Quantum fields in curved spacetime," Phys. Rept. **574**, 1 (2015).

J. Holland and S. Hollands, "Recursive construction of operator product expansion coefficients," Commun. Math. Phys. **336**, no. 3, 1555 (2015).

S. Hollands and A. Ishibashi, "Instabilities of extremal rotating black holes in higher dimensions," Commun. Math. Phys. **339**, no. 3, 949 (2015).

J. Holland and S. Hollands, "Associativity of the operator product expansion," J. Math. Phys. **56**, no. 12, 122303 (2015).

K. Sanders, "On the construction of Hartle-Hawking-Israel states across a static bifurcate Killing horizon," Lett. Math. Phys. **105**, no. 4, 575 (2015).

M. B. Fröb and E. Verdaguer, "Quantum corrections to the gravitational potentials of a point source due to conformal fields in de Sitter," JCAP **1603**, no. 03, 015 (2016).

A. Di Dato and M. B. Fröb, "Mapping AdS to dS spaces and back," Phys. Rev. D **91**, no. 6, 064028 (2015).

M. Constantinou, R. Horsley, H. Panagopoulos, H. Perlt, P. E. L. Rakow, G. Schierholz, A. Schiller and J. M. Zanotti, "Renormalization of local quark-bilinear operators for N_f=3 flavors of stout link nonperturbative clover fermions," Phys. Rev. D **91**, no. 1, 014502 (2015).

A. J. Chambers *et al.* [QCDSF Collaboration], "A novel approach to nonperturbative renormalization of singlet and nonsinglet lattice operators," Phys. Lett. B **740**, 30 (2015).

R. Horsley *et al.*, "Lattice determination of Sigma-Lambda mixing," Phys. Rev. D **91**, no. 7, 074512 (2015).

F.-K. Guo *et al.*, "The electric dipole moment of the neutron from 2+1 flavor lattice QCD," Phys. Rev. Lett. **115**, no. 6, 062001 (2015).

A. J. Chambers *et al.*, "Disconnected contributions to the spin of the nucleon," Phys. Rev. D **92**, no. 11, 114517 (2015).

J. Zahn, "The current density in quantum electrodynamics in time-dependent external potentials and the Schwinger effect," J. Phys. A **48**, no. 47, 475402 (2015).

J. Schlemmer and J. Zahn, "The current density in quantum electrodynamics in external potentials," Annals Phys. **359**, 31 (2015).

H. C. Steinacker and J. Zahn, "Self-intersecting fuzzy extra dimensions from squashed coadjoint orbits in $\mathcal{N}$ = 4 SYM and matrix models," JHEP **1502**, 027 (2015).

J. Zahn, "Locally covariant charged fields and background independence," Rev. Math. Phys. **27**, no. 07, 1550017 (2015)

in press

S. R. Green, S. Hollands, A. Ishibashi and R. M. Wald, "Superradiant instabilities of asymptotically anti-de Sitter black holes," Class. Quant. Grav. **33**, no. 12, 125022 (2016).

J. Holland, S. Hollands and C. Kopper, "The operator product expansion converges in massless φ^4_4-theory," Commun. Math. Phys. **342**, no. 2, 385 (2016)

M. B. Fröb, A. Higuchi and W. C. C. Lima, "Mode-sum construction of the covariant graviton two-point function in the Poincaré patch of de Sitter space," Phys. Rev. D **93**, no. 12, 124006 (2016).

R. Horsley *et al.*, "QED effects in the pseudoscalar meson sector," JHEP **1604**, 093 (2016).

A. P. Isaev, D. Karakhanyan and R. Kirschner, "Orthogonal and symplectic Yangians and Yang–Baxter R-operators," Nucl. Phys. B **904**, 124 (2016).

Talks

For some talks of Prof. S. Hollands, see the TET group page
http://www.uni-leipzig.de/~tet/?page_id=551

J. Zahn, "Applications of local gauge covariance: Anomalies and QED in external potentials," invited talk at DPG Frühjahrstagung, Berlin, March 2015.

K. Sanders, "Hartle-Hawking-Israel states for radiating static black holes," seminar at Brazilian Center for Research in Physics (CBPF), Rio de Janeiro (BRA), February 2015.

K. Sanders, "Ground states for radiating static black holes," invited talk at the minisymposium"Algebraic QFT on Lorentzian manifolds", annual DMV meeting, Hamburg, September 2015.

K. Sanders, "Modular Nuclearity: a generally covariant perspective," invited talk at workshop "QFT: Infrared problems and constructive aspects", Munich, October 2015.

K. Sanders, "Modular Nuclearity: a generally covariant perspective," colloquium of Graduiertenkolleg 1493, Göttingen, December 2015.

D. Karakhanyan and R. Kirschner, "Yang-Baxter relations with orthogonal or symplectic symmetry," Contribution to the Prag workshop QSIS-23, June 2015.

14.17 Graduations

Bachelor

- Jonathan Wernersson
  A massless Klein-Gordon field minimally coupled with a static electric field on a finite interval in 1+1 dimensions
  June 4, 2015.

14.18 Guests

- Prof. Ralf Schützhold
  U Duisburg-Essen
  January 6, 2015.

- Prof. Hoger Gies
  U Jena
  January 27, 2015.
- Prof. Volker Bach
  TU Braunschweig
  February 3, 2015.
- Prof. Detlev Buchholz
  U Göttingen
  April 14, 2015.
- Prof. Klaus Fredenhagen
  U Hamburg
  May 5, 2015.
- Prof. Christoph Schweigert
  U Hamburg
  May 5, 2015.
- Dr. Michal Wrochna
  U Grenoble (France)
  June 1–3, 2015.
- Dr. Daniela Cadamuro
  U Bristol (UK)
  June 23, 2015.
- Prof. Nicola Pinamonti
  U Genova (Italy)
  June 21 – July 10, 2015.
- Dr. David Hilditch
  U Jena
  June 30, 2015.
- Prof. Dominik Schwarz
  U Bielefeld
  July 7, 2015.
- Dr. Alexander Schenkel
  Heriot-Watt U Edinburgh (UK)
  July 8–15, 2015.
- Dr. Norihiro Tanahashi
  U Cambridge (UK)
  October 18–20, 2015.
- Dr. Paul de Medeiros
  U Cardiff (UK)
  October 19–22, 2015.
- Prof. Stoytcho Yazadjiev
  U Sofia (Bulgaria)
  October 25–28, 2015.

- Dr. Stephen Green
  Perimeter Institute (Canada)
  December 7–11, 2015.
- Dr. Andree Lischewski
  HU Berlin
  December 14, 2015.
- Prof. Harvey Reall
  U Cambridge (UK)
  December 14–16, 2015.

Author Index

F

G

H

I

J

K

L

M

N

O

P

R

S

T

U

V

W

Y

Z

ISSN 0268-1242

Semiconductor Science and Technology

Volume 30 Number 2 February 2015

Special issue

Semiconductor functional oxides

Guest editors: Saskia F Fischer and Marius Grundmann

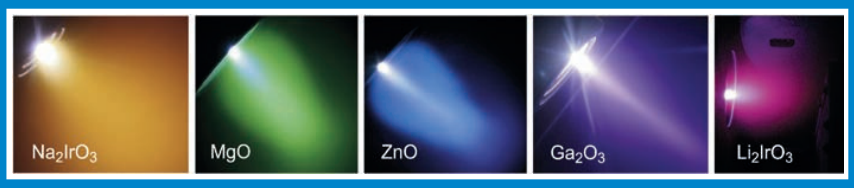

iopscience.org/sst

IOP Publishing

IOP Expanding Physics

Physics of Cancer

Claudia Tanja Mierke

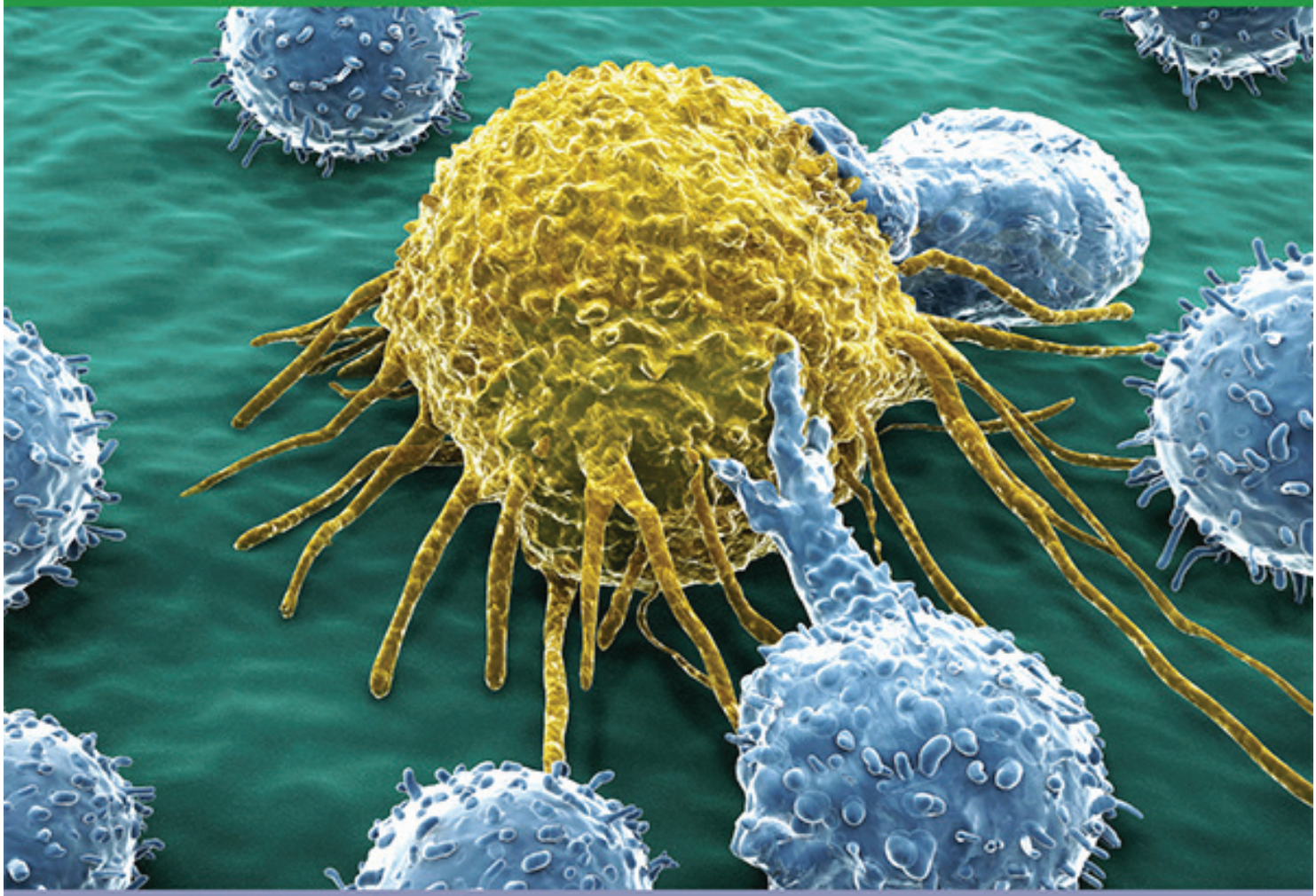

IOP | ebooks